

## Review

DOI: [10.55085/ads.2022.611](https://doi.org/10.55085/ads.2022.611)

### Periodontal Microsurgery: A Boon for Precision

Rituparna Dhir , Jayasheela M , Triveni MG , Manjunath Nandihalli Shetru 

Department of Periodontics, Bapuji Dental College and Hospital, Karnataka, India.

#### ABSTRACT

The surgical operating microscope increases illumination and visual acuity for the periodontist to perform clinical procedures with improved precision over conventional surgeries. Presently, using a surgical microscope gives an impression of being the best option which helps in better diagnostic ability and treatment quality. This review highlights the basics of periodontal plastic surgery, including the role of magnification and microsurgical instruments, knot tying, clinical applications, and microsurgical effects on aesthetics. This mini-literature review infers that improved visual acuity of microsurgery provides significant advantages of less patient discomfort, rapid healing, improved esthetics, and patient compliance. Periodontal microsurgery combined with minimally invasive surgical techniques benefits the ability of a clinician's precision in manipulating the tissues, thereby offering the simplest and the best probable outcome.

**Keywords:** Microsurgery, Magnification, Surgical Microscope, Illumination, Periodontal Surgery.

Received: 30 Nov 2021  
Revised: 10 Mar 2022  
Accepted: 14 Mar 2022  
Published: 10 Apr 2022

Academic Editor:

Gustavo Fernandes 

Correspondence: Rituparna Dhir,  
Department of Periodontics, Bapuji  
Dental College and Hospital, Karnataka,  
India.  
Email: [gustfernandes@gmail.com](mailto:gustfernandes@gmail.com)

Cite this article as: Dhir R, Jayasheela M, Triveni MG. Periodontal Microsurgery: A Boon for Precision. *Ann Dent Sci.* 2022;1:611. [\[https://doi.org/10.55085/ads.2022.611\]](https://doi.org/10.55085/ads.2022.611)

Copyright © 2022 Dhir R et al. This is an open access article distributed under the [Creative Commons Attribution 4.0 International License](https://creativecommons.org/licenses/by/4.0/), which permits unrestricted use, distribution, and reproduction in any medium, provided the original work is properly cited.

#### Authors' contributions

The participation of each author corresponds to the criteria of authorship and contributorship emphasized in the [Recommendations for the Conduct, Reporting, Editing, and Publication of Scholarly work in Medical Journals of the International Committee of Medical Journal Editors](https://www.sciencedirect.com/journal/annals-of-dental-sciences/policy). Indeed, all the authors have actively participated in the redaction, the revision of the manuscript, and provided approval for this final revised version.

#### Acknowledgments

None.

#### Funding

No funding was received from any organization to conduct the present study.

#### Conflict of interest

The authors declare that there is no conflict of interest regarding the publication of this article.

#### INTRODUCTION

The development in technology has improved our understanding of the etiopathogenesis, diagnosis, and treatment modality to perform a simple, minimally invasive surgical procedure to obtain better outcomes. Hence, the concept of microsurgery came into practice in 1993 in periodontics. Magnification achieved with loupes or surgical microscopes is widespread in medical and dental practice; however, its usage in periodontics needs to be broadened. This dilemmatic condition for its use in their daily practice may be because of a lack of didactic studies showing benefits or owing to a lack of familiarity with the surgical operating microscope [1]. The potential for treating periodontal tissues increases with the use of an operating microscope and microsurgical instruments by elevating the ability of a clinician to handle it. The success of surgical and non-surgical periodontal therapies, especially periodontal plastic surgeries and implant therapy, has been revolutionized by the use of magnification [2].

Microsurgery basically uses tools called the operating microscope or high-powered loupes, which aids in the precision technique outcome. At this juncture, the “criterion standard” of performing microsurgery is under the microscope, which is used diligently. Leknius and Geissberger have shown a direct relationship between magnification and significantly enhanced performance of technique-sensitive dental procedures. However, some published articles embrace the benefits of magnification. Hence, the present mini-review discussed the efficacy of surgical microscopes and microsurgical instruments for their clinical usage in managing periodontal diseases [2].

#### History of Evolution

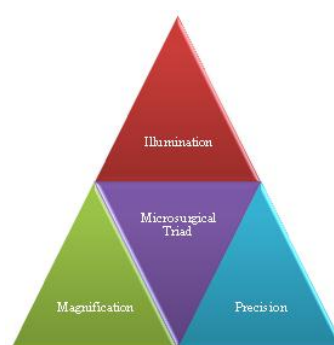
The evolution of magnification from a simple meniscus lens to the presently known operating microscope has been a long journey. Modern periodontology is linked to periodontal plastic surgery and esthetic dentistry. The timeline of evolution is shown in Table 1 [3,4].

#### Definition and Terminology

A surgical procedure performed under a microscope is called microsurgery. Broadly, it can be defined as “the surgery performed under the magnification provided by the operating microscope,” given by Daniel RK in 1979. As defined by Serafin in 1980, microsurgery is

**Table 1:** The timeline of evolution

SL. NO	YEAR	PROPOSED BY	FIELD
1.	2800	Egyptians	Simple glass meniscus
2.	19 <sup>TH</sup> century		Field of medicine
3.	1921	Carl Nylen	Microscope for operating ear surgery
4.	1950	Barraquer	Corneal surgery
5.	1960	Jacobsen Suarez	Microvascular anastomosis
6.	1964	Antonvan Leuwenhook	Compound microscope
7.	1978	Apothekar Jako	Dentistry
8.	1992	Carr	Endodontics
9.	1993	Shanelec Tibbets	Periodontics

**Figure 1:** Pictorial depiction of Microsurgical Triad.

a methodology that assures modification and refinement of existing surgical techniques using magnification to improve visualization, with applications to all specialties [3,4]. The working principle of the microscope used in dentistry is based on co-axial illumination [3,5]. Working of a surgical operating microscope is listed under the following headings- magnification, illumination, documentation, accessories [5,6].

### MAGNIFICATION

Magnification is determined by the power of the eyepiece, focal length of binoculars, magnification change factor, and focal length of the objective lens.

#### Magnification changer

The magnification changer is located in the head of the microscope. It is available in two forms, such as three or five steps manual changers or power zoom changers. (Figure 2 a) Magnification in the range of 2.5x to 30x is usually recommended [2,5]. The lower magnification (2.5x to 8x) is used for orientation to the surgical field and allows a wide field of view. Midrange magnification (10x to 16x) is used for operating. High range magnifications (20x to 30x) are used for observing fine detail. [6].

The equation for calculating total magnification [5]

$$MT = fT \times Me \times Mc$$

Where MT= total magnification, fT= focal length of the binocular tube, fO= focal length of the objective lens, Me= magnification of the eyepiece, Mc= magnification factor

#### Objective lens

It forms an image of the object processed by the magnification changer while projecting illumination from the light source onto the field of view (Figure 2 b). Ideally, an objective lens with a focal length of 200 to 250 mm should be used [2,5]. However, in periodontal surgery, a focal length of 200 to 300 mm can be used [6].

#### Binocular tube

The conventional binocular tube contains two inverting prisms that rectify the inverted image produced by the objective lens and collected by the lenses in the end region of the tube [2] (Figure 2 c) wherein, straight and inclined binocular tubes are available which are positioned either parallel or inclined at 45- degree angle to the axis of the microscope [5,6].

#### Eyepieces



The role of eyepieces or ocular lenses is to magnify the intermediate image generated in the binocular tube [2]. Eyepieces with magnification factors of 10x to 20x are available for operating microscopes (Figure 2 d). They can achieve 3x to 40x total magnification, but in dentistry, magnification ranging from 4x to 24x is generally used [5,7].

### ILLUMINATION

Illumination shows the path that light takes as it travels through the microscope (100W halogen bulb). A rheostat controls the light intensity, and a fan cools the lamp. The pathway of the reflected light follows through a condensing lens to a series of prisms and then to the surgical field through the objective lens. The important things to contemplate are- eye-to-object distance, light sources, coaxial illumination, parfocality, and beam splitter [5,6,7].

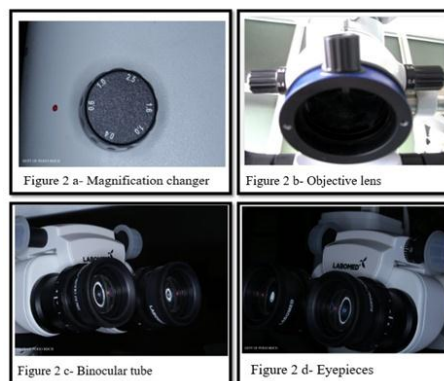


**Figure 2:** Diagrammatic representation of parts of Microscope.

### DOCUMENTATION

The purpose of documentation is to communicate with the referring dentist, educate patients and students and maintain the record of each case. It requires a video adapter, video camera, and video printer. The advancements in the documentation include a three-dimensional view of the surgical field on a video monitor and an HDTV single camera. [3] The charged coupled device sensors in the camera require less light than 35mm film for capturing digital images. Therefore, photos of the surgical field can be taken even without illumination with the flashlight. [5] This prevents the shadowing and vignetting of digital images. It also has the added advantage of assessing the images immediately and, if necessary, deleting the image and retaking the photograph. [6]

Using a video adapter by attaching video cameras to the beam splitter, direct photos and video can be documented. These adapters provide the necessary focal length, thereby providing the same magnification and field of view on the monitor as seen by the surgeon. [7] The most important thing to consider is the resolution of the video camera which should match the recording capability of the video cassette recorder and the resolution of the video monitor. [5] By documenting every case through the microscope, real-time surgeries of all kinds of procedures and techniques can be accessed by the students and practitioners. In the field of teaching and learning, the use of a microscope and documentation has become the single most important development. [4]

Digital documentation capabilities enhance the clinician's ability to efficiently capture surgical procedures of the patient with greater rates of acceptance, thereby increasing the patient's level of reliance and time required. [6]

#### Principles of Microsurgery

It embraces three key points-

- Enhancement of motor skills for increased precision.
- Reduces surgical field and decreases tissue trauma.
- Superior wound healing [4].

Microsurgery is steadily gaining acceptance among periodontists, the reason being not reduced morbidity. Rather the end-point therapeutic appearance of microsurgery is simply superior compared to that of conventional surgery. The difference is clearly shown in cleaner précised incisions, better closer wound apposition, reduced hemorrhage and tissue trauma at the surgical site [4,8,12].

#### Microsurgical Instruments

Specific instruments and sutures are used to carry out the microsurgical techniques [10]. Titanium made is superior to stainless steel instruments. However, stainless steel is more

popular as it provides a greater degree of hardness and flexibility [5]. The specifications of these are shown (Table 2).

**Table 2:** Specifications of microsurgical instruments [6].

Sl. No.	Specifications	Features	Advantages
1.	Design	Top-heavy	precised work and fine motor control
2.	Cross-section	Circular	allows secure rotation between digits
3.	Length	18cm	held securely
4.	Weight	15-20g	avoid fatigue of hand and arm muscles
5.	Color coating	Coated	avoid reflection from light of microscope
6.	Material	Titanium/ steel	stronger, lighter, and non-magnetized

### Ophthalmic knives

Offer the dual advantages of being small and extremely sharp to produce a more precise wound edge and better treatment outcomes than standard no. 15 blade. [11,13,14] (Figure 3 a) [3] [15]. The various types of microsurgical knives used are as follows [13,14,15] (Table 3).

**Table 3:** Types of microsurgical knives used.

Sl. No.	Types	Specifications
1.	Blade-breaker knife	used in place of a no. 15 blade
2.	Crescent knife	intrasulcular incisions, connective tissue graft procedures
3.	Spoon knife	undermine the flap

### Needle holders

They are available in various sizes and are designed to grasp very fine needles. They have smooth jaws to give a simple and controlled knot. The most commonly used needle holder is 14 cm and 18 cm [11] (Figure 3 b). The tip of the needle holder should be 1-mm for 5-0 and 6-0 sutures, whereas 0.3 mm for suturing 8-0 and 10-0 sutures [5,6,16].

### Microsurgical needles and sutures

Needles have high flexural and ductile strength to prevent breakage. Curved needles are easier to enter into tight spaces. So, needles with 3/8 or 1/2 curve circular and arc length of 8-15 mm are preferred to use in periodontal surgery [5,10]. Needles with a range of 6-0 to 9-0 are frequently used. According to length, 13–15-mm, 10–12-mm, 5–8 mm long needles are considered for posterior areas, anterior region, and for vertical incisions, respectively [5]. The commonly used suture sizes are 5-0, 6-0, and 7-0, either absorbable or non-absorbable type [9].

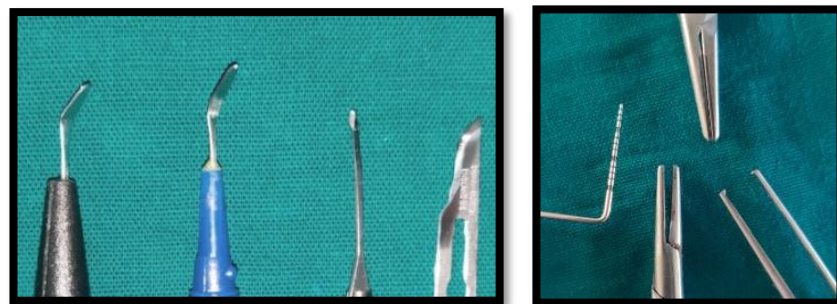


**Figure 3:** Microsurgical instruments.

### Microsurgical knot tying

Knot tying using the microscope is done using instrument ties, with a microsurgical needle holder in the dominant hand and microsurgical tissue pick-up in the non-dominant hand. Three common techniques are used- non-dominant, dominant, and a combination of two; however, non-dominant and combination are the most commonly used. A surgeon's knot followed by a square knot is the preferred knot combination.

### Applications of Microsurgery in Periodontics

Periodontal microsurgery is the descendant of conventional periodontal therapy to reduce surgical trauma and open the horizons for better patient care [9,17]. Table 4 outlines the various studies done under a microscope in chronological order.

**Table 4: Studies showing the clinical applications of microsurgery.**

Clinical application	Aim of the study	Conclusion
<b>Diagnostic procedures 2009</b>	The study was done with the use of high-powered magnification or microscopes in general dentistry [30].	It elaborates on specific general dental applications for high-powered magnification in different fields of dentistry.
<b>Non-surgical periodontal therapy 2005</b>	The study was done on the exposed root surfaces for enhanced periodontal debridement using micro ultrasonics and periodontal endoscopy [39,46].	Endoscopic technology enhances visualization and debridement of the roots in a minimally invasive way.
<b>Management of periodontal flaps 2009</b>	The study assessed the regeneration of lost periodontal tissues using microscope [12].	It concluded the use of a surgical microscope offers definite advantages in terms of increased acceptance, improved visual acuity; superior approximation of wounds, rapid wound healing, and decreased postoperative morbidity.
<b>Regenerative therapy 2021</b>	A study was done to treat intrabony defect using periodontal minimally invasive surgery (MIST) with and without the use of regenerative materials [48].	It is concluded that MIST is an effective treatment for intrabony defects with the use of regenerative materials.
<b>Mucogingival surgery 2004</b>	Treatment of gingival recession using microsurgery by free rotated papilla autograft technique combined with the coronally advanced flap [40].	Statistically significant root coverage without additional second surgical site and reducing patient morbidity. Microscopes permitted less traumatic and minimally invasive procedures. Both groups showed convincing improvement in clinical parameters.
<b>2018</b>	Comparative evaluation of treatment of localized gingival recessions with coronally advanced flap using microsurgical vs conventional techniques [49].	Microscopes permitted less traumatic and minimally invasive procedures. Both groups showed convincing improvement in clinical parameters.
<b>Implant therapy 2021</b>	A study was done to treat peri-implant osseous defects using papilla preservation and minimally invasive surgery, a 5-year retrospective study [50].	All implants survived up to 5 years with significant clinical and radiographic outcomes.
<b>Sinus elevation procedure 2021</b>	Treatment of preliminary results of a minimally invasive microsurgical approach to sinus floor elevation and bone reconstruction using a palatal septum window [51].	Bone augmentation was evaluated six months after preservation by computed tomography and histology, and it demonstrated positive preliminary results in bone reconstruction with reduced morbidity.

#### Advantages of Microscope

The surgical microscope offers advantages to the practicing personnel and gaining its popularity [18,21]. Table 5 highlights it. However, it also has certain disadvantages like high cost of equipment, a restricted working field of about 11-55 mm only, and also the perception and orientation takes time [19,20].

**Table 5: Advantages of microscope**

Postural	Procedural	Psychological	Educational
<b>Perfect posture avoids discomfort to back and neck muscles</b>	Manual operating abilities are magnified.	Decreases occupational, physical and postural stress	Due to inbuilt camera, documentation of images and videos for further referral.
<b>Working distance is maintained, eyes to the surgical field is constant</b>	Appropriate lighting without overshadowing	Increased personal and professional satisfaction.	Recording of diagnostic sequences and treatment in video format
<b>Inbuilt corrective mechanisms are present in microscopic binoculars to compensate for different eye powers.</b>	Collateral vision decreases: unnecessary visual information avoided	Reduced post-operative discomfort with improved clinical results	

## DISCUSSION

The current surgical trend in periodontal therapy entails changing the perception from the use of traditional methods to minimally invasive microsurgery. The practitioner first adapts visually to the microscope before acquiring the new microsurgical skills such as instrument grip and posture through structured training programs [22]. The hands and instruments while operating the microscope are moved by kinaesthetic movement. Wherein there is visual movement without reference to background clues [3,23,24]. The beginners in the microsurgical practice should undergo training to familiarize themselves with the operating microscope, handling of micro-instruments, and technique of knot tying on surgical simulations like surgical gauze, flesh models, and animals to produce high-quality treatment [25,26]. Once completely trained, the practitioner and assistant could steadily introduce it into their practice.

Periodontal microscopy allows high-level motor skills and accuracy when performed at 10x to 20x magnification [3]. With normal vision, the highest possible visual resolution is only 0.2 mm. This can be improved at 20x, wherein hand movement accuracy approaches ten  $\mu$  with a visual resolution of 1  $\mu$ . This means that the surgical site can be accurately focussed [3,24,27,28].

High magnification in surgical microscope gives advantages to treat regenerative [35,42,43,46] and periodontal plastic surgery [23,33,34,49,50] and implant therapy [43,51] successfully over conventional surgery. Clinicians can perform precise work using microsurgical instruments, probably due to fine and sharp blades that extend hard-to-reach areas [31, 36, 38,47].

Also, flaps can be elevated atraumatically as the margins of the flap are sharp. This benefits the fine suturing and accelerated healing outcomes [39, 41, 42]. Hence, the use of microsurgical procedures makes it possible for the clinician to perform completely different from those of conventional procedures [3].

The utilization of a surgical microscope proved to be a boon in various periodontal surgical procedures. Published literature definitely showed a comparison of microscopic periodontal surgery to conventional surgery [29, 32, 35, 49]. Results are superior to a traditional approach. Added advantages were noted, such as less traumatic, enhanced revascularization, higher incidence of primary wound closure, and minimally invasive procedure [41, 42]

Any challenge to visual reality is a fundamental challenge and is not readily believable. Keeping the above advantages in mind, it is necessary that change be accepted with the use of a microscope rather than challenged.

## CONCLUSION

Microsurgery offers new knowledge and technology for periodontics that can dramatically improve the therapeutic outcomes of many periodontal plastics and esthetic treatment modalities. This technique will shift the focus of periodontal procedures from a macro to a micro field, thus achieving precise results. As health care professionals become familiar with the benefits of microsurgery, applications of this philosophy in periodontics will likely become a treatment standard. Microsurgical periodontics requires a different practitioner mindset. Periodontal microsurgery and esthetic and plastic periodontal microscopic surgeries afford a natural evolution in the advancement in the field of periodontics. The "magnification escalation" is likely to continue, and tomorrow's dentistry will see increasing use of magnification.

## REFERENCES

- [1] Belcher JM. A perspective on periodontal microsurgery. *Int J Periodontics Restorative Dent*. 2001;21(2):191–6. Available from: <https://pubmed.ncbi.nlm.nih.gov/11829393/>
- [2] Kumar MP, Jaswitha V, Gautami SP, Ramesh KSV. Applications of microscope in periodontal therapy- Role in magnification really matters! *IP Int J Periodontology Implantology*. 2019;4(1):1–5. DOI: [10.18231/j.ijpi.2019.001](https://doi.org/10.18231/j.ijpi.2019.001)
- [3] Tibbetts L, Shanelac D. Principles and Practice of Periodontal Microsurgery. 2009 [Accessed 2022 Apr 10]. Available from: [http://www.quintpub.com/journals/micro/pdf\\_temp/micro\\_1\\_1\\_Tibbetts\\_3.pdf](http://www.quintpub.com/journals/micro/pdf_temp/micro_1_1_Tibbetts_3.pdf)
- [4] Tripathi S, Gupta DS, Khan M, Piyush, Gowrav, Jalali V. Periodontal Microsurgery - The Growing Wave of Magnification. 2019 [Accessed 2022 Apr 10]. Available from: <https://www.semanticscholar.org/paper/PERIODONTAL-MICROSURGERY-THE-GROWING-WAVE-OF-Tripathi-Gupta/18ca5dc91c0da182a875ef4e758629a5afa26629>
- [5] Zuhler O, Huzler M. Plastic esthetic Periodontal and implant surgery.
- [6] Kim S. Color atlas of microsurgery in endodontics. 2010.



- [7] García Calderín M, Torres Lagares D, Calles Vázquez C, Usón Gargallo J, Gutiérrez Pérez JL. The application of microscopic surgery in dentistry. *Med Oral Patol Oral Cir Bucal*. 2007;12(4):E311-316. Available from: <https://pubmed.ncbi.nlm.nih.gov/17664918/>
- [8] Shanelec DA. Periodontal Microsurgery. *J Esthet Restor Dent*. 2003;15(7):402–7. <https://doi.org/10.1111/j.1708-8240.2003.tb00965.x>
- [9] Vikender Singh Yadav, Sanjeev Kumar Salaria, Anu Bhatia, Renu Yadav. Periodontal microsurgery: Reaching new heights of precision. *J Indian Soc Periodontol*. 2018;22(1):5. DOI: [10.4103/jisp.jisp\\_364\\_17](https://doi.org/10.4103/jisp.jisp_364_17)
- [10] Sitbon Y, Attathom T. Minimal intervention dentistry II: part 6. Microscope and microsurgical techniques in periodontics. *BDJ*. 2014;216(9):503–9. DOI: [10.1038/sj.bdj.2014.356](https://doi.org/10.1038/sj.bdj.2014.356)
- [11] Mamoun J. Use of high-magnification loupes or surgical operating microscope when performing prophylaxes, scaling or root planing procedures. *N Y State Dent J*. 2013;79(5):48–52. Available from: <https://pubmed.ncbi.nlm.nih.gov/24245463/>
- [12] Hegde R, Sumanth S, Padhye A. Microscope-enhanced periodontal therapy: a review and report of four cases. *J Contemp Dent Pract*. 2009;10(5):E088-096. Available from: <https://pubmed.ncbi.nlm.nih.gov/19838615>
- [13] Suryavanshi P, Bhongade M. Periodontal Microsurgery: A New Approach to Periodontal Surgery. 2015 [Accessed 2022 Apr 10]. Available from: <https://www.ijsr.net/archive/v6i3/ART20171566.pdf>
- [14] Tibbetts LS, Shanelec D. Periodontal microsurgery. *Dent Clin North Am*. 1998;42(2):339–59. Available from: <https://pubmed.ncbi.nlm.nih.gov/9597340/>
- [15] Tibbetts LS, Shanelec DA. An overview of periodontal microsurgery. *Current Opinion in Periodontology*. 1994;187–93. Available from: <https://pubmed.ncbi.nlm.nih.gov/8032459/>
- [16] Price PB. Stress, Strain and Sutures. *Ann Surg*. 1948;128(3):408–20. Available from: <https://www.ncbi.nlm.nih.gov/pmc/articles/PMC1514080/>
- [17] Maytreyye R, Jain P, Hamid H, Narang S, Jain K. Periodontal Microsurgery: An Overview. 2016 [Accessed 2022 Apr 10]. Available from: <https://idauttarakhand.files.wordpress.com/2017/09/periodontal-microsurgery-an-overview.pdf>
- [18] García Calderín M, Torres Lagares D, Calles Vázquez C, Usón Gargallo J, Gutiérrez Pérez JL. The application of microscopic surgery in dentistry. *Med Oral Patol Oral Cir Bucal*. 2007 Aug 1;12(4):E311-316. Available from: <https://pubmed.ncbi.nlm.nih.gov/17664918/>
- [19] Shanelec DA, Tibbetts LS. A perspective on the future of periodontal microsurgery. *Periodontology* 2000. 1996;11(1):58–64.
- [20] Belcher JM. A perspective on periodontal microsurgery. *Int J Periodontics Restorative Dent*. 2001;21(2):191–6. Available from: <https://pubmed.ncbi.nlm.nih.gov/11829393/>
- [21] Vikender Singh Yadav, Sanjeev Kumar Salaria, Anu Bhatia, Renu Yadav. Periodontal microsurgery: Reaching new heights of precision. *Journal of Indian Society of Periodontology*. 2018;22(1):5. Available from: <http://www.jisponline.com/article.asp?issn=0972-124X;year=2018;volume=22;issue=1;spage=5;epage=11;aulast=Yadav>
- [22] Rubinstein R. The anatomy of the surgical operating microscope and operating positions. *Dent Clin North Am*. 1997;41(3):391–413. Available from: <https://pubmed.ncbi.nlm.nih.gov/9248682/>
- [23] Burkhardt R, Hürzeler MB. Utilization of the surgical microscope for advanced plastic periodontal surgery. *Pract Proced Aesthet Dent: PPAD*. 2000;12(2):171–80. Available from: <https://pubmed.ncbi.nlm.nih.gov/11404959/>
- [24] Strassler HE, Syme SE, Serio F, Kaim JM. Enhanced visualization during dental practice using magnification systems. *Compend Contin Educ Dent*. 1998;19(6):595–8. Available from: <https://pubmed.ncbi.nlm.nih.gov/9693517/>
- [25] Bergmeister KD, Aman M, Kramer A, Schenck TL, Riedl O, Daeschler SC, et al. Simulating Surgical Skills in Animals: Systematic Review, Costs & Acceptance Analyses. *Front Vet Sci*. 2020 [Accessed 2021 Dec 29];7. DOI: [10.3389/fvets.2020.570852](https://doi.org/10.3389/fvets.2020.570852)
- [26] Demirseren ME, Tosa Y, Hosaka Y. Microsurgical Training with Surgical Gauze: The First Step. *J Reconstr Microsurg*. 2003;19(6):385–6. DOI: [10.1055/s-2003-42634](https://doi.org/10.1055/s-2003-42634)
- [27] Mohan R, Gundappa M. Magnification Tools: Surgical Operating Microscope And Magnifying Loupe In Dental Practice. [Accessed 2022 Apr 10]. Available from: [https://www.researchgate.net/publication/258023254\\_Magnification\\_Tools\\_Surgical\\_Operating\\_Microscope\\_And\\_Magnifying\\_Loupe\\_In\\_Dental\\_Practice](https://www.researchgate.net/publication/258023254_Magnification_Tools_Surgical_Operating_Microscope_And_Magnifying_Loupe_In_Dental_Practice)
- [28] Hegde R, Hegde V. Magnification-enhanced contemporary dentistry: Getting started. *Journal of Interdisciplinary Dentistry*. 2016;6(2):91. DOI: [10.4103/2229-5194.197695](https://doi.org/10.4103/2229-5194.197695)
- [29] Shetty S. Comparative Evaluation of Microsurgical and Conventional Open Flap Surgical Procedure Outcomes in Patients with Periodontitis – A Histopathological & Scanning Electron Microscopy Study. *Biomedical Journal of Scientific & Technical Research*. 2018;6(5). DOI: [10.26717/bjstr.2018.06.001407](https://doi.org/10.26717/bjstr.2018.06.001407)
- [30] Mamoun JS. A rationale for the use of high-powered magnification or microscopes in general dentistry. *Gen Dent*. 2009;57(1):18–26. Available from: <https://pubmed.ncbi.nlm.nih.gov/19146139/>
- [31] Padhye A, Hegde R, Sumanth S. Microscope-Enhanced Periodontal Therapy: A Review and Report of Four Cases. *J Contemp Dent Pract*. 2009;10(5):88–100. DOI: [10.5005/jcdp-10-5-88](https://doi.org/10.5005/jcdp-10-5-88)
- [32] Burkhardt R, Lang NP. Coverage of localized gingival recessions: comparison of micro- and macrosurgical techniques. *J Clin Periodontol*. 2005;32(3):287–93. DOI: [10.1111/j.1600-051x.2005.00660.x](https://doi.org/10.1111/j.1600-051x.2005.00660.x)



- [33] Bittencourt S, Del Peloso Ribeiro É, Sallum EA, Nociti Jr. FH, Casati MZ. Surgical Microscope May Enhance Root Coverage With Subepithelial Connective Tissue Graft: A Randomized-Controlled Clinical Trial. *J Periodontol.* 2012;83(6):721–30. DOI: [10.1902/jop.2011.110202](https://doi.org/10.1902/jop.2011.110202)
- [34] Francetti L, Del Fabbro M, Calace S, Testori T, Weinstein RL. Microsurgical treatment of gingival recession: a controlled clinical study. *Int J Periodontics Restorative Dent.* 2005;25(2):181–8. Available from: <https://pubmed.ncbi.nlm.nih.gov/15839595/>
- [35] Andrade PF, Grisi MFM, Marcaccini AM, Fernandes PG, Reino DM, Souza SLS, et al. Comparison Between Micro- and Macrosurgical Techniques for the Treatment of Localized Gingival Recessions Using Coronally Positioned Flaps and Enamel Matrix Derivative *J Periodontol.* 2010;81(11):1572–9. DOI: [10.1902/jop.2010.100155](https://doi.org/10.1902/jop.2010.100155)
- [36] Ribeiro FV, Casarin RCV, Palma MAG, Júnior FHN, Sallum EA, Casati MZ. Clinical and Patient-Centered Outcomes After Minimally Invasive Non-Surgical or Surgical Approaches for the Treatment of Intrabony Defects: A Randomized Clinical Trial. *J Periodontol.* 2011;82(9):1256–66. DOI: [10.1902/jop.2011.100680](https://doi.org/10.1902/jop.2011.100680)
- [37] Cortellini P, Tonetti MS. Microsurgical Approach to Periodontal Regeneration. Initial Evaluation in a Case Cohort. *J Periodontol.* 2001;72(4):559–69. DOI: [10.1902/jop.2001.72.4.559](https://doi.org/10.1902/jop.2001.72.4.559)
- [38] Abou El Nasr HM. The use of Dental Operating Microscope for Retrieval of different types of Fractured Implant Abutment Screws: Case Reports. *Dentistry.* 2018;08(08). DOI: [10.4172/2161-1122.1000507](https://doi.org/10.4172/2161-1122.1000507)
- [39] Suryavanshi P, Bhongade M. Periodontal Microsurgery: A New Approach to Periodontal Surgery. *Int J Sci Res.* 2015 [Accessed 2022 Apr 10];6:2319–7064. Available from: <https://www.ijsr.net/archive/v6i3/ART20171566.pdf>
- [40] Kwan JY. Enhanced periodontal debridement with the use of micro ultrasonic, periodontal endoscopy. *J Calif Dent Assoc.* 2005;33(3):241–8. Available from: <https://pubmed.ncbi.nlm.nih.gov/15918406/>
- [41] Francetti L, Del Fabbro M, Testori T, Weinstein RL. Periodontal microsurgery: report of 16 cases consecutively treated by the free rotated papilla autograft technique combined with the coronally advanced flap. *The International Journal of Periodontics & Restorative Dentistry.* 2004;24(3):272–9. Available from: <https://pubmed.ncbi.nlm.nih.gov/15227775/>
- [42] Nordland WP, Sandhu HS, Perio C. Microsurgical technique for augmentation of the interdental papilla: three case reports. *Int J Periodontics Restorative Dent.* 2008;28(6):543–9. Available from: <https://pubmed.ncbi.nlm.nih.gov/19146049/>
- [43] Shanellec DA, Tibbetts LS. Implant Microsurgery: Immediate Implant Placement With Implant-Supported Provisional. *Clinical Advances in Periodontics.* 2011;1(3):161–72. DOI: [10.1902/cap.2011.110040](https://doi.org/10.1902/cap.2011.110040)
- [44] Cairo F, Carnevale G, Billi M, Prato GPP. Fiber retention and papilla preservation technique in the treatment of infrabony defects: a microsurgical approach. *Int J Periodontics Restorative Dent.* 2008;28(3):257–63. Available from: <https://pubmed.ncbi.nlm.nih.gov/18605601/>
- [45] Harrel SK. A minimally invasive surgical approach for periodontal bone grafting. *Int J Periodontics Restorative Dent.* 1998;18(2):161–9. Available from: <https://pubmed.ncbi.nlm.nih.gov/9663094/>
- [46] Clark D. The operating microscope and ultrasonics; a perfect marriage. *Dentistry Today.* 2004;23(6):74–6. Available from: <https://pubmed.ncbi.nlm.nih.gov/15218673/>
- [47] Feuillet D, Keller J-F, Agossa K. Interproximal Tunneling with a Customized Connective Tissue Graft: A Microsurgical Technique for Interdental Papilla Reconstruction. *Int J Periodontics Restorative Dent.* 2018;38(6):833–9. DOI: [10.11607/prd.3549](https://doi.org/10.11607/prd.3549)
- [48] Liu B, Ouyang X, Kang J, Zhou S, Suo C, Xu L, et al. Efficacy of periodontal minimally invasive surgery with and without regenerative materials for treatment of intrabony defect: a randomized clinical trial. *Clinical Oral Investigations.* 2021;26(2):1613–23. DOI: [10.1007/s00784-021-04134-w](https://doi.org/10.1007/s00784-021-04134-w)
- [49] Joshi S, Patel C, Mehta R, Hirani T, Joshi C. Comparative evaluation of treatment of localized gingival recessions with coronally advanced flap using microsurgical and conventional techniques. *Contemp Clin Dent.* 2018;9(4):613. DOI: [10.4103/ccd.ccd\\_571\\_18](https://doi.org/10.4103/ccd.ccd_571_18)
- [50] Cortellini P, Cortellini S, Bonaccini D, Tonetti MS. Papilla preservation and minimally invasive surgery for the treatment of peri-implant osseous defects. Clinical and radiographic outcomes of a 5-year retrospective study. *Clin Oral Implants Res.* 2021;32(11):1384–96. DOI: [10.1111/clr.13826](https://doi.org/10.1111/clr.13826)
- [51] Moreno Rodríguez J, Pecci-Lloret M, Ruiz E, Ruiz A. Preliminary Results of a Minimally Invasive Microsurgical Approach to Sinus Floor Elevation and Bone Reconstruction Using a Palatal Septum Window. *Int J Periodontics Restorative Dent.* 2021;41(6):e255–63. DOI: [10.11607/prd.4810](https://doi.org/10.11607/prd.4810)

Content available at: <https://www.ipinnovative.com/open-access-journals>

Indian Journal of Microbiology Research

Journal homepage: <https://www.ijmronline.org/>

## Original Research Article

***In vitro* lytic efficacy of bacteriophages against multidrug-resistant pathogenic bacterial species isolated from pyogenic skin infections****Manjunath Nandihalli Shetru<sup>1,\*</sup>, Maribasappa Karched<sup>2</sup>, Dayanand Agsar<sup>3</sup>, Rangaswamy B E<sup>1</sup>**<sup>1</sup>Dept. of Biotechnology, Bapuji Institute of Engineering and Technology, Davangere, Karnataka, India<sup>2</sup>Oral Microbiology Research Laboratory, Faculty of Dentistry, Kuwait University, Kuwait<sup>3</sup>Dept. of Microbiology, Gulbarga University, Gulbarga, Karnataka, India

## ARTICLE INFO

## Article history:

Received 16-11-2021

Accepted 25-11-2021

Available online 11-04-2022

## Keywords:

Antibiotics

Multidrug resistance

Skin infection

Bacteriophage therapy

## ABSTRACT

**Introduction:** Bacterial multidrug resistance has worsened the situation by adding to economic burden but also poses a greater risk of patient death. The aim of the study was to characterize the multidrug resistance (MDR) properties of the bacterial isolates from skin infections and then to isolate and evaluate lytic efficacy of bacteriophages against the pathogenic bacteria.

**Materials and Methods:** Antimicrobial susceptibilities of the isolates (n=84) from pyogenic skin infections against 14 antibiotics was studied using CLSI guidelines. Phylogenetic analyses of the MDR strains from each species was performed. Lytic efficacy of the sewage-derived phages was assessed by spot test.

**Results:** *Staphylococcus aureus* was the most predominant (57, 68%) of the total of 84 isolates. The number of Gram-negative isolates that were resistant to all antibiotics (except amikacin) were significantly higher ( $P < 0.05$ ). On the other hand, significant number of *S. aureus* strains were susceptible only to clindamycin and erythromycin ( $P < 0.05$ ). Phylogenetic analysis based on the 16S rRNA gene revealed close relatedness of the strains with MDR strains previously reported. *In vitro* analysis of select MDR strains (n=20) showed that the bacteriophages  $\Phi$ DMSA-2,  $\Phi$ DMEC-1 and  $\Phi$ DMPA-1 against *S. aureus*, *E. coli*, and *P. aeruginosa*, respectively, showed lytic efficacy against 4 of 5 MDR strains tested from each species.

**Conclusions:** These preliminary, but still important results emphasize the potential of phages as an effective alternative therapy against MDR bacteria. Further, the lytic efficacy of phages underscores the importance of developing need-based and locally isolated bacteriophages as potential antimicrobial therapy alternative to antibiotics.

This is an Open Access (OA) journal, and articles are distributed under the terms of the [Creative Commons Attribution-NonCommercial-ShareAlike 4.0 License](https://creativecommons.org/licenses/by-nc-sa/4.0/), which allows others to remix, tweak, and build upon the work non-commercially, as long as appropriate credit is given and the new creations are licensed under the identical terms.

For reprints contact: [reprint@ipinnovative.com](mailto:reprint@ipinnovative.com)

## 1. Introduction

Skin and soft tissue infections are a major healthcare issue worldwide and are of particular importance in developing countries.<sup>1</sup> Factors that exacerbate skin infection cases in the developing countries are low level of hygiene, lack of access to clean water, malnutrition, and overcrowded living conditions in lower socio-economic classes.<sup>2</sup>

\* Corresponding author.

E-mail address: [nsm.microb1973@gmail.com](mailto:nsm.microb1973@gmail.com) (M. N. Shetru).

Pyogenic bacteria such as *Staphylococcus aureus*, *Pseudomonas aeruginosa*, *Escherichia coli* and *streptococci* are the prominent species involved in intricate multibacterial infections of deeper skin structures, major abscesses, burns and ulcers, bite wounds and diabetic.<sup>3</sup> Even though most skin infections begin as local induration, erythema, pain or tenderness at the site of infection, the impact may be so worse that it can progress to life-threatening necrotizing fasciitis. When a healthy skin encounters a

bacterial onslaught, epidermal cells (keratinocytes) stage robust innate immune response producing antimicrobial peptides and proinflammatory cytokines.<sup>4</sup> However, with a progressing infection, pathogenic bacteria succeed in gaining entry to keratinocytes and evade host immune response. Since the majority of antibiotics cannot freely enter eukaryotic cells, cutaneous intracellular accumulation of pathogens like methicillin-resistant *S. aureus* (MRSA) poses a great challenge to treat skin infections using antibiotics.<sup>5</sup> Further, the indiscriminate and reckless use of antibiotics has led to a crisis of multidrug resistance among bacterial pathogens. Infections caused by multidrug resistant microorganisms often fail to respond to conventional treatment, resulting in prolonged illness and greater risk of death. New resistance mechanisms have emerged in various bacteria, making the antibiotic therapy difficult.<sup>6</sup> The longer duration of illness and treatment often in hospitals increases health-care costs and the economic burden to families and societies where it increases the costs of health care.<sup>7</sup>

During the recent past bacteriophage therapy has gained a renewed interest as a potential alternative therapy for multidrug-resistant (MDR) bacterial infections.<sup>8</sup> Importantly, phages possess remarkable species specificity to bacterial pathogens. Further, an important clinical significance is that phage therapy can be very effective in biofilm infections where antibiotics fail to kill bacterial cells in biofilms, which are impermeable to antibiotics.<sup>9</sup> Phage therapy finds special advantage for localized use, because phages penetrate deeper as long as the infection is present, rather than decrease rapidly in concentration below the surface. The phages stop reproducing once specific bacteria they target are destroyed. This prevents the development of secondary resistance to phages, which is quite often the case in antibiotics. Since phages live in the same niche as their host bacteria,<sup>10</sup> and that they exhibit very high specificity (both species- and strain-specificity), it is crucial that phages are isolated and characterized for their bacteria-lytic ability locally in the affected regions. We recently demonstrated in an *in vivo* skin excisional wound model that the survival rate in mice was significantly high when a locally isolated phage against methicillin-resistant *S. aureus* was applied to the wounds.<sup>11</sup> In this study we took up a systematic approach at first to isolate clinically important pathogenic bacterial species from pyogenic skin infections, determined antibiotic susceptibility of the isolates and then tested phages for lytic efficacy against MDR bacterial pathogen isolates.

## 2. Materials and Methods

### 2.1. Collection of clinical samples

The study was approved by the institutional Ethics Committee (Institutional Animal Ethics Committee-IAEC, Sree Siddaganga College of Pharmacy, Tumkur,

Karnataka state, India-572 102 with an Approval reference No:SSCPT/IAEC.Clear/130/12-13). Written informed consent was obtained from all study patients (n=114). Swab samples from pyogenic skin infections were collected from patients of different age groups including males (n=82 median age 41 yrs) and females (n=32 median age 28 yrs). Swabs were immersed in 1% sterile peptone water and immediately subjected to microbial culture in aseptic conditions within 30-45 min of collection.

### 2.2. Isolation, identification and characterization of bacterial pathogens

The samples were at first cultured on general nutrient agar medium and suspect colonies were subsequently subcultured on selective agar media for different species. The major clinically important bacterial species from pyogenic infections were isolated using selective growth medium for each species. Identification of the species was achieved by extensive microbiological and biochemical characterization of presumptive colonies.

### 2.3. Antibiotic susceptibility of the bacterial isolates

The confirmed clinical isolates of each species were screened for antibiotic susceptibility by Kirby Bauer's disc diffusion method.<sup>12,13</sup> according to Clinical and Laboratory Standard Institute (CLSI) guidelines (2005). Six hours old cultures were spread uniformly on the surface of Mueller-Hinton agar plates, antibiotic discs were placed on the agar surface and the plates were incubated at 37°C for 24 hr. The zone of inhibition was recorded in millimetres. The results were interpreted as susceptible or resistant as per the CLSI guidelines, 2005.<sup>14</sup> Blank discs without antibiotic were used as negative controls in each experiment. The minimum inhibitory concentration (MIC) of methicillin was performed on *S. aureus* using the broth microdilution methods as described previously.<sup>15</sup>

### 2.4. DNA extraction, 16SrRNA gene amplification and phylogenetic analysis

Genomic DNA from the bacterial isolates was extracted by following a previously described method.<sup>16</sup> Complete 16S rRNA gene from select strains from each species were amplified using the primers 16S-1-GGT GGA GCA TGT GGT TTA and 16S-2 (5'-16S-2 CCA TTG TAG CAC GTG TGT).<sup>17</sup> PCR reaction mixture consisted of 200  $\mu$ M dNTPS, 2.5 U Taq DNA polymerase and DNA template. After thermal cycling, the PCR products were gel purified using the QIAquick PCR Purification Kit. Following a nested PCR strategy,<sup>17</sup> a 256-bp internal region of the amplified 16S rRNA gene was sequenced with an ABI 3100 automated sequencer (Applied Biosystems). The sequence of the PCR product was compared with known 16S rRNA gene sequences in the Gene Bank by multiple sequence

alignment using the CLUSTAL W Program . Phylogenetic trees were constructed using Mega 5 program.

### 2.5. PCR amplification of *mecA* gene

To test whether the methicillin resistant *S. aureus* strains harbored a methicillin resistance gene (*mecA*), 4 of the MRSA isolates were subject to PCR by using the primers *mecA*-F (5'- CCT AGT AAA GCT CCG GAA) and *mecA*-R Primer (5'- CTA GTC CAT TCG GTC CA) as describe previously.<sup>18</sup> The 25- $\mu$ l reaction mixture included 200  $\mu$ M dNTPs, 2.5  $\mu$ M primers, 2.5 U of Taq DNA polymerase. Thermal profile was as follows: Initial denaturation for 5 min at 94°C, followed by 30 cycles of denaturation for 30s at 94°C; annealing for 30s at 53°C; and primer extension for 40 sec at 72°C and a final extension for 10 min at 72°C. A 10- $\mu$ l PCR product was loaded onto a 1.2% agarose gel the bands were visualized under a UV transilluminator.

### 2.6. Isolation of bacteriophages

A cocktail of sewage originated from hospital, municipal and domestic waste in Davangere city, Karnataka, India, was used as a source for the isolation of phages. Initially, 25 ml of the cocktail sewage sample was pre-treated with 200  $\mu$ l of chloroform for 15 minutes and to this, 2 ml of 16-18 hours old bacterial cultures, each species separately, were added and incubated overnight at 37°C. The lysate was centrifuged (4000  $\times$ g, 10 min) and the supernatant was filtered through a 0.22  $\mu$ m membrane filter and serially diluted using SM phage buffer. One hundred microliter from this stock was mixed with 100  $\mu$ l of host bacterial suspensions. Bacterial cell suspension without phage filtrate was used as a negative control. After incubation (37 °C, 20 min), luria bertani agar (0.7%) was added to the above, mixed gently and poured on LB agar plates followed by incubation at 37°C for 15-16 hours. A few prominent and isolated plaques were recovered using a sterile gel cutter followed by suction. The bacteriophage particles were diffused out of agarose by adding chloroform. The phage preparations were stored at 4°C for further use.

### 2.7. Transmission electron microscopy

Transmission electron microscopy was carried out at the laboratory of Hans-W Ackermann, Professor Emeritus, Department of Microbiology and Immunology, Laval University, Quebec, Canada. A high titer bacteriophage lysate of 10<sup>8</sup> pfu ml<sup>-1</sup> previously filtered through 0.22  $\mu$ m Minisart Sartorius filter was centrifuged and treated with a fixative 1% glutaraldehyde. A drop of purified and fixed phage lysate was deposited on Formvar carbon-coated copper grids and negatively stained with 1% phosphotungstic acid (PTA). The grids were examined in Tecnai G<sup>2</sup> Biotwin (Philips-Netherland) transmission electron microscope. The images of phages were captured

and the sizes of head and tail were measured.

### 2.8. Determination of Phage host range (Spot test)

Bacterial isolates (4 from each species) were screened for phage lysis by a spot test. The suspensions of log-phase bacteria were added to 15 ml sterile tubes with molten 3 ml agarose maintained at 47°C. The contents were mixed and overlaid on pre-dried LB agar plates. The dried plates having bacterial layer, on which 5  $\mu$ l of phage suspension (10<sup>8</sup> pfu ml<sup>-1</sup>) was dropped and incubated at 37°C without inverting the plates. The results were scored as a clear zone of complete lysis (++), partial lysis with turbidity (+) and no lysis (0).

### 2.9. Effect of storage period, pH, temperature and chloroform on the stability of the phages

The storage stability of the phages was determined at temperatures -40°C, -20°C, 4°C, and 20°C and also in presence of 20% (v/v) glycerol at -40°C and -20°C. Stability was also tested at pH 2, 4, 5, 6, 7, 8, 9 and 10. Phage titres were determined after 3, 6, 9 and 12 months of storage by double agar layer technique.

### 2.10. Statistics

Antibiotic resistance or susceptibility differences between the groups were determined using McNemar test. Differences in plaque titre values (pfu/ml) were determined using a non-parametric Mann-Whitney U test. A P value of < 0.05 was considered statistically significant. The statistical software SPSS version 25.0 (IBM Corp, Armonk, NY, USA) was used for all analyses.

## 3. Results

### 3.1. Bacterial pathogens from pyogenic skin infections

Among the 84 bacterial strains isolated from pyogenic skin infections of the study (Table 1), *S. aureus* was the most prevalent with 57 (67.85%) isolates followed by *P. mirabilis* 14 (16.66%), *P. aeruginosa* 7 (8.33%), *E. coli* 5 (5.95%) and *S. xylosus* 1 (1.19%). The highest prevalence of all bacteria (41, 48.80%) was recorded from abscess, followed by pyoderma (11, 13.09%), ulcers (9, 10.71%), cellulitis (5, 5.95%), wounds (5, 5.95%), diabetic foot (5, 5.95%), and post-operative infections (4, 4.76%). Only one *S. aureus* strain was isolated from burn wound infections.

### 3.2. Antibiotic susceptibility of the bacterial pathogens from pyogenic infections

All bacterial isolates (n=74) were subjected to antibiotic susceptibility testing (Table 2). *S. aureus* isolates were found to be resistant to most of the common antibiotics, with a highest (22/46, 48%) resistance for amikacin followed

by 40% (18/46 strains) of the strains for ciprofloxacin. However, clindamycin and erythromycin were the only antibiotics to which significantly higher number of *S. aureus* isolates were susceptible ( $P < 0.05$ ). The single isolate from the *S. xylosus* species was sensitive to clindamycin and methicillin and resistant to all other antibiotics tested for Gram positive bacteria. From Gram negatives, significantly higher number of isolates were resistant to all the antibiotics tested except amikacin ( $P < 0.05$ ). *P. aeruginosa* isolates were resistant 100% (10 of 10 strains) for amoxicillin, 80% (8/10) for cephataxime, 80% (8/10) for cefoperazone, 60% (6/10) and 40% for each of ceftazidime, ciprofloxacin, levofloxacin, tobramycin and amikacin respectively. *E. coli* isolates were resistant 50% (2/4) for amikacin and ceftazidime, 100% for cefoperazone (4/4), 75% (3/4) for each of the other antibiotics (Table 2).

### 3.3. Methicillin resistance among *S. aureus* strains

Considering the clinical significance of methicillin-resistant *S. aureus* strains, we also looked at the occurrence of MRSA strains among our *S. aureus* isolates. All strains of *S. aureus* having methicillin MIC of  $> 4 \mu\text{g/ml}$  were considered methicillin-resistant. As evidenced by antibiotic susceptibility tests, 41% of all *S. aureus* isolates were found to be methicillin-resistant (Table 2). When a molecular confirmation of methicillin resistance in these strains was sought, 3 strains showed an amplicon corresponding to the size of *mecA* gene (Figure 1). Similar to isolates from other species, these MDR *S. aureus* strains were selected for investigating the host range of the bacteriophage  $\Phi\text{DMSA-2}$ .

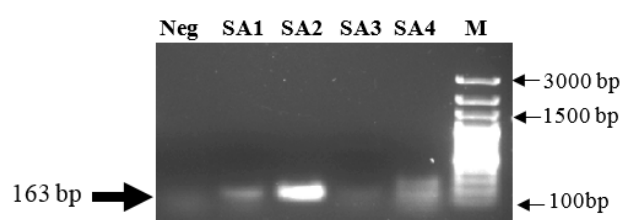


**Fig. 1:** Detection of *mecA* gene among methicillin resistant *S. aureus* isolates. Four of the multidrug resistant *S. aureus* strains (SA1-SA4) that were also resistant to methicillin were tested for the presence of *mecA* gene that encodes methicillin resistance. The amplicons were separated on a 2% agarose gel, stained with ethidium bromide and visualized under UV transilluminator.

### 3.4. 16S rRNA gene sequencing and phylogenetic analysis

Phylogenetic trees were constructed using 16S rRNA gene sequences from each of the MDR pathogens from this study against the sequences of MDR strains from NCBI (Figure 2

). The phylogenetic trees revealed that the isolates formed a cluster with other MDR strains of the same species, but not with non-MDR strains or strains belonging to different species.

### 3.5. Isolation and morphological features of the phages

Figure 3 depicts transmission electron micrographs of all 5 phages, i.e.,  $\Phi\text{DMSA-2}$ ,  $\Phi\text{DMSX-1}$ ,  $\Phi\text{DMPA-1}$ ,  $\Phi\text{DMEC-1}$ , and  $\Phi\text{DMPM-1}$ . All phages possessed an isometric icosahedral capsid of varying sizes. The details of phage dimensions and their classification are given in Figure 3. The phages  $\Phi\text{DMSA-2}$ ,  $\Phi\text{DMEC}$ , and  $\Phi\text{DMPM}$  exhibited a head size in the range 60-90 nm and tail of 200-240 nm long. These 3 phages were assessed to be belonging to the family *Siphoviridae*. The morphological characteristics of phage was examined and confirmed as phage belonging to the family *Siphoviridae*. On the other hand, phages  $\Phi\text{DMSX}$  and  $\Phi\text{DMPA}$  appeared to possess a bigger head size with 100-137 nm and a tail of 210-217 nm. Interestingly, the phage  $\Phi\text{DMSX}$  for *S. xylosus* had a head with a triangular aspect, which was different from all other phages.  $\Phi\text{DMSX}$  belongs to a group of "twort-like phages" under the sub family *Spounavirinae* of the family *Myoviridae*. Its tail measured about 210 nm showing conspicuous striations and terminate in a base plate with a set of spikes.

### 3.6. Host range

Four multidrug-resistant strains from each species were chosen for determining the *in vitro* lytic efficacy of the phages  $\Phi\text{DMSA-2}$ ,  $\Phi\text{DMSX-1}$ ,  $\Phi\text{DMEC-1}$ ,  $\Phi\text{DMPA-1}$ , and  $\Phi\text{DMPM-1}$  Table 3 shows the degree of lytic activity of all five phages against their specific host MDR isolates from each species. The results were scored as a clear zone of complete lysis (++), partial lysis with turbidity (+) and no lysis (0). The phages against *S. aureus* ( $\Phi\text{DMSA-2}$ ), *P. aeruginosa* ( $\Phi\text{DMPA-1}$ ) and *E. coli* ( $\Phi\text{DMEC-1}$ ) exhibited strong lytic activity and could completely lyse 3 of 4 (75%) tested strains. Importantly, no bacteriophage-insensitive mutants (BIM) were observed for this phage. The *S. xylosus* phage was able to completely lyse 1 strain (25%), partially lyse 2 strains (50%) and no lysis in the case of 1 strain (25%). The phage  $\Phi\text{DMPM-1}$  against *P. mirabilis* showed only partial lysis of all 4 strains tested. The occurrence of bacteriophage-insensitive mutants (BIM) based on the growth of bacterial colonies within the plaque were noticed in the case of three phages ( $\Phi\text{DMSX-1}$ ,  $\Phi\text{DMEC-1}$  and  $\Phi\text{DMPA-1}$ ).

### 3.7. Factors influencing the stability of the phages

The stability of hage lysates was tested in different storage conditions and period. The level of phage titre ( $10^8$  pfu) did not decrease significantly ( $P < 0.05$ ) after 3 month storage at all of the tested temperatures, i.e., 6 months at  $-20^\circ\text{C}$



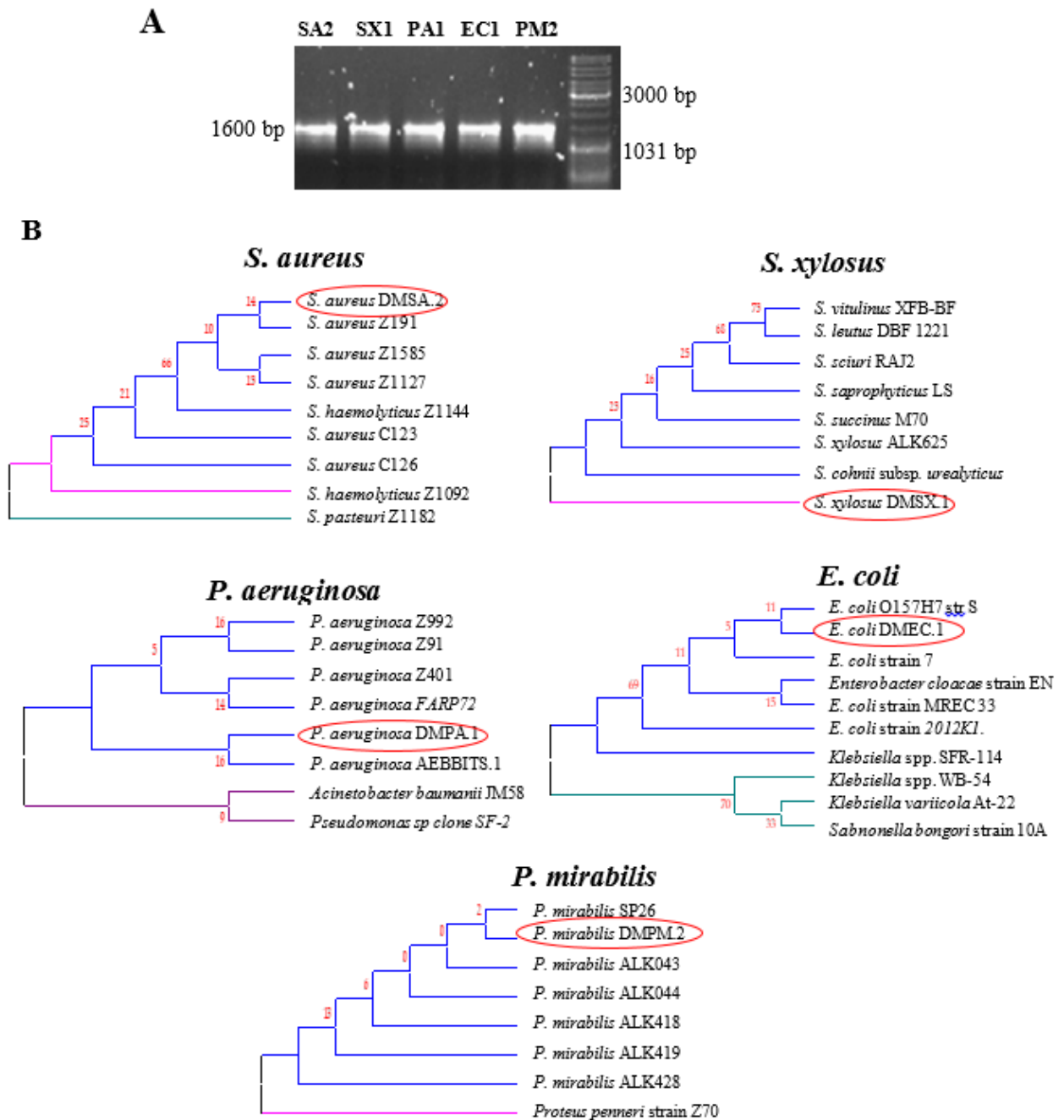


**Fig. 2:** 16S rRNA gene sequence based phylogenetic analysis of the MDR pathogen isolates. PCR amplification of the 16S rRNA gene from the representative strains from each pathogenic species (A). 16S rRNA gene sequences from the MDR bacterial isolates were compared with those from known MDR pathogens of the same species. Multiple sequence alignment and phylogenetic trees were constructed using the bioinformatics tool MEGA5 (B). Circled isolates are from this study

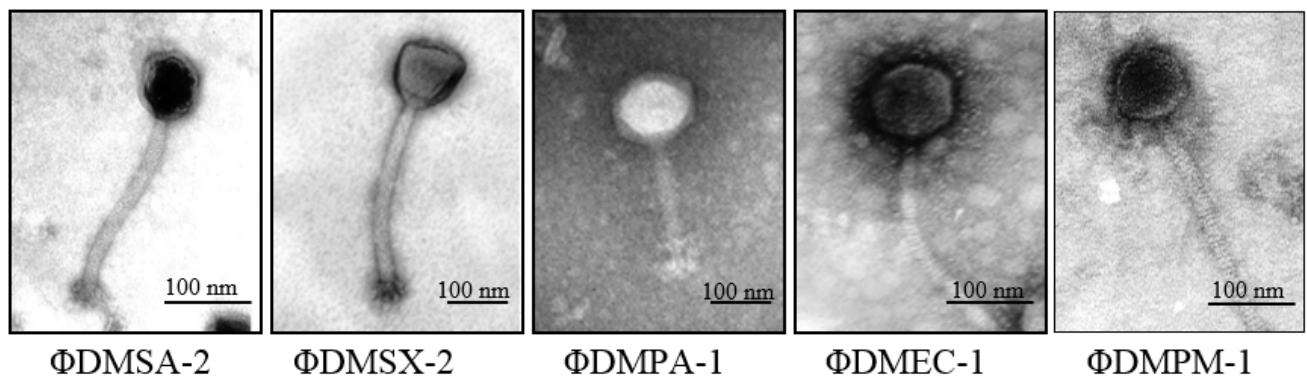


**Fig. 3:** Electron micrographs of phages specific to the MDR pathogen isolates. Glutaraldehyde-fixed phage lysate was deposited on formvar carbon-coated copper grids and negatively stained with 1% phosphotungstic acid. TEM images were acquired on a Tecnai G Biotwin (Philips-Netherlands) transmission electron microscope. Using the scale from the image acquiring software, sizes of head and tail were measured

and 9 months at  $-40^{\circ}\text{C}$  with glycerol. However, at room temperature, the titer was reduced 30% from  $10^8$  pfu/ml to  $7 \times 10^7$  pfu/ml. When phages were exposed to a high temperature of  $60^{\circ}\text{C}$  for 15 minutes, phage titers decreased significantly up to  $10^6$  pfu/ml ( $P < 0.05$ ). Phages were stable between pH range 6-9 and completely lysed at pH 2 and 4. Incubation at pH 4 and  $37^{\circ}\text{C}$  caused a 30% ( $7 \times 10^7$  pfu/ml) and 60% ( $4 \times 10^7$  pfu/ml) decrease in phage titre after 1 and 5 h of incubation, respectively.

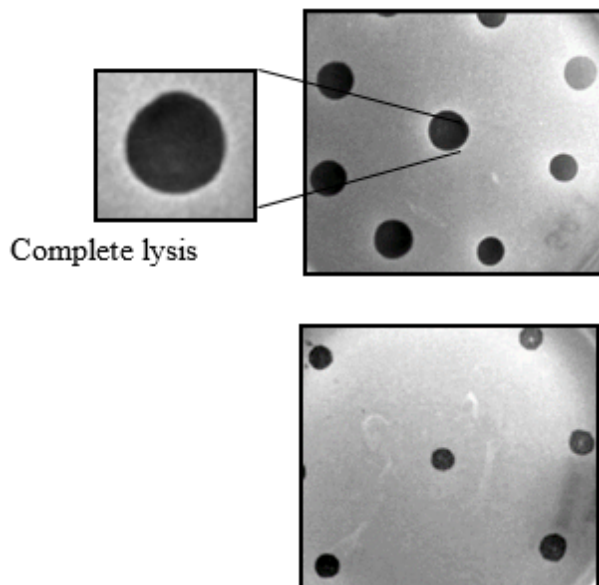


**Fig. 4:**

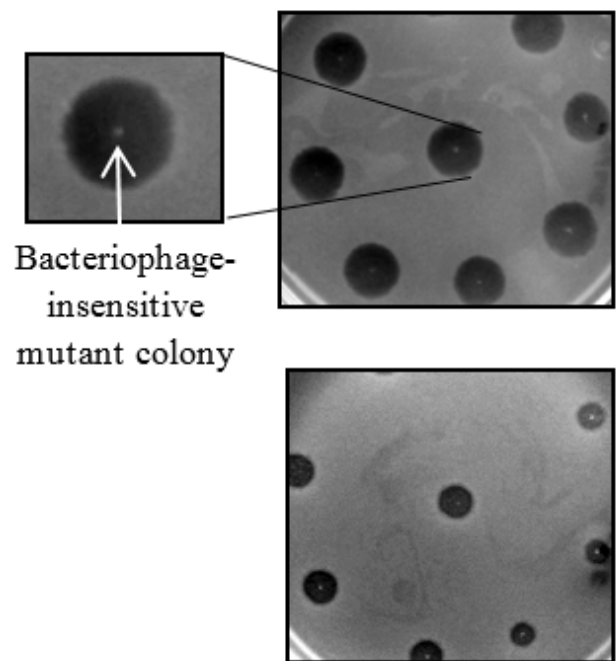


**Fig. 5:**

#### 4. Discussion

In this study, locally isolated phages lysed multi drug resistant bacterial isolates belonging to important pathogenic species from skin infections. Clinical samples collected from pyogenic skin infections were collected from a total of 114 patients. The highest prevalence of bacteria, i.e., 41 (48.80%) was recorded from abscess, followed by pyoderma, ulcers, cellulitis, wounds and diabetic foot. Existing literature has revealed that the general microbiota of human skin infections includes *S. aureus* as a highly

**Table 1:** Profile of pathogenic bacterial isolates from pyogenic skin infections

Type of infection	Pathogenic bacterial isolates					TotalN (%)
	<i>S. aureus</i> N (%)	<i>P. mirabilis</i> N (%)	<i>P. aeruginosa</i> N (%)	<i>E. coli</i> N (%)	<i>S. xylosus</i> N (%)	
Abscess	26 (30.95)	9 (10.71)	3 (3.57)	3 (3.57)	0 (0)	<b>41 (48.80)</b>
Pyoderma	8 (9.52)	1 (1.19)	2 (2.38)	0 (0)	0 (0)	<b>11 (13.09)</b>
Ulcer	7 (8.33)	1 (1.19)	1 (1.19)	0 (0)	0 (0)	<b>9 (10.71)</b>
Cellulitis	3 (3.57)	1 (1.19)	1 (1.19)	0 (0)	0 (0)	<b>5 (5.95)</b>
Wound	4 (4.76)	1 (1.19)	0 (0)	0 (0)	0 (0)	<b>5 (5.95)</b>
Diabetic foot	1 (1.19)	1 (1.19)	0 (0)	2 (2.38)	1 (1.19)	<b>5 (5.95)</b>
Post-Operative Infection	4 (4.76)	0 (0)	0 (0)	0 (0)	0 (0)	<b>4 (4.76)</b>
Folliculitis	3 (3.57)	0 (0)	0 (0)	0 (0)	0 (0)	<b>3 (3.57)</b>
Burn Wound Infection	1 (1.19)	0 (0)	0 (0)	0 (0)	0 (0)	<b>1 (1.1)</b>
<b>Total</b>	<b>57 (67.85)</b>	<b>14 (16.66)</b>	<b>7 (8.33)</b>	<b>5 (5.95)</b>	<b>1 (1.19)</b>	<b>84 (100)</b>

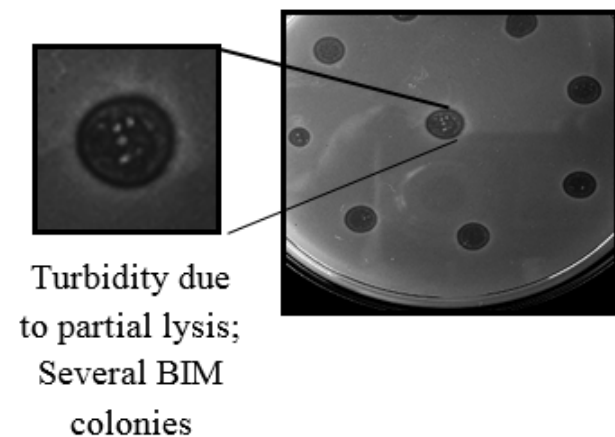
**Table 2:** Antibiotic resistance of the bacterial pathogens from pyogenic infections

Species	Antibiotic resistance N (%)							
	Ak	Cf	Cd	E	M	Of	Ox	P
<b>Gram-positive species</b>								
<i>S. aureus</i> (n=46)	22 (48)	18 (40)	7 (15)*	14 (31)*	19 (41)	19 (41)	19 (41)	19 (41)
<i>S. xylosus</i> (n=1)	R <sup>#</sup>	R	S <sup>#</sup>	R	S	R	R	R
<b>Gram-negative species</b>								
<i>P. aeruginosa</i> (n=10)	4 (40)	10 (100)	6 (60)	8 (80)	6 (60)	8 (80)	6 (60)	6 (60)
<i>E. coli</i> (n=4)	2 (50)	3 (75)	2 (50)	3 (75)	3 (75)	4 (100)	3 (75)	3 (75)
<i>P. mirabilis</i> (n=13)	10 (77)	6 (46)	10 (77)	7 (54)	9 (69)	11 (85)	12 (92)	11 (85)

Ak, Amikacin; Cf, Ciprofloxacin; Cd, Clindamycin; E, Erythromycin; M, Methicillin; Of, Ofloxacin; Ox, Oxacillin; P, Penicillin G; Ac, Amoxicillin; Ca, Cefazidime; Cs, Cefoperazone; Le, Levofloxacin; Tb, Tobramycin; Ce, Cephalexime

#R=resistant, S=susceptible

\*P=0.02

**Fig. 6:**

predominant species,<sup>19</sup> but species from other genera such as *Pseudomonas*, *Enterococcus*, *Escherichia*, *Enterobacter*, *Klebsiella*, *Proteus*, *Acinetobacter*, and coagulase-negative *Staphylococcus* spp. are also commonly present.<sup>3</sup>

Nearly 40% of the *S. aureus* strains showed resistance to all major antibiotics available for Gram-positive bacteria during the period this study was conducted. The only other Gram-positive species, *S. xylosus*, was resistant to all tested antibiotics except clindamycin and methicillin. Among Gram-negative bacteria, 50-100% of all three species, *P. aeruginosa*, *E. coli*, and *P. mirabilis*, were resistant to all antibiotics tested except amikacin. Multidrug resistance among bacterial pathogens occurring in skin infections in India has been reported in a number of studies. These studies found that major pathogens such as *S. aureus*, *E. coli*, *P. aeruginosa* etc. were resistant (>60%) to major antibiotics including penicillin, erythromycin, co-trimoxazole, clindamycin, cefepime, and ciprofloxacin.<sup>20</sup> Even though Gram-negatives are most frequently encountered, *S. aureus* is of immense clinical significance due to its role in skin infections. In our study, 41% of the *S. aureus* isolates were resistant to methicillin. MRSA have become a major challenge worldwide with varied prevalence depending on geographic region.<sup>21,22</sup> MRSA develop resistance through the acquisition of the *mecA* gene, which facilitates production of “penicillin-binding protein 2a” (PBP2a) that strengthens the cell wall and increases resistance to  $\beta$ -lactam antibiotics by blocking

**Table 3:** Host range of the bacteriophages against MDR bacterial strains

	<b>Bacterial isolates</b>	<b>Lytic activity of Phages</b>	<b>BIM*</b>
Complete lysis (Figure 4)	<b><i>S. aureus</i></b>	<b>Φ DMSA.2</b>	
	DMSA.1	++	
	DMSA.2	++	
	DMSA.3	++	
	DMSA.4	-	
	<b><i>S. xylosus</i></b>	<b>Φ DMSX.1</b>	
	DMSA.1	++	
	DMSA.2	+	
Bacteriophage-insensitive mutant colony (Figure 5)	DMSA.3	-	+
	DMSA.4	+	
	<b><i>P. aeruginosa</i></b>	<b>Φ DMPA.1</b>	
	DMPA.1	++	
	DMPA.2	+	
	DMPA.3	++	+
	DMPA.4	++	
	<b><i>E. coli</i></b>	<b>Φ DMEC.1</b>	
Turbidity due to partial lysis; Several BIM colonies (Figure 6)	DMEC.1	++	
	DMEC.2	++	
	DMEC.3	-	+
	DMEC.4	++	
	<b><i>P. mirabilis</i></b>	<b>Φ DMPM.1</b>	
	DMPM.1	+	
	DMPM.2	+	
	DMPM.3	+	
	DMPM.4	+	

the  $\beta$ -lactam binding site.<sup>23</sup> Penicillin-resistant strains of *S. aureus* predominate the nosocomial infections and currently only <5% of the *S. aureus* strains are penicillin-susceptible.<sup>24</sup>

Biological and geographical relationship among MDR strains is generally studied using 16S rRNA gene sequences and allows sequence comparison among strains from different geographic regions. In the present study, each of the representative MDR pathogen species formed a close clade in the phylogenetic tree with other MDR strains. Horizontal transfer of antibiotic resistance genes in the environment is a continuous natural phenomenon. Thus, phylogenetic analysis of MDR strains provides important information about their geographic distribution and may therefore help devise better treatment strategies.<sup>25</sup>

Phages against *S. aureus*, *P. aeruginosa* and *E. coli* exhibited highest lytic activity as evidenced by spot test. The phage against *P. mirabilis* was able to lyse all 4 strains but only moderately and no complete lysis was observed for any strain. In earlier studies, phages have been reported to display broad host range, killing different strains from the same species, e.g., phage Stau2 could lyse 80% of the *S. aureus* isolates obtained from hospitals in Taiwan.<sup>13</sup>

In another study, *E. coli* pathogenic strains EHEC, EPEC, ETEC, and UPEC were effectively lysed by a phage.<sup>26</sup> High selectivity and specificity of phages to their respective host bacteria provide a convenient yet effective way to eradicate bacterial pathogens both intracellular and otherwise in skin infections.

In our study, except for *S. aureus*, all other species produced bacteriophage insensitive mutants (BIMs). Even though phages have been successfully tested as alternative therapeutic agents in several human infections,<sup>27</sup> emergence of BIMs is a serious concern. The bacterial resistance to phages can occur through different mechanisms, e.g., restriction modification, abortive infection, and more commonly through mutations in phage receptor sites on the bacterial cell surface, preventing them from attachment. However, bacteriophage insensitivity is known to come at a cost for the host bacteria, i.e., the BIM trait makes the bacteria compromise with their performance in other traits resulting in slower growth, decreased virulence, and even diminished resistance to various antibiotics.<sup>28</sup>

From the perspective of phage therapy in clinical medicine, stability of phages upon storage and implementation of appropriate storage conditions is

critical for a successful outcome. Storage stability of all four phages examined under different parameters showed that there was no significant decrease in the phage titre except at room temperature. Interestingly, only  $\Phi$ DMSA-2 was stable for 9 months, the longest duration of storage as compared to the other phages. There are a few studies reporting the use phage as in hand sanitizer solutions and as disinfectants to sanitize operating rooms and medical equipment.<sup>29</sup> Further, a gel containing a cocktail of phages targeted nasal carriage of MRSA significantly reducing the incidence of MRSA transmission.<sup>18,30</sup> Thus, our data showing remarkable stability of the phages in a variety of conditions is an important step forward in developing phage therapy for skin infections.

One of the serious concerns about the use of phage therapy in vivo is a strong antibody response which would clear the phages more quickly.<sup>31</sup> To circumvent this problem, phages with different antigenicity or with low immunogenicity could be prepared. Other drawbacks of phages as therapeutic agents are their often-narrow host ranges and the fact that phages are not always lytic under certain physiological conditions. Further, phage therapy triggers release of endotoxins from the target pathogen due to widespread bacterial cell lysis. This occurs also when antibiotics are used, but it could be countered with regulated use of phages.

## 5. Conclusions

Predominant occurrence of clinically important, multidrug resistant bacterial pathogens in skin infections highlights the severity of the problem. Multidrug resistance among the majority of the bacterial isolates underscores the existing global problem with the current antibiotic therapies. Phages have special advantage for localized use in skin infections, because, unlike antibiotics, they penetrate deeper in an infected tissue rather than decrease rapidly in concentration below the surface. Importantly, in our recent study,<sup>11</sup> lytic efficacy of the phage  $\Phi$ DMSA-2 against MRSA, was shown to significantly enhance the survival of mice in an in vivo skin excisional model. Thus, our study emphasizes the importance of need-based and locally isolated bacteriophages as potential alternative antimicrobial therapy.

## 6. Ethics

All procedures performed in studies involving human participants were in accordance with the ethical standards of the institute and with the 1975 Helsinki declaration and its later amendments (revised in 2000) or comparable ethical standards. The study's experimental design and protocol were approved by the Ethics Committee at Bapuji Institute of Engineering and Technology.

## 7. Author Contribution

MNS: Conception, design, experimentation, data analysis and manuscript writing. MK: Experimentation, data analysis and manuscript writing. DA: Data analysis, manuscript writing.

## 8. Source of Funding

The corresponding author is grateful to Vision Group on Science and Technology (VGST), Govt. of Karnataka Secretariat, India for the facilities created through funding in the department of Biotechnology for research under the schemes Seed Money to Young Scientist for Research (SMYSR) and Centers of Innovative Science and Engineering Education (CISEE).

## 9. Conflict of Interest

The authors declare that they do not have any conflict of interest.

## Acknowledgements

We are grateful to Hans-W Ackerman, Professor Emeritus, Laval University, Quebec, Canada and former Vice-President of International Committee on Taxonomy of Viruses (ICTV) for his generous help and support with electron microscopy and bacteriophage classification. We thank Skanda Life Sciences, Bengaluru for their lab facility. Lastly, Oral Microbiology Research Laboratory (SRUL 01/14), Kuwait University is acknowledged for the co-author M Karched's collaboration on this study.

## References


1. Afsar FS. Skin infections in developing countries. *Curr Opin Pediatr*. 2010;22(4):459–66.
2. WHO. Epidemiology and management of common skin diseases in developing countries World Health Organization; 2005. Available from: <https://apps.who.int/iris/handle/10665/69229>.
3. Esposito S, Noviello S, Leone S. Epidemiology and microbiology of skin and soft tissue infections. *Curr Opin Infect Dis*. 2016;29(2):109–15.
4. DiMeglio P, Perera GK, and FON. The multitasking organ: recent insights into skin immune function. *Immunity*. 2011;35(6):857–69.
5. Soong G, Paulino F, Wachtel S, Parker D, Wickersham M, Zhang D, et al. Methicillin-resistant *Staphylococcus aureus* adaptation to human keratinocytes. *mBio*. 2015;6(2):e00289–15.
6. Chang HH, Cohen T, Grad YH, Hanage WP, O'brien TF, Lipsitch M. Origin and proliferation of multiple-drug resistance in bacterial pathogens. *Microbiol Mol Biol Rev*. 2015;79(1):101–117.
7. Naylor NR, Atun R, Zhu N, Kulasabanathan K, Silva S, Chatterjee A, et al. Estimating the burden of antimicrobial resistance: a systematic literature review. *Antimicrob Resist Infect Control*. 2018;7:58.
8. Hesse S, Adhya S. Phage Therapy in the Twenty-First Century: Facing the Decline of the Antibiotic Era; Is It Finally Time for the Age of the Phage? *Annu Rev Microbiol*. 2019;73:155–74.
9. Lusiak-Szelachowska M, Weber-Dabrowska B, Gorski A. Bacteriophages and Lysins in Biofilm Control. *Virol Sin*. 2020;35(2):125–33.
10. Szafranski SP, Kilian M, Yang I, Wieden GB, Winkel A, Hegermann J, et al. Diversity patterns of bacteriophages infecting *Aggregatibacter*



- and Haemophilus species across clades and niches. *ISME J.* 2019;13(10):2500–22.
11. Shetru MN, Karched M, Agsar D. Locally isolated broad host-range bacteriophage kills methicillin-resistant *Staphylococcus aureus* in an in vivo skin excisional wound model in mice. *Microb Pathog.* 2021;152:104744. [doi:10.1016/j.micpath.2021.104744](https://doi.org/10.1016/j.micpath.2021.104744).
  12. Bauer AW, Kirby WM, Sherris JC, Turck M. Antibiotic susceptibility testing by a standardized single disk method. *Am J Clin Pathol.* 1966;45(4):493–6.
  13. Hsieh SE, Lo HH, Chen ST, Lee MC, Tseng YH. Wide host range and strong lytic activity of *Staphylococcus aureus* lytic phage Stau2. *Appl Environ Microbiol.* 2011;77(3):756–61.
  14. Institute CaLS. Guidelines by CLSI/NCCLS - CLSI informational supplement. Approved standard M100-S15. Wayne, PA: CLSI; 2005.
  15. Bou G. Minimum inhibitory concentration (MIC) analysis and susceptibility testing of MRSA. *Methods Mol Biol.* 2007;391:29–49.
  16. Geha DJ, Uhl JR, Gustaferrero CA, Persing DH. Multiplex PCR for identification of methicillin-resistant staphylococci in the clinical laboratory. *J Clin Microbiol.* 1994;32(7):1768–72.
  17. Sauer P, Gallo J, Kesselova M, Kolar M, Koukalova D. Universal primers for detection of common bacterial pathogens causing prosthetic joint infection. *Biomed Pap Med Fac Univ Palacky Olomouc Czech Repub.* 2005;149(2):285–8.
  18. Thompson JM, Gundogdu A, Stratton HM, Katouli M. Antibiotic resistant *Staphylococcus aureus* in hospital wastewaters and sewage treatment plants with special reference to methicillin-resistant *Staphylococcus aureus* (MRSA). *J Appl Microbiol.* 2013;114(1):44–54.
  19. Tong SYC, Davis JS, Eichenberger E, Holland TL, Fowler VG. *Staphylococcus aureus* infections: epidemiology, pathophysiology, clinical manifestations, and management. *Clin Microbiol Rev.* 2015;28(3):603–61.
  20. Sardana K, Manchanda V, Rajpal M, Garg VK, Chauhan DS. Bacterial pyoderma in children and therapeutic options including management of community-acquired methicillin resistant *Staphylococcus aureus*. *Int J Dermatol.* 2007;46(3):309–13.
  21. Ki V, Rotstein C. Bacterial skin and soft tissue infections in adults: A review of their epidemiology, pathogenesis, diagnosis, treatment and site of care. *Can J Infect Dis Med Microbiol.* 2008;19(2):173–84.
  22. Leclercq R. Mechanisms of resistance to macrolides and lincosamides: nature of the resistance elements and their clinical implications. *Clin Infect Dis.* 2002;34(4):482–92.
  23. Ito T, Katayama Y, Asada K, Mori N, Tsutsumimoto K, Tiensasitorn C, et al. Structural comparison of three types of staphylococcal cassette chromosome mec integrated in the chromosome in methicillin-resistant *Staphylococcus aureus*. *Antimicrob Agents Chemother.* 2001;45(5):1323–36.
  24. Ladhani S, Garbashi M. Staphylococcal skin infections in children: rational drug therapy recommendations. *Paediatr Drugs.* 2005;7(2):77–102.
  25. Sagova-Mareckova M, Ulanova D, Sanderova P, Omelka M, Kamenik Z, Olsovska J, et al. Phylogenetic relatedness determined between antibiotic resistance and 16S rRNA genes in actinobacteria. *BMC Microbiol.* 2015;15:81. [doi:10.1186/s12866-015-0416-6](https://doi.org/10.1186/s12866-015-0416-6).
  26. Manohar P, Tamhankar AJ, Lundborg CS, Nachimuthu R. Therapeutic Characterization and Efficacy of Bacteriophage Cocktails Infecting *Escherichia coli*, *Klebsiella pneumoniae*, and *Enterobacter* Species. *Front Microbiol.* 2019;10:574. [doi:10.3389/fmicb.2019.00574](https://doi.org/10.3389/fmicb.2019.00574).
  27. Mattila S, Ruotsalainen P, Jalasvuori M. On-Demand Isolation of Bacteriophages Against Drug-Resistant Bacteria for Personalized Phage Therapy. *Front Microbiol.* 2015;6:1271. [doi:10.3389/fmicb.2015.01271](https://doi.org/10.3389/fmicb.2015.01271).
  28. Oechslin F. Resistance Development to Bacteriophages Occurring during Bacteriophage Therapy. *Viruses.* 2018;10(7):351.
  29. O'Flaherty S, Ross RP, Meaney W, Fitzgerald GF, Elbreki MF, Coffey A. Potential of the polyvalent anti-*Staphylococcus* bacteriophage K for control of antibiotic-resistant staphylococci from hospitals. *Appl Environ Microbiol.* 2005;71(4):1836–42.
  30. Mann NH. The potential of phages to prevent MRSA infections. *Res Microbiol.* 2008;159(5):400–5.
  31. Clark JR, March JB. Bacteriophages and biotechnology: vaccines, gene therapy and antibacterials. *Trends Biotechnol.* 2006;24(5):212–8.

## Author biography

**Manjunath Nandihalli Shetru**, Associate Professor & Head

**Maribasappa Karched**, Associate Professor  <https://orcid.org/0000-0001-8927-6617>

**Dayanand Agsar**, Professor & Vice Chancellor

**Rangaswamy B E**, Professor

**Cite this article:** Shetru MN, Karched M, Agsar D, Rangaswamy B E. *In vitro* lytic efficacy of bacteriophages against multidrug-resistant pathogenic bacterial species isolated from pyogenic skin infections. *Indian J Microbiol Res* 2022;9(1):14-23.

# Thermogravimetric and combustion efficiency analysis of *Jatropha curcas* biodiesel and its derivatives

Vinay Atgur, G. Manavendra, G. P. Desai, B. Nageswara Rao, I. M. Rizwanul Fattah, Badr A. Mohamed, Nazaruddin Sinaga & H. H. Masjuki

To cite this article: Vinay Atgur, G. Manavendra, G. P. Desai, B. Nageswara Rao, I. M. Rizwanul Fattah, Badr A. Mohamed, Nazaruddin Sinaga & H. H. Masjuki (2022): Thermogravimetric and combustion efficiency analysis of *Jatropha curcas* biodiesel and its derivatives, *Biofuels*, DOI: [10.1080/17597269.2022.2090136](https://doi.org/10.1080/17597269.2022.2090136)

To link to this article: <https://doi.org/10.1080/17597269.2022.2090136>



Published online: 01 Jul 2022.



Submit your article to this journal [↗](#)





View related articles [↗](#)



View Crossmark data [↗](#)



# Thermogravimetric and combustion efficiency analysis of *Jatropha curcas* biodiesel and its derivatives

Vinay Atgur<sup>a,b</sup> , G. Manavendra<sup>b</sup>, G. P. Desai<sup>c</sup>, B. Nageswara Rao<sup>a</sup> , I. M. Rizwanul Fattah<sup>d,e</sup>, Badr A. Mohamed<sup>f</sup>, Nazaruddin Sinaga<sup>g</sup> and H. H. Masjuki<sup>h</sup>

<sup>a</sup>Department of Mechanical Engineering, Koneru Lakshmaiah Education Foundation (KLEF), Guntur, Andhra Pradesh, India; <sup>b</sup>Department of Mechanical Engineering, Bapuji Institute of Engineering and Technology (BIET), Davangere, Karnataka, India; <sup>c</sup>Department of Chemical Engineering, Bapuji Institute of Engineering and Technology (BIET), Davangere, Karnataka, India; <sup>d</sup>Centre for Green Technology, Faculty of Engineering and IT, University of Technology Sydney, Ultimo, NSW, Australia; <sup>e</sup>Department of Mechanical/Electrical Engineering, College of Engineering, Universiti Tenaga Nasional, Kajang, Selangor, Malaysia; <sup>f</sup>Department of Agricultural Engineering, Cairo University, Giza, Egypt; <sup>g</sup>Mechanical Engineering Department, Engineering Faculty, Diponegoro University, Semarang, Central Java, Indonesia; <sup>h</sup>Department of Mechanical Engineering, Faculty of Engineering, International Islamic University, Malaysia, Kuala Lumpur, Malaysia

## ABSTRACT

Thermal behavior of diesel, *Jatropha curcas* methyl ester (JOME), and its B20 blend (20% biodiesel and 80% diesel) are examined from the profiles of thermogravimetry – differential scanning calorimetry (TG-DSC) under air. TG profiles of samples indicate the mass loss steps to volatilization and combustion of methyl esters. Due to the higher temperature combustion of the intermediate stable compounds that are formed, the peak temperature of combustion is high for JOME compared to diesel and B20 blend. DSC profiles of diesel and B20 JOME indicate an endothermic peak associated with the vaporization of methyl esters for B20 JOME and the volatilization of a small fraction of the diesel. The ignition temperature for diesel and B20 blend is 128 °C, whereas JOME has an ignition temperature of 220 °C. The burnout temperatures for the diesel, JOME, and B20 blend are 283.24, 470.02, and 376.92 °C, respectively. The ignition index for the B20 blend was found to be 73.73% more compared to diesel. The combustion index for the B20 blend was found to be 37.81% higher compared to diesel. The B20 blend exhibits high enthalpy, better thermal stability, and a reduced peak temperature of combustion, with an improved combustion index and an intensity of combustion making it nearly comparable with diesel.

## ARTICLE HISTORY

Received 10 February 2022  
Accepted 11 June 2022

## KEYWORDS

Combustion; *jatropha* oil methyl ester; heat flow; thermal degradation

## Introduction

The rate at which global warming is accelerating is concerning and must be addressed. One of the fundamental reasons is the indiscriminate use of fossil fuels, which has resulted in the degradation of natural resources. Diesel engines effectively delivered efficient power while drastically harming living beings. Because these nonrenewable energy supplies are depleting, the world is focusing on alternate fuel sources [1,2]. Biofuel is a green fuel considered to be renewable [3–5]. Fuels derived from vegetable oils or animal fat have less sulfur content, low particulate emission, and a neutral contribution of CO<sub>2</sub> to the environment [6–9].

Stability is the major concern with using *Jatropha curcas* oil as engine fuel. Poor oxidation and thermal stability result in gum formation leading to problems with long storage [10,11]. Among various non-edible oil sources, *jatropha* oil has the potential to produce a large quantity of biodiesel [12,13]. Double bonds in the mono-alkyl esters of biodiesels are responsible for the oxidation process, which begins with the loss of hydrogen atoms [14]. After that, newly developed radicals react with oxygen, forming peroxide, giving rise to more alkyl radicals. Furthermore,

this process consumes esters and ends with the formation of stable compounds like ketones, aldehydes, etc. [5,15,16]. These are more harmful emissions than HC and CO. Petroleum oils are stable at distillation temperature. Straight-run gasoline (or 'naphtha') is a result of fractional distillation of crude oil that boils between 30 °C and roughly 200 °C [17]. Vegetable oils contain unsaturated compounds that oxidize at room temperature to 250 °C, leading to the formation of polymeric compounds by a condensation reaction [18].

Thermal analysis techniques are being used to analyze thermal stability, oxidative reaction, volatilization, decomposition, and combustion [19–21]. One technique used to evaluate thermal stability is thermogravimetric analysis (TGA). This approach elucidates the physical (adsorption, desorption, and phase transitions) and chemical (chemisorption and thermal decomposition) phenomena of the substances being described [20]. Several researchers conducted thermal analyses to better understand the combustion behavior and stability of fossil fuels, which has a substantial impact on the industrial economy [22,23]. Farias *et al.* [24] examined biodiesel blends' thermal stability in 20% passion fruit, 20% castor oil biodiesel, and 20% biodiesel blend of passion fruit and castor oil. The TG curve

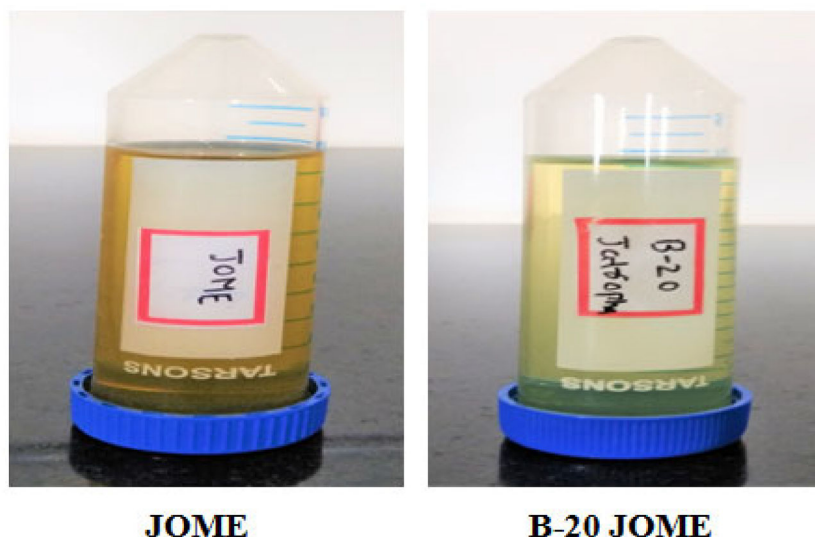


**Figure 1.** Biodiesel and its blends produced from *Jatropha curcas*.

JOME: Jatropha oil methyl ester B-20: JOME/B20 JOME: 20% jatropha biodiesel blend with diesel

**Table 1.** Composition (wt%) of diesel, JOME and ASTM biodiesel.

Element	Diesel	Jatropha methyl ester	ASTM biodiesel
Carbon (C)	83.80	75.02	77
Hydrogen (H)	12.2	12.00	12
Nitrogen (N)	0	–	–
Sulfur (S)	0.23	–	0.05
Oxygen (O <sub>2</sub> )	1	9.82	11
C/H ratio	7.0	6.3	–

indicated a higher stability of castor oil biodiesel when compared to that of passion fruit. The presence of oleic and linoleic acids in the passion fruit leads to low thermal stability due to high oxidation. Blends of passion fruit and castor oil biodiesel (1:1 proportions) indicate high thermal stability, whereas high stability in 1:2 proportions is due to the ricinoleic acid content in castor oil. Santos *et al.* [25] have investigated the thermal stability and physicochemical properties of biodiesels produced from cotton, sunflower, palm oil, and their B10 blends. The TG curve of the palm oil indicates a high initial temperature of decomposition and two mass loss steps, whereas there is one mass loss in the case of sunflower oil and cotton oil. The high onset temperature of cotton oil biodiesel indicates high thermal stability compared to palm and sunflower oil biodiesel. Blends have a high decomposition temperature. Volli and Purkait [26] have examined the thermo-chemical behavior of mustard, soybean, olive, and karanja oils. They conducted Thermogravimetry-Derivative Thermogravimetry (TG-DTG) experiments in a nitrogen atmosphere up to 600 °C with heating rates of 10, 20, 30, 50, and 100 °C/min. They observed a single stage of decomposition. High activation energy was noticed in karanja, followed by soybean, mustard and olive oils. Dwivedi and Sharma [27] studied the oxidation and thermal stability of *Pongamia* biodiesel deterioration in long storage. They examined the oxidation stability, onset and offset temperature, and activation energy for various blends of *Pongamia* biodiesel with 100–500 ppm of pyrogallol (PY) antioxidant and 0.5–2 mg/L iron metal contaminants. Thermal degradation of the samples follows the first-order reaction. The addition of PY antioxidants increases the induction period and activation energy, which will be decreased with the addition of iron metal contaminants. John *et al.* [28] used fuel properties

following spectrometric methods like Gas Chromatography Mass Spectrometry (GC-MS), and Fourier-transform infrared spectroscopy (FTIR) with TG-DSC to assess the quality of hemp (*Cannabis sativa* L.) biodiesel. The results of Differential scanning calorimetry (DSC) and TG-DTG are in good agreement with the GC-MS and FTIR results. Wnorowska *et al.* [29] examined the effect of fuel additives on different fuels to analyze the combustion profiles. Halloysite was used as a fuel additive and generated TG-DTG profiles for analyzing the combustion profile.

Leonardo *et al.* [30] used thermogravimetry methods to determine the volatility parameters for diesel S10 fuel. Platinum and aluminum pans are used for experimentation from ambient temperature to 580 °C with a heating rate of 10 °C/min. Experiments were performed in both closed and open pans. When using open pans, boiling occurs at a lower temperature due to the dragging effect of purge gas. Donoso *et al.* [31] considered the biowaste generated from the wine industry in their oxidation stability study. Grapeseed oil fatty acid ethyl ester and methyl esters were obtained from grape marc and bioethanol. Grapeseed oil ethyl ester satisfies the European Standard (EN) 14214 standard except for oxidation stability. Natural antioxidants obtained from the extraction process were added to bio-fuel. Grapeseed oil fatty acid methyl ester showed improved oxidation stability compared to ethyl esters. The addition of an antioxidant improved the oxidation stability of grapeseed oil ethyl ester, but has no effect on methyl esters.

The bulk of the publications in the literature completed engine research by empirical testing; this is time-consuming and it takes a huge quantity of fuel to forecast the combustion behavior. These experiments can be minimized through TG-DSC analysis. In the present work, thermoanalytical methods have been adopted to analyze the combustion behavior, which requires small samples. This paper examines the thermal behavior of diesel, Jatropha oil methyl ester (JOME), and its 20% JOME blend with diesel (B20) blend from the profiles of DSC and TG-DTG under atmospheric air. The novelty of this study is to compare diesel, *Jatropha curcas* biodiesel, and a 20% blend of jatropha biodiesel and diesel using the abovementioned

**Table 2.** Properties of diesel and biodiesel.

Fuel	Calorific value (MJ/kg)	Kinematic viscosity @40 °C (cSt)	Cetane value	Density (kg/m <sup>3</sup> )	Flash point (°C)	Pour point (°C)	Cloud point (°C)
Diesel	44.22	2.87	47.8	840	76	−3	6.5
JOME	39.79	4.73	52	862.2	182.5	3	3
B20 JOME	44.10	3.99	49	840.2	93.5	−3	4

**Table 3.** Structure and fatty acid composition (%) of JOME.

Fatty acids	Structure	Composition (%)
Lauric	12:0	–
Myristic	14:0	5
Palmitic	16:0	22
Stearic	18:0	5.5
Oleic	18:1	49.5
Linoleic	18:2	12
Linolenic	18:3	0.2
Arachidic	20:0	0.5
Others		4
Saturated		38.5
Unsaturated		61.5

methods. Peak combustion temperature, enthalpy, onset–offset temperature, stability, ignition, and burnout temperature are reported. The DTG curve is utilized to evaluate the combustion index (S) and intensity of combustion ( $H_f$ ). This study analyzes combustion behavior and storage conditions, which will be helpful in optimizing fuel blends, thereby reducing the number of engine bench tests.

## Materials and testing

### Materials

JOME was procured from the Centre for Information and Demonstration of Biofuels Production and Research (CIDBPR), Biofuel Park Madenur, Hasan. *Jatropha curcas* L. is a poisonous, semi-evergreen shrub or small tree, reaching a height of 6 m. This plant originated from Mexico. Portuguese traders spread it across Asia and Africa as a hedge plant. It belongs to the family Euphorbiaceae [32]. The blends of JOME (i.e. B20 JOME) were homogenized initially with a magnetic stirrer for 10 min, followed by 20 min in an ultrasonicator. Appropriate glassworks are used while preparing the blends by volumetric proportion (pipette, graduate beaker, and volumetric flask). Figure 1 shows the prepared biodiesels (JOME and B20 JOME).

Table 1 gives the composition of diesel, JOME and American Society for Testing and Materials (ASTM) biodiesel, whereas Table 2 presents the properties of diesel, JOME, and its B20 blend. JOME has less carbon and hydrogen content and a lower calorific value compared to diesel due to its significant content of O<sub>2</sub> [33]. Table 3 gives the fatty acid content of JOME. A high level of unsaturated fatty acids, 61.5%, reduces the fuel quality [34]. Saturated fatty acids like palmitic (16:0) and stearic (18:0) acids are more stable than unsaturated fatty acids like oleic (18:1) and linoleic (18:2) acids, resulting in lower fuel quality.

### Fourier transformer infrared spectroscopy

FTIR is used to determine the presence of different functional groups in the sample. It is also used to investigate the compounds formed by the transesterification of JOME. Interpreting infrared (IR) spectra is of immense help in structural determination. IR spectroscopy analysis also clarifies the

**Figure 2.** Hot Disk TPS 500 Thermal Constants Analyzer.

concentration of bands using transmittance values. IR spectra are recorded in the range of 3000–700 cm<sup>−1</sup>. A Perkin Elmer Spectrum Two FT-IR instrument made in the USA was used for the experimentation.

### Thermal property analyzer

Physical properties (like density, viscosity, thermal conductivity, and specific heat) are essential for analyzing the transient phase. Experimental evaluation of these transport properties is involved due to variation in composition from one fuel to another. Because of decomposition, measurements are complex over-temperature levels. They are useful in understanding the intermolecular interaction among different biodiesel molecules and the combustion behavior. Thermal conductivity, specific heat, and thermal diffusivity were determined using a Hot Disk TPS 500 Thermal Constants Analyzer made by the Hot Disk Corporation, Sweden (see Figure 2). The TPS 500 measures the properties accurately and rapidly using two types of sensors: Kapton sensors (:7577\*, 5465, 5501) and Teflon sensors (:7577\*, 5465, 5501). The TPS method is based on the transiently heated plane source.

### TG-DSC combustion experiment

DSC measures the heat flow of transition in materials in terms of temperature and time. DSC curves were obtained using an model NETZSCH STA 449F3 calorimeter made by the NETZSCH group, Germany (Figure 3). Atmospheric air was chosen as a medium. The heating rate was 10 °C/min. DSC consists of T-Zero calibration and enthalpy/temperature calibration. Two experiments were performed in T-Zero calibration: (i) without a sample to obtain the baseline and (ii) with a large (95 mg) sapphire disk on both samples and reference positions (without the pans). In enthalpy/temperature calibration, a standard metal (viz. indium) was heated to its melting transition and the heat of fusion was compared with its theoretical value. During experimentation, the alumina crucible pan was selected and hermetically sealed with a universal crimper, avoiding the splashing of the sample outside the pans and preventing sensor failure. Care was taken while



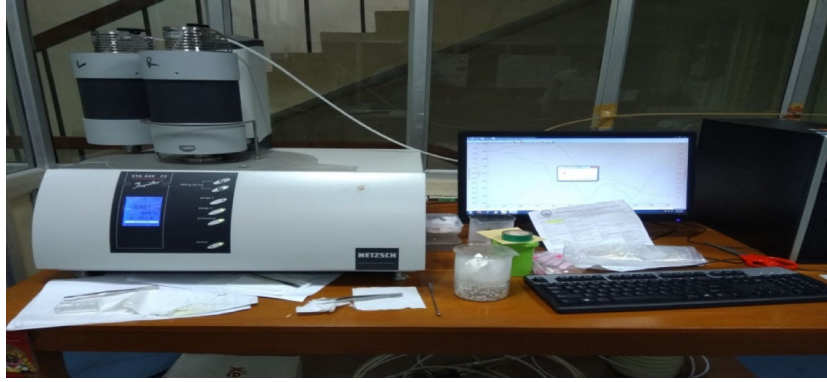


Figure 3. TG- DSC Instrument, make NETZSCH STA 449F3.

performing experiments with liquid samples. DSC curves were analyzed in terms of reaction intervals, peak temperature, heat flow, and enthalpy. TG analysis was performed to record mass loss in terms of increasing temperature in a controlled environment. TG-DTG curves provide data for pure compounds or mixtures. The curves are analyzed for stability, weight loss, maximum decomposition temperature, and onset and offset temperatures.

### Combustion characteristics of biodiesels

The combustion characteristics of diesel, JOME, and their B20 blend were evaluated in the air. Ignition temperature ( $T_i$ ) is calculated as follows. Let  $T_{max}$  be the temperature at  $DTG_{max}$ . Draw tangent lines on the TG-curve at the beginning of the TG curve and at  $T_{max}$ . The intersection of these tangent lines will be at the ignition temperature ( $T_i$ ), as shown in stages 1 and 3 of Figure 4. At burnout temperature ( $T_b$ ), 98% of conversion ( $\alpha$ ) occurs at the single stage of the combustion process.

The conversion ( $\alpha$ ) is defined as

$$\alpha_T = \frac{w_0 - w_T}{w_0 - w_f} \times 100\% \quad (1)$$

Here,  $w_0$  and  $w_f$  are the weights at the beginning and at the end of combustion.  $w_T$  is the mass at temperature  $T$ .

The ignition index ( $D_i$ ) and the burnout index ( $D_b$ ) are defined as

$$D_i = \frac{DTG_{max}}{T_{max} \times T_i} \quad (2)$$

$$D_b = \frac{DTG_{max}}{\Delta T_{0.5} \times T_{max} \times T_i} \quad (3)$$

$\Delta T_{0.5}$  is the half peak width of the DTG curve.

The combustion index ( $S$ ) is defined as

$$S = \frac{DTG_{max} \times DTG_{mean}}{T_b \times T_i^2} \quad (4)$$

$DTG_{mean}$  is defined as

$$DTG_{mean} = \frac{\alpha T_b - \alpha T_i}{((T_b - T_i)/\beta)} \quad (5)$$

The intensity of combustion,  $H_f$ , is defined as

$$H_f = T_{max} \times \ln \left( \frac{\Delta T_{0.5}}{DTG_{max}} \right) \times 10^{-3} \quad (6)$$

$S$  is the parameter of combustion index and ignition, and a high value for burnout characteristics represents better combustion properties in Equation (5).  $H_f$  is the

intensity of the combustion process, where a lower value indicates better combustion properties in Equation (6).

## Results and discussion

### Fourier transformer infrared spectroscopy

The FTIR spectrum of diesel is shown in Figure 5, indicating two strong bands of symmetric and asymmetric stretching vibration of C-H, at  $2922 \text{ cm}^{-1}$  and  $2854 \text{ cm}^{-1}$ , respectively. The band at  $1745 \text{ cm}^{-1}$  indicates a small variation in stretching vibration due to the carbonyl group ( $\text{-C=O}$ ).

Figure 6 shows the FTIR spectrum for JOME. As in diesel, the stretching vibration results in two strong bands (viz. symmetric and asymmetric stretching vibrations of C-H), at  $2923 \text{ cm}^{-1}$  and  $2854 \text{ cm}^{-1}$ , respectively [36]. The band at  $1742 \text{ cm}^{-1}$  indicates a small variation in stretching vibration due to the carbonyl group ( $\text{-C=O}$ ). The bending vibration of  $\text{CH}_2$  and  $\text{CH}_3$  groups of biodiesel shows variations in the strong peak at  $1463 \text{ cm}^{-1}$ . Due to the wagging vibrations of the  $\text{CH}_2$  group, the biodiesel has a strong peak at  $1169 \text{ cm}^{-1}$  [37], while the peak at  $722 \text{ cm}^{-1}$  indicates the rocking vibration of  $\text{=C-H}$  groups.

Figure 7 shows FTIR spectra for B20 JOME. As in diesel and JOME, the stretching vibration results in two strong bands (viz. symmetric and asymmetric stretching vibrations of C-H), at  $2922 \text{ cm}^{-1}$  and  $2854 \text{ cm}^{-1}$ , respectively. The band at  $1745 \text{ cm}^{-1}$  indicates a small variation in stretching vibration due to the carbonyl group ( $\text{-C=O}$ ). The bending vibration of  $\text{CH}_2$  and  $\text{CH}_3$  groups of the biodiesel shows variations in strong two peaks, at  $1465 \text{ cm}^{-1}$  and  $1378 \text{ cm}^{-1}$ . Due to the wagging vibrations of the  $\text{CH}_2$  group, the biodiesel has a strong peak at  $1170 \text{ cm}^{-1}$ , while the peak at  $723 \text{ cm}^{-1}$  indicates the rocking vibration of  $\text{=C-H}$  groups.

### Thermal properties

Transport properties, shown in Table 4, varied in the following order: diesel > B20 JOME > JOME. Diesel possesses a high calorific value compared to JOME and B20 JOME [36]. In diesel, carbon numbers range from  $\text{C}_5$  to  $\text{C}_{12}$  (i.e. a low carbon number is attached to hydrogen). Decomposition of this structure is easy compared to fatty acid methyl esters (FAME) of biodiesel. Therefore, diesel possesses better transport properties when compared to JOME and B20 JOME.

Due to weaker double bond presence and a structure possessing oxygen content, biodiesels exhibit low transport properties compared to diesel and B20 blends [38]. Diesel molecules have long-chain hydrocarbons and low ignition

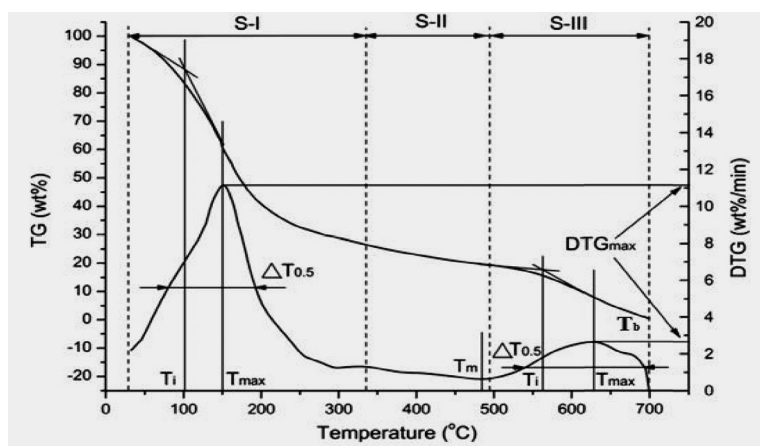


Figure 4. Combustion stages from the TG-DTG curve [35].

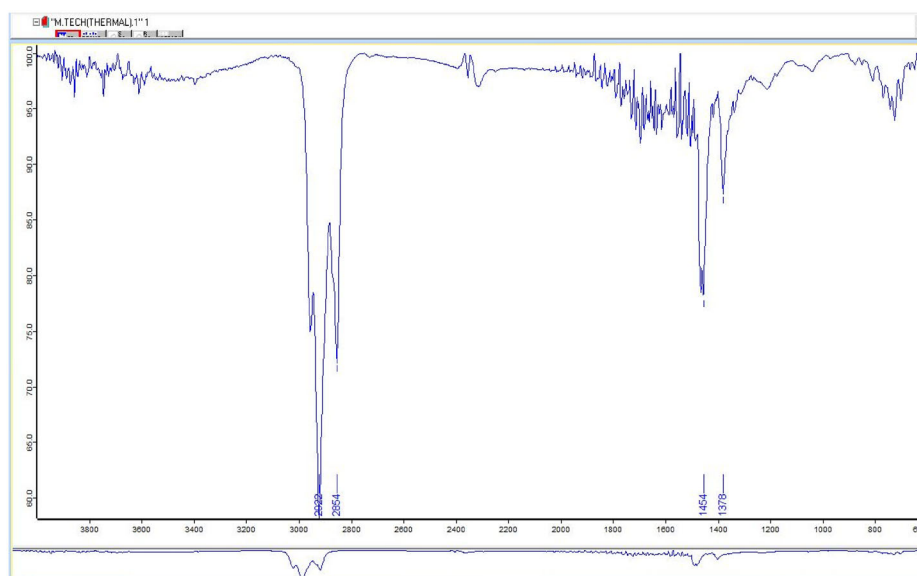


Figure 5. FTIR spectrograph of diesel.

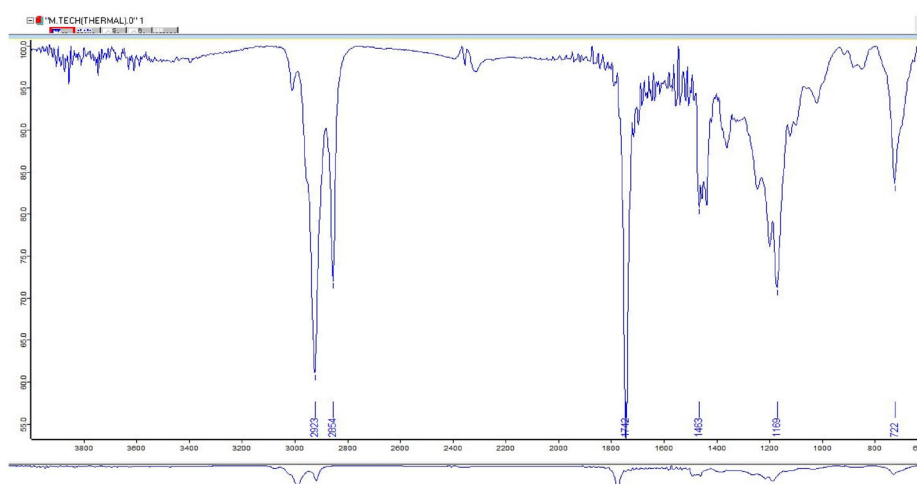


Figure 6. FTIR spectrograph of JOME.

temperature when compared to JOME. B20JOME properties merely match those of the diesel. This is the reason why the transport properties of the B20 blend are within the range of diesel and biodiesel. Kinematic viscosities of diesel, JOME, and B20 JOME are 2.87, 4.73, and 3.99 cSt, respectively. The diesel, JOME, and B20 JOME densities are 840, 862.2, and 840.2 kg/m<sup>3</sup>, respectively. Both viscosity and density decrease with increasing temperature, leading to buoyancy force. It will be

opposed by the viscous force for the heat flow. Transport properties decrease with increasing biodiesel content [39,40]. B20 JOME will be an alternative to diesel.

### DSC analysis

Generally, the combustion of hydrocarbons exhibits an exothermic reaction. The DSC thermogram of diesel (Figure 8)

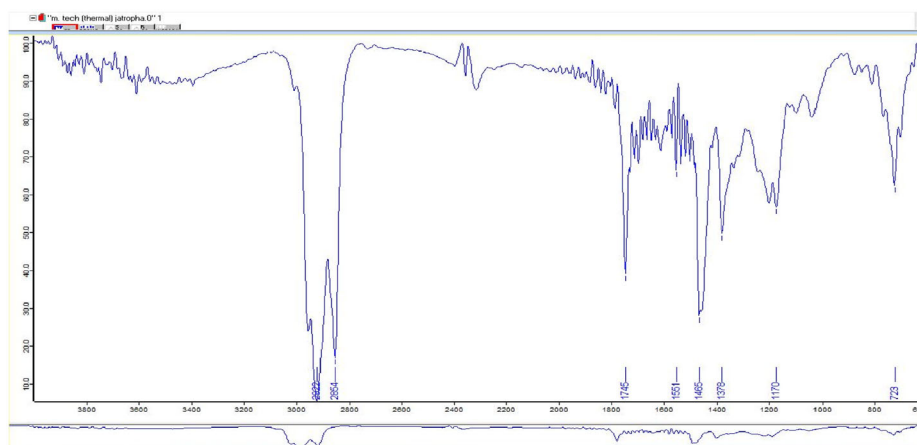


Figure 7. FTIR spectrograph of B20 JOME.

Table 4. Thermal conductivity, thermal diffusivity and specific heat capacity.

Sample	Thermal conductivity (W/mK)	Thermal diffusivity (mm <sup>2</sup> /s)	Specific heat (MJ/m <sup>3</sup> K)
Diesel	0.3381	1.325	0.2553
JOME	0.2358	0.4116	0.5728
B20 JOME	0.3087	0.7944	0.3886

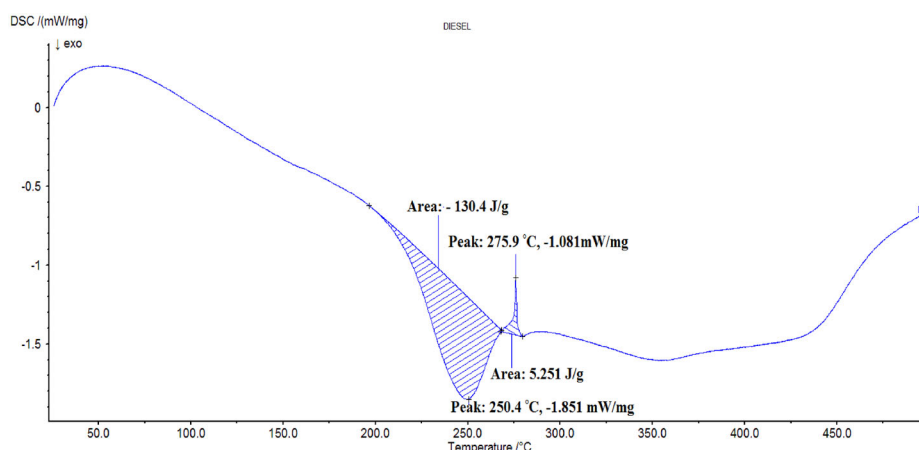


Figure 8. DSC combustion curve for diesel.

indicates an endothermic reaction at 34–100 °C. This is known as an evaporation zone, and it is where the fuel prepares for combustion by evaporating a small fraction occurring through one step endothermic cracking reaction. It is termed diesel distillation [41,42]. Combustion peak temperature occurs at 250.4 °C with enthalpy 130.4 J/g as diesel consists of C<sub>5</sub>–C<sub>12</sub> with a boiling range of 180–371 °C. Further, it starts burning and dissipating more energy to the environment.

The DSC combustion curve of JOME (Figure 9) exhibits a reaction zone occurring at 43–435 °C with a peak at 292.1 °C. The combustion reaction zone of biodiesel occurs at a high-temperature range when compared to diesel; the direct use of biodiesel results in hard burning in engine motors. A high cetane number of fuels in engines means they experience a short delay in biodiesel burning [9]. Biodiesels with a low cetane number have a lead time that produces a delay in burning, resulting in insufficient engine performance [43,44]. Biodiesel has a faster combustion behavior and a higher combustion temperature than conventional diesel due to its higher oxygen content. A higher cetane number in JOME yields a short delay time in fuel combustion, and more time is taken for complete combustion. JOME's combustion reaction range, as well as its combustion peak temperature, can be expected to be higher compared to those of diesel [38].

The combustion of JOME exhibits an exothermic reaction in the air due to a weaker double bond presence [45,46].

The combustion thermogram of the B20 blend (Figure 10) is very close to that of diesel, with a reaction zone occurring at 63–465 °C. Initially, it shows an endothermic reaction up to 63 °C. The peak temperature of combustion in Table 5 is 266.5 °C, close to that of diesel, with an enthalpy of 147.5 J/g. In the first reaction, interval combustion of diesel takes place, whereas in the second reaction, interval biodiesel combustion takes place [47]. Biodiesel and diesel molecules create a homogeneous mixture. Hence, B20 combustion is close to that of diesel, and the reaction starts early, resulting in easy combustion. From the action region of the DSC combustion curve [48,49], the cetane number of biodiesel is found to be lower than that of diesel. Blending is necessary. Otherwise, direct use of biodiesel in the engine results in a time delay leading to insufficient engine performance. Table 5 compares the reaction region, peak temperature of combustion, heat flow, and enthalpy.

### Thermal stability analysis

The TG-DTG curve of diesel in synthetic air presents one complex mass loss step at 40–280 °C. Behavior and

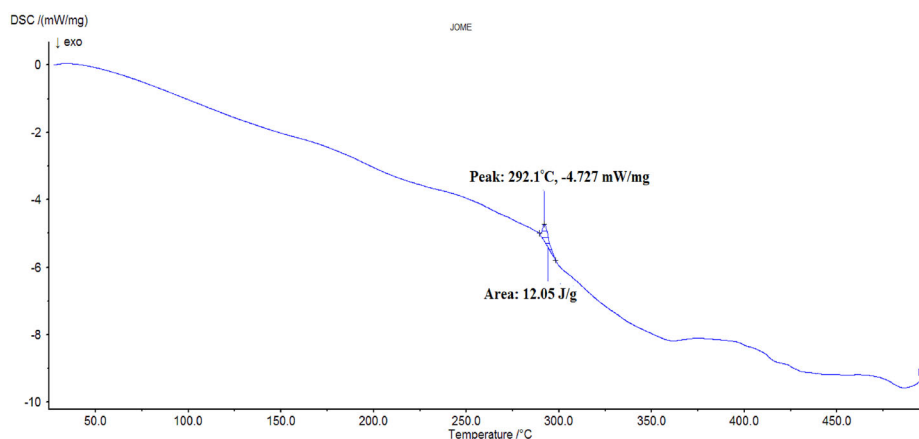


Figure 9. DSC combustion curve for JOME.

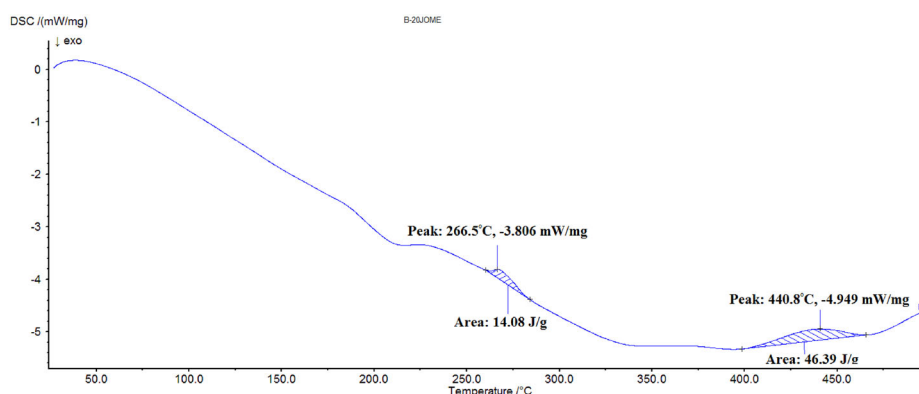


Figure 10. DSC combustion curve for B20 JOME.

Table 5. Heat flow and enthalpy at peak temperature.

Sample	Reaction region (°C)	Peak temperature (°C)	Heat flow (mW/mg)	Enthalpy (J/g)
Diesel	34–270	250.4	−1.851	130.4
JOME	43–435	292.1	−4.727	12.05
B20 JOME	63–465	266.5	−3.808	147.5

properties depend on the length of diesel molecules [50]. Longer chains of molecules have higher boiling points. The opposite properties of gasoline characterize diesel. Hydrocarbon molecules must oxidize with the formation of peroxides initially. Other products of incomplete oxidation are for auto-ignition to start easily [51]. Initially, there is evaporation and combustion of methyl esters, as well as the evaporation and combustion of the other components of diesel-like naphthenes, paraffin, olefins and aromatics with  $C_{12}$ – $C_{18}$ .

In the diesel TGA-DTG curve shown in Figure 11, the combustion reaction occurs between 40 and 495.74 °C, with a peak temperature of 184.5 °C. Diesel fuel mainly contains  $C_5$ – $C_{12}$  with a boiling range of 180–376 °C; at around 45 °C, diesel starts to burn and dissipate energy to the environment, and 99.50% of mass loss occurs at 498.1 °C in a 47.49 min time span; the remaining 0.5% mass loss represents soot particles which are not burned out [52].

JOME exhibits the reaction at 140–490 °C with a peak temperature of 277.3 °C (Figure 12). Biodiesel shows two steps of the reaction. According to the literature, JOME has major fatty acid contents of oleic acid, palmitic acid, linolenic acid, and stearic acid, which are 49.5%, 22%, 12%, and 5.5%, respectively. The transesterification reaction mechanism makes the biodiesel less stable. Also, the

monoglyceride molecules make the sample less stable [53]. Initially, there is an evaporation of methyl esters followed by the decomposition of mono, di, and triglycerides and fatty acids with high-carbon oleic and linoleic acids [40,54]. The carbonization of the sample occurs with 1.64% weight loss. The total loss is  $\approx$ 98.36%. The combustion process takes place over an interval of 47.43 min. B20 JOME exhibits only one reaction interval, indicating better diesel and biodiesel mixing.

Figure 13 shows the TG-DTG curve for B20 JOME. The TG-DTG thermograms for diesel and the B20 blend are very close to each other, and weight losses are lower than that of pure biodiesel [55,56]. The blend starts to decompose from 40 °C to 430 °C, with a peak temperature of 182.8 °C. Combustion of the B20 blend takes place over a span of 47.39 min with a residual mass loss of 0.73%. The first reaction is the evaporation of the methyl esters and the light fraction of carbons [57,58]. The second reaction is the decomposition of the mono, di, and triglycerides and methyl esters of fatty acids with high carbon content [59,60]. Finally, the carbonization of the sample occurs from 400 to 500 °C with a mass loss of 99.27%.

Diesel is less thermally stable when compared to biodiesel due to greater tension in the chains of the complex structured biodiesel [56]. Hence, the thermal stability of the blends decreases with an increasing proportion in the

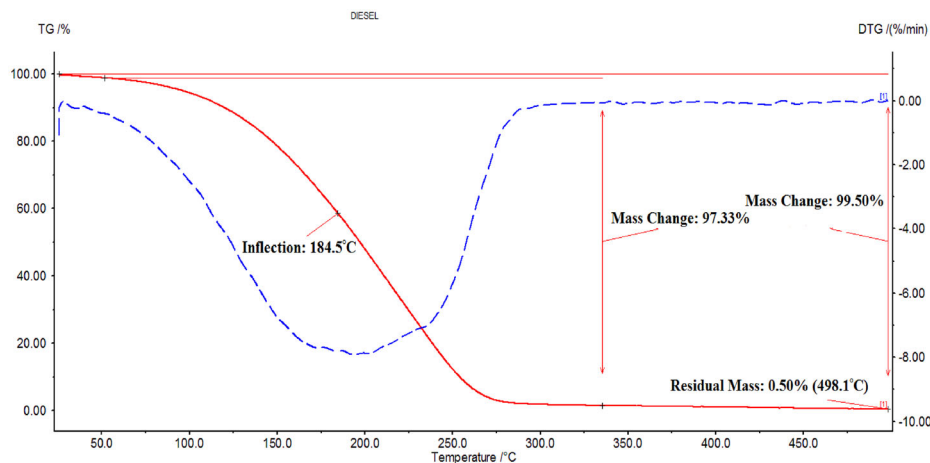


Figure 11. TG-DTG curve for diesel.

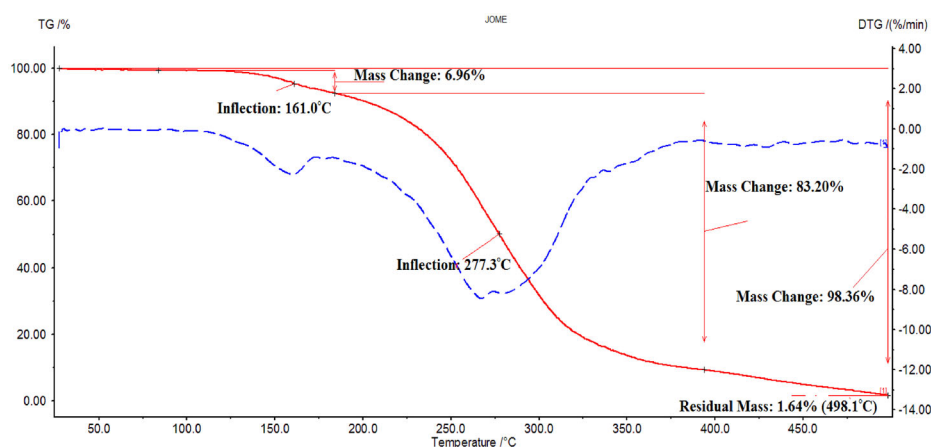


Figure 12. TG-DTG curve for JOME.

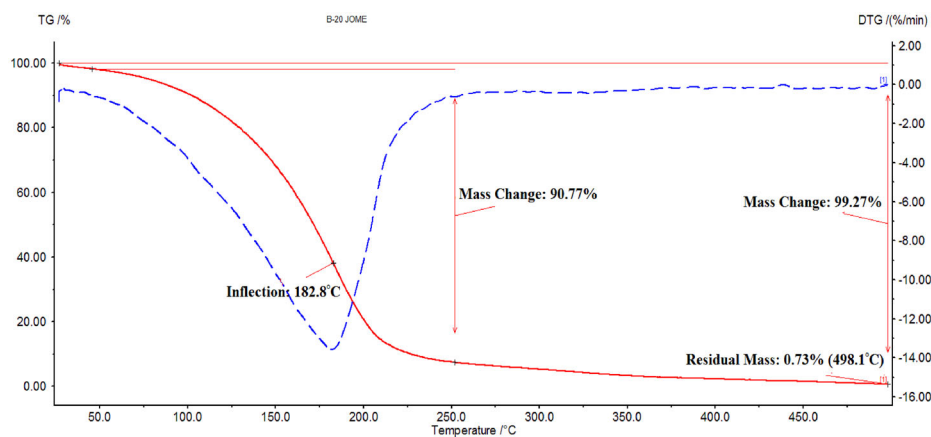


Figure 13. TG-DTG curve for B20 JOME.

T G-DT G: Thermogravimetry-Derivative Thermogravimetry B-20 JOME/B20 JOME: 20% jatropha biodiesel blend with diesel

Table 6. Onset, offset, reaction region, maximum temperature, and weight loss of biodiesels.

Sample	Onset temperature $T_e$ (°C)	Offset temperature $T_o$ (°C)	Reaction region (°C)	Decomposition temperature, $T_{max}$ (°C)	Weight loss (%) at 498.1 °C
Diesel	140	265	40–280	184.5	99.50
JOME	146	334	140–490	277.3	98.36
B20 JOME	130	230	40–430	182.8	99.27

blend. The high viscosity of the biodiesel leads to a slow evaporation process and high thermal stability of fuels [61]. It is observed that initially, the TG curves ascend because of buoyancy and the molecular adsorption effect, while TGA curves show a descending trend with increasing temperature due to volatilization of weak chemical bonds and

small molecules of biodiesel blends [25,62]. A single well-defined mass loss step could be clearly observed for all TG curves, which describes the volatilization and decomposition. The decomposition temperature increases with an increasing proportion of biodiesel in the blend. Table 6 compares the onset, offset, reaction region, maximum



**Table 7.** Ignition, burnout temperature, DTG<sub>max</sub> and T<sub>max</sub> of diesel, JOME and B20 JOME.

Sample	Ignition temperature (°C)	Burnout temperature (°C)	DTG max	Tmaxcorres DTG max (°C)
Diesel	128	283.24	7.92	184.5
JOME	220	470.02	8.44	267.52
B20 JOME	128	376.96	13.56	181.965

**Table 8.** Combustion characteristics of diesel, JOME and B20 JOME.

Sample	Ignition index $D_i \times 10^{-4}$ (wt% min <sup>-1</sup> °C <sup>-2</sup> )	Burnout index $D_b \times 10^{-6}$ (wt% min <sup>-1</sup> °C <sup>-3</sup> )	Combustion index parameter $S \times 10^{-6}$ (wt% min <sup>-2</sup> °C <sup>-3</sup> )	Intensity of combustion
Diesel	3.35	3.35	41.6	0.467
JOME	1.43	6.87	77.74	0.591
B20 JOME	5.82	4.6	57.33	0.318

temperature and weight loss. JOME demonstrates low-onset temperature and high volatility. It approaches the characteristics of diesel and improves the fuel properties.

Table 7 presents ignition temperature, burnout temperature, and maximum DTG. Compared to JOME, diesel and B20 blends have a shorter devolatilization stage, and JOME degradation represents three stages of the process as described by Ren *et al.* [35]. Table 8 presents the combustion index, which differs in air and oxidation environments due to combustion's high degradation temperature [63]. Low mass degradation in the later stage is due to a low combustion index. JOME has significant mass degradation after the third stage, leading to high combustion and hard burning intensity.

## Conclusion

DSC and TG-DTG are useful tools for assessing the combustion behavior and thermal stability of biodiesel and its blends. Thermogravimetry and calorimetric profiles of the samples indicate the relationship of mass loss steps to volatilization and combustion methyl esters. On the basis of TG curves, thermal stability is established as JOME > B20 JOME > diesel. Diesel and B20 JOME degradation start from 40 °C, whereas JOME degradation starts from 140 °C. JOME is thermally stable up to 140 °C. This matches well with the onset and offsets temperatures. JOME presents a lower onset temperature and high volatility. It approaches the characteristics of diesel and improves the fuel properties. JOME presents more decomposition steps with high decomposition temperatures indicative of the formation of a more stable compound due to the oxidation process. The combustion of the stable compounds that are formed takes place at high temperatures. The peak temperature of combustion for diesel, JOME, and B20 JOME is 250.4, 292.1, and 266.5 °C, respectively. DSC profiles of the diesel and B20 JOME show an endothermic peak related to the vaporization of methyl esters for B20 JOME and the volatilization of a small fraction of the diesel. Biodiesel exhibits high enthalpy despite satisfactory performance as a fuel; its high viscosity causes poor fuel atomization in the combustion of the engine and serious engine problems, requiring blending with petroleum diesel. The B20 blend exhibits high enthalpy when compared to diesel, with a reduced peak temperature.

## Acknowledgements

The authors express their gratitude to the Visvesvarayya Technological University, Belgaum, and the Sophisticated Analytic Instrumentation Facility Center, Indian Institute of Technology, Madras, for providing facilities to carry out experiments.

## Competing interests

The authors declare that they have no competing interests.

## Funding

This work is supported by the Universiti Tenaga Nasional grant no. IC6-BOLDREFRESH2025 (HCR) under the BOLD2025 Program.

## ORCID

Vinay Atgur  <http://orcid.org/0000-0001-6423-770X>

B. Nageswara Rao  <http://orcid.org/0000-0003-1620-6188>

## Data availability statement

The data supporting this study's findings are available from the corresponding author upon reasonable request.

## References

- [1] Kumar S, Dinesha P. Use of alternative fuels in compression ignition engines: a review. *Biofuels*. 2019;10(4):525–535.
- [2] Mishra VK, Goswami R. A review of production, properties and advantages of biodiesel. *Biofuels*. 2018;9(2):273–289.
- [3] Thiagarajan S, Varuvel E, Karthickeyan V, et al. Effect of hydrogen on compression-ignition (CI) engine fueled with vegetable oil/biodiesel from various feedstocks: a review. *Int J Hydrogen Energy*. 2022. <https://doi.org/10.1016/j.ijhydene.2021.12.147>
- [4] Fattah IMR, Ong HC, Mahlia TMI, et al. State of the art of catalysts for biodiesel production. *Front. Energy Res*. 2020;8:101.
- [5] Viswanathan K, Ikhsan Taipabu M, Wu W. Novel petit grain bitter orange waste peel oil biofuel investigation in diesel engine with modified fuel injection pressure and bowl geometry. *Fuel*. 2022;319:123660.
- [6] Seela CR, Ravi Sankar B, Sai Kiran D. Influence of biodiesel and its blends on CI engine performance and emissions: a review. *Biofuels*. 2017;8(1):163–179.
- [7] Kumar A, Subramanian KA. Experimental investigation on effects of karanja biodiesel (B100) on performance, combustion, and regulated and GHG emissions characteristics of an automotive diesel engine. *Biofuels*. 2020;11(3):239–250.
- [8] Swaminathan C, Sarangan J, Michael BS. Investigation of performance and emission characteristics of IC engine using sunflower oil methyl ester as fuel with oxygenated additive and EGR. *Biofuels*. 2019;10(5):583–589.

- [9] Veza I, Afzal A, Mujtaba MA, et al. Review of artificial neural networks for gasoline, diesel and homogeneous charge compression ignition engine. *Alexandria Eng J.* **2022**;61(11): 8363–8391.
- [10] Manaf ISA, Embong NH, Khazaai SNM, et al. A review for key challenges of the development of biodiesel industry. *Energy Convers Manage.* **2019**;185:508–517.
- [11] Iyer R. A review on the role of allylic and bis allylic positions in biodiesel fuel stability from reported lipid sources. *Biofuels (London).* **2017**;8(5):543–554.
- [12] Kavitha KR, Beemkumar N, Rajasekar R. Experimental investigation of diesel engine performance fuelled with the blends of *Jatropha curcas*, ethanol, and diesel. *Environ Sci Pollut Res Int.* **2019**;26(9):8633–8639.
- [13] Borah N, Mapelli S, Pecchia P, et al. Variability of growth and oil characteristics of *Jatropha curcas* L. in North-east India. *Biofuels.* **2021**;12(3):327–337.
- [14] Azad AK, Adhikari J, Halder P, et al. Performance, emission and combustion characteristics of a diesel engine powered by macadamia and grapeseed biodiesels. *Energies.* **2020**;13(11): 2748.
- [15] Viswanathan K, Wang S, Esakkimuthu S. Impact of yttria stabilized zirconia coating on diesel engine performance and emission characteristics fuelled by lemon grass oil biofuel. *J Therm Anal Calorim.* **2021**;146(5):2303–2315.
- [16] Taipabu MI, Viswanathan K, Wu W, et al. Production of renewable fuels and chemicals from fats, oils, and grease (FOG) using homogeneous and heterogeneous catalysts: design, validation, and optimization. *Chem Eng J.* **2021**;424:130199.
- [17] Thomas A. Chapter five – automotive fuels. In: Arcoumanis C, editor. *Internal combustion engines*. London: Academic Press; **1988**. p. 213–270.
- [18] Xia Y, Larock RC. Vegetable oil-based polymeric materials: synthesis, properties, and applications. *Green Chem.* **2010**;12(11): 1893–1909.
- [19] Rial RC, de Freitas ON, Santos G, et al. Evaluation of the oxidative and thermal stability of soybean methyl biodiesel with additions of dichloromethane extract ginger (*Zingiber officinale* Roscoe). *Renew Energy.* **2019**;143:295–300.
- [20] Balajii M, Niju S. Biochar-derived heterogeneous catalysts for biodiesel production. *Environ Chem Lett.* **2019**;17(4):1447–1469.
- [21] Lamprecht I. Chapter 4 – combustion calorimetry. In: Kemp RB, editor. *Handbook of thermal analysis and calorimetry*. Amsterdam, The Netherlands: Elsevier Science B.V.; **1999**. p. 175–218.
- [22] Chauhan BS, Kumar N, Cho HM. A study on the performance and emission of a diesel engine fueled with *Jatropha* biodiesel oil and its blends. *Energy.* **2012**;37(1):616–622.
- [23] Banapurmath NR, Tewari PG, Hosmath RS. Performance and emission characteristics of a DI compression ignition engine operated on Honge, *Jatropha* and sesame oil methyl esters. *Renew Energy.* **2008**;33(9):1982–1988.
- [24] Farias RMC, Conceição MM, Candeia RA, et al. Evaluation of the thermal stability of biodiesel blends of castor oil and passion fruit. *J Therm Anal Calorim.* **2011**;106(3):651–655.
- [25] Santos AGD, Caldeira VPS, Souza LD, et al. Study of the thermal stability by thermogravimetry for oil, biodiesel and blend (B10) of different oilseeds. *J Therm Anal Calorim.* **2016**;123(3): 2021–2028.
- [26] Volli V, Purkait MK. Physico-chemical properties and thermal degradation studies of commercial oils in nitrogen atmosphere. *Fuel.* **2014**;117:1010–1019.
- [27] Dwivedi G, Sharma MP. Experimental investigation on thermal stability of Pongamia biodiesel by thermogravimetric analysis. *Egypt J Pet.* **2016**;25(1):33–38.
- [28] John CB, Solamalai AR, Jambulingam R, et al. Estimation of fuel properties and characterization of hemp biodiesel using spectrometric techniques. *Energy Sources Part A.* **2020**;1–18. doi: [10.1080/15567036.2020.1842559](https://doi.org/10.1080/15567036.2020.1842559)
- [29] Wnorowska J, Ciukaj S, Kalisz S. Thermogravimetric analysis of solid biofuels with additive under air atmosphere. *Energies.* **2021**;14(8):2257.
- [30] Leonardo RS, Murta Valle ML, Dweck J. Thermovolumetric and thermogravimetric analysis of diesel S10. *J Therm Anal Calorim.* **2020**;139(2):1507–1514.
- [31] Donoso D, Bolonio D, Lapuerta M, et al. Oxidation stability: the bottleneck for the development of a fully renewable biofuel from wine industry waste. *ACS Omega.* **2020**;5(27):16645–16653.
- [32] Fattah IMR, Masjuki HH, Kalam MA, et al. Performance and emission characteristics of a CI engine fueled with Cocos nucifera and *Jatropha curcas* B20 blends accompanying antioxidants. *Ind Crops Prod.* **2014**;57:132–140.
- [33] Singh D, Sharma D, Soni SL, et al. A comprehensive review of physicochemical properties, production process, performance and emissions characteristics of 2nd generation biodiesel feedstock: *Jatropha curcas*. *Fuel.* **2021**;285:119110.
- [34] Swathi D, Gopa BV, Rao PV, et al. Optimization of *Jatropha* methyl ester and study of its physico-chemical properties using GC-MS and FT-IR analysis. *Austin Chem Eng.* **2016**;3(2):1027.
- [35] Ren X, Meng J, Moore AM, et al. Thermogravimetric investigation on the degradation properties and combustion performance of bio-oils. *Bioresour Technol.* **2014**;152:267–274.
- [36] Posom J, Sirisomboon P. Evaluation of the thermal properties of *Jatropha curcas* L. kernels using near-infrared spectroscopy. *Biosyst Eng.* **2014**;125:45–53.
- [37] El-Seesy AI, Xuan T, He Z, et al. Enhancement the combustion aspects of a CI engine working with *Jatropha* biodiesel/decanol/propanol ternary combinations. *Energy Convers Manage.* **2020**;226:113524.
- [38] Atgur V, Manavendra G, Desai GP, et al. Thermogravimetry and calorimetric evaluation of honge oil methyl ester and its B-20 blend. *Cleaner Eng Technol.* **2022**;6:100367.
- [39] Giuliano Albo PA, Lago S, Wolf H, et al. Density, viscosity and specific heat capacity of diesel blends with rapeseed and soybean oil methyl ester. *Biomass Bioenergy.* **2017**;96:87–95.
- [40] Freire LMS, Bicudo TC, Rosenhaim R, et al. Thermal investigation of oil and biodiesel from *Jatropha curcas* L. *J Therm Anal Calorim.* **2009**;96(3):1029–1033.
- [41] Abdullah BM, Yusop RM, Salimon J, et al. Physical and chemical properties analysis of *Jatropha curcas* seed oil for industrial applications. *Int J Chem Sci Eng.* **2013**;7(12):183–186.
- [42] Vossoughi S, El-Shoubary YM. Kinetics of liquid hydrocarbon combustion using the DSC technique. *Thermochim Acta.* **1990**;157(1): 37–44.
- [43] Xue J, Grift TE, Hansen AC. Effect of biodiesel on engine performances and emissions. *Renew Sustain Energy Rev.* **2011**; 15(2):1098–1116.
- [44] Teoh YH, Masjuki HH, Kalam MA, et al. Effects of *jatropha* biodiesel on the performance, emissions, and combustion of a converted common-rail diesel engine. *RSC Adv.* **2014**;4(92):50739–50751.
- [45] Garcia-Perez M, Adams TT, Goodrum JW, et al. DSC studies to evaluate the impact of bio-oil on cold flow properties and oxidation stability of bio-diesel. *Bioresour Technol.* **2010**;101(15):6219–6224.
- [46] Atgur V, Manavendra G, Desai GP, et al. Thermal characterisation of dairy washed scum methyl ester and its b-20 blend for combustion applications. *Int J Ambient Energy.* **2021**;1–11. doi: [10.1080/01430750.2021.1909651](https://doi.org/10.1080/01430750.2021.1909651)
- [47] Dunn RO. Thermal analysis of alternative diesel fuels from vegetable oils. *J Am Oil Chem Soc.* **1999**;76(1):109–115.
- [48] Mohammed MN, Atabani AE, Uguz G, et al. Characterization of Hemp (*Cannabis sativa* L.) biodiesel blends with euro diesel, butanol and diethyl ether using FT-IR, UV-vis, TGA and DSC techniques. *Waste Biomass Valor.* **2020**;11(3):1097–1113.
- [49] Peer MS, Kasamani R, Rajamohan S, et al. Experimental evaluation on oxidation stability of biodiesel/diesel blends with alcohol addition by rancimat instrument and FTIR spectroscopy. *J Mech Sci Technol.* **2017**;31(1):455–463.
- [50] Silva WC, Castro MPP, Perez VH, et al. Thermal degradation of ethanolic biodiesel: physicochemical and thermal properties evaluation. *Energy.* **2016**;114:1093–1099.
- [51] Misutsu MY, Cavaleiro LF, Ricci TG, et al. Thermoanalytical methods in verifying the quality of biodiesel. In: Biernat K, editor. *Biofuels – status and perspective*. London: IntechOpen; **2015**. doi: [10.5772/59479](https://doi.org/10.5772/59479)
- [52] de Oliveira TF, Dweck J. Liquid phase oxidation quantitative analysis of biodiesel/diesel blends by differential TG and DTA. *J Therm Anal Calorim.* **2018**;134(3):1953–1963.
- [53] Almazrouei M, Janajreh I. Thermogravimetric study of the combustion characteristics of biodiesel and petroleum diesel. *J Therm Anal Calorim.* **2019**;136(2):925–935.

- [54] Damasceno SS, Rosenhaim R, Gondim AD, et al. Flow properties of biodiesel: correlation between TMDSC and dynamic viscosity. *J Therm Anal Calorim.* **2013**;114(3):1239–1243.
- [55] Nicolau CL, Klein ANV, Silva CAA, et al. Thermal properties of the blends of methyl and ethyl esters prepared from babassu and soybean oils. *J. Braz. Chem. Soc.* **2018**;29(8):1672–1679.
- [56] Candeia RA, Freitas JCO, Souza MAF, et al. Thermal and rheological behavior of diesel and methanol biodiesel blends. *J Therm Anal Calorim.* **2007**;87(3):653–656.
- [57] Dantas MB, Albuquerque AR, Soledade LEB, et al. Biodiesel from soybean oil, castor oil and their blends. *J Therm Anal Calorim.* **2011**;106(2):607–611.
- [58] Mujtaba MA, Muk Cho H, Masjuki HH, et al. Critical review on sesame seed oil and its methyl ester on cold flow and oxidation stability. *Energy Rep.* **2020**;6:40–54.
- [59] Conceição MM, Fernandes VJ, Araújo AS, et al. Thermal and oxidative degradation of castor oil biodiesel. *Energy Fuels.* **2007**;21(3):1522–1527.
- [60] Zhao H, Cao Y, Orndorff W, et al. Thermal behaviors of soy biodiesel. *J Therm Anal Calorim.* **2012**;109(3):1145–1150.
- [61] Shancita I, Masjuki HH, Kalam MA, et al. Comparative analysis on property improvement using Fourier transform infrared spectroscopy (FT-IR) and nuclear magnetic resonance (NMR) (<sup>1</sup>H and <sup>13</sup>C) spectra of various biodiesel blended fuels. *Energy Fuels.* **2016**;30(6):4790–4805.
- [62] Jain S, Sharma MP. Correlation development between the oxidation and thermal stability of biodiesel. *Fuel.* **2012**;102:354–358.
- [63] Niu S-l, Han K-h, Lu C-m. Characteristic of coal combustion in oxygen/carbon dioxide atmosphere and nitric oxide release during this process. *Energy Convers Manage.* **2011**;52(1):532–537.



# Thermogravimetry and calorimetric evaluation of honge oil methyl ester and its B-20 blend

Vinay Atgur<sup>a,b,\*</sup>, G. Manavendra<sup>b</sup>, G.P. Desai<sup>c</sup>, B. Nageswara Rao<sup>a</sup>

<sup>a</sup> Department of Mechanical Engineering, Koneru Lakshmaiah Education Foundation (KLEF), Deemed to Be University, Green Fields, Vaddeswaram, Guntur, 522502, Andhra Pradesh, India

<sup>b</sup> Department of Mechanical Engineering, Bapuji Institute of Engineering and Technology (BIET), Davangere, 577055, Karnataka, India

<sup>c</sup> Department of Chemical Engineering, Bapuji Institute of Engineering and Technology (BIET), Davangere, 577055, Karnataka, India

## ARTICLE INFO

### Keywords:

Combustion

Diesel

Differential scanning calorimeter (DSC)

HOME

Pyrolysis

## ABSTRACT

Thermal characterization of biofuels is useful in design, modeling and operation of the systems. This article examines thermal behavior of honge oil methyl ester (HOME) and its B-20 blend (20% of HOME and 80% of diesel) along with diesel. Differential scanning calorimetry (DSC) and thermogravimetry (TG) experiments were performed for a heating rate of 4.72 K/s. The range of combustion temperature is high for HOME when compared to that of diesel and B-20 blend due to the formation of intermediate stable compounds during combustion. Reduction in peak temperature of combustion is noticed for diesel, whereas reverse trend is for HOME and B-20 blend in oxygen to nitrogen atmosphere. TG curves indicate two phases of decomposition for diesel as well as B-20 blend and three phases for HOME. Diesel and B-20 blend starts to decompose from 313K onwards whereas HOME is thermally stable up to 408K. B-20 blend exhibits low offset temperature when compared to diesel and HOME, whereas the reaction range occurs from 331 to 578K when compared to that of diesel from 313 to 553K. Complete degradation occurs at 572.9, 596 and 696K for diesel, B-20 blend and HOME. The behavior of B-20 blend is similar to diesel with reduced emission of harmful gases. Present TG-DSC tests will be useful in optimizing the engine tests with blends.

## 1. Introduction

Biodiesel is one of the alternate energy sources, which exhibits clean burning and have benefit of non toxic, biodegradable free of sulphur and carcinogenic ring components. It consists of alkyl esters of the fatty acids like methyl and methyl esters (medium length  $C_{16}$ – $C_{18}$ ) (Swathi et al., 2016; Abdullah et al., 2013). The non-toxic, nonflammable and environmentally friendly biodiesel blends are designated by BXX in which XX is the %volume of biodiesel. The chemical composition of biodiesel is different to that of diesel, whereas it has identical fuel characteristics (Saxena et al., 2013; Conceição et al., 2007). Table 1 gives a comparison of diesel and biodiesel properties. Table 2 gives composition of diesel and biodiesels, whereas Table 3 presents the composition of diesel, HOME and ASTM biodiesel. The heating value of the biodiesel is less when compared to that of the diesel. Cetane number of the biodiesel is higher than the diesel which indicates that the biodiesel burns quickly (Ramkumar and Kirubakaran, 2016; Singh and Padhi, 2006). Sulphur emission from the biodiesel is less when compared to that of diesel.

Biodiesel has less than 24 ppm. The fuel is environmentally friendly (Posom and Sirisomboon, 2014). Among the blends tested in engine, B-20 blend gives better efficiency close to that of the diesel (Banapurmath et al., 2008a). Hence, 20% blending is economically good. Honge oil methyl esters (HOME) consist of carbon, hydrogen and significant oxygen. Having significant  $O_2$  content, HOME possesses less carbon and hydrogen content. Due to the reduced content of carbon and hydrogen, HOME will have less calorific value when compared to that of diesel. Being obtained from the transesterification process, it has high percentage of saturated fatty acid content and less unsaturated fatty acid contents. It exhibits high Cetane value, high viscosity leading to better biodiesel stability (Freire et al., 2009; Ren et al., 2014).

Fig. 1 shows the overall transesterification reaction of the biodiesel. Structures in Fig. 2 show triglycerides, biodiesel and pyrolysis products. Experiments carried out so far described the evaporation and combustion mechanism of vegetable oils under different conditions of temperature and pressure. Heating and dilation takes place before the fuel vaporization when they are introduced in the diesel engine. To analyze the this transient phase knowledge of thermal properties like density,

\* Corresponding author. Department of Mechanical Engineering Koneru Lakshmaiah Education Foundation Vaddeswaram, 522502, Andhra Pradesh, India.

E-mail address: [atgurvinay@kluniversity.in](mailto:atgurvinay@kluniversity.in) (V. Atgur).

<https://doi.org/10.1016/j.clet.2021.100367>

Received 14 December 2020; Received in revised form 8 December 2021; Accepted 12 December 2021

Available online 16 December 2021

2666-7908/© 2021 The Authors.

Published by Elsevier Ltd.

This is an open access article under the CC BY-NC-ND license

(<http://creativecommons.org/licenses/by-nc-nd/4.0/>).

### Abbreviations

B-20 blend	Biodiesel 20%, Diesel 80%
HOME	Honge oil Methyl Ester
DSC	Differential Scanning Calorimetry
TG-DTG	Thermogravimetry Derivative Thermogravimetry
TPS	Transient Plane Source

viscosity, Thermal Conductivity, Specific heat and Thermal diffusivity required which are rarely available in literature.

This paper examines the thermal behavior of biodiesel viz., HOME and its B-20 blend by performing differential scanning calorimetry (DSC) and thermogravimetric analyses. Experiments are carried out in oxygen atmosphere and in nitrogen atmosphere with heating rate of 4.72 K/s to analyze the combustion and pyrolysis properties as in (Candeia et al., 2007) utilizing the thermal advantage (TA) universal analysis software. Peak temperatures, reaction intervals, percentage of mass loss and the enthalpy presented. TG-DTG curves are generated and analyzed for onset, offset temperatures, thermal stability, and maximum temperature of decomposition and weight losses in air.

## 2. Methodology & experiments

DSC calibration has to be done for temperature as well as for heat flow. Temperature calibration is done by two experiments. First calibration is performed without samples to get the baseline, whereas in the second experiment the sapphire material alumina without pan placing on both the reference positions. In both experiments cell is preheated, followed by an initial equilibrium temperature holding in isothermal for 5 min. Temperature as well as sensitivity calibration is done in Al<sub>2</sub>O<sub>3</sub> furnace. Second calibration is performed with large sapphire disk (without pan) on both the samples and reference position. In the heat flow calibration standard metal is heated through its melting transition. The calculated heat fusion is compared with the theoretical value. The samples of biodiesel, diesel and their blends exhibit a unique reaction zone. The samples are homogenous in nature having nearly the same reaction interval zone. DSC combustion experiments are carried out on aluminum pan with heating rate of 4.72 K/s using the instrument make Universal TA DSC Q-20 as shown in Fig. 3.

As studied by (Souza et al., 2007), the curve is analyzed in terms of peak temperature, reaction intervals and heat flow of the reactions. Some materials in air undergo partial combustion forming char, whereas in oxygen environment organics will go through complete combustion. This is the reason why combustion experiments are performed in oxygen environment (Kök., 2002). Pans are hermetically sealed to avoid damage formation in the DSC cell. The sample (3–5 ml) is placed into the pan and loaded into the DSC. As in (Zhao et al., 2012), selected the temperature range of 303–573 K at the starting of the experimentation and heating rate of 4.72 K/s. Oxygen is selected as purge gas for combustion experiments, whereas nitrogen as purge gas for pyrolysis experiment. The selected signals to analyze the data are: time (min), temperature (°C), heat flow (W/g) and gas flow rate (ml/min). DSC pyrolysis curves are analyzed using the Shimadzu instrument, DSC-60 detector. The samples are analyzed for the heating rate of 4.72 K/s and the flow rate of

**Table 2**

Composition of fatty acids of HOME.

Fatty acids	Structure	Composition (%)
Saturated fat		20.5
Monounsaturated fatty acid		46
Polyunsaturated fatty acid		33.4
Palmitic acid	16:00	10.8
Stearic acid	18:00	8.7
Oleic acid	18:01	46
Linoleic acid	18:02	27.1
Arachidic acid	20:00	0.8
Linolenic acid	18:03	6.3
Behenic acid	22:00	3.2
Myristic acid	14:00	0.23
Capric acid	10	0.1
Lauric acid	12:00	0.1

**Table 3**

Composition of diesel, HOME and ASTM biodiesel.

Element weight%	Diesel	HOME	ASTM Biodiesel
Carbon (C)	83.80	73.20	77
Hydrogen (H)	12.2	11.6	12
Nitrogen (N)	0	–	–
Sulfur (S)	0.23	–	0.05
Oxygen (O <sub>2</sub> )	1	10.8	11
C/H ratio	7.0	6.5	–

80 ml/min with nitrogen as atmosphere. Since the DSC analysis of liquid samples are difficult due to evaporation which may lead to damage of sensor. Whereas DSC analysis of liquid fuels still becomes difficult due to evaporation, non stability of complex while heating and burn out. So, two different DSC equipments are used. Thermal Conductivity, Specific heat and Thermal diffusivity are determined by experimentally by using Hot Disk TPS-500(Transient Plane Source) Thermal Constants Analyzer shown in Fig. 4. TPS-500 measures the properties accurately and rapidly by using two sensors Kapton sensors-7577\*, 5465, 5501 and Teflon sensors: 7577\*, 5465, 5501.

## 3. Result and discussion

Fig. 5 shows the DSC combustion curve for diesel. Combustion of hydrocarbons exhibits exothermic reaction. During combustion evaporation zone occurs. Fuel prepares for combustion a small fraction of diesel volatile up which occur only one step cracking reaction (it is termed as the diesel distillation). Combustion peak temperature occurs at 486.6 K (point B) with enthalpy  $5.923 \times 10^5$  J/kg as diesel consists of C<sub>17</sub>–C<sub>22</sub> with boiling range of 523–623 K. Burning continues dissipating more energy to the environment. Premixed burning phase in atmospheric air is found to be more when compared to nitrogen. This could be the reason why the peak temperature of combustion reduces and enthalpy increases with high heat release rate.

DSC combustion curve of HOME in Fig. 6 exhibits reaction zone in the temperature range 303.01–616.28 K with a peak temperature of 616.28 K (Point C) and with enthalpy of  $3.51 \times 10^5$  J/kg Combustion phenomena of organic fuels like HOME generally exhibit exothermic reaction in air due to the presence of a weaker double bond (Atgur et al., 2020). Most of the components in the range C<sub>14</sub>–C<sub>20</sub> will decompose.

**Table 1**

Comparison of biodiesel and diesel properties.

Fuel	Calorific value (MJ/kg)	Kinematic viscosity(cSt) @313 K	Cetane value	Density (kg/m <sup>3</sup> )	Flash point (K)	Pour point (K)	Cloud point (K)
DIESEL	44.22	2.87	47.8	840	349	270	279.5
HOME	38.66	4.92	51.0	870	413	277.3	286.2
B-20 BLEND	43.85	2.98	–	835	359	275.8	280.8



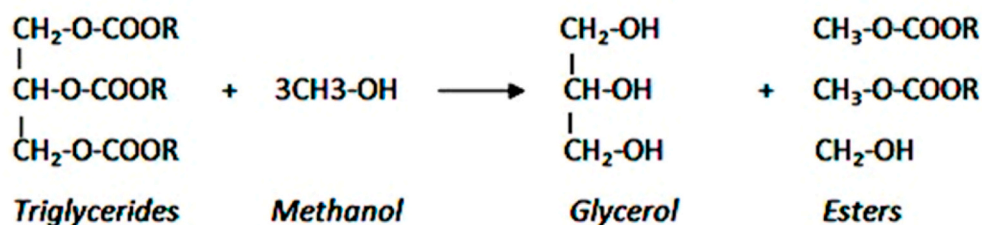


Fig. 1. Overall transesterification reaction of biodiesel.

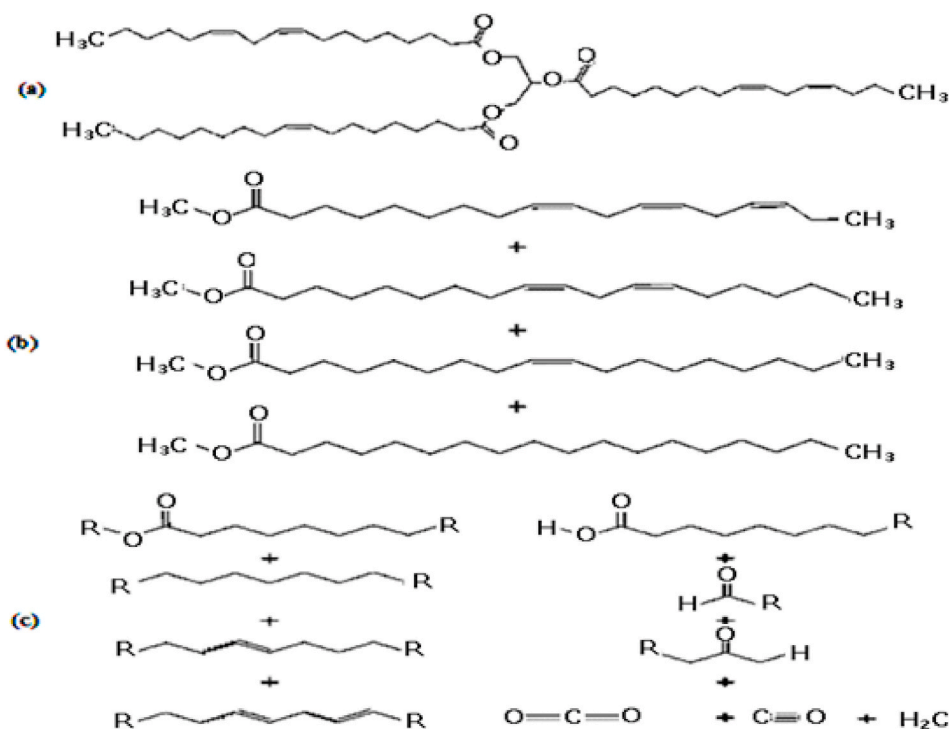


Fig. 2. Structures of (a) triglycerides; (b) biodiesel; and (c) pyrolysis products.



Fig. 3. Dsc Q-20, instrument make universal TA

Endothermic reactions range for the HOME is 616.28–673 K (see Fig. 6 from C to D). The combustion reaction of the HOME occurs at higher temperature when compared to that of the diesel (Dwivedi and Sharma, 2016). The oxidation of the HOME hardly compares to that of the diesel (Dantas et al., 2011). Use of biodiesel in engine causes hard burning. In a specific motor engine higher Cetane number fuels have shorter delay



Fig. 4. Hot disk TPS 500 thermal constants analyzer.

period (Banapurmath and Tewari, 2010; Rajasekar and Selvi, 2014).

The DSC combustion graph of B-20 blend is shown in Fig. 7. From combustion thermograph, the reaction zone is 303.05–573 K with a peak temperature of 468.22 K (Point C). DSC combustion of the biodiesel and its blends exhibits only one reaction interval at which the combustion takes place. DSC thermo grams of the biodiesel and its blend indicate continuous heat flow to surroundings (*i.e.* exothermic reaction) during the combustion phenomena (Chabane et al., 2018; Conconi and Manoel, 2013). From the DSC curve, one can conclude that the cetane number of

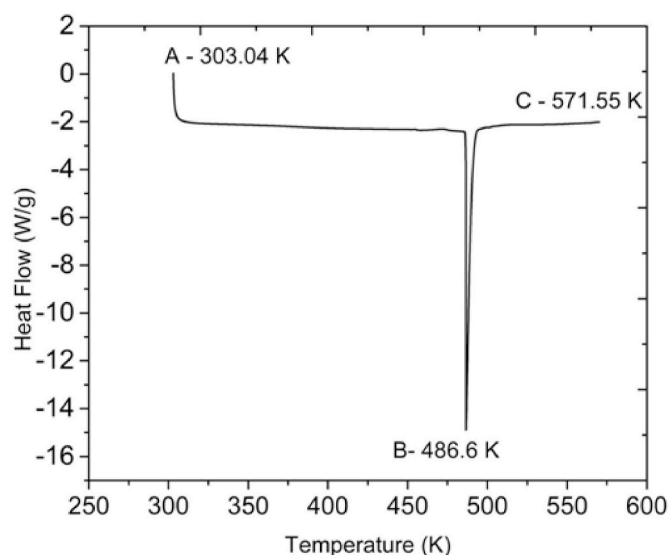


Fig. 5. DSC Combustion curve for Diesel.

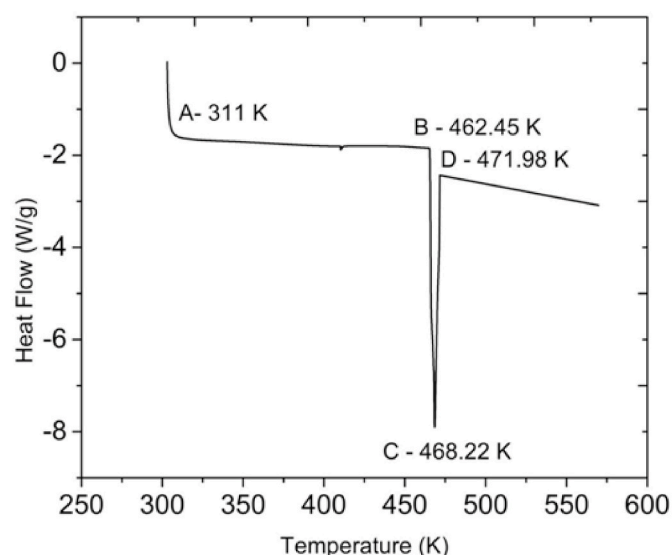


Fig. 7. DSC Combustion curve for B-20 BLEND.

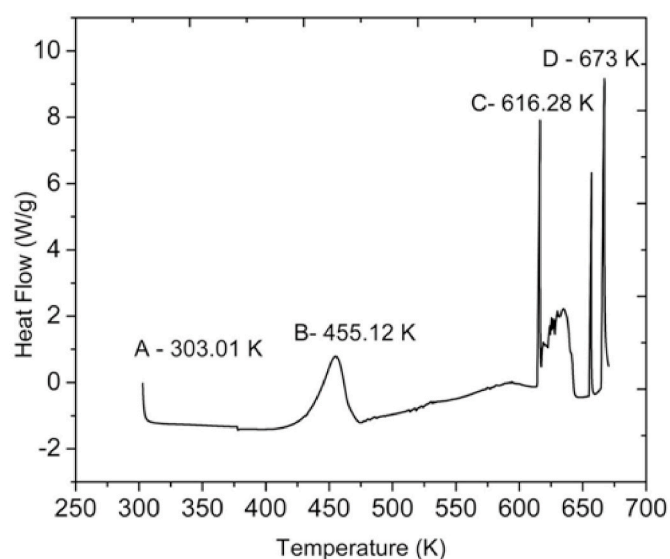


Fig. 6. DSC Combustion curve for HOME (C to D Endothermic region).

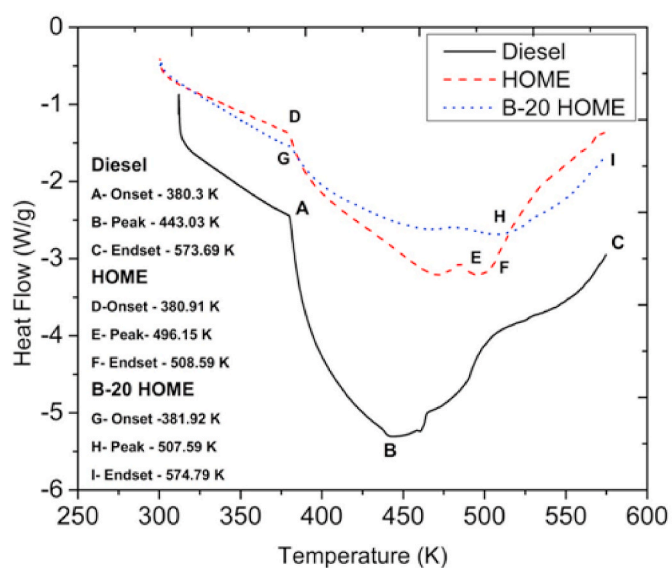


Fig. 8. DSC Pyrolysis curve for DIESEL, HOME and B-20 blend.

the biodiesel is less when compared to that of the diesel. Usage of biodiesel in the engine results in a time delay leading to the insufficient motor performance (Banapurmath et al., 2008b).

For analyzing the pyrolysis mechanism of diesel, biodiesel and their B-20 blends, the specimens are exposed to constant heating rate of 4.21 K/s under nitrogen atmosphere. Under the oxygen atmosphere samples exhibit exothermic reaction showing active oxidation reaction (Volli and Purkait, 2014). At high temperature (above 573K) samples exhibit endothermic reaction, which takes the heat from the surroundings to crack the molecules and release heat (Jain and Sharma, 2012).

Fig. 8 shows the DSC pyrolysis of diesel, HOME and B-20 blend. Temperature in the range of 311–386 K is termed as the first reaction interval is going on and cracked the monoglycerides molecules. Being an organic type homogenous fuel, biodiesel does not require any heat for the small fraction volatile (Nicolau et al., 2018). Second reaction interval shows dissipation of more heat from the cracked molecules to the surroundings. During the reaction interval oxygen bonds are broken. C<sub>11</sub>–C<sub>24</sub> alkyl will be going to form and the remaining molecules (C<sub>7</sub>–C<sub>11</sub> carboxyl group in Fig. 2) will form the sequence of reaction (Damasceno et al., 2013). End set temperature for diesel and B-20 blend occurs at

nearly same temperature of 574 K, whereas for HOME endset temperature occurs at 508.59 K its due to the endothermic behavior from this point onwards reaction region shifts to endothermic. Reaction intervals are analyzed from the area under the reaction curve to assess the reaction enthalpies. From Fig. 8 for the B-20 blend, the mixing rate of biodiesel increases temperature for increasing the cracking reaction. More heat is required to crack the molecule, which means mixing of biodiesel makes the fuel more stable (Mohammed et al., 2018).

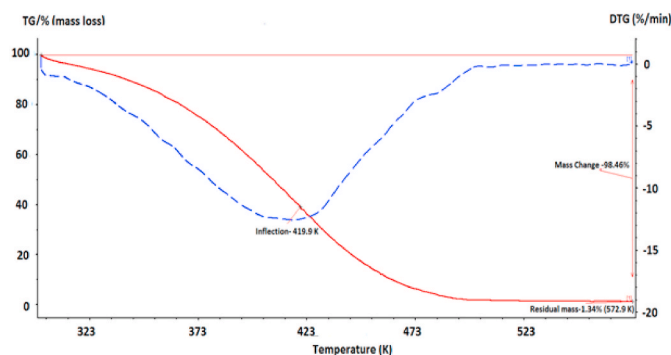
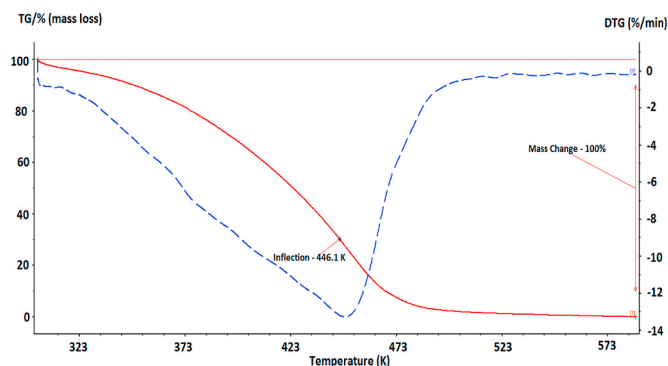
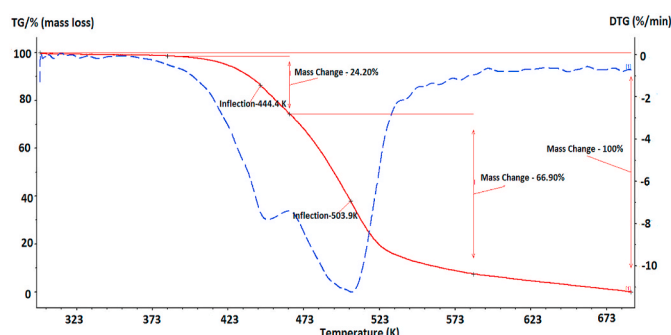
A combustion curve of hydrocarbons under an oxidizing environment normally exhibits exothermic reactions. Generally, crude oil samples exhibit an evaporation zone (additional zone of reaction), which is endothermic in nature. Similar observations in biodiesel and its blends are referred as fuel preparatory phase. Some biodiesels exhibit endothermic reaction at different structural levels for a certain range of temperature. Table 4 gives the peak temperature, reaction region and enthalpy for diesel, HOME and B-20 blend in oxygen and nitrogen atmosphere.

Fig. 9 shows the TGA/DTG of diesel. Combustion reaction occurs between 313 and 529K with a peak temperature of 419.9K. Diesel contains C<sub>17</sub>–C<sub>22</sub> with boiling range of 523–623K. At 318K, diesel starts

**Table 4**

Comparison of peak temperature, reaction temperature range and enthalpy.

Fuel	Oxygen atmosphere			Nitrogen atmosphere		
	Peak Temp. (K)	Reaction range (K)	Enthalpy (J/kg)	Peak Temp. (K)	Reaction range (K)	Enthalpy (J/kg)
DIESEL	486.6	355.6–563	$5.92 \times 10^5$	443.03	380.3–573.69	$4.32 \times 10^5$
HOME	455.52	354.1–608	$3.51 \times 10^5$	496.15	380.91–508.59	$4.05 \times 10^5$
B-20 Blend	468.22	338–571	$4.78 \times 10^5$	507.59	381.92–574.79	$2.98 \times 10^5$

**Fig. 9.** TG-DTG curve for Diesel.**Fig. 11.** TG-DTG curve for B-20 blend.**Fig. 10.** TG-DTG curve for HOME.

to burn and dissipates energy to the environment at 98.46% of mass loss at 572.9K with a 27 min of time span. Remaining 1.34% mass loss represents soot particle which are not burned out (Santos et al., 2016; Vinay et al., 2021). TG-DTG of HOME in Fig. 10 starts to decompose under nitrogen atmosphere with heating rate of 273 K/min around 385K with a peak temperature of 503.9K. HOME decomposition shows three steps of mass loss as in (Almazrouei and Janajreh, 2019). Phase-1 decomposition (means low temperature oxidation) for HOME, corresponds to the removal of water content in addition to the low temperature volatiles (like alcohols) (Yao et al., 2014). According to literature major content of HOME is oleic acid, linoleic acid and palmitic acid and the boiling point of these acids are 541K, 503K and 623K respectively. Remaining acid stearic, linolenic and behenic degrades above 573K. Third phase of decomposition (related to the last 2% of mass, by-products of the fuel oxidation process) is nothing but the impurities (like degradation of residuals from previous phase 1 and 2) aldehydes, ketones, hydroperoxides and carboxylic acids. HOME degrades completely at 696K with a 39.28 min of time span (Silva et al., 2014). From the DTG curve we can analyze that from temperature 444.4K–503.9K reaction is active and from 573K onwards reactivity stops.

Broader thermal decomposition is observed in Fig. 11 for diesel due to the presence of several organic compounds. From the DTG profile, constant curve is observed beyond 503K. Above this temperature reactivity is zero. TG/DTG thermogram of B-20 BLEND as shown in Fig. 11 is

very close to diesel and weight loss are lower than HOME. B-20 blend shows one reaction region from 331 to 578K which indicates that both the fuels mixed perfectly. Peak temperature occurs at 446.1K (Niu et al., 2017). Biodiesel and diesel molecules perform a homogenous mixture at 20%. At 596K complete mass degraded with a time of 28.33 min. Blend decomposes at high offset temperature. Its temperature increases with increasing biodiesel content. In phase-1, lighter fractions of Napthenes, olefins, paraffins and aromatics are present in diesel. Decomposition starts followed by evaporation and combustion of methyl esters in HOME prior to carbonization (Chouhan et al., 2013). TG-DTG curves indicate shifting of oxidative atmosphere combustion process to lower temperature and reaction occurs quickly. Table 5 provides the onset, offset temperature, reaction region, maximum decomposition temperature and weight loss for diesel, HOME and B-20 blend in atmospheric air. B-20 blend properties in Table 6 matches closely with those of the diesel. These properties are in good agreement with the calorimetric data. Future work is towards the DSC-TG experiments on various biofuel samples and heating rates.

#### 4. Conclusion

From the DSC combustion curves, combustion temperature takes place for the samples in the following order: Biodiesel  $\Rightarrow$  Diesel  $\Rightarrow$  B-20. Transesterification reaction of the biodiesel makes the triglycerides more ignitable. Diesel molecules have long chain hydrocarbons and low ignition temperature. From the combustion thermo grams the B-20 blend has better combustion properties lower combustion temperature exhibiting high enthalpy. Calorimetric data presented in Table-4 reveal higher number of enthalpy in the oxygen environment. The first exothermic transition is related to the combustion of organic compounds. In the nitrogen atmosphere, a complete exothermic reaction reveals the evaporation or pyrolysis of the organic compounds.

B-20 blend exhibits maximum enthalpy and reduced peak temperature of combustion, which indicates its suitability for combustion applications. Thermal stability is in the following order HOME > B-20 blend > Diesel. High range of offset temperature is observed for the HOME followed by the B-20 blend. This indicates more duration of combustion process when compared to that of diesel. Biodiesel presents more decomposition steps with higher decomposition temperature by indicating the formation of more stable compounds due to the oxidation

**Table 5**

Onset, Offset temperature, reaction region, maximum decomposition temperature and weight loss.

Sample	Onset temp. Te (K)	Offset temp. To (K)	Reaction Region (K)	Maximum decomposition temperature T <sub>max</sub> (K)	Weight loss (%)	Temp. (K)
HOME	440	547	373–733	444.4 & 503.9	100	696
B-20 Blend	396	531	331–578	446.1	100	596
DIESEL	413	513	313–553	419.9	98.46	572.9

**Table 6**

Comparison of thermal conductivity, thermal diffusivity and specific heat.

Sample	Thermal Conductivity (W/mK)	Thermal Diffusivity (m <sup>2</sup> /s)	Volumetric Heat Capacity (MJ/m <sup>3</sup> K)
DIESEL	0.3381	1.325×10 <sup>-6</sup>	0.2553
HOME	0.3067	6.310×10 <sup>-5</sup>	0.4861
B-20 blend	0.2396	9.913×10 <sup>-5</sup>	0.2417

process. From the combustion profiles it is concluded that the diesel biodiesel blend exhibits similar behavior to diesel with major advantage of reduced emission of harmful gases.

### Disclosure statement

The authors declare that there is no conflict of interests regarding the publication of this paper.

### Declaration of competing interest

The authors declare that they have no known competing financial interests or personal relationships that could have appeared to influence the work reported in this paper.

### Acknowledgement

The author would like to express their gratitude to the Visvesvarayya Technological University Belgaum, University Scientific Instrumentation and Facility Center, Karnataka University, Dharwad, Sophisticated Analytic instrumentation facility centre Indian Institute of Technology Madras and Thermal Laboratory National Institute of Technology Calicut. They are grateful to the reviewers for their constructive criticism to improve the clarity in presenting the work.

### References

- Abdullah, B.M., Yusop, R.M., Salimon, J., Yousif, E., Salih, N., 2013. Physical and chemical properties analysis of jatropha curcas seed oil for industrial applications. *World Academy of Science, Engineering and Technology, International Journal of Chemical and Molecular Engineering* 7 (12), 893–896.
- Almazrouei, M., Janajreh, I., 2019. Thermogravimetric study of the combustion characteristics of biodiesel and petroleum diesel. *Journal of Thermal Analysis and Calorimetry* 136 (2), 925–935. <https://doi.org/10.1007/s10973-018-7717-6>.
- Atgur, V., Manavendra, G., Desai, G.P., Rao, B.N., 2020. Experimental investigation on thermal conductivity and thermal degradation of Honge oil methyl ester with B-20 blend. *J. Therm. Eng.* 7 (7), 1604–1613, 2021.
- Banapurmath, N.R., Tewari, P.G., 2010. Performance, combustion, and emissions characteristics of a single-cylinder compression ignition engine operated on ethanol-biodiesel blended fuels. *Proceedings of the Institution of Mechanical Engineers, Part A: Journal of Power and Energy* 224 (4), 533–543. <https://doi.org/10.1243/09576509JPE850>.
- Banapurmath, N.R., Tewari, P.G., Hosmath, R.S., 2008a. Combustion and emission characteristics of a direct injection, compression-ignition engine when operated on honge oil, HOME and blends of HOME and diesel. *International Journal of Sustainable Engineering* 1 (2), 80–93. <https://doi.org/10.1080/19397030802221265>.
- Banapurmath, N.R., Tewari, P.G., Hosmath, R.S., 2008b. Performance and emission characteristics of a DI compression ignition engine operated on Honge. *Jatropha and sesame oil methyl esters* 33, 1982–1988. <https://doi.org/10.1016/j.renene.2007.11.012>.
- Candeia, R.A., Freitas, J.C.O., Souza, M.A.F., Conceição, M.M., Santos, I.M.G., Soledade, L.E.B., Souza, A.G., 2007. Thermal and rheological behavior of diesel and methanol biodiesel blends. *Journal of Thermal Analysis and Calorimetry* 87 (3), 653–656. <https://doi.org/10.1007/s10973-006-7861-2>.
- Chabane, S., Benziane, M., Khimeche, K., Trache, D., Didaoui, S., Yagoubi, N., 2018. Low-temperature behavior of diesel/biodiesel blends: solid–liquid phase diagrams of binary mixtures composed of fatty acid ethyl esters and alkanes. *Journal of Thermal Analysis and Calorimetry* 131 (2), 1615–1624. <https://doi.org/10.1007/s10973-017-6614-8>.
- Chouhan, A.P.S., Singh, N., Sarma, A.K., 2013. A comparative analysis of kinetic parameters from TGDTA of Jatropha curcas oil, biodiesel, petroleum diesel and B50 using different methods. *Fuel* 109, 217–224. <https://doi.org/10.1016/j.fuel.2012.12.059>.
- Conceição, M.M., Fernandes, V.J., Araújo, A.S., Farias, M.F., Santos, I.M.G., Souza, A.G., 2007. Thermal and oxidative degradation of castor oil biodiesel. *Energy and Fuels* 21 (3), 1522–1527. <https://doi.org/10.1021/ef0602224>.
- Conconi, C.C., Manoel, P., 2013. Thermal behavior of renewable diesel from sugar cane, biodiesel, fossil diesel and their blends. *Fuel Processing Technology* 114, 6–11. <https://doi.org/10.1016/j.fuproc.2013.03.037>.
- Damasceno, S.S., Rosenhaim, R., Gondim, A.D., Tavares, M.L.A., Queiroz, N., Santos, I.M.G., Souza, A.G., Santos, N.A., 2013. Flow properties of biodiesel: correlation between TMDSC and dynamic viscosity. *Journal of Thermal Analysis and Calorimetry* 114 (3), 1239–1243. <https://doi.org/10.1007/s10973-013-3146-8>.
- Dantas, M.B., Albuquerque, A.R., Soledade, L.E.B., Queiroz, N., Ary, S.M., Santos, I.M.G., Souza, A.L., Cavalcanti, E., Barro, A.K., Souza, A.G., 2011. Biodiesel from soybean oil, castor oil and their blends: oxidative stability by PDSC and rancimat. *Journal of Thermal Analysis and Calorimetry* 106 (2), 607–611. <https://doi.org/10.1007/s10973-011-1410-3>.
- Dwivedi, G., Sharma, M.P., 2016. Experimental investigation on thermal stability of Pongamia Biodiesel by thermogravimetric analysis. *Egyptian Journal of Petroleum* 25 (1), 33–38. <https://doi.org/10.1016/j.ejpe.2015.06.008>.
- Freire, L.M.S., Bicudo, T.C., Rosenhaim, R., Sinfônio, F.S.M., Botelho, J.R., Carvalho Filho, J.R., Santos, I.M.G., Fernandes Jr., V.J., Antoniosi Filho, J.R., Souza, A.G., 2009. Thermal investigation of oil and biodiesel from jatropha curcas L. *Journal of Thermal Analysis and Calorimetry* 96 (3), 1029–1033. <https://doi.org/10.1007/s10973-009-0055-y>.
- Jain, S., Sharma, M.P., 2012. Correlation development between the oxidation and thermal stability of biodiesel. *Fuel* 102, 354–358. <https://doi.org/10.1016/j.fuel.2012.06.110>.
- Kök, M.V., 2002. Thermal analysis applications in fossil fuel science. *Literature survey. Journal of Thermal Analysis and Calorimetry* 68 (3), 1061–1077. <https://doi.org/10.1023/A:1016119428815>.
- Mohammed, M.N., Atabani, A.E., Uguz, G., Lay, C.H., Kumar, G., Al-Samarae, R.R., 2018. Characterization of hemp (cannabis sativa L.) biodiesel blends with euro diesel, butanol and diethyl ether using FT-IR, UV–vis, TGA and DSC techniques. *Waste and Biomass Valorization* 1–17. <https://doi.org/10.1007/s12649-018-0340-8>.
- Nicolau, C.L., Klein, A.N.V., Silva, C.A.A., Fiorucci, A.R., Stropa, J.M., Santos, E.O., Borges, K.C.S., da Silva, R.C.L., de Oliveira, L.C.S., Simionatto, E.L., Dilamara, R., Scharf, D.R., Simionatto, E., 2018. Thermal properties of the blends of methyl and ethyl esters prepared from babassu and soybean oils. *Journal of the Brazilian Chemical Society* 29 (8), 1672–1679. <https://doi.org/10.21577/0103-5053.20180040>.
- Niu, S., Zhou, Y., Yu, H., Lu, C., Han, K., 2017. Investigation on thermal degradation properties of oleic acid and its methyl and ethyl esters through TG-FTIR. *Energy Conversion and Management* 149 (17923), 495–504. <https://doi.org/10.1016/j.enconman.2017.07.053>.
- Posom, J., Sirisomboon, P., 2014. Evaluation of the thermal properties of Jatropha curcas L. kernels using near-infrared spectroscopy. *Biosystems Engineering* 125, 45–53. <https://doi.org/10.1016/j.biosystemseng.2014.06.011>.
- Rajasekar, E., Selvi, S., 2014. Review of combustion characteristics of CI engines fueled with biodiesel. *Renewable and Sustainable Energy Reviews* 35 (x), 390–399. <https://doi.org/10.1016/j.rser.2014.04.006>.
- Ramkumar, S., Kirubakaran, V., 2016. Biodiesel from vegetable oil as alternate fuel for C. I engine and feasibility study of thermal cracking: a critical review. *Energy Conversion and Management* 118, 155–169. <https://doi.org/10.1016/j.enconman.2016.03.071>.
- Ren, X., Meng, J., Moore, A.M., Chang, J., Gou, J., Park, S., 2014. Thermogravimetric investigation on the degradation properties and combustion performance of bio-oils. *Bioresource Technology* 152, 267–274. <https://doi.org/10.1016/j.biortech.2013.11.028>.
- Santos, A.G.D., Caldeira, V.P.S., Souza, L.D., Oliveira, D.S., Araújo, A.S., Luz, G.E., 2016. Study of the thermal stability by thermogravimetry for oil, biodiesel and blend (B10) of different oilseeds. *Journal of Thermal Analysis and Calorimetry* 123 (3), 2021–2028. <https://doi.org/10.1007/s10973-015-4943-z>.



- Saxena, P., Jawale, S., Joshipura, M.H., 2013. A review on prediction of properties of biodiesel and blends of biodiesel. *Procedia Engineering* 51, 395–402. <https://doi.org/10.1016/j.proeng.2013.01.055>. NUICONE 2012.
- Silva, T.A., De Assunção, R.M.N., Vieira, A.T., De Oliveira, M.F., Batista, A.C.F., 2014. Methylic and ethylic biodiesels from pequi oil (*Caryocar brasiliense* Camb.): production and thermogravimetric studies. *Fuel* 136, 10–18. <https://doi.org/10.1016/j.fuel.2014.07.035>.
- Singh, R.K., Padhi, S.K., 2006. Characterization of jatropha oil for the preparation of biodiesel. *Indian Journal of Natural Products and Resources* 8 (2), 127–132.
- Souza, A.G., Danta, H.J., Silva, M.C.D., Santos, I.M.G., Fernandes, V.J., Sinfrônio, F.S.M., Teixeira, L.S.G., Novák, Cs., 2007. Thermal and kinetic evaluation of cotton oil biodiesel. *Journal of Thermal Analysis and Calorimetry* 90 (3), 945–949. <https://doi.org/10.1007/s10973-006-8199-5>.
- Swathi, D., Goipal, B.V., Rao, P.V., Raju, G.M.J., 2016. Optimization of jatropha methyl ester and study of its physico-chemical properties using GC-MS and FT-IR analysis. *Austin Chemical Engineering* 3 (2), 1–6.
- Vinay, Atgur, Manavendra, G., Desai, G.P., Nageswara Rao, B., 2021. Thermal characterisation of dairy washed scum methyl ester and its b-20 blend for combustion applications. *International Journal of Ambient Energy*. <https://doi.org/10.1080/01430750.2021.1909651>.
- Volli, V., Purkait, M.K., 2014. Physico-chemical properties and thermal degradation studies of commercial oils in nitrogen atmosphere. *Fuel* 117, 1010–1019. <https://doi.org/10.1016/j.fuel.2013.10.021>.
- Yao, D.W., Jiang, J.Y., Yu, Z.Z., Yao, D.Q., Yang, D.J., Zhao, Y.B., 2014. Canine babesiosis in China caused by babesia gibsoni: a molecular approach. *Iranian Journal of Parasitology* 9 (2), 163–168. <https://doi.org/10.1016/j.renene.2007.11.012>.
- Zhao, H., Cao, Y., Orndorff, W., Cheng, Y.H., Pan, W.P., 2012. Thermal behaviors of soy biodiesel. *Journal of Thermal Analysis and Calorimetry* 109 (3), 1145–1150. <https://doi.org/10.1007/s10973-012-2551-8>.



# A Study on Different Combination of Shear Walls Using ETABS

Syed Irfan<sup>1</sup> and Dr. C. S. Vijay Kumar<sup>2</sup>

<sup>1</sup>Post Graduate

Student, Structural Engineering, Bapuji Institute of Engineering Technology, Davanagere, Karnataka, India

<sup>2</sup>Professor, Department of Civil

Engineering, Bapuji Institute of Engineering Technology, Davanagere, Karnataka, India

---

**Abstract.** Shear wall could be considered as a structural component which is designed to take care of the sideway forces which are imposed on it. These types of all play a very important role in seismically dynamic areas where the shear forces on the structural members increase because of earthquakes. Structural members like shear walls will have more stiffness strength and are resistant to in-plane forces acting along the height of the structure. Any structure which is provided with shear walls that are structurally designed in correct way and detailed out properly will demonstrate an excellent performance during the earthquake conditions. In the present project report a building is provided with shear wall three different locations in 3 different models and the performance of the structure is observed. This way we can analyze the performance of the structure as well as the shear with respect to the position of the provided shear wall. This project is carried out to calculate the performance of provided shear wall with reference to seismic activities.

**Keywords:** Shear wall, shear forces, structural component, seismic activities

---

Date of Submission: 02-04-2022

Date of acceptance: 16-04-2022

---

## I. INTRODUCTION

The reaction of any structure during seismic loading will straight away depend on the sideway load resisting structural system. We have varieties of sideway load resisting structural system to take care of sideway load like seismic and wind forces but only a few of them are really very effective w.r.t performance and cost. However, when one type of sideway load resisting structural system doesn't prove itself sufficient or effective we can still go with combination of different sideway load resisting structural systems to face the lateral loads. It has been observed that rather than regular shaped buildings or structures irregular shaped structures are more unstable against lateral loads. Hence in such structures provision of sideway load resisting structural system becomes very critical. By providing these types of system we can reduce the damage to the structure by controlling various seismic parameters like story drift, displacement etc.

The selection of type of building structures becomes very important in earthquake prone areas. A very common source of damage during the earthquake to the structure is the shape of the structure itself. Second reason is the placement of the shear wall in the structure. A poor placement of a shear wall done during the design may cause damage to the structure rather than reducing the damage. This may even become the reason for the failure of the entire structure. Especially now a day's architects are proposing a lot of irregular shaped structures which look unique by their shapes. In such structures position of shear wall becomes a challenge as we have to bear in mind that the purpose, functionality of the building should not be disturbed and at the same time the beauty of the building should not also be affected. This becomes a challenge since we as a design engineers have to fulfill the structural as well as architectural requirements.

### a. Shear Wall

A shear wall can easily be considered as one of the structural elements whose primary function is to resist and withstand sideway forces i.e. the forces which are acting at right angles to the plane of the shear walls. In case of slender/long walls in which the deformation due to bending is predominant, these shear walls will withstand the loads by cantilever action. Or we can say shear walls are those category of vertical structural members which can also be called as sideway force resisting system. For lean walls in which the bending buckles is high, shear wall takes care of the loads due to cantilever action. Or we can also say, it can be considered as upright elements which work as horizontal force resisting system.

In structural engineering field a shear wall could be taken into consideration as a structural system which is consisting of shear panels, these are also called as braced panels. These are provided to encounter the effect of sideway forces which may act on the structure in the form of seismic forces or wind loads.

In any structure a inflexible and upright diaphragm will be able to transfer any sideway forces from the exterior walls, floors and roofs to the earth through the foundation in the direction which is parallel to the plane of shear-walls.

A strong sideway forces along with torsion forces are produced during the earthquake, wind, differential settlement of the foundations, uneven distribution of live load. All or any one of these or combination of these may cause damage to the structure or even the failure of the structures.

## II.

## OBJECTIVES

Below are the major objectives of this project.

- Carrying out analysis using response spectrum method for seismic zone V
- To ascertain the effect of earthquake on high rise structures which have different shear wall configurations.
- To ascertain the behavior of the building during earthquake by providing shear wall at predefined and well planned location of the building.
- To compare the results of various analysis results w.r. to earthquake for different position of the shear walls.
- To gain knowledge of behavior of shear wall and its configurations.

## III. SCOPE OF THE PROJECT

Analyzing all the three models using response spectrum analysis method zone V using three different combinations of shear wall using a commonly used analysis and design software Etabs and obtaining the analysis results.

## IV. PROBLEM STATEMENT

In this project a G+12 floors building is used to perform the required task. The building has 7 spans of 6.0 m each on X direction & 5 spans of 7.0 m on Y direction, Floor to floor height of 3.2 m is considered. Height between the plinth and foundation is considered as 1.52 m. Column of 700 mm X 700 mm is considered. Beams of 500 mm X 600 mm are considered. Slab thickness of 200 mm is accounted. It is assumed to be an office building hence in general office area live load of 4.0 kN/sqm and in common area like corridor, balcony and staircase it is taken as 3.0 kN/sqm. To obtain live load IS 875 part 2 is followed. Whereas self weight of various building materials like bricks, concrete, plastering, mortar etc are obtained from IS 875 Part-1.

After obtaining all these values from code, wall load in the form of UDL is calculated after deducting the beam depths and the same is applied along the periphery of the building which acts as exterior wall.

Three models were generated using ETABS. First model is provided with the shear wall at all the four corners in L shape. The second one is provided with shear wall at the centre of each face, thus 4 shear walls were provided on all the four faces. In the third model shear wall is provided at the centre or core of the building where lift & staircase are located. In third model both lift and staircase are surrounded by shear walls.

Once all the three models were created analysis was performed on all the three models and then the comparison of various results was carried out by tabulating the results. Comparison was also done in graph format. At the end of the report conclusion is drawn. Response spectrum analysis (RSA) method is used in this project to obtain the results.

Ground +12 floor building structure is created which is a conventional reinforced concrete building. The building is rectangle in shape and the dimensions are expressed in subsequent pages. Loads taken in to account are dead load, imposed load as per IS 875 part-1 and part-

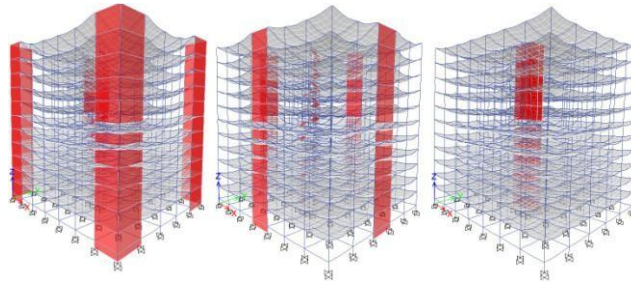
2 respectively and seismic load as per IS:1893(Part-1)- 2002. Analysis is carried out by RSA for seismic zone V of India.  $Z=0.36$ ,  $I=1.0$ ,  $R=5.0$ , damping ratio = 5.0% and soil type = II is considered.

During the entire process some assumptions were made and are listed below.

- 1) This is an office building, thus the main focus is on the response of frame configuration's.
- 2) Story 1 has plinth beam only and no labs are provided as these plinth beams will rest directly on the ground.
- 3) The centre of columns and beams are inline. This is done in order to avoid any eccentricity. The software will do it by default.
- 4) For all the structural elements concrete grade of M30 and steel grade of Fe500 are considered.
- 5) All the lower ends of columns where represents the footings are considered as fixed ends

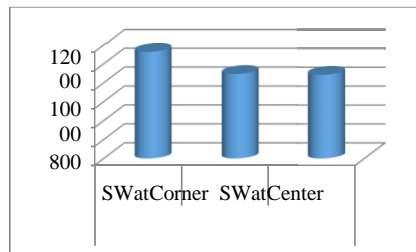
## V. RESULT

### a. Deflection Shape for all 3 Buildings



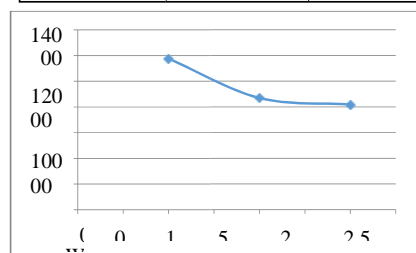
### b. Base Reactions in X direction

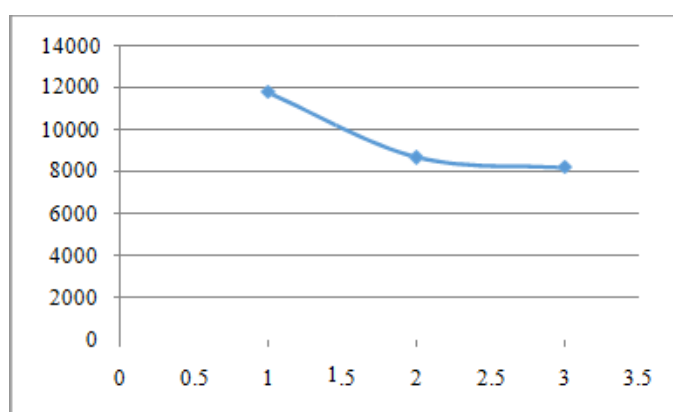
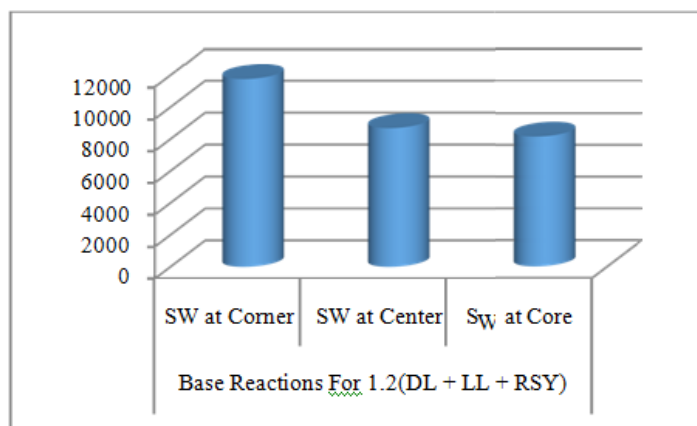
BaseReactionsInXDir	
SWatCorner	SWatCenter



### c. Base Reactions in Y direction

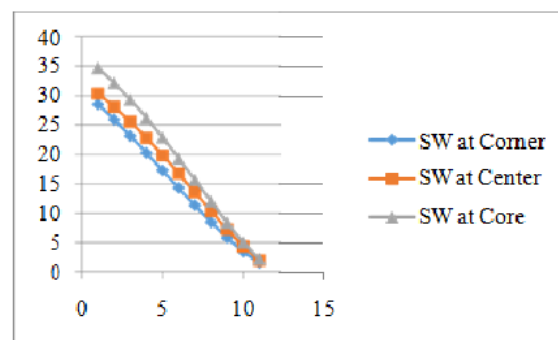
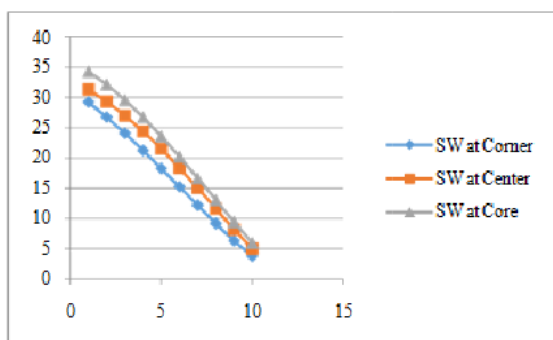
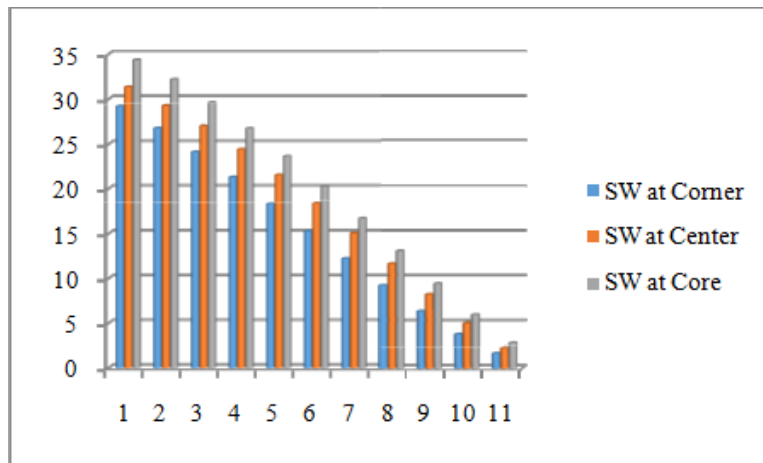
BaseReactionsInYDir	
SWatCorner	SWatCenter





d. Story Displacement in X direction

Story displacement in X direction		
Floor	SW at Corner	SW at Center
Story 11	26.78	29.325
Story 10	24.107	27.01
Story 9	21.279	24.406
Story 8	18.318	21.516
Story 7	15.271	18.377
Story 6	12.202	15.048
Story 5	9.192	11.619

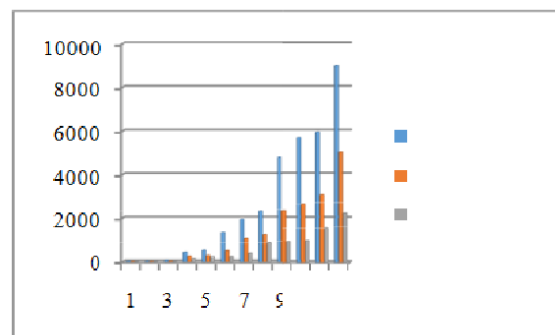
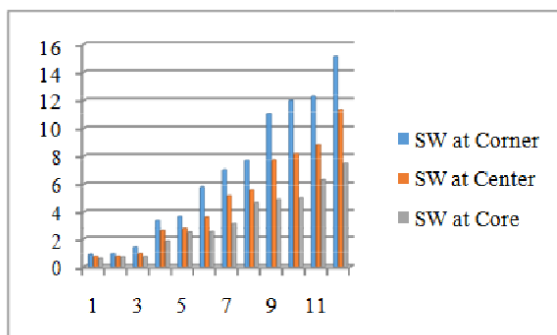


g. Modal Frequencies

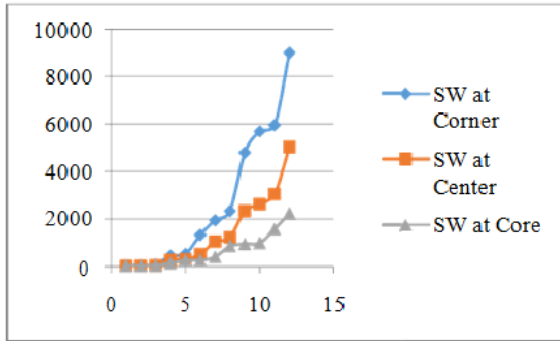
Modal Frequency, Mode v/s Frequency cyc/sec			
	SW at Corner	SW at Center	SW at Core
1	0.886	0.742	0.59
2	0.934	0.758	0.7
3	1.398	0.944	0.729
4	3.346	2.573	1.813
5	3.643	2.717	2.459
6	5.79	3.6	2.491
7	7.005	5.16	3.154
8	7.68	5.564	4.638
9	11.016	7.703	4.886
10	11.994	8.152	5
11	12.271	8.788	6.292
12	15.09	11.289	7.51

h. Modal Eigen Values

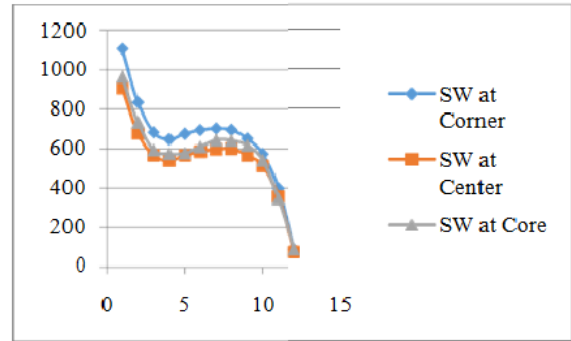
Modal Frequency, Mode v/s Eigenvalue rad <sup>2</sup> /sec <sup>2</sup>			
	SW at Corner	SW at Center	SW at Core
1	30.98	21.74	13.76
2	34.44	22.70	19.35
3	77.12	35.19	20.95
4	441.9	261.30	129.
5	523.80	291.41	238.68
6	1323.40	511.72	245.04
7	1937.27	1051.07	392.71
8	2328.27	1222.39	849.38
9	4790.36	2342.56	942.54
10	5679.26	2623.42	986.87
11	5944.82	3048.66	1563.03
12	8990.07	5030.81	2226.77







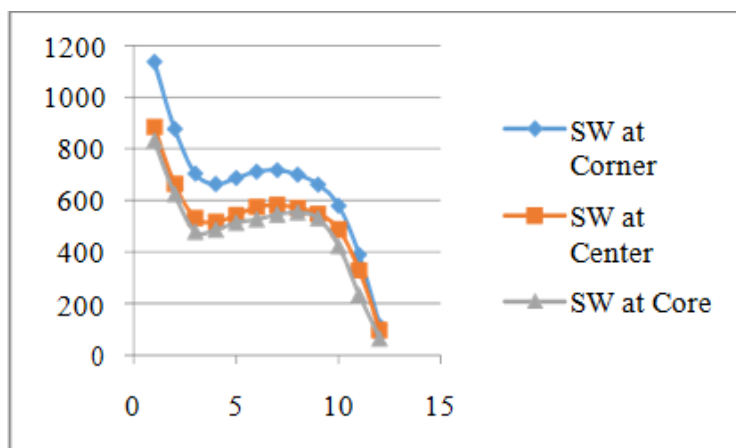
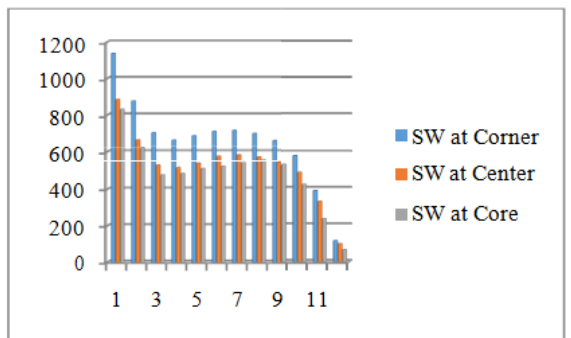
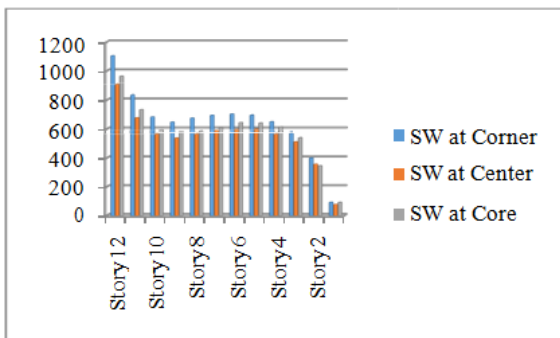
i. Story Acceleration for RS Function X dir



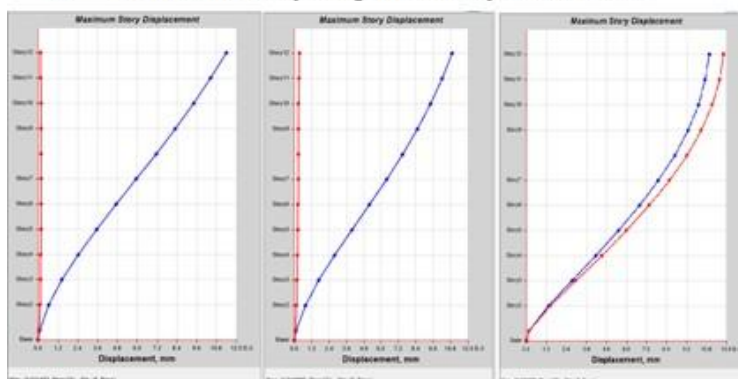
j. Story Acceleration for RS Function Y dir

Story Accelerations in X dir, mm/sec <sup>2</sup>			
	SW at Corner	SW at Center	SW at Core
Story12	1104.05	907.87	963.46
Story11	834.29	676.55	732.69
Story10	682.13	565.12	592.81
Story9	647.13	538.33	573.64
Story8	674.65	564.92	576.99
Story7	693.66	584.44	608.47
Story6	701.85	596.24	643.63
Story5	694.53	598.84	641.22
Story4	649.78	564.79	615.38
Story3	572.26	511.65	539.83
Story2	399.61	356.03	345.64
Story1	91.31	75.8	91.05

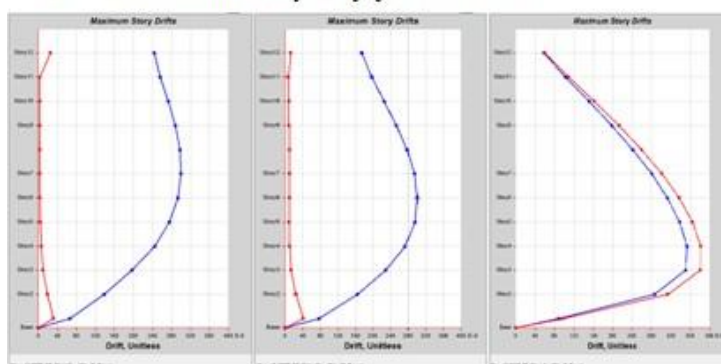
Story Accelerations in Y dir, mm/sec <sup>2</sup>			
	SW at Corner	SW at Center	SW at Core
Story12	1136.6	884.65	831.11
Story11	876.44	663.51	622.72
Story10	703.42	532.16	478.5
Story9	662.9	517.34	486.14
Story8	686.51	542.69	513.09
Story7	710.77	574.34	525.43
Story6	716.53	581.93	544.69
Story5	699.45	570.45	552.04
Story4	660.6	547.87	530.44
Story3	578.56	487.27	422.14
Story2	388.94	328.83	234.1
Story1	114.12	97.04	64.24



### k. Maximum Story Displacement for 1st Mode



### l. Maximum Story Drift for 1st Mode



## VI. CONCLUSION

On the basis of above study for G+ 12 building with 3 different configuration of shear wall below conclusions were drawn:

- 1) A building which is provided with shear wall at right places will have more rigidity to resist sideways loads like seismic and wind loads.
- 2) Base shear is maximum in the building with shear wall at corner due to obvious reason that the total weight of structure is more in first model as the area and volume of shear wall is more in comparison with the other two.
- 3) In building with shear wall at corners is the most rigid when compared with the other two buildings. This is evident from story displacement for all the 3 buildings.
- 4) The modal period is also the least in the building with corner shear wall in comparison to the other two.
- 5) Thus by looking at the above values, points and comparison it is clear that for the chosen shape, size of the building if we provide the shear wall at the corner the building will be more rigid and will be able to face these seismic waves for the given zone effectively.

## REFERENCES

- [1]. Bureau of Indian Standards, IS:456(2000), Plain and Reinforced Concrete Code of Practice
- [2]. IS 875 (Part 2):1987, Indian Standard Code of Practice for Design Loads (Other Than Earthquake) For Building and Structures, Part 2 Imposed Loads (Second Revision), Bureau of Indian Standards, New Delhi.
- [3]. Duggal S.K., "Earthquake Resistant Design Structure", Tata McGraw Hill Publication, 10th Edition 2004.
- [4]. Mahesh N. Patil, Yogesh N. Sonawane, "Seismic Analysis of Multi-Storied Building"
- [5]. Indian Standard Criteria for Earthquake Resistant Design Structure 1839-2002 and IS 875 (Part 2):1987.
- [6]. "Ductility Detailing of RC Structures Subjected to Seismic Forces IS 13920 :1993"
- [7]. IS 875 (Part 2):1987, Indian Standard "Code of Practice For Design Loads (Other Than Earthquake) For Building And Structures", Part 2 Imposed Loads (Second Revision), Bureau of Indian Standards, New Delhi.



## Cyclic Dissimilarity in Physico-Chemical Variables in Groundwater Quality of Honnali Taluk, Davangere District Karnataka, India

Bindu Pavan V <sup>1\*</sup>, S Manjappa <sup>2</sup>, MH Moinuddin Khan <sup>3</sup>, Sachin HP <sup>4</sup>, Suresh B <sup>5</sup>

<sup>1, 3, 4</sup> Department of Chemistry, J N N College of Engineering, Shivamogga, Karnataka, India

<sup>2</sup> Department of Chemistry, University BDT College of Engineering, Davangere-577005, Karnataka, India

<sup>5</sup> Department of Civil Engineering, Bapuji Institute of Engineering & Technology, Davangere-577 005, Karnataka, India

\* Corresponding Author: **Bindu Pavan V**

### Article Info

**ISSN (online):** 2582-7138

**Volume:** 03

**Issue:** 02

**March-April 2022**

**Received:** 22-03-2022;

**Accepted:** 10-04-2022

**Page No:** 533-536

### Abstract

Ground Water quality plays a key role in groundwater management and quality protection; hence it is very much essential to appraise the groundwater quality not only for its current needs but also a probable source of water for upcoming consumption. The study area selected was ground water of Honnali Taluk, Davangere district, Karnataka, India. In our study, first we mark the sampling locations in twenty five different zones of the city, then locations were established and groundwater samples were collected. In the present work an attempt has been made to identify the ground water quality of the region in Pre monsoon, monsoon and Post monsoon phase in year 2020. The physico-chemical variables like pH, electrical conductivity, total hardness, total alkalinity, chloride, fluoride, sulphate, sodium, potassium, calcium, magnesium and nitrate were chosen to analyze the potable ground water quality of the city. Better water quality was found in Pre-monsoon season than Post-monsoon season. Extent of pollution happened due to over utilization of ground water, urbanization and anthropogenic activities. TDS shows highly positive correlation with EC in pre monsoon and post monsoon indicating. In some of the area, nitrate concentration increases in post monsoon.

**Keywords:** cyclic, ground water, TDS, EC, correlation, topography

### Introduction

Groundwater, the water present in an aquifer matrix locked below the sub-surface in the waterlogged zone, act as the primary shield against deficiency for both human necessities and flora production (Siebert, 2010) <sup>[1]</sup>. Significance of groundwater for irrigation in India has been enhanced in the current years, especially due to the fact that groundwater proposes consistency and elasticity in contact to water that irrigation channel can play competition (Abbas Abbasnia, *et al.*, 2018) <sup>[1]</sup>.

Ground water is the most significant source of water supply for drinking purposes in rural zones. Ground water quality acting an chief role in groundwater security and quality conservation. Hence, it is very important to appraise the ground water quality not only for its current use but also from the view point of a probable source of water for upcoming utilization (Kori, *et al.*, 2006) <sup>[7]</sup>. Water sources accessible for drinking and other household needs must acquire high degree of purity, free from contamination (Machiwal, *et al.*, 2018) <sup>[8]</sup>.

In India severe water shortage is becoming common in several parts of the country, especially in arid and semi-arid provinces. Due to enhanced in population and human activities, the quality of groundwater is degrading in day to day life. The opportunity of groundwater contamination is due to the current usage, application and decreasing in the surface water availability, the discharging industrial waste into surface water, municipal and household into the nearby watercourse and surface water bodies. The majority usage of groundwater for agricultural activity are enhancing the ionic strength of the groundwater and making it more salty (Karthikeyan, *et al.*, 2013) <sup>[6]</sup>. Water pollution is the situation of deviation from pure condition, whereby its normal reactions and properties are affected. Motivated environment problems often reproduce the changes in technology (Singh, *et al.*, 2002) <sup>[12]</sup>.

## Materials and methods

### Location Details

Geologically rocks of granodiorite and granite associated with iron and manganese ore bands. The rock formations are joined and are traversed by doleritic Dykes, Weathering in hard rock's is limited to 5 meters from ground level where as in schist and phyllite extends upto 20 meters.

### Experimental Work

Present study comprises of interpretation and analysis of ground water samples collected from different locations at all over Honnali taluk. In our study, first we mark the sampling locations in five different zones of the city, then locations were established and groundwater samples were collected. The samples were analyzed for different physico-chemical parameters and results were carefully studied and analyzed. The present study provides a detailed description of the physicochemical parameters level in groundwater. Total twenty five representative ground water samples were collected during the year 2020.

### Collection and Analytical procedure for Samples

Ground water samples were collected in plastic bottles, which were previously thoroughly washed with tap water and rinsed with double distilled water. Groundwater level in the wells is documented and pH of groundwater samples is measured in the field using a handy pH meter. In the present study bore well water samples are collected after pumping the water for 10 min. Samples collected are transported to the laboratory and filtered using 0.45-µm Millipore filter paper. The fluoride concentration of groundwater samples is determined using Specific Ion Electrode method (APHA 2005). The samples were collected in both pre and post periods. Preservation of water samples and chemical analyses were carried out as using standard methods. Analysis was carried out for various water quality variables such as pH, electrical conductivity (EC), Total Dissolved Solids (TDS), total hardness (TH), calcium ( $\text{Ca}^{++}$ ), total alkalinity (TA), chloride ( $\text{Cl}^-$ ), magnesium ( $\text{Mg}^{++}$ ), sodium ( $\text{Na}^+$ ), potassium ( $\text{K}^+$ ), Sulphate ( $\text{SO}_4^-$ ), Fluoride ( $\text{F}^-$ ) and nitrate ( $\text{NO}_3^-$ ) were estimated using standard method laid out by the American Public Health Association (APHA 2005). The groundwater sampling locations and dumpsite are depicted in Fig. 4.

## Results and discussion

### Groundwater quality for drinking purposes

**Electrical Conductivity (EC) in  $\mu\text{mhos/cm}$ :** Electrical conductivity (EC) is a measure of water capacity to convey electric current. It signify the amount of total dissolved salts EC values were in the range of 2460.0  $\mu\text{mhos/cm}$  at Anjaneyapura [S-11] to 552.0  $\mu\text{mhos/cm}$  at Benakanahalli (Infront of Govt.Hospital) [S-25] during pre monsoon period given in Table 1. High EC values were observed in Anjaneyapura [S-11] during post monsoon season and minimum EC value in Benakanahalli (Infront of Govt. Hospital) [S-25] during pre monsoon period indicating the presence of high amount of dissolved inorganic salts in ionized form.

**Total Alkalinity (TA) in mg/L:** Alkalinity of water is its capacity to neutralize a strong acid and it is normally due to the presence of bicarbonate, carbonate and hydroxide compound of calcium, sodium and potassium. Total alkalinity values for most of the investigated samples were found to be higher value prescribed by WHO. Alkalinity was

found in the range of 713.0 mg/L in Channambapura (infront of Mallikarjuna house) [S-23] to 363.0 mg/L in Bidaragadde (Basavanadurga) [S-4] Post monsoon and 263.0 mg/L Bidaragadde (Basavanadurga) [S-4] to 679.0 mg/L in Chikkahalivana (Opp to SriKari college) [S-5] Pre monsoon given in Table 1. Alkaline water may reduce the solubility of metals. The alkalinity varies in agreement with the fluctuation in the pollution load (Parashar, *et al.*, 2006) [9].

**Total Hardness (TH) in mg/L:** Hardness is the property of water which prevents the lather formation with soap and swells the boiling points of water hardness of water mainly depends upon the amount of calcium or magnesium salts or both. The hardness values shown range from 170.05 mg/L to 745.02 mg/L. The values for sample from point in Bijogatte (In front of Primary Health Centre) [S-16] and Channambapura (in front of Hospital) [S24] were higher than the prescribed limit. In some areas of the city, the hardness is very high, also beyond permissible limit. It is due to rocks bearing salts of Calcium and Magnesium. BIS has prescribed desirable limit of total hardness is 200 mg/L and permissible limit in the absence of alternate source is 600 mg/lit (De, 2002).

**Calcium ( $\text{Ca}^{++}$ ) in mg/L:** Calcium is directly related to hardness. Calcium concentration ranged between 40.10 mg/L [S-17] during pre monsoon season to 196.40 mg/L [S-10] and found below permissible limit of WHO and BIS in the entire study period and all the sampling locations.

**Magnesium ( $\text{Mg}^{++}$ ) in mg/L:** Magnesium is directly related to hardness. Magnesium content in the investigated water samples was ranging from 7.01 in Belimallur (Near Main road) [S-2] mg/L to 43.20 mg/L in Chilapura [S-22] during which were found within WHO limit.

**Sodium ( $\text{Na}^+$ ) in mg/L:** Sodium concentrations were found in between 16.90 mg/L and 17.61 [S-5] to 50.60 mg/L and 54.60 mg/L [S-7]. In the entire study all the sampling locations were showed lower sodium concentration than the prescribed limit by WHO and BIS.

**Potassium ( $\text{K}^+$ ) in mg/L:** The major source of potassium in natural fresh water is weathering of rocks but the quantities increase in the polluted water due to disposal of waste water Potassium content in the water samples varied from 0.89 mg/L [S-3] during pre monsoon season to 4.73 mg/L [S-17] during post monsoon season. It is found that the contents of potassium in site S-17 and S-12 is higher ie 4.73 and 4.12 mg/L, whereas all other locations are showing below 4.0 mg/L potassium content.

**Chloride ( $\text{Cl}^-$ ) in mg/L:** The chloride concentration serves as an indicator of pollution by sewage. People accustomed to higher chloride in water are subjected to laxative effects. In the present analysis, chloride concentration was found in the range of 367.05 mg/L [S-18] to 39.31 mg/L [S-8]. The values are within the limit in all ground water sample collected from Hospet taluk. Higher chloride concentration in samples from sites [S-18] may be due to big discharge of sewage near the sampling location.

**Nitrate ( $\text{NO}_3^-$ ) in mg/L:** Groundwater contains nitrate due to leaching of nitrate with the percolating water. Groundwater can also be contaminated by sewage and other wastes rich in nitrates. The nitrate content in the study area varied in the range 7.94 mg/L and 9.20 mg/L to 58.09 mg/L and 56.41 mg/L during pre and post monsoon season respectively. In the entire study all the collected ground water samples are found within the prescribed limit except [S-3, S-7, S-8, S-9, S-10, S-11] during pre monsoon season. In all other locations



were showing below the permissible limit of WHO and BIS. **Sulphate ( $\text{SO}_4^{2-}$ ) in mg/L:** Sulphate occurs naturally in water as a result of leaching from gypsum and other common minerals. Discharge of industrial wastes and domestic sewage tends to increase its concentration. The sulphate concentration varied between 13.92 mg/L [S-11] and 84.32 mg/L [S-10] to 18.60 [S-20] mg/L to 82.70 mg/L [S-10] during post and pre monsoon seasons respectively and found within the prescribed limit.

Descriptive statistics of 13 measured variables at 25 sampling locations for the whole sampling period are summarized in Table 1. The results shows that pH (mean range, 7.62–7.67), TDS – (mean range, 739.68 – 802.56 mg/L),  $\text{Ca}^{++}$  (mean range, 102.55–117.53mg/L),  $\text{Mg}^{++}$  (mean range, 27.20–52.40 mg/L),  $\text{Cl}^-$  (mean range, 130.34–156.38 mg/L), Fluoride (mean range, 1.14–1.24 mg/L),  $\text{SO}_4$  (mean range, 32.10–37.42 mg/L), Na (mean range 29.86–30.86 mg/L) and K (mean range, 1.69–2.66 mg/L) is within the permissible levels, while all other parameters exceed average levels set by national guidelines for drinking purposes and other needs. It is evident that distribution of TDS, Cl and alkalinity was significantly correlated with EC in Pre monsoon and post monsoon seasons (Table 2 and 3) indicating the high mobility of these ions. EC is positive correlated with pH, TH,  $\text{Ca}^{++}$ ,  $\text{Mg}^{++}$ , and K and negatively correlated with Na, F-,  $\text{NO}_3$  and  $\text{SO}_4$ . Highly positive correlation is observed between TDS and pH, TH, Cl, Ca, Mg and alkalinity (Jothivenkatachalam, *et al.*, 2010) [5], pH, F and Cl, Cl and F, Na and Cl, Na and F. While highly negative correlation is seen among Na and all parameters except CL,  $\text{SO}_4$  and Alkalinity. Positive correlation occurs between pH and Na, TDS and TH (Udayalaxami, *et al.*, 2010) [13]. Good relation to Ca and TH indicating that Hardness in groundwater is mainly due to  $\text{CaCO}_3$  (Ramakrishna, *et al.*, 2009) [10]. TDS shows highly positive correlation with EC in pre monsoon and post monsoon indicating in Figures 1 and 2.

## Conclusions

Higher concentration of Total Dissolved Solids during Post Monsoon samples exhibits poor quality of water as compared to Pre Monsoon due to leaching of various salts into Post Monsoon ground water by infiltrating recharge waters. In pre monsoon only one sample out of 12 shows high value of total hardness than the prescribed limit by WHO but in Post Monsoon 8 samples show high value of total hardness. According to study in urban area of Hospet have high value of hardness in post monsoon. In some of the area, nitrate concentration increases in post monsoon. Study of water quality indices revealed that the drinking water in most locations of Hospet taluk region was found to be slightly contaminated.

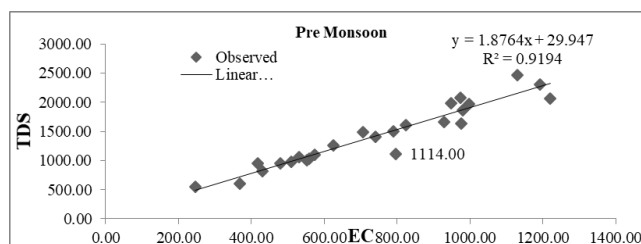


**Fig 1:** Correlation between TDS and EC during Pre Monsoon Season

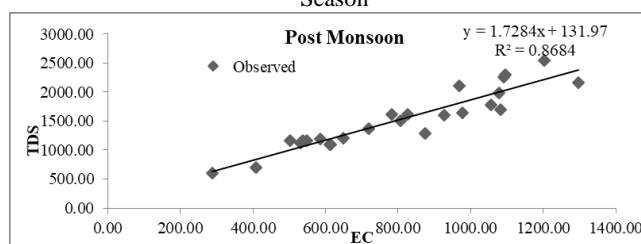


**Fig 2:** Correlation between TDS and EC during Post Monsoon Season

**Table 1:** Descriptive statistical value for pre and post monsoon seasons

Sample No	Pre-Monsoon				Post-Monsoon				Standards	
	Max	SD	SD	Mean range	Max	Min	SD	Mean range	WHO	BIS
EC	2460.0	499.99	531.33	1417.88	2538.0	602.0	499.99	1519.08	-	-
TDS	1220.0	269.58	271.51	739.68	1298.0	288.0	269.58	802.56	500-1500	500-2000
pH	8.3	0.28	0.27	7.67	8.5	7.1	0.28	7.62	6.5 - 8.5	6.5 - 8.5
TA	679.0	99.93	108.93	449.84	713.0	363.0	99.93	522.80	-	200 - 600
TH	690.0	145.98	149.72	399.71	745.0	223.1	145.98	435.86	-	200 - 600
$\text{Ca}^{2+}$	196.4	40.48	39.13	102.55	192.4	54.6	40.48	117.53	75 - 200	75 - 200
$\text{Mg}^{2+}$	40.2	7.64	7.25	27.20	43.2	7.0	7.64	52.40	50 - 150	30 - 100
$\text{Cl}^-$	264.2	75.95	67.89	156.38	387.1	39.3	75.95	130.34	200-600	250-1000
$\text{F}^-$	2.1	0.56	0.52	1.14	2.5	0.7	0.56	1.24	1.0 - 1.5	0.6 - 1.2
$\text{SO}_4^{2-}$	82.7	22.33	19.62	37.42	84.3	13.9	22.33	32.10	200-400	200-400
$\text{NO}_3^{2-}$	56.4	16.23	17.41	28.81	58.1	7.9	16.23	26.52	> 45	> 45
$\text{Na}^+$	54.6	7.83	8.43	30.86	50.6	17.6	7.83	29.86	200	-
$\text{K}^+$	2.8	0.85	0.47	1.69	4.7	1.6	0.85	2.66	-	-

**Table 2:** Correlation matrix of Ground water in Hospet taluk during pre monsoon season

	pH	TH	Cl-	Ca	Mg	TDS	ALK	K	Na	F	$\text{NO}_3$	$\text{SO}_4$	EC
pH	1.000												
TH	-0.071	1.000											
Cl-	0.176	0.163	1.000										
Ca	-0.323	0.878	-0.080	1.000									
Mg	-0.187	0.612	0.237	0.497	1.000								
TDS	0.340	0.258	0.729	0.008	0.094	1.000							
ALK	0.158	-0.238	0.338	-0.235	-0.058	0.490	1.000						



<b>K</b>	-0.044	0.062	0.019	0.267	0.122	0.040	0.330	1.000					
<b>Na</b>	-0.402	-0.150	-0.077	-0.095	0.086	-0.234	-0.203	-0.264	1.000				
<b>F</b>	-0.123	0.275	-0.260	0.415	-0.170	-0.250	-0.104	0.138	-0.139	1.000			
<b>NO<sub>3</sub></b>	-0.205	0.088	-0.182	0.234	-0.146	-0.212	0.173	0.170	-0.094	0.840	1.000		
<b>SO<sub>4</sub></b>	0.268	0.087	-0.246	0.173	-0.324	-0.093	-0.155	0.087	-0.307	0.385	0.101	1.000	
<b>EC</b>	0.252	0.226	<b>0.741</b>	0.024	0.075	<b>0.959</b>	<b>0.401</b>	0.083	-0.124	-0.253	-0.211	-0.117	1.000

**Table 3:** Correlation matrix of Ground water in Hospet taluk during pre monsoon season

	pH	TH	Cl-	Ca	Mg	TDS	ALK	K	Na	F	NO <sub>3</sub>	SO <sub>4</sub>	EC
pH	1.000												
TH	-0.071	1.000											
Cl-	0.176	0.163	1.000										
Ca	-0.323	0.878	-0.080	1.000									
Mg	-0.187	0.612	0.237	0.497	1.000								
TDS	0.340	0.258	0.729	0.008	0.094	1.000							
ALK	0.158	-0.238	0.338	-0.235	-0.058	0.490	1.000						
K	-0.044	0.062	0.019	0.267	0.122	0.040	0.330	1.000					
Na	-0.402	-0.150	-0.077	-0.095	0.086	-0.234	-0.203	-0.264	1.000				
F	-0.123	0.275	-0.260	0.415	-0.170	-0.250	-0.104	0.138	-0.139	1.000			
NO <sub>3</sub>	-0.205	0.088	-0.182	0.234	-0.146	-0.212	0.173	0.170	-0.094	0.840	1.000		
SO <sub>4</sub>	0.268	0.087	-0.246	0.173	-0.324	-0.093	-0.155	0.087	-0.307	0.385	0.101	1.000	
EC	0.252	0.226	<b>0.741</b>	0.024	0.075	<b>0.959</b>	0.401	0.083	-0.124	-0.253	-0.211	-0.117	1.000

## References

1. Abbas Abbasnia, Mahmood Alimohammadi, Amir Hossein Mahvi, Ramin Nabizadeh, Mahmood Yousefi, Ali Akbar Mohammadi *et al.* Assessment of groundwater quality and evaluation of scaling and corrosiveness potential of drinking water samples in villages of Chabahr city, Sistan and Baluchistan province in Iran, Data in Brief. 2018; 16; pp. 182-192.
2. APHA. Standard methods for the examination of water and wastewater. 21<sup>st</sup> ed. Washington D.C.: American Public Health Association, 2005.
3. Bureau of Indian Standards –BIS. Drinking Water Specifications. 2012, IS: 10500.
4. Guidelines for drinking water quality. 2th Ed., World Health Organization, Geneva, Gajendran, C.; Thamarai, P., (2008) Study on Statistical relationship between ground water quality parameters in Nambiyar River basin, Tamilnadu, India. Poll. Res. 1996; 27(4): 679-683 (5 pages).
5. Jothivenkatachalam K, Nithya A, Mohan S C. Correlation analysis of drinking water quality in and around Perur Block of Coimbatore District, Tamil Nadu, India, Rasayan. J. Chem. 2010; 3(4):649-654 (6 pages).
6. Karthikeyan N, A Saranya, MC Sashikkumar. Spatial Analysis of Groundwater Quality for Virudhunagar District, Tamil Nadu Using GIS, International Journal of Remote Sensing and Geoscience (IJRSG). 2013; 2(4):pp. 23-30.
7. Kori R, Saxena A, Upadhyay N. Groundwater quality Assessment of Mandideep Industrial area, National Seminar on Environment and Development, Bhopal, 2006.
8. Machiwal D, Jha MK, Singh VP, Mohan C. Assessment and mapping of groundwater vulnerability to pollution: current status and challenges. Earth Sci. Rev. 2018; 185:201-227.
9. Parashar C, Dixit S, Srivastava R. Seasonal Variations in Physico-chemical characteristics in upper lake of Bhopal, Asian.J. Exp. Sci. 2006; 20(2):pp.297-302.
10. Ramakrishna CH, Rao DM, Rao KS, Srinivas N. Studies on groundwater quality in slums of Visakhapatnam, Andhra Pradesh, Asian J. Chem. 2009; 21(6):4246-4250 (5 pages).
11. Siebert S. Groundwater use for irrigation-a global inventory, Hydrology and Earth System Sciences. 2010; 14: pp. 1863-1880.
12. Singh SP, Pathak D, Singh R. Hydrobiological studies of two ponds of satna (M.P.) India, Eco. Env. and Cons. 2002; 8(3):pp. 289-292.
13. Udayalaxami G, Himabinda D, Ramadass G. Geochemical evaluation of ground water quality in selected areas of Hyderabad, A.P. India. Indian J. Sci. Tech. 3 (1- 5): 2010, 546-553 (8 pages).



# **iJRASET**

International Journal For Research in  
Applied Science and Engineering Technology



---

# **INTERNATIONAL JOURNAL FOR RESEARCH**

IN APPLIED SCIENCE & ENGINEERING TECHNOLOGY

---

**Volume: 10    Issue: V    Month of publication: May 2022**

**DOI: <https://doi.org/10.22214/ijraset.2022.42784>**

**[www.ijraset.com](http://www.ijraset.com)**

**Call:  08813907089**

**E-mail ID: [ijraset@gmail.com](mailto:ijraset@gmail.com)**

# Waste Vegetable Peels as Bioplastics: A Review

Suresh B<sup>1</sup>, Poojitha<sup>2</sup>

<sup>1,2</sup>Department of Civil Engineering, M. Tech Programme in Environmental Engineering, Biotechnology, Bapuji Institute of Engineering and Technology, Davanagere - 577004, Karnataka, India

**Abstract:** Bio-plastic is a significant role in our ecosystem as it is eco-friendly and compatible, when matched to plastic carry bags. Bio-plastic are produced by organic waste in environment and it degrading faster than plastic which was made of chain of polymers. Plastic made our environment poisonous, aquatic animals to die and many more. Environmental friendly plastic is made of many organic wastes like banana peel, sugarcane bagasse, newspaper, shrimps etc. Bio-plastic mostly utilised in food packaging so that they are edible to humans and doesn't cause any disease and disintegrates fast. Bio-plastic is helpful to mankind and useful to reduce environmental pollution. Bio-plastics are not affected to nature ecosystem because it can changes back into carbon dioxide. The plastics are substituted by number of varieties of bio-plastics. In this research paper chiefly discussed on utilization of substrates like vegetable waste, fruit and green leaves including water hyacinth as alternate substrate as bio-plastics. Market demand for bio-plastic is developing due to consumer-friendly products. It is less related with conventional plastics production than other bio-plastics.

**Keywords:** bio-plastic, environmental friendly, organic substance.

## I. INTRODUCTION

Plastics are long chain artificial polymeric molecules that are low-cost, lightweight and durable (Scott, 1999). The species in the ocean and the ecosystem get affected everyday due to the addition of plastic substance and the effects is called Trash islands also garbage patches (Jefferson, et al., 2009). The macro-plastics are renewed into micro-plastics, to convert into still small fragments takes nearly about 400 years (Ezeoha, et al., 2013). The plastics which contains chlorine releases the destructive chemical substance into the soil then enters into ground water through water cycle. This changes in the food chain and also harmful to species that intake through mixed water (Kathiresan, et al., 2003).

## II. EXPERIMENTS OF BIO-PLASTICS

Literate survey summarises, collected, represented and analytical data by academic and industrial researchers from bio-plastics and their effects on the ecosystem. The scholar's relevant work searched by placing the relevant studied to discuss in the present study. Bio plastics prepared using petroleum based, biomass based, biodegradability, disposal as waste, recycling and life cycle appraisal. Industrial research work done by the researchers like primary data accessible on company and agencies websites, was included from this review as such data gives information about the bio-plastic as economic, cutting-edge research and development activities. To specifically meet the objectives of the current review, discussed presenting a new categories of bio-plastics including its positive and negative impact on ecosystem were also discussed. The outcome of this literature review are represented in four parts. The first part is Plastics and Ecosystem, discusses currently using conventional plastics, their bio-degradability including impact on the natural and artificial systems. The second part consists about bio-plastics and replacement of currently using plastics including some of the significance of bio-plastics for commercial and industrial activities. The third part presents advantages and disadvantages of bio-plastics including effects on materials. The fourth part defines the life cycle assessment including the eco-friendliness of bio-plastics with reference to primary analysis reported by the various authors.

## III. CURRENT TRENDS OF BIO-PLASTIC

Bio-plastics are one of the supreme innovative substances that are bio-degradable and bio-based, which is created from waste, renewable sources and bio-mass are used by many authors like as jackfruit (Lothfy, et al., 2018), banana peels (Mohapatra, et al., 2015), organic waste (Goswami, et al., 2015), agriculture waste (Zulkafli, 2014), paper waste (Joshi, et al., 2015), oil palm hollow fruit bunch (Isroi, et al., 2017), sugar cane (Khosravi-Darani and Bucci, 2015), corn starch (Keziah, et al., 2018), potato (Schon, et al., 2014), rice straw (Agustin, et al., 2014), rapeseed oil (Delgado, et al., 2018), vegetables oil, cellulose from floras, starch, cotton, bacteria (Shamsuddin, et al., 2017) and occasionally from several Nano-particles like polysaccharides (carbohydrate chains) (Jabeen, et al., 2015).



Bio-plastic degraded by the natural microorganisms such as bacteria (Ali, et al., 2017, Pradhan, S. 2014, Das, et al., 2018), algae and fungi (Momani, B. 2009). In this research paper chiefly discussed on utilization of substrates like vegetable waste, fruit and green leaves including water hyacinth as alternate substrate as bio-plastics. Describes the classification of bio-plastics then followed by merits and demerits of bio-plastics. The article also includes the processing, applications, experiments of bio-plastics and finally describe on future scenarios of bio-plastics.

#### A. *Types of Bio-plastics-Material and Methods*

Bio-plastics classified based on the type of manufactured using raw materials and its properties which are available in the market. Bio-plastics are also considered under biodegraded by microbes within a period of time in the environment. Generally, bio-plastics are classified into biodegradable (Polylactic acid, Polyhydroxy alkanates, Cellulose, Starch) and non-biodegradable (Biopolypropylene, Biopolyethylene) plastics (Emadian et al., 2017, Mohapatra, et al., 2015, Ilyas, et al., 2016, Soykeakaew, et al., 2017, Lackner, 2015, Sun, 2015 and Rugenstein, and Angelova, 2013). Depends upon this bio-plastics are classified into four types like biomass based polymers, monomers from polymers, polymers from microbial biodegradable including fermentation, monomers and recyclable and compostable bio-plastics. Bio-plastics available in global market is assumed to be growing about 20% to 25% per year. Nearly out of total available plastics, about 10% to 15% bio-plastics will increase its market share to 26% to 34% by 2021. The bio-plastic market attained over 75 billion rupees in 2008 and it will be over 750 billion by 2021. More and more establishments are entering and investing in this market (Krzan, et al., 2006, Kaith, et al., 2010).

#### B. *Merits and Demerits of Bio-plastics*

Plastic is one of the chief pollutant which causes pollution in the ecosystem and also used in the daily life (Pradhan, 2014). Therefore, to reduce the pollution in the system, find out a substitute for alternate as plastics material to change the practice of conventional plastics. The progress was observed in the nature and world the contribution of bio-plastics. Many environmental issues can be renewed by using with polymers based on natural renewable resources like biopolymers starch based, cellulose based and other polylactides and polyhydroxyalkanoates (Kalia, et al., 2011). The properties of bio-plastics makes a good alternatives for conventional plastics. Along with this bio-plastics is having a unique properties like eco-friendly, energy efficient and biodegradable including compostable (Shamsuddin, et al., 2017). Conventional plastics affects the environment, difficulty to recycle and also creates pollutants into the ecosystem and creates pollution have various hazardous effects to the environment (Kalia, et al., 2011). Therefore, there is urgently require to rethink about the usage of kind of materials is difficult to protect air environment. Hence, bio-plastics is a replacement of conventional plastic also revolutionary way for sustainable development since both plastic are showing similar properties. Moreover, in certain condition bio-plastic shows better properties with some mechanical and thermal properties also water transmission rate (Pandey, et al., 2014). Some of the Bio-plastics having advantage like sustainable, reduced carbon foot print, reduce energy efficiency and partly prepared with natural feedstock. Like that some of the disadvantages costly, thermal instability, recycling problem and brittleness. Comparatively, bio-plastic and conventional plastics are showing similar properties observed by previous researchers (Shamsuddin, et al., 2017, Chen, Y. J. 2014, Jabeen, et al., 2015, Ilyas, et al., 2016, Lackner, M. 2015, Shivam, P. 2016, Reddy, et al., 2013, El-kadi, 2014, Andrady, et al., 2009, Arikian, et al., 2015, Pandey, et al., 2014).

#### C. *Bio-plastic as Packaging Material*

The bio-plastics introduced in 1980s, as packaging material and market accounted for roughly 68% of the world-wide manufacturing of bio-plastic (European Bioplastics, 2019). Some presently created and applied bio-polymers using renewable resources contains cellulose and starch, which are biopolymers that are obtained directly from agricultural waste (de Moura, et al., 2017). However, bio-based does not considered as biodegradable and compostable (Dammer, et al., 2016, European Bioplastics, 2019, Van Den Oever, 2017). Bio-based goods products contains raw materials that are renewable and can be recycled through natural processes (Niaounakis, 2015). Biodegradable products consists polymers which consumed by microorganisms through degradation process.

### IV. PROCESSING AND APPLICATION

Bio-plastics produced using PHAs as biomass source can be used for packaging material and disposable products on the other hand biofuels can also be generated using PHAs. PHAs find countless applications in industry, agriculture, pharmaceuticals and health. Soon a whole variety of day-to-day products will be produced with bio-plastics; along with the things you might expect like packaging and food-services products but also components in consumer electronics and automotive components. In relation to the manufacturing of packaging, conventional plastics are being substituted by bio-plastics at a rapid pace.

There's a big demand for bio-plastic packaging and it is the largest segment of the European bio-plastic market- estimated at around 44% of 2.05 million tonnes in 2017.

Bio-plastics provide an alternative approach to packaging and are a real solution to the need for a reduction in conventional plastic use and waste. Plant based polymers are able to fully compost at the end of their useful life. Biodegradable plastics are also being used for medical devices. Dentist are also getting on board and are using bio-plastics for dental implants that fill in the hole that remains after a tooth has been extracted. The cosmetics products are another big creator of packaging for its products. Many of these products have a short life span once disposed of they end up in landfills.

Biodegradable polymers have been at the forefront of research for biomedical applications in the last 50 years. The advancements have been seen in the areas of using biodegradable polymers as delivery vehicles for controlled drug release (Lyu, et al., 2016, Sung, et al., 2019 and Maya, et al., 2017). Bio-plastics have been the great of motivating exploration like in construction and building activities. However not only builder but home owners are also attracted to use bio-plastics for different products such as in fencing, decking and so on (Souza, et al., 2012).

## V. FUTURE SCENARIO OF BIO-PLASTICS

To control the disposal of plastic waste released from the various sources, most environmentally innovative and eco-friendly solution is adopt biodegradable plastic in daily life and applications. Currently non-biodegradable petroleum products are source for plastic pollution and main treats to the ecosystem especially in the absence of waste management. (Temoor Ahmed, et al., 2018) Now a day's bio and fossil based plastics are adopted as alternate for petrochemical plastics. The demand of these type of plastics are increasing constantly in certain applications. These type of materials focused in future especially for manufacturing and packaging industries including disposable medical waste. Moreover, bio-degradable plastics should be used where diffusion into the ecosystem is imminent and challenging to segregate the garbage (Vijaya and Reddy 2008 and Chen and Patel 2011). On the other hand, proper management of waste and littering control is required to take benefits of such polymers in the community.

## VI. CONCLUSION

Bio-plastics have significant potential as substitutes of fossil-based plastics in many applications especially in food packaging and carry bags. They have been used in several food packaging units. Molenveld et al. [1] reported that PLA and bio-PE are adopted as bottles to cover fruits, milk, and dairy foodstuffs. PLA, starch based, and cellophane are used as films, trays/dishes, and bowls to store food, like vegetables including meats and other food items. Bio-plastics can be used as single-use plastic substances and packaging material, which was produced by seaweed as raw material. Significantly, however, bio-plastics are related with some deficiencies. It should be understood that many degradable bio-plastics end up with the landfills, which degrades slowly and releases methane gas. Hence, public are starting to use bio-plastics.

## VII. ACKNOWLEDGEMENTS

The authors gratefully acknowledge Bapuji Institute of Engineering and Technology, Davangere – 577005, Karnataka for the library and support through this work.

## REFERENCES

- [1] Agustin, M. B., Ahmmad, B., Alonso, S. M. M and Patriana, F. M. 2014. Bio-plastic based on starch and cellulose nanocrystals from rice straw. *Journal of Reinforced Plastics and Composites*. 33(24), 2205–2213.
- [2] Ali, S., Zaki, N. H., Yassen, N and Obiad, S. 2017. Production of bioplastic by bacteria isolated from local soil and organic wastes. *Current Resouces in Microbiology and Biotechnology*. 5 (2), 1012–1017.
- [3] Andrady A. L and Neal, M. A. 2009. Applications and societal benefits of plastics. *Philosophical Transactions of the Royal Society B: Biological Sciences*. 364 (1526), 1977–1984.
- [4] Arikan, E. B and Ozsoy, H. D. 2015. A Review: Investigation of Bio-plastics. *Journal of Civil Engineering and Architecture*. 9, 188–192.
- [5] Chen G Q and Patel M K. 2011. Plastics derived from biological sources: present and future: a technical and environmental review. *Chem Rev* 112:2082–2099.
- [6] Chen, Y. J. 2014. Bio-plastics and their role in achieving global sustainability. *Journal of Chemical and Pharmaceutical Research*. 6 (1), 226–231.
- [7] Dammer L and Partanan A. 2016. The EU Ecolabel and bio-based products. *Bioplastics Mag* 11:44–46.
- [8] Das, S. K., Sathish, A and J. Stanley, J. 2018. Production of Biofuel and Bio-plastic from *Chlorella Pyrenoidosa*. *Materials Today: Proceedings*. 5 (8), 16774–16781.
- [9] De Moura IG, de Sá AV and Sofia A. (2017) Bio-plastics from agro-wastes for food packaging applications. In: Grumezescu AM, *Food Packaging*, Academic Press, 7: 223–263.
- [10] Delgado, M., Felix and M., Bengoechea, C. 2018. Industrial Crops and Products Development of bio-plastic materials : From rapeseed oil industry by products to added-value biodegradable bio-composite materials. *Industrial Crops and Product*. 125, 401–407.
- [11] Rugenstein, E and E., Angelova, D. 2013. Bio-plastics: an alternative with a future. *International Trade Fair No.1 Plastics Rubber Worldwide*. 1–11.
- [12] El-kadi, S. 2014. Bio-plastic production from inexpensive sources. 1-144.



- [13] Emadian, S. M., Onay, T. T and Demirel, B. 2017. Biodegradation of bio-plastics in natural environments. *Waste Management*. 59, 526–536.
- [14] European Bio-plastics, Applications for bio-plastics, 2019. Available from: <https://www.european-bioplastics.org/market/applications-sectors/>.
- [15] European Bio-plastics, What are bioplastics. 2019. Available from: <https://www.europeanbioplastics.org/bioplastics/>.
- [16] Ezeoha S L and Ezenwanne J N. 2013. Production of Biodegradable Plastics Packaging Film from Cassava Starch, *IOSR Journal of Engineering*, 3(10), 14-20.
- [17] Goswami, G., Goswami, M. G and Purohit, P. 2015. Bioplastics from Organic Waste. *International Journal of Engineering Research and Technology*. 3 (23), 1–3.
- [18] Ilyas, R. A., Sapuan, S. M., Sanyang, M. L and Ishak, M. R. 2016. Nanocrystalline cellulose reinforced starch-based nanocomposite: A review. *Conference Paper*. 82–87.
- [19] Isroi, I., Cifriadi, A. Panji, T., Nendyo, A. W and Syamsu, K. 2017. Bioplastic production from cellulose of oil palm empty fruit bunch. *IOP Conference series: Earth and Environmental Science*. 65.
- [20] Jabeen, N., Majid, I and Nayik, G. A. 2015. Bio-plastics and Food Packaging: A review. *Cogent Food and Agriculture*. 42(1), 1-6.
- [21] Jefferson Hopewell, Robert Dvorak and Edward Kosior, *Plastics recycling: challenges and opportunities*, *Philosophical Transactions of The Royal Society Biological Sciences*, 364, 2009, 1526.
- [22] Joshi, S., Sharma, U and Goswami, D. G. Bio-Plastic from Waste Newspaper. 2015.
- [23] Kaith, B. S., Jindal, R., Jana, A. K and Maiti, M. 2010. Development of Corn Starch Based Green Composites Reinforced with Saccharum Spontaneum L Fiber and Graft Copolymers-Evaluation of Thermal, Physico-chemical and Mechanical Properties. *Bio-resource Technology* 101: 6843-5.
- [24] Kalia S., Dufresne, A., Cherian, B. M., B. S. Kaith, B. S., Averous, L., Njuguna, J and Nassiopoulou, E. 2011. Cellulose-based bio- and nano-composites: A review. *International Journal of Polymer Science*. 2011, 35.
- [25] Kathiresan. 2003. Polythene and Plastics degrading microbes from the mangrove soil, *Research gate, Revista de biologia tropical*, 51, 2003, 3-4.
- [26] Keziah, V. S., Gayathri, R and Priya, V. V. 2018. Biodegradable plastic production from corn starch. *Drug Invention Today*. 10 (7), 1315–1317.
- [27] Khosravi-Darani, K and Bucci, D. Z. 2015. Application of Poly (hydroxyalkanoate) In Food Packaging: Improvements by Nanotechnology. *Chemical and Biochemical Engineering Quarterly*. 29 (2), 275–285.
- [28] Krzan, A., Hemjinda, S., Miertus, S., Corti, A and Chiellini, E. 2006. Standardization and Certification in the Area of Environmentally Degradable Plastics. *Polymer Degradation and Stability* 91: 2819-33.
- [29] Lackner, M. 2015. Bio-plastics – Bio-based plastics as renewable and/or biodegradable alternatives to petroplastics. *Kirk-Othmer Encyclopedia of Chemical Technology*.
- [30] Lothfy, F. A., Haron, M. F and Rafea, H. A. 2018. Fabrication and Characterization of Jackfruit Seed Powder and Polyvinyl Alcohol Blend as Biodegradable Plastic. *Journal Polymer Science Technology*. 3 (2), 1–5.
- [31] Lyu Y., Fang Y., Miao Q., Zhen X., Ding D and Pu K. 2016. Intraparticle Molecular Orbital Engineering of Semiconducting Polymer Nanoparticles as Amplified Theranostics for in Vivo Photoacoustic Imaging and Photothermal Therapy. *ACS Nano*. 10: 4472-4481. doi: 10.1021/acsnano.6b00168.
- [32] Maya Vetencourt J. F., Ghezzi D., Antognazza M.R., Colombo E., Mete M., Feyen P., Desii A., Buschiazzi A., Di Paolo M and Di Marco S. 2017. A fully organic retinal prosthesis restores vision in a rat model of degenerative blindness. *Nat. Mater*. 16:681–689. doi: 10.1038/nmat4874.
- [33] Mohapatra, A., Prasad, S and Sharma, H. 2015. Bio-plastics Utilization of Waste Banana Peels for Synthesis of Polymeric Films.
- [34] Molenveld K, Van Den Oever M J A and Bos H L. 2015. Bio-based Packaging Catalogue, Wageningen: Wageningen UR-Food and Biobased Research.
- [35] Momani, B. 2009. Assessment of the Impacts of Bio-plastics: Energy Usage, Fossil Fuel Usage, Pollution, Health Effects, Effects on the Food Supply, and Economic Effects Compared to Petroleum Based Plastics. *Worcester Polytechnic Institute*.
- [36] Niaounakis M. 2015. Definitions of terms and types of biopolymers, *Biopolymers: Applications and Trends*, Oxford: William Andrew Publishing, 1–90.
- [37] Pandey, A., Kumar, P and Singh, V. 2014. Application of Bioplastics in Bulk Packaging: A Revolutionary. *University of Science & Technology, Hisar, Haryana, India*.
- [38] Pradhan, S. 2014. Optimization and Characterization of Bioplastic Produced by *Bacillus Cereus* SE1. *National Institute of Technology Rourkela, Odisha*
- [39] Reddy, R. L., Reddy, V. S and Gupta, G. A. 2013. Study of Bio-plastics As Green & Sustainable Alternative to Plastics. *International Journal of Emerging Technology and Advanced Engineering*. 3 (5), 82–89.
- [40] Schon, M and Schwartz, P. 2014. Production of Bioplastic.
- [41] Scott G, *Environmental stability of polymers- In Polymers and the Environment*, Royal Society of Chemistry, 1999.
- [42] Shamsuddin, I. M., Jafar, J. A., Shawai, A. S. A., Yusuf, S., Lateefah, M and Aminu I. 2017. Bio-plastics as Better Alternative to Petroplastics and Their Role in National Sustainability: A Review. *Advances in Bioscience and Bioengineering*. 5 (4), 63–70.
- [43] Shivam, P. 2016. Recent Developments on biodegradable polymers and their future trends. *Int. Res. J. Sci. Eng.* 4(1), 17–26.
- [44] Sivan, A. 2011. New Perspectives in Plastic Biodegradation. *Current Opinion in Biotechnology* 22:422-6.
- [45] Souza, A.C., Benze, R., Ferrão, E.S., Ditchfield, C., Coelho, A.C.V and Tadini, C.C. 2012. Cassava starch biodegradable films: Influence of glycerol and clay nanoparticles content on tensile and barrier properties and glass transition temperature. *LWT - Food Science and Technology*. 46, 110–117.
- [46] Soykeabkaew, N., Tawichai, N., Thanomsilp, C., O and Suwantong, O. 2017. Nano-cellulose Reinforced Green Composite Materials. *Walailak Journal Science & Technology*. 14(5), 353–368.
- [47] Sun, Q. 2015. Development of Bio-based and Biodegradable Film from Carbon Dioxide Based Polymer and Poly (Lactic acid). *University of Guelph*.
- [48] Sung Y.C., Jin P.R., Chu L.A., Hsu F.F., Wang M.R., Chang C.C., Chiou S.J., Qiu J.T., Gao D.Y and Lin C.C. 2019. Delivery of nitric oxide with a nanocarrier promotes tumour vessel normalization and potentiates anti-cancer therapies. *Nat. Nanotechnol.* 2019; 14:1160–1169. doi: 10.1038/s41565-019-0570-3.
- [49] Temoor Ahmed, Muhammad Shahid, Farrukh Azeem, Ijaz Rasul, Asad Ali Shah, Muhammad Noman, Amir Hameed, Natasha Manzoor, Irfan Manzoor and Sher Muhammad. 2018. Biodegradation of plastics: current scenario and future prospects for environmental safety. *Environmental Science and Pollution Research*, 25:7287–7298
- [50] Van Den Oever M, Molenveld K and Van Der Zee M. 2017. Bio-based and Biodegradable Plastics–Facts and Figures: Focus on Food Packaging in the Netherlands, *Netherlands: Wageningen Food & Biobased Research*.
- [51] Vijaya C and Reddy R M. 2008. Impact of soil composting using municipal solid waste on biodegradation of plastics. *Indian J Biotechnol* 7: 235–239.
- [52] Zulkafli, N. N. Production of Bioplastic from Agricultural Waste. 2014.



10.22214/IJRASET



45.98



IMPACT FACTOR:  
7.129



IMPACT FACTOR:  
7.429



# INTERNATIONAL JOURNAL FOR RESEARCH

IN APPLIED SCIENCE & ENGINEERING TECHNOLOGY

Call : 08813907089  (24\*7 Support on Whatsapp)

# Framework of Infotainment using Predictive Scheme for Traffic Management in Internet-of-Vehicle

Reshma S<sup>1</sup>

Department of Computer Science & Engineering  
Global Academy of Technology  
Bangalore, India

Chetanaprakash<sup>2</sup>

Department of Computer Science & Engineering  
Bapuji Institute of Engineering & Technology  
Davangere, India

**Abstract**—Infotainment system potentially contributes towards controlling accident fatalities in the era of Internet-of-Vehicles (IoV). Review of existing system is carried out to find that irrespective of various methods towards infotainment system, the quality of data being retrieved as well as issues associated with power and traffic congestion in vehicular communication is still an impending challenge. Therefore, this manuscript introduces a novel predictive scheme that offers enriched set of information from the environment to assists in decision making. Reinforcement learning is adopted for controlling traffic signal and power while the proposed system introduce augmented Long Short Term Memory scheme in order to predict the best possible traffic scenario for assisting the infotainment system to make a precise decision. The simulation is carried out for proposed system with existing learning schemes to find out proposed scheme offers better performance in every respect over challenging scene of an IoV.

**Keywords**—Infotainment system; internet-of-vehicle; reinforcement learning; decision making; power; long short term memory

## I. INTRODUCTION

The concept of vehicular communication system arrives from vehicular adhoc network two decades back in order to facilitate comfortable and safer driving experience [1]. However, owing to the complex structural implementation and various problems associated with such forms of adhoc network, a reliable and safer communication cannot be guaranteed. So, the most recent innovations of Internet-of-Things (IoT) have introduced an Internet-of-Vehicle (IoV) system that is mainly formed to minimize the event of fatal accidents on road [2]. This is carried out by installing IoT objects within the vehicle which is known to facilitate various functionalities. One such form of system which creates a bridge of communication between the vehicle and external entities is infotainment system [3][4]. The contribution of infotainment system is quite significant especially when deployed over an IoV with respect to essential data transmission [5]. It doesn't only pertain to data transmission based on real-time data, but it also carry out various analytical operation to judge the traffic system. This analyzed outcome is disseminated to drivers via infotainment system in order to ensure safer driving over road [6]. A study shows that out of all deaths happened in country of Sri Lanka, maximum of deaths were due to road accidents [7]. Among the road accidents, maximum of them occur during morning hours

of 9:00 AM to 10:00 AM and also during evening hours of 6:00 PM to 7:00 PM [8]. This clearly indicates that during rush hours, there will be more accidents and fatalities. Hence an efficient traffic management system is required to manage the traffic and avoid congestion and ultimately accidents. The travel time of the emergency vehicles is also an important factor. It is shown that risk of death due to cardiac arrest will increase by 95% during initial 3 hours of time. Hence, the travel time of emergency vehicles should be much lesser compared to travel time of ordinary vehicles. The infotainment system can be used to transfer vital information and entertainment information together. Since the Infotainment system is aware of GPS co-ordinates and health information of the vehicle, the same information can be used to perform several important tasks e.g. redirecting the driver to roads which have less traffic congestion with connected Infotainment system this can be used to manage entire city's traffic. CityFlow provides an excellent platform for simulating city's traffic and urban mobility in general [9]. The CityFlow platform is built in python and is 20 times faster than the other popular alternatives [10]. It is also found to be compatible with Reinforcement Learning (RL) techniques and hence it can be used along with RL agents. Reviews show that studies towards infotainment system and IoV still demands lot of improvisation that motivates to carry out proposed study.

The proposed study presents a unique computational framework of an infotainment system that is meant for data dissemination over congestion-free traffic using machine learning. The contributions of this study are: i) a unique traffic model is implemented for an IoV considering power consumption, ii) a better traffic management is presented to control power and traffic signaling operation in distributed manner applicable for an IoV operation, and, iii) an analytical model is built which is responsible for carrying predictive analysis of data dissemination for infotainment system with an effective decision making system considering the dynamicity of practical IoV environment. The organization of the manuscript is as follows: Section II discusses about existing investigation towards infotainment system followed by research problem highlights in Section III. Briefing of adopted research methodology is carried out in Section IV while an elaborated discussion about the system implementation is carried out in Section V. Discussion of Result analysis is carried out in Section VI while conclusive remarks of proposed contribution is carried out in Section VII.

## II. RELATED WORK

This section discusses about the existing studies being carried out towards IoV with a special emphasis towards infotainment system supportability. Recent studies towards IoV have been reviewed with respect to various methodologies and its effectiveness is studied.

The recent work carried out by Wu et al. [11] has constructed a hybrid communication system which mainly targets towards energy-efficient data transmission system using infotainment. The study also introduces a selection of cache nodes for all the intelligently connected vehicles. The limitation of the study is associated with non-inclusion of spatial complexity associated with streaming over such caching system. Adoption of machine learning towards communication system via infotainment system is carried out by Xu et al. [12] where a reinforcement learning algorithm has been used. The purpose is to encapsulate fluctuating patterns of channel condition in order to select a specific frame. The limitation of the study is that it emphasizes mainly on achieving throughput without consideration of vehicle density or emergency condition. Din et al. [13] have developed a caching system which assists in placing an appropriate content over the target vehicle. The limitation of this model is its non-consideration of uncertain traffic situation which could adversely affect the caching process. Vasudev et al. [14] have developed a unique communication system that emphasize over the mutual authentication scheme in vehicle-to-vehicle communication system. The limitation of this approach is that it uses cryptographic operation over a constraint device, which cannot be considered over a long run without performing any form of optimization of key management. Benarous et al. [15] have implemented a secure communication scheme in IoV where maintains privacy of location-based services utilized by the vehicles. The limitation of this scheme is that it doesn't present any identification system towards intruders and implementation is carried out considering known adversarial scenario.

A robust infotainment system over an IoV also demands an efficient resource management scheme as seen in work of Ni et al. [16]. The study uses allocation of resources as well as broadcasting of beacons over arbitrary access points for performing congestion control. However, the limitation of the study is that the model carry out the resource allocation without considering dynamic traffic scenario as well as it doesn't cater up any emergency services too during communication. Adoption of deep learning is witnessed in work of Chang et al. [17] where a model for accident detection system is developed. Upon detecting the collision, the information is transmitted to cloud-services which release notification. The limitation of the study is that its response time of notification completely depends upon the traffic and priority system, which may fail to cater up emergency transmission of accident notification. Silva et al. [18] have carried out a study towards social IoV system which uses conventional communication system in order to perform exchange of data among the vehicles. The paper concludes that there is still an unsolved problem associated with ethical guidelines about such communication in IoV. The work carried out by Sharma and Liu [19] have addressed the problem of misbehavior detection using machine learning in

IoV. The study has used supervised learning model for this purpose. The limitation of this work is it is applicable only for specific attack. The work carried out by Wang et al. [20] has developed a behavioral modelling that predicts the driving strategy for safer driving. However, this model completely lacks associating with traffic system in order to exchange such information using infotainment system.

The work presented by Qureshi et al. [21] has presented a mechanism of data propagation using clustering approach in IoV. The method calls for a selection of a cluster head using self-assessment approach as well as routing attributes for data exchange within one-hop nodes. The limitation of this paper is that it consumes too much time in clustering process and does leads to delay in case of heavy traffic in IoV. The work carried out by the Fu et al. [22] have presented a transcoding operation for multimedia streaming in IoV over fog computing. The study uses a reinforcement learning scheme which assists in optimizing the allocation of an appropriate resource for facilitating streaming in IoV. The limitation of this work is its it cannot be used for large stream of data in dense traffic. Mechanism of content caching is implemented in work of Xue et al. [23] where a dynamic programming has been used for minimizing the problem of content caching in data transmission of vehicular network. Irrespective of reduced delay, the study model suffers from poor scalability issues in presence of massive number of vehicle density as well as there is no scheme for prioritization of certain vehicle that seems quite impractical. Existing system has also witnessed modelling of task orchestration in vehicular network as reported in work of Sonmez et al. [24]. The study has used machine learning approach considering the success score of task completion. However, the limitation of the study is its non-inclusion of traffic-lights or centralized controlling system, without which the model is not practical to implement. Hong et al. [25] have presented a cost optimization based scheme using analytical framework in order to enhance the transmission time in IoV network. The model suffers from pitfall of using static threshold for cost, which is impractical in real-world traffic. The work carried out by Hou et al. [26] has used Q-learning-based strategy for content management in IoV. Although, the model is capable of making prediction for movement of vehicle, it doesn't have any inclusion of multiple path decision over urban traffic. Apart from these, there are various work carried out by Xia et al. [27], Su et al. [28], Ni et al. [29], and Heo et al [30] towards improving communication system with respect to infotainment system in an IoV.

Existing approaches discussed about offers a claim to better outcome; however, they are also associated with some significant issues. The next section outlines the research problems explored from this review.

## III. MOTIVATION FOR THE RESEARCH

- The traffic congestion is a daily day problem especially in a country like India. The traffic congestion can be easily mitigated with the existing infrastructures and roads. The issue is not of the infrastructure but of the poor management of the infrastructure. Hence an efficient system needs to be designed to manage all the infrastructure and get a better results for the same.



- The connected vehicles are no longer a dream of the future. With several car companies like Tesla and Morris Garage supporting the connected cars by default, the system does not require a hardware upgrade anymore. The computing power of the cars is more than the horsepower of themselves as of now. Since the computing power already exists in the car they only need a software update to support the smart Internet of Vehicle infrastructure now a days.
- The Road accidents due to congestion are a serious cause of the concern now a days. With the systems like autopilot from tesla and several other cutting edge technologies, it is possible to automatically redirect the city's traffic easily with the modern technological systems. And hence there is a scope for a system that can plan the city's traffic and redirect it to a suitable destination on the go.
- The heart attack and other serious emergencies must be addressed immediately. There is a limit to which people cooperate with the emergency vehicles. Green corridor is a very much common phenomenon in cities where an emergency vehicle is given zero traffic and fully allowed to pass through. This is traditionally done for VIP vehicles. However for the genuine emergency vehicles, people give way with understanding. This is possible to be modified based on traffic signal where the emergency vehicles can be made to reach destinations much faster that they are now.
- The Infotainment systems make the driving experience less of a hassle but more of an enjoyable experience. This can be achieved with the proposed study.

#### IV. RESEARCH PROBLEM

After reviewing the existing system in infotainment system in IoV, following are the open end problems identified in proposed study:

- Restricted Coverage Issues in IoV: The conceptual definition of an IoV calls for an interconnected vehicles; however, they still have a dependencies towards a fixed infrastructure at one point. It could be in the form of a hotspots mounted on road or embedded within traffic signal in order to guide the vehicles for congestion free direction. However, the existing studies don't report to consider this coverage issue from Road Side Units (RSU) and mainly focus on vehicle to vehicle communication. This is incomplete implementation for any IoV system to assists the infotainment system within the vehicle.
- Non-inclusion for Density Monitoring: Majority of existing studies on IoV and infotainment system fixes the number of vehicles on specific route. However, in real-time, there are fair possibilities of either increase or decrease of such density over an uncertain instance of time. Without this consideration, the infotainment system will either faces congestion issue or face scarcity of information to undertake decision of data transmission.

- More Focus on Navigation: Majority of existing studies towards infotainment system only focuses on route navigation, whereas infotainment system can also be used for various other forms of data transmission at same time. This requires a dedicated and congestion-free communication channel to be explored by the infotainment system in vehicles. Even if this concept is implemented within present state of implementation in infotainment system, it will significantly cause a serious bottleneck condition for the traffic among the vehicles.
- Less Emphasis towards Data Quality: In IoV system, there are numerous numbers and types of data being required to fulfill the process of data dissemination within an infotainment system. Although usage of mobile edge computing and cloud services makes the operation easier, but still there is a serious pitfalls of almost all the existing architecture of data transmission in IoV. This generates a massive set of traffic data which pertains to road attributes as well as vehicle attributes. Apart from this, there is also a need of multi-objective function to develop a model, which can extract only the productive traffic-related information within IoV system. Hence, ensuring data quality is quite a challenging scenario within current state of infotainment system.
- Uses of Sophisticated Technique: Existing system adopts sophisticated technique targeting for data transmission within vehicles ignoring the resource efficiency of the infotainment system. Adoption of machine learning demands higher training, which is again not much reported to be resource friendly for all implementation carried out in IoV till date.

Therefore, it can be seen that above mentioned issues do exist in present time of IoV deployment scenario. From practical viewpoint, this problem is much dominantly seen in a road network  $R_n$  with multiple junction point. It is because of the decision to find the optimal path owing to the problems identified in this section. Therefore, the prime problem formulation of the proposed system can be stated as follow:

$$R_n(S) \rightarrow [\text{opt}(r_i)] \approx A_i \quad (1)$$

In the above problem formulation, the core idea is to obtain a better form of road network  $R_n$  for all state attributes associated with intersection points. The idea is to optimize the set of reward  $r_i$  parameters for all the set of actions  $A_i$  considered in environment of IoV.

This problem is tackled by developing a computational framework that implements a conditional logic for vehicles considering its properties. Further reinforcement learning approach is used to redefine various state attributes that resolves the decision making problem further using LSTM attention network.

#### V. RESEARCH METHODOLOGY

The core aim of the proposed system is to design and develop a smart traffic system which is capable of facilitating



enriched information to the infotainment system embedded within the vehicle in IoV. Adopting an analytical research methodology, the proposed system make use of machine learning approach in a unique manner which assists in better decision making in the form of direction as well as seamless data transmission in IoV. The proposed system emphasizes more on data quality, where data is associated with both traffic and vehicles in order to assist the infotainment system to undertake correct decision of route formation and resource-efficient seamless data dissemination in IoV. The architecture developed for this notion is highlighted in Fig. 1 as follows:

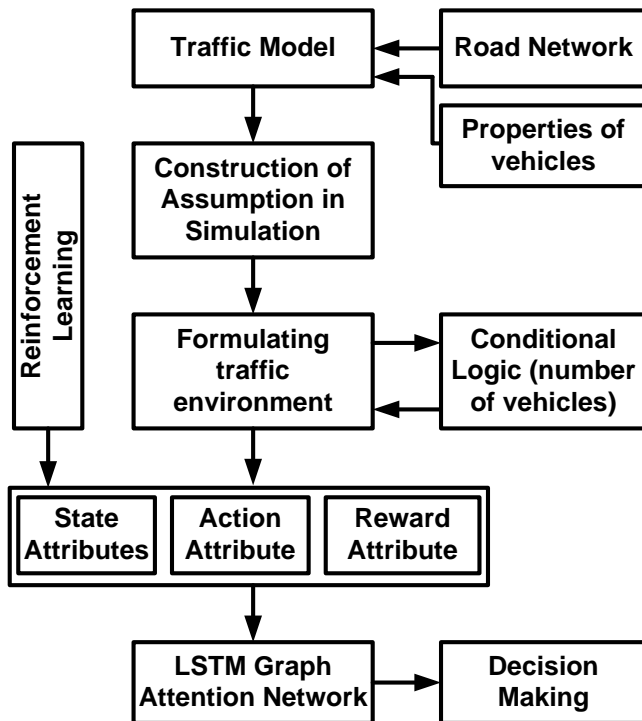


Fig. 1. Architecture of Proposed System.

According to Fig. 1, the proposed system develops a traffic model that mainly consists of formation of road network and properties of vehicle. The proposed modelling considers various attributes in order to develop the topology of traffic model. Further the proposed scheme also constructs assumption which is used for simulation study followed by considering all the essential challenges involved in developing this model. A traffic environment is formed where specific conditional logic is constructed. The proposed system makes use of reinforcement learning scheme which is used over framing up state attributes, action attributes, and reward attributes. Further, Long Short Term Memory (LSTM) graph attention network is utilized which is basically used for decision making towards opting for congestion free and reserving resources while performing vehicular communication in IoV. The next section elaborates further about the operation being carried out by each block towards infotainment system.

## VI. SYSTEM IMPLEMENTATION

In order to design an infotainment platform/scenario, it is required to realize that all vehicles in IoV are required to be

strongly interconnected with each other in order to make a seamless transmission. There might be some vehicles connected directly to internet via 4G/5G; however it is required to ensure that the connectivity is given to all vehicles in order to ensure transmission of vital data like traffic and emergency data. Before simulation of the infotainment system itself, the traffic and the congestion is needed to be simulated first and therefore the proposed system is simulated using standard CityFlow simulator [9]. This section discusses about the various aspects of the system implementation.

### A. Traffic Model

In order to simulate the traffic scenario, A road network  $R_n$  with 4 junctions as  $\{J_1, J_2, J_3, J_4\}$  is considered with three level of congestion as i) highly congested, ii) moderately congested, and iii) less congested. The model defines a vehicle  $V$  with characteristic elements from the set of properties viz. length, width, maximum positive acceleration, maximum negative acceleration, usual positive acceleration, usual negative acceleration, minimum gap, maximum speed, headway time. The brief highlights of these properties are as follows:

- Length refers to the length of vehicle including the luggage space and bumpers.
- Width of vehicle refers to physical width of the vehicle including mirrors.
- Maximum positive acceleration is the change in speed of the vehicle when accelerator is applied in full throttle.
- Maximum negative acceleration is change in speed of the vehicle when sudden break is applied.
- Typical positive acceleration is the usual acceleration of the vehicle.
- Typical negative acceleration is usual change in speed occurred when breaks are applied.
- Minimum gap is recommended gap that should be maintained between the vehicles.
- Maximum speed is top speed of the vehicle.
- Headway time is the time taken by the following vehicle to reach the position of leading vehicle.

### B. Assumptions on Traffic Simulation

The assumptions being considered while developing the proposed schema of infotainment are as follows:

- Everyone respects traffic rules and lane discipline.
- It is assumed that no mishaps happen like accidents.
- All roads are in good condition.
- There are no two wheelers and three wheelers. All the vehicles are assumed to be cars or emergency vehicles.
- Everyone tend to move at similar speeds.

Another, important properties defined for a vehicle are: {Interval, Start time, End time} with default values of {5.0, 0, -1} respectively. These values are considered using 5.0 Likert Scale which signifies 5 as highest and -1 as lowest score. The design process of the model defines a definite simulation time ( $T_s$ ). If the start time is equal to zero, it means that at the beginning of simulation, the vehicles will appear at their respective junction, however if the end time is equal to -1, it means that it is uncertain to say that when again a particular vehicle will re-appear on the same junction. Moreover, if the interval is defined say interval=5, it means that at every 5 units of time, that vehicle will re-appear on respective junction.

### C. Challenges of Modelling

In the present study, the problem is being formulated as a Markov chain model. Each intersection in the system is controlled by an agent. The infotainment system which is present within the vehicle is an embedded system hence it only has a routing table to forward the information. Since all the information is encrypted only the end node can see the required information. SNR of the multimedia signals are noted at the cars and average SNR is calculated. SNR is calculated for 4 different types of data viz. i) text data, ii) video data, iii) audio data, and iv) security data.

### D. Traffic Environment from CityFlow

The CityFlow simulator is used to generate the traffic data for three years' time period. Apart from the traffic scenarios of junctions and vehicle characteristics, the program (simulator) also keep adding vehicles with random start time and end time parameters over the span of simulation. Hence, the number of vehicles on the roads keep increasing and creates a dynamic and uncertain stage of congestion. In addition the simulator is internally programmed to model seasonal traffic in such a way that the number of vehicles on the road will be comparatively lower in the month of July and august due to rainy season. The problem of mitigating the congestion, require information as in the Table I.

In the Table I, the parameter of MED is computed as following expression (1),

MED (S)=

$$\begin{cases} S \left[ \frac{1}{2} \times (\sum_{j=1}^n V_j) \right] & \text{if number of vehicles are even} \\ S \left[ \frac{1}{2} \times (\sum_{j=1}^n V_j - 1) \right] + S \left[ \frac{1}{2} \times (\sum_{j=1}^n V_j + 1) \right] & \text{if number of vehicles are odd} \end{cases} \quad (1)$$

TABLE I. FORMULATION USED IN PROPOSED STUDY

Junction ID	Total number of vehicles	Speed	Congestion
{J1,J2,J3,J4, .. Jn}	$\sum_{j=1}^n V_j$	MED (S)	$\left( \frac{\sum_{j=1}^n V_j, speed = 0}{\sum_{j=1}^n V_j} \right) \times 100$

### E. Formulating State Attribute

State is definitive term that represents the state of the particular intersection. Since it has multiple values, it is represented in form of a vector  $S$  as follows,

$$S = \{\vec{S_1}, \vec{S_2}, \vec{S_3} \dots \vec{S_n}\}$$

$$\vec{S_i} = [L_q, P] \quad (2)$$

In the above expression (2), the variable  $L_q$  represents the average queue length of the intersection that is mathematically represented as follows,

$$L_q = \frac{1}{4} \sum_{i=1}^4 u_i \quad (3)$$

$u_i$  is the queue length of the individual road in the intersection.

### F. Formulating Actions Attribute

Actions are execution attribute that Reinforcement Learning RL agent can perform on the environment. Since a single RL agent is assigned to an intersection, there are possibilities of  $n$  number of actions  $A$  as follows,

$$A = \{A_1, A_2, A_3 \dots A_n\}$$

$$A_i = [\vec{T_v}, P_i] \quad (4)$$

In the above expression (4), the variable  $P_i$  represents the power input of the base station. If the RL agent sets a higher power then the signal can be transmitted further and results in a higher useful information ratio. At the same time, it also results in higher overall power consumption. The first variable in expression (4) is represented as follows,

$$\vec{T_i} = [X_1, X_2, X_3, X_4] \quad (5)$$

In the above expression (5), the variable  $X_i$  represents the traffic signal. Since there are 4 signals in each intersection it is represented by  $X_1$  to  $X_4$  and its generalized form is as follows,

$$X_i \in \{R, Y, G\} \quad (6)$$

In the above expression (6), the variable  $R$ ,  $Y$ , and  $G$  represents three different lights in the traffic signal. Red, Yellow and Green.

### G. Formulating Reward Attribute

Reward  $r_i$  is a real number representing the overall performance of the system.

$$r_i = - \frac{\sum_{i=1}^4 u_i}{4} - P_i + \frac{\sum_{i=1}^N S_i}{N} \quad (7)$$

The RL system proposed in this study is programmed in such a way that both traffic congestion as well as information SNR are optimized. The information is passed through a software Defined Network (SDN) created by Mobile Adhoc Networks (MANET) by the vehicles. The parameters which are being optimized here are,

- Useful information ratio of 4 different types of data (varying preference) (MAX).
- Traffic congestion (Average queue length) (MIN).

- Average Travel time of the regular vehicles (MIN).
- Average Travel time of the emergency vehicles (Only ambulances are considered) (MIN).
- Overall Power consumption by the base stations (MIN).

#### H. Methodology for Implementing LGAT Neural Network

The proposed system implements a neural network in the form of regular Long Short-Term Memory LSTM itself; however, one of the hidden layers in this network is common for all the networks over the grid. This essentially makes each neural network to be aware of its surroundings. Hence this is named as LSTM Graph Attention Network (LGAT). LGAT has two parts involved in its module i.e. i) First part which is before the GAT layer and ii) second part is after the GAT layer. Before GAT layer rectified linear unit ReLU Activation function is used whereas after GAT layer, Sigmoid function is used. This is done since the output is always expected to be residing between 0 and 1. The power input of the base station is controlled by considering the input of the percentage of maximum power consumption. The traffic signals are always controlled by considering the input of 1 or 0 to each signal lamp with the one hot encoding strategy. The Adam optimizer is used to train the neural network and the loss function used here is MSE. It should be taken into special attention that MSE is used here instead of commonly used binary cross entropy. This is due to the fact that the network should output an analog value for power consumption in terms of percentage.

Fig. 2 shows the structure of the proposed LGAT neural network where the second hidden layer is the shared layer whose weights and biases are shared with all the other networks. The weight sharing mechanism here is very similar to that of the Siamese neural networks. The output layer contains 13 outputs 12 of which corresponds to the traffic signals and one corresponds to the base station input power percentage.

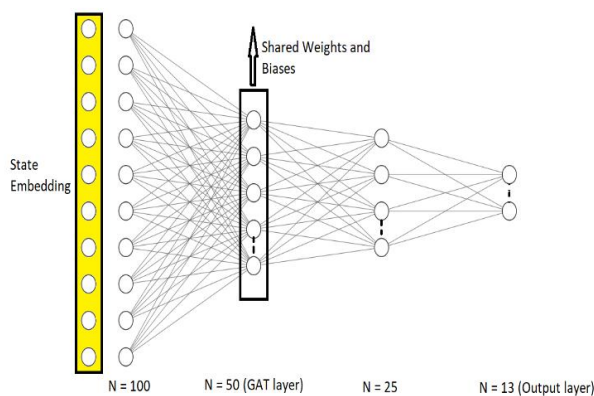


Fig. 2. Structure of Proposed Neural Network.

#### I. Training the Agent

The agent is trained for 4000 episodes in the study and the ANN shown here is trained for one epoch in every episode. Effectively the ANN is trained for 4000 epochs with dynamically changing data. However, since this is an LSTM network, the changing nature of the data is also learnt by the network. The central shared hidden layer enables multiple agents to cooperate with each other. Due to this cooperation the agents are able to produce a good output. Here, the competition behind agents must be avoided at all costs as that will result in selfish agents which may just shut down their base stations in order to save power.

### VII. RESULT ANALYSIS

This section discusses about results being obtained from the simulation study by implementing the proposed scheme discussed in prior section. The recommended hardware and software stack for training the agent are as follows.

- CPU: Intel Core I7 10th Generation.
- GPU: Nvidia GeForce RTX 2060.
- OS: Kali Linux 2021.
- C compiler: GCC 10.2.1.
- GPU C library: Nvidia CUDA 10.1.
- GPU python bridge: Nvidia CuDNN.
- Python: 3.8.2.
- TensorFlow: 2.5.0.

The above-mentioned stack is used in order to get the best results since the TensorFlow works better when it is executed on GPU. Above stack must be used in order to run TensorFlow over GPU. Table II highlights about the properties of vehicles considered for proposed scheme.

TABLE II. PROPERTIES OF A VEHICLE (V)

#	Property	Value	Units
1	Length	5	Feet
2	Width	2	Feet
3	Maximum Positive Acceleration	2	m/sec <sup>2</sup>
4	Maximum Negative Acceleration	4.5	- m/sec <sup>2</sup>
5	Typical Positive Acceleration	2	m/sec <sup>2</sup>
6	Typical Negative Acceleration	4.5	- m/sec <sup>2</sup>
7	Minimum Gap	2.5	Feet
8	Maximum Speed	16.67	m/sec
9	Headway Time	1.5	second

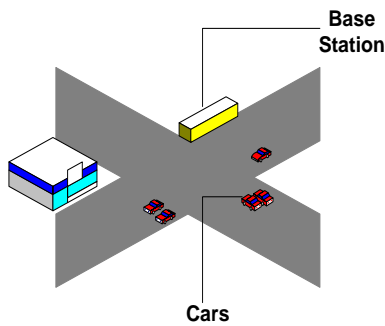


Fig. 3. Simulation Environment.

As it can be observed from Fig. 3 that the simulation is a set up in such a way that there is always a base station in every intersection. Fig. 4 exhibits the higher level overview of system implementation. It is powerful enough to transmit till next base station. However, since the signal strength of the base station can be controlled by the RL agent, the base station's power consumption will vary and the range also varies. If there are vehicles closer to each other, then it is enough if the base station transmits the signal to nearest car. That car can act as a repeater and transmit the message further to other cars. Hence if a particular junction is congested, then the base station may spend less amount of power to transmit the signal further.

The reward depends on both travel time and power consumption. Hence the agent is expected to optimize both of these parameters. The environment is built in such a way that it can support one agent per every intersection. Hence this is a multi-agent environment. Every agent can perform the optimization of power and congestion in their own intersections however, they are expected to co-operate with each other and optimize the entire city's power consumption and travel time of entire city in average.

There are several base stations are present in the city as well as vehicles act as relay to the signal. If the vehicles are far apart, then the base stations have to send signal far hence there will be more power consumption by the base stations. The system must optimize the over power consumption as well.

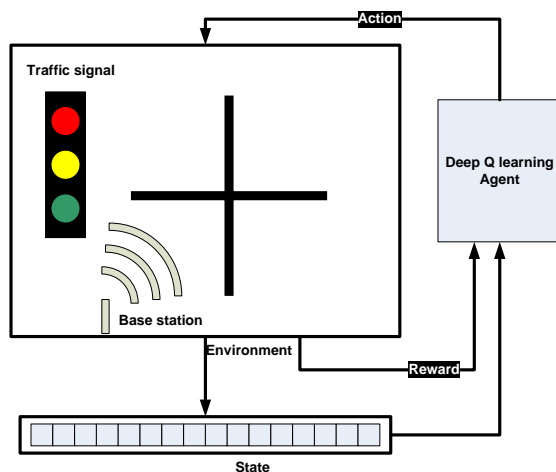


Fig. 4. Higher Level Overview of the System.

Following are the parameters which are being optimized

- **Useful Information Ratio:** Every vehicle needs to receive the information required for itself. More it acts as a relay, more the battery consumption and lower the bandwidth utilization for itself. Hence base station must provide higher power for better data transmission.
- **Queue Length:** Queue length is defined as the distance between front of the first stopped car in the intersection to the back of the last stopped car in the intersection (Feet). Traffic congestion is the average of all 4 incoming queue lengths in each intersection.
- **Average Travel Time:** Average travel time is nothing but average time taken by all cars to travel from source to destination (Entry intersection, Exit intersection). It is considered for Regular vehicles and Emergency vehicles.
- **Overall Power Consumption:** This is the sum of power consumed by all base stations in the city. The order in which the priority is given to the parameters viz. Travel time of Emergency vehicles, Congestion, Travel time of Regular vehicles, Useful info ratio for emergency data, Useful info ratio for text data, Useful info ratio for audio/video data, Power consumption Simulation parameters are set as following.

Fig. 5 highlights the consideration of 6X6 grid for proposed simulation with 36 intersections in total while there are two simulations done using this layout. Uniflow assumes that the traffic moves in a single direction during morning and opposite direction in the evening. Biflow assumes that the traffic moves in both directions during all times of the day.

Fig. 6 highlights the map to shows the area considered in Hangzhou junction of China. It contains total of 16 junctions and traffic is the real recorded traffic.

Fig. 7 highlights the map to shows the area considered in New York city that contains 196 junctions in total. The proposed system is assessed with existing system of learning-based model of vehicular network in IoV.

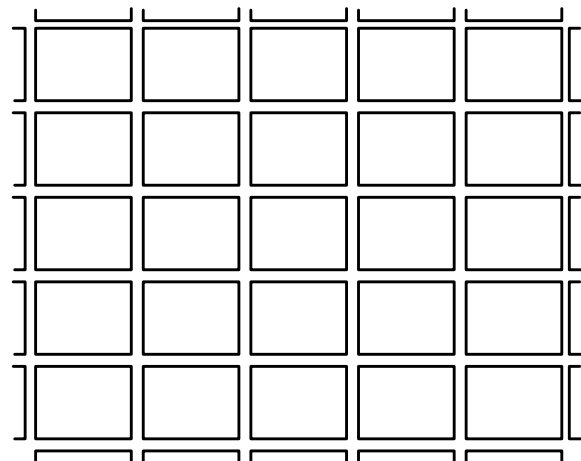


Fig. 5. 6X6 Grid for Simulation.



Fig. 6. Hangzhou Simulation Setup.



Fig. 7. New York Simulation Setup.

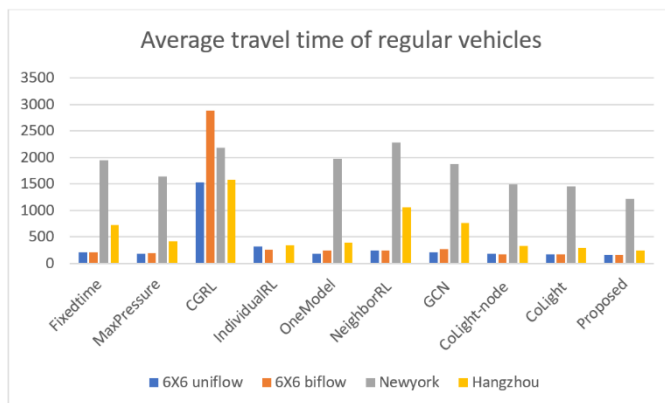


Fig. 8. Average Travel Time for Various Methods.

The above graph in Fig. 8 clearly indicates that the proposed method performs better for every scenario. As it can be observed, New York City is the most difficult scenario. For individual RL, data isn't available. The overall travel time is reduced because of the LGAT architecture. The vehicular traffic follows a particular pattern during the day. LGAT can learn the temporal patterns as well and be able to predict the future vehicular traffic.

An extra parameter which is considered in this study is that average travel time of emergency vehicles (Fig. 9) in which the proposed system is performing better compared to CoLight model. The performance is better in the proposed system since the LSTM layer is used. From Fig. 10, can be observed that the travel time of emergency vehicle is half of regular vehicles.

The graph in Fig. 11 shows that the overall power consumption is less for proposed method. This evidently shows that proposed system has better performance score when evaluated with existing CoLight model in perspective of different available dataset of data dissemination in vehicles of urban scenario.

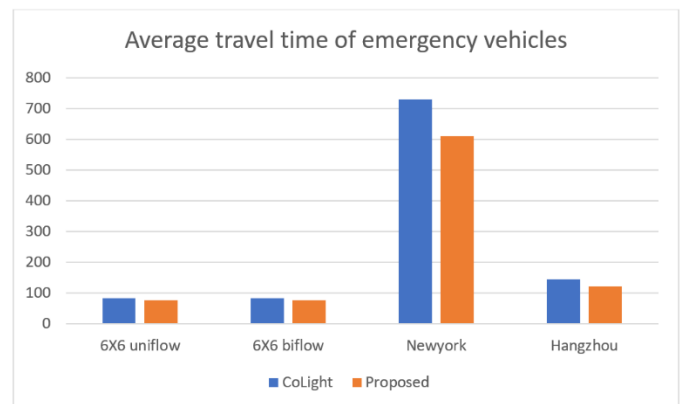


Fig. 9. Comparison of Travel Time for Emergency Vehicles.

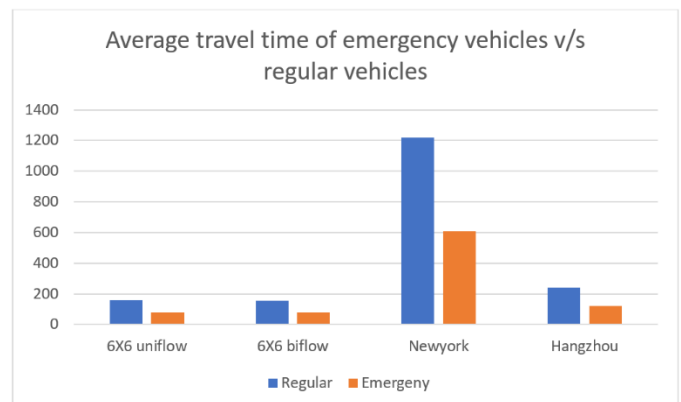


Fig. 10. Average Travel Time for Emergency Vehicle vs Regular Vehicle.



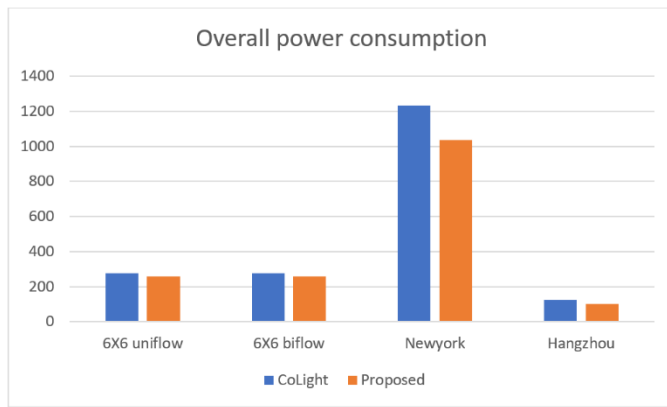


Fig. 11. Overall Power Consumption in MWH.

### VIII. CONCLUSION

This study presents a novel mechanism to manage the urban traffic system and prevents the congestion at the same time. The system can be used to redirect emergency vehicles to shorter paths where there is less congestion and reduce their travel time. The presented model considers the aspect of power consumption by the system. This is carried out in order to address the problem about infotainment system that not only consists of the in-vehicle system but also the sensors, gateways and signal repeaters. Such forms of devices consume a lot of power in order to make sure the quality information is transferred. The implementation of proposed study also optimizes the power consumption by the infotainment system and ensures overall transmission efficiency. The proposed system constructs an optimal environment for the city traffic management and its reward system so that the system rewards the agent based on both power consumption and the travel time. While the environment is a single environment, this is a multi-agent system. An RL agent is assigned at every intersection and they control the traffic signal and power input of the transmitter at the intersection. An agent will also be aware of actions and states of other agents through a novel neural network architecture proposed in this study, LGAT architecture. The proposed system implements an LGAT that is a special type of LSTM in which one of the layer's weights and biases are shared with all other agent's weights and biases. The neural network here uses the DQN architecture for RL. The DQN architecture means the NN takes the action as input and outputs Q values for all possible actions. Q values are nothing but the future rewards for the system. The system is trained over multiple episodes with a single epoch per episode. The proposed study considers several existing methods and considers various parameters to study the traffic. There are two synthetic environments and two realistic environments in this study. The two realistic environments are the traffic data from Network city and Hongzow junction from Hong Kong. The synthetic environment contains two different environments which are 6x6 uniflow and 6x6 Biflow.

### REFERENCES

- [1] N. Chowdhury, L. M. Mackenzie, Vehicular Communications for Smart Cars Protocols, Applications and Security Concerns, Taylor & Francis Limited, ISBN: 9780367457440, 036745744X, 2021.
- [2] G. Zhao, G. Zhu, Big Data Transportation Systems, World Scientific Publishing Company, ISBN: 9789811236013, 9811236011, 2021.
- [3] J. Aulinas, H. Sjafrie, AI for Cars, CRC Press, ISBN: 9781000417166, 1000417166, 2021.
- [4] W. Xu, H. Zhou, X. Shen, Internet Access in Vehicular Networks, Springer International Publishing, ISBN: 9783030889913, 3030889912, 2021.
- [5] W. Shi, L. Liu, Computing Systems for Autonomous Driving, Springer International Publishing, ISBN: 9783030815646, 3030815641, 2021.
- [6] A. Khanna, D. Gupta, P. L. Mehta, V. H. C. de Albuquerque, Smart Sensors for Industrial Internet of Things Challenges, Solutions and Applications, Springer International Publishing, ISBN: 9783030526245, 3030526240, 2021.
- [7] <https://www.worldbank.org/en/news/feature/2021/11/04/sri-lanka-s-journey-to-road-safety>.
- [8] S. K. Singh, "Road Traffic Accidents in India: Issues and Challenges", Elsevier-ScienceDirect, Transportation Research Procedia, vol.25, pp.4708-4719, 2017.
- [9] <https://cityflow-project.github.io/>.
- [10] L. Raes, P. Michiels, T. Adolphi, C. Tampere, "DUET: A Framework for Building Secure and Trusted Digital Twins of Smart Cities", IEEE Internet Computing, 2021, DOI:10.1109/MIC.2021.3060962.
- [11] H. Wu, J. Zhang, Z. Cai, F. Liu, Y. Li and A. Liu, "Toward Energy-Aware Caching for Intelligent Connected Vehicles," in IEEE Internet of Things Journal, vol. 7, no. 9, pp. 8157-8166, Sept. 2020, doi: 10.1109/IIOT.2020.2980954.
- [12] W. Xu, S. Guo, S. Ma, H. Zhou, M. Wu and W. Zhuang, "Augmenting Drive-Thru Internet via Reinforcement Learning-Based Rate Adaptation," in IEEE Internet of Things Journal, vol. 7, no. 4, pp. 3114-3123, April 2020, doi: 10.1109/IIOT.2020.2965148.
- [13] I. Ud Din, B. Ahmad, A. Almogren, H. Almajed, I. Mohiuddin and J. J. P. C. Rodrigues, "Left-Right-Front Caching Strategy for Vehicular Networks in ICN-Based Internet of Things," in IEEE Access, vol. 9, pp. 595-605, 2021, doi: 10.1109/ACCESS.2020.3046887.
- [14] H. Vasudev, V. Deshpande, D. Das and S. K. Das, "A Lightweight Mutual Authentication Protocol for V2V Communication in Internet of Vehicles," in IEEE Transactions on Vehicular Technology, vol. 69, no. 6, pp. 6709-6717, June 2020, doi: 10.1109/TVT.2020.2986585.
- [15] L. Benarous, S. Bitam and A. Mellouk, "CSLPPS: Concerted Silence-Based Location Privacy Preserving Scheme for Internet of Vehicles," in IEEE Transactions on Vehicular Technology, vol. 70, no. 7, pp. 7153-7160, July 2021, doi: 10.1109/TVT.2021.3088762.
- [16] Y. Ni et al., "Toward Reliable and Scalable Internet of Vehicles: Performance Analysis and Resource Management," in Proceedings of the IEEE, vol. 108, no. 2, pp. 324-340, Feb. 2020, doi: 10.1109/JPROC.2019.2950349.
- [17] W. Chang, L. Chen and K. Su, "DeepCrash: A Deep Learning-Based Internet of Vehicles System for Head-On and Single-Vehicle Accident Detection With Emergency Notification," in IEEE Access, vol. 7, pp. 148163-148175, 2019, doi: 10.1109/ACCESS.2019.2946468.
- [18] R. Silva and R. Iqbal, "Ethical Implications of Social Internet of Vehicles Systems," in IEEE Internet of Things Journal, vol. 6, no. 1, pp. 517-531, Feb. 2019, doi: 10.1109/IIOT.2018.2841969.
- [19] P. Sharma and H. Liu, "A Machine-Learning-Based Data-Centric Misbehavior Detection Model for Internet of Vehicles," in IEEE Internet of Things Journal, vol. 8, no. 6, pp. 4991-4999, 15 March 2021, doi: 10.1109/IIOT.2020.3035035.
- [20] X. Wang, S. Han, L. Yang, T. Yao and L. Li, "Parallel Internet of Vehicles: ACP-Based System Architecture and Behavioral Modeling," in IEEE Internet of Things Journal, vol. 7, no. 5, pp. 3735-3746, May 2020, doi: 10.1109/IIOT.2020.2969693.
- [21] K. N. Qureshi, M. M. Idrees, J. Lloret and I. Bosch, "Self-Assessment Based Clustering Data Dissemination for Sparse and Dense Traffic Conditions for Internet of Vehicles," in IEEE Access, vol. 8, pp. 10363-10372, 2020, doi: 10.1109/ACCESS.2020.2964530.
- [22] F. Fu, Y. Kang, Z. Zhang, F. R. Yu and T. Wu, "Soft Actor-Critic DRL for Live Transcoding and Streaming in Vehicular Fog-Computing-

- Enabled IoV," in IEEE Internet of Things Journal, vol. 8, no. 3, pp. 1308-1321, 1 Feb.1, 2021, doi: 10.1109/JIOT.2020.3003398.
- [23] Z. Xue, Y. Liu, G. Han, F. Ayaz, Z. Sheng and Y. Wang, "Two-Layer Distributed Content Caching for Infotainment Applications in VANETs," in IEEE Internet of Things Journal, vol. 9, no. 3, pp. 1696-1711, 1 Feb.1, 2022, doi: 10.1109/JIOT.2021.3089280.
- [24] C. Sonmez, C. Tunca, A. Ozgovde and C. Ersoy, "Machine Learning-Based Workload Orchestrator for Vehicular Edge Computing," in IEEE Transactions on Intelligent Transportation Systems, vol. 22, no. 4, pp. 2239-2251, April 2021, doi: 10.1109/TITS.2020.3024233.
- [25] X. Hong, J. Jiao, A. Peng, J. Shi and C. -X. Wang, "Cost Optimization for On-Demand Content Streaming in IoV Networks With Two Service Tiers," in IEEE Internet of Things Journal, vol. 6, no. 1, pp. 38-49, Feb. 2019, doi: 10.1109/JIOT.2018.2873085.
- [26] L. Hou, L. Lei, K. Zheng and X. Wang, "A  $Q^2$ -Learning-Based Proactive Caching Strategy for Non-Safety Related Services in Vehicular Networks," in IEEE Internet of Things Journal, vol. 6, no. 3, pp. 4512-4520, June 2019, doi: 10.1109/JIOT.2018.2883762.
- [27] S. Xia, F. Lin, Z. Chen, C. Tang, Y. Ma and X. Yu, "A Bayesian Game Based Vehicle-to-Vehicle Electricity Trading Scheme for Blockchain-Enabled Internet of Vehicles," in IEEE Transactions on Vehicular Technology, vol. 69, no. 7, pp. 6856-6868, July 2020, doi: 10.1109/TVT.2020.2990443.
- [28] Z. Su, M. Dai, Q. Xu, R. Li and H. Zhang, "UAV Enabled Content Distribution for Internet of Connected Vehicles in 5G Heterogeneous Networks," in IEEE Transactions on Intelligent Transportation Systems, vol. 22, no. 8, pp. 5091-5102, Aug. 2021, doi: 10.1109/TITS.2020.3043351.
- [29] Y. Ni et al., "Toward Reliable and Scalable Internet of Vehicles: Performance Analysis and Resource Management," in Proceedings of the IEEE, vol. 108, no. 2, pp. 324-340, Feb. 2020, doi: 10.1109/JPROC.2019.2950349.
- [30] S. Heo, W. Yoo, H. Jang and J. -M. Chung, "H-V2X Mode 4 Adaptive Semipersistent Scheduling Control for Cooperative Internet of Vehicles," in IEEE Internet of Things Journal, vol. 8, no. 13, pp. 10678-10692, 1 July1, 2021, doi: 10.1109/JIOT.2020.3048993.



# Monitoring activity and detecting unexpected events in surveillance footage using Deep CNN

Gururaj T<sup>1</sup>, Nirmala C R<sup>2</sup>, Naveen K R<sup>3</sup>

<sup>1</sup> Associate Professor, CSE, Bapuji Institute of Engineering and Technology, Davangere, Karnataka, India, [raj80guru@gmail.com](mailto:raj80guru@gmail.com)

<sup>2</sup> Professor, CSE, Bapuji Institute of Engineering and Technology, Davangere, Karnataka, India, [nirmala.cr@gmail.com](mailto:nirmala.cr@gmail.com)

<sup>3</sup> Assistant Professor, CSE, Bapuji Institute of Engineering and Technology, Davangere, Karnataka, India, [naveenkr@bietdvg.edu](mailto:naveenkr@bietdvg.edu)

Received Date : April 05, 2022 Accepted Date : April 29, 2022 Published Date : May 07, 2022

## ABSTRACT

Security is always a primary concern in any domain, because there is an increasing in crime rate and illegal activities. Computer vision learning places a premium on abnormal detection and monitoring, which has numerous applications for dealing with a wide range of issues. We are all aware that there is a high demand for safety protection, personal properties and security, in recent years, video surveillance in systems has become a major focus in people's lives, particularly in government agencies and businesses. The technique we are employing is anomaly detection, which aids in distinguishing various patterns and identifying unusual patterns in a short period of time; these patterns are referred to as outliers. Surveillance videos provide real-time output of unusual events. Anomaly detection in video surveillance entails breaking the process down into three layers: video labelers, image processing, and activity detection. As a result, it detects abnormalities in videos for video surveillance, providing an application by providing accurate results in real-time scenarios. In this proposed work, abnormal events are detected with 98.5 percent accuracy using images and videos. To prevent virus transmissions across the world the government forced to announce the lockdown due to COVID-19 pandemic. As a result, production at manufacturing plants in most areas was halted, resulting in the cessation of all economic activity. There is an even greater need to ensure the safety of youngsters. While there is a pressing need to revive workforce production. The work helps in maintaining social distance and wearing face masks while at work clearly reduces the risk of transmission. Monitor activity decided to identify violations using computer vision (Not Wearing Mask) Real-time alerts that send a trigger and an email with a photo of a rule violation to the appropriate authority as evidence of a rule violation.

**Key words:** Covid-19, Deep CNN, Pandemic, Surveillance, Yolo.

## 1. INTRODUCTION

At that moment and area pass, technology is widely leaking around the earth. The motive of this is to boost us in our everyday residence. Technology has been used for surveillance for decades[8]. Government agencies, businesses, and private properties alike have been interested in video surveillance systems for many years. In today's world, people want better image quality, less expense, and a wider variety of different quantities and scalability. For protection purposes, cameras are the same as they have to be monitor real-time actions, receive data, and break down calculations of what's going on. Often, monitor the real-time activities, collect data, and give out analyses.

The most important thing is to improve an algorithm that can detect mortal activity quickly and easily on video surveillance to take advantage of it [8]. In this case, we're combining simplicity and the necessities of the market. The nation is directly moving towards the end of mechanization as a result of workers' loads. Also, safety issues are a problem in the world. So why not just expand a modern strategy that fulfills the market demands? An easy task doesn't have to be complex. In this work, we discuss a simple software algorithm that let us classify events that occur in a video as normal or abnormal via the content of the video.

- Globally the COVID-19 Pandemic has been severely affecting the World, affecting more than eight million people, according to data obtained by the end of the World Health Organization. To avoid the reach of the infection in common places, face masks should be worn and safe social distance should be followed.

- For detecting masks and social distance, we employ cascade classifiers. With the use of machine learning, a

cascade process can be tested from a pair of beneficial and negative visions to identify odd information.

- In this technique, initially the representation stands with several favorable and unfavorable snapshots or data. Then features like line features, edge features & four rectangle features are extracted from it. This is achieved with the help of Cascade of Classifiers.

- Following these steps, the extracted features from both models are evaluated by comparing with the previously loaded data to figure out whether the image under study contains a weapon, or the person is wearing a mask securely or whether the country in the structure is maintaining a safe distance from among us.

- If any deviation from the training data is observed, the object is labelled to be a weapon and alerts are let out in the form of a buzzing sound, a mobile phone notification and an email notification to the registered email address on the Cloud platform.

- If the individuals in the scene are found to be not wearing a face mask or not located at the specified safe distance, an output window appears displaying the appropriate message.

## 2. LITERATURE SURVEY

[1] explains about low resolution frames, and can handle uncommon events like crowding and fights without require classifiers and training data sets, this methodology is low cost and able to recognize uncommon events as they occur. This method will increase ATM security by enhancing user authentication. Video surveillance systems face the challenge of detecting unusual events, although the light conditions within the environment may also affect the captured image.

In proposed methodology [2] of cost again rises if we are handling with the event detection. An Algorithm is developed recently to detect an unusual events and also for enhancement of ATM's security by using a low resolution cameras and with the lower cost. It can be used in low resolution frames but require proper light condition.

We are now seeing theft and robbery attacks on the general public in ATMs.[3]. Investigation agencies often have difficulty tracking cases. Our system detects odd events even with videos with low resolution, which use ARM 7 LPC 2148, to provide an enhanced ATM security system. At the moment of detecting a suspicious event in the ATM, a buzzer will sound and SMS will be sent from the GSM module to the ARM 7 telling it what to do.

In [4] USA Social distancing has been shown to be an effective method of preventing the spread of the infectious Corona Virus Disease (COVID-19). It is challenging to track the 6-foot (2-meter) distance between you and your surroundings as individuals are unaccustomed to doing so. The system monitors for violations and releases a warning

signal over audio and visual mediums without directly targeting the violator. Its accuracy, however, is lower.

Using [5] open-source Computer Vision (OpenCV) software, which is used for Image processing operations, the system is implemented on the credit card sized Raspberry Pi.

The paper [6] describes a video surveillance system that can be used in a crowded environment and describes an unusual event that occurred on the Lebanese International University Saida Campus.. Here with the help of Histogram of Magnitudes (HOM) we implement our results and we met our expectations.

## 3. PROPOSED SYSTEM

Activity models occur hardly used for picturing the passionate essence, of a network but are furthermore utilized to establish the executable policy by using advanced and reverse engineering skills.

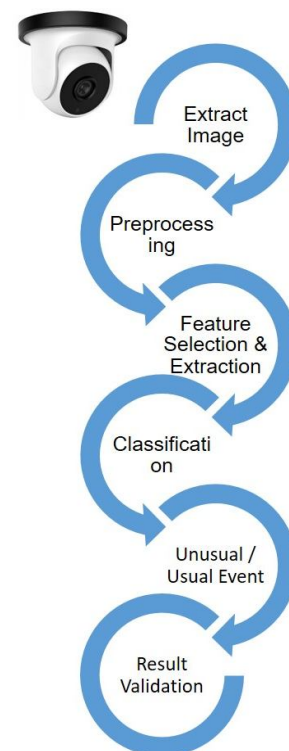
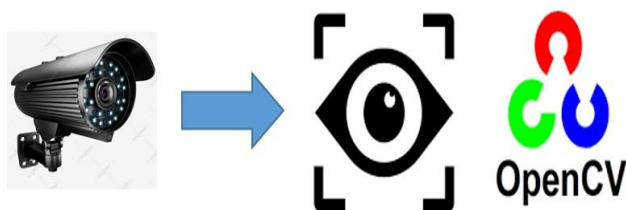


Figure 1: Activity model of proposed system

The figure 1 shows the Activity model of how their laboring technique will be accomplished characterizes the dynamic factors of the network. It occurs in a flowchart that illustrates the sequence from one of the activities to another. The flow can exist sequential, branched, or concurrent. Here the working starts with the camera and then it will extract the image, preprocessing procedure will be applied then it will select the features and extract it next it undergoes for classification if the event is unusual or usual and then it sends a message alert here comes the end of procedure.

## OBJECTIVES

- Our project is designed to create an Enhanced security system with automatic alert system of abnormal events.
- It helps in environment to work safe in schools, colleges and in public area and it is a user friendly.
- It helps in detecting who are not wearing a proper mask and who are all not maintaining social distance.



**Figure 2: Training model using camera**

The Figure 2 shows how we trained our model by using the Web camera, and the camera captures the live video and from that video live, we are going to observe the expression by taking the portrayal of the person into frames. We trained this by using algorithms to detect any unusual activity it must observe all the unusual events and detect them.

## 4. DESIGN AND IMPLEMENTATION OF ANOMALY DETECTION

It explains how to detect a weapon by observing the figure 3 in that first step, we initialize the web camera and start capturing the video frame. After that it will preprocess the image and reduce the noise, it will extract the feature. In weapon detection, we are using YOLOU3 framework has we seen in the figure 3.

The YOLOU3 framework has been designed to detect objects in the cloud. It takes the entire image in a single object & divides it in a grid format & predict the sounding box coordinates. The advantages of YOLOU3 is increased speed which is necessary for real time applications.

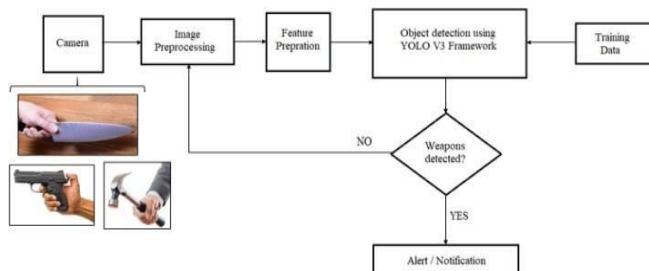


**Figure 3: Block Diagram for Weapon Detection**

Once weapon is detected, it will send the Alert Notification to authorized person for sending SMS we are using Twilio module.

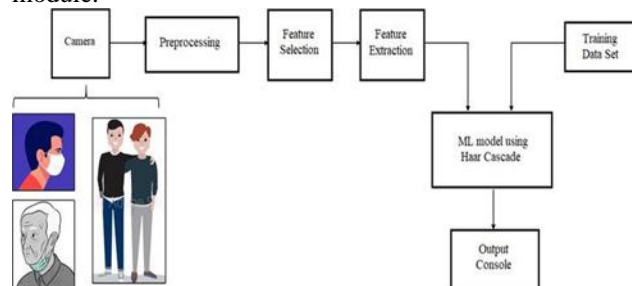


**Figure 4- Block Diagram for Face mask and Social distance Detection**

In figure 4 it explains detection of Face mask and Social Distancing, and in this diagram first camera will open in here. We are using open cv packages in that we are using cv2 library.

After that it will initialize the video frame & start capture the face of the person image preprocess the image means it will remove noise and unwanted images it will select only person image. After that it will select only person image. After that it will extract the features. We are using Haar cascade algorithm.

In this algorithm, initially, the prototype is to be provided with various beneficial and unfavorable pictures or data.

Then the features like line, edge, and four-rectangle features are extracted from it. After feature extraction it will train the image and create the model once the model is created it will test the image. The person is wearing a mask securely, or the people in the frame are keeping their distance from each other.

## 5. IMPLEMENTATION OF CASCADE OBJECT DETECTOR (HAAR CASCADES)

In Figure 5 Our benefit will be implemented utilizing the Haar Cascade classifier. In the 2001 journal "Rapid Object Detection using a Boosted Cascade of Simple Features", Paul Viola and Michael Jones proposed a multi-class Haar Cascade classifier as a beneficial object detection approach. Through the cascade function, a lot of favorable and unfavorable images are trained. This method is then used to detect items in other images based on the training. As you can see, they are huge individuals

Matching templates find identical tracts in the bigger portraits by comparing them to a minor image, or template. Blob estimation observes items in attention by segmenting and analyzing blob property. With the Viola-Jones algorithm, pre trained objects such as faces, noses, and eyes can be identified by features similar to those in the Haar algorithm. A custom classifier could also be trained.



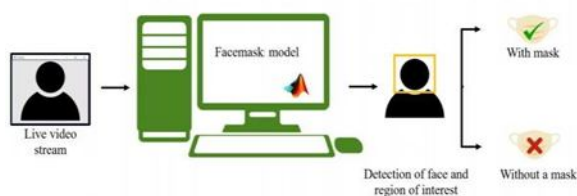


**Figure 5: Live video stream is given as an input to the Facemask model**

### FACIAL RECOGNITION ALGORITHM

This section describes Viola-Jones algorithm here, as it is one of the popular features-based algorithms. The Viola-Jones framework is a powerful framework despite its age. It has shown exceptional results in real-time face recognition. In spite of its slow training time, this algorithm can detect faces in real-time very quickly. The algorithm (which works on grayscale images, seeks out specific features in each sub region) takes a large portion of an image and looks at many smaller sub regions. In an image there are often many faces of varied sizes, so different positions and scales must be checked. Using this algorithm, Viola and Jones identified faces using features similar to those in the Haar algorithm.

1. The video should be captured.
2. By dividing the video into frames, you will be able to understand what's happening.
3. You can also use YOLOv3 to get the bounding boxes around people in each frame. If it reaches the end of the frame, stop
4. Furthermore, you should use Haar cascade to see where the faces are captured so that you can calculate their positions.
5. If a person is wearing a mask, you need to detect the mask with the mask net and face net models.
6. You can detect masks on a person and learn how much distance exists between their faces by using bounding boxes.
7. Show the results on a results board above the video.
8. The results should be displayed in an output stream.
9. Repeat this process until the file is full

### DETECTION AND IDENTIFICATION OF WEAPONS

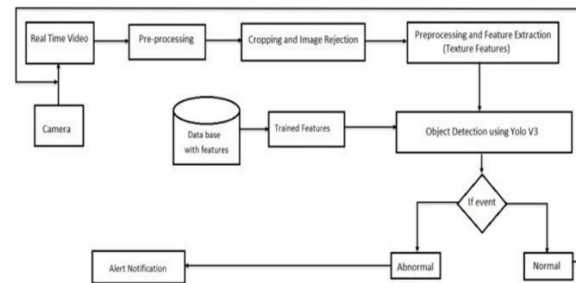


**Figure 6: Block Diagram**

We build a machine learning model using the Tensor flow backend and Python Programming Language as shown in figure 6. We train this model by passing a good amount of data and teaching it to distinguish between various types of detection made.

**Photographic, film, or video camera: A device that records visual images.** It constantly works like a surveillance system.

Pre-processing an image is a method of improving the data of images, aiming to suppress undesired distortions or enhance certain features that will be in the image once further analysis is completed. The image information content is not increased.

**Cropping and Image rejection:** Cropping the image lets us extract the area of interest in an image. Rejection removes background details.

**Feature extraction:** This process reduces the weight of dimensionality of raw data by dividing it up into smaller, more manageable sets

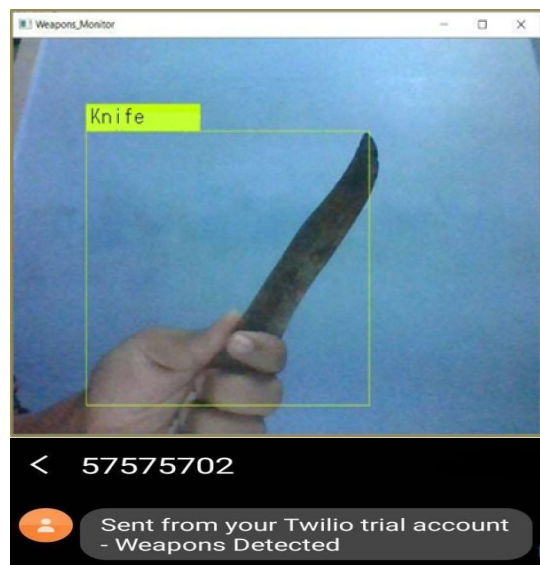
**Object detection using YOLO V3:** One of the earliest possible real-time objective detection algorithms is YOLO (You Only Look Once) which is approximately 4.5 frames per second faster than the R-CNN clan (R-CNN, Fast R-CNN, Faster R-CNN, etc.)

**If statement for Event:** It triggers an alarm if there's an unusual event detected otherwise it continues scanning for Weapons within video frames.

**Alert Notification:** If a weapon is detected then it sends an alert notification to the registered user and emails them a picture of the offender along with the weapon detected.

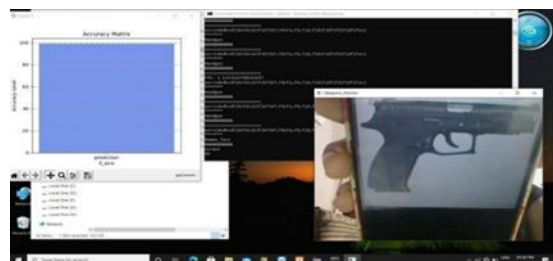
**Database:** Dark net is a C and CUDA-based neural network framework. The framework brings out You Only Look Once (YOLO), a state-of-the-art, real-time object detection system  
**Trained features:** We train our model using COCO datasets for weapons and human detection.

## 6.RESULTS



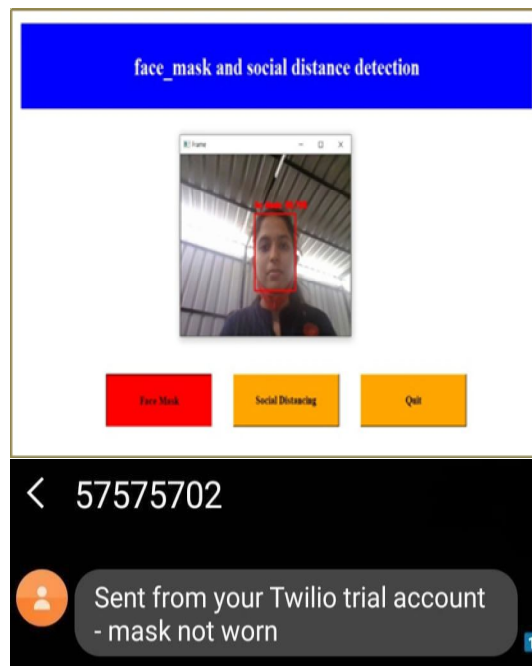
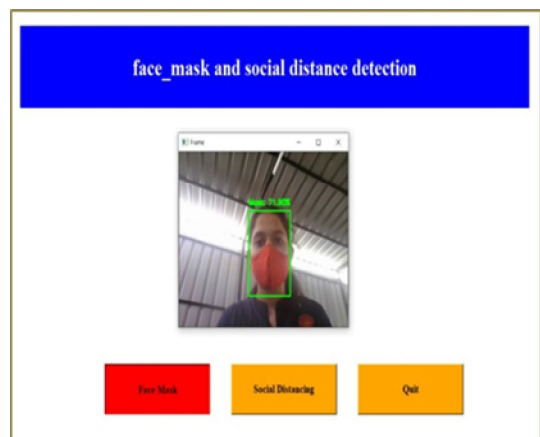
**Figure 7: Output of Weapon Detection**

In Figure 7 it shows an Output of Weapon Detection as Security is the main thing in today's situation in public places, like if any events going on as so many people are getting together we can't check all so here we implemented to detect a weapon by training all the types of weapons before itself. Here in figure knife is detected and it gives us a message alert by using Twilio account i.e. "WEAPON DETECTED".



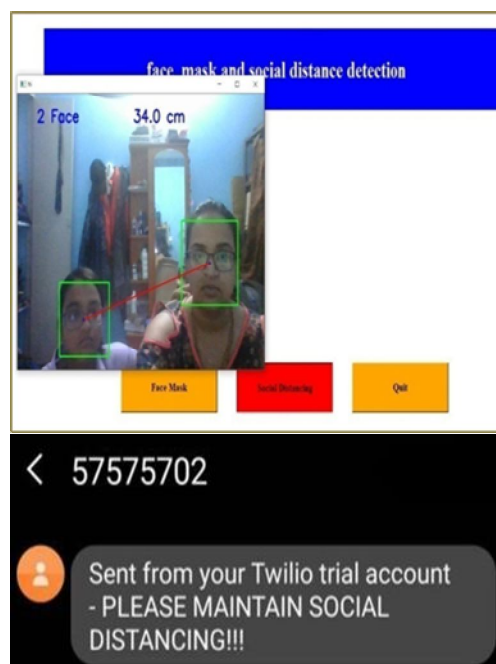
**Figure 8: Handgun Detection**

We get a 98.5% of accuracy matrix graph which shown in above figure 8 and it gives an message alert by using Twilio account i.e. "HANDGUN DETECTED".



**Figure 9 : Output of Face Mask Detection**

In figure 9 it shows an Output of Face mask detection, Wearing a Face Mask is one of the great meaningful creatures in this Pandemic Situation but people are neglecting and not wearing the face mask properly, So here we implement that the people who wearing a face mask and who are not wearing a face mask, as the figure tells u that the people who are wearing a face mask it marks all them as in GREEN color and people who are not wearing the face mask with the RED color mark along with this it gives a message alert like "PLEASE WEAR FACE MASK".



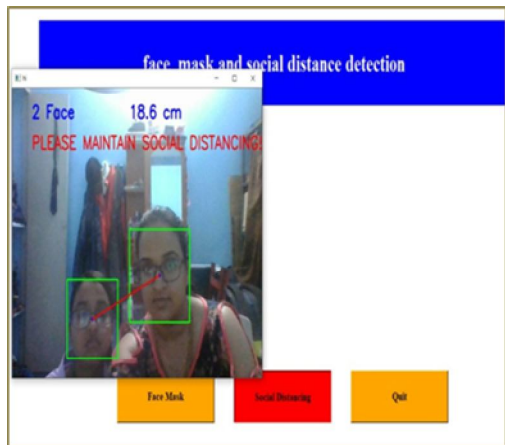


**Figure 10: Output of Social Distance Detection**

In figure 10 it shows a Output of Social Distance Detection, as you know that maintaining a Social Distance is also one of the important criteria in today's pandemic condition, as the people are not maintaining the distance properly so here by using camera we can identify who are all not maintaining the minimum distance of 19cm it gives an RED color mark to that person it sends an message alert like "PLEASE MAINTAIN SOCIAL DISTANCE" and the people who are all maintaining the social distance shows as GREEN color mark.

## 7. CONCLUSION AND FUTURE ENHANCEMENT

This model is more reliable in providing security. This is also much anticipated solution to the problem of illegal or rules violation in any places and also it can be used to monitor social distance and also mask detection by interfacing a camera to capture live face images. If mask is not detected and not maintaining social distance then it send a alert about the violation to authorized person.

Also our model also helps in detecting Weapon and unusual activity and sending alert to the consult person.

Advantage and Disadvantage:

Advantage:

- ☐ Gives Assurance of safety from contagious COVID-19
- ☐ It Increases safety due to detection and alert system
- ☐ Opportunities to avoid greater loss or damage due to prior alerts and notifications
- ☐ Helps in detection of particular objects like dangerous weapons, face mask

Disadvantage:

- ☐ Fake weapons are also detected
- ☐ Social distancing detection applicable for 3 or less people

Applications:

- Our Model Can be set up in crowded places like
- Railway stations
- Airports
- Bus stand
- Malls

It also useful in buildings that requires high security like

- Banks
- Museums
- Jewelry shop
- ATMs

Future Enhancements:

- ☐ Algorithm can be modified and more intricate data can be fed to make the machine capable of Crowd Detection in order to ensure social distancing as a contribution to prevailing pandemic situation.
- ☐ Sensors and required circuits can be paired with the hardware model in order to detect and monitor accidents like fire breakouts, gas leaks, explosions.
- ☐ The project can make good use of upcoming advancements in CCTV surveillance technology to improve its efficiently, ease of access and output accuracy.
- ☐ Model can be upgraded and trained much more efficiently to differentiate between real and fake objects and situations.

## REFERENCES

1. S. A. Radzi, M. K. M. Alif, Y. N. Athirah, A. S. Jaafar, A. H. Norihan, and M. S. Saleha, "IOT based facial recognition door access control home security system using Raspberry Pi," *International Journal of Power Electronics and Drive Systems (IJPEDS)*, vol. 11, no. 1, p. 417, 2020.
2. P. Priyanka and T. R. R. Kumar, "Real-time facial expression recognition system using Raspberry Pi," *NCTET-2K17*, 2017.
3. Y. Shatnawi, M. Alsmirat, and M. Al-Ayyoub, "Face recognition using Eigen-faces and Extension Neural Network," *2019 IEEE/ACS 16th International Conference on Computer Systems and Applications (AICCSA)*, 2019.
4. P. A. Avirachmi Gresy Narwati, A. K. Mahamad, S. Saon, M. A. Azlan, and R. Nurmalasari, "Automated door accessing system with face recognition and NFC," *Lecture Notes in Electrical Engineering*, pp. 589–599, 2021.
5. W. Donat, "The Home Security System," *Learn Raspberry Pi Programming with Python*, pp. 111–126, 2014.
6. S. K. J, R. K. K, and S. V.S, "Security system with face recognition, SMS alert and Embedded Network Video Monitoring Terminal," *International Journal of Security*,

Privacy and Trust Management, vol. 2, no. 5, pp. 9–19, 2013.

7. M. Sahani, C. Nanda, A. K. Sahu, and B. Pattnaik, “Web-based online embedded door access control and home security system based on Face Recognition,” 2015 International Conference on Circuits, Power and Computing Technologies [ICCPCT-2015], 2015.
8. M. R. Mulla, R. P. Patil, and S. K. Shah, “Facial image based security system using PCA,” 2015 International Conference on Information Processing (ICIP), 2015.



\*Correspondence: Naveen S Pagad, Visvesvaraya Technological University, Belagavi, Karnataka, India, naveenspagad@gmail.com

# End-to-End Relation Extraction on Clinical Text Data using Natural Language Processing

Naveen S Pagad<sup>1</sup>, Pradeep N<sup>2</sup>

<sup>1</sup> Visvesvaraya Technological University, Belagavi, Karnataka, India, naveenspagad@gmail.com

<sup>2</sup> Bapuji Institute of Engineering and Technology, Davangere, Karnataka, India, nmnpadeep@gmail.com

## Abstract

In light of the increasing number of clinical narratives, a modern framework for assessing patient histories and carrying out clinical research has been developed. As a consequence of using existing approaches, the process for recognizing clinical entities and extracting relations from clinical narratives was subsequently error propagated. Thus, we propose an end-to-end clinical relation extraction model in this paper. Clinical XLNet has been used as the base model to address the discrepancy issue, and the proposed work has been tested with the N2C2 corpus.

**Keywords:** Clinical entity, Relation extraction, Error propagation, End-to-end model

## 1. Introduction

Data is the collection of facts and statistics concerning an object or originated an event. The processed data is information whose objective is to increase its usefulness of the data. Knowledge represents an understanding of certain information. The unstructured nature of text data makes automated understanding difficult and has led to the development of several text mining (TM) techniques in the last decade (Bose, P., et al., 2021).

In the clinical context, clinical data is raw data in a patient's Electronic Health Record (EHR). The clinical narrative written by a healthcare practitioner originated in the occurrence of an event, such as admission reports written during patient admission, lab reports, and discharge summaries. Clinical data from electronic health records are used for computerized clinical applications (e.g., clinical decision support systems) and clinical and translational research. EHR data can serve as a challenge because patient information can be embedded in the clinical text, which is not directly accessible through other computerized applications that utilize structured data (Tang, B., Cao, H., Wu, Y., Jiang, M., & Xu, H., 2013, April).

The clinical terms found and extracted from the clinical data, such as medication or diseases, is clinical information. Clinical knowledge comprises comprehension of the clinical data extracted, such as establishing clinical relations between the patient diagnosis and the clinical terms found in the patient's EHR. An example of clinical knowledge could be discovering which medications are more prescribed in a given clinical specialty based on the clinical information extracted from the EHRs' clinical



data, written in narratives.

NLP technologies have been introduced in the medical domain in the past decade that extracts structured clinical information from narrative text (Friedman, C., et al., 1994). The term Natural Language Processing (NLP) refers to the methods used by computers to interpret spoken or written information. Several high-level tasks are needed to process human languages with NLP, such as machine translation, question-answering systems, information extraction, and natural language understanding. As part of data analysis, KDD, and data mining, knowledge extraction is essential to extracting structured information from unstructured data. A significant amount of continuous medical information is acquired, maintained, and available digitally, including background information, blood tests, medications, therapies, and therapeutic interventions.

Clinical Named Entity Recognition (NER) is an essential step in extracting patient data from medical records. A need for clinical NER in the mining of clinical data has attracted research attention. Specifically, it aims to build a database of unique medical entities from medical texts, where the target entities include diseases, medications, examinations, and remedies (Zhang, R., Zhao, P., Guo, W., Wang, R., & Lu, W., 2022). However, medical NER differs from generic NER in several important ways. There are many alternative spellings and synonyms that contribute to the development of vocabulary. As a result, medicine interpretation is negatively affected.

This research aims to extract end-to-end relation extraction from text data using natural language processing, discovering clinical concepts within the texts and their relationships. Current solutions often resolve the problem in two steps: identifying the named entities and classifying any relations between them (Giorgi, J., et al., 2019). These two steps can be regarded as two traditional subtasks, namely named entity recognition (NER) and relation classification (RC), which propagate errors from NER to RC without giving feedback from RC to NER (Bethard, S., et al., 2015, June; Lee, H. J., et al., 2016, June).

Due to the limitation of error propagation between subtasks, we developed the clinical XLNet model based on natural language processing to achieve end-to-end relation extraction from clinical text data.

The structure of the paper has been structured as follows: Section 2 presents the recent works of literature; section 3 depicts the detailed description of the proposed methodology; section 4 deliberates the implementation results; finally, section 5 concludes the paper.

## ***2. Literature Survey***

This section provides a survey of some existing research related to clinical relations extraction from electronic health records.

Mahendran, D., & McInnes, B. T. (2021) use relation extraction techniques to examine the relationship between drugs and associated attributes. An outline of three approaches is provided: a rule-based approach, a deep learning approach, and a contextualized language model approach. Experimental results demonstrated that the contextualized language model-based approach outperformed other approaches and reached the highest ADE extraction performance.

Hasan, F., Roy, A., & Pan, S. (2020, November) investigate whether word and

sentence embeddings can be used to improve the accuracy of relation extractions using traditional NLP features. In order to extract clinical relationships, different neural network architectures have been explored for combining text embeddings (e.g., Word2Vec and BERT) and traditionally syntactic and semantic features. Comparison between models employing static word embedding (e.g., Word2Vec) and models employing contextual embedding (e.g., BERT). Even though conventional contextual embedding with BERT is very effective, models that combine the technique with traditional syntactic and semantic features perform worse than those that combine conventional contextual embedding with static Word2Vec embedding.

Perera, N., Dehmer, M., & Emmert-Streib, F. (2020) describe approaches to Named Entity Recognition (NER) and Relation Detection (RD), which can be used to determine relationships between proteins and drugs or genes and diseases. A specific biomedical or clinical problem can be summarized using large-scale details integrated into networks, allowing easy data management and analysis.

Liao, W., & Veeramachaneni, S. (2009, June) presented a semisupervised learning algorithm that used CRFs in the NER. Their algorithm provided high-precision labels for unlabeled data based on independent evidence. This allows for the automatic extraction of high-accuracy data without redundant information. A more accurate classifier would be the result of the next iteration.

Jiang, S., Zhao, S., Hou, K., Liu, Y., & Zhang, L. (2019, October) modeled Chinese electronic medical records using a BERT-BiLSTM-CRF model. A pre-trained BERT language model improves word semantics, followed by a biLSTM network with a CRF layer, with word vectors used as inputs. In contrast to previous approaches that aimed to utilize feature engineering and domain knowledge, the BERT model improves semantic representation. At the same time, the BiLSTM network solves the issue of previous methods that relied on feature engineering and domain knowledge. The CRF model is a new approach that focuses on context annotation information instead of other approaches.

Shi, X., et al. (2019) proposed a novel joint deep learning method to recognize clinical entities or attributes and extract entity-attribute relations simultaneously. This method combines two state-of-the-art methods for named entity recognition and relationship extraction, such as bidirectional long short-term memory with conditional random fields and long short-term memory.

Xu, J., He, H., Sun, X., Ren, X., & Li, S. (2018) introduced a unified model which allows semi-supervised learning to learn in-domain unlabeled data by self-training. Large amounts of unlabeled data are combined to enhance the performance of the NER.

Li, F., Zhang, M., Fu, G., & Ji, D. (2017), using a joint neural model to extract biomedical entities and relationships, investigated how knowledge could be extracted from biomedical data. This methodology combines several state-of-the-art neural models for entity recognition and relation classification in natural language processing and text mining. Besides extracting adverse events related to drug-induced diseases, their model also extracted residences related to bacteria.

Throughout the analysis, the use of relation extraction techniques to examine the relationship between drugs and associated attributes requires a lot of manual work

(Mahendran, D., & McInnes, B. T., 2021). The word and sentence embeddings are used to improve the accuracy of relation extractions using traditional NLP features [9]. The clinical problem can be summarized using large-scale details integrated into networks (Perera, N., Dehmer, M., & Emmert-Streib, F., 2020). The high-precision labels for unlabeled data for automatic data extraction (Liao, W., & Veeramachaneni, S., 2009, June). Word semantics, a pre-trained BERT language model, is used, followed by a biLSTM network with a CRF layer, which provokes discrepancy issues (Jiang, S., Zhao, S., Hou, K., Liu, Y., & Zhang, L., 2019, October). A novel joint deep learning method to recognize clinical entities or attributes (Shi, X., et al., 2019). Large amounts of unlabeled data are combined to enhance the performance of the NER, but more memory is required for training (Xu, J., He, H., Sun, X., Ren, X., & Li, S., 2018). A joint neural model to extract biomedical entities and relationships, but there are high possibilities of error propagation (Li, F., Zhang, M., Fu, G., & Ji, D., 2017). A novel relation extraction technique is proposed, elaborated in the next section, to eliminate the issues mentioned above.

### 3. End-to-End Clinical Relation Extraction

A new framework for assessing patient histories and conducting clinical research has evolved due to the expanding number of clinical reports. Clinical entity recognition and relation extraction are two of the most critical challenges for extracting valuable information from clinical text data. The existing research developed a pipeline for performing entity recognition and relation extraction tasks separately, which could propagate the error from the former task to the latter one, provoking error propagation and performance degradation is provoked. A novel strategy named end-to-end clinical relation extraction has been proposed to overwhelm the issues mentioned above. To deal with the issue of error propagation, both entity recognition and relation extraction

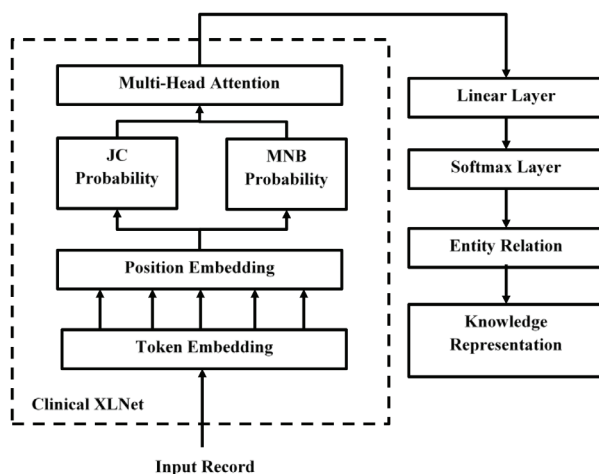


Fig. 1. Block diagram of the proposed end-to-end clinical knowledge discovery strategy

are performed solely rather than separately. Clinical XLNet, a large bidirectional transformer model, has been incorporated as a base model to resolve BERT-based models' discrepancies. Here, the position embedding has been incorporated upon clinical XLNet to take advantage of the entities' positional data of the entities by entity markers with the existing [CLS] vector. To leverage the dependent event relation association and the independent events, the multinomial Naïve Bayes probability function has been performed parallel to the joint conditional probability function. Whereas the multinomial Naïve Bayes leverages the prior probability with conditional probability to determine the probability of the dependent event relation association; furthermore, if the entity pairs are presented in consecutive sentences, the relations between them have been learned through incorporating multi-head attention layer at the top of the clinical XLNet. The transformer outputs are concatenated through a linear layer. Finally, the softmax classifier can be employed to present the entity relation, which might be drug-adverse drug event, drug-reason, etc. At last, the absolute and abundant knowledge discovered from the entity relation extraction will be portrayed in a graphical or statistical form. The block diagram of the proposed methodology is depicted in figure 1.

### ***3.1. Clinical Entity Recognition***

The clinical image or clinical text has been utilized for clinical knowledge discovery, whereas we have extracted the knowledge by adopting clinical text data. Initially, the clinical text data has been pre-processed to retain the eminence of the input corpus for data miners to gain knowledge. The pre-processing steps include data cleaning, tokenization, parts of speech tagging, parsing, stemming, and lemmatization. After the data cleaning process, the sentences are split into several tokens, and then the parts of the speech process have been carried out. In order to resolve the structural ambiguity, parsing is carried out, which identifies the constituents.

Consequently, stemming and lemmatization have been performed. The procedure for stemming is to remove and replace word suffixes to arrive at a common root for the term. A lemma is a canonical form of a word, whereas a stem may or may not be an actual word. This reduces a word's inflectional forms and certain derivationally related forms to a single base form.

The clinical named entity recognition is the task that is crucial for relation extraction. If the entities are not recognized appropriately, the error of entity recognition was carried forward into the relation extraction task on the knowledge discovery pipeline. This provokes error propagation, implying performance degradation and the erroneous discovery of knowledge. To prevent this, the clinical entity recognition and the relation extraction tasks were performed solely on the single model. Most existing approaches rely on sequence labeling models like BERT with Bi-LSTM or CRF, which suffered from discrepancy issues while tuning with contextual embedding. In order to overcome this, the XLNet, a large bidirectional transformer model, has been adopted as a base model in our research.

The XLNet, on the other hand, has been fine-tuned by utilizing smaller clinical data to maximize the task-specific knowledge to make XLNet a clinical XLNet, where the named entity recognition has been taken place. The embedding layers are mainly contributed to clinical entity recognition. The XLNET embedding should be pre-trained with the clinical notes datasets using Permutation Language Modeling. The permuted

language model (PLM) maintains the benefits of autoregressive modeling while simultaneously allowing systems to include bidirectional context. If a sentence is given as  $y = (y_1, y_2, y_3 \dots y_m)$  with the length of  $m$ , there is  $m!$  Possible permutations. Symbolize  $H_m$  as the permutations of set  $\{1, 2, 3, \dots, m\}$ . For a permutation  $h \in H_m$ , represents  $h_T$  as the  $T$ -th element in  $h$  and  $h < T$  as the first  $T-1$  element in  $h$ . PLM pre-trains the model by achieving the preceding criteria,

$$\log P(y; \theta) = E_{h \in H_m} \sum_{T=c+1}^m \log P(y_{hT} | y_{h < T}; \theta) \quad (1)$$

During the autoregressive pre-training, each predicted token in PLM can only view its previous tokens in a permuted phrase and has no knowledge of the whole sentence's position. The permutation Language modeling has been done in the embedding layer to generate a better clinical embedding from clinical notes. The embedding layer processes are depicted in figure 2. Initially, the pre-processed data has been inputted to the clinical XLNet model, whereas the token embedding layer generates the inputs as tokens for further processing. In clinical XLNet, the [CLS] token has been employed as a classification token; the [SEP] token is for the separation of sentences. However, the [CLS] token utilizes only partial knowledge from the input sequence, which affects the positioning of entities. Thus to resolve this, the position embedding has been incorporated upon clinical XLNet to leverage the position information of the entities by entity markers with the existing [CLS] vector, which contributed to carrying forward the entire knowledge up to the end of the task. In figure 2, the entity tokens are represented as entity markers  $\{E_1, E_2, \dots, E_N\}$ , which has been appropriately identifying the clinical entities in the input clinical text data.

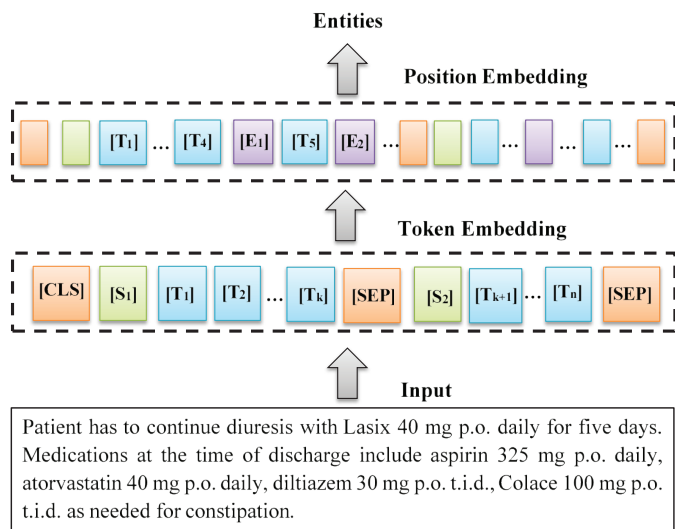


Fig. 2. Embedding Process

As with the entity markers, each entity is preserved until the end of the knowledge discovery process. The clinical entities are drug, class, dosage, frequency, duration, route, and condition. Thus the relation between the drug with the different entities has been extracted by the relation extraction process, which is explained in the next section.



4. Result and Discussion

This section provides a detailed explanation of the implementation results and the evaluation metrics of the proposed system. A comparison has also been provided to demonstrate that the proposed model's performance is superior to existing models.

4.1. Experimental Setup

This work has been implemented in the working platform of python with the following system specification, and the simulation results are discussed below.

Platform	: Python
OS	: Windows 10
Processor	: 64-bit Intel processor
RAM	: 8 GB RAM
Dataset	: N2C2 dataset

4.1.1. Dataset Description

The corpus utilized in the proposed methodology is National NLP Clinical Challenges (n2c2) 2018 dataset. The n2c2 corpus contains the electronic health record of several patients in 10 classes. The medical history, diagnosis, drug name, class of the drug, treatment plans, vaccination dates, allergies, the frequency of the intake of drugs, duration, route, condition, radiological pictures, and laboratory and test results of a patient are all kept in the record. The discharge summaries of patients presented in the corpus are considered for knowledge discovery. The n2c2 corpus contains entity annotations: drug, strength, form, dosage, frequency, route, duration, reason, and ADR. There are eight different kinds of clinical entity relations: strength–drug (severity), form–drug (form), dosage–drug (do), frequency–drug (fr), route–drug (route), duration– drug (du), reason–drug (reason), ADR–Drug (adverse).

The n2c2 corpus has been employed as the input to the proposed clinical XLNet model for knowledge discovery. The corpus is grouped into 10 classes, each containing several patients' health records that have been initially pre-processed for cleaning, then represented statistically in figure 3.

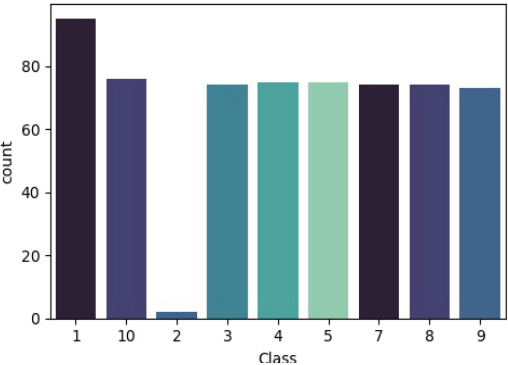


Fig. 3. Statistical representation of n2c2 corpus

humulin', 'hydralazine', 'hydroxide', 'hypertension', 'id', 'imdur', 'improved',  
ns affecting', 'information', 'information override', 'information override add',  
, 'instructed', 'instructed follow', 'instruction', 'instruction avoid', 'instr  
grapefruit unless', 'instructiongive', 'instructiongive stomach', 'instructiongive  
tructiontake consistently meals', 'instructs', 'instructs override', 'instructs  
ril maleate', 'interaction instruction', 'interaction instruction avoid', 'inte  
ctiongive', 'interaction instructiongive stomach', 'interaction instructiontake  
ssium chloride', 'interaction simvastatin', 'interaction simvastatin amp', 'int  
'iv', 'june', 'kcl', 'kcl slow', 'klonopin', 'known', 'lab', 'lad', 'lantus', 'l  
acin', 'levofloxacin po', 'levofloxacin po ref', 'levothyroxine', 'likely', 'li  
isinopril reason', 'lisinopril reason override', 'liter', 'long', 'lopressor',  
agnesium', 'make', 'maleate', 'maleate amp', 'maleate amp potassium', 'mcg', 'm  
, 'medical center', 'medication', 'medications acetylsalicylic', 'medications  
harge', 'medications ecasa', 'medications ecasa aspirin', 'medications tylenol'  
rate', 'mg 24', 'mg 24 dose', 'mg 8h', 'mg atenolol', 'mg colace', 'mg colace 1  
insomnia', 'mg iv', 'mg lasix', 'mg po', 'mg po bid', 'mg po bidfood', 'mg po d  
, 'mg po qhsfood', 'mg qd', 'mg times', 'mg twice', 'mg twice day', 'mgp', 'mi  
o', 'minutes', 'ml', 'moderate', 'monday', 'monday wednesday', 'monday wednesda  
al', 'na', 'nasal', 'nausea', 'neb', 'nebulizer', 'nebulizer mg', 'needed', 'ne

Fig. 4. Tokenization

DISCHARGE MEDICATIONS:/ Medications at the time of dischargeinclude aspirin CHEMICAL  
325 mg p.o. daily , atorvastatin CHEMICAL 40 mg p.o. daily , diltiazem CHEMICAL 30 mg  
p.o. t.i.d CHEMICAL ., Colace CHEMICAL 100 mg p.o. t.i.d CHEMICAL . as neededfor  
constipation DISEASE , Zetia CHEMICAL 10 mg p.o. daily , fenofibrate CHEMICAL 145  
mg p.o.daily , Lasix CHEMICAL 40 mg p.o. daily x5 days , K-Dur 20 mEq p.o. daily x5days  
CHEMICAL , metformin CHEMICAL 500 mg p.o. daily , Toprol-XL 25 mg p.o. daily ,and  
oxycodone CHEMICAL 5-10 mg p.o. q.4 h. as needed for pain DISEASE .DISCHARGE  
Activate Win

Fig. 5 (a)

TEXT	START	END	ENTITY	TYPE
aspirin	68	75	CHEMICAL	
atorvastatin	96	108	CHEMICAL	
diltiazem	127	136	CHEMICAL	
t.i.d	148	153	CHEMICAL	
Colace	157	163	CHEMICAL	
t.i.d	176	181	CHEMICAL	
constipation	196	208	DISEASE	
Zetia	211	216	CHEMICAL	
fenofibrate	236	247	CHEMICAL	
Lasix	267	272	CHEMICAL	
x5days	324	330	CHEMICAL	
metformin	333	342	CHEMICAL	
oxycodone	395	404	CHEMICAL	
pain	439	443	DISEASE	
Lasix	635	640	CHEMICAL	
type II diabetic	846	862	DISEASE	
Diabetes	955	963	DISEASE	
metformin	1019	1028	CHEMICAL	

fig. 5 (b)

Fig. 5. Entity Relation Extraction

For knowledge discovery, the clinical entity recognition task is the one that has to be focused on to enhance the proposed model's efficiency. To do that, the tokenization takes place with token embedding, which is depicted in figure 4. On the obtained tokens, the incorporation of position embedding has been identifying the position of the entities and the entity relation with the drug, which is portrayed in figure 5. In figure 5(a), the entity types marked in the input record have been illustrated. In figure 5(b), the identified entity relations with the drug are listed in the output window with the position of entities, whereas the entity drug is indicated as chemical.

### 5. Conclusion

In this paper, a novel end-to-end clinical relation extraction strategy has been proposed with clinical XLNet. The proposed model has considered the extraction of entity pairs in consecutive sentences, and this provides vast knowledge from the clinical text data, which has been implemented with the n2c2 corpus.

### References

- Bethard, S., et al. (2015, June). Semeval-2015 task 6: Clinical tempeval. In *proceedings of the 9th International Workshop on Semantic Evaluation (SemEval 2015)* (pp. 806-814).
- Bose, P., et al. (2021). A Survey on Recent Named Entity Recognition and Relationship Extraction Techniques on Clinical Texts. *Applied Sciences*, 11(18), 8319.
- Friedman, C., et al. (1994). A general natural-language text processor for clinical radiology. *Journal of the American Medical Informatics Association*, 1(2), 161-174.
- Giorgi, J., et al. (2019). End-to-end named entity recognition and relation extraction using pre-trained language models. *arXiv preprint arXiv:1912.13415*.
- Hasan, F., Roy, A., & Pan, S. (2020, November). Integrating Text Embedding with Traditional NLP Features for Clinical Relation Extraction. In *2020 IEEE 32nd International Conference on Tools with Artificial Intelligence (ICTAI)* (pp. 418-425). IEEE.
- Jiang, S., Zhao, S., Hou, K., Liu, Y., & Zhang, L. (2019, October). A BERT-BiLSTM-CRF model for Chinese electronic medical records named entity recognition. In *2019 12th International Conference on Intelligent Computation Technology and Automation (ICICTA)* (pp. 166-169). IEEE.
- Lee, H. J., et al. (2016, June). UTHealth at SemEval-2016 task 12: an end-to-end system for temporal information extraction from clinical notes. In *Proceedings of the 10th International Workshop on Semantic Evaluation (SemEval-2016)* (pp. 1292-1297).
- Li, F., Zhang, M., Fu, G., & Ji, D. (2017). A neural joint model for entity and relation extraction from biomedical text. *BMC bioinformatics*, 18(1), 1-11.
- Liao, W., & Veeramachaneni, S. (2009, June). A simple semi-supervised algorithm for named entity recognition. In *Proceedings of the NAACL HLT 2009 Workshop on Semi-Supervised Learning for Natural Language Processing* (pp. 58-65).
- Mahendran, D., & McInnes, B. T. (2021). Extracting Adverse Drug Events from Clinical Notes. In *AMIA Annual Symposium Proceedings* (Vol. 2021, p. 420). American Medical Informatics Association.
- Perera, N., Dehmer, M., & Emmert-Streib, F. (2020). Named entity recognition and relation detection for biomedical information extraction. *Frontiers in cell and developmental*

*biology*, 673.

Shi, X., et al. (2019). Extracting entities with attributes in clinical text via joint deep learning. *Journal of the American Medical Informatics Association*, 26(12), 1584-1591.

Tang, B., Cao, H., Wu, Y., Jiang, M., & Xu, H. (2013, April). Recognizing clinical entities in hospital discharge summaries using Structural Support Vector Machines with word representation features. In *BMC medical informatics and decision making* (Vol. 13, No. 1, pp. 1-10). BioMed Central.

Xu, J., He, H., Sun, X., Ren, X., & Li, S. (2018). Cross-domain and semisupervised named entity recognition in chinese social media: A unified model. *IEEE/ACM Transactions on Audio, Speech, and Language Processing*, 26(11), 2142-2152.

Zhang, R., Zhao, P., Guo, W., Wang, R., & Lu, W. (2022). Medical named entity recognition based on dilated convolutional neural network. *Cognitive Robotics*, 2, 13-20.

**Submitted: 03.09.2021**

**Accepted: 25.11.2021**

## Research Article

# Clinical Text Data Categorization and Feature Extraction Using Medical-Fissure Algorithm and Neg-Seq Algorithm

**Naveen S Pagad** <sup>1,2</sup> **Pradeep N** <sup>3</sup> **Khalid K. Almuzaini** <sup>4</sup> **Manish Maheshwari** <sup>5</sup>  
**Durgaprasad Gangodkar** <sup>6</sup> **Piyush Shukla**<sup>7</sup> and **Musah Alhassan** <sup>8</sup>

<sup>1</sup>Department of Information Science and Engineering, Sri Dharmasthala Manjunatheshwara Institute of Technology, Ujire 574 240, India

<sup>2</sup>Visvesvaraya Technological University, Belagavi, Karnataka, India

<sup>3</sup>Department of Computer Science and Engineering, Bapuji Institute of Engineering and Technology, Davangere, Karnataka, India

<sup>4</sup>National Center for Cybersecurity Technologies (C4C), King Abdulaziz City for Science and Technology (KACST), Riyadh 11442, Saudi Arabia

<sup>5</sup>Department of Computer Science and Applications, MCNUJC, Bhopal 462003, Madhya Pradesh, India

<sup>6</sup>Department: Computer Science & Engineering, Graphic Era Deemed to Be University, Dehradun, Uttarakhand, India

<sup>7</sup>UIT-RGPV, Bhopal, India

<sup>8</sup>University of Development Studies, Electrical Engineering Department, School of Engineering, Nyankpala Campus, Nyankpala, Ghana

Correspondence should be addressed to Musah Alhassan; [musahalhassan@uds.edu.gh](mailto:musahalhassan@uds.edu.gh)

Received 7 January 2022; Revised 22 January 2022; Accepted 27 January 2022; Published 7 March 2022

Academic Editor: Vijay Kumar

Copyright © 2022 Naveen S Pagad et al. This is an open access article distributed under the Creative Commons Attribution License, which permits unrestricted use, distribution, and reproduction in any medium, provided the original work is properly cited.

A large amount of patient information has been gathered in Electronic Health Records (EHRs) concerning their conditions. An EHR, as an unstructured text document, serves to maintain health by identifying, treating, and curing illnesses. In this research, the technical complexities in extracting the clinical text data are removed by using machine learning and natural language processing techniques, in which an unstructured clinical text data with low data quality is recognized by Halve Progression, which uses Medical-Fissure Algorithm which provides better data quality and makes diagnosis easier by using a cross-validation approach. Moreover, to enhance the accuracy in extracting and mapping clinical text data, Clinical Data Progression uses Neg-Seq Algorithm in which the redundancy in clinical text data is removed. Finally, the extracted clinical text data is stored in the cloud with a secret key to enhance security. The proposed technique improves the data quality and provides an efficient data extraction with high accuracy of 99.6%.

## 1. Introduction

Clinical data is a standard source of information in most clinical and medical studies. Medical information is gathered either as part of routine hospital treatment or as part of a systematic clinical research plan. Clinical evidence is divided into six categories: Administrative reports, claims data, patient/disease registries, health audits, clinical trial data, and electronic health records. The purest type of electronic clinical data is collected at a treatment institution, hospital,

clinic, or internship at the point of service. The electronic medical record (EMR), also known as the electronic health record (EHR), is normally not accessible to outside researchers. A longitudinal database of electronic health information about particular patients and communities is known as an electronic health record (EHR) [1]. EHRs are often used to track healthcare procedures. EHRs provide a wealth of knowledge that makes them useful for a variety of other purposes [2]. Reducing prescription mistakes, implementing improved coordination and information-



sharing practices between physicians, lowering healthcare rates, better control of patients' medical records, improving care quality, and contributing to better outcomes are only a few examples.

An electronic health record is an electronic version of a patient's medical records [3] maintained by a health care professional for some time, and it includes all of the essential statistical healthcare details related to the care provided to a person by a specific provider, such as profiles, success notes, complications, prescriptions, important signs, and medical history [4]. Privacy, secrecy, and confidentiality are all concerns that must be resolved in an electronic health record system [4]. Even though security and privacy are closely linked, they are fundamentally separate. Privacy refers to a person's ability to choose when, how, and to what extent personal information is [5, 6] exchanged or transmitted by others, while confidentiality refers to the degree to which access to someone's personal information is limited and permitted. An individual's trust in the safety and confidentiality of their medical history had a positive impact on their motivation to create an electronic health record [7]. Patients' ability to encourage health care providers to exchange their medical data by using cloud computing techniques has been [8] limited as a result of privacy issues. Antivirus tools, chief information security officers, and cloud computing are other security methods that are used, but their deployment is [9] budget-dependent.

Even though the cloud storage infrastructure seems to be successful, antivirus protection remains a more widely used security measure. Security concerns have been raised as a result of IT developments such as hosting health data on remote servers managed by third-party cloud service providers [10]. Specific skills for interpreting and collecting information would be needed as information about the patient's condition continues to grow rapidly. Graphics, icons, free text, and numbers are all examples of data formats that can be contained in the EHR program [11]. There are two types of data formats: structured and unstructured. [12] Since the data already has a defined structure, traditional mathematical or machine learning approaches may be used to analyze structured data types with little effort. Hospital notes, surgical history, discharge summaries, radiology reports, diagnostic photographs, and pathology reports are the unstructured data contained in EHR.

Natural language processing (NLP) refers to a computer's capacity to comprehend the more recent human speech words and text. Natural language processing is gaining popularity in healthcare due to its ability to scan, review, and translate massive volumes of patient data. In the healthcare media, NLP will accurately give voice to the unstructured data of the universe, [13] providing incredible insight into understanding efficiency, refining processes, and improving patient outcomes. Natural language processing in healthcare employs sophisticated engines capable of scrubbing vast amounts of unstructured health data for previously ignored or incorrectly written medical conditions. Using [14–16] machine-learned algorithms to interpret medical records in natural language, an illness that

could not have been coded before may be discovered. Algorithms are the building blocks in a machine learning program and are a series of instructions for completing a set of tasks. The algorithms are programmed to learn from data without the need for human interference. [17] Machine learning algorithms increase prediction accuracy over time without the need for scripting. Machine learning applications can potentially improve the accuracy of treatment protocols and health outcomes through algorithmic processes.

Thus, the analysis of unstructured data with a novel solution for data sensitivity, security, quality, and accessibility using machine learning and natural language processing should be proposed. The main goal of this research is to develop machine learning and natural language processing method for recognizing unstructured clinical text data. Even though several data extraction strategies have been proposed, recognizing the unstructured clinical text data remains difficult. The content of the paper is organized as follows: Section 1 represents the introduction; Section 2 presents the literature survey of clinical text data; the novel solutions are presented in Section 3; the implementation results and its comparison are provided in Section 4; finally, Section 5 concludes the paper.

## 2. Literature Survey

Digital Imaging and Communication in Medicine (DICOM) is considered to be the most commonly used medical image format among hospitals. Dorgham et al. [18] proposed to enhance the secure transfer and storage of medical images on the cloud by using hybrid encryption algorithms. One of today's most important priorities is the security of data processed in cloud data centers. When confidential data, such as medical images, is uploaded or shared on the cloud, it must be treated with extreme caution to ensure its reliability. They are made up of one or more compact files that cannot be seen on a screen and saved in a folder. As a result, the data can be accessed at any time. As a result, preserving data protection and denying unauthorized access becomes critical.

Agrwal et al. [19] have used a hybrid integrated Fuzzy Analytical Hierarchy Process-Technique for Order of Preference by Similarity to Ideal Solution (Fuzzy AHP-TOPSIS) method for evaluating various information security. It is essential and sufficient to evaluate information security using an integrated fuzzy MCDM methodology and to define various security attributes in a systematic and step-by-step (tree-based) fashion. This web application did not focus on data quality and data based on electronic health records.

Clinical data synthesis aims at generating realistic data for healthcare research, system implementation, and training. It is a promising tool for situations where real-world data is difficult to obtain or unnecessary. Chen et al. [20] examined an open-source well-documented synthetic data generator Synthea, which was composed of key advancements in this emerging technique. They selected a representative 1.2-million Massachusetts patient cohort

generated by Synthea. Synthea and other synthetic patient generators do not use model for treatment anomalies or the possible results that could emerge from them. So synthetic data generators consider critical quality measurements in their logic and model when clinicians can deviate from the standard to produce a more practical data collection.

In recent years, deep learning techniques have demonstrated superior performance over traditional machine learning (ML) techniques for various general-domain NLP tasks. Clinical documents pose unique challenges compared to general-domain text due to the widespread use of acronyms and nonstandard clinical jargon by healthcare providers. The study by Hasan et al. [21] shows that compared to methods using linear models such as support vector machines (SVMs) or logistic regression, nonlinear neural network models have promising outcomes. The obtained state-of-the-art outcomes as opposed to the lexicon-, knowledge-source-, and conventional machine learning-based systems, demonstrating the usefulness of deep learning approaches to solve different clinical NLP issues, do not state the accessibility of unstructured data.

Identifying chronic conditions in the electronic health record is an important but challenging task. Here, systems adopt methods that allow for automated “noisy labeling” of positive and negative controls. Murray et al. [22] combined a variant of the Easy Ensemble method with the technique of Learning with Noisy Labels. Each of the individual models was trained by using all the 583 positive cases and a random pool of 583 negative patients. All the models in the ensemble were trained with 1:1 class balance and shared the same positive set. This is important for conditions such as systemic lupus erythematosus SLE, for which diagnostic uncertainty is common, and there is often incomplete documentation.

Kumar et al. [23] presented an overview of the current state of healthcare information and a tiered model for healthcare information management in businesses. The report also assesses the numerous elements that play a role in healthcare information security breaches. AHP-TOPSIS’ hybrid fuzzy-based symmetrical technique. Furthermore, to examine the impact of the estimated results, the authors tested the results on Varanasi’s local hospital software. The comparison and sensitivity analysis verify the tested outcomes of the parameters. However, the efficient and accurate extraction of clinical text data is not considered in this work.

Harnoun et al. [24] presented an end-to-end strategy for information extraction and analysis from biological, clinical notes using the Bidirectional Encoder Representations from Transformers (BERT) model and the Conditional Random Field (CRF) layer. They also constructed a named entity recognition model capable of recognizing entities such as drug, strength, duration, frequency, adverse drug responses, the rationale for taking medicine, method of administration, and form. However, the security and authority of clinical data during storage are not considered in this work.

In [18], cloud transfer of data was a tedious process [19]. Security should be maintained in clinical data [20] as

sensitive information needs more privacy [21] and data quality to improve the accessibility [22] of unstructured data. [23] requires efficient and accurate data extraction and in [24], there is a need to consider the security and authority in the clinical text data. Hence, it is understood that the existing techniques face problems in improving the quality of clinical text data; the accessibility of unstructured data is not provided, and it is difficult to maintain data security and authority. Based on an overview of the literature survey, the problem faced on data security, data quality, accessibility of unstructured data should be processed, and a new novel solution had to be implemented based on machine learning and natural language processing. The proposed methods will contribute to all stages of clinical text data extraction, starting with splitting the clinical text data and ending with extraction and storage. The approaches that are already in use in clinical data extraction are explained above. The next section explains the techniques and benefits of the algorithms in the proposed method.

### **3. Discovery of Knowledge in Clinical Data Using Machine Learning and Natural Language Processing in Cloud**

The machine learning approach focuses on advanced computational techniques to identify data and the natural language processing methods enabled to process and analyze textual data written in human languages. Recognition of clinical text data was a tedious process; existing techniques have used several methods for structured data but not in unstructured data, so it could not determine the effective results and data quality. Using our novel Halve Progression, we recognize unstructured clinical text data based on machine learning techniques to split the unstructured clinical text data according to the disease condition. The novel Halve Progression technique utilizes a novel Medical-Fissure algorithm that uses cross-validation based on structured data and thus, the recognition terms are made to be more efficient. After recognizing text data, extraction of data is required to obtain extensive knowledge in clinical data. This can be processed based on clinical language processing; existing techniques could not determine the ambiguity, and mapping with medical terms was not accurate. Our proposed Clinical Data Progression technique uses Neg-Seq algorithm that uses statistical features and Unified Medical Language System (UMLS) with unique identification for mapping. Hence, the resultant data can be used for further diagnosis activity. Extracted data can be stored in a cloud platform since it is considered to be best for accessibility and storage, so an effective cloud framework is required to store clinical data as it contains vast data and sensitive information. Our Cloud Progression uses RS access control that.

It performs validation and authorizes and has a private key for data sharing. So the clinical text data is stored in the cloud with security and authority. Hence, as shown in Figure 1, in our proposed novel method, clinical text data is recognized, extracted, and stored efficiently by machine learning techniques and natural language processing in a cloud environment.

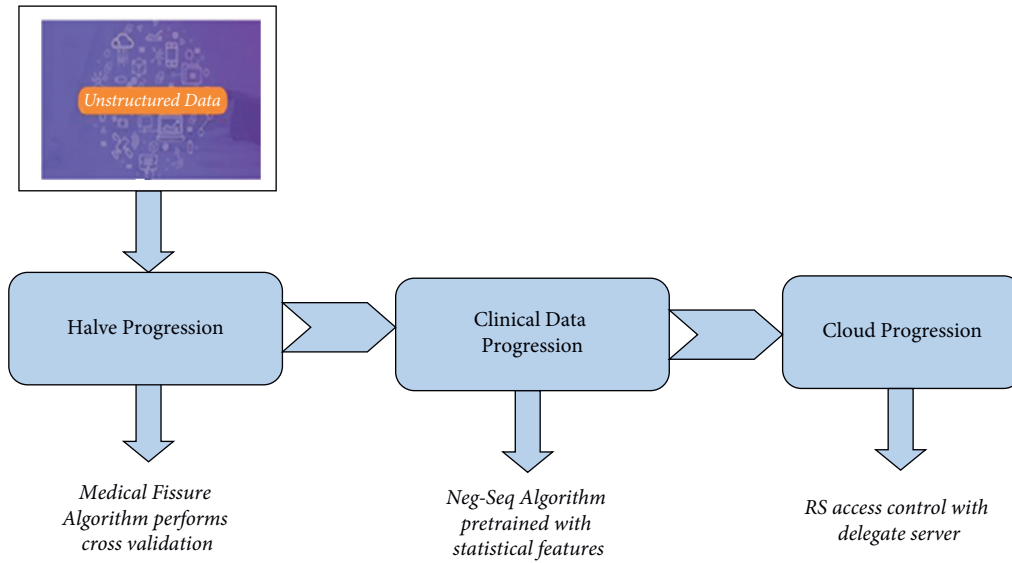


FIGURE 1: Proposed framework.

**3.1. Halve Progression.** The clinical text data recognition was challenging, particularly unstructured clinical text data recognition, and the prior approach could not identify the effective outcome because it required many conversion procedures. A machine learning approach is employed in this work to detect unstructured clinical text data. Using a cross-validation approach, the Medical-Fissure Algorithm divides clinical text data based on illness state.

Halve progression is used to split the clinical text data towards a more advanced state, thereby increasing the data quality. Halve progression uses the Medical-Fissure algorithm for the clinical text data categorization. In the Medical-Fissure algorithm, the original clinical text data, which contains much clinical information, is divided into reduced categories of clinical text data according to some specific condition. Halve Progression based on Medical-Fissure Algorithm provides the best result with F-score in cross-validation trials, indicating the need to split the text data depending on the sick state. For example, the trained five classifiers are needed to detect arterial hypertension (AH), myocardial infarction (MI), stroke, diabetes mellitus (DM), and angina pectoris (AP). For stroke, MI, and AH, using negation classifiers is critical. The classifiers for MI and AH learn context and assist in the discovery of more examples of these illnesses. The most important words for identifying MI, including illness terminology and treatment options, are included in surgery and medications.

When the negations are recognized, a logistic loss is used to categorize each phrase in the anamnesis as containing or not containing negation. Sentences or portions of sentences with negations are deleted from anamnesis so that these texts may be utilized to create additional models that solely address the patient's current situations, such as topic modeling.

The basic goal of the Medical-Fissure Algorithm is to detect unstructured clinical text data and split it based on a unique sick state. As shown in Figure 2, First, unstructured clinical data is used as input, which implies data that does not follow any

conventional format. Second, the Medical-Fissure Method calculates the count in the clinical text data, and the prerequisite for this algorithm is that the clinical text data be present in the input. Third, using a cross-validation technique, the clinical text data is separated into distinct illness conditions. Finally, the filtered clinical text data is the output of this Medical-Fissure Algorithm. As a result, data quality improves and recognition words become more efficient. After recognizing text data, data extraction is required to obtain extensive knowledge in clinical data; this can be processed using clinical language processing because ambiguity determination and mapping with medical terms were not accurate. The next subsection explains the next approach, Clinical Data Progression.

**3.2. Clinical Data Progression.** The Halve Progression improves data quality, but the mapping and extraction of medical words are ineffective. Clinical Data Progression employs the Neg-Seq Algorithm, which is pretrained using statistical characteristics, which include the size, provenance, collection methods, and annotation of the clinical text data. Statistical characteristics accurately collect data, conduct appropriate analyses, and effectively increase the efficiency of data extraction. The Neg-Seq Algorithm uses statistical features for the extraction of clinical text data. By using statistical features, the clinical text data is extracted based on medical terms. For example, if a medical term related to heart is taken means the features are extracted based on the information related to the heart, such as heart operation, heart diseases, treatments taken by the heart patients, medicines for heart diseases, etc. UMLS with unique identifiers is utilized for mapping. It is essential to eliminate any additional brackets, points, commas, colons, semicolons, dashes, hyphens, parentheses, apostrophes, quotation marks, and so on from the medical transcript. Neg-Seq Algorithm is mainly used to remove the redundant data present in the reduced categories of clinical text data obtained from Halve Progression technique. Since Neg-Seq Algorithm

Input: unstructured clinical text data  
Output: filtered categories of clinical text data  
Step 1: start  
Step 2: take the Unstructured clinical text data as input.  
Step 3: calculate the word count in the clinical text data.  
Sent\_count = sent\_count + len (sentences)  
Step 4: assign a condition in which the clinical text data should be present in the clinical text data list.  
Step 5: split the clinical text data according to the disease condition.  
Categories = clinicaldata.groupby (clinicaldata ['medical\_specialty'])  
Step 6: finally get the filtered categories of clinical text data.  
Step 7: end

ALGORITHM 1: Medical-Fissure Algorithm.

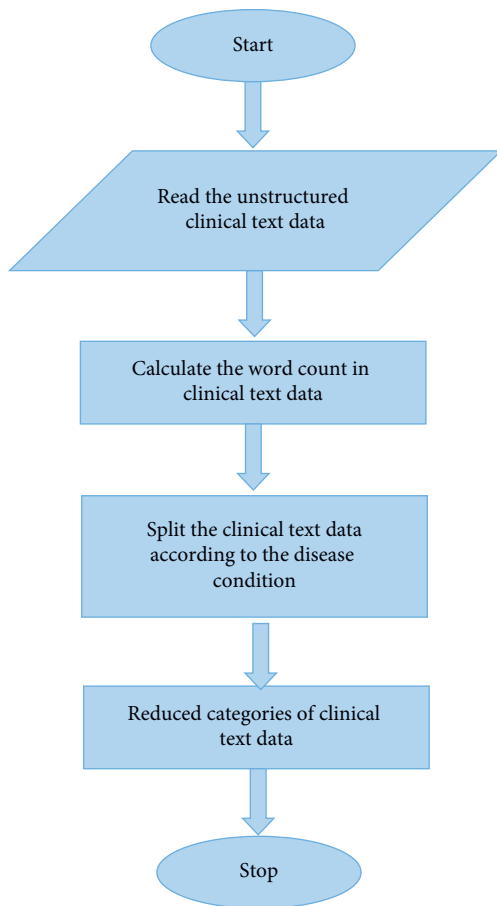


FIGURE 2: Flowchart for halve progression.

uses statistical features, it can detect redundant data and even redundant punctuations and thereby makes the redundant features absent in the reduced categories of clinical text data.

The Neg-Seq Algorithm is syntactically nonredundant; however, it can create semantically redundant patterns in reality. For pairings of patterns like (a b -b c) and (a -b b c), redundancy exists, and it is easy to avoid creating both effectively. To overcome this problem, the method describes the negative datasets as a collection of negative items before composing the final dataset with new items.

Mapping medical terms with Unified Medical Language System (UMLS) involves the following steps:

- (1) Create a class model for your development domain
- (2) Use the model to identify persistent classes
- (3) Assume that each persistent class in the model maps to one relational table
- (4) For each class hierarchy, choose an appropriate inheritance technique
- (5) Add a unique ID (OID) for each class or choose an appropriate primary key
- (6) Map basic data types to table columns for each class
- (7) Map complicated characteristics (association, aggregation) to  $P_k$ ,  $F_K$  pairs for each class
- (8) Keep an eye out for the strong and weak aggregation types
- (9) Map  $P_k$ ,  $F_K$  pairs identifying the role ends according to the specified key for associated classes
- (10) Classify relationship roles according to their cardinality

By using UMLS with unique identification, the major issues in mapping the clinical text data are solved and it makes the mapping more accurate.

The Neg-Seq Algorithm, as shown in Figure 3, improves the extraction and mapping methods by using the result of Halve Progression, which is the categorized clinical text data, as input and removing the unwanted punctuations that are repeated in the input; thus, this algorithm aims to remove redundancy in the clinical text data. The redundancy is then eliminated from every row and column. Finally, precise data is obtained. As a result, the extracted data can be used for further diagnostic purposes.

Extracted data can be stored in a cloud platform because it is the best option for accessibility and storage; however, an effective cloud framework is required to store clinical data because it contains a large amount of data and private information. The next subsection explains the next approach, Cloud Progression.

**3.3. Cloud Progression.** The data collected from the Clinical Data Progression is kept in the cloud, which should keep critical information secure. The clinical text data is saved in the cloud to improve security and authority. For storage, cloud advancement uses a framework as a service. Storage as

Input: filtered categories of clinical text data  
Output: clinical text data without redundancy

Step 1: start

Step 2: take the filtered categories of clinical text data as the input.

Data = filtered\_categories [['transcription', 'medical\_specialty']]

Step 3: remove unwanted punctuations which are repeated in the input.

REPLACE\_BY\_SPACE\_RE = re.compile('[/(){}\\[\\]\\|@,; ]')

Step 4: find similarities by checking each row and column of the clinical text data

Step 5: if two or more rows or columns are similar, then remove the redundancy by considering the rows or columns only once.

Step 6: thus, the data is extracted without any redundancy and the extracted data is more accurate.

Step 7: end

ALGORITHM 2: Neg-Seq Algorithm.

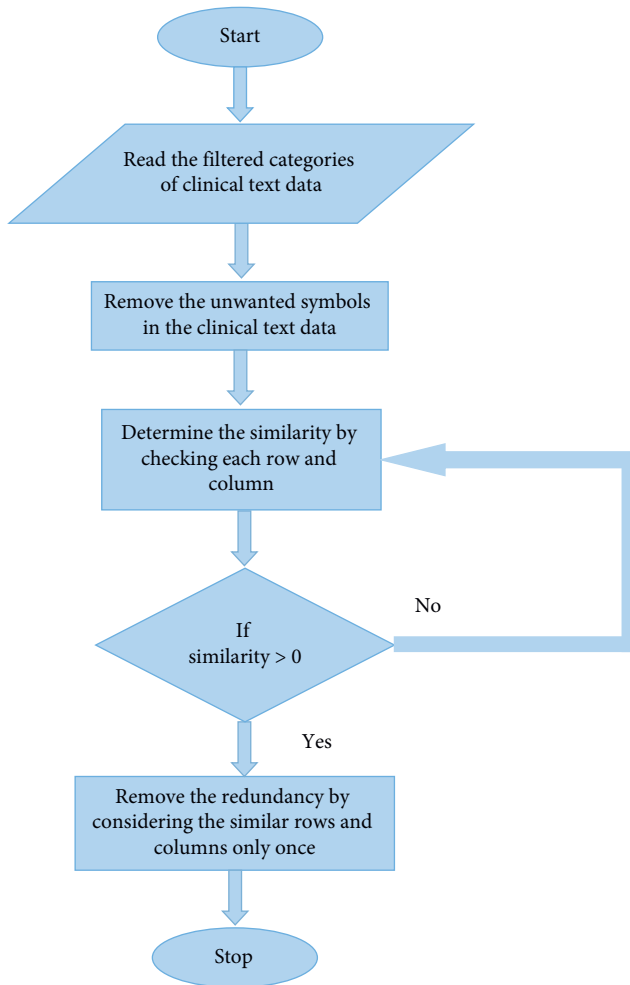


FIGURE 3: Flowchart for Neg-Seq algorithm.

a service refers to the practice of storing data on public cloud storage facilities. However, it needs to improve privacy; therefore, it is required to employ RS (Recommended Standard) access control, in which a delegate server performs validation and grants authorization. The delegate server acts as an intermediary and stores the security key for data exchange. The main objective of RS access control is identification, authorization, authentication, confidentiality, integrity, availability, and accountability.

Figure 4 shows the cloud progression using cryptography for cloud storage. Cloud cryptography uses encryption techniques to protect data that will be utilized or stored there. It enables users to use shared cloud services simply and safely since all data held by cloud providers is encrypted. Cloud cryptography secures sensitive data without slowing down information flow. The encryption method encrypts data on the client-side before sending it to the cloud for storage. Plaintext will be converted to ciphertext, preventing data theft from man-in-the-middle attacks. That is, even if an attacker intercepts the data, he will be unable to read it or derive any useful information from it. This secret key is used for both encryption and decryption algorithms.

The private key is taken as  $\langle j, k \rangle$  and the clinical text data is taken as  $t$  and the ciphertext that is the encrypted clinical text data is taken as  $q$

To determine the ciphertext  $q$  the below formula is used:

$$q = t^j \bmod k. \quad (1)$$

To determine the clinical text data  $t$  the below formula is used:

$$t = q^j \bmod k, \quad (2)$$

where

$q$ : encrypted clinical text data

$t$ : original clinical text data

$\langle j, k \rangle$ : secret key

Decryption is the process of restoring data to its original unencrypted state after it has been rendered unreadable via encryption. Users receive encryption keys from cloud storage providers, which encrypt data. When data must be decrypted, these keys are utilized to do it safely. The hidden data is decrypted and made readable again. Figure 5 shows a flowchart for cloud encryption and decryption algorithm.

As a result, clinical text data is securely and authoritatively kept in the cloud. This enables machine learning and natural language processing techniques to detect, retrieve, and save the clinical text data in the cloud environment efficiently. Overall, the Discovery of Knowledge in Clinical Data Using Machine Learning and Natural Language Processing includes  $n$  major techniques. The first is Halve



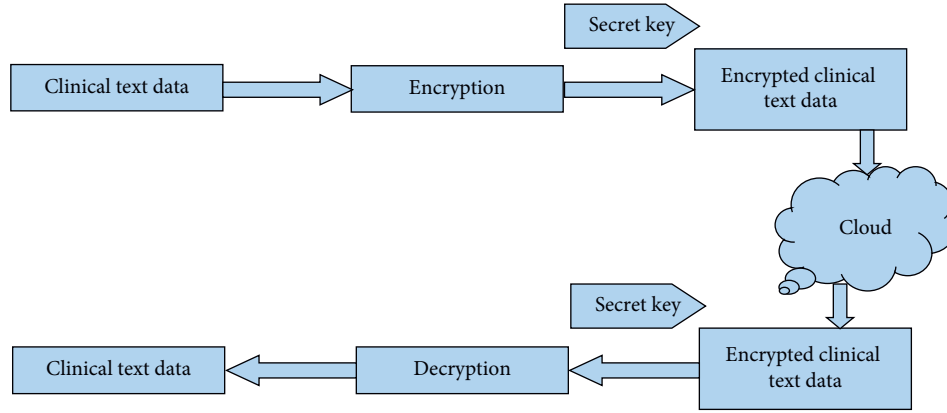


FIGURE 4: Cloud Progression using cryptography for cloud storage.

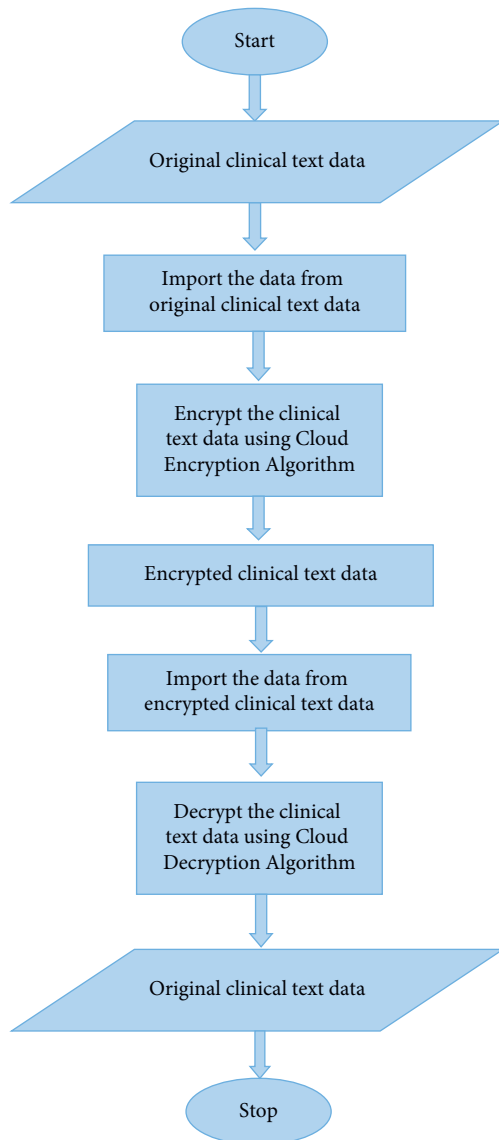


FIGURE 5: Flowchart for cloud encryption and decryption algorithm.

Progression, which uses a Medical Fissure algorithm to split clinical data based on diseased conditions, making diagnosis easier and improving data quality. Second, Clinical Data Progression employs the Neg-Seq Algorithm, which is pretrained using statistical characteristics to extract relevant data while also increasing the significance of the mapping. Third, Cloud Progression is used to securely store data on the cloud. Thus Discovery of Knowledge in clinical data using machine learning and natural language processing provides authorization and validation to clinical text data. The next section explains the results obtain from the Discovery of knowledge in clinical data using machine learning and natural language processing in the cloud and discusses it in detail.

#### 4. Results and Discussion

This segment provides a detailed description of the implementation results and the performance of the proposed system and a comparison section to ensure that the proposed system performs valuable.

**4.1. Experimental Setup.** This work has been implemented in the working platform of python with the following system specification and the simulation results are discussed below.

Platform: Python

OS: Windows 7

Processor: 64 bit Intel processor

RAM: 8 GB RAM

Dataset: Medical Transcription (MTSamples) Dataset

**4.1.1. Dataset Description.** The MTSamples dataset contains 5,000 sample medical transcription reports from various specialties. The dataset includes 40 medical specialties, including 'Surgery', 'Consult - History and Phy', and 'Cardiovascular/Pulmonary'. Each specialization has a set of sample reports ranging from 6 to 1103 [25–27]. The medical

Step 1: start  
 Step 2: generate the secret key  $\langle j, k \rangle$ .  
 Step 3: encrypt the clinical text data. The encrypted data is given by  
 $q = t^j \text{mod } k$   
 Step 4: store the encrypted data in the cloud.  
 Step 5: cloud user decrypts the encrypted data by determining the original clinical text data,  
 $t = q^j \text{mod } k$ .  
 Step 6: original clinical text data is obtained.  
 Step 7: stop

ALGORITHM 3: Cloud Encryption Algorithm and Decryption Algorithm.

history, diagnosis, medicines, treatment plans, vaccination dates, allergies, radiological pictures, and laboratory and test results of a patient are all kept in this dataset. By using the proposed method, these 40 categories are often divided into 21 categories (hence 1000 samples are considered for experimentation) based upon some specified conditions, that is, by splitting the clinical text data according to the disease condition using the proposed halve progression technique.

**4.2. Results Obtained from Each Methodology.** The clinical text data used as input and the obtained results from various techniques are explained in a detailed manner.

The MTSamplesdataset contains 40 classes that are unstructured, whereas some classes do not have any useful information for knowledge discovery from clinical data, which are not considered as a training samples. In order to exclude those uninformative classes, the halve progression technique is employed in the proposed framework. The resulted classes from 40 are 21, along with a number of records from the given 5000 record samples. The resulting 21 classes with the record count are graphically represented in Figure 6 and are statistically represented in Table 1. The records contained in those 21 classes are utilized for further processing.

**4.3. Performance Metrics of the Proposed Method.** The performance of the proposed methodology and the obtained clinical text data are detected by the following equation.

**4.3.1. Accuracy.** The accuracy of the clinical text data is calculated using

$$\text{accuracy} = \left[ \frac{\text{TP} + \text{TN}}{\text{TP} + \text{TN} + \text{FP} + \text{FN}} \right] * 100. \quad (3)$$

TP: true positive value

TN: true negative value

FP: false positive value

FN: false negative value

Figure 7 represents the overall accuracy of the proposed system; from the graph, it is clear that the proposed system gives high accuracy with 99.6% of resultant clinical text data. The accuracy of the proposed system is increased to 99.6% by

using Clinical Data Progression Approach since this approach extracts the data with statistical features, which is interpreted in Table 2.

**4.3.2. Specificity.** Specificity is derived from the equation:

$$\text{specificity} = \frac{\text{true negative}}{\text{true negative} + \text{false positive}}. \quad (4)$$

Table 3 and Figure 8 clearly explain the specificity of the proposed model, and the specificity of the proposed model is about 98.6%. The highest of about 98.6% specificity is attained overall by the proposed methodology. The specificity of the proposed model is increased to 98.6% by using Halve Progression approach since the quality of data is maintained by using this approach.

**4.3.3. Sensitivity.** Sensitivity is deduced using the formula

$$\text{sensitivity} = \frac{\text{true positive}}{\text{true positive} + \text{false negative}}. \quad (5)$$

The sensitivity of the proposed is determined as 98.68%, which is illustrated in Figure 9 and Table 4. The sensitivity is overall between 97.2 and 98.68 percent. The sensitivity of the proposed system is determined by using Halve Progression approach since the recognition and division of data makes the clinical text data more sensitive.

**4.3.4. F1 Score.** F1 Score is defined as follows:

$$F1 = \frac{2 \times (\text{precision} * \text{recall})}{\text{precision} + \text{recall}}, \quad (6)$$

where

$$\text{recall} = \frac{\text{TP}}{\text{TP} + \text{FN}}, \quad (7)$$

$$\text{precision} = \frac{\text{TP}}{\text{TP} + \text{FP}}.$$

Table 5 and Figure 10 clearly show the F1 Score of the suggested model, which is about 97.6 percent. As the number of samples increases, the specificity of the model also increases. Overall, the suggested technique achieves a high level of F1-score of around 97.6 percent. The F1-score

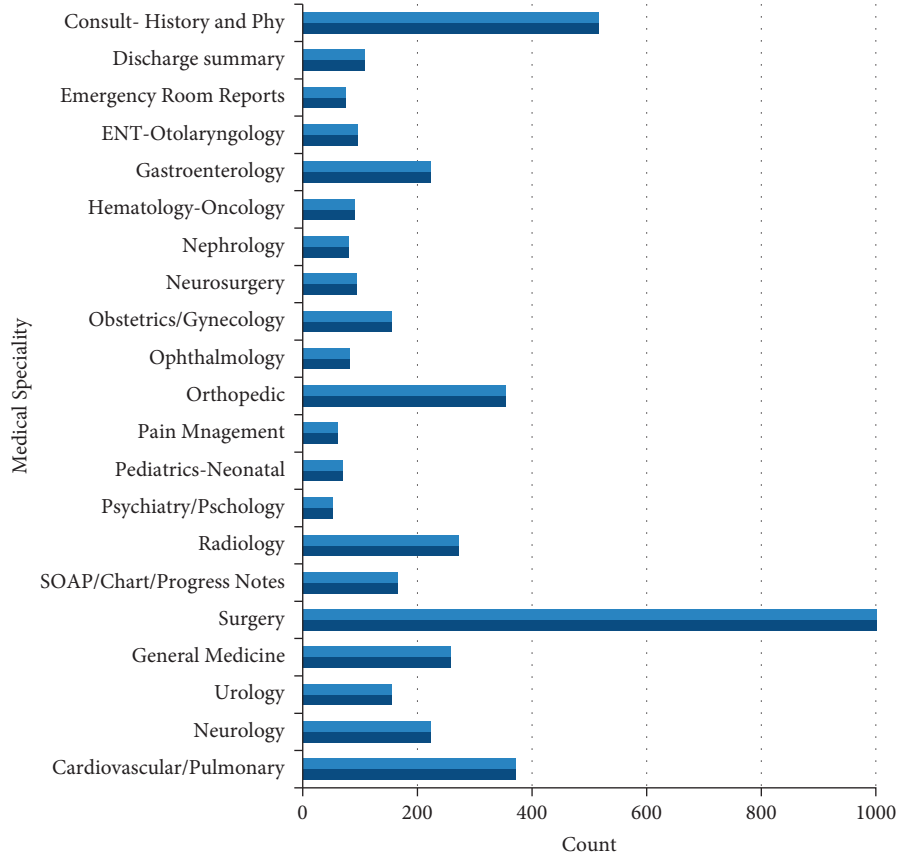


FIGURE 6: Halve progression output as reduced categories.

TABLE 1: Statistical representation of halve progression output as reduced categories.

Medical speciality	Statistical count
Cardiovascular/Pulmonary	371
Neurology	223
Urology	156
General medicine	259
Surgery	1088
SOAP/Chart/Progress notes	166
Radiology	273
Psychiatry/Psychology	53
Pediatrics-neonatal	70
Pain management	61
Orthopedic	355
Ophthalmology	83
Obstetrics/Gynecology	155
Neurosurgery	94
Nephrology	81
Hematology-oncology	90
Gastroenterology	224
ENT-otolaryngology	96
Emergency room reports	75
Discharge summary	108
Consult- history and phy	516

of the proposed system is determined by using the Clinical Data Progression approach in which unique identification is required.

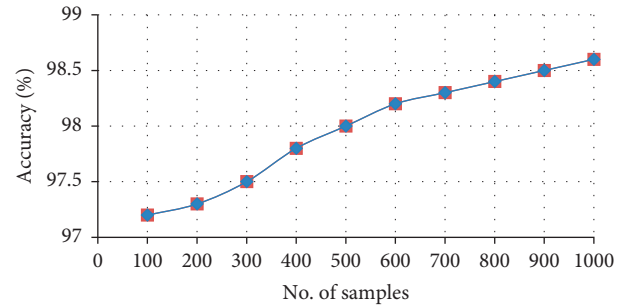


FIGURE 7: Overall accuracy of the proposed system.

**4.3.5. Precision.** The closeness of two or more measurements to each other is known as precision. The formula is presented as follows:

$$\text{Precision} = \frac{TP}{TP + FP}, \quad (8)$$

where

TP: true positive

FP: false positive

Figure 11 represents the overall precision of the proposed system; from the graph, it is clear that the proposed system gives high precision with 98.6% of resultant clinical text data, which is listed in Table 6. The precision of the

TABLE 2: Accuracy of the proposed system.

No. of samples	Accuracy
100	97.2
200	97.3
300	97.5
400	97.8
500	98
600	98.2
700	98.3
800	98.4
900	98.5
1000	98.6

TABLE 3: Specificity of the proposed system.

No. of samples	Specificity
100	97.146
200	97.27
300	97.457
400	97.757
500	98
600	98.134
700	98.2
800	98.365
900	98.544
1000	98.6

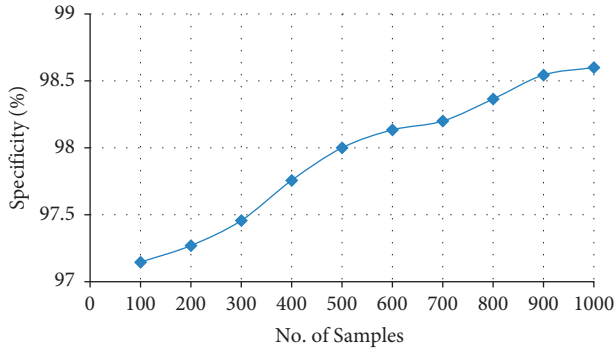


FIGURE 8: Overall specificity of the proposed system.

proposed method is increased to 98.6% by using the Clinical Data Progression approach since the mapping is done with the help of UMLs.

**4.3.6. Recall.** Recall is defined as the ability of the model to accurately predict the output. The formula of recall is defined as follows:

$$\text{Recall} = \frac{\text{TP}}{\text{TP} + \text{FN}}, \quad (9)$$

where

TP: true positive

FN: false negative

From Figure 12 and Table 7, it is observed that the recalls of the proposed system are about 98.64%. Hence, the recalls increase with the increase in the number of samples. The

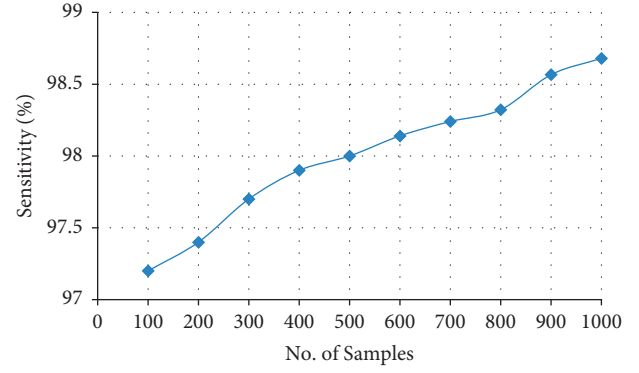


FIGURE 9: Overall sensitivity of the proposed system.

TABLE 4: Sensitivity of the proposed system.

No. of samples	Sensitivity
100	97.2
200	97.4
300	97.7
400	97.9
500	98
600	98.14
700	98.24
800	98.322
900	98.566
1000	98.68

TABLE 5: F1-score of the proposed system.

No. of samples	F1-score
100	96.2
200	96.3
300	96.5
400	96.8
500	97
600	97.2
700	97.3
800	97.4
900	97.5
1000	97.6

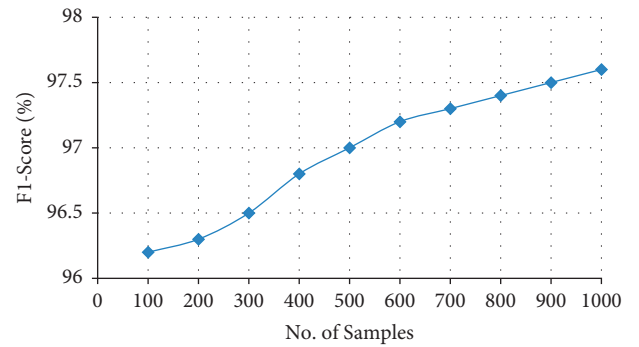


FIGURE 10: F1-score of the proposed system.

recall of the proposed system is determined by using the Cloud Progression approach. This approach stores the entire clinical text data in the cloud with an encryption process.

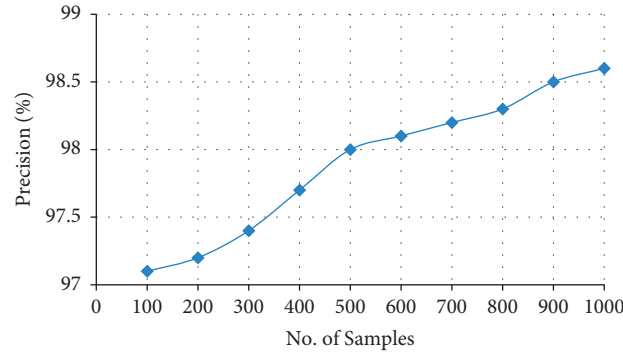


FIGURE 11: Overall precision of the proposed system.

TABLE 6: Precision of the proposed system.

No. of samples	Precision
100	97.1
200	97.2
300	97.4
400	97.7
500	98.0
600	98.1
700	98.2
800	98.3
900	98.5
1000	98.6

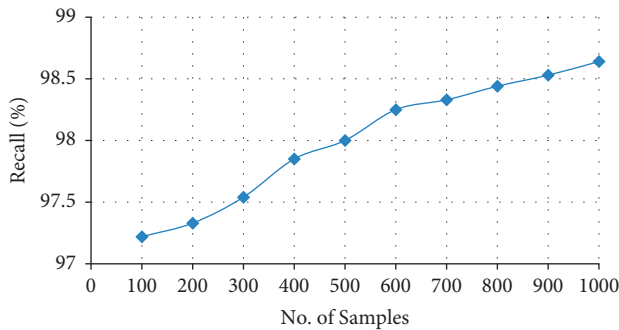


FIGURE 12: Recall of the proposed system.

TABLE 7: Recall of proposed system.

No. of samples	Recall
100	97.22
200	97.33
300	97.54
400	97.85
500	98.00
600	98.25
700	98.33
800	98.44
900	98.53
1000	98.64

This section describes the resultant performance of the proposed system. The next section describes a comparison of various performances of the previous research with the performance of the proposed method.

**4.4. Comparison Results of the Proposed Method.** This section describes various performances of the proposed method, comparing with the results of previous methodologies and depicting their results based on various metrics.

The accuracy of clinical text data is compared with the accuracy of the various previously proposed techniques. From Table 8 and Figure 13, it is clear that the stack accuracy of the proposed output achieves 97.9% which is 16% higher than the existing output when compared with Support Vector Machine (SVM) [27], Naïve Bayes (NB) [28], K-Nearest Neighbor (KNN) [29], XGBoost [30], Random forest [31], AdaBoost [32] and CatBoost [33].

The precision of clinical text data is compared with the precision of the various previously proposed techniques. From Table 9 and Figure 14, it is clear that the stack precision of the proposed output achieves 98.9% which is 11% higher than the existing output when compared with SVM [27], NB [28], KNN [29], XGBoost [30], Random forest [31], AdaBoost [32], and CatBoost [33].

The recalls of clinical text data are compared with the recalls of the various previously proposed techniques. From Table 10 and Figure 15, it is clear that the stack recalls of the proposed output achieve 98.7%, which is 12% higher than the existing output when compared with SVM [27], NB [28], KNN [29], XGBoost [30], Random forest [31], AdaBoost [32], and CatBoost [33].

The  $F1$ -score of clinical text data is compared with the  $F1$ -score of the various previously proposed techniques. From Table 11 and Figure 16, it is clear that the stack  $F1$ -score of the proposed output achieves 98.7%, which is 14% higher than the existing output when compared with SVM [27], NB [28], KNN [29], XGBoost [30], Random forest [31], AdaBoost [32], and CatBoost [33].

The performance in terms of accuracy and  $F1$ -score in HoC Dataset is compared with various previously proposed techniques. From Table 12 and Figure 17, it is clear that the stack accuracy of the proposed output achieves 97.7%, which is 17% higher than the existing output when compared with Random forest [31], AdaBoost [32], and CatBoost [33], and the  $F1$ -score of the proposed output achieves 98% which is 1% higher than the existing output when compared with Random forest [31], AdaBoost [32], and CatBoost [33].

The performance in terms of accuracy and  $F1$ -score in the ChemProt Dataset is compared with various previously



TABLE 8: Accuracy comparison.

Methodologies	Accuracy
SVM	82.17
NB	81.08
KNN	64.9
XGBoost	82.87
Random forest	81.4
AdaBoost	78.1
CatBoost	81
Proposed	97.9

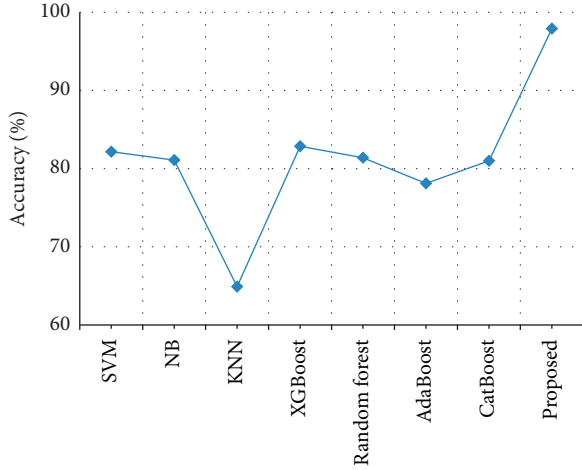


FIGURE 13: Accuracy comparison.

TABLE 9: Precision comparison.

Methodologies	Precision
SVM	81.17
NB	82.08
KNN	63.9
XGBoost	84.87
Random forest	85.4
AdaBoost	76.1
CatBoost	87
Proposed	98.9

proposed techniques. From Table 13 and Figure 18, it is clear that the stack accuracy of the proposed output achieves 97.8%, which is 19% higher than the existing output when compared with Random forest [31], AdaBoost [32], and CatBoost [33] and the *F1*-score of the proposed output achieves 98% which is 16% higher than the existing output when compared with Random forest [31], AdaBoost [32], and CatBoost [33].

The performance in terms of precision and recall in the ChemProt dataset is compared with various previously proposed techniques. From Table 14 and Figure 19, it is clear that the precision of the proposed output achieves 97.85%, which is 22% higher than the existing output when compared with Random forest [31], AdaBoost [32] and CatBoost [33], and the recall of the proposed output achieves 98.8% which is 17% higher than the existing output when compared with Random forest [31], AdaBoost [32] and CatBoost [33].

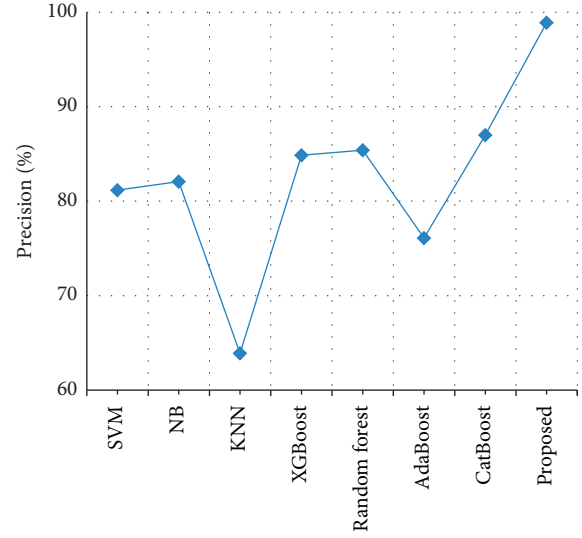


FIGURE 14: Precision comparison.

TABLE 10: Recall comparison.

Methodologies	Recall
SVM	82.17
NB	83.08
KNN	66.9
XGBoost	84.67
Random forest	85.8
AdaBoost	73.1
CatBoost	86
Proposed	98.7

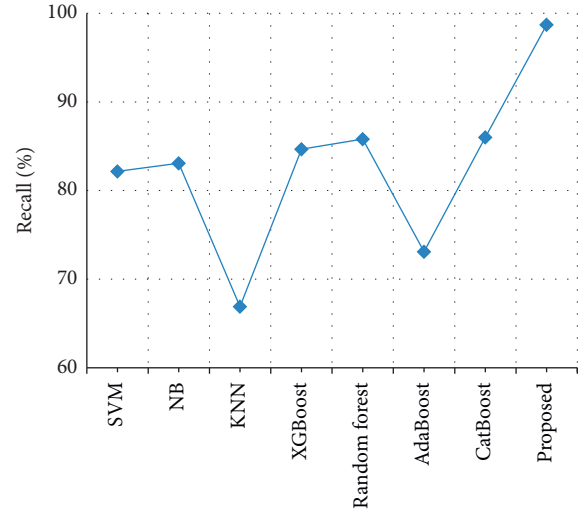
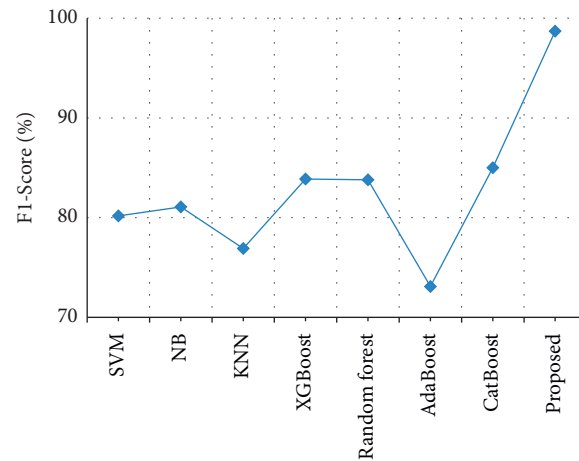


FIGURE 15: Recall comparison.

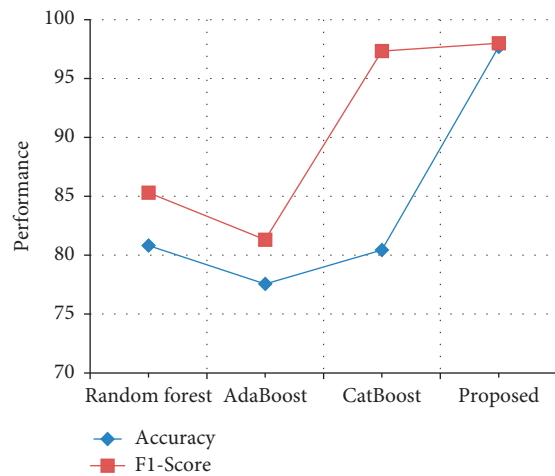
The performance in terms of precision and recall in the HoC Dataset is compared with various previously proposed techniques. From Table 15 and Figure 20, it is clear that the precision of the proposed output achieves 97.71%, which is 12% higher than the existing output when compared with Random forest [31], AdaBoost [32] and CatBoost [33], and the recall of the proposed output achieves 98.5%, which is 1%

TABLE 11: *F1*-score comparison.

Methodologies	<i>F1</i> -score
SVM	80.17
NB	81.08
KNN	76.9
XGBoost	83.87
Random forest	83.8
AdaBoost	73.1
CatBoost	85
Proposed	98.7

FIGURE 16: *F1*-score comparison.TABLE 12: Accuracy and *F1*-score comparison in HoC Dataset.

HoC dataset	Methodologies	Accuracy	<i>F1</i> -score
	Random forest	80.82	85.31
	AdaBoost	77.56	81.32
	CatBoost	80.45	97.34
	Proposed	97.7	98

FIGURE 17: Performance in terms of accuracy and *F1*-score comparison in HoC Dataset.TABLE 13: Accuracy and *F1*-score comparison in ChemProt Dataset.

ChemProt dataset	Methodologies	Accuracy	<i>F1</i> -score
	Random forest	74.82	80.22
	AdaBoost	72.88	76.40
	CatBoost	76.78	82.01
	Proposed	97.8	98

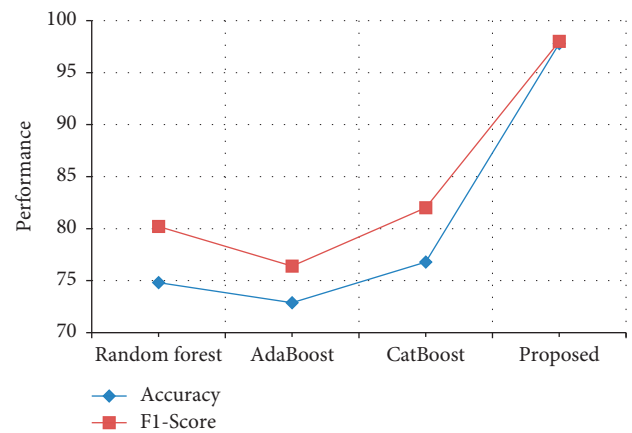
FIGURE 18: Performance in terms of accuracy and *F1*-score comparison in ChemProt dataset.

TABLE 14: Precision and recall comparison in ChemProt Dataset.

ChemProt dataset	Methodologies	Precision	Recall
	Random forest	74.87	80.72
	AdaBoost	72.48	76.10
	CatBoost	76.68	81.01
	Proposed	97.85	98.8

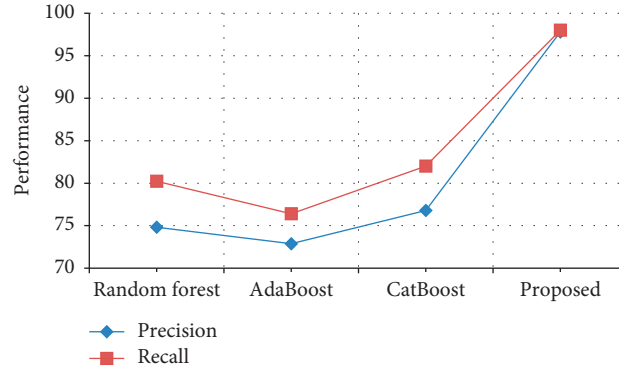


FIGURE 19: Performance in terms of precision and recall comparison in ChemProt Dataset.

TABLE 15: Precision and Recall comparison in HoC Dataset.

HoC dataset	Methodologies	Precision	Recall
	Random forest	81.82	84.31
	AdaBoost	77.56	82.32
	CatBoost	85.45	97.64
	Proposed	97.71	98.5

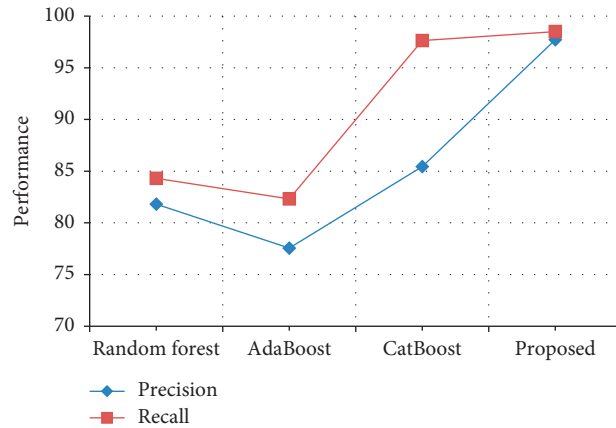


FIGURE 20: Performance in terms of precision and recall comparison in HoC Dataset.

higher than the existing output when compared with Random forest [31], AdaBoost [32], and CatBoost [33]. Thus, the proposed method functions are proved to have the best performance by comparing with results of previous research.

## 5. Conclusion

The technical complexities in extracting the clinical text data are removed by using machine learning and natural language processing techniques. Halve Progression, Clinical

Data Progression, and Cloud Progression provide a solution for major issues like difficulty in diagnosis, reduced data quality, difficulty in extraction and mapping, and risk in security by using Medical-Fissure Algorithm to split the clinical text data and Neg-Seq Algorithm to remove redundancy and usage of the secret key to provide better security. The clinical text data is extracted with high accuracy of 99.6%. The results of the proposed method are compared with other existing techniques and the proposed method outperforms all the other existing techniques. To further

improve the quality and accuracy of data extraction, the relation extraction using Transformer based models in clinical text data can be developed for knowledge discovery.

## Data Availability

The data that support the findings of this study are available upon request from the corresponding author.

## Conflicts of Interest

The authors declare no conflicts of interest.

## Acknowledgments

The authors wish to thank King Abdulaziz City for Science and Technology (KACST) for its support partially in this research.

## References

- [1] E. Kim, S. M. Rubinstein, K. T. Nead, A. P. Wojcieszynski, P. E. Gabriel, and J. L. Warner, "The evolving use of electronic health records (EHR) for research," in *Seminars in Radiation Oncology*, vol. 29, no. 4, pp. 354–361, WB Saunders, 2019.
- [2] C. Huang, J. Zhao, W. Yeming et al., "Clinical Features of Patients Infected with 2019 Novel Coronavirus in Wuhan," *China Lancet*, vol. 395, no. 10223, 2020.
- [3] I. Keshta and A. Odeh, "Security and privacy of electronic health records: concerns and challenges," *Egyptian Informatics Journal*, vol. 22, no. 2, 2021.
- [4] H. O. Alanazi, A. A. Zaidan, and B. B. Zaidan, M. L. M. Kiah, M. L. Kiah, and S. H. Al-Bakri, Meeting the security requirements of electronic medical records in the ERA of high-speed computing," *Journal of Medical Systems*, vol. 39, no. 1, pp. 165–213, 2015.
- [5] D. F. Sittig and H. Singh, "A new socio-technical model for studying health information technology in complex adaptive healthcare systems," in *Cognitive Informatics for Biomedicine*, pp. 59–80, Springer, Cham, Switzerland, 2015.
- [6] B. B. Gupta, *Computer and Cyber Security: Principles, Algorithms, Applications, and Perspectives*, CRC Press, Boca Raton, FL, USA, 2018.
- [7] M. Whetstone and R. Goldsmith, "Factors influencing intention to use personal health records," *International Journal of Pharmaceutical and Healthcare Marketing*, vol. 3, no. 1, 2019.
- [8] T. Ermakova, B. Fabian, and R. Zarnekow, "Security and Privacy System Requirements for Adopting Cloud Computing in Healthcare Data Sharing Scenarios," in *Proceedings of the 19th Americas Conference on Information Systems (AMCIS 2013)*, Chicago, Illinois, USA, August, 2013.
- [9] B. B. Gupta and P. Dharma, *Handbook of Research on Cloud Computing and Big Data Applications in IoT*, IGI Global, Pennsylvania, USA, 2019.
- [10] E. S. Hunter and S. Euzelia, "Electronic health records in an occupational health setting-Part I. A global overview," *Workplace Health & Safety*, vol. 61, no. 2, pp. 57–60, 2013.
- [11] S. Yu, C. Tianrun, and C. Tianxi, "NILE: fast natural language processing for electronic health records," 2013, <https://arxiv.org/abs/1311.6063>.
- [12] W. Sun, Z. Cai, Y. Li, F. Liu, S. Fang, and G. Wang, "Data processing and text mining technologies on electronic medical records: a review," *Journal of Healthcare Engineering*, vol. 2018, Article ID 4302425, 9 pages, 2018.
- [13] D. W. Bates, A. Auerbach, P. Schulam, A. Wright, and S. Saria, "Reporting and implementing interventions involving machine learning and artificial intelligence," *Annals of Internal Medicine*, vol. 172, no. 11\_Supplement, pp. S137–S144, 2020.
- [14] J. Devlin, M.-W. Chang, K. Lee, and K. Toutanova, "Bert: pre-training of deep bidirectional transformers for language understanding," 2018, <https://arxiv.org/abs/1810.04805>.
- [15] M. G. Kersloot, F. J. P. Van Putten, A. Abu-Hanna, R. Cornet, and D. L. Arts, "Natural language processing algorithms for mapping clinical text fragments onto ontology concepts: a systematic review and recommendations for future studies," *Journal of Biomedical Semantics*, vol. 11, no. 1, pp. 14–21, 2020.
- [16] B. De Bruijn, C. Cherry, S. Kiritchenko, J. Martin, and X. Zhu, "Machine-learned solutions for three stages of clinical information extraction: the state of the art at i2b2 2010," *Journal of the American Medical Informatics Association*, vol. 18, no. 5, pp. 557–562, 2011.
- [17] J. B. Edgcomb and B. Zima, "Machine learning, natural language processing, and the electronic health record: innovations in mental health services research," *Psychiatric Services*, vol. 70, no. 4, pp. 346–349, 2019.
- [18] O. Dorgham, B. Al-Rahamneh, A. Almomani, M. d. Al-Hadidi, and K. F. Khatatneh, "Enhancing the security of exchanging and storing DICOM medical images on the cloud," *International Journal of Cloud Applications and Computing*, vol. 8, no. 1, pp. 154–172, 2018.
- [19] A. Agrawal, A. K. Pandey, A. Baz et al., "Evaluating the security impact of healthcare Web applications through fuzzy based hybrid approach of multi-criteria decision-making analysis," *IEEE Access*, vol. 8, Article ID 135770, 2020.
- [20] J. Chen, D. Chun, M. Patel, E. Chiang, and J. James, "The validity of synthetic clinical data: a validation study of a leading synthetic data generator (Synthea) using clinical quality measures," *BMC Medical Informatics and Decision Making*, vol. 19, no. 1, pp. 44–49, 2019.
- [21] S. A. Hasan and O. Farri, "Clinical natural language processing with deep learning," in *Data Science for Healthcare*, pp. 147–171, Springer, Cham, Switzerland, 2019.
- [22] S. G. Murray, A. Avati, G. Schmajuk, and J. Yazdany, "Automated and flexible identification of complex disease: building a model for systemic lupus erythematosus using noisy labeling," *Journal of the American Medical Informatics Association*, vol. 26, no. 1, pp. 61–65, 2019.
- [23] R. Kumar, A. K. Pandey, A. Baz et al., "Fuzzy-based symmetrical multi-criteria decision-making procedure for evaluating the impact of harmful factors of healthcare information security," *Symmetry*, vol. 12, no. 4, p. 664, 2020.
- [24] A. Harnoune, M. Rhanoui, M. Mikram, S. Yousfi, Z. Elkaimbillah, and B. El Asri, "BERT based clinical knowledge extraction for biomedical knowledge graph construction and analysis," *Computer Methods and Programs in Biomedicine Update*, vol. 1, Article ID 100042, 2021.
- [25] F. Moramarco, D. Juric, A. Savkov, and E. Reiter, "Towards objectively evaluating the quality of generated medical summaries," 2021, <https://arxiv.org/pdf/2104.04412.pdf>.
- [26] N. Sadman, M. H. Rahman, M. A. Haque, and K. D. Gupta, *Medical Speciality Detector Application (MSDA) Using AI*, Association for the Advancement of Artificial Intelligence, Menlo Park, CA, USA, 2021.
- [27] V. Garla, C. Taylor, and C. Brandt, "Semi-supervised clinical text classification with Laplacian SVMs: an application to

- cancer case management,” *Journal of Biomedical Informatics*, vol. 46, no. 5, pp. 869–875, 2013.
- [28] M.-S. Ong, F. Magrabi, and E. Coiera, “Automated categorisation of clinical incident reports using statistical text classification,” *BMJ Quality and Safety*, vol. 19, no. 6, p. e55, 2010.
  - [29] K. Shah, H. Patel, S. Devanshi, and M. Shah, “A comparative analysis of logistic regression, random forest and KNN models for the text classification,” *Augmented Human Research*, vol. 5, no. 1, pp. 1–16, 2020.
  - [30] S. Li and X. Zhang, “Research on orthopedic auxiliary classification and prediction model based on XGBoost algorithm,” *Neural Computing & Applications*, vol. 32, no. 7, pp. 1971–1979, 2020.
  - [31] A. Thielmann, C. Weisser, A. Krenz, and B. Säfken, “Unsupervised document classification integrating web scraping, one-class SVM and LDA topic modelling,” *Journal of Applied Statistics*, 2021.
  - [32] X.-A. Bi, X. Hu, H. Wu, and Y. Wang, “Multimodal data analysis of Alzheimer’s disease based on clustering evolutionary random forest,” *IEEE Journal of Biomedical and Health Informatics*, vol. 24, no. 10, pp. 2973–2983, 2020.
  - [33] A. Samat, E. Li, P. Du, S. Liu, Z. Miao, and W. Zhang, “CatBoost for RS image classification with pseudo label support from neighbor patches-based clustering,” *IEEE Geoscience and Remote Sensing Letters*, vol. 19, pp. 1–5, 2022.



## Research Article

# Machine Learning Techniques for Human Age and Gender Identification Based on Teeth X-Ray Images

**K. C. Santosh,<sup>1</sup> Nijalingappa Pradeep,<sup>1</sup> Vikas Goel,<sup>2</sup> Raju Ranjan,<sup>3</sup> Ekta Pandey,<sup>4</sup> Piyush Kumar Shukla<sup>5</sup> and Stephen Jeswinde Nuagah<sup>6</sup>**

<sup>1</sup>CS&E Department, Bapuji Institute of Engineering and Technology, Davangere, Karnataka, India

<sup>2</sup>Department of Information Technology, KIET Group of Institutions, Delhi-NCR Meerut Road (NH-58), Ghaziabad 201206, Uttar Pradesh, India

<sup>3</sup>School of Computing Science and Engineering, Galgotias University, Greater Noida, Uttar Pradesh, India

<sup>4</sup>Applied Science Department, Bundelkhand Institute of Engineering and Technology, Jhansi, Uttar Pradesh, India

<sup>5</sup>Computer Science & Engineering Department, University Institute of Technology, Rajiv Gandhi Proudyogiki Vishwavidyalaya, Technological University of Madhya Pradesh, Bhopal 462033, India

<sup>6</sup>Department of Electrical Engineering, Tamale Technical University, Tamale, Ghana

Correspondence should be addressed to Stephen Jeswinde Nuagah; [jeswinde@tatu.edu.gh](mailto:jeswinde@tatu.edu.gh)

Received 29 October 2021; Accepted 17 December 2021; Published 4 January 2022

Academic Editor: Liaqat Ali

Copyright © 2022 K. C. Santosh et al. This is an open access article distributed under the Creative Commons Attribution License, which permits unrestricted use, distribution, and reproduction in any medium, provided the original work is properly cited.

The use of digital medical images is increasing with advanced computational power that has immensely contributed to developing more sophisticated machine learning techniques. Determination of age and gender of individuals was manually performed by forensic experts by their professional skills, which may take a few days to generate results. A fully automated system was developed that identifies the gender of humans and age based on digital images of teeth. Since teeth are a strong and unique part of the human body that exhibits least subject to risk in natural structure and remains unchanged for a longer duration, the process of identification of gender- and age-related information from human beings is systematically carried out by analyzing OPG (orthopantomogram) images. A total of 1142 digital X-ray images of teeth were obtained from dental colleges from the population of the middle-east part of Karnataka state in India. 80% of the digital images were considered for training purposes, and the remaining 20% of teeth images were for the testing cases. The proposed gender and age determination system finds its application widely in the forensic field to predict results quickly and accurately. The prediction system was carried out using Multiclass SVM (MSVM) classifier algorithm for age estimation and LIBSVM classifier for gender prediction, and 96% of accuracy was achieved from the system.

## 1. Introduction

Technological advancement in modern medicine helps medical professionals to diagnose the nature of the medical condition of a person more effectively and medicate accurately. Technical advancement in the field of medicine shows several types of evolution in radiologic technology, such as radiographic fluoroscopy, molecular imaging, and digital imaging. The present study was conducted by using digital radiographs of teeth, also known as orthopantomogram (OPG), considered as input for gender identification and age

estimation of humans. However, the traditional method followed by forensic practitioners for identification is time-consuming; hence, a complete automated system was developed for personal identification, which produces results quickly and accurately.

The human body has a tendency to undergo changes in lifetime due to any external cause or internal metabolism changes. In such case, teeth are the only structure that will not be affected by any causes due to their hardness nature and low metabolism [1]. Dental X-ray images provide useful information in identification, and it is considered a good

material in either living or nonliving populations for genetic study and odontological, anthropological, and forensic investigation. Identification based on teeth images has higher accurate results than any other parts in humans. Teeth development stages and dental eruption factors depicted in a few atlases help manual investigation process in forensic dentistry. Identification of an individual in forensic medicine is most challenging and confidential in the matter of civil law and crime investigation [2, 3]. Hence, prediction based on observing anatomical features of teeth should be conducted with higher accuracy. Teeth images are publicly unavailable and have to be collected from the dental college, dental hospitals, or clinics that have X-ray imaging facilities.

Forensic odontology is a department in dentistry that is associated with the scientific study of the anatomy of teeth that should handle properly and analyze eruption of teeth as evidence of gender determination and age assessment. Various techniques exist in estimation of age like anthropological study, psychological and radiological method, and odontological and skeletal analysis [4, 5]. The cuspids or eyeteeth mainly show the sexual difference from other teeth in humans. These teeth are rugged in nature and have resistance to disease. The main goal of this paper is to deliver a state of art evidence and trends and to fill gaps in the experiments on age and gender determination that was based on machine learning methods. In particular, medical image analysis is the trending and challenging research area in machine learning communities. Though the dental structures and features are almost the same in males and females, few changes in the size of the tooth will exhibit some clues about gender differences. Forensic experts manually identify gender and age differences by tooth dimensions and craniofacial morphologies [6, 7]. Figure 1 illustrates a standard numbering for each tooth. Panoramic image of teeth is divided into four quadrants; each quadrant has 8 sets of teeth. A number of denotation systems for teeth are available in the dentition field, but FDI (Federation Dentaire International) is a global standard labeling system used by many researchers. FDI uses a 2-digit global standard labeling system for tooth identification, where the first number represents the quadrant of the tooth and the second number represents the number of the tooth from the midline, as depicted in Figure 1.

A sample of FDI dental labeling on an adult panoramic image is depicted in Figure 1. It has four quadrants, upper jaw right (Q1), upper jaw left (Q2), lower jaw left (Q3), and lower jaw right (Q4). It can be evaluated in a clockwise direction [8]. The teeth number begins from 1 to 8 in each quadrant that starts from the middle line and moves towards the distal end. For example, an upper jaw right is a wisdom tooth that can be called tooth number “18” or a lower jaw left tooth that can be numbered as “38.” A complete set (32 teeth) of an adult human is depicted in Figure 2.

Human teeth have two parts, upper jaw and lower jaw, called maxillary and mandible jaw, respectively. Each jaw has 8 teeth on the left side and 8 teeth on the right part with a universal numbering and palmer numbering system [9]. Table 1 illustrates the numbering system of each tooth.

Orthopantomogram, known as OPG, and cephalogram are two different types of X-ray images in dental analysis. OPG creates a panoramic vision of teeth, which consist of both the maxillary jaw and mandible jaw, whereas a cephalogram is an X-ray image of facial structure. Age and gender determination required a complete view of teeth rather than a partial view like cephalogram [10, 11]. Hence, OPG is used widely in individual identification. Figure 3 depicts the different types of dental X-ray imaging available.

Figure 3(a) is bitewing X-ray imaging that depicts details of lower teeth and upper teeth in a particular part of the mouth. The exposed area in bitewing X-ray imaging shows the features of teeth from the crown to the root of teeth. In Figure 3(b), periapical X-ray imaging type, one can notice minute parts inside a tooth that depicts the entire tooth with roots and soft tissues. Every periapical tooth image depicts a complete portion of a tooth, either lower jaw tooth or upper jaw tooth. Figure 3(c) is the orthopantomogram X-ray image. This type of imaging displays a complete panoramic view of teeth [12–14]. Dataset of orthopantomogram (OPG) was used in this paper for detection of gender and age estimation.

## 2. Literature Review

Many researchers have focused on the manual method of identification using teeth, but very few contributions were made on machine learning approaches and computer vision for automated gender and age identification based on teeth. In this section, we briefly focus on the latest articles that illustrate the methodology, technical aspects, and other significant contributions of researchers in the prediction of age and gender.

Wallraff et al. [15] in 2021 proposed a method for age determination based on panoramic digital X-ray images of teeth using deep learning. The authors used a supervised regression-based deep learning technique by considering a dataset of 14000 images.

Saloni et al. [16] in 2020 proposed a method based on digital images of teeth in the identification of teeth by analyzing morphometric means of mandible ramus of 250 OPG samples. The mandible ramus may be used as an alternate tool in determining gender based on the OPG of the selected population. The authors studied mandible ramus measurements by discriminant function analysis. This outcome indicates that mandible ramus exhibits better sexual dimorphism. In 2020, Poornima Vadla et al. [17] introduced a technique based on permanent mandible teeth of the left-sided jaw. Their study focused on estimating age with high accuracy based on the Camerier method applied from an Indian-specific formula on the left and right sides of mandibular teeth. The authors used radiographs of 50 samples (25 males and 25 females) of range 5–15 years. The outcome values were recorded based on the Camerier technique in estimation of age based on Indian-specific equations. Okkesim and Erhamza [18] in 2020 conducted a study for determination of human gender based on mandibular ramus. Mandibular teeth play a vital role in determining human gender since mandible bone is the largest,

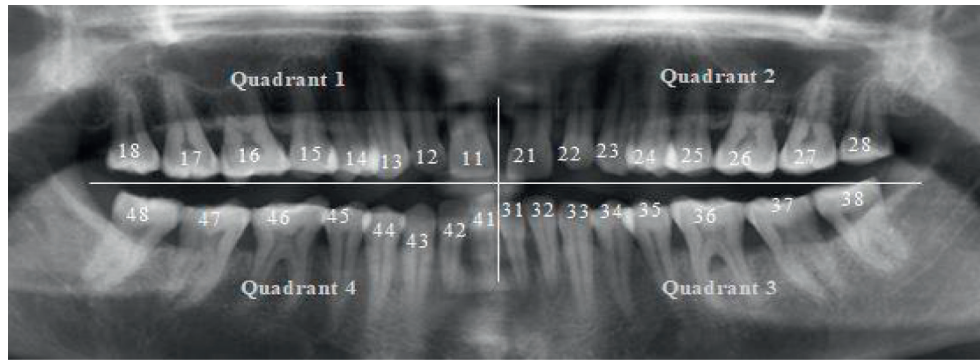


FIGURE 1: FDI nomenclature illustrated on a panoramic radiograph.

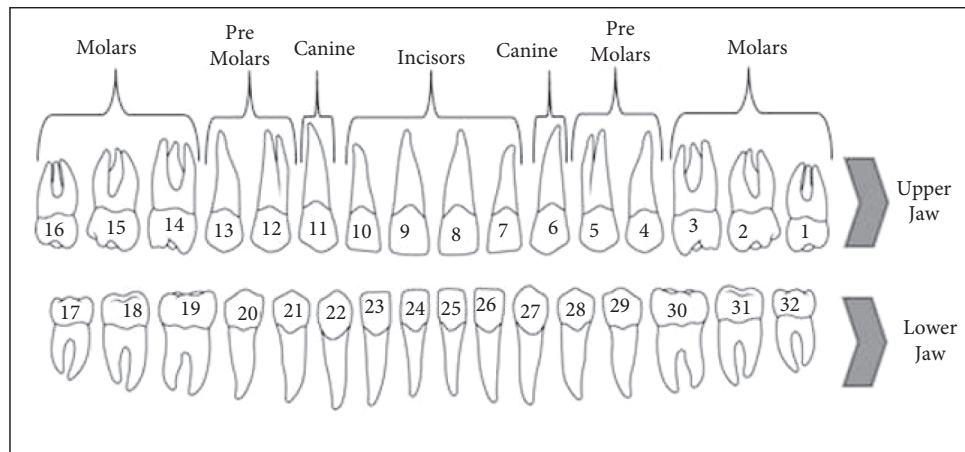


FIGURE 2: Anatomy of human teeth.

TABLE 1: Numbering system and names of teeth.

Maxillary jaw (upper jaw)			Mandibular jaw (lower jaw)		
Universal numbering	Palmer numbering system	Tooth name	Universal numbering	Palmer numbering system	Tooth name
Right	1	Up. Rt. 8	32	L. Rt. 1	3rd molar
	2	Up. Rt. 7	31	L. Rt. 2	2nd molar
	3	Up. Rt. 6	30	L. Rt. 3	1st molar
	4	Up. Rt. 5	29	L. Rt. 4	2nd premolar
	5	Up. Rt. 4	28	L. Rt. 5	1st premolar
	6	Up. Rt. 3	27	L. Rt. 6	Canine
	7	Up. Rt. 2	26	L. Rt. 7	Lateral incisor
	8	Up. Rt. 1	25	L. Rt. 8	Central incisor
Left	9	Up. Lt. 1	24	L. Lt. 8	Central incisor
	10	Up. Lt. 2	23	L. Lt. 7	Lateral incisor
	11	Up. Lt. 3	22	L. Lt. 6	Canine
	12	Up. Lt. 4	21	L. Lt. 5	1st premolar
	13	Up. Lt. 5	20	L. Lt. 4	2nd premolar
	14	Up. Lt. 6	19	L. Lt. 3	1st molar
	15	Up. Lt. 7	18	L. Lt. 2	2nd molar
	16	Up. Lt. 8	17	L. Lt. 1	3rd molar

dimorphic, and strongest bone in the skull. Most recent studies highlighted that CBCT (cone-beam computed tomography) is better than any traditional technique. Some of

the important features in mandible teeth like-gonial angle, ramus measurement, and a few morphologic parameters are reported. Researchers studied different parameters in the

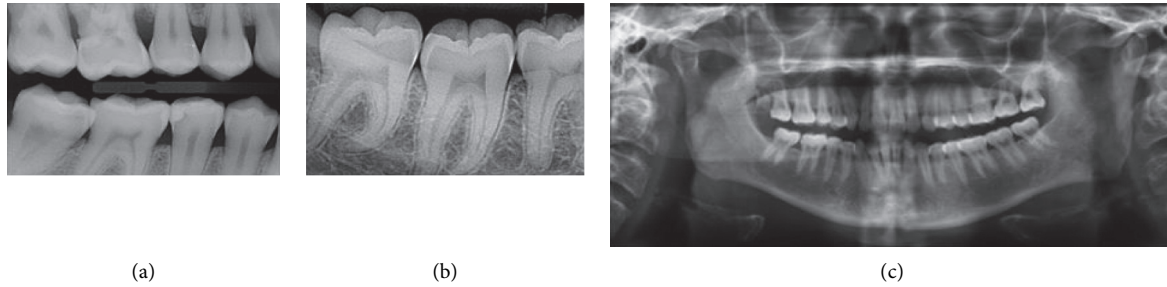


FIGURE 3: Types of dental imaging. (a) Bitewing X-ray. (b) Periapical X-ray. (c) Orthopantomogram X-ray.

mandible. Vila et al. [19] built a gender classification technique based on CNN approaches like the DASNet method and VGG-16 architecture methods. Their classification system was carried out using 3500 OPG images. Patil et al. [20] conducted a study to determine the gender of humans using discriminant analysis and logistic regression based on mandible parameters. They conducted a study using 509 panoramic images. The accuracy of their experimental results is tabulated in Table 2.

In 2020, Neves et al. [21] developed a predictive model for gender identification based on mesiodistal widths using a permanent dental cast. A total of 168 dental casts were considered for classification. Mesiodistal width of first right molar to left molar was calculated for every cast. In 2020, Dalessandri et al. [22] reviewed articles on 2D radiological method versus 3D radiological for determination of age based on teeth of 18 years old. The authors' review assesses the present trend with reliability and accuracy of OPG versus CBCT for determination of age and gender. The final outcome of their survey illustrated that CBCT was found to be accurate when compared with OPG in teeth anatomy evaluation. Stella and Thirumalai [23] developed an automation tool for estimation of age based on dental OPG images. The authors developed two methods for individual age assessment using the Demirjian and Nolla methods. This application was developed by using MS excel Visual Basic Application (VBA). This helps in the automation technique using any programming environment. Bali Behl et al. [24] proposed a method based on panoramic evaluation for mandible morphometric changes in postpubertal and prepubertal in the Turkish population. The authors measured bicondylar breadth (BB), gonial angle measurement, antegonial angle (AGA), ramus height, and ramus breadth (RHRB), which were captured from the Turkish population. They conducted this experiment on 750 digital radiographic images of ages from 5 years to 50 years. All parameters values from OPG radiographs were recorded and analyzed using the software Java Image Process. In 2019, Andrade et al. [25] developed a system for determination of gender and age estimation using pulp cavity volumes based on the CBCT method. They used 120 experimental samples of CBCT scans from the Brazilian population of both genders of ages ranging from 13 years to 70 years. Pearson's correlation evaluation methods were used in assessing the relation between pulp volume and chronological age. Higher accuracy can be achieved by using this formula when it is applied

to pulp volume for one or both teeth. Good results can be fetched for samples of age more than 35 years in age estimation.

### 3. Feature Extraction

Feature extraction is the process of identifying key features in the dataset available. It is a part of the dimensionality reduction process in which an initial set of images were divided into many manageable groups. Determination of humans based on skeletal parts available is the most challenging task for forensic experts when only fragmented parts of the body are recovered [26]. In this situation, forensic dentistry will help in gender identification and age estimation based on the dental remaining and skull part. Some of the salient and dominant features in teeth for the identification process are illustrated in this section. In this paper, the most dominant features of teeth which help in determination of age and gender were identified. Few features identified from teeth are intercanine distance, incisor width, and canine width; they play a significant role in judging age and gender using teeth. Feature values extracted and recorded the values of these features in a feature matrix form. The next phase in the identification process is the conversion of feature matrix values to an understandable classifier format [27].

The odontometric features identified and analyzed for gender and age assessment are as follows:

- (i) Incisor width: central incisors' width from both mandible and maxilla was analyzed and measured. The measurement of the incisor in the mandible differs from the maxillary jaw in males and females.
- (ii) Distance measured between canine: distance between canine from maxilla and mandible jaw is noted. This intercanine distance is the measurement between teeth numbers 13 and 23 in the maxillary jaw and the distance between teeth numbers 33 and 43 in the mandible. Figures 4(a) and 4(b) represent the samples of measurement of maxillary incisor teeth and mandible intercanine distance.

### 4. Materials and Methods

The present experimental study for the prediction of individuals was conducted based on digital X-ray images of teeth. Dental X-ray images were publicly not available. Hence, they were collected from local dental colleges and dental clinics, which

TABLE 2: Literature review summary.

SN	Authors	Year	Research findings	Remark
01	Saloni, Pradhuman V, P Mahajan, Ankush, Sukhleen Kaur, and Sakshi [16]	2020	Three parameters out of five mandible ramus variables studied showed statistically ( $p < 0.05$ ) significant differences in gender	Mandible ramus may be used as an alternate tool in determining gender based on OPG
02	Poornima V, Surekha, Venkateswara Rao, G. Deepthi, Naveen S, and Arun Kumar [17]	2020	Right and left permanent mandible teeth were evaluated in OPG using the Camerier technique	High accuracy is achieved based on the Camerier method applied from an Indian-specific formula
03	A Okkesim and S Erhamza [18]	2020	The average value in min ramus width for males is 31.7 mm and for females is 29 mm. The average projection height value of ramus in females is measured 53.9 mm and in males is 48 mm	Mandible ramus in CBCT-based model exhibits significant differences in gender determination
04	N Vila, R. R. Vilas, and M. J. Carreira [19]	2020	Gender is evaluated based on DASNet and VVG 16 architecture	Accuracy of gender classification is 83% for DASNet and 90% for VGG-16
05	Vathsala Patil, Ravindranath, Saumya, Adithya, and Namesh [20]	2020	Gender determination based on mandible parameters using a logistic regression technique	In discriminant analysis, accuracy is 69%, in logistic regression, accuracy is 70%, and ANN shows the highest accuracy of 75%
06	J Albernaz, Nathalie A, Ferreira, Vanessa, and Proença [21]	2020	Teeth cast was used for the experimental procedure. Mesiodistal width of Rt. 1st molar to Lt. 1st molar was measured on each cast	Gender determination was classified with accuracy of 75%
07	Dalessandri D, Ingrid Tonni, Laura L, Marco Migliorati, Gaetano I, LVisconti, Stefano B, and C Paganelli [22]	2020	Reliability and accuracy of OPG versus CBCT for determination of age and gender	CBCT was found to be accurate when compared with OPG images in prediction
08	Stella A and Thirumalai [23]	2020	Tooth was divided into different stages starting from A stage to H stage	Individual age assessment using the Demirjian and the Nolla methods
09	Ahima Bali Behl [24]	2020	Measurement of bicondylar breadth (BB), gonial angle measurement, antegonial angle (AGA), ramus height, and ramus breadth (RHRB)	Upper and lower breadths of ramus were calculated. Ramus condylar height and coronoid height were measured appropriately
10	Vanessa M A, Rocharles, Andreia D'Souza, Casimiro, Andrea, Francisco C, and Deborah Q Eduardo Jr. [25]	2019	Equations for prediction of age and gender using pulp volumes from upper canine and upper central incisor	High accuracy can be achieved by using this formula when it is applied to pulp volume
11	Wallraff Sarah, Vesal Sulaiman, Syben Christopher, Lutz Rainer, and Maier Andreas [15]	2021	Unisex and sex-specific approaches based on deep learning methods achieve better results on the test data set	Male gender is slightly estimated younger than female gender

have digital X-ray imaging facilities [28]. The local dataset was obtained with proper proceedings and academic agreement between two dental colleges. A total of 995 samples of teeth were collected from the College of Dental Sciences, Davangere, and 147 samples were collected from Bapuji Dental College and Hospital, Davangere, Karnataka, India. In total, we have 1142 datasets available for research analysis.

Figure 5(a) depicts the distribution of datasets based on the age of 5-year interval, segregating male and female count per group. The age distributions of available 1142 datasets of teeth were divided into 11 groups of 5 years of range per group except the first and last groups since the first group is datasets of the age group of 1–10 years and the last group is for the age group of 60 years and above. Figure 5(b) illustrates the total samples of males and females (total 632 male and 510 female samples).

**4.1. Methodology.** The proposed system for age assessment and determination of gender has a systematic methodology depicted in Figure 6. Basic blocks in methodology are data

collection, preprocessing of input image [29], features extraction, feature matrix, conversion of feature matrix into understandable classifier format, and classification. Out of 1142 local samples, 80 percent of dataset samples (913 samples) were used as the training dataset, and 20 percent of dataset samples (229 samples) were used as the unseen testing dataset. Subjects that came under the decayed tooth, missing tooth, or broken tooth were excluded from the experimental study. A normal healthy state and caries-free teeth were considered for the study. An OPG of teeth was provided as input for the model. The initial stage of the identification system was preprocessing the image. This input sample was preprocessed by removing unwanted labels and noise present in the sample. The outcome of preprocessing stage was an enhanced image, which was essential for better accuracy in prediction. The most important and dominant features in teeth that helped in the identification process were extracted. Feature values of teeth like incisor width and intercanine distance were extracted from an input OPG image. Feature matrix was constructed,



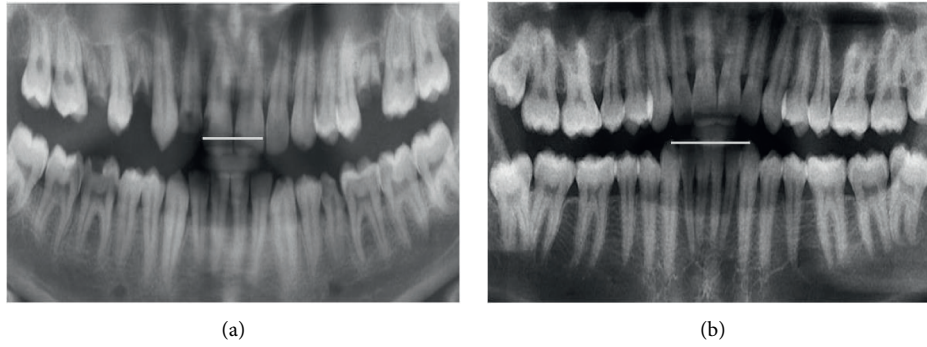


FIGURE 4: (a) Central incisor teeth measurement. (b) Inter canine measurement.

and feature matrix values were converted to classifier understandable format. Figure 6 depicts the methodology for age and gender identification. Finally, the model classified age and gender from an input OPG image. The age and gender identification system were implemented using a Support Vector Machine (SVM) classifier.

Gender identification based on teeth was carried out using the LIBSVM classifier tool and training with several kernels and with different values of hyperparameters [29]. Since gender determination required two classes, the age estimation process was carried out using the Multiclass SVM (MSVM) classifier tool, and images were trained with several kernels and with different hyperparameter values. Age estimation required multiple classes. Hence, the LIBSVM classifier and MSVM classifier were used for gender and age identification [30], respectively.

Few samples of teeth datasets collected from College of Dental Sciences, Davangere, and Bapuji Dental College and Hospital, Davangere, are shown in Figures 7 and 8, respectively. These images were received in Tagged Image File Format (TIFF) format.

## 5. Experimental Results and Discussion

The human age and gender classification model is a fully automated system that predicts the gender of humans with an estimation of age. The model displays the result by taking only the input of an OPG of teeth. It produces results in less than a minute with higher accuracy. Classification techniques used and outputs obtained from classifiers with various kernels and hyperparameters are highlighted in this section. Age estimation and gender determination are carried out by MSVM and LIBSVM, respectively. The initial stage in the prediction model is to preprocess the input image by removing image noises, which may be adjoined while capturing images. The subsequent task of image preprocessing is to enhance the brightness and quality of the image [31].

**5.1. Pixel Brightness Transformation.** Brightness transformations modify pixel brightness, and the transformation depends on the properties of a pixel. Contrast enhancement is an important area in image processing. It is widely used for medical image processing. The function used is *cv2.cvtColor*

(*img, cv2.COLOR\_BGR2GRAY*). The outcome of this stage is an enhanced version of the original image. The result after the preprocessed image is depicted in Figure 9.

**5.1.1. Edge Detection Using Canny Edge Detection Algorithm.** Image segmentation is a technique of partitioning the images into multiple segments. Specifically, the image segmentation method is used to locate objects and boundaries of images. The Canny detection algorithm is used to detect edges of teeth, which aids the model in predicting age and gender accurately.

The Canny edge detection technique uses five steps for the detection of edges of input images. The following steps are used in this paper to detect edges from teeth OPG. Figure 10 depicts the outcome of the Canny edge detection technique performed on an OPG image.

Steps in edge detection using the Canny edge detection algorithm are as follows:

- (1) Conversion of image based on Gaussian filter.  
Sigma = 1.5, G Kernel size ( $5 \times 5$ )
- (2) Gradient Calculation.  
Horizontal filter  $K_X$  and Vertical filter  $K_Y$   
 $I_x = \text{filters.convolve}(\text{image}, K_x)$   
 $I_y = \text{filters.convolve}(\text{image}, K_y)$
- (3) Nonmax suppression: To achieve thin edges  
 $\text{angle} = A * 180 / \text{np.pi}$   
 $\text{angle}[\text{angle} < 0] += 180$
- (4) Double Threshold  
 $\text{high\_Threshold} = \text{image.max}() * \text{highThresholdratio}$   
 $\text{low\_Threshold} = \text{high\_Threshold} * \text{lowThresholdratio}$
- (5) Tracking edge-based hysteresis  
 $\text{Low\_T} = \text{Low\_T} * \text{max}(\text{max}(b-w))$   
 $\text{High\_T} = \text{Low\_T} * \text{max}(\text{max}(b-w))$

**5.1.2. Mathematical Modeling for Prediction Based on Teeth.** Mathematical equations involved in prediction of age and gender are described in this section. Equation (1) is used in

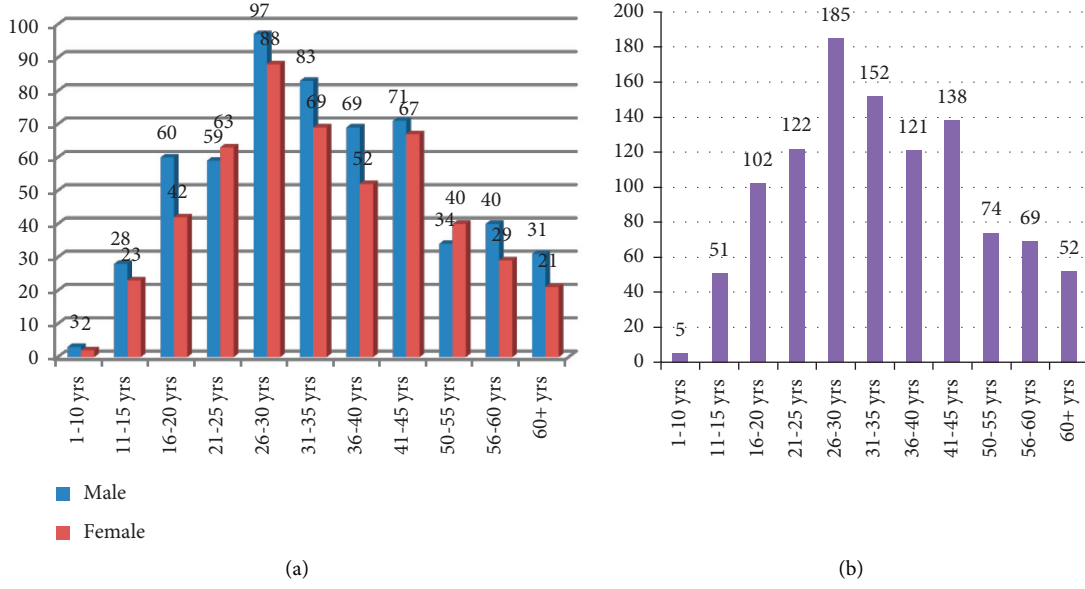


FIGURE 5: (a) and (b) Dataset distribution based on gender and age group.

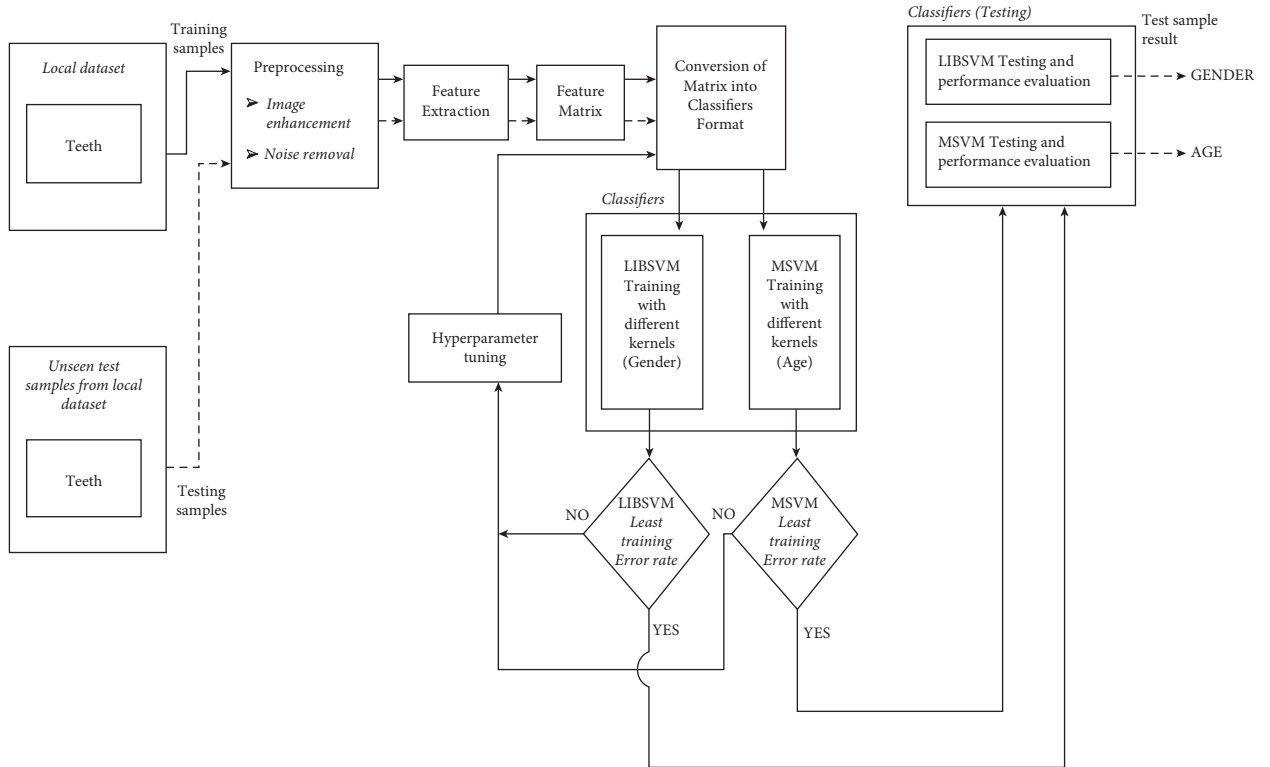


FIGURE 6: Methodology for gender and age assessment system using OPG of teeth.

calculation for gender differences that appeared on the left and right part of maxillary and mandible canines:

$$\text{gender difference} = \frac{(X_m/X_f - 1)}{100}, \quad (1)$$

where  $X_m$  is the average of canine teeth width in males and  $X_f$  is the average of canine teeth width in females.

Noise removal from digital images is done by applying a Gaussian filter, as shown in equation (2). To perform this operation, the image convolution method was used by applying a Gaussian kernel of  $3 \times 3$ ,  $5 \times 5$ ,  $7 \times 7$ , and so on. Sizes of Gaussian kernel depend on image blurring effects. In the present model, a  $5 \times 5$  kernel size has been used. The formula for Gaussian kernel filter  $(2k + 1) * (2k + 1)$  is given as

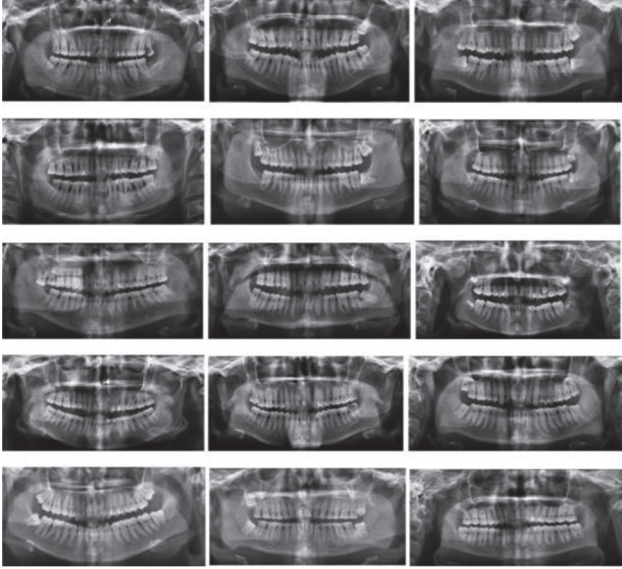


FIGURE 7: Dataset collected from College of Dental Science, Davangere.

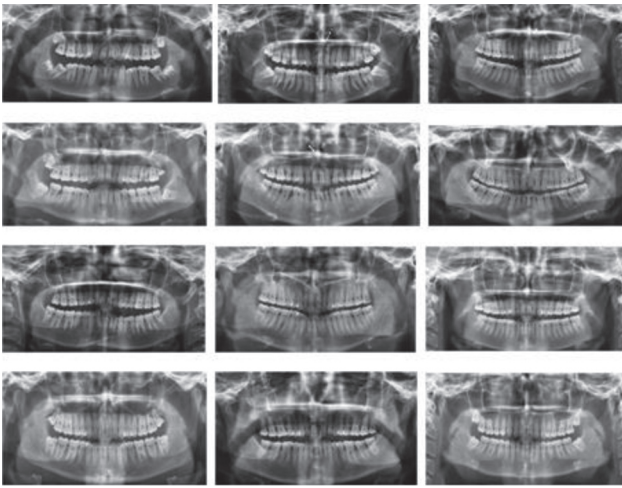


FIGURE 8: Dataset collected from Bapuji Dental College and Hospital, Davangere.

$$H_{ij} = \frac{1}{2\pi\sigma} \exp\left(-\frac{(m - (k+1))^2 + (n - (k+1))^2}{2\sigma^2}\right). \quad (2)$$

Some part of mathematics is involved behind the scene, mainly depending on derivatives. This mathematical-based formula was converted to equivalent python codes. Table 3 is the comparison between feature values of central incisor width and intercanine width in millimeters.

## 5.2. SVM Training

**5.2.1. LIBSVM Training for Gender Determination.** The LIBSVM classifier is used for gender determination from teeth images. LIBSVM is trained with different kernels of SVM, namely, Linear, Polynomial, Gaussian Radial Basis Function (RBF), and Sigmoid kernels. These are trained with

different parameters of SVM like  $C$ ,  $\gamma$ , and  $d$ . The LIBSVM executable *svmtrain* is employed for SVM training with various *svm\_type* and *kernel\_type*. Kernel parameters also have a significant effect on the decision boundary. Two features values from the teeth were extracted for age and gender determination [29]. The values of these features are extracted from the GUI from a teeth X-ray image. The training (memorization) accuracy of the SVM classification engine is calculated using the following expression:

$$\text{training accuracy} = \frac{T_C}{T_S} \times 100, \quad (3)$$

where  $T_C$  represents the total number of samples correctly classified by the SVM and  $T_S$  represents the total number of samples used for testing.

Figure 11 depicts the training dataset feature matrix of teeth for gender identification. Each row in the feature matrix represents the feature of each image in the dataset [30]. The first column represents the class for gender determination, where 0 is for male and 1 indicates female. The second and third columns represent the feature values extracted from teeth.

LIBSVM classifier uses two classes for gender, and the description of the class label used in the LIBSVM classifier is depicted in Table 4, since gender determination has only two classifications.

**5.2.2. MSVM Training for Age Estimation.** The MSVM classifier is used for age estimation from teeth images. Different kernels of MSVM, namely, Linear, Polynomial, Gaussian Radial Basis Function (RBF), and Sigmoid kernels, are used for training teeth datasets. The training dataset feature matrix of teeth is depicted in Figure 12, where 832 indicates the number of data (images in the dataset) and 2 indicates the dimension (number of features) of the data. Each row in the feature matrix represents the feature of each teeth image in the dataset [31]. The last column represents the class of the age classification.

MSVM classifier uses multiple class labels for age estimation. The class label description used in the M-SVM classifier is depicted in Table 5, since age estimation has multiple age groups, and hence it is classified using multiple class label SVM.

**5.3. SVM Testing.** For the testing phase, 20 percent of unseen data samples were used for gender and age classification system.

**5.3.1. LIBSVM Testing for Gender.** The LIBSVM executable command *svm-predict.exe* is used for testing and validating the classification results. Once the best hyperparameters are determined using the grid search technique, the training model with the best cross-validation accuracy [15] is considered for LIBSVM testing.

Accuracy from teeth unseen dataset is depicted in Table 6 and in Figure 13, respectively. From Table 6, we can notice that the RBF kernel shows the best classification results of



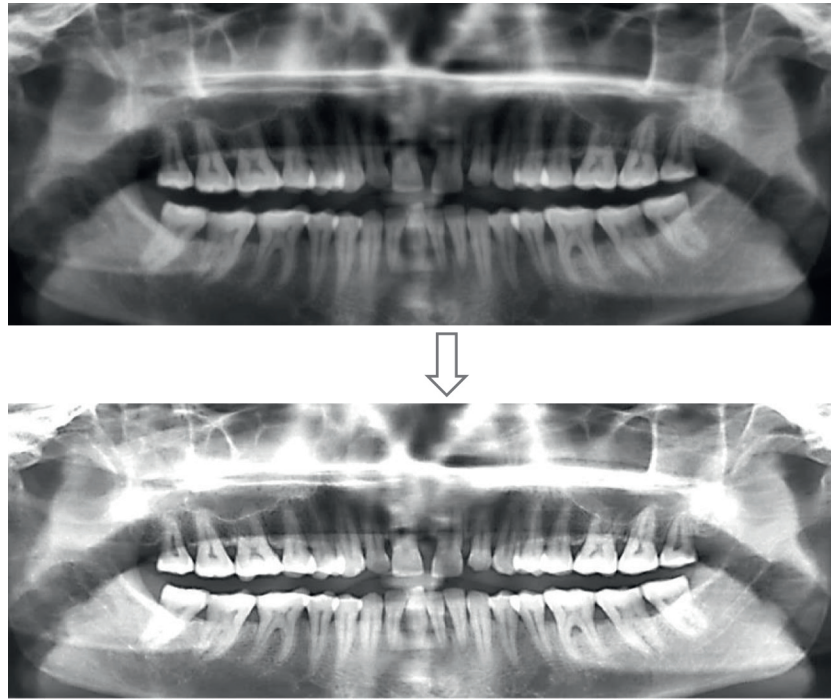


FIGURE 9: Result of preprocessing.

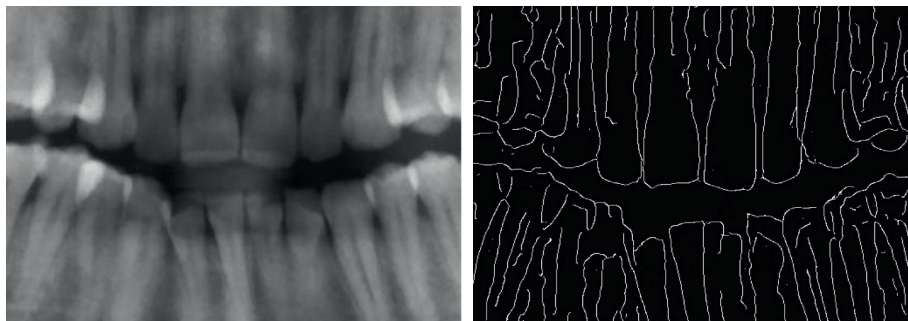


FIGURE 10: Detection of edge in teeth image using Canny edge detector.

TABLE 3: Central incisor and intercanine width (male versus female).

Sl. no.	Parameters	Gender	Mean (in mm)
01	Central incisor width	Male	9.4
		Female	8.3
02	Intercanine distance	Male	29.14
		Female	25.7

accuracy of 95.83 percent for the teeth dataset. Since the classification result is above 95 percent, the models generated for the teeth dataset using RBF kernel by LIBSVM training are acceptable. Comparisons of different LIBSVM kernels for gender determination with various hyperparameters are illustrated in Figure 14. Figures 14(a)–14(d) show the accuracy of gender classification performed by using Polynomial, Linear, RBF, and Sigmoid kernels, respectively. The highest accuracy of 95.83% is achieved for gender classification from the RBF kernel for hyperparameter values  $d = 3$ ,  $c = 28$ , and  $g = 0.04167$ .

**5.3.2. MSVM Testing for Age.** The MSVM executable command *predmsvm.exe* is used for testing and validating the classification results. The best hyperparameters are selected using the grid search technique, and the training model with the best cross-validation accuracy is considered for MSVM testing. Figure 15 depicts the age classification test case results validated for unseen dataset samples of teeth. MSVM classifiers with various kernels are used to build the best model for accuracy.

RBF kernel yields best classification results of accuracy of 97.91 percent for teeth testing dataset as depicted in Table 7.

1	0	1:9.1	2:29.2
2	1	1:8.4	2:24.4
3	1	1:8.2	2:26.3
4	0	1:9.2	2:36.1
5	1	1:8.5	2:27.8
6	1	1:8.3	2:24.1
7	1	1:8.8	2:29.2
8	1	1:8.1	2:30.9
9	1	1:8.4	2:27.1
10	0	1:9.4	2:34.9
11	0	1:9.9	2:35
12	0	1:9.5	2:34.1
13	1	1:8.3	2:29.2
14	1	1:8.5	2:28.1
15	0	1:9.1	2:34
16	1	1:8.9	2:33.2
17	0	1:10.0	2:39.6

FIGURE 11: Feature matrix of teeth dataset for gender.

TABLE 4: Class label description.

Class label	Gender
Class 0	Male
Class 1	Female

1	832		
2	2		
3	9.3	35.3	02
4	8.7	34.8	12
5	8.6	34.7	17
6	9.2	35.1	01
7	8.7	34.8	18
8	8.3	34.5	15
9	8.8	34.9	19
10	8.1	34.3	14
11	9.4	35.4	02
12	9.9	35.9	05
13	8.8	34.9	19
14	8.0	34.1	13
15	9.8	35.7	04
16	10.3	36.4	08
17	9.3	35.3	02
18	8.0	34.2	13
19	8.1	34.3	14
20	10.0	35.0	05

FIGURE 12: Feature matrix of teeth dataset for age.

TABLE 5: MSVM class label description.

Class label_M	Age_M (years)	Class label_F	Age_G (years)
Class 1	1–15	Class 11	1–15
Class 2	16–20	Class 12	16–20
Class 3	21–25	Class 13	21–25
Class 4	26–30	Class 14	26–30
Class 5	31–35	Class 15	31–35
Class 6	36–40	Class 16	36–40
Class 7	41–45	Class 17	41–45
Class 8	46–50	Class 18	46–50
Class 9	51–55	Class 19	51–55
Class 10	56+	Class 20	56+



TABLE 6: LIBSVM testing for Gender with different kernels.

Kernel with hyperparameters	Number of samples correctly classified	Number of samples misclassified	Accuracy (%)
Linear ( $C = 256$ )	43	05	89.5833
Polynomial ( $d = 2$ , $C = 64$ , $g = 0.09153$ )	42	06	85.41
RBF ( $C = 16$ , $g = 0.08245$ )	46	02	95.8333
Sigmoid ( $C = 512$ , $g = 0.31626$ )	40	08	83.3333

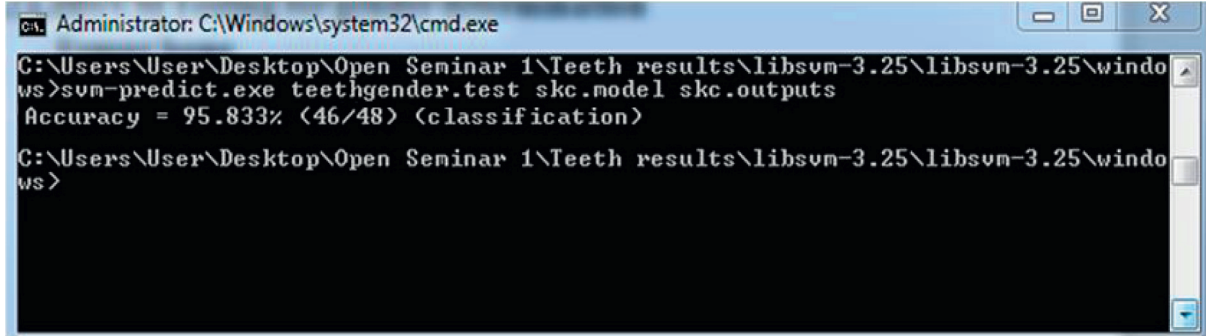


FIGURE 13: Gender accuracy of teeth dataset.

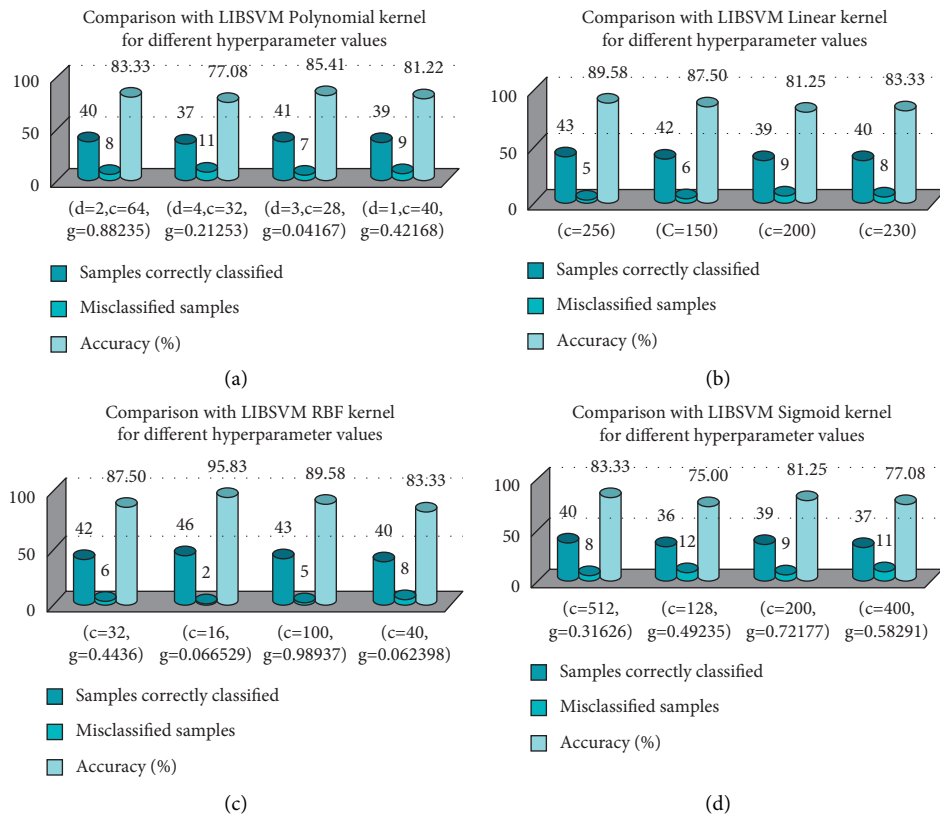


FIGURE 14: Comparison of different LIBSVM kernels with different hyperparameter values. (a) Polynomial kernel, highest accuracy = 85.41% ( $d = 3$ ,  $c = 28$ , and  $g = 0.81032$ ). (b) Linear kernel, accuracy = 89.58% ( $c = 256$ ). (c) RBF kernel, accuracy = 95% ( $c = 16$ ;  $g = 0.08245$ ). (d) Sigmoid kernel, accuracy = 83.33% ( $c = 512$ ;  $g = 0.31626$ )).

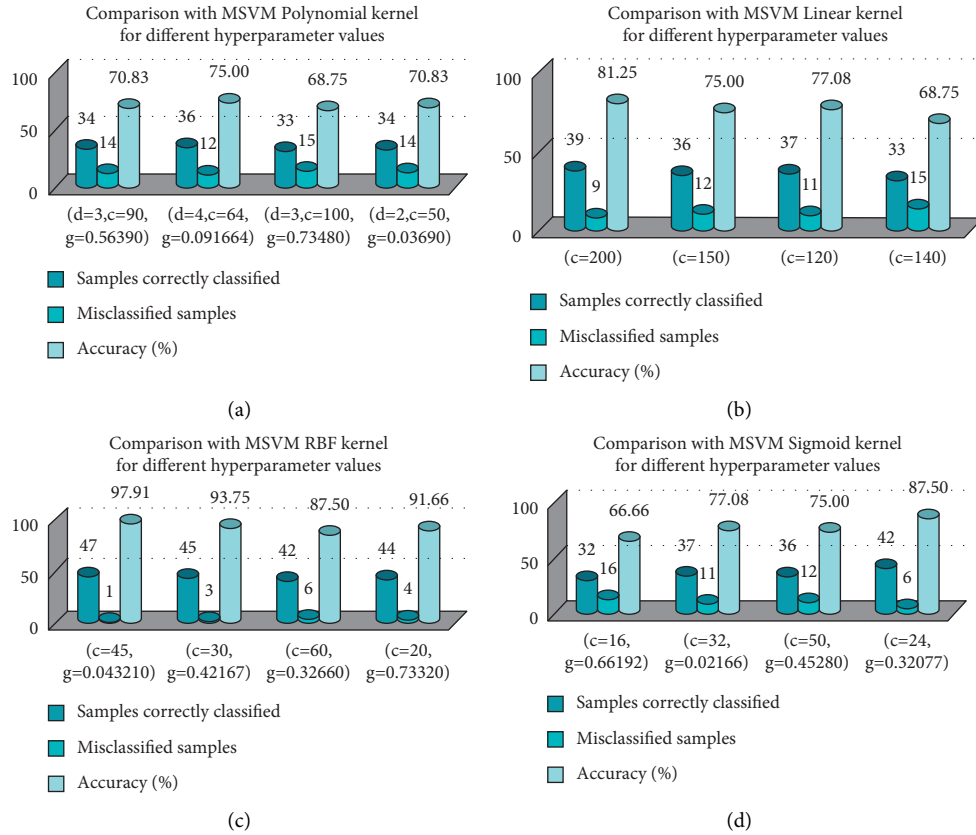


FIGURE 15: Comparison of different MSVM kernels with different hyperparameter values. (a) Polynomial kernel, highest accuracy = 75.41% ( $d=4$ ,  $c=64$ , and  $g=0.09164$ ). (b) Linear kernel, accuracy = 81.25% ( $c=200$ ). (c) RBF kernel, accuracy = 97.91% ( $c=45$  and  $g=0.043216$ ). (d) Sigmoid kernel, accuracy = 87.50% ( $c=24$  and  $g=0.32077$ ).

TABLE 7: MSVM testing for age with different kernels.

Kernel with hyperparameters	Number of samples correctly classified	Number of samples misclassified	Accuracy (%)
Linear ( $C=200$ )	39	09	81.25
Polynomial ( $d=4$ , $C=64$ , and $g=0.05273$ )	36	12	75.0
RBF ( $C=45$ and $g=0.04317$ )	47	48	97.916
Sigmoid ( $C=256$ and $g=0.63419$ )	42	06	87.50

Since the classification result is above 97 percent, the models generated for femur and teeth dataset using RBF kernel by MSVM training can be acceptable.

## 6. Conclusion and Future Scope

From the present study, the morphological differences in identifying age and gender in the teeth were observed. Incisor width and intercanine distance in male teeth were found to be more compared to female teeth. The majority of all the parameters from the teeth of the male tended to be

slightly more than female. The formula that was developed and used in this paper provided good and accurate results in prediction by using LIBSVM classifier and MSVM classifier. 95% of accuracy was achieved for gender determination, and 97% of accuracy was achieved for estimation of age. In conclusion of this paper, we were able to meet the goal of prediction by achieving the experimental results, which were nearly matching to ground truth values. This system may be used further as a novel model in personal identification without human intervention. It can be effectively used and applicable in the forensic science department for accurate and fast test results. In this paper, we have developed a system that makes the task easier in studying and analysing the femur digital radiographs for age and gender identification. This paper can be elaborated by identifying and extracting some more important teeth features and by standardizing those new features from the datasets. Furthermore, this research work can be elaborated on other parts of the human body, such as pelvis bone, skull, wrist, and other long bones. These digital images may also contribute to the identification of gender and age. In this paper, we have developed a system that makes the task easier in studying and analysing the femur digital radiographs for age and gender identification. This paper can be further carried out by developing a web-based application or on a smart-phone-based application that can be user-friendly to access.

## Data Availability

The data that support the findings of this study are available from the corresponding author upon request.

## Conflicts of Interest

The authors declared that they do not have any conflicts of interest.

## References

- [1] N. Pandey and M. S. Ma, "Evaluation of sexual dimorphism in maxillary and mandibular canine using mesiodistal, labiolingual dimensions, and crown height," *Indian Journal of Dental Research: Official Publication of Indian Society for Dental Research*, vol. 27, pp. 473–476, 2016.
- [2] E. Avcu and F. Bas\_çiftçi, *The Determination of Age and Gender by Implementing New Image Processing Methods and Measurements to Dental X-ray Images*, pp. 0263–2241, Elsevier, Amsterdam, Netherlands, 2019.
- [3] R. Srivastava, B. Jyoti, J. Prakash, M. Gupta, P. Devi, and R. Jayaram, "Gender determination from the mesiodistal dimension of permanent maxillary incisors and canines: an odontometric study," *Journal of Indian Academy of Oral Medicine and Radiology*, vol. 26, no. 3, 2014.
- [4] N. Mohan and T. Aravinth Raja, "Comparasion of the position mental foramen and permanent maxillary canine width in gender determination," *IOSR Journal of Dental and Medical Science*, vol. 17, no. 5, pp. 12–18, 2018.
- [5] R. Cameriere, L. Ferrante, and M. Cingolani, "Age estimation in children by measurement of open apices in teeth," *International Journal of Legal Medicine*, vol. 120, no. 1, pp. 49–52, 2006.
- [6] A. Omar and S. Azab, "Applicability of determination of gender from odontometric measurements of canine teeth in a sample of adult Egyptian population," *Cairo Dent J*, vol. 25, pp. 167–180, 2009.
- [7] V. K. Asrani and J. S. Shah, "Mental foramen: a predictor of age and gender and guide for various procedures," *Forensic Sci Med*, vol. 4, pp. 76–84, 2018.
- [8] A. Sklavos, D. Beteramia, S. N. Delpachitra, S. N. Delpachitra, and R. Kumar, "The panoramic dental radiograph for emergency physicians," *Emergency Medicine Journal*, vol. 36, no. 9, pp. 565–571, 2019.
- [9] V. Sairam, G. R. Potturi, B. Praveen, and G. Vikas, "Assessment of effect of age, gender, and dentoalveolar changes on mandibular morphology: a digital panoramic study," *Contemporary Clinical Dentistry*, vol. 9, pp. 49–54, 2018.
- [10] Ch. Sai kiran, T. Khaitan, P. Ramaswamy, S. Sudhakar, B. Smitha, and G. Uday, "Role of mandibular canines in establishment of gender," *Egypt J Forensic Sci*, vol. 4, no. 3, pp. 71–74, 2014.
- [11] Y. Kaeswaren and A. Z. Weinheimer, "The use of mandibular and maxillary canine teeth in establishing sexual dimorphism in the Malaysian population of selangor," *J Forensic Sci & Criminal Inves*, vol. 11, no. 3, Article ID 555815, 2019.
- [12] G. Suragimath, S. R. Ashwinirani, V. Christopher, S. Bijjargi, R. Pawar, and A. Nayak, "Gender determination by radiographic analysis of mental foramen in the Maharashtra population of India," *Journal of Forensic Dental Sciences*, vol. 8, p. 176, 2016.
- [13] Z.-P. Ge, Y. Pan, G. Li, J.-Z. Zhang, and X.-C. Ma, "Age estimation based on pulp cavity/chamber volume of 13 types of tooth from cone beam computed tomography images," *International Journal of Legal Medicine*, vol. 5, no. 4, pp. 2421–2425, 2016.
- [14] C. Monali, P. Pritam, M. Tapan, and D. Kajal, "Gender determination: a view of forensic odontologist," *Indian Journal of Forensic Medicine and Pathology*, vol. 4, no. 4, 2011.
- [15] S. Wallraff, S. Vesal, C. Syben, R. Lutz, and A. Maier, "Age estimation on panoramic dental X-ray images using deep learning," *Bildverarbeitung für die Medizin 2021*, Springer, Berlin/Heidelberg, Germany, pp. 186–191, 2021.
- [16] P. V. Saloni, P. Mahajan, A. Puri, S. Kaur, and S. Mehta, "Morphometric analysis of mandibular ramus: a panoramic study," *Indian Journal of Dental Research*, vol. 31, no. 3, 2020.
- [17] P. Vadla, R. Surekha, G. V. Rao, G. Deepthi, S. Naveen, and C. Arun Kumar, "Assessing the accuracy of Cameriere's Indian-specific formula for age estimation on right and left sides of orthopantomogram," *Egyptian Journal of Food Science*, vol. 10, no. 1, 2020.
- [18] A. Okkesim and S. Erhamza, "Assessment of mandibular ramus for sex determination: retrospective study," *Journal of Oral Biology and Craniofacial Research*, vol. 10, no. 4, pp. 569–572, 2020.
- [19] N. Vila, R. R. Vilas, and M. J. Carreria, *Towards Deep Learning Reliable Gender Estimation from Dental Panoramic Radiographs*, STAIRS, Santiago de Compostela, Spain, 2020, <http://ceur-ws.org/>.
- [20] V. Patil, R. Vineetha, S. Vatsa et al., "Artificial neural network for gender determination using mandibular morphometric parameters: a comparative retrospective study," *Cogent Engineering*, vol. 7, no. 1, Article ID 1723783, 2020.
- [21] J. A. Neves, N. Antunes-Ferreira, V. Machado et al., "Sex prediction based on MesiodistalWidth data in the Portuguese population," *Applied Sciences*, vol. 10, p. 4156, 2020.
- [22] D. Dalessandri, I. Tonni, L. Laffranchi et al., "2D vs. 3D radiological methods for dental age determination around 18 Years: a systematic review," *Applied Sciences*, vol. 10, no. 9, p. 3094, 2020.
- [23] A. Stella and S. Thirumalai, "Age assessment automation tool using VBA with OPG," *International Journal of Scientific & Technology Research Volume*, vol. 9, no. 1, 2020.
- [24] A. Bali Behl, S. Grewal, K. Bajaj, P. S. Baweja, G. Kaur, and P. Kataria, "Mandibular ramus and gonial angle—identification tool in age estimation and sex determination: a digital panoramic radiographic study in north Indian population," *Journal of Indian Academy of Oral Medicine and Radiology*, vol. 32, no. 1, p. 31, 2020.
- [25] V. M. Andrade, R. C. Fontenele, A. C. de Souza et al., "Age and sex estimation based on pulp cavity volume using cone beam computed tomography: development and validation of formulas in a Brazilian sample," *Dentomaxillofacial Radiology*, vol. 48, Article ID 20190053, 2019.
- [26] E. Michael Onyema, P. Kumar Shukla, S. Dalal, M. Neeraj Mathur, M. Zakariah, and B. Tiwari, "Enhancement of patient facial recognition through deep learning algorithm: ConvNet," *Journal of Healthcare Engineering*, vol. 2021, Article ID 5196000, 8 pages, 2021.
- [27] P. K. Shukla, J. Kaur Sandhu, A. Ahirwar, D. Ghai, P. Maheshwary, and P. K. Shukla, "Multiobjective genetic algorithm and convolutional neural network based COVID-19 identification in chest X-ray images," *Mathematical Problems in Engineering*, vol. 2021, Article ID 7804540, 9 pages, 2021.
- [28] V. Roy, P. K. Shukla, A. K. Gupta, V. Goel, P. K. Shukla, and S. Shukla, "Taxonomy on EEG artifacts removal methods,

- issues, and healthcare applications,” *Journal of Organizational and End User Computing*, vol. 33, no. 1, pp. 19–46, 2021.
- [29] P. K. S. M. Agrawal and A. U. Khan, “Stock price prediction using technical indicators: a predictive model using optimal deep learning,” *International Journal of Recent Technology and Engineering (IJRTE) ISSN*, vol. 8, no. 2, pp. 2297–2305, 2019.
- [30] R. Gupta, P. K. Shukla, and P. Kumar Shukla, “Performance analysis of anti-phishing tools and study of classification data mining algorithms for a novel anti-phishing system,” *International Journal of Computer Network and Information Security*, vol. 7, no. 12, pp. 70–77, 2015.
- [31] M. Kumar Ahirwar, P. K. Shukla, and R. Singhai, “CBO-IE: a data mining approach for healthcare IoT dataset using chaotic biogeography-based optimization and information entropy,” *Scientific Programming*, vol. 2021, Article ID 8715668, 14 pages, 2021.

## Performance analysis of different intonation models in Kannada speech synthesis

Sadashiva Veerappa Chakrasali<sup>1,2</sup>, Krishnappa Indira<sup>1</sup>, Sunitha Yariyur Narasimhaiah<sup>3</sup>,  
Shadaksharaiah Chandraiah<sup>4</sup>

<sup>1</sup>Department of Electronics & Communication Engineering, Ramaiah Institute of Technology, Bengaluru, India

<sup>2</sup>Department of Electronics & Communication Engineering, VTU Research Center, Ramaiah Institute of Technology, Bengaluru, India

<sup>3</sup>Department of Electronics & Communication Engineering, SJB Institute of Technology, Bengaluru, India

<sup>4</sup>Department of Electrical & Electronics Engineering, Bapuji Institute of Engineering and Technology, Davangere, India

### Article Info

#### Article history:

Received Mar 23, 2021

Revised Jan 10, 2022

Accepted Feb 21, 2022

#### Keywords:

CART model  
Fujisaki parameters  
Intonation models  
Kannada TTS  
Neural network  
Pitch frequency  
Tilt model

### ABSTRACT

Text to speech (TTS) is a system that generates artificial speech from text input. The prosodic models used improve the quality of the synthesized speech especially naturalness and intelligibility. The prosody involves intonation, intonation refers to the variations in the pitch frequency (F0) with respect to time in an utterance. This work mainly concentrates on building feedback neural network model to predict F0 contour in the utterances using Fujisaki intonation model parameters as the input features to the network since the Fujisaki intonation model is data driven and not a rule based one. In this work we have built 4-layer feedback neural network in the festival framework. Finally, the synthetically generated Kannada speech using the neural network model, is compared for its performance with the classification and regression tree (CART) model and Tilt model. Database of simple declarative Kannada sentences created by Carnegie Mellon University have been deployed in this work. From the study it is very clear that F0 contours can be accurately predicted using CART and neural network models, whereas naturalness and intelligibility is high in CART model rather than neural network model.

This is an open access article under the [CC BY-SA](https://creativecommons.org/licenses/by-sa/4.0/) license.



### Corresponding Author:

Sadashiva Veerappa Chakrasali  
Department of Electronics & Communication Engineering, VTU Research Center  
Ramaiah Institute of Technology  
Bengaluru, India  
Email: sadashivavc@gmail.com

## 1. INTRODUCTION

Recent developments in voice synthesis are huge in foreign languages, but they are almost non-existent in Indian languages like Kannada. In a previous paper [1], we created a Kannada speech synthesiser based on the hidden markov model (HMM) and the festival framework for simple declarative sentences, with prosody generated using the Tilt model. The developed Kannada speech synthesizer was able to produce a speech with m-nary-coded-decimal (MCD) score ranging between 3.5 dB to 5 dB, which is considered to be a good synthesizer but the generated speech is unsteady and unnatural sounding. Mixdorff and others [2], [3] have demonstrated that integrating prosody models improves the quality (naturalness and intelligibility) of synthetic speech. Prosody refers to the duration, gain, and intonation (pitch pattern) of speech portions. In the case of spoken speech sounds, intonation provides information on the glottal pulse source's periodicity. Depending on the nature or style of speech, different utterances for the same phoneme segment may have different intonation patterns. To forecast intermediate peaks and valleys, Madhukumar *et al.* [4] have made



available a model for linear intonation for the Hindi language for common sentences which are declarative in nature and its content limited to most commonly used functional words. This model fails to capture abrupt changes in pitch. In the paper, Patel *et al.* [5] have reported that the naturalness of the synthesized language can be increased by using proper models for the variations in the pitch, its rise and fall in the phrases and accent used in the language synthesized. Fujisaki and others [6], [7] have demonstrated the improvement in the synthesized speech in Japanese language by incorporating prosodic model. Details on Fujisaki model and extraction of model parameters are available in [7]–[11]. In the paper, Mnasri *et al.* [12] have built a neural network model to predict pitch frequency using Fujisaki parameters to synthesize Arabic language. In the paper, Rao and Yegnanarayana [13] has developed a neural network model to predict F0 of a syllable for Telugu and Bengali languages by feeding the attributes obtained directly from the utterances. In this work, Fujisaki Intonation Model features are used as input attributes of the neural network (NN) Model to predict the pitch of the phoneme in an utterance. Section 2, explains Fujisaki model and extraction of its parameters, whereas neural network model built in this work along with input and output features is explained in section 3. Section 4 explains the performance of neural network model and its performance analysis in synthesis.

## 2. FUJISAKI MODEL

From the literature it is evident that the Fujisaki model is widely used in intonation modeling, the main reason to use this is that it is a data driven method which is independent of language. The Fujisaki model provides a high-accuracy method for generating fundamental frequency (F0) changes in natural speech. The supplied pitch contour is decomposed into various components for parameters like Fb, the base frequency, the language phrases commonly used and the accent in which the words and phrases are pronounced. These three parameters of F0 are compared by superimposing their contours generated on a log scale. The Figure 1 displays the contour generated on the log scale for the pitch F0. The components or the phrases of the language are obtained as a result of the impulse reaction caused due to exposure of the linear system to critical damping to the second order. The accent components were seen to develop when the above dampening system was actuated by accent commands which were in the form of rectangular pulses, varying in length and amplitude. When the value of the speech which is constant is superimposed on two different components of the same utterance, it is seen to result in a basic model of the pitch contour relating to the utterance.

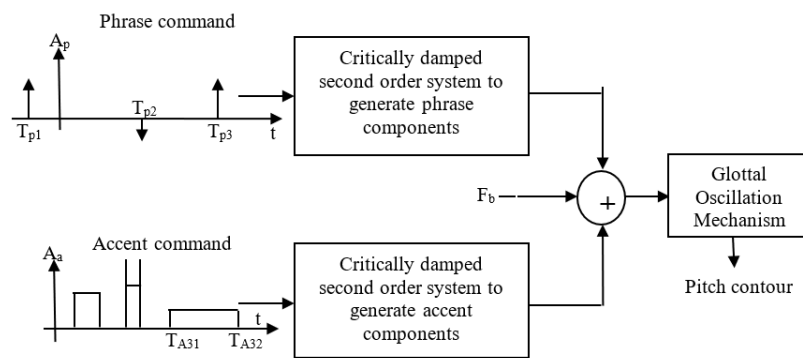


Figure 1. Block diagram for pitch contour generation

$$\ln(F_0(t)) = \ln(F_b) + \sum_{i=1}^I A_{pi} G_{pi}(t - T_{pi}) + \sum_{j=1}^J A_{aj} \{G_{aj}(t - T_{aj1}) - G_{aj}(t - T_{aj2})\}$$

where,

$$G_{pi}(t) = \begin{cases} \alpha_i^2 t \exp(-\alpha_i t), & t \geq 0 \\ 0, & t < 0 \end{cases}$$

$$G_{aj}(t) = \begin{cases} \min[1 - (1 + \beta_j t) \exp(-\beta_j t), \theta_j], & t \geq 0 \\ 0, & t < 0 \end{cases}$$

F<sub>b</sub>: represents the utterance base frequency

I: represents the quantity of phrase commands available in any utterance

$J$ : represents the quantity of accent commands available in any utterance

$A_{pi}$  and  $A_{aj}$ : respectively represent the amplitude of the  $i^{\text{th}}$  phrase command and accent command in the utterance

$T_{pi}$ : represents the instant of occurrence of the  $i^{\text{th}}$  phrase command available in the utterance

$T_{aj1}$  and  $T_{aj2}$ : respectively represent the Starting Time and End Time of the  $j^{\text{th}}$  accent command available in the utterance

$\alpha_i$ : represents the natural angular frequency of phrase control mechanism of  $i^{\text{th}}$  phrase command

$\beta_j$ : represents the natural angular frequency of accent control mechanism of  $j^{\text{th}}$  accent command

## 2.1. Parameter extraction

When a language is spoken by different individuals there is a quite naturally a marginal difference in the contours with regard to the pitch at a micro level. The individual prosodic changes caused by different individuals at the micro level need to be ironed out or eliminated to arrive at a pitch contour specific to a particular utterance and phrase. Only then it would be possible to extract the parameters of the Fujisaki model. This is possible by using an interpolation technique known as Cubic Spline Interpolation [6], [8], [9]. This interpolation creates a continuous pitch contour by removing silence portions from the speech, which is very essential to take derivatives of interpolated pitch contour. By taking derivatives we get high frequency contours (HFC) and low frequency contour (LFC). LFC is obtained by deducting the HFC from the obtained contour for interpolated pitch (IC). The IC is processed through a high pass filter with a cut off frequency of 0.5 Hz. to separate the accent and phrase components. As shown in Figure 2(a)-(d), the LFC is produced by subtracting HFC from the interpolated contour. The approximation derivative is used to HFC to extract the accent commands, i.e. the accent commands are analysed between successive minima in HFC. The largest F0 in the Log scale is obtained based on the value of  $A_a$ , the accent command maxima.  $F_b$  the base frequency is revealed by the LFC Global minimum. In view of the fact that the commencement of any new phase is distinctly marked by a local minima in that phrase component, the phrase components are spaced 1 second apart and the LFC searched for local minimas. The segment of the LFC after the potential onset time  $T_p$  is searched for the next local maximum to initialize the magnitude value of  $A_p$  assigned to each phrase command. At this stage,  $A_p$  is determined in proportion to  $F_0$ , taking into account the contributions of previous orders. 1/S, 20/S, and 0.9 are the values for the remaining model parameters [11].

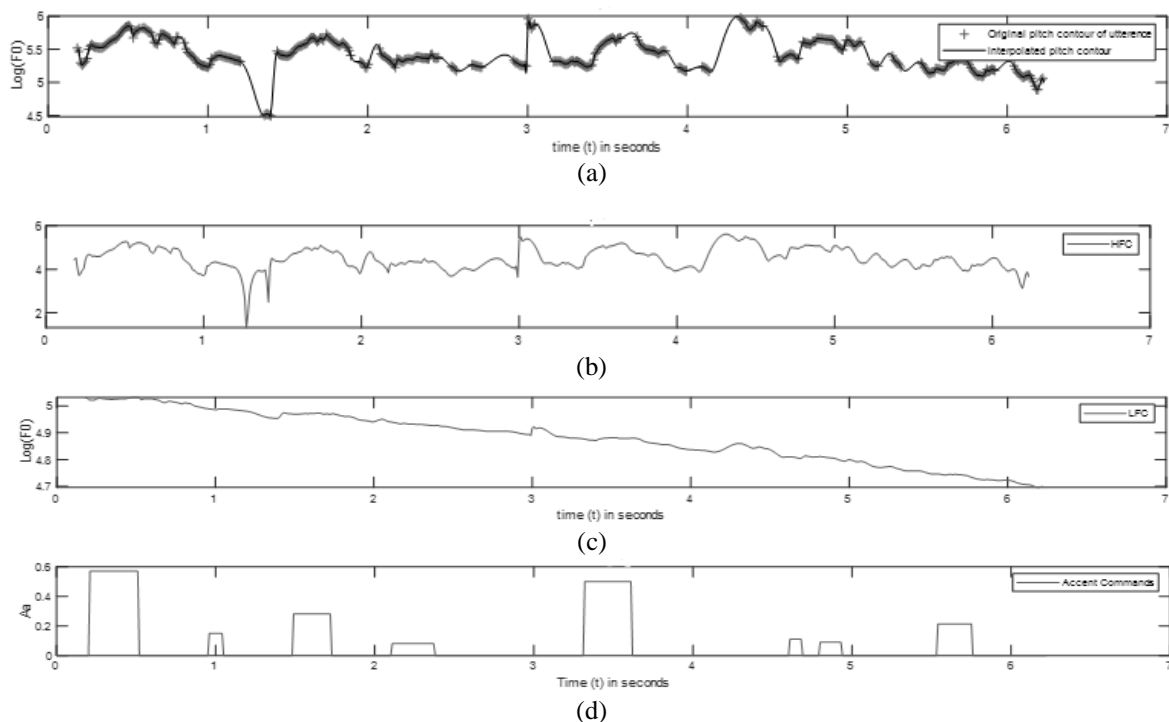


Figure 2. Extraction of the Fujisaki Parameters in an utterance, (a) cubic interpolation of pitch contour, (b) HFC, (c) LFC of interpolated pitch contour, and (d) extracted phrase and accent commands of an utterance

### 3. NEURAL NETWORK MODEL

Neural network (NN) model is nothing but the mutual functional relation between the input and output. This study uses a four layered feedback neural network (FBNN) shown in Figure 3, which is used to predict the average F0 [14], [15] value for each phoneme in an utterance. The positional, contextual and phonological features are used to train the neural network. There are 23 input feature vectors and 1 output feature vector. The list of features affecting the F0 of a phoneme are given in Table 1 and Table 2 respectively. The first layer in the four-layer neural network is the input layer with 23 input feature vectors and the first layer is having linear activation function. The middle two layers are the hidden layers with sigmoid as an activation function. The third layer is having a single node whereas the performance of the network is analyzed by varying number of nodes in the second layer. The last or the fourth layer is the output layer with 1 output feature vector that is a non-linear unit. The back-propagation method is used in order to achieve minimum mean square error (MSE).

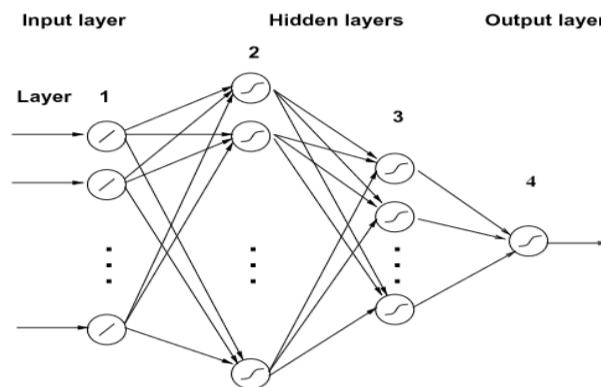


Figure 3. Four-layer FBNN

#### 3.1. Training of neural network

In this work, we used a four layered FBNN shown in Figure 3, which consists of one input layer, two hidden layers and one output layer. There are 23 input feature vectors and 1 output feature vector considered that are fed to train the network. The input features are based on the positional, contextual and phonological constraints of a phoneme and the output feature vector is the pitch of the respective phoneme as shown in Table 1.

Table 1. List of the input attributes and the number of nodes needed for training the neural network

Factors	Input attributes	No. of Nodes
Phoneme position in the word	Position of phoneme from the beginning of the word	3
	Position of phoneme from the end of the word	
	Number of phonemes in the word	
Phoneme position in the phrase	Position of phoneme from the beginning of the phrase	3
	Position of phoneme from the end of the phrase	
	Number of phonemes in the phrase	
Word position in the phrase	Position of the word (corresponding to required phoneme) from the beginning of the phrase	3
	Position of the word from the end of the phrase	
	Number of words in the phrase	
Context of phoneme	Present phoneme	3
	Previous phoneme	
	Successive phoneme	
Fujisaki model parameters	Phrase command amplitude	9
	Accent command amplitude ( $A_a$ ) at Present phoneme	
	Duration of the accent command at present phoneme	
	Accent command amplitude at Previous phoneme	
	Duration of the accent command at previous phoneme	
	Accent command amplitude at successive phoneme	
Pitch	Duration of the accent command at successive phoneme	2
	Base frequency of the utterance	
	Number of accent commands in the utterance	
	Pitch of the previous phoneme	
	Pitch of the successive phoneme	

For an example the utterance corresponding to the text “ಶ್ರೀ ಅವರ ಜೊತೆಗೆ ದುಡಿದ ಗೆಳೆಯರು ಪ್ರೊಫೆಸರ್ ನರಸಿಂಹಾಚಾರ್ ಕಸ್ತೂರಿ ರಂಗಾಚಾರ್ ಮುಂತಾದವರುಗಳು”, tabulation is prepared to depict the input to the neural network. Table 2, indicates part of that Table 3, indicates the codepoints of Kannada vowels along with its corresponding English transliteration. The details of codepoints and the corresponding transliteration for the consonants in Kannada is given in appendix. Out of 696 simple Kannada declarative utterances taken from Carnegie Mellon University’s Indic data base, in this work we have used 130 utterances to train the neural network with 70% training and 15% testing and 15% validation. The detailed discussion of performance of this network in prediction of F0 is discussed in next section by varying number of neurons in layer 2. Then we measure the performance of the proposed network in speech synthesis in comparison to Tilt and Cart model.

Table 2. Input and output attributes for the words “\” ಶ್ರೀ ಯವರ “\”

Pho neme	Phoneme position in the word			Phoneme position in the phrase			Word position in the phrase			Context of phoneme			Fujisaki Model Parameters										Pitch of previous and succeeding phoneme		Pitch of current phoneme
C}	1	3	3	1	78	78	1	10	10	3254	3200	3248	0.4	0	0	0	0	0.57	0.035	110	8	0	270	0	
9r	2	2	3	2	77	78	1	10	10	3248	3254	3208	0.4	0.57	0.035	0	0	0.57	0.185	110	8	0	327	270	
I:	3	1	3	3	76	78	1	10	10	3208	3248	3247	0.4	0.57	0.185	0.57	0.035	0.57	0.015	110	8	270	315	327	
j	1	6	6	4	75	78	2	9	10	3247	3208	3205	0.4	0.57	0.015	0.57	0.185	0.57	0.085	110	8	327	300	315	
a	2	5	6	5	74	78	2	9	10	3205	3247	3253	0.4	0.57	0.085	0.57	0.015	0	0	110	8	315	300	322	
v	3	4	6	6	73	78	2	9	10	3253	3205	3205	0.4	0	0	0.57	0.085	0.2	0.1	110	8	322	260	300	
a	4	3	6	7	72	78	2	9	10	3205	3253	3248	0.4	0.2	0.1	0	0	0	0	110	8	300	260	280	
9r	5	2	6	8	71	78	2	9	10	3248	3205	3205	0.4	0	0	0.2	0.02	0.26	0.04	110	8	280	270	260	
a	6	1	6	9	70	78	2	9	10	3205	3248	3228	0.4	0.26	0.08	0.2	0.02	0	0	110	8	260	265	270	

Table 3. Vowels and their code points with English transliteration

Kannada Grapheme	ಅ	ಆ	ಇ	ಈ	ಉ	ಊ	ಋ
Codepoint	3205	3206	3207	3208	3209	3210	3211
English utterance	A	A:	i	i:	u	u:	9r
Kannada Grapheme	ಎ	ಏ	ಐ	ಒ	ಓ	ಔ	ಅಂ
Codepoint	3214	3215	3216	3218	3219	3220	3202
English utterance	e	e:	aI	o	o:	aU	n

## 4. RESULTS AND DISCUSSION

### 4.1. Prediction of F0 by neural network model

The training of the neural network is carried to predict the pitch frequency of the phoneme. The performance of the network for the intended work is measured with different number of neurons in the hidden layer 1 (layer 2 in entire network). From the following regression graphs shown in Figure 4, representing correlation coefficient (R) for training, testing and validation. It is very clear that network is well performing when the network is having 5 neurons in the hidden layer 1. Comparative analysis with different number of neurons is indicated in Table 4.

Table 4. Performance analysis of proposed neural network with different neurons in hidden layer 1

Number of Neurons in hidden layer 1	Correlation Coefficient		
	Training	Validation	Testing
5	0.972	0.857	0.808
10	0.925	0.584	0.353
15	0.584	0.185	0.192
20	0.938	0.696	0.519
25	0.741	0.534	0.610
30	1	0.638	0.405

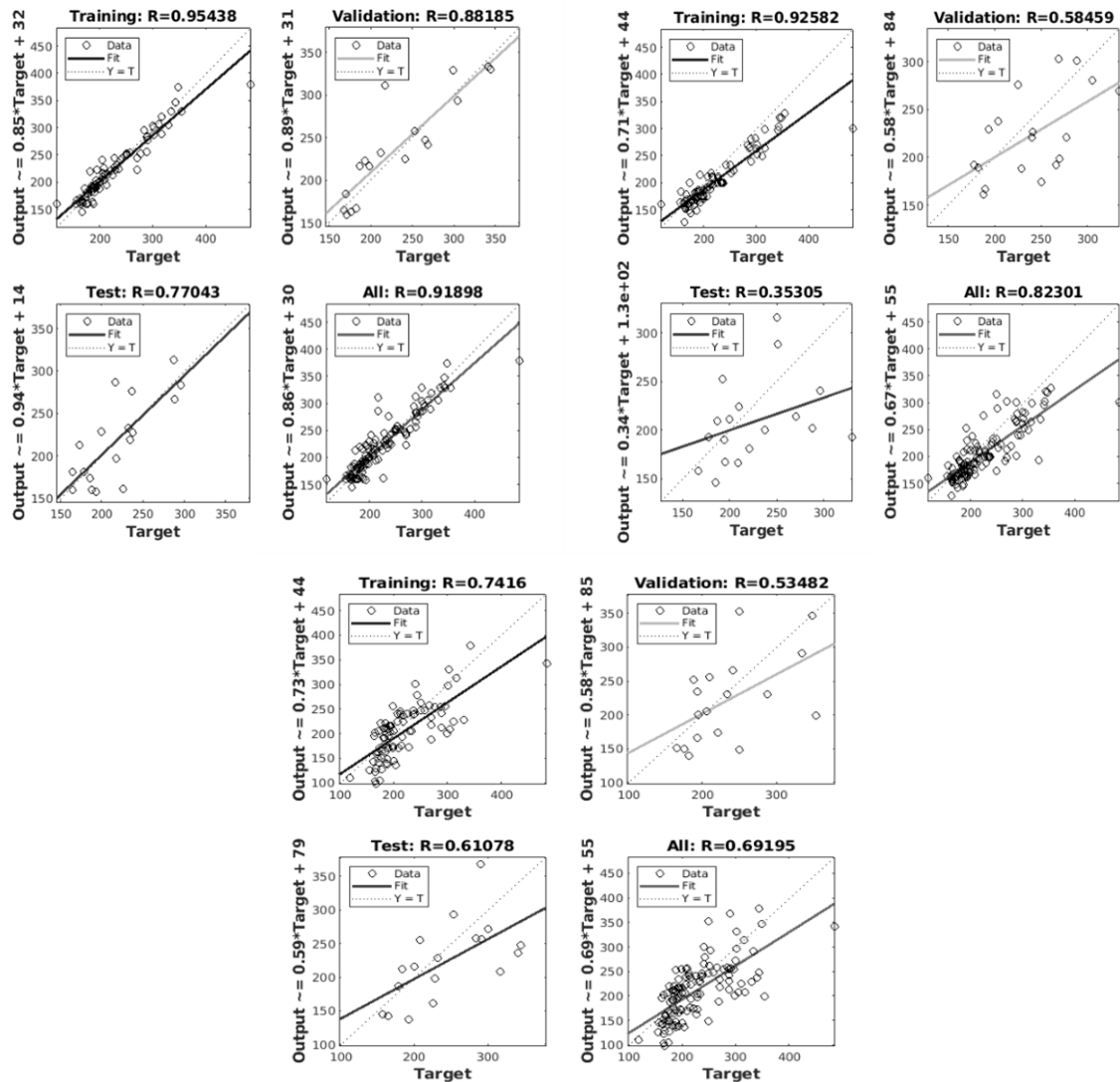
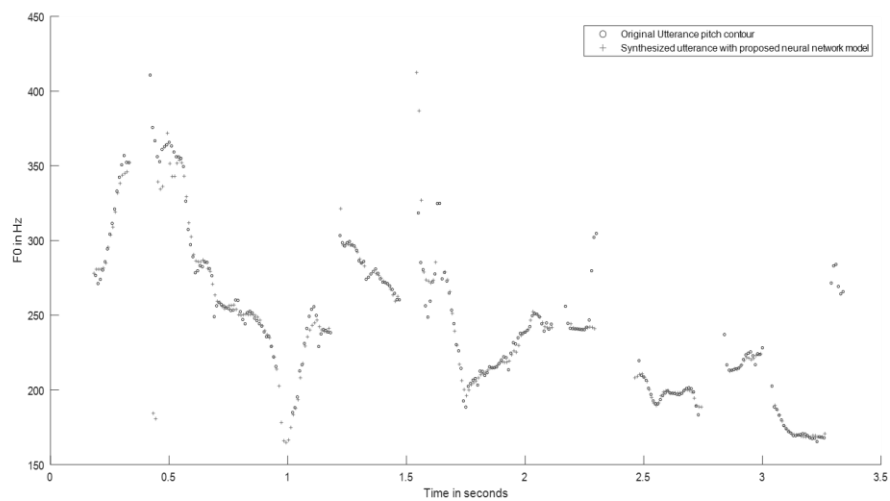


Figure 4. Regression plots of trained neural network with hidden neurons=5, 10 and 25

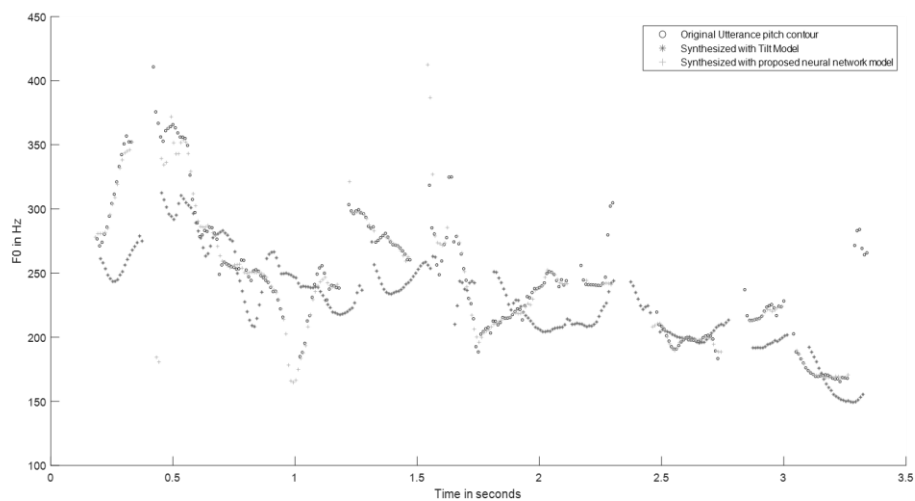
#### 4.2. Synthesis and MCD score analysis

Synthesis of simple Kannada declarative sentences are synthesized using festival framework [16]–[20] by considering three different prosodic models, namely Tilt [21], [22], classification and regression tree (CART) [23]–[25] and proposed neural network model. In this work we have done qualitative analysis. Qualitative analysis involves subjective analysis in which persons of different age group are asked to listen original and synthesized utterances and noted their opinions, which is indicated in Table 5, whereas another qualitative analysis involves plotting the F0 contours of original and synthesized utterances. From the observations of pitch contours of the synthesized utterances with Tilt model is having high variations in comparison to original utterance, whereas CART model developed based on Fujisaki parameters is matching very close with original utterance. This is also reflected in another qualitative analysis done using MCD score. It is very clear that the pitch contours of the synthesized speech with the proposed neural network model is highly matching with the pitch contours of the original utterance. The comparison of the F0 contours of the synthesized utterances using different models are shown in Figures 5(a)–(c). But the proposed model is lacking in naturalness and intelligibility though the F0 contour is almost following the original one. The main reason for poor performance of proposed neural network model is due to, the model is only able to predict pitch frequency of the phoneme but unable to predict duration of the phoneme, whereas CART model with Fujisaki parameters is very accurate in predicting F0 and duration both.

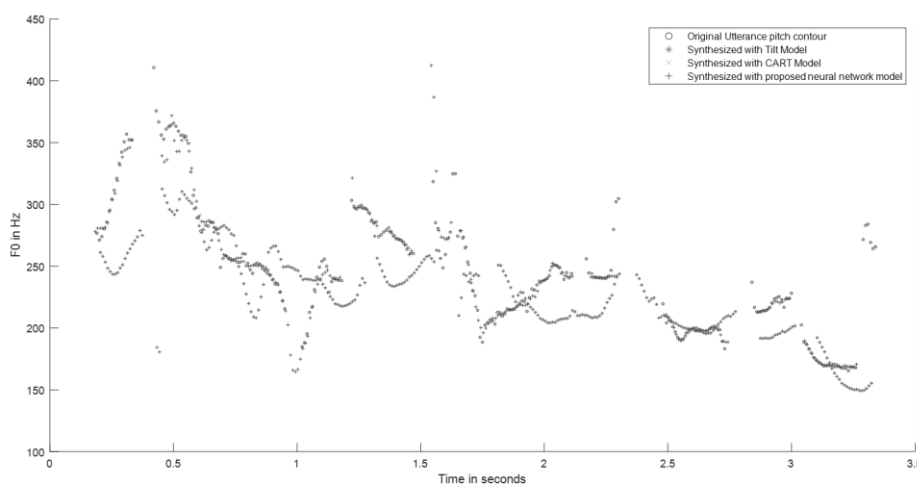




(a)



(b)



(c)

Figure 5. Comparison of pitch contour of original utterance and synthesized utterance, (a) with Tilt model, (b) CART model, and (c) proposed neural network model

Table 5. Subjective analysis of synthesized utterances

Person	Synthesized utterances														
	Tilt model					CART Model					neural network model				
	1	2	3	4	5	1	2	3	4	5	1	2	3	4	5
1	1	1	2	1	1	4	4	4	4	4	2	2	2	2	2
2	1	1	1	1	1	3	4	4	4	4	2	2	2	2	2
3	1	1	1	1	1	4	4	4	4	4	1	1	1	2	1
4	2	1	2	1	1	4	4	4	4	4	2	2	2	2	2
5	1	1	1	1	1	4	4	4	3	4	2	2	2	1	2
6	1	2	1	1	1	4	3	4	4	4	2	2	2	2	2
7	1	1	1	1	1	4	4	4	4	4	2	1	1	2	1
8	1	1	1	2	1	4	4	4	4	4	1	1	2	2	1
9	1	1	1	1	1	4	4	4	4	4	1	2	1	1	2
10	1	1	1	1	1	4	4	4	4	4	2	2	2	2	2

1. Poor, 2. Average, 3. Good, and 4. Very good

Mel cepstral distortion (MCD score): A vital entity that is very much necessary in deciding the quality of the speech which has been synthesized is the MCD Score. The mathematical formal that is commonly used to arrive at the MCD is as shown in:

$$MCD = \frac{10\sqrt{2}}{\ln 10} \sqrt{\sum_d \left( mc_{(d)}^{(t)} - mc_{(d)}^{(e)} \right)^2}$$

where,

$mc_{(d)}^{(t)}$  : Mel - Cepstral parameters of training utterance

$mc_{(d)}^{(e)}$  : Mel - Cepstral parameters of synthesized utterance

d : index of Mel - Cepstral parameters array

Since MCD is the yardstick to measure the proximity of the synthesized speech to the actual speech, it is normally considered that a MCD value between 4.5 to 6 dB is acceptable. In a work carried out earlier by us where synthesizing using the Tilt model was carried out, we were able to achieve MCD value between 3.52 and 5.02 dB. Despite the fact that value could be considered fairly good, we found that in the Tilt method the synthesized speech was rather unnatural and shaky. On working with the CART model where the Fujisaki parameters were used for synthesizing speech we achieved MCD values in the range of 1.62 dB and 2.43 dB while a value in the range of 3 to 4.5 dB was achieved applying the Neural Network technique. All these details are shown in Table 6 for different 10 utterances. There is a slight improvement seen in MCD score for synthesis using neural network model, but still this model lacks in generating quality synthesized speech though the F0 contour is very close to original utterances.

Table 6. Performance analysis of different models based on MCD score

Utterance	MCD Score of Synthesized Speech in dB			Utterance	MCD Score of Synthesized Speech in dB		
	Tilt Model	CART Model	NN Model		Tilt Model	CART Model	NN Model
1	3.52	1.68	3.21	1	4.65	1.89	3.19
2	4.16	2.10	3.48	2	4.80	2.37	4.02
3	3.87	1.78	3.07	3	4.21	1.65	3.63
4	4.32	2.43	3.62	4	5.02	2.29	3.94
5	4.34	1.62	3.87	5	4.56	1.67	3.54

## 5. CONCLUSION

From the performance analysis it is very clear that F0 contours of utterances can be predicted with high accuracy in the feedback neural network with 5 neurons in the hidden layer. But prediction of F0 contour alone is not sufficient to generate quality speech as it requires additional factors such as duration models. However neural network model is able to perform better than Tilt model. Naturalness is very high in speech synthesized using CART model built using Fujisaki parameters.




## REFERENCES

- [1] S. V. Chakrasali, K. Indira, S. B. Sharma, N. M. Srinivas, and S. S. Varun, "HMM based Kannada speech synthesis using festvox," *International Journal of Recent Technology and Engineering*, vol. 8, no. 3, pp. 2635–2639, Sep. 2019, doi: 10.35940/ijrte.C4934.098319.





- [2] H. Mixdorff and D. Mehnert, "Exploring the naturalness of several German high-quality-text-to-speech systems.," *Eurospeech*, 1999, Accessed: Feb. 17, 2022. [Online]. Available: [http://public.beuth-hochschule.de/~mixdorff/thesis/files/mixdorff\\_mehnert\\_eurosp1999.pdf](http://public.beuth-hochschule.de/~mixdorff/thesis/files/mixdorff_mehnert_eurosp1999.pdf)
- [3] H. Mixdorff and O. Jokisch, "Evaluating the quality of an integrated model of German prosody," *International Journal of Speech Technology*, vol. 6, no. 1, pp. 45–55, 2003, doi: 10.1023/A:1021099922328.
- [4] A. S. Madhukumar, S. Rajendran, and B. Yegnanarayana, "Intonation component of a text-to-speech system for hindi," *Computer Speech and Language*, vol. 7, no. 3, pp. 283–301, Jul. 1993, doi: 10.1006/csla.1993.1015.
- [5] T. B. Patel and H. A. Patil, "Analysis of natural and synthetic speech using Fujisaki model," in *ICASSP, IEEE International Conference on Acoustics, Speech and Signal Processing - Proceedings*, Mar. 2016, vol. 2016-May, pp. 5250–5254, doi: 10.1109/ICASSP.2016.7472679.
- [6] K. Hirose, *Speech Prosody in Speech Synthesis: Modeling and generation of prosody for high quality and flexible speech synthesis*, February. Springer Berlin Heidelberg, 2015.
- [7] H. Fujisaki and K. Hirose, "Analysis of voice fundamental frequency contours for declarative sentences of Japanese," *Journal of the Acoustical Society of Japan (E) (English translation of Nippon Onkyo Gakkaishi)*, vol. 5, no. 4, pp. 233–242, 1984, doi: 10.1250/ast.5.233.
- [8] S. Narusawa, N. Minematsu, K. Hirose, and H. Fujisaki, "Automatic extraction of model parameters from fundamental frequency contours of English utterances," *7th International Conference on Spoken Language Processing, ICSLP 2002*, pp. 1725–1728, 2002, Accessed: Feb. 17, 2022. [Online]. Available: <http://www.iscaspeech.org/archive>
- [9] H. Mixdorff, "A novel approach to the fully automatic extraction of Fujisaki model parameters," in *ICASSP, IEEE International Conference on Acoustics, Speech and Signal Processing-Proceedings*, 2000, vol. 3, pp. 1281–1284, doi: 10.1109/ICASSP.2000.861811.
- [10] H. Zen *et al.*, "The HMM-based speech synthesis system (HTS) Version 2.0," *6th ISCA Workshop on Speech Synthesis*.
- [11] S. Chakrasali, S. Y. N, and C. M. Patil, "Performance analysis of fujisaki intonation model in Kannada speech synthesis," *Turkish Journal of Physiotherapy and Rehabilitation*, vol. 32, no. 3, Accessed: Feb. 17, 2022. [Online]. Available: [www.turkjphysiotherrehabil.org](http://www.turkjphysiotherrehabil.org)
- [12] Z. Mnasri, F. Boukadida, and N. Ellouze, "F<sub>0</sub> contour parametric modeling using multivariate adaptive regression splines for arabic text-to-speech synthesis," in *Eighth International Multi-Conference on Systems, Signals & Devices*, Mar. 2011, pp. 1–6, doi: 10.1109/ssd.2011.5981479.
- [13] K. Sreenivasa Rao and B. Yegnanarayana, "Intonation modeling for Indian languages," *Computer Speech and Language*, vol. 23, no. 2, pp. 240–256, Apr. 2009, doi: 10.1016/j.csl.2008.06.005.
- [14] T. F. Quatieri, "Discrete-time speech signal processing: principles and practice," p. 816, 2001, Accessed: Feb. 17, 2022. [Online]. Available: <http://www.amazon.com/Discrete-Time-Speech-Signal-Processing-Principles/dp/013242942X>
- [15] D. O'Shaughnessy, *Speech Communications: Human and Machine*, 2nd Editio. University Press, 2004.
- [16] S. King, "An introduction to statistical parametric speech synthesis," *Sadhana - Academy Proceedings in Engineering Sciences*, vol. 36, no. 5, pp. 837–852, Oct. 2011, doi: 10.1007/s12046-011-0048-y.
- [17] H. Zen, H. Zen, H. Zen, M. J. F. Gales, Y. Nankaku, and K. Tokuda, "Product of experts for statistical parametric speech synthesis," *IEEE Transactions on Audio, Speech and Language Processing*, vol. 20, no. 3, pp. 794–805, Mar. 2012, doi: 10.1109/TASL.2011.2165280.
- [18] T. Koriyama, T. Nose, and T. Kobayashi, "Statistical parametric speech synthesis based on gaussian process regression," *IEEE Journal on Selected Topics in Signal Processing*, vol. 8, no. 2, pp. 173–183, Apr. 2014, doi: 10.1109/ISTSP.2013.2283461.
- [19] J. Tao, K. Hirose, K. Tokuda, A. W. Black, and S. King, "Introduction to the issue on statistical parametric speech synthesis," *IEEE Journal on Selected Topics in Signal Processing*, vol. 8, no. 2, pp. 170–172, Apr. 2014, doi: 10.1109/ISTSP.2014.2309416.
- [20] K. Tokuda, Y. Nankaku, T. Toda, H. Zen, J. Yamagishi, and K. Oura, "Speech synthesis based on hidden Markov models," *Proceedings of the IEEE*, vol. 101, no. 5, pp. 1234–1252, May 2013, doi: 10.1109/JPROC.2013.2251852.
- [21] J. Yamagishi, "An introduction to HMM-based speech synthesis," *October*, no. October, 2006, Accessed: Feb. 17, 2022. [Online]. Available: <https://wiki.inf.ed.ac.uk/twiki/pub/CSTR/TrajectoryModelling/HTS-Introduction.pdf>
- [22] H. G. Assistant, "Acoustic phonetic characteristics of Kannada language," *International Journal of Computer Science Issues*, vol. 8, no. 6, pp. 332–339, 2011, Accessed: Feb. 17, 2022. [Online]. Available: [www.IJCSI.org](http://www.IJCSI.org)
- [23] P. Bhaskararao, "Salient phonetic features of Indian languages in speech technology," *Sadhana - Academy Proceedings in Engineering Sciences*, vol. 36, no. 5, pp. 587–599, Oct. 2011, doi: 10.1007/s12046-011-0039-z.
- [24] Z. H. Ling *et al.*, "Deep learning for acoustic modeling in parametric speech generation: a systematic review of existing techniques and future trends," *IEEE Signal Processing Magazine*, vol. 32, no. 3, pp. 35–52, May 2015, doi: 10.1109/MSP.2014.2359987.
- [25] S. Imai, K. Sumita, and C. Furuichi, "Mel log spectrum approximation (MLSA) filter for speech synthesis," *Electronics and Communications in Japan (Part I: Communications)*, vol. 66, no. 2, pp. 10–18, 1983, doi: 10.1002/ecja.4400660203.

## BIOGRAPHIES OF AUTHORS







**Sadashiva Veerappa Chakrasali**    is currently working as an assistant professor in E & C department, M S Ramaiah Institute of Technology, Bangalore. His research interests are statistical signal processing and communication. He has completed BE and M.Tech from Kuvempu university and VTU Belgaum in the year 2000 and 2004 respectively. He can be contacted at email: [sadashiva.c@msrit.edu](mailto:sadashiva.c@msrit.edu).







**Dr. Krishnappa Indira**     is currently working as a Professor in E & C Dept., M S Ramaiah Institute of Technology, Bangalore. Her research interests are in the field of Image and speech processing. She has published several technical papers in peer reviewed journals. She has completed B. E and M.E from Bangalore University in the year 1988 and 1992 respectively. She has done her PhD from VTU, Belagavi in the year 2012. She is a senior member IEEE. Currently she is working on Machine Learning, Neural Networks, Pattern recognition and speech processing. She can be contacted at email: [indira@msrit.edu](mailto:indira@msrit.edu).



**Dr. Sunitha Yariyur Narasimhaiah**     is currently working as an assistant professor in E & C Department, SJB Institute of Technology, Bangalore. Her research interests are Image processing and communication. She has completed B.E. from Mysore University in the year 2000, MTech and PhD from VTU Belgaum in the year 2003 and 2021, respectively. She can be contacted at email: [sunithayn@sjbit.edu.in](mailto:sunithayn@sjbit.edu.in).



**Shadaksharaiah Chandraiah**     is working as an assistant Professor in Electrical and Electronics Engineering department of BIET, Davangere. Prior to this he has worked in Information science department of the same institute. He is a well known programmer in LINUX and C++. His current research are in the area of fault detections in computer networking using Artificial Intelligence techniques. He has done his M. Tech in Computer science and engineering from PDA college of Engineering, Gulbarga in the year 2004. He can be contacted at email: [cshadaksharaiah@gmail.com](mailto:cshadaksharaiah@gmail.com).



## Design of Decimation Filters for Wireless Local Area Network Applications

**Kantharaj S P\***

BIET, Davangere, Karnataka,  
INDIA

**G. S. Sunitha**

BIET, Davangere, Karnataka,  
INDIA

**G. H. Leela**

BIET, Davangere, Karnataka,  
INDIA

**S. O. Nirmala**

BIET, Davangere, Karnataka,  
INDIA

### Article Info

#### Article history:

Received: January 22, 2022

Revised: April 25, 2022

Accepted: June 5, 2022

#### Keywords:

Sampling Rate Conversion;  
WLAN-b; FIR Filter; Decimator.

### Abstract

Multirate signal processing is critical to realizing the digital frequency converter in WLAN technologies. In this paper, we focus on designing and analyzing the different structures of decimators that support WLAN-b applications to reduce the frequency by 12 for an IEEE. The structure modeling of the decimator used Simulink. Implementing a single-stage decimator required a higher-order filter, extra storage space, and a long simulation time. Results showed that the necessary storage elements for 2-stage design are 55% and for 3-stage design is 65% of single stage. For 133 MHz WLAN-b application, a two-stage decimator is proved to be efficient.

**To cite this article:** K. S P, and G. S. Sunitha, G. H. Leela, S. O. Nirmala "Design of Decimation Filters for Wireless Local Area Network Applications," *Int. J. Electron. Commun. Syst.*, vol. 2, no. 1, pp. 9-13, 2022.

## INTRODUCTION

In many signal processing and communication applications, it is necessary to convert the audio signal at a given frequency to some other signals with different sampling rates. In digital audio, three different sampling rates are 32 kHz for broadcasting, 44.1 kHz for CD, and 48 kHz for digital audiotape. A wireless local area network (WLAN) uses a wireless distribution technique to two or more devices. It also allows users to shift around within a geographical local coverage area, connect to the network, and connect to the wider internet [1], [2].

Sample Rate Conversion (SRC) is a process by which the audio sample rate gets changed without affecting the audio pitch [3]. It is comfortable to design and analyze the implementation of transmultiplexer by multirate DSP systems [4]. The systems which operate at different sampling rates throughout the processing are called multirate systems. In multirate systems, the sampling frequency changes during signal processing [5]. Multirate systems have gained popularity since the early

1980s, and they are commonly used for audio and video processing, communications systems, and transform analysis, to name a few. Multirate systems play a central role in many areas of signal processing [6]. The primary operations of multirate systems are Decimation and Interpolation. Decimation and interpolation are the two basic building blocks of multirate digital signal processing systems [7]. Decimation reduces the sampling rate, whereas interpolation is used to increase the sampling rate [8].

In practice, decimation usually implies low pass-filtering of a signal, then throwing away some of its samples [9]. The most immediate reason to decimate is simply to reduce the sampling rate at the output of a system so the system operating at a lower sampling rate can input the signal [10]. The main task of a decimation filter is to remove the quantization noise away from the band of interest and avoid aliasing of high-frequency components down to the low-frequency region or within the signal bandwidth [11].

#### Corresponding author:

Kantharaj S P, Bapuji Institute of Engineering and Technology, Davanagere-577004, India. ✉ [kantharajsp@gmail.com](mailto:kantharajsp@gmail.com)

© 2021 The Author(s). **Open Access.** This article is under the CC BY SA license (<https://creativecommons.org/licenses/by-sa/4.0/>)

Khalid et al. presented the decimation filter simulated using Matlab, and its complete architecture was realized using DSP Blockset and Simulink. The filter was implemented using Mentor Graphic ModelSim and Calibre Tool in FPGA technology. The resulting architecture is hardware efficient and consumes less power than conventional decimation filters [12]. Jing showed that Compared with a conventional digital filter, the more efficient filter has a great advantage in the real-time and the use of hardware resources, which can improve the real-time performance of the signal processing and greatly reduce the rate of the back-end digital signal processing [13]. Kim also said that the complexity of the circuit is reduced by applying the required down-sampling rate twice instead of once. In addition, CIC decimation filters without a multiplier are used as the decimation filter of the first stage. The second stage is implemented using a CIC filter and a down sampler with an anti-aliasing filter, respectively [14]

Multirate signal processing is the key technology to realizing the digital frequency converter in WLAN technologies. For a wireless local area network, multirate systems perform a processing task with improved efficiency and offer higher performance at a lower cost and reduced complexity [15]. In this paper, we focus on designing and analyzing the different structures of decimators that support WLAN-b applications to reduce the frequency by 12 for an IEEE. The design is subjected to retaining the passband aliasing in the desired bounds.

## METHOD

### *Sampling Rate Conversion*

The sampling rate change may be achieved in one fell swoop or multi fell swoops. Sampling rate conversion by integer factors in a single stage is useful but can be too restrictive in some practical applications [16]. The structure modeling of the decimator used Simulink. Implementing a single-stage decimator requires a higher-order filter, extra storage space, and a long simulation time. The multistage design approach has advantages over the single-stage sampling rate converters. In a multistage structure, the conversion factor is translated into a product of integer values such that conversion can be carried out in

more than one stage. But no systematic approach is formulated in the literature to determine the optimal number of stages and factors to minimize storage space and computation time. The trial-and-error method may mostly be applied for such designs [17], [18].

For sampling rate converters, additional efficiency is achieved by cascading two or more stages design. Depending upon the application and the required response, a suitable filter and design method can be adopted for frequency conversion in the case of WLAN. This paper uses symmetric Linear FIR filters designed by the optimal method for sampling rate converters because of their advantages [19]. In WLAN applications, frequency converter system performance can be enhanced by simplifying arithmetic operations determined by the number of multiplications per sample and the number of total storage elements [20].

## RESULTS AND DISCUSSION

### *Structure Modelling of Decimator Using Simulink*

In this paper, we focus on designing and analyzing the different structures of decimators that support WLAN-b applications. For interoperating between two WLAN-b's, consider designing the decimator to down-convert 132 MHz frequency input signal to 11 MHz as specified in table 1.

**Table 1.** Design Specification for WLAN Application.

Specifications	Values
Input sampling frequency	132 MHz
Output frequency	11 MHz
Pass band frequency	3 MHz
Stop band frequency	5 MHz
Frequency deviation	0.015
Pass band attenuation	0.5 db
Stop band attenuation	44 db

### *Single-stage implementation*

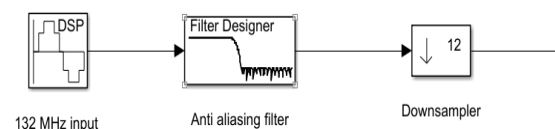


**Figure 1.** Block Modelling of Single Stage Decimator.



The sampling rate reduction required for WLAN is 12, which is realized with a single stage and multistage decimator structure. To compare performances, the decimator is designed using the above specifications as a single stage and multistage structure. We have implemented the same using MatLab Simulink. These structures' performance metrics like MPS and TSR are evaluated and compared. In one fell swoop design, the decimator consists of an anti-aliasing filter followed by a 12-fold down sampler, as shown in figure 1. Decimator specifications are listed in table 2.

**Table 2.** Single Stage Decimator Specifications.

Specifications	Values
Input sampling frequency	132 MHz
Decimation Factor	12
Pass band frequency	3 MHz
Stop band frequency	5 MHz
Frequency deviation	0.015
Pass band attenuation	0.5 db
Stop band attenuation	44 db
Order	101
Multiplications (in terms of 106)	1100
Storage Elements	101

#### Two-stage decimator implementation

Figure 2 shows a two-stage structure for the down sampling. In the two-stage decimator model, sampling rate reduction factor 12 is considered  $M1 \times M2$  (possibly as  $4 \times 3$  and  $3 \times 4$ ). The design aspects and performance measures of two-stage decimators are listed in table 3.

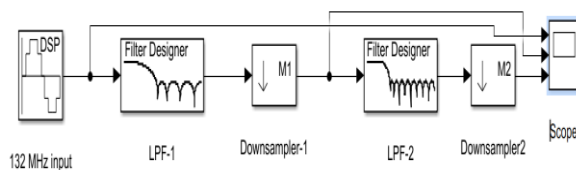


**Figure 2.** Block Modelling of Two Stage Decimator.

#### Three-stage decimator implementation

In 3-stage approach, the decimation factor 12 is factorized as  $M1 \times M2 \times M3$  (possibly as  $4 \times 2 \times 2$ ,  $2 \times 4 \times 2$  and  $2 \times 2 \times 4$ ). Figure 4 shows the three-stage structures for the rate conversion. Table 3 shows the performance measures of three-stage decimators for converting 132MHz signal to 11MHz signal. Decimator design computational efficiency can be analyzed based on the number of multiplications per input sample and the number of delay elements required to perform the sampling rate conversion of WLAN-b.

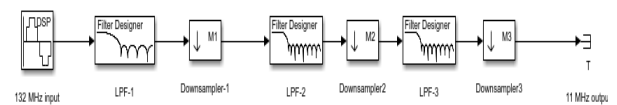


**Figure 3.** Block Modelling of Three Stage Decimator.

Tables 2, 3, and 4 show the multiplications and number of storage elements (number of delay elements which are the same as storage elements) required. We believe that reducing the number of filters reduces the complexity involved in designing the decimators. Results show that the required storage elements for 2-stage design are 55% and for 3-stage design is 65% of single stage. For multistage decimators in WLAN-b, the better approach to finding the optimal number of stages and set of integers is apropos computational complexity and total storage requirements. To the specified WLAN-b application, two stages decimator is appeared to be the most efficient in the dimension of the number of multiplications and storage elements. More precisely, to achieve better performance during the multistage decimator design, it is good to choose the largest integer of all the possible factors of M as M1.

**Table 3.** Two Stage Decimator Specifications

Two stage decimator				
Parameters	Factors: M1=4, M2=3		Factors: M1=3, M2=4	
Input frequency	132 MHz	33 MHz	132 MHz	44 MHz
Pass band frequency	3 MHz	3 MHz	3 MHz	3 MHz
Stop band frequency	27.5 MHz	5.5 MHz	38.5 MHz	5.5 MHz
Frequency deviation	0.18	0.075	0.27	0.045
Pass band attenuation	0.006	0.006	0.006	0.006
Stop band attenuation	0.05	0.05	0.05	0.05
Order	11	33	7	43
Multiplications (in terms of 10 <sup>6</sup> )	583		737	
Storage Elements	44		50	

**Table 4.** Three Stage Decimator Specifications

Parameters	Factors: M1=3, M2=2, M3=2			Factors: M1=2, M2=3, M3=2			Factors: M1=2, M2=2, M3=3		
Input frequency	132 MHz	44 MHz	22 MHz	132 MHz	66 MHz	22 MHz	132 MHz	66 MHz	33 MHz
Pass band frequency	3 MHz	3 MHz	3 MHz	3 MHz	3 MHz	3 MHz	3 MHz	3 MHz	3 MHz
Stop band frequency	38.5 MHz	16.5 MHz	5.5 MHz	60.5 MHz	16.5 MHz	5.5 MHz	60.5 MHz	27.5 MHz	5.5 MHz
Frequency deviation	0.26	0.3	0.11	0.43	0.2	0.11	0.43	0.35	0.07
Pass band attenuation	0.016	0.016	0.016	0.016	0.016	0.016	0.016	0.016	0.016
Stop band attenuation	0.006	0.006	0.006	0.006	0.006	0.006	0.006	0.006	0.006
Order	7	6	23	7	9	21	5	5	25
Multiplications (in terms of $10^6$ )		693			891			770	
Storage Elements		36			37			35	

### CONCLUSION

Symmetric linear phase FIR filters designed by the optimal method are used to design the decimator. Results show the multistage designs yield significant reductions in computation speed and storage requirements compared with single-stage designs. For 133 MHz WLAN-b application, a two-stage decimator is proved to be efficient.

### REFERENCES

- [1] V. Jayaprakasan and K. Pavitra, "Comparative Analysis of Interpolation/Decimation FIR Filter Structures for WLAN-b and WLAN-g Applications," *Int. J. Innov. Res. Sci. Technol.*, vol. 2, no. 2, 2016.
- [2] R. E. Crochiere and L. R. Rabiner, "Interpolation and Decimation of Digital Signals-A Tutorial Review," *Proc. IEEE*, vol. 69, no. 3, pp. 300-331, 1981, doi: 10.1109/PROC.1981.11969.
- [3] M. Sabraj, "Spectral Analysis of Sample Rate Converter," *Sign. Processing: An Intern. J. (SPIJ)*, vol. 4, no. 4, pp. 219-227, 2014.
- [4] Arunkumar and K. Ganesh, "Performance and Analysis of Transmultiplexers," *J. Circuits, Syst. Comput.*, vol. 28, no. 1, pp. 1-8, 2019, doi: 10.1142/S0218126619500099.
- [5] S. A. Kumar and P. G. Kumar, "Elegant and Practical Method of FIR Decimation Using Comb Filters in the Field of Digital Signal Processing," *Circuits Syst.*, vol. 7, no. 9, pp. 2476-2488, 2016, doi: 10.4236/cs.2016.79214.
- [6] V. M. Student, "Sub Band Coding of Speech Signal by using Multi-Rate Signal Processing," vol. 2, no. 9, pp. 45-49, 2013, [Online]. Available: [www.ijert.org](http://www.ijert.org)
- [7] N. B. Bahadure, "Multirate Digital Signal Processing System for Digital Communication Multirate Digital Signal Processing System for Digital Communication," no. 1, pp. 1-2, 2016.
- [8] S. Xu, Y. Chai, Y. Hu, L. Huang, and L. Feng, "The analysis of decimation and interpolation in the linear canonical transform domain," *Springerplus*, vol. 5, no. 1, 2016, doi: 10.1186/s40064-016-3479-4.
- [9] S. Sarswat and M. Kaur, "Decimation Filter Design Optimization of ADC for ECG Processing," *IOSR J. Electr. Electron. Eng.*, vol. 13, no. 2, pp. 63-66, 2018, doi: 10.9790/1676-1302036366.
- [10] P. E. Howland, D. Maksimiuk, and G. Reitsma, "FM radio based bistatic radar," *IEE Proc. Radar, Sonar Navig.*, vol. 152, no. 3, pp. 107-115, 2005, doi: 10.1049/ip-rsn:20045077.
- [11] G. G. Moon and S. N. Joshi, "Design Approach for Decimation Filter for ADC Application," *Int. J. Eng. Trends Technol.*, vol. 10, no. 12, pp. 597-600, 2014, doi: 10.14445/22315381/ijett-v10p320.
- [12] K. H. Abed and S. Colaco, "Design and Implementation of a Decimation Filter For High Performance Audio Applications," pp. 812-815, 2007.

- [13] Q. Jing, Y. Li, and J. Tong, "Performance analysis of multi-rate signal processing digital filters on FPGA," *Eurasip J. Wirel. Commun. Netw.*, vol. 2019, no. 1, 2019, doi: 10.1186/s13638-019-1349-9.
- [14] S. Kim, J. Oh, and D. Hong, "Design of Low Area Decimation Filters Using CIC Filters," vol. 20, no. 3, pp. 71–76, 2021.
- [15] A. V. Babu and L. Jacob, "Fairness analysis of IEEE 802.11 multirate wireless LANs," *IEEE Trans. Veh. Technol.*, vol. 56, no. 5, pp. 3073–3088, 2007, doi: 10.1109/TVT.2007.898397.
- [16] J. G. Proakis, *Digital Signal Processing, 4th Edition*, 4th ed. Massachusetts: Massachusetts Institute of Technology, Lincoln Laboratory, 2007.
- [17] F. Francesconi, G. Lazzari, V. Liberali, F. Maloberti, and G. Torelli, "A novel interpolator architecture for  $\Sigma\Delta$  DACs," no. March, pp. 249–253, 2002, doi: 10.1109/edac.1993.386468.
- [18] G. S. Gawande, Khanchandani, and Marode, "Performance analysis of FIR digital filter design techniques," *Int. J. Comput. Corp. Res.*, vol. 2, no. 1, 2012.
- [19] G. S. Gawande, B. Pawar, and Khanchandani, "Performance Evaluation of Efficient Structure for Fir Decimation Filters Using Polyphase Decomposition Technique," *Inter. J. Electron. Commun. Eng. Technol. (IJCET)*, vol. 6, no. 5, pp. 1–8, 2015.
- [20] M. P. Chaudhari and M. T. Pce, "The Fir Filter Design and Analysis and Code Generation Using HDLCODER for Area and Power Efficient FPGA Implementation," *Int. J. Emerg. Technol. Eng. Res.*, vol. 4, no. 7, pp. 99–102, 2016.

# Video quality assessment using optimization algorithms

Ganesh K.<sup>1</sup>, Chandrashekhar M. Patil<sup>2</sup>

<sup>1</sup>Department of Electronics & Communication Engineering, BIET, VTU, India

<sup>2</sup>Department of Electronics & Communication Engineering, VVCE, VTU, India

**Abstract.** Video quality assessment has seen more importance due to vast data entering the internet and multimedia communication network. This necessitates to predict the human observer's opinion for the video instead of perceptual quality estimation by human individuals. Two methods exist in video quality assessment based on involvement of human observer – subjective and objective methods. Subjective estimation of quality of video is based on rating of video quality perceived by human individuals and objective estimation is based on prediction of video quality using mathematical models which is well correlated with human observer quality scores. Objective video quality assessment research is gaining momentum because of amount of multimedia data entering into different media. Machine learning algorithms are making it easier to predict the quality of video using objective methods. Features of machine learning model are different individual visual metrics. In this paper, complete reference objective video quality assessment done with optimization algorithm applied for feature selection to predict video quality. In this paper, optimization algorithms-based feature selection is performed on LIVE and CSIQ Full Reference Video Database. Predominant features are selected to model video quality assessment. Regression is used to build the model. The results show the improvement in classification accuracy with the proposed method.

*Keywords:* Optimization, Feature selection, objective video quality metric, Regression, Machine learning models, Quality assessment

## 1. INTRODUCTION

Due to the advancement in the digital technologies, visual quality of digital media awareness has increased. Quality of the video is affected during the acquisition, transmission, compression and editing process of the video. Hence there is a need for video quality evaluation. To evaluate the visual quality qualitatively, human observers need to be shown both reference and test videos and asked to rate on a scale. Mean of these opinion scores of different individuals is the quality mark of the test video. But, with the voluminous data entering to internet and communication system, qualitative assessment poses a challenge. So, objective quality assessment is the way

ahead. Objective quality of assessment aims to predict the quality of video without a human visual assessment. Objective video quality metrics rely on mathematical models to predict the quality of the video.

Video Quality Assessment (VQA) is a major research area which aims to design algorithms and to evaluate objective scores well correlated with subjective scores of the human visual system. Image quality assessment metrics also applied on frames of video for the video quality assessment with pooled temporal. Image and video quality analysis plays an vital role in the image and video processing applications like enhancement, compression, reconstruction etc.

Countless objective video quality metrics proposed in the past few decade. The challenge of video quality prediction lies in choosing right quality metric for the application. A single quality metric will not be sufficient to quantify the video. So, more than one quality metrics have to be preferred. Since, more and more objective video quality metrics are being proposed, it becomes difficult to include all the quality metrics in the model of prediction. So, best performing quality metrics have to be selected among the set of quality metrics considered. This process is also susceptible for errors since there are different categories of quality metrics like pixel based, information based, and similarity based etc. as well as single quality metric quantification may give false narrative of being a good quality metric than the set of quality indicators. In our work, we have tried to select best performing quality metrics for predictive model using optimization-based feature selection.

In our model, we have considered LIVE and CSIQ database. LIVE database is given by Laboratory of the Image and Video Engineering, University of 'Texas', Austin. CSIQ database is provided by 'Laboratory of Computational and Subjective Image Quality', Shizuoka University. These databases will help for the validation of objective video quality assessment algorithms.

## CSIQ VIDEO DATABASE

The CSIQ video database[1] consists of twelve (12) high-quality reference videos and two hundred and sixteen (216) distorted videos from six (6) different types of distortion. SAMVIQ procedure was used to collect subjective ratings of quality during the experiment.

Videos which are in CSIQ database will be in YUV420 format having resolution with 832x480, duration of 10 seconds and has the frame rates of 24,25,30,50 and 60fps. For each reference video in database, distortion videos have six types of distortions at three levels. Compression and transmission-

based distortion types are used to generate sample videos.

## LIVE DATABASE

The LIVE Video Database[2][3] consists of ten(10) reference videos in YUV format. Sample videos in LIVE database are created using 'MPEG2' compression, 'H.264' compression, simulated transmission of 'H.264' compressed bit streams through the error prone IP network and the wireless networks. For each of the reference video, 15 distorted test videos are created. Hence, it has 150 distorted videos. 38 human subjects have assessed distorted videos in single stimulus mode with hidden reference removal. The mean and difference of Mean Opinion Score (DMOS) obtained from subjective assessment.

Machine learning (ML) and deep learning (DL) are playing an important role in predictive video quality assessment. Machine learning will be used for building model of quality video assessment for predicting the video quality quantitatively. In our approach, we have done regression based.

## 2. LITERATURE SURVEY

In this session, we discuss about the quality metrics considered for machine learning model and optimization methods used for feature selection.

### 2.1. QUALITY METRICS

Various quality measures have been proposed based on availability of reference image. There are three (3) types of metrics-based availability of reference image. They are (FR) Full Reference, (NR) No Reference and (RR) Reduced Reference quality metrics. In our study, we have considered 16 FR video quality metrics.

SSIM (Structural Similarity Index Measure) [4] is a top-down approach for functionality of the overall (HVS) Human Visual System. Overall similarity of metric  $S(x, y)$  has 3 components: local luminance  $l(x, y)$ , local contrast  $c(x, y)$  and structures  $(x, y)$  comparison between the original and the distorted images.

FSIM (Feature Similarity Index Measure) [5] points the features and measures the similarities between the two images. In this metric, (PC) Phase Congruency and (GM) Gradient Magnitude are taken for evaluation.

CWSSIM (Complex Wavelet Structural Similarity Index Measure) is syntactic similarity metric in the complex wavelet domain [6]

GMSD (Gradient Magnitude Similarity Deviation) uses the gradient magnitude similarity of digital images to assess the image quality [7]

DSS (DCT Sub-band Similarity) DCT (Discrete Cosine transform) is linear transformation used for quality analysis [8]

SVD (Singular Value Decomposition) predicts the quality, based on the singular value decomposition. SVD will be applied on each 8x8 block of reference and test image. Differences of SVD's in reference and sample frames weighted by the edge-strength in every block, are used [9]

QILV (Quality Index based on Local Variance) is based on the consideration that variance distribution corresponds to high structural information. [10]

CORR2D (2D Correlation) is used to analyze how similar (or dissimilar) two spectral signals change. The correlation analysis describes in a quantitative manner how similar these two signals behave [11]

NCC (Normalized Cross Correlation) is the measure of finding similarity between two set of images. In image processing applications where the brightness of the image might vary due to lighting and exposure conditions, the images will be first bring into normalized and used in finding the incidences of a pattern or an objects in the image [12].

PSNR (Peak Signal - Noise Ratio) [13] refer to the measure of logarithmic representation of MSE (Mean Square Error). It is used in earlier video quality research because of its simplicity and fast calculation. But, even additive noise will give higher PSNR suggesting of higher video quality. So, it is ignorant of spatial relationship and structure in the image.

MSE [14] points to the mean of squared error between the reference and sample frames of the video. It represents the simple pixel to pixel difference between reference and test frames of the video.

SSIM (Structural Similarity Index Measure) [4] has 3 comparisons namely luminance, contrast and structure and is one of the major metrics in the image and video quality assessment. Variants of SSIMs do exist.

Multi Scale - SSIM [15] is calculated on different scales of image. In our case, 5 scales are considered.

3SSIM - Three Component Structural Similarity [16] is using 'edges', 'textures' and 'smooth regions' of images and evaluates the metric value using weighted average of the SSIM metric for the said regions. Human visual system is the sensitive to texture and edge regions than smooth regions.

Delta - It represents the difference of mean brightness of distorted image and mean original brightness

DCT based VQM [17] - This Video Quality Metric (VQM) is based on Discrete Cosine Transform (DCT) for predicting human rank for the test video. It involves color transformation, DCT transformation of blocks 8x8, local contrast values are obtained from DCT coefficients, local contrast values are converted to noticeable difference and finally, weights are assigned for pooling of mean and maximum distortions.

Mean Sum of Absolute Differences (MSAD) - This metric depends only on difference of original and distorted, it is absolute of difference and will show real value of the difference between reference and test image. Value of zero indicates completely equivalent images.

### 2.2 OPTIMIZATION METHODS

Different optimization techniques and algorithms are proposed in the literature. Here, we list the optimization algorithms we have used for our implementation.

ASO (Atom search optimization) [18], is developed to address a diverse of optimization of the problems. this mathematically models and mimics the atomic motion model is its character, where it interact through interaction forces resulting from the Lennard-Jones potential and constraint forces resulting from the bond length potential.

GNDO (Generalized Normal Distribution Optimization) [19] introduces a generalization of the normal distribution also provide a comprehensive treatment of its mathematical properties.

EO (Equilibrium Optimizer) [20] in this, each particle is the solution with its concentration (position) acts as a search pool. The search pool randomly updates their concentration with respect to best-so-far solutions, namely equilibrium candidates, to finally reach to the equilibrium state i.e. optimal result. A well-defined "generation rate" term is proved to invigorate EO's ability in exploration, exploitation, and local minima avoidance.

MRFO (Manta Ray Foraging Optimization) [21] is outcome from intelligent behavior of the manta rays. This optimization mimics chain foraging, cyclone foraging and somersault foraging strategies of the manta rays for efficient optimization.

SMA (Slime Mould Algorithm Optimization) [22] is inspired on the oscillation mode of the slime mould in nature. Adaptive weights are used in this mathematical model. This optimization can mimic the process of positive and negative response of the propagation wave of slime mould to find short path.

ABC (Traditional Artificial Bee Colony Optimization) [23] is an optimization algorithm grounded on the intelligent geste of the honey freak mass.

Traditional Ant Colony Optimization [24] is inspired from ant colony. It is a computational method based on probabilistic technique to find optimum path through graphs. Artificial ants represent methods inspired by the real ant's behavior.

TPS (Traditional Particle Swarm Optimization) [25] is a computational method that will optimizes a problem by iteratively trying to improve the candidate problem solution with respect to a given measure of the quality. It solves a problem by having several seeker results, then dubbed patches, and moving these patches around in the hunt-space according to simple fine formulae over the particle's position and velocity.

### 2.3. AKAIKE INFORMATION CRITERION (AIC)

For a set of data provided, estimation of prediction error and relative quality of statistical models can be accomplished with AIC. It is based on information theory. AIC can be used for model selection.

## 3. METHODOLOGY

Proposed methodology is shown in Figure 1. In our method, raw YUV420 videos of LIVE and CSIQ datasets are considered.

YUV method says, 'Y' refers to the brightness, or 'luma' value, and 'UV' refers to the color, or 'chroma' values. Since we haven't considered the color in our quality analysis, we are accessing only the luminance component of the video. Y part of reference frame of reference videotape of dataset and Y part of distorted video (test videotape) frame are considered for objective video tape quality scores like SSIM, CWSSIM etc. We have considered first 100 frames of these datasets for our analysis. Hence, 100 quality scores for each quality metric are obtained. Pooling of these 100 quality scores will give a quality metric value for the particular dataset video.

### 3.1. FILTER FEATURE SELECTION METHOD

In this, statistical measures applied to assign a point to each feature. Ranking of the features by point is done and features are retained nor removed from the dataset. Many exemplifications of sludge point selection styles are chi-square test, information gain and correlation measure.

### 3.2. WRAPPER FEATURE SELECTION METHOD

Wrapper methods aim to search and select the set of features among all the features. Here, combinations of different features are made, evaluated, and compared to another combinations. Accuracy of the predictive model is used in assign a score to combination of the features and can be used to evaluate a combination of features.

The search process to find the subset of features may have best fit search, random hill climbing, heuristics like forward and backward passes or metaheuristics like optimization algorithms.

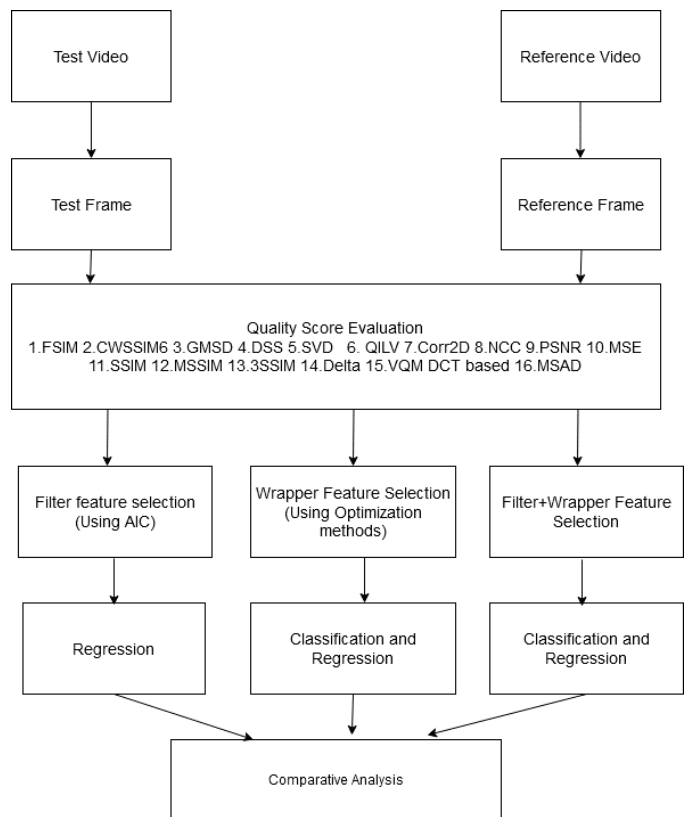


Figure 1: Methodology

### 3.3. EMBEDDED METHOD

In this method, feature selection process is embedded in the learning or model building phase. Regularization methods like LASSO, ridge regression, elastic net are examples for embedded methods.

While filter methods measure the relevance of the features, wrapper methods measure usefulness and give better performance. Embedded method lies in between these methods.

#### Selection of predominant feature from wrapper optimization methods

In this proposed method, we select the predominant features of a dataset based on repetition of same feature in different optimization methods. Among the 8 wrapper feature selection methods, if a feature is recurring in more than 3 optimization algorithm, we have considered that feature (quality metric) as predominant feature. This process is done for both LIVE and CSIQ database separately.

#### Algorithm for quality estimation model using predominant feature selection using wrapper optimization based feature selection methods

1. Find the Full Reference quality score between reference video frame and test(distorted) video frame
2. Pooling of quality scores of frames of video (Averaging as pooling strategy)
3. Repeat steps 1 and 2 for 16 image or video quality metrics considered in literature
4. Wrapper optimization-based feature selection with 8 optimization methods considered in literature
5. Listing of predominant features – metrics which appeared more than thrice in 8 different optimization methods.



- Building the model of prediction using regression analysis with all the 16-quality metrics discussed in literature survey and finding RMSE.
- Building the model of prediction with predominant features obtained in step 5, using regression analysis and finding RMSE
- Comparative analysis of RMSE of step 6 and 7

#### Algorithm for quality estimation model with features selected from each of 5 category – Filtering method

- Find the Full Reference quality score between reference video frame and test (distorted) video frame for LIVE and CSIQ databases.
- Pooling of quality scores of frames of video (Averaging as pooling strategy) to obtain a individual quality metric value for a sample video in the dataset.
- Repeat steps 1 and 2 for 16 image/video quality metrics considered in literature
- In our case, 16 metrics are divided into 5 categories as a) similarity-based metrics b) pixel-based metrics c) Block-wise evaluation metrics d) Correlation based metrics e) Deviation/Variance based metrics
- Akaike Information Criterion is calculated for each of the quality metric(feature) in each category and metric with highest AIC is taken for next step.
- For each of the feature selected/filtered in step 5, regression model is built and RMSE is evaluated for both LIVE and CSIQ databases separately.
- Comparative analysis of RMSE

#### Algorithm for quality estimation model with features selected from each of 5 category using filtering and wrapper methods for further reduction in feature set – Filtering + Wrapper method

- Quality metrics obtained from filtering using Akaike Information Criterion as filtering method are taken for this algorithm.
- 8 Wrapper feature selection methods discussed in literature are applied for quality metrics considered in step 1
- Features selected using 8 wrapper feature selection methods have consistency in feature selection and are used for building regression model
- Comparative analysis of RMSE with different algorithms proposed is done.

## 4. RESULTS AND DISCUSSION

In this part, we focus on the analysis of results. LIVE and CSIQ database are utilized to understand the performance analysis of video quality metrics. LIVE database videos have wide variety of content. Table 1 shows optimization algorithms used for feature selection for LIVE and CSIQ full reference video database along with the accuracy for each of the optimization algorithm. We have done the implementation using Matlab 2020a. Regression learner is used for the evaluation of RMSE.

#### Quality metrics (features)

- FSIM
- CWSSIM6
- GMSD
- DSS
- SVD
- QILV
- Corr2D
- NCC
- PSNR
- MSE
- SSIM
- MSSIM
- 3SSIM
- Delta
- VQM
- DCT based
- MSAD

Table 1 shows the features selected using wrapper feature selection methods. Table 2 shows features selected using filter method and wrapper method. Table #3 shows the RMSE (Root Mean Square Error) result of regression model built using predominant features

obtained so far. First two columns show results of regression RMSE with predominant feature selection whereas third and fourth columns show the regression results for without feature selection. It can be noted from Table 2 that, instead of all the 16 quality metrics used for training, only predominant features can be considered and higher accuracy of predictability could be achieved. Table 3 enlists regression RMSE with and without predominant feature selection through feature selection algorithms. Table 4 provides the results related to regression RMSE with AICs as filter feature selection criterion. This evaluation has considered filter feature selection criterion and without wrapper feature selection. Table 5

**Table 1. Feature selection from 16 features using wrapper feature selection methods**

Sl. NO	Optimization Algorithm	Database	Features Selected (Among 16 features)	Accuracy
1.	Atom Search Optimization (ASO)	LIVE	8,7	47.61
		CSIQ	6 7 8 9 10 11	34.88
2.	Generalized Normal Distribution Optimization (GNDO)	LIVE	2 3 4 6 13	42.85
		CSIQ	9 10 11 16	37.20
3.	Equilibrium Optimizer (EQ)	LIVE	1 3 12	61.90
		CSIQ	1 9 10	37.20
4.	Manta Ray Foraging Optimization (MRFO)	LIVE	6 7 12 16	61.90
		CSIQ	9 10 11	37.20
5.	Slime Mould Algorithm Optimization (SMA)	LIVE	6	42.85
		CSIQ	7 9 10	37.20
6.	Traditional Artificial Bee Colony Optimization (ABC)	LIVE	1 3 6 7 8 12 14	66.66
		CSIQ	9 10 15	37.20
7.	Traditional Ant Colony Optimization	LIVE	8 7	47.62
		CSIQ	9 7 10	37.21
8.	Traditional Particle Swarm Optimization	LIVE	4 7 11 12 14	42.85
		CSIQ	1 9 10	37.21

Optimization based feature selection process is done for both LIVE and CSIQ database separately. We found that for LIVE database, GMSD, QILV, Corr2D, NCC, MSSIM appeared 3 or more times in 8 optimization algorithms for feature selection. For CSIQ database, Corr2D, PSNR, SSIM and MSSIM appeared 3 or more times in feature selection using optimization algorithms. So, we can consider these

features as predominant features in respective databases. These predominant features are used for building regression model for prediction of video quality

Akaike Information Criterion (AIC) is used as filtering mechanism to select features for both LIVE and CSIQ databases.

Quality metrics for CSIQ database and indices used – using filtering method with AIC 1'. CWSSIM 2'. Delta 3'. DSS 4'. CORR2D 5'. GMSD

Quality metrics for LIVE database and indices used – using filtering method with AIC 1'. MSSIM 2'. PSNR 3'. VQM 4'. Corr2D 5'. QILV

**Table 2 Features selected using BOTH filtering and wrapper feature selection methods using different optimization methods for LIVE and CSIQ databases**

Sl. NO	Optimization Algorithm	Database	Features Selected (Among 5 category)	Accuracy (%)
1.	Atom Search Optimization (ASO)	LIVE	1' 2' 4'	52.38
		CSIQ	2' 3' 4'	34.88
2.	Generalized Normal Distribution Optimization (GNDO)	LIVE	1' 2' 4'	52.38
		CSIQ	2' 3' 4'	34.88
3.	Equilibrium Optimizer (EQ)	LIVE	1'	42.86
		CSIQ	2' 3' 4'	34.88
4.	Manta Ray Foraging Optimization (MRFO)	LIVE	1' 2' 4'	52.38
		CSIQ	2' 3' 4'	34.88
5.	Slime Mould Algorithm Optimization (SMA)	LIVE	1' 2' 4'	52.38
		CSIQ	1' 4'	30.23
6.	Traditional Artificial Bee Colony Optimization (ABC)	LIVE	1' 2' 4'	52.38
		CSIQ	2' 3' 4'	34.88
7.	Traditional Ant Colony Optimization	LIVE	1' 2' 4'	52.38
		CSIQ	2' 3' 4'	34.88
8.	Traditional Particle Swarm Optimization	LIVE	1' 2' 4'	52.38
		CSIQ	2' 3' 4'	34.88

Table 2 and 3 show the classification accuracies for wrapper feature selection methods and filter + wrapper feature selection methods. It can be noted that with hybrid feature selection using filter and wrapper methods, features from 5 groups may be selected. Consistency is achieved in classification accuracy with this hybrid method. This method worked well for LIVE database and among 8 optimization algorithms used for feature selection, classification accuracy improved in 5 algorithms.

**Table 3. Regression RMSE with and without predominant feature selection through wrapper feature selection algorithms (Without filter feature selection)**

Regression learner	LIVE	CSIQ	LIVE w/o	CSIQ w/o
Linear regression - linear	0.16	1.43	0.79	1.38
Linear regression - Interactions linear	0.21	1.50	160.61	59.42
Linear regression - Robust Linear	0.16	1.44	0.83	1.38
Stepwise linear regression	0.16	1.46	0.81	1.45
Fine tree	0.18	1.60	0.90	1.65
Medium tree	0.20	1.55	0.98	1.46
Coarse tree	0.23	1.46	1.08	1.42
Linear SVM	0.16	1.44	0.85	1.39
Quadratic SVM	0.18	1.53	1.50	2.44
Cubic SVM	0.22	1.76	16.53	5.33
Fine Gaussian SVM	0.24	1.42	0.94	1.43
Medium Gaussian SVM	0.13	1.41	0.74	1.37
Coarse Gaussian SVM	0.16	1.44	0.84	1.39
Ensemble Boosted trees	0.20	1.49	0.77	1.41
Ensemble Bagged Trees	0.19	1.45	0.96	1.39
Gaussian Process Regression Matern 5/2 GPR	0.13	1.43	0.71	1.37
Gaussian Process Regression - Exponential GPR	0.13	1.43	0.71	1.37
Gaussian Process Regression - Rational Quadratic GPR	0.13	1.43	0.72	1.37

**Table 4. Regression RMSE with AIC as filter feature selection criterion (Without wrapper feature selection)**

Regression learner	LIVE AICC	CSIQ AICC	LIVE w/o	CSIQ w/o
Linear regression - linear	0.94	1.39	0.79	1.38
Linear regression - Interactions linear	1.16	1.44	160.61	59.42
Linear regression - Robust Linear	1.38	1.39	0.83	1.38

Stepwise linear regression	0.75	1.39	0.81	1.45
Fine tree	0.89	1.68	0.90	1.65
Medium tree	0.94	1.47	0.98	1.46
Coarse tree	1.02	1.39	1.08	1.42
Linear SVM	1.04	1.42	0.85	1.39
Quadratic SVM	0.79	1.52	1.51	2.44
Cubic SVM	47.04	5.44	16.53	5.34
Fine Gaussian SVM	0.90	1.48	0.94	1.43
Medium Gaussian SVM	0.73	1.43	0.74	1.37
Coarse Gaussian SVM	0.83	1.41	0.84	1.39
Ensemble Boosted trees	0.78	1.46	0.77	1.41
Ensemble Bagged Trees	0.91	1.45	0.96	1.39
Gaussian Process Regression Matern 5/2 GPR	0.72	1.39	0.71	1.37
Gaussian Process Regression - Exponential GPR	0.71	1.40	0.71	1.37
Gaussian Process Regression - Rational Quadratic GPR	0.72	1.39	0.72	1.37

**Table 5. Regression RMSE with BOTH filter feature selection with AIC and wrapper feature selection using predominant features**

Regression learner	LIVE AICC +Pred. Features	CSIQ AICC +Pred. Features	LIVE w/o	CSIQ w/o
Linear regression - linear	1.10	1.40	0.79	1.38
Linear regression - Interactions linear	0.88	1.41	160.61	59.42
Linear regression -Robust Linear	1.37	1.40	0.83	1.38
Stepwise linear regression	0.78	1.41	0.81	1.45
Fine tree	0.91	1.63	0.90	1.65
Medium tree	0.90	1.46	0.98	1.46
Coarse tree	0.98	1.41	1.08	1.42
Linear SVM	1.16	1.41	0.85	1.39
Quadratic SVM	1.18	1.43	1.51	2.45
Cubic SVM	18.61	2.48	16.53	5.34
Fine Gaussian SVM	0.82	1.45	0.94	1.43
Medium Gaussian SVM	0.76	1.42	0.74	1.38
Coarse Gaussian SVM	0.81	1.42	0.84	1.39
Ensemble Boosted trees	0.81	1.47	0.77	1.41
Ensemble Bagged Trees	0.89	1.50	0.96	1.39
Gaussian Process Regression Matern 5/2 GPR	0.76	1.40	0.71	1.37
Gaussian Process Regression - Exponential GPR	0.73	1.41	0.71	1.37
Gaussian Process Regression - Rational Quadratic GPR	0.74	1.40	0.72	1.37

## 5. CONCLUSION

The paper says, the proposed optimization methods are based predominant feature selection of predictive video quality analysis. Wrapper feature selection based on optimization is used to select the quality metrics. Eight optimization algorithms are used to select features. The metrics which appeared more than thrice have been taken as predominant features of the particular database. We found that for LIVE database, GMSD, QILV, Corr2D,

NCC and MSSIM are predominant features. For CSIQ database, Corr2D, PSNR, SSIM, MSSIM are found to be predominant features. We can conclude that we can build hybrid metric using these features. RMSE for with predominantselection feature is less than the 1 without selectionfeature. In our case, we have used wrapper optimization methods-based feature selection. We can improve the feature selection using both filter-based approach and wrapper feature selection approach if we have large subset of features. We have obtained consistent

features from 5 categories with usage of both filter feature selection process using AIC as well as wrapper feature selection process. Hence, hybrid feature selection using filter and wrapper methods help in obtaining consistent and best performing features for building the model.

## REFERENCES

1. P. V. Vu and D. M. Chandler, "ViS3: an algorithm for video quality assessment via analysis of spatial and spatiotemporal slices," *J. Electron. Imaging*, 2014.
2. K. Seshadrinathan, R. Soundararajan, S. Member, A. C. Bovik, and L. K. Cormack, "Study of Subjective and Objective Quality Assessment of Video," vol. 19, no. 6, pp. 1427–1441, 2010.
3. K. Seshadrinathan, R. Soundararajan, A. C. Bovik, and L. K. Cormack, "A Subjective Study to Evaluate Video Quality Assessment Algorithms," 2000.
4. Z. Wang, A. C. Bovik, H. R. Sheikh, and E. P. Simoncelli, "Image quality assessment: From error visibility to structural similarity," *IEEE Trans. Image Process.*, vol. 13, no. 4, pp. 600–612, Apr. 2004.
5. L. Zhang, L. Zhang, X. Mou, and D. Zhang, "FSIM: A feature similarity index for image quality assessment," *IEEE Trans. Image Process.*, 2011.
6. M. P. Sampat, Z. Wang, S. Gupta, A. C. Bovik, and M. K. Markey, "Complex wavelet structural similarity: A new image similarity index," *IEEE Trans. Image Process.*, 2009.
7. W. Xue, L. Zhang, X. Mou, and A. C. Bovik, "Gradient magnitude similarity deviation: A highly efficient perceptual image quality index," *IEEE Trans. Image Process.*, vol. 23, no. 2, pp. 668–695, 2014.
8. A. Balanov, A. Schwartz, Y. Moshe, and N. Peleg, "Image quality assessment based on DCT subband similarity," in *Proceedings - International Conference on Image Processing, ICIP*, 2015.
9. O. F. Ismael and Z. M. Hussain, "SVD-structural similarity in the wavelet-gabor domain: Improved confidence for face recognition under noise, blur and haze," *J. Comput. Sci.*, 2019.
10. S. Aja-Fernández, R. S. J. Estépar, C. Alberola-López, and C. F. Westin, "Image quality assessment based on local variance," in *Annual International Conference of the IEEE Engineering in Medicine and Biology - Proceedings*, 2006.
11. J. Blaber, B. Adair, and A. Antoniou, "Ncorr: Open-Source 2D Digital Image Correlation Matlab Software," *Exp. Mech.*, 2015.
12. J. C. Yoo and T. H. Han, "Fast normalized cross-correlation," *Circuits, Syst. Signal Process.*, 2009.
13. S. Winkler and P. Mohandas, "The Evolution of Video Quality Measurement: From PSNR to Hybrid Metrics," vol. 54, no. 3, pp. 1–9, 2008.
14. M. Wang, E. Y. Wang, and G. Pan, "Image quality assessment based on invariant moments similarity," in *Advanced Materials Research*, 2012, vol. 546–547, pp. 565–569.
15. Z. Wang, E. P. Simoncelli, and A. C. Bovik, "Multi-scale structural similarity for image quality assessment," *Conf. Rec. Asilomar Conf. Signals, Syst. Comput.*, vol. 2, no. Ki L, pp. 1398–1402, 2003.
16. A. C. Bovik, "Content-weighted video quality assessment using a three-component image model," *J. Electron. Imaging*, vol. 19, no. 1, p. 011003, 2010.
17. F. Xiao, "DCT-based video quality evaluation," *Final Proj. EE392J*, no. Figure 1, p. 769, 2000.
18. W. Zhao, L. Wang, and Z. Zhang, "Atom search optimization and its application to solve a hydrogeologic parameter estimation problem," *Knowledge-Based Syst.*, vol. 163, pp. 283–304, Jan. 2019.
19. S. Nadarajah, "A generalized normal distribution," *J. Appl. Stat.*, vol. 32, no. 7, pp. 685–694, Sep. 2005.
20. A. Faramarzi, M. Heidarinejad, B. Stephens, and S. Mirjalili, "Equilibrium optimizer: A novel optimization algorithm," *Knowledge-Based Syst.*, vol. 191, p. 105190, Mar. 2020.
21. W. Zhao, Z. Zhang, and L. Wang, "Manta ray foraging optimization: An effective bio-inspired optimizer for engineering applications," *Eng. Appl. Artif. Intell.*, vol. 87, p. 103300, Jan. 2020.
22. S. Li, H. Chen, M. Wang, A. A. Heidari, and S. Mirjalili, "Slime mould algorithm: A new method for stochastic optimization," *Futur. Gener. Comput. Syst.*, vol. 111, pp. 300–323, Oct. 2020.
23. D. Karaboga and B. Basturk, "Artificial Bee Colony (ABC) optimization algorithm for solving constrained optimization problems," in *Lecture Notes in Computer Science (including subseries Lecture Notes in Artificial Intelligence and Lecture Notes in Bioinformatics)*, 2007, vol. 4529 LNAI, pp. 789–798.
24. M. Dorigo, V. Maniezzo, and A. Colomi, "Ant system: Optimization by a colony of cooperating agents," *IEEE Trans. Syst. Man, Cybern. Part B Cybern.*, vol. 26, no. 1, pp. 29–41, Feb. 1996.
25. J. Kennedy and R. Eberhart, "Particle swarm optimization," in *IEEE International Conference on Neural Networks - Conference Proceedings*, 1995.



# Hybrid time centric recommendation model for e-commerce applications using behavioral traits of user

B. R. Sreenivasa<sup>1</sup> · C. R. Nirmala<sup>2</sup>

Accepted: 7 September 2021

© The Author(s), under exclusive licence to Springer Science+Business Media, LLC, part of Springer Nature 2022

## Abstract

In today's online market, recommendation systems have become universal and are an aspect of any online shopping portal. The traditional approach uses the subscriber's historical knowledge, and this technique is not adequate for resolving problems with a cold start. These issues include recommendations for non-registered users or newly added customers and new items added. Session-based recommendations based on recurrent neural networks are gaining popularity for product recommendations. This is due to recurrent neural networks' ability to record sequential feature data more effectively throughout the current session, which results in more similarity between consumer behaviour sequences. Nevertheless, most state-of-the-art recurring neural networking systems completely ignore the long-term details of multiple sessions and concentrate solely on short-term communication in a single session. This paper presents a hybrid time-centric prediction model to address research issues that learn the customers' short and long-term behaviours. Experiments on the recsys challenge data set are carried out to assess the efficiency of the hybrid time-centric prediction models over the existing hybrid models in terms of HitRate and Mean-Reciprocal Rate.

**Keywords** Deep learning · Machine learning · Bayesian personalized recommendation · Behaviour modelling · Recommendation system · Recurrent neural network · Session-based

## 1 Introduction

Online shopping has become a ubiquitous way of shopping. More than 79% of people in the United States visit online shopping portals, as stated in [1]. However, the purchase of products ends at just 2–5% of these portions [1, 25]. This process is called the procurement conversion rate of online shopping portals (PCR). Considering that, as indicated by [40], present e-Commerce is estimated at more than US\$ 460 billion. The income/revenue of the e-commerce platform would be increased even if the PCR online is little

changed. The e-commerce modelling behaviour of subscribers is a research interest field for quite a long time to gain insight into subscriber decision making (DM). They are also used by visiting online shopping sites to boost customer service and increase sales.

Recently, numerous online shopping portals use RS techniques [26, 31, 32] to create customized items that may satisfy the user's favourites/preferences. The CF [9, 34] and content-based (CB) techniques are widely utilized RS strategies. The CB method utilizes the user's history log data stored in the e-Commerce portal to extract user preferences. By and large, a subscriber's log information is constructed using the historical data of items procured or viewed by the subscribers or using comments. The ratings are given to items by the subscribers and so on. The collaborative filtering-based techniques [29] suggest that the items depend on the clients with identical preferences for a specific client. While the content-based techniques suggest the items that resemble similarities for items accessible in the subscriber's preference historical log data. In [19], a content-based collaborative filtering technique for fashion

✉ B. R. Sreenivasa  
br.sreenu@gmail.com

C. R. Nirmala  
nirmala.cr@gmail.com

<sup>1</sup> Department of Information Science & Engineering, Bapuji Institute of Engineering & Technology, Visvesvaraya Technological University, Karnataka, Davangere, India

<sup>2</sup> Department of Computer Science & Engineering, Bapuji Institute of Engineering & Technology, Visvesvaraya Technological University, Karnataka, Davangere, India

retail shopping environments was introduced. The model built recommendations using both online and offline data.

This model, however, does not produce a successful outcome over time. Also, the precise use of content-based and collaborative filters is limited by the accessibility of the subscriber's preferences' historical data. Those content-based and collaborative filtering techniques cannot provide legitimate/appropriate item advice to their subscribers if their historical preferential information is not accessible [4, 6].

Besides, personalized recommendation [24] is considered one of the most challenging tasks of the user rating system [37]. Customer intent/compliance is complex to predict/model. During the present and previous sessions, different internal and external features affect. Several state-of-the-art methods are running on a context-based recommendation system [27], investigating context data, including spatial position, temporal data [11], historical log data of the subscriber [30] or domain unique characteristics [28], using past user rating and query information employing reinforcement learning [37].

Similarly, numerous other refined neural network methods have been modelled, similar to time-based multi-task behavioural modelling [7, 33], and [42]. In [16], it is essential to consider both items and attribute session information to build a recommendation model. Further, they presented a Feature weighted session-based recommendation model that combines multiple attribute sessions using different feature weighting mechanisms. However, the model only considers a single session, and it is better to consider various sequences together [22] as it will give a better understanding of user preferences. Furthermore, deep learning (DL) approaches can be used to improve their conversion probability model. The RS method modelled in recent times [13, 14], and [38] show that the RNN-based RS model can outclass state-of-art other well-known options in some session-based forecasting undertakings.

The research aims to utilize both inter-session information of long-term context and intra-session of short-term context to build superior personalized time-centric RS. The following concerns and challenges must be addressed in order to develop such a model. First, a state-of-art Recurrent Neural Network (RNN) can't learn efficiently using extensive sequential information. Thus, it induces high memory usage and training latency. Then, the communication exchange information is composed of noise: as few clicks are done accidentally, few clicks are useful. Lastly, data from previous historical sequential sessions should assume various norms as the current session, yet there is no particular norm for combining session-based long-term information with session-centric short-term information. In this way, a progressively efficient method to deal with time-centric information with varied recommendation significance needs. This work considered the abovementioned challenge and issues

in building a hybrid time-centric prediction model (HTCP) for the e-Commerce recommendation system.

The research contribution is as follows.

- This work modelled time-centric behaviour modelling for recommending items to its customers.
- We are designing a hybrid time-centric prediction model for modelling both short-term and long-term sequence information.
- The HTCP model outperforms the existing hybrid recommendation model in terms of HitRate and Mean Reciprocal Rank.

The rest of the paper is laid out as follows. Section II reviews the studies that have been used hybrid techniques in recommendations exclusively, which was the critical approach used in the existing systems. Section III then provides observations and discussions about the implemented HTTP model using the customer framework's dynamic behaviour trait. Conventional model performance metrics is presented. An experimental discussion is carried out in the penultimate segment. In the final section, we can see the conclusion and future work.

## 1.1 Literature survey

This section discusses the work done so far building efficient RS for the online shopping portal environment. Further, it discusses the techniques used, benefits, drawbacks, and limitations of these state-of-art RS models. Rating Matrix was used in RS for exploiting and extracting relationships among subscribers and the items for obtaining the subscriber's preferences in the current session (RM). Thus, a single outcome of RM depicts a user's preference outcome for particular item [14, 23, 26, 39], and [35]. For maintaining RM, the RS model can request the subscriber to rate an item explicitly.

Similarly, even the model can rate an item based on a subscriber's behaviour towards an item. In this way, RS, the matrix-factorization (MF) method, is used to deal with subscribers' favourite list or preferences within the RM [14, 23, 26, 39], and [35]. In [11], to build people's sequential actions, the author created a new LSTM (Long Short-Term Memory) updated version implemented in Time-LSTM. Time-LSTM trains LSTM with time gates to design time intervals. These time gates are deliberately built in such a way that Time-LSTM combines customers' short- and long-term wishes to improve the reliability of the recommendation compared to traditional RNN approaches.

Matrix factorization-based collaborative filtering strategies utilizes the rating matrix for learning subscriber's preferences. However, these techniques suffer from problems of CS and data sparsity issues [39]. If an item is not rated by any subscribers, it is difficult to recommend



it to the users. This sort of issue is known as the cold start issue. Correspondingly, if barely any clients have given a rating to an item, or a client has given a rating to a few things, at that point, there is less information for carrying out forecasting. This sort of issue is described as a data sparsity issue. Subsequently, for overcoming the research issues, some work has been modelled using content-based strategies that utilize the content of the items or the metadata alongside the RM for item forecasting [39]. The author [8] presented RS using collaborative filtering and gated recurrent network [5] to learn subscriber favourite lists. The paper [26] proposed an RS using collaborative filtering alongside a gated recurrent network [5] for distinguishing subscriber behaviour from the current sessions. While [5] utilized the CF with gated recurrent unit learning user behaviour in recent sessions. The author [26] focused on a session-based recommendation and proposed a recurrent neural hierarchical network to transfer cross-session knowledge. A model-based hierarchical RNN (HRNN) that extends previous RNN-based session modelling by an additional GRU stage, predicting user behaviour through sessions and time transformation to predict personalized session-based recommendations. HRNNs offer a streamlined means of transferring information on long-term customer interest patterns to the session level and thereby delivering personalized user-oriented session-based suggestions.

In [26] and [5], authors have demonstrated that utilizing the gated recurrent network method handled sequential information from the current session superior to the other deep learning-based approaches. Existing session-based recommendation techniques use the metadata of the items click of the subscriber for forecasting items in the current session; consequently, these strategies don't consider the historical information of the client's traits from the recent sessions [5, 26]. The work states that item forecasting accuracy can be enhanced by efficiently learning the short-term feature sets (i.e., hidden items feature sets) from the client's behavioural information in the current sessions. This work presents a hybrid time-centric recommendation model for extracting the essential features from the customer's behaviour to overcome the research problem.

In [42], a multi-task learning system was suggested to predict consumer return times and jointly recommend products. A survival analysis model is used to assess patients' probability of survival to determine the return time. The authors have extended this model to predict customer return times using LSTM. LSTM also makes product recommendations from the previous customer session activities. This work aimed at presenting intersession proposals instead of the aforementioned

session-based suggestions that concentrated on the advice from the same session.

## 2 Summary of the literature

Most techniques proposed for session recommendations are based on some sequence learning in the literature; A recent survey of the broader class of sequence-aware recommenders was found in [44]. Early techniques placed more importance on identifying recurrent sequential patterns to forecast a user's future behaviour at the time of the recommendation. These early algorithms were used in the context of forecasting user-online navigation behavior. Pattern mining approaches are then used to next-item suggestion problems in e-Commerce and the music industry [45]. While frequent pattern approaches are simple to use and result in comprehensible models, the mining process can be computationally intensive. Finding acceptable algorithm parameters, especially a reasonable minimum support threshold, might be difficult at the same time. Finally, it appears that in some application domains, employing frequent item sequences does not produce better recommendations than employing simpler item co-occurrence patterns [45].

More advanced sequence learning algorithms that incorporate some type of sequence modeling have been presented in a number of recent papers. Markov Chain (MC) models are commonly used in such sequence modeling approaches [46].

Over the last few years, the quantity of research papers on deep learning-based recommendation systems has exploded. Since 2016, RecSys, the world's leading international conference on recommendation systems, has hosted monthly deep learning seminars. Deep learning can characterize non-linear correlations in data by employing non-linear activations such as ReLU, Sigmoid, and Tanh. This characteristic enables the capture of sophisticated and complex user-item interaction patterns. Factorization machines and matrix factorization, for example, are inherently linear models.

RNNs are used in the most current efforts on sequence modeling. For example, Zhang et al. [37] employed them to forecast user actions in an advertisement situation. Hidasi et al. [14] were among the first to investigate Gated Recurrent Units (GRUs), a type of RNN that may predict the next user action in a session. In [13][44] and [47] all enhanced their gru4rec approach in different ways. Approaches based on recurrent neural networks (RNNs) are the most recently studied group of approaches for session-based recommendation challenges. gru4rec is a brand-new deep learning algorithm explicitly designed for session-based recommendation applications [14][47]. gru4rec uses an

RNN with Gated Recurrent Units to model user sessions to forecast the likelihood of succeeding events (e.g., item clicks) given a session starting point.

## 2.1 Memory usage and training latency

The neural networks must store input data, weight parameters, and activations in their memory to transport data across the network. The activations from the forward pass must be retained during training before the error gradients in the reverse pass can be computed. The 50-layer ResNet network, for example, has 26 million weight parameters and calculates 16 million forward activations. If you have a floating-point value of 32 bits to store every weight and activation, that will provide 168 MB of storage. We may reduce this storage requirement by half or a quarter by adding the lower precision value to store these weights and activations.

It is impossible to hold the GPU processor's data with such large quantities of storage state required. In reality, many high-performance GPU processors only have 1 KB of memory per core processor that can be read quickly enough to saturate the floating-point datapath. This means that it must save the state in an external DRAM at each layer of the DNN, load up the next network layer, and load the data back into the device. Therefore, the already limited off-chip memory interface bandwidth and latency suffer from the added pressure of continuous recharge and re-activation. This decreases training time substantially and increases power demand considerably.

Although parallelism in large mini-batches improves computational efficiency, research demonstrates that large mini-batches result in generalizing networks that take longer to train. Furthermore, machine learning model graphs already reveal a great deal of parallelism.

During decades of compilation work for sequential languages, many techniques are available to minimize the memory further. First, there should be "in-place" operations, such as activation functions, to transcribe input data directly from the output. This allows for the reuse of the memory state. Second, the data dependencies between network activities can be reused by evaluating and assigning the same memory to operations that fail to use it simultaneously.

Researchers from Google DeepMind with recurring neural networks have established a similar memory-reuse approach (RNNs). RNNs are a special form of DNN that has a structure that encodes behavior cycles over input sequences. Re-computing for RNN's has shown that the memory is reduced by 20 for 1000-long sequences with only 30 percent overhead efficiency.

## 2.2 Proposed work

The goal of phase-1 of the research aims to create a recommendation model based on the client's geographical location. Customers' dynamic behavior traits were taken into account when developing the hybrid location-centric e-Commerce recommendation model. The work considers the dynamic behavior of the user and learns both short-term and long-term context. The RNN model is described in detail in HLCP and how RNN is used to model the long-term context. When people/users are exposed to a new environment, their behavior changes quickly (short-term). The priority of items may vary when a user goes to a different country or place.

Similarly, when certain advertising is posted to a specific user interface, user preferences change quickly (AUT). As a result, the RNN model can't be used to describe such a short-term scenario. The paper provides the operational structure of the feed-forward neural network for modeling short-term context in dynamic behavior features of the user in order to address the challenges.

In addition, the research includes static behavior modeling, such as a customer viewing a product list and spending some time on an e-Commerce website. On an e-Commerce website, more dynamic behavior was also considered, such as user clicks, views, purchases, spending time, and so on. The dynamic behavior model is then exhibited in the HLCP model. Finally, the Bayesian personalized ranking is utilized to train a recurrent neural network to predict e-Commerce customers' behavior traits.

In phase-2, the research work provides a hybrid time-centric e-Commerce recommendation model based on the dynamic behavioral traits of the customer. The architecture of the HTCP model is shown in Fig. 3. The HTCP model is designed for recommending items based on users' dynamic behavior and session-centric information on the ongoing session. For obtaining a relationship between user current sessions and past behavior for recommending items, it is essential to model both short and long-term behavior contexts (i.e., time-centric HLCP model). The hybrid time-centric prediction (HTCP) model is designed by substituting location-centric (LC) transition matrices (TM) with session-centric TM's.

## 3 Hybrid time centric recommendation model for online shopping environment

The HTCP model recommends items based on the user's dynamic behaviour and session-centric information on the ongoing session. For obtaining a relationship between user current session and past behaviour for recommending items, it is essential to consider both short-term and long-term

behaviour context (i.e., Location centric HLCP model [36]). Let's consider a set of items like clothes, furniture, computer accessories, as follow

$$\mathcal{U}\{u_1, u_2, \dots, u_n\}, \quad (1)$$

where  $u_n$ , No.\_of\_items and set\_of\_users like a male, female, chilen, etc. as follows

$$\mathcal{V} = \{u_1, u_2, \dots, u_n\}. \quad (2)$$

where  $u_n$ , total number of users. The proposed work considers e-Commerce application, which includes different behaviour such as

$$\mathcal{C} = \{c_1, c_2, c_3, c_4\}. \quad (3)$$

where  $c_1$  clickstream,  $c_2$  items\_added to cart list,  $c_3$  adding to favourite\_list, and  $c_4$  purchased items. The job is to predict what clients will buy in the current session using the hybrid time-centric prediction model.

### 3.1 Long-term and short-term behaviour modelling

For modelling the long-term behaviour context, this work employs RNN. The architecture of RNN is shown in Fig. 1

The RNN architecture comprises an input layer, numerous hidden layers, output layers, and inner weight matrices. The activation parameter of the hidden layers is obtained as follows

$$i_{\ell}^v = f(\mathcal{X}i_{\ell}^v + \mathcal{D}s_{w_{\ell}}^v), \quad (4)$$

where  $i_{\ell}^v \in \mathbb{S}^c$  illustration of user  $v$  at  $\ell$ . in a trait,  $\mathcal{D}_{j_{\ell}} \in \mathbb{S}^c$ .  $\ell^{th}$ . input item of user  $v$ . The activation parameter is represented by  $f(i)$  and the present item transition matrix is represented as follows

$$\mathcal{D} \in \mathbb{S}^c \quad (5)$$

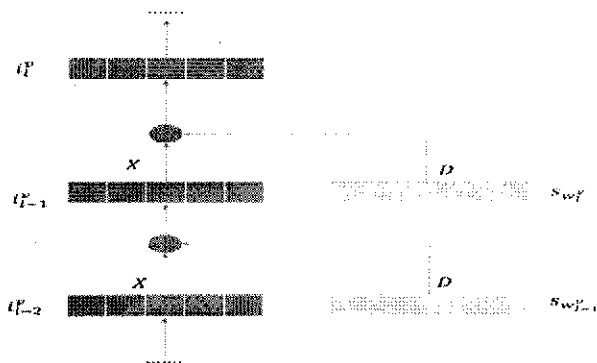


Fig. 1 The architecture of the RNN model

$\mathcal{D}$ . can obtain the user's present behaviour, and  $\mathcal{X}$  can propagate traits signals. Equation (4) is executed iteratively to get the status of each location in traits. The hidden layer information of the RNN is dynamic for behavioural characteristics, wherein the pattern is repetitive. Thus, RNN faces issues in adapting short-term contexts in behavioural traits. or learning short-term behavioural context productively, this work utilizes a feed-forward neural network (FFNN) with a solitary linear hidden layer [15, 20]. The usage of FFNN aid in learning recent behaviour more efficiently and improves behaviour classification accuracy [19]. The author's prior work [36] has additional details on the RNN and FFNN models depicted in Fig. 1 and Fig. 2. The architecture of FFNN is shown in Fig. 2.

Thus, behaviour traits in the ongoing session window are extracted using items clicked and their transition matrices in each session. The next position can be estimated using a linear prediction model using the following equation

$$i_{\ell}^v = \sum_{j=0}^{a-1} \mathcal{D}_j s_{w_j}^v, \quad (6)$$

where  $\mathcal{D}_j \in \mathbb{S}^{c \times c}$  transition-matrix for each location in a behaviour trait, and  $a$  number of components modelled in a trait.

To capture the consumer's complex behaviour, the proposed study considers behavior-based matrices to obtain characteristics of different forms of behaviour. Then, the illustration of subscriber  $\underline{u}$  at  $\hat{\ell}$  is estimated using the following equation

$$i_{\ell}^v = \mathcal{X}i_{\ell}^v + \sum_{j=0}^{a-1} \mathcal{D}_j \mathcal{N}_{c_{\ell}^v - j r_{\ell}^v - j}^v \quad (7)$$

where  $\mathcal{N}_{c_{\ell}^v - j r_{\ell}^v - j}^v \in \mathbb{S}^{c \times c}$  behaviour-based transition matrix on the  $j^{th}$ . product of subscribe  $u$ . The cold-start problem can be addressed by considering  $i_0^v = v_0$ , nothing etial to be outwardly seen here is that the behaviour-based matrices can be eliminated if there is one kind of behaviour. LCP can get the underlying features of whether various types of behaviour in past traits.

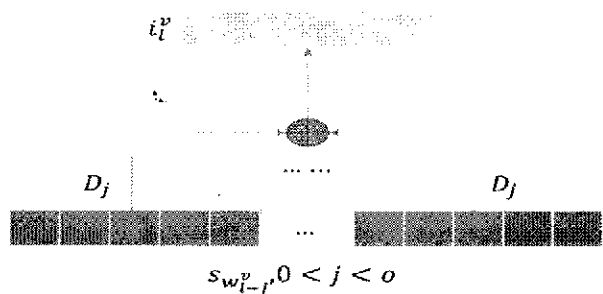


Fig. 2 The architecture of the FFNN model

Further, by computing whether user  $v$ , would perform behaviour  $c$ , on product  $w$  at session sequence  $\ell + 1$  can be obtained as

$$z_{v,\ell+1,c,w} = (i_\ell^v)^{\mathcal{U}} \mathcal{N}_{cs_w} = (i_\ell^v + v_v)^{\mathcal{U}} \mathcal{N}_{cs_w} \quad (8)$$

where  $i_\ell^v$  current\_position of user  $v$  at the traits position  $\ell$ , static hidden representation  $v_v \in \mathbb{S}^v$  and containing a dynamic representation  $i_\ell^v$ .

### 3.2 Time-centric behaviour modelling

The sequence-based model generally neglect continuous session variance (SV) among input feature sets. The session variance feature is handy in forecasting as short-term session window variances have typically higher effects on future buying than using long-term session variances. For example, let consider two product,  $w_a$ , and  $w_b$ , in a customer's procuring log. The customer purchased the product  $w_a$  the previous night or a few hours back and product  $w_b$  a few weeks back. There is a high chance that a customer's choice of product to purchase in the future may be impacted by product  $w_a$ . On the way around, if the product  $w_b$  are purchased the previous day, then there is a high probability that that product  $w_a$  and  $w_b$  have an identical effect on customer's selection due to similar interest in a short-term instance. Besides, the behaviour of purchasing individual items is periodic. For instance, if you are buying soaps and shampoos on a monthly basis, the influence of session variances results in a more dynamic environment. Considering these conditions, we improve the HLCP model [36] by incorporating session variances knowledge and model time-centric prediction models. 3. The architecture of HTCP: HTCP is modelled to capture both short-term and long-term context in behavioural traits.

### 3.3 Hybrid time-centric prediction-based recommendation system

In the above, this work discussed how user preference changes when they move to different regions/locations. For learning the user's preference HLCP model is presented in [36]. However, it is still essential to consider and incorporate time/session variance data into HLCP. Thus, this work presents a hybrid time-centric prediction (HTCP) model by substituting location-centric (LC) transition matrices (TM) with session-centric TM's. The HTCP model is shown in Fig. 3. From Fig. 3, for a given customer  $v$ , the location  $l$  is computed as follows

$$i_l^v = Xi_{l-0}^v + \sum_{j=0}^{o-1} U_{u_l^v - u_{l-1}^v} s_{w_{l-j}}^v, \quad (9)$$

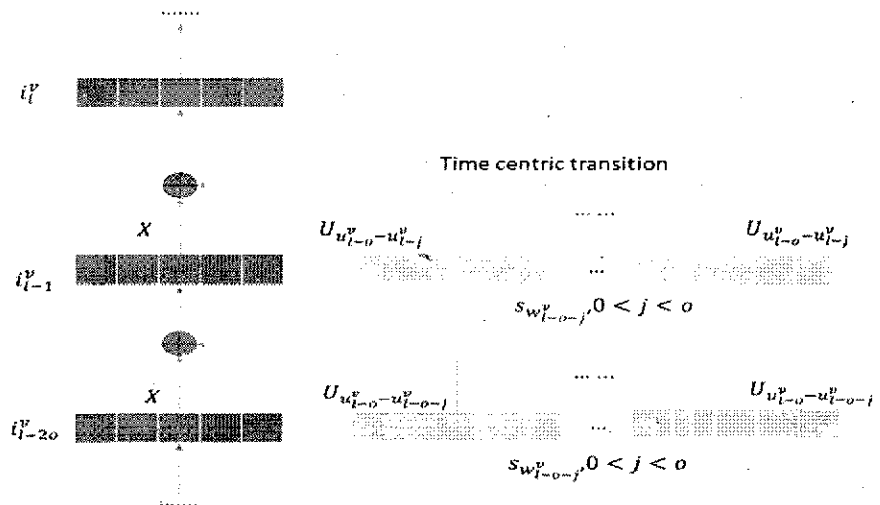
where  $u_l^v$ , present time,  $u_{l-1}^v$ , time of every product of each HTCP, and  $U_{u_l^v - u_{l-1}^v}$ , time-centric TM of time variance  $u_{l-1}^v - u_l^v$  among time  $u_{l-1}^v$ , and  $u_l^v$ . The time-centric TM helps in capturing session-specific behaviour based on the most recent activity log. Further, Eq. (9) is rewritten similarly with the HLCP model as follow

$$i_l^v = Xi_{l-0}^v + \sum_{j=0}^{l-1} U_{u_l^v - u_{l-1}^v} s_{w_{l-j}}^v, \quad (10)$$

where  $i_l^v = v_{l-0}$ , depicting the initial condition of customers. For modelling dynamic behavioural traits, behavioural-centric TM's is used in the HTCP model as follows

$$i_l^v = Xi_{l-0}^v + \sum_{j=0}^{l-1} U_{u_l^v - u_{l-1}^v} N_{c_{l-j}}^v s_{w_{l-j}}^v, \quad (11)$$

**Fig. 3** The architecture of HTCP: HTCP is modelled to capture both short-term and long-term context in behavioural traits



Then, carry out forecasting operation whether a customer  $v$  will carry out certain behaviour  $c$  on particular product  $w$  at sequential location  $l + 1$  is estimated similarly to HLCP using the following equation

$$z_{v,l+1,c,w} = (t_l^v)^U N_{c,w} = (t_l^v + v_v)^U N_c \quad (12)$$

### 3.4 Transition matrix learning

Suppose we have to continuously learn unique conceivable session variance, then we must compute a higher number of session-centric TM's and result overfitting problems. Thus, it is essential to segment all probable session variance parameters equally into a separate window for addressing the issue. This work considers estimating only TM's of the lower and upper limits of the session window (SW). Using linear interpolation (LI) for all session variance in SW, their TM's are computed. The time-centric TM  $U_{ue}$  for session variance parameter  $u_e$  is mathematically expressed as follows

$$U_{ue} = \frac{[U_{M(u_e)}(V(u_e) - u_e) + U_{V(u_e)}(u_e - M(u_e))]}{[(V(u_e) - u_e) + (u_e - M(u_e))]} \quad (13)$$

where  $M(u_e)$  and  $V(u_e)$  depicts the lower and upper limit of session variance  $u_e$ ,  $U_{V(u_e)}$  and  $U_{M(u_e)}$  depict the session-centric TM's for  $V(u_e)$  and  $M(u_e)$ , respectively. Using LI, we can address the problem in learning time-centric TM for continuous session variances. Note that optimizing time-centric TM's in every separate session window is linear. However, the global optimization in the comprehensive range of every probable session variance is non-linear. The HLCP model is efficient in modelling the sequence of behavioural traits of the user.

Furthermore, when the user's location changes, the HLCP model is particularly efficient. This is because the HLCP model stores the entirety of the user's behaviour in a single session window. However, for modelling session-centric data, the HTCP model outperforms HLCP since the session is partitioned into multiple-session windows in HTCP. The session windows are then compared to one another. As a result, the HTCP model is useful when time-centric information is provided; otherwise, HLCP is more efficient.

### 3.5 Learning of TC-LCP model

The Bayesian Personalized Ranking (BPR) model [30] is a pairwise ranking method used for implicit feedback. It is an objective parameter widely used to learn RNN and for

predicting customer behaviour traits. In general Bayesian personalized ranking considers that a customer desires a chosen set than a negative one. That is, it aims to maximize the probability using the below equation

$$p(v, l + 1, c, w > w') = h(z_{v,l+1,c,w} - z_{v,l+1,c,w'}) \quad (14)$$

where  $w'$  negative features,  $h(y)$  is a non-linear function selected using the below equation

$$h(y) = \frac{1}{1 + e^{-y}} \quad (15)$$

Thus, by considering negative log-likelihood, the fourth coming objective function can be minimized equivalently as follows

$$K_1 = \sum \log(1 + e^{-(z_{v,l+1,c,w} - z_{v,l+1,c,w'})}) + \frac{\mu}{2} \|\Theta\|_1^2 \quad (16)$$

where  $\mu$  regularization power control parameter and  $\Theta_1 = \{V, S, X, U, N\}$  depicts parameter to be computed. The experiment is conducted to evaluate the performance outcome of HTCP in terms of Hit Rate (HR) and Mean Reciprocal Rank (MRR) performance.

### 4 Inter and Intra-session RNN

Intra-session RNN generates suggestions by analyzing the order in which items are presented in a session. A large amount of memory can be used to create a mini-batch of one hot-vectors when the collection of items is extensive, which may be a problem and dropout is applied to these levels once the embedded item representation is transmitted through one or more levels of GRU. The vector is then scaled up to RNN using a feed-forward layer. The result is  $[ov_1, ov_2, \dots, ov_{N}]$ , where  $ov_i$  is the score for item  $v_i \in N$ . Rjs then developed a list of recommendations by sorting things belonging to the  $k$  highest scores by their score. Although the RNN intra-session can attain high efficiency, it begins at any session without any user knowledge. In the session, the model will learn about the user's needs, but all data will once again be discarded at the end of the session.

Long-term user profiles are included for personalized session-based RS to learn the intersession pattern in a smooth manner by using a temporal dynamics model. User embedding, short-term interest, user taste evolution, user survival time, and local negative sampling are integrated into the temporal changes in session RNN. The inter-session RNN will boost the intra-session RNN because it considers the user's previous sessions, and at the beginning of each session, it provides information to the intra-session feature.

We differentiate the above two kinds of session contexts because they require different types of relationships for the recommendation task: the context of intra-session embeds

the dependency of the intra-session. At the same time, inter-session primarily conveys the inter-session dependency.

## 5 Result and discussion

This section presents the experimental analysis of the HTCP model over the existing hybrid recommendation model [18]. The existing hybrid recommendations [18] are designed by combining both RNN and k-nearest neighbour algorithms using static customer behavioural information [41], and also GRU-based methods are used for comparison. On the other hand, the hybrid recommendation models combine both FFNN and RNN using dynamic customer behaviour. The RNN model is then learned by maximizing objective function using BPR [30] [12].

Inter-session and intra-session approaches are used in this study to improve the accuracy of the proposed work in comparison to existing methodologies. The user's actions in the time-centric prediction model may be influenced by all past activities in the session, not just the earlier one. Session-based recommendations benefit from RNNs' ability to process user activity sequences and internally represent the user's interests. It also doesn't imply that all actions indicate a willingness to learn more about anything. It can learn to recognize other people's indifferent behaviour. Short-term dependencies between actions within a session, as well as long-term dependencies between actions from distinct sessions, are prevalent. For example, a user who was interested in research papers in their prior session(s) is likely to be interested in them again in their present session. Similarly, a user who purchased a new gadget in a previous session is unlikely to purchase another in the present session, although they may be interested in accessories for the gadgets they purchased. For instance, a user who has shown an interest in research articles during his/her previous session(s) is likely to express that interest again during his/her current session. Likewise, a user who acquired a new gadget during a prior session is unlikely to purchase another during this session, albeit he/she may be interested in accessories for the gadgets he/she purchased. Thus, if the user's behaviour does not change in response to the location, the model employs RNN and operates efficiently through the use of historical data.

However, humans have a tendency to shift their behavioural patterns when exposed to different environments such as location, climate, and even in this pandemic circumstance, the user's surfing patterns change dramatically. Existing RNNs struggle to learn unexpected changes in the user's behavioural patterns since the RNN's hidden layer data is complex in terms of behavioural features, especially when the pattern is recurrent.

**Table 1** Characteristics of the Yoochoose datasets

Dataset Behaviours	Yoochoose Dataset
Clicks Streams	31,637,239
Sessions	7,996,257
Items	37,483
Timespan in days	182
Actions per sessions	3.97
Action per Day	174,222
Session per Day	43,854

**Table 2** Characteristics of the TMall datasets

Dataset Behaviours	TMall Dataset
Clicks Streams	13,421,239
Sessions	1,776,154
Items	25,348
Timespan in days	91
Actions per sessions	7.56
Action per Day	149,096
Session per Day	19,719

To efficiently learn short-term behavioural contexts, the work employs a Feed-Forward Neural Network (FFNN) with a single linear hidden layer. For instance, if a person is always engaged in browsing, his or her smartphone's browsing habits may change as the person changes its locations. In this case, recommendations would be generated solely on the basis of current intrasession browsing patterns, as advising on the basis of previous sessions' data would diminish the model's accuracy. In this work, the Feed Forward neural network is employed to successfully interpret the user's short-term behavioural context. Then the intrasession information will be stored in the RNNs memory for better recommendations.

### 5.1 Dataset characteristics

First, the experiment is conducted on the Yoochoose dataset used in the Recsys Challenge 2015 [2], as shown in Table 1. The Yoochoose dataset contains a collection of a sequence of clickstreams (click sessions) from yoochoose.com. Given a sequence of click streams, the objective is to foresee what things the client will purchase, if any. Such data is profoundly significant to e-businesses since it can indicate what stuff to recommend to the client and urge them to turn into a purchaser. The trial information generally contains 31,637,239 clicks on 37,483 items and involving 7,996,257 sessions gathered from yoochoose.com. This dataset includes the clicks of a customer (such as session id, timestamp, product id, and category) and the date of



purchase of a customer (session-id, timestamp, product id, price, and quantity).

Second, the experiment is conducted on the TMall data set [10], and its characteristics are shown in Table 2. The recommendation model's preliminary job is to forecast what the customer will buy in the current ongoing session using time-centric prediction and the existing recommendation model. The TMall dataset comprises two lakhs of shopping records composed of thousands of users considering twenty-five thousand products. It is one of china's biggest e-commerce web portals. The HTCP utilizes both the dataset to predict the items a client will purchase in the progressing session. These datasets contain redundant data. Thus in pre-processing steps, redundant data are removed for experiment analysis. Then, we establish the session information using clickstreams. Also, utilize the data from each customer's previous session as the testing data, and the remaining session information is used to train the model. The experiment is conducted on the Yoochoose and TMall dataset to evaluate the performance of HTCP over the existing hybrid forecasting model in terms of Precision/Mean reciprocal rate (MRR) and Recall/Hit rate (HR). (Tables 3 and 4).

## 5.2 Baselines methods used

### 5.2.1 Gated Recurrent Unit(GRU4Rec)

gru4rec is a new deep learning methodology that was created with session-based recommendation scenarios in mind [13][14]. gru4rec uses an RNN with GateRecurrentUnits to model user sessions to forecast the probability of subsequent events (e.g., item clicks) given a session start. To learn the model, it employs a method of session-parallel

mini-batch training and frequently employs ranking-based loss functions.

### 5.3 Sequential Rules (SR)

In [15] suggested a sequential rule method that is a version of Markov Chains (MC) or Association Rules (AR). It considers the order of events as well, but in a less restrictive way. We generate a rule when an item-M appears after an item-N in a session, even if additional events occur between M and N, unlike the MC method. We examine the number of elements appearing between p and q in the session when allocating weights to the rules. We employ the weight function  $w_{sr}(x) = 1/(x)$ , where x denotes the number of steps between the two objects.

#### 5.3.1 Session-based Matrix Factorization (SMF)

Session-Based Matrix Factorization is a novel factorization-based method explicitly built for the purpose of session-based recommendation.

It combines Factorised Markov Chains with classical matrix factorization, similar to Factorised Sequential Prediction with Item Similarity Models (FOSSIL)[18]. In the smf technique, we replace the latent user vector  $M_u$  with a session preference vector  $s_u$ , in contrast to the conventional factorization-based prediction model  $r_{u,i} = M_u N_i^T$ .

#### 5.3.2 Session-based kNN (SKNN)

Rather than just looking at the last event in the current session, the sknn methodology compares the current session to past sessions in the training data to identify the items to

**Table 3** Results comparison with proposed work and existing works in terms of HR and MRR for Yoochoose dataset

Algorithm	Metrics MRR@20	Metrics MRR@10	Metrics HR@20	Metrics HR@10
HTCP	0.394	0.308	0.783	0.614
gru4rec (ER)	0.308	0.301	0.683	0.591
Sequential Rule (SR)	0.304	0.298	0.653	0.569
Session Based Matrix Factorization (SMF)	0.302	0.295	0.666	0.575
Sequential session based KNN(S-SKNN)	0.272	0.267	0.602	0.531

**Table 4** Results comparison with proposed work and existing works in terms of HR and MRR for TMall dataset

Algorithm	Metrics MRR@20	Metrics MRR@10	Metrics HR@20	Metrics HR@10
HTCP	0.298	0.197	0.534	0.457
gru4rec (ER)	0.129	0.125	0.277	0.225
Sequential Rule (SR)	0.128	0.125	0.242	0.206
Session Based Matrix Factorization (SMF)	0.121	0.118	0.261	0.213
Sequential session based KNN(S-SKNN)	0.185	0.181	0.387	0.331

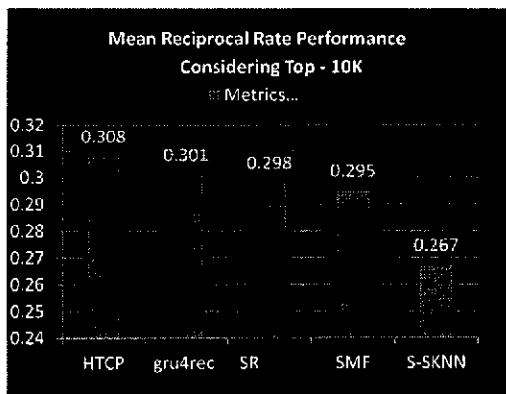


Fig. 4 Average MRR performance attained by the HTCP considering the top-10 k recommendation for Yoochoose Dataset

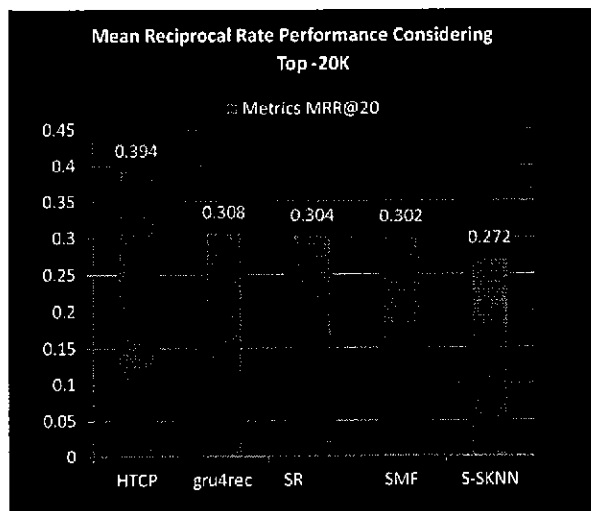


Fig. 5 Average MRR performance attained by the HTCP considering the top-20 k recommendation for Yoochoose Dataset

recommend(see also [45] and [18]). Technically, given a session  $s$ , we find the  $k$  most similar previous sessions (neighbors)  $N_s$  by smearing a suitable session similarity measure to binary vectors over the item space, such as the Jaccard index or cosine similarity [45].

### 5.3.3 Mean Reciprocal Rate/Precision performance

The accuracy performance of both the HTCP model and the existing model is evaluated on the Yoochoose dataset in MRR for a top-10 k recommendation top-20 k recommendation considering the Yoochoose data set. Figure 4 shows that the HTCP achieves an MRR outcome of 0.308, and the ER method achieves an MRR outcome of 0.301, considering the top-10 k recommendation. Similarly, the

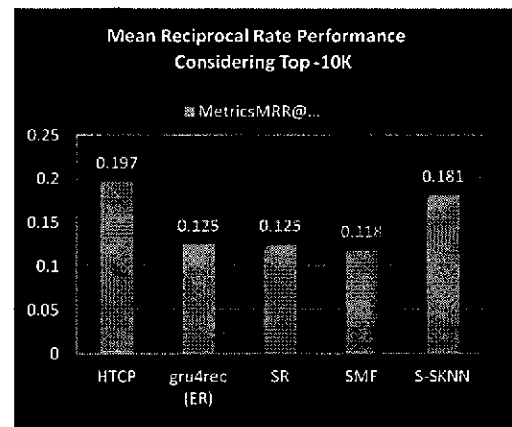


Fig. 6 Mean reciprocal rate performance considering the top-10 k recommendation for TMall Dataset

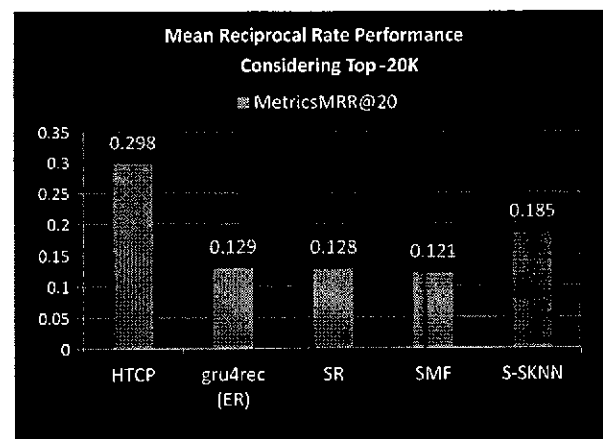


Fig. 7 Mean reciprocal rate performance considering the top-20 k recommendation for the TMall Dataset

HTCP achieves an MRR outcome of 0.3945, and the existing method achieves an MRR outcome of 0.308, considering the top-20 k recommendations. The result attained in Figs. 4 and 5 shows that the HTCP model attains significant improvement in the performance over the existing baseline model in terms of MRR considering the Yoochoose dataset. Further, the experiment is conducted using the TMall dataset to evaluate the MRR performance of HTCP and the existing recommendation (ER) model. The accuracy outcome is evaluated considering the top-10 k recommendations, as shown in Fig. 6. The HTCP achieves an MRR outcome of 0.1978, and the existing research method, an MRR achieves an outcome of 0.0986. The result attained shows the HTCP method achieves a much superior MRR outcome than existing approaches, considering the top-10 k recommendation.

Further, the accuracy outcome is evaluated considering top-20 k recommendations, as shown in Fig. 7. The HTCP achieves an MRR outcome of 0.2984, and the ER method achieves an MRR outcome of 0.1852. The result attained shows the HTCP method achieves a much superior MRR outcome than ER methodologies, considering the top-20 k recommendation. The overall result attained considering the top-10 k recommendation and top-20 k recommendation considering both Yoochoose and TMall dataset shows HTCP achieves superior MRR outcomes. HTCP achieving better MRR will aid in improving better profitability for the e-Commerce environment.

### 5.3.4 Hit Rate performance

The performance evaluation based on both the HTCP model's accuracy and the existing hybrid recommendation model is evaluated considering the Yoochoose dataset in HR for a top-10 k recommendation and top-20 k recommendation shown in Figs. 8 and 9. Figure 8 indicates that the HTCP achieves a HitRate outcome of 0.6145, and the ER method achieves a HitRate outcome of 0.155, considering the top-10 k recommendation. Similarly, the HTCP achieves a HitRate outcome of 0.7832, and the ER method achieves a HitRate outcome of 0.6827, considering the top-20 k recommendations. The result attained in Figs. 8 and 9 shows that the HTCP model attains significant improvement in the performance over the existing baseline model in terms of HR considering the Yoochoose dataset. Further, the experiment is conducted using the TMall dataset to evaluate the MRR performance of the HTCP and the existing recommendation (ER) model. The accuracy outcome (i.e., HitRate) of HTCP and existing recommendation methodologies are evaluated in this section. The accuracy outcome is evaluated considering top-10 k recommendations, as shown in Fig. 10. The HTCP achieves a HitRate outcome of 0.4571, and ER (i.e., ES (existing system)) method achieves an HitRate outcome

of 0.2119. The result shows that the HTCP method achieves a much superior HitRate outcome than ER methodologies, considering the top-10 k recommendation.

Further, the accuracy outcome is evaluated considering top-20 k recommendations, as shown in Fig. 11. The HTCP achieves a HitRate outcome of 0.5347, and the ER method achieves a HitRate outcome of 0.4038. The result shows that the HTCP method achieves a much superior HitRate outcome than ER methodologies, considering the top-20 k recommendation. The overall result attained considering the top-10 k recommendation, and top-20 k recommendation shows HTCP achieves superior HitRate outcomes considering two dynamic behaviour datasets such as Yoochoose and TMall dataset. Higher HitRate outcome of the HTCP model will help achieve better recommendations for the user and

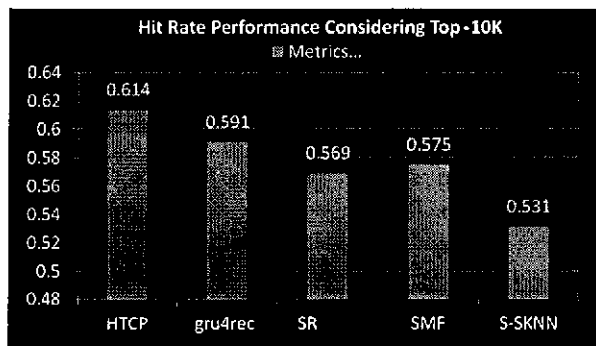


Fig. 8 Average HR performance attained by the HTCP considering the top-10 k recommendation for Yoochoose Dataset

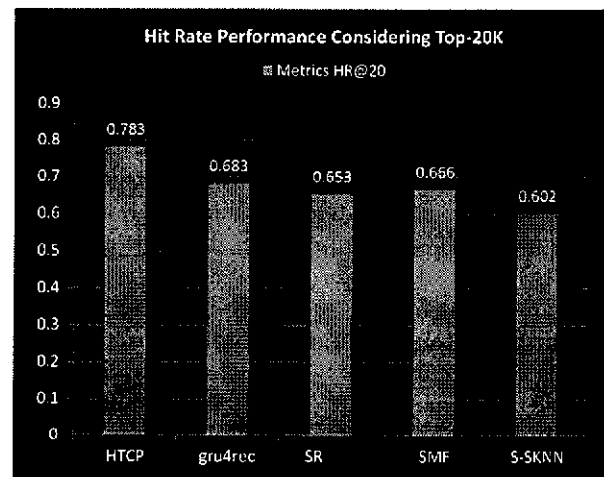


Fig. 9 Average HR performance attained by the HTCP considering the top-20 k recommendation for Yoochoose Dataset

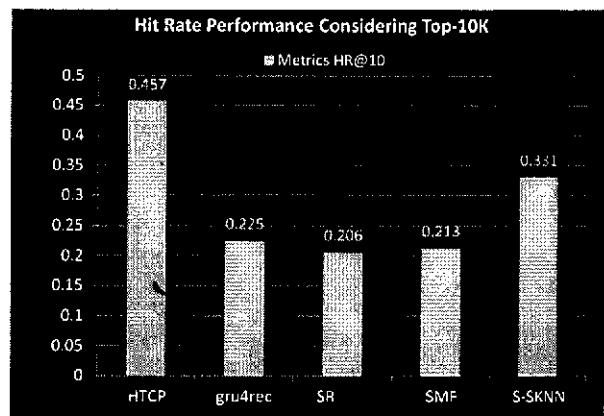


Fig. 10 Hit rate performance considering the top-10 k recommendation for the TMall Dataset

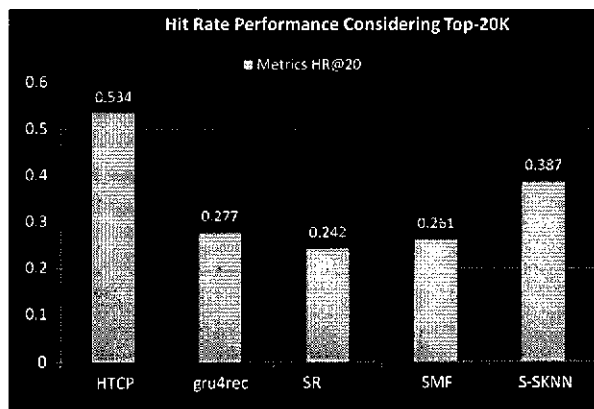


Fig. 11 Hit rate performance considering the top-20 k recommendation for the TMall Dataset

increase the quality of subscribers' experience aiding better profitability of the online shopping portal.

## 6 Conclusion

The research first explores how creating an effective session-based recommendation framework increases the online shopping portal's conversion rate. The comprehensive study shows that RNN is commonly used in numerous current session-based recommendation models with good performance. However, they are not effective for modelling the subscriber's short-term behaviour sequences. It has been presented to boost the efficiency of the hybrid model using RNN. Using FFNN as an attenuation layer for weight optimization in RNN has helped build a better recommendation model. However, the existing hybrid model is not productive for modelling the present ongoing session's suggestions that end in purchases.

To address research issues, the research work demonstrates the usefulness of using hybrid forecasting to combine RNN and FFNN to predict user choices in the current session. It is shown by combining RNN and FFNN, and the hybrid model is sufficient to reduce the issue of cold start and data sparseness in the time-centric recommendation method, which is experimentally proved by experimenting with a better outcome than the existing recommendation models. HTCP has helped solve data sparsity issues using the session window where the model will suggest items based on previous session sequences even though a specific sequence is missing—further, modelling the dynamic behaviour of customers aid in improving the learning efficiency of the time-biased feature of the user's interest in the particular item for certain session intervals. This aids

in extracting significant item feature-sets for a user in the present session.

The experiment is conducted on Yoochoose and the TMall dataset to evaluate the performance accuracy of implemented HTCP over the existing hybrid recommendation model. The results show that, respectively, HTCP and existing hybrid models for the yoochoose dataset achieve the hit-rate efficiency of 0.6145 and 0.595 for top-10 K recommending and 0.7832 and 0.6827 for a Top-20 k recommendation. Also, an average mean reciprocal rate performance of 0.308 and 0.301 for top-10 k recommendations and 0.3945 and 0.308 for top-20 k recommendations is attained by HTCP and the existing hybrid model.

The result shows that the Hit Rate performance of 0.4571 and 0.3312 for top-10 k recommendation is attained by the HTCP and existing hybrid model for the TMall dataset. Similarly, for a top-20 k recommendation, an average hit rate performance of 0.5347 and 0.3871 is attained by HTCP and existing hybrid models for the TMall dataset, respectively. Furthermore, an average mean reciprocal rate performance of 0.1978 and 0.185 for top-10 k recommendations and 0.2984 and 0.1852 for top-20 k recommendations is attained by HTCP and the existing hybrid model for the TMall dataset, respectively.

The overall result shows that significant performance achieved by HTCP over the existing hybrid recommendation model in terms of MMR and HR. Future work would consider performance evaluation considering varied datasets such as Amazon, Movie Lens, etc. Along with would carry out comparative analysis over various state-of-art methods.

## Declarations

**Conflict of interest** I declare that I am the sole author and exclusive owner of my work and declares that the following contribution has No conflict of interest with any commercial product or service related to the submitted article.

## References

1. Aaron Smith MA (2016). Online Shopping and E-Commerce. In: Pew Research Center, December, 2016, "Online Shopping and E-Commerce."
2. Ben-Shimon D, Shapira B, Tsikinovsky A, Rokach L, Friedmann M, Hoerle J (2015) RecSys Challenge 2015 and the YOOCHOOSE Dataset. In: RecSys 2015 - Proceedings of the 9th ACM Conference on Recommender Systems (pp 357–358). Association for Computing Machinery, Inc. <https://doi.org/10.1145/2792838.2798723>
3. Campos PG, Díez F, Cantador I (2014) Time-aware recommender systems: a comprehensive survey and analysis of existing evaluation protocols. *User Modell User-Adapt Interact* 24:67–119. <https://doi.org/10.1007/s11257-012-9136-x>

4. Cheng HT, Koc L, Harmsen J, Shaked T, Chandra T, Aradhye H et al. (2016) Wide & Deep Learning for Recommender Systems. In: DLRS 2016: Proceedings of the 1st Workshop on Deep Learning for Recommender Systems (Vol. 15–Septemb, pp 7–10). <https://doi.org/10.1145/2988450.2988454>
5. Chung J, Gulcehre C, Cho K, Bengio Y (2014) Empirical evaluation of gated recurrent neural networks on sequence modelling. In: Neural and Evolutionary Computing (pp 1–9). <http://arxiv.org/abs/1412.3555>
6. Covington P, Adams J, Sargin E (2016) Deep neural networks for youtube recommendations. In: RecSys 2016 - Proceedings of the 10th ACM Conference on Recommender Systems (pp 191–198). Association for Computing Machinery, Inc. <https://doi.org/10.1145/2959100.2959190>
7. Dai H, Wang Y, Trivedi R, Song L (2016) Recurrent coevolutionary latent feature processes for continuous-time recommendation. In: DLRS 2016: Proceedings of the 1st Workshop on Deep Learning for Recommender Systems (pp 29–34). Association for Computing Machinery. <https://doi.org/10.1145/2988450.2988451>
8. Donkers T, Loepp B, Ziegler J (2017) Sequential user-based recurrent neural network recommendations. In: RecSys 2017 - Proceedings of the 11th ACM Conference on Recommender Systems (pp 152–160). <https://doi.org/10.1145/3109859.3109877>
9. Fu M, Qu H, Yi Z, Lu L, Liu Y (2019) A novel deep learning-based collaborative filtering model for recommendation system. *IEEE Trans Cybernet* 49(3):1084–1096. <https://doi.org/10.1109/TCYB.2018.2795041>
10. Gao C, Jin D, He X, Gan D, Chen X, Feng F et al (2019) Learning to recommend with multiple cascading behaviours. *IEEE Trans Knowl Data Eng.* <https://doi.org/10.1109/tkde.2019.2958808>
11. Ge H, Caverlee J, Lu H (2016). TAPER: A contextual tensor-based approach for personalized expert recommendation hancheng. In: RecSys 2016 - Proceedings of the 10th ACM Conference on Recommender Systems (pp 261–268). <https://doi.org/10.1145/2959100.2959151>
12. He Y, Wang C, Jiang C (2019) Correlated matrix factorization for recommendation with implicit feedback. *IEEE Trans Knowl Data Eng* 31(3):451–464. <https://doi.org/10.1109/TKDE.2018.2840993>
13. Hidasi B, Karatzoglou A (2018) Recurrent Neural Networks with Top-k Gains for Session-based Recommendations. In: CIKM '18: Proceedings of the 27th ACM International Conference on Information and Knowledge Management (pp 843–852). <https://doi.org/10.1145/3269206.3271176>
14. Hidasi B, Karatzoglou A, Baltrunas L, Tikk D (2016) Session-Based Recommendations with Recurrent Neural Networks. In: 4th International Conference on Learning Representations, ICLR 2016 (pp 1–10). <http://arxiv.org/abs/1511.06939>
15. Fang H, Guo G, Zhang S DY (2019) Deep learning-based sequential recommender systems: concepts, algorithms, and evaluations hui. *Deep Learn-Based Sequential Recommend Syst* 577(11496):574–577. <https://doi.org/10.1007/978-3-030-19274-7>
16. Hwangbo H, Kim Y (2019) Session-based recommender system for sustainable digital marketing. *Sustain (Switzerland)* 11(3336):1–19. <https://doi.org/10.3390/SU11123336>
17. Hwangbo H, Kim YS, Cha KJ (2018) Recommendation system development for fashion Retail e-commerce. *Electron Commer Res Appl* 28:94–101. <https://doi.org/10.1016/j.elcrap.2018.01.012>
18. Jannach D, Ludewig M, Lerche L (2017) Session-based item recommendation in e-commerce: on short-term intents, reminders, trends and discounts. *User Modell User-Adapt Interact* 27(3–5):351–392. <https://doi.org/10.1007/s11257-017-9194-1>
19. Kang WC, McAuley J (2018) Self-attentive sequential recommendation. In: Proceedings - IEEE International Conference on Data Mining, ICDM (Vol. 2018–Novem, pp 197–206). <https://doi.org/10.1109/ICDM.2018.00035>
20. Ko YJ, Maystre L, Grossglauser M (2016) Collaborative Recurrent Neural Networks for Dynamic Recommender Systems. In: *Journal of Machine Learning Research* (Vol. 63, pp 366–381).
21. Koren Y (2010). Collaborative Filtering with Temporal Dynamics. In: KDD '09: Proceedings of the 15th ACM SIGKDD international conference on Knowledge discovery and data mining (pp 447–456). <https://doi.org/10.1145/1721654.1721677>
22. Lika B, Kolomvatsos K, Hadjiefthymiades S (2014) Facing the cold start problem in recommender systems. *Exp Syst Appl* 41:2065–2073. <https://doi.org/10.1016/j.eswa.2013.09.005>
23. Liu M, Pan W, Liu M, Chen Y, Peng X, Ming Z (2017) Mixed similarity learning for recommendation with implicit feedback. *Knowl-Based Syst* 119:178–185. <https://doi.org/10.1016/j.knosys.2016.12.010>
24. Mu D, Guo L, Cai X, Hao F (2017) Query-focused personalized citation recommendation with mutually reinforced ranking. *IEEE Access* 6:3107–3119. <https://doi.org/10.1109/ACCESS.2017.2787179>
25. Posts R (2020). Online Retailing : Britain , Europe , US. *The Property Chronicle*. 1–6. <https://www.propertychronicle.com/online-retailing-britain-europe-us-canada-2017/TH>
26. Quadrana M, Karatzoglou A, Hidasi B, Cremonesi P (2017) Personalizing Session-based Recommendations with Hierarchical Recurrent Neural Networks. In: RecSys 2017 - Proceedings of the 11th ACM Conference on Recommender Systems (pp 130–137). <https://doi.org/10.1145/3109859.3109896>
27. Gediminas Adomavicius and Alexander Tuzhilin (2011) Context-Aware Recommender Systems. In: *Recommender Systems Handbook* (pp 217–253). Springer US. <https://doi.org/10.1007/978-0-387-85820-3>
28. Reddy S, Mascia J (2006) Lifetrak: Music In Tune With Your Life. In: Proceedings of the ACM International Multimedia Conference and Exhibition (pp 25–34). <https://doi.org/10.1145/1178745.1178754>
29. Rendle S (2012) Factorization machines with libFM. *ACM Trans Intell Syst Technol.* <https://doi.org/10.1145/2168752.2168771>
30. Rendle S, Freudenthaler C, Gantner Z, Schmidt-Thieme L (2009) BPR: Bayesian personalized ranking from implicit feedback. In: *Information Retrieval* (pp 452–459).
31. Sedhain S, Menon AK, Sanmery S, Xie L (2015) AutoRec: Autoencoders Meet Collaborative Filtering. In: *WWW 2015 Companion - Proceedings of the 24th International Conference on World Wide Web* (pp 111–112). <https://doi.org/10.1145/2740908.2742726>
32. Shams B, Haratizadeh S (2017) Graph-based collaborative ranking. *Exp Syst Appl* 67:59–70. <https://doi.org/10.1016/j.eswa.2016.09.013>
33. Shen J, Karimzadehgan M, Bendersky M, Qin Z, Metzler D (2018) Multi-Task Learning for Email Search Ranking with Auxiliary Query Clustering. In: CIKM '18: Proceedings of the 27th ACM International Conference on Information and Knowledge Management (pp 2127–2136). <https://doi.org/10.1145/3269206.3272019>
34. Shengyu L, Beizhan W, Hongji W, Q H (2018) A Hybrid Collaborative Filtering Algorithm Based On KNN and Gradient Boosting. In: *The 13th International Conference on Computer Science & Education (ICCSE 2018)* (pp 1–5). <https://doi.org/10.1109/ICCSE.2018.8468751>
35. Shi Y, Larson M, Hanjalic A (2014) collaborative filtering beyond the user-item matrix: a survey of the state of the art and future challenges. *ACM Comput Surv* 47(1):1–45. <https://doi.org/10.1145/2556270>
36. Sreenivasa BR, Nirmala CR (2019) Hybrid location-centric e-commerce recommendation model using dynamic behavioural

- traits of customer. *Iran J Comput Sci* 2(3):179–188. <https://doi.org/10.1007/s42044-019-00040-3>
37. Sun Y, Zhang Y (2018) Conversational Recommender System. In: 41st International ACM SIGIR Conference on Research and Development in Information Retrieval, SIGIR 2018 (pp 235–244). <https://doi.org/10.1145/3209978.3210002>
  38. Tan YK, Xu X, Liu Y (2016) Improved recurrent neural networks for session-based recommendations. In: ACM International Conference Proceeding Series (Vol. 15-September-2016, pp 17–22). Association for Computing Machinery. <https://doi.org/10.1145/2988450.2988452>
  39. Wei J, He J, Chen K, Zhou Y, Tang Z (2017) Collaborative filtering and deep learning based recommendation system for cold start items. *Exp Syst Appl* 69:29–39. <https://doi.org/10.1016/j.eswa.2016.09.040>
  40. Young J (2020) US ecommerce sales grow. *Digital Commerce* 360:1–9
  41. Yu F, Liu Q, Wu S, Wang L, Tan T (2016) A Dynamic Recurrent Model for Next Basket Recommendation. In: SIGIR 2016 - Proceedings of the 39th International ACM SIGIR Conference on Research and Development in Information Retrieval (pp 729–732). <https://doi.org/10.1145/2911451.2914683>
  42. Zhu Y, Li H, Liao Y, Wang B, Guan Z, Liu H, Cai D (2017) What to Do Next: Modelling User Behaviours by Time-LSTM. In: Proceedings of the Twenty-Sixth International Joint Conference on Artificial Intelligence (IJCAI-17) (pp 3602–3608).
  43. Jing H, Smola AJ (2017) Neural survival recommender, WSDM 2017 - Proc. 10th ACM Int. Conf. Web Search Data Min., pp 515–524. [doi:https://doi.org/10.1145/3018661.3018719](https://doi.org/10.1145/3018661.3018719)
  44. Massimo Q, Paolo C, Dietmar J (2018) Sequence-Aware Recommender Systems. *ACM Comput. Surv.* 51, 4, Article 66 (September 2018), 36 pages. <https://doi.org/10.1145/3190616>
  45. Geoffray Bonnin and Dietmar Jannach. 2014. Automated Generation of Music Playlists: Survey and Experiments. *ACM Comput. Surv.* 47, 2, Article 26 (January 2015), 35 pages. <https://doi.org/10.1145/2652481>
  46. Mehdi HA, Negar H, Bamshad M, Robin B (2015) Adapting Recommendations to Contextual Changes Using Hierarchical Hidden Markov Models. In: Proceedings of the 9th ACM Conference on Recommender Systems. Association for Computing Machinery, New York, NY, USA, pp 241–244. <https://doi.org/10.1145/2792838.2799684>
  47. Hidasi B, Quadrana M, Karatzoglou A, Tikk D (2016) Parallel recurrent neural network architectures for feature-rich session-based recommendations, RecSys 2016 - Proc. 10th ACM Conf. Recomm. Syst., pp 241–248 <https://doi.org/10.1145/2959100.2959167>

**Publisher's Note** Springer Nature remains neutral with regard to jurisdictional claims in published maps and institutional affiliations.



# Session-based Personalized Recommender System for Online Shopping



B. R. Sreenivasa, C. R. Nirmala, and M. V. Manoj Kumar

## 1 Introduction

The development of web and smartphone innovations have brought about changing how individuals shop. Individuals purchase increasingly more items online through the web or mobile application instead of performing traditional-style shopping. Recommendation systems [1] help customers in taking care of data over-burden by suggesting new things (i.e. products) that suit the client's needs (i.e. favourites) and requirements. Recommendation systems gather data on the client's inclinations for the products in a respective area such as an online shopping environment and movie and afterwards endeavour to forecast what different products the customer is probably going to discover significant (i.e. useful). Data related to customers' inclinations might be procured in an explicit manner through likes/dislikes, a rating, etc. and on. Similarly, the data can be procured in an implicit manner by verifiably observing the customer's activities. The well-known RS methods are content-based, collaborative or by combining multiple methods in designing hybrid methodologies. Collaborative filtering (CF) methodologies [2, 3] depend on the collaborative information of historical information of subscribers as well as of product for carrying out forecasting operation. The content-based methodologies endeavour to forecast products using content features likeness/similarities. The hybrid forecasting method [4,

---

B. R. Sreenivasa (✉)

Department of Information Science and Engineering, Bapuji Institute of Engineering and Technology, Davangere, India

C. R. Nirmala

Department of Computer Science and Engineering, Bapuji Institute of Engineering and Technology, Davangere, India

M. V. Manoj Kumar

Department of Information Science and Engineering, Nitte Meenakshi Institute of Technology, Bangalore, India

© The Author(s), under exclusive license to Springer Nature Singapore Pte Ltd. 2022  
N. R. Shetty et al. (eds.), *Emerging Research in Computing, Information, Communication and Applications*, Lecture Notes in Electrical Engineering 790,  
[https://doi.org/10.1007/978-981-16-1342-5\\_49](https://doi.org/10.1007/978-981-16-1342-5_49)

641

5) generally combines multiple methodologies discussed above for building efficient forecasting designs.

The state-of-the-art forecasting method concentrated on modelling customers' preferences and choices of likeness under users' historical behaviour on particular items and in general and consistently disregards the sequence behaviour data. Consider that shopper inclination/choice changes considering different customers' behaviour sequence. In this way, as opposed to considering one sort of behaviour, for example adding to cart, click stream and buying, there exist different behavioural sequences corresponding to products qualities cases with various conduct towards an item. Thus, it is preliminary to incorporate multiple behaviour sequences and forecast collaboratively what a user will purchase, select or prefer in future considering the certain behavioural context. In recent times, a few endeavours have been placed into creating forecast techniques using customer behaviour sequence data [6, 7]. Nonetheless, none of the current techniques is intended for learning sequence information considering a multi-behaviour sequence by our knowledge. Furthermore, if we straightforwardly treat various behaviours towards a product as different components in sequence, or just disregard the variance among behaviour sets, existing forecasting strategies will pose issues in establishing a correlation concerning behaviour sets and product sets. In [8, 9], utilized artificial intelligence (AI) and recurrent neural network (RNN) for session-based product forecasting. RNN has been widely used in the most existing method as a natural choice for addressing the issue of learning behaviour sequences efficiently. The model is applied to various sequence-based forecasting issues in time series forecasting, signal processing (SP), pattern recognition, etc. in a productive manner. In RS, RNN is widely used for modelling a session-based forecasting environment with good results.

This work focuses on building efficient session-based RS for the e-commerce environment [10]. His work endeavours to establish if a set of products looked into by the customer during an ongoing session is probably going to end with a buy. For meeting real-world challenges and circumstances, the above-discussed problems are challenging because the forecasting model needs to learn inter-product dependencies and its relationship. Recent work modelled based on session-based RS [5, 11] and [12] centre around forecasting future top-k products list of the session, as opposed to foreseeing the utilization purpose/goal. This paper accepts that forecasting the purpose of the customers early in the session may aid the number of strategies improving the session result. For example if the model can predict the session purpose (i.e. if the RS model predicts the user leaves the ongoing session without purchase), then the system might provide a certain discount for changing the mood or intent of the customer. Along with this, this paper addresses the cold-start issues for purchasing purpose forecasting in the current ongoing session where customers' purchase history is not available for new entrant products in the e-commerce environment. This circumstance generally occurs in an e-commerce environment when new products are added frequently. However, these issues have not yet been overcome by existing methodologies. For overcoming research challenges, this work presents a time-centric predication model for online shopping environment using a hybrid learning technique. Research contribution as follows:

- This work presented a time-centric prediction model combining both short and long-term behaviour sequences.
- TCP model attains good performance considering hit rate (HR) and mean reciprocal rate (MRR) concerning state-of-the-art RS methods.

The manuscript is articulated as follows. In Sect. 2, some baseline methods are described. In Sect. 3, the proposed time-centric recommendation model for online shopping portal is presented. In Sect. 4, the experiment is conducted using online shopping portal data and the performance of TCP, and the existing recommendation model is evaluated. The conclusion and future work are described in the last section.

## 2 Literature Baseline Methods

Many research work has been carried out in literature to overcome the shortcomings of traditional recommender system by considering user preferences based on the characteristics of items to provide more accurate recommendations [13], and it is been used in many product-based RS [14], tourisms RS [15], restaurant RS problems [16] and many others. In [17], the author described how the RNN model is used to predict the user next buying pattern based on the previous history log files. To minimize the costs and to increase the prediction accuracy, all older states are combined into single window and keeps only latest states. Quadrana et al. [18] presented a hierarchical recurrent neural network for session-based RS, and it mainly focuses on user identities. Methods based on recurrent neural networks concentrate on session-oriented proposal issues. Out of these techniques, gru4rec is a significant method used for effectively planning for session-based recommendation scenarios [11, 12]. Then, gru4rec constructs gated recurrent units with the help of RNN [19, 20] to predict the likelihood of possible events (e.g. click streams) at the start of every session. The solitary item determines the contribution of the method, which is based on vector in one-hot encoded form and yield. It gives a positioning circulation. Typical GRU layer screens a state that encodes existing items in the same session. While predicting with the help of GRU, the items of a session must be fed of into the system. As far as activation functions, tanh functions to work best for GRU and the ranking layer. Use of RNNs for prediction issues is a characteristic decision. Decision of the loss function and utilization of session parallel mini-batches to accelerate the training phase are key components of the approach.

## 3 Time-Centric Recommendation Model for Online Shopping Portal Environment

This section presents a time-centric prediction/recommendation (TCP) model for online shopping portal using session-centric behaviour information of customers. For

obtaining a relationship between user current session and past behaviour for recommending items, it is important for modelling both short and long-term behaviour contexts (i.e. time-centric HLCP model [21]). As discussed in [21], the RNN model is efficient in modelling the long-term behaviour of the customer. Thus, this work uses RNN for modelling long-term dynamic behaviour. The architecture of the RNN model is shown in Fig. 1. Similarly, in [21] showed that FFNN is efficient in modelling short-term behaviour context of the customer when compared with RNN. Thus, this work uses FFNN for modelling short-term sequence. The architecture of FFNN is shown in Fig. 2.

For capturing the dynamic behaviour of the customer, this paper uses behaviour-based matrices for obtaining feature sets of various sorts of behaviour sets. Then, the illustration of subscriber  $v$  at  $\ell$  is estimated using the following equation

$$i_t^v = \mathcal{X}i_{t-1}^v + \sum_{j=0}^{o-1} \mathcal{D}_j \mathcal{N}_{c_{t-j}^v r_{t-j}^v}, \quad (1)$$

where  $\mathcal{N}_{c_{t-j}^v} \in \mathbb{S}^{p \times o}$  depicts a behaviour-based transition matrix design concerning behaviour on the  $j$ th product of subscriber  $v$ .

The cold-start problem can be addressed by considering  $i_0^v = v_0$ . Further, the existing sequence-based model generally neglects continuous session variance (SV)

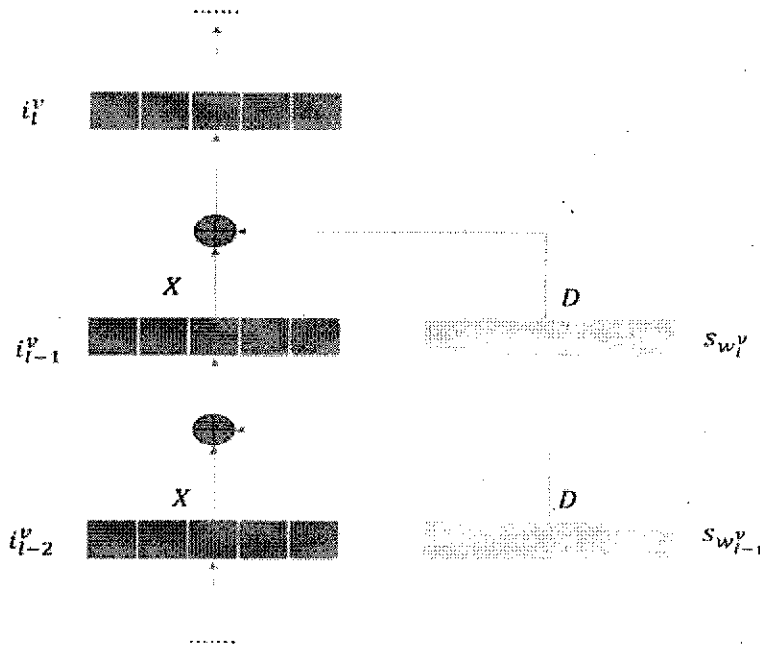
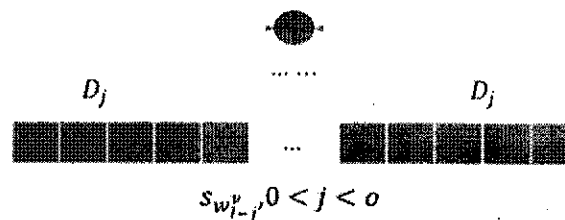


Fig. 1 Architecture of RNN model

**ii**



Using [21], user preference can be learned better considering customer location. However, it is still important to consider incorporating time/session variance data into HLCP. Thus, this work presents an efficient time-centric prediction (TCP) model by substituting location-centric (LC) transition matrices (TM) with session-centric TM's. The TCP model is shown in Fig. 3. From Fig. 3, for a given customer  $v$ , the location  $l$  is computed as follows

$$i_l^v = Xi_{l-o}^v + \sum_{j=0}^{o-1} U_{u_l^v - u_{l-1}^v} S w_{l-j}^v, \quad (2)$$

where  $u_l^v$  depicts the present time,  $u_{l-1}^v$  depicts the time of every product of each layer of TCP, and  $U_{u_l^v - u_{l-1}^v}$  depicts the time-centric TM of time variance  $u_{l-1}^v - u_l^v$  among time  $u_{l-1}^v$  and  $u_l^v$ . The time-centric TM aids in capturing session-specific effects behaviour on the most recent activity log. Further, Eq. (2) is rewritten similarly with the HLCP model as follows

$$i_l^v = Xi_0^v + \sum_{i=0}^{l-1} U_{u_i^v - u_{i-1}^v} s_{w_{i-j}^v}, \quad (3)$$

where  $i_l^v = v_0$  is depicting the preliminary condition of customers. From modelling dynamic behavioural traits, behavioural-centric TM's is used in the TCP model as follows

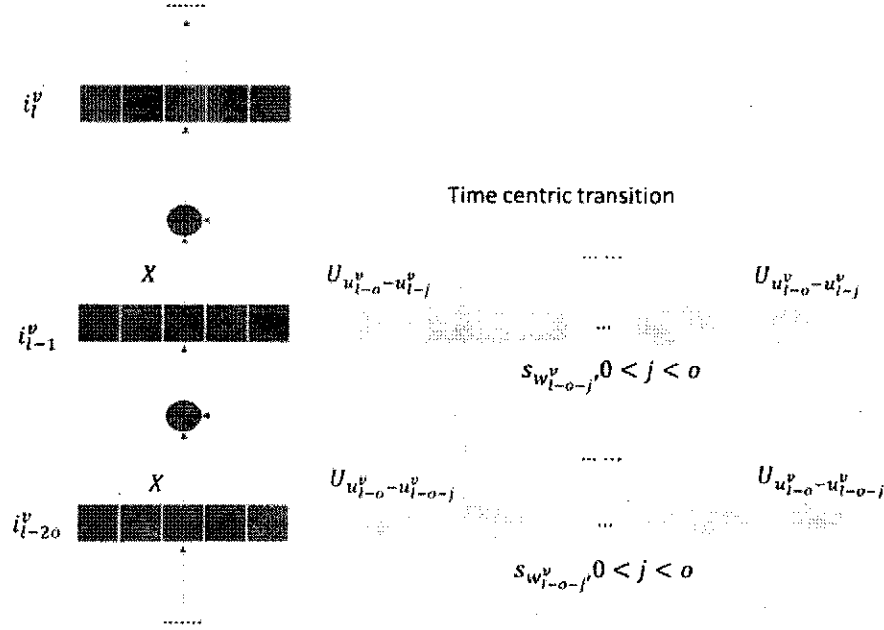


Fig. 3 Architecture of TCP that combines both short and long-term session behaviour sequences

$$i_l^v = X i_{l-o}^v + \sum_{j=0}^{l-1} U_{u_l^v - u_{l-j}^v} N_{c_{l-m}^v} s_{w_{l-j}^v}. \quad (4)$$

Then, carry out forecasting operation whether a customer  $v$  will carry out certain behaviour  $c$  on particular product  $w$  at sequential location  $l+1$  is estimated similarly to HLCP using following equation

$$z_{v,l+1,c,w} = (i_l^v)^U N_{c,w} = (i_l^v + v_v)^U N_{c,w}. \quad (5)$$

The experiment is conducted using an online shopping portal dataset for both proposed TCP and existing recommendation models. The TCP model attains significant recommendation accuracy performance when compared with the existing recommendation model which is experimentally shown below.

#### 4 Experiment Results and Discussions

This section discusses the results of the proposed algorithm and comparison in reference to evaluation benchmark, performance metrics and accuracy based on various standard datasets.



**Table 1** Characteristics of the e-commerce datasets

Dataset RSC15	TMALL
Actions	13.42 M
Sessions	1.77
Items	425,348
Timespan in days	91
Action per session	7.56
Unique items per session	5.56
Action per day	149,096
Session per day	19,719

### Evaluation Protocol and Performance Measures

The general computational error and in session-based recommendation issues are to produce a list of ranked items that in some structure “matches” a given session starting. What speaks to a decent match relies upon the particular application situation. It could be a set of alternative shopping things in an online business situation or a continuation of a given music listening meeting. The experiment is conducted on the Tmall dataset [11]. This dataset was distributed with regards to the Tmall competition and contains user-interaction logs of the tmall.com site for one year. For Tmall, each split comprises of 30 days of training and 1 day of test information. It is one of china’s greatest Internet business web-based interface. Then, the preliminary job of the RS model is to forecast what the customer will buy in the current ongoing session using time-centric prediction and existing recommendation model. The performance of TCP and existing recommendation (ER) methodologies are evaluated using HR and MRR metrics. The characteristics of the data set used for the implementation of the proposed work is shown in Table 1. The Hit Rate and Mean Reciprocal Rank performance for different cases using Tmall dataset is shown in Table 2. Table 3 represents the comparison of of proposed and the existing work. Figures 4 and 5 represents the Mean Reciprocal rank and Hit Rate of the proposed work for Top 20 and 10 recommendations respectively with different iterations.

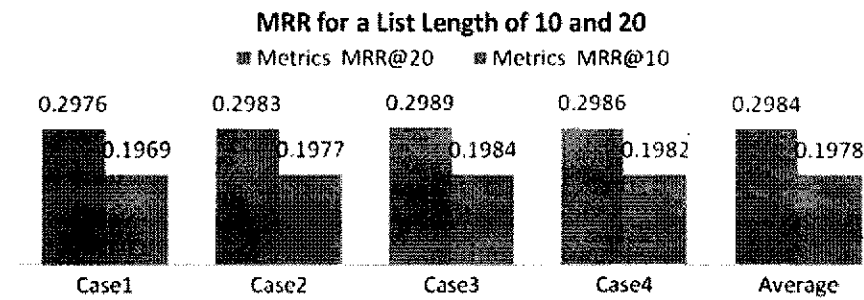
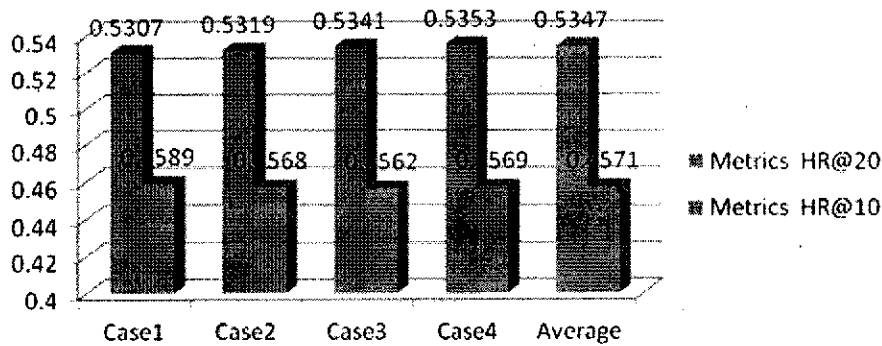
(a) *Hit rate/Accuracy outcome achieved by TCP and ER methodologies:*

**Table 2** Hit rate (HR) and mean reciprocal rank (MRR) for a list length of 10 and 20 obtained for the e-commerce TMALL datasets considering different cases

Case	Metrics	Metrics MRR@20	Metrics HR@20	Metrics MRR@10	Metrics HR@10
Case1	Proposed HTCP	0.2976	0.5307	0.1969	0.4589
Case2		0.2983	0.5319	0.1977	0.4568
Case3		0.2989	0.5341	0.1984	0.4562
Case4		0.2986	0.5353	0.1982	0.4569
Average		<b>0.2984</b>	<b>0.5347</b>	<b>0.1978</b>	<b>0.4571</b>

**Table 3** Result comparison with proposed work and existing work in terms of HR and MRR

Metrics	Metrics MRR@20	Metrics HR@20	Metrics MRR@10	Metrics HR@10
Proposed HTCP	0.2984	0.5347	0.1978	0.4571
Existing gru4rec (ER)	0.1852	0.4038	0.0986	0.2119

**Fig. 4** Mean reciprocal rank for the list length of 20 and 10 with different cases for Tmall dataset**Fig. 5** Hit rate for the list length of 20 and 10 with different cases for Tmall dataset

The accuracy outcome (i.e. HR) of TCP and existing recommendation methodologies is evaluated in this section. The accuracy outcome is evaluated considering top-10 k recommendation as shown in Fig. 6. The TCP achieves an HR outcome of 0.4571, and ER (i.e. existing system (ES)) method achieves an HR outcome of 0.2119. From the result attained, it shows the TCP method achieves much superior HR outcome when compared with ER methodologies considering the top-10 k recommendation. Further, the accuracy outcome is evaluated considering top-20 k recommendation as shown in Fig. 7. The TCP achieves an HR outcome of 0.5347, and the ER method achieves an HR outcome of 0.4038. From the result attained, it shows the TCP method achieves much superior HR outcome when compared with ER methodologies considering the

Fig. 6 Hit rate performance considering the top-10 k recommendation

Hit Rate Performance Considering Top-10K

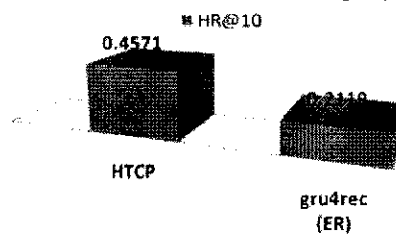
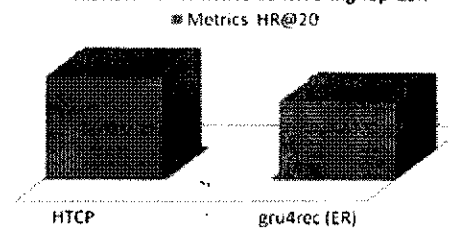


Fig. 7 Hit rate performance considering the top-20 k recommendation

Hit Rate Performance Considering Top-20K



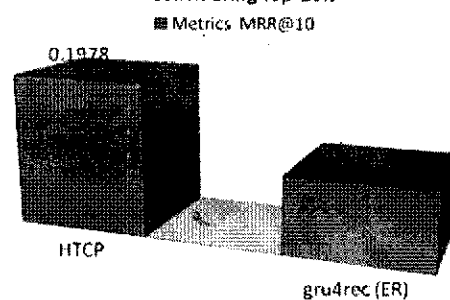
top-20 k recommendation. The overall result attained considering the top-10 k recommendation and top-20 k recommendation shows TCP achieves much superior HR outcomes.

- (b) *Mean reciprocal rate/Accuracy outcome achieved by TCP and ER methodologies:*

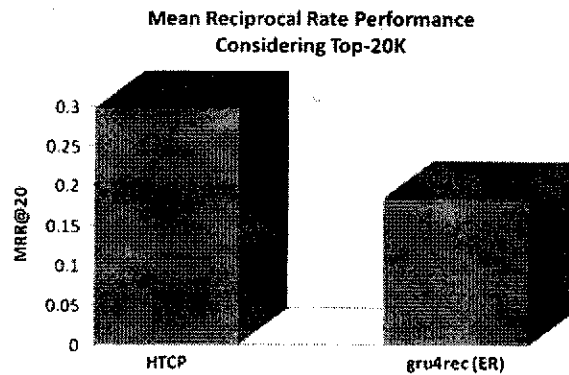
The accuracy outcome (i.e. MRR) of TCP and existing recommendation methodologies is evaluated in this section. The accuracy outcome is evaluated considering top-10 k recommendation as shown in Fig. 8. The TCP achieves an MRR outcome of 0.1978, and the ER method achieves an MRR outcome of 0.0986. From the result attained, it shows the TCP method achieves much superior MRR outcome when compared with ER methodologies considering the top-10 k recommendation.

Fig. 8 Mean reciprocal rate performance considering the top-10 k recommendation

Mean Reciprocal Rate Performance Considering Top-10K



**Fig. 9** Mean reciprocal rate performance considering the top-20 k recommendation



Further, the accuracy outcome is evaluated considering top-20 k recommendation as shown in Fig. 9. The TCP achieves an MRR outcome of 0.2984, and the ER method achieves an MRR outcome of 0.1852. From the result attained, it shows the TCP method achieves much superior MRR outcome when compared with ER methodologies considering the top-20 k recommendation. The overall result attained considering the top-10 k recommendation and top-20 k recommendation shows TCP achieves many superior MRR outcomes. TCP achieving better HR and MRR will aid in improving better profitability for the e-commerce environment.

## 5 Conclusion

Having the option to predict the users short-term interest for an online session is an exceptionally applicable issue practically speaking, which has brought expanded intrigue additionally up in the academic field as of late. Despite the fact that various diverse algorithmic methodologies were proposed throughout the years, no standard benchmark datasets and baseline algorithm exist today. In this work, we have looked at some of the recent and computationally complex calculations for session-based product recommendation. The experiment investigations on various diverse datasets show in many cases one of the simpler methods is able to outperform even the most recent methods based on recurrent neural networks in terms of the prediction accuracy. The work showed the effectiveness of using hybrid forecasting combining RNN and FFNN for forecasting user's choices in the current session. It is seen by combining RNN and FFNN, the hybrid model is efficient enough to minimize the cold-start and data sparseness problems in time-centric recommendation system. The experiment is carried out for evaluating the outcome achieved by the proposed TCP concerning existing recommendation methodologies. The overall result attained describes that HR outcome of 0.4571 and 0.2119 achieved by TCP and ER methodologies, respectively. Then, the HR outcome of 0.5347 and 0.4038 is achieved by TCP and ER methodologies for a list length of 10 and 20, respectively. Along with, MRR outcome

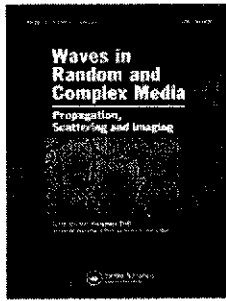
of 0.1978 and 0.0986 and 0.2984 and 0.1852 is achieved by TCP and ER methodologies for a list length of 10 and 20, respectively. Result attained in this work shows that the proposed TCP model is very efficient when compared with ER methodologies considering HR and MMR evaluation metrics. Thus, will aid in improving better productivity (i.e. better sales resulting in good profit) of the e-commerce environment. Further work will study performance evaluation considering varied datasets and also consider refining mathematically the TCP model.

## References

1. Jesús Bobadilla D, Ortega F, Hernando A, Gutiérrez A (2013) Recommender systems survey. *Knowledge-based systems* 46:109–132
2. Herlocker JL, Konstan JA, Borchers A, Riedl J (2017) An algorithmic framework for performing collaborative filtering. In *ACM SIGIR Forum*. vol 51. ACM, pp 227–234
3. Ricci F, Rokach L, Shapira B (2015) Recommender systems: introduction and challenges. In *Recommender systems handbook*. Springer, pp 1–34
4. Jannach D, Ludewig M, Lerche L (2017) Session-based item recommendation in e-Commerce: on short-term intents, reminders, trends, and discounts. *User Model User-Adapt Interact* 27(3–5):351–392. <https://doi.org/10.1007/s11257-017-9194-1>
5. Yu F, Liu Q, Wu S, Wang L, Tan T (2016) A dynamic recurrent model for next basket recommendation. In: *Proceedings of the 39th international ACM SIGIR*
6. REF: Hernández S, Álvarez P, Fabra J, Ezpeleta J (2017) Analysis of users' behavior in structured e-commerce websites. In *IEEE Access* 5:11941–11958
7. Yu X, Jiang F, Du J, Gong D (2017) A user-based cross domain collaborative filtering algorithm based on a linear decomposition model. *IEEE Access* 5:27582–27589
8. Fu M, Qu H, Yi Z, Lu L, Liu Y (2018) A novel deep learning-based collaborative filtering model for recommendation system. *IEEE Trans Cybernet*. <https://doi.org/10.1109/TCYB.2018.2795041>
9. Mu D, Guo L, Cai X, Hao F (2018) Query-focused personalized citation recommendation with mutually reinforced ranking. *IEEE Access* 6:3107–3119
10. Ludewig M, Jannach D (2018) In: *Evaluation of session-based recommendation algorithms*. arXiv preprint arXiv:1803.09587
11. Hidasi B, Karatzoglou A (2017) Recurrent neural networks with top-k gains for session-based recommendations. arXiv preprint arXiv:1706.03847
12. Hidasi B, Karatzoglou A, Baltrunas L, Tikk D (2015) Session-based recommendations with recurrent neural networks. arXiv preprint arXiv:1511.06939
13. Hassan M, Hamada M (2017) A neural networks approach for improving the accuracy of multi-criteria recommender systems. *Appl Sci* 7:868
14. Palanivel K, Sivakumar R (2011) A study on collaborative recommender system using fuzzy-multicriteria approaches. *Int J Bus Inf Syst* 7:419–439
15. Jannach D, Gedikli F, Karakaya Z, Juwig O (2012) Recommending hotels based on multi-dimensional customer ratings. In: *Information and communication technologies in tourism*. Vienna, Austria, Springer, pp 320–331
16. Sanchez-Vilas F, Ismoilov J, Lousame FP, Sanchez E, Lama M (2011) Applying multicriteria algorithms to restaurant recommendation. In *Proceedings of the 2011 IEEE/WIC/ACM international conferences on web intelligence and intelligent agent technology*, Lyon, France, 22–27 August 2011, pp 87–91
17. Adrana M, Karatzoglou A, Hidasi B, Cremonesi P (2017) Personalizing session-based recommendations with hierarchical recurrent neural networks. In: *Recsys* pp 130–137

18. Wu S, Ren W, Yu C, Chen G, Zhang D, Zhu J (2016) Personal recommendation using deep recurrent neural networks in NetEase. In ICDE. pp 1218–1229
19. Malte L, Jannach D (2018) Evaluation of session-based recommendation algorithms. *User Model User-Adapted Interact* 28.4–5:331–390. Crossref. Web.
20. Greenstein-Messica A, Rokach L, Friedman M (2017) Session based recommendations using item embedding. In: *Proceedings of the 22nd international conference on intelligent user interfaces*. ACM, pp 629–633
21. Sreenivasa BR, Nirmala CR (2019) Hybrid location-centric e-Commerce recommendation model using dynamic behavioral traits of customer. *Iran J Comput Sci*. <https://doi.org/10.1007/s42044-019-00040-3>





## Numerical study of heat transfer mechanism in the flow of ferromagnetic hybrid nanofluid over a stretching cylinder

B. R. Sreenivasa, Alaa J. Faqeeh, Abdulmohsen Alsaiani, Hassan A. H. Alzahrani & M. Y. Malik

To cite this article: B. R. Sreenivasa, Alaa J. Faqeeh, Abdulmohsen Alsaiani, Hassan A. H. Alzahrani & M. Y. Malik (2022): Numerical study of heat transfer mechanism in the flow of ferromagnetic hybrid nanofluid over a stretching cylinder, Waves in Random and Complex Media, DOI: [10.1080/17455030.2022.2061084](https://doi.org/10.1080/17455030.2022.2061084)

To link to this article: <https://doi.org/10.1080/17455030.2022.2061084>



Published online: 02 May 2022.



Submit your article to this journal [↗](#)



View related articles [↗](#)



View Crossmark data [↗](#)

## Numerical study of heat transfer mechanism in the flow of ferromagnetic hybrid nanofluid over a stretching cylinder

B. R. Sreenivasa<sup>a</sup>, Alaa J. Faqeeh<sup>b</sup>, Abdulmohsen Alsaiani<sup>c,d</sup>, Hassan A. H. Alzahrani<sup>e</sup> and M. Y. Malik<sup>f</sup>

<sup>a</sup>Department of Information Science, Bapuji Institute of Engineering and Technology, Davanagere, India;

<sup>b</sup>General Studies Department, Jubail Industrial College, Royal Commission, Jubail Industrial City, Saudi Arabia; <sup>c</sup>Centre of Excellence in Desalination Technology, King Abdulaziz University, Jeddah, Saudi Arabia;

<sup>d</sup>Mechanical Engineering Department, King Abdulaziz University, Jeddah, Saudi Arabia; <sup>e</sup>Department of Chemistry, College of Science and Arts at Khulis, University of Jeddah, Jeddah, Saudi Arabia; <sup>f</sup>Department of Mathematics, College of Sciences, King Khalid University, Abha, Saudi Arabia

### ABSTRACT

In electrical and engineering equipment, heat transfer analysis is critical. Scientists and engineers examined many models in this approach for this intent. The use of various solid particles to advance the thermal characteristics of base liquids is being investigated. In this direction, the aluminum alloys (AA7075 and AA7072) are considered nanoparticles suspended in base liquid (50% of ethylene glycol) at room temperature. The influence of chemical reaction and heat source/sink on hybrid nanofluid flow past a stretching cylinder with magnetic dipole and porous medium is analyzed in this current study. The modeling equations are converted to the system of nonlinear coupled ordinary differential equations (ODEs) by choosing appropriate similarity variables. To solve these reduced equations the fourth-fifth order Runge Kutta process is used by adopting a shooting technique. The impact of influencing parameters on respective profiles is explained graphically. The outcomes reveal that the rise in ferromagnetic interaction parameter decreases the fluid velocity but increases the temperature profile. The increase in values of the chemical reaction parameter declines the mass transfer. Finally, the rise in heat generation/absorption parameter decline the heat transfer rate.

### ARTICLE HISTORY

Received 17 August 2021


Accepted 29 March 2022

### KEYWORDS

Hybrid nanofluid; heat source/sink; magnetic dipole; porous medium; stretching cylinder

### Nomenclature

$(u, v)$	Velocity components
$\varepsilon$	Dimensionless Curie temperature
$R$	Radius of the cylinder
$\nu$	Kinematic viscosity
$\mu$	Dynamic viscosity
$K^*$	Porous medium permeability
$\mu_0$	Magnetic permeability

CONTACT Hassan A. H. Alzahrani  hahalzahrani@uj.edu.sa

© 2022 Informa UK Limited, trading as Taylor & Francis Group

$\rho$	Density
$k$	Thermal conductivity
$(\rho C_p)$	Heat capacitance
$M$	Magnetization
$\theta_1(\eta), \theta_2(\eta)$	Dimensionless temperature
$Q_0$	Heat generation/absorption coefficient
$C_f$	Skin friction coefficient
$\sigma$	Chemical reaction parameter
$\chi_1(\eta), \chi_2(\eta)$	Dimensionless Concentration
$Re_x$	Local Reynolds number
$l$	Reference length
$T$	Temperature
$D$	Diffusion coefficient
$C_p$	Specific heat
$f(\eta), f'(\eta)$	Dimensionless fluid velocity
$H$	Magnetic field
$Q$	Heat generation/absorption parameter
$(x, r)$	Directions
$U_0$	Reference velocity
$\psi$	Flow function
$K^{**}$	Porosity parameter
$\lambda$	Viscous dissipation parameter
$\phi_1, \phi_2$	Volume fraction
$\gamma$	Curvature parameter
$Pr$	Prandtl number
$U_w(x)$	Stretching velocity
$K_r$	Reaction rate
$\beta$	Ferromagnetic interaction parameter
$Sc$	Schmidt number
$\rho_M = \nabla \cdot M$	Magnetic charge density

### Subscript

$f$	Fluid
$bf$	Base fluid
$hnf$	Hybrid nanofluid
$\infty$	Ambient
$c$	Curie
$s_1, s_2$	Solid particle

## 1. Introduction

Nanofluids have emerged high heat transfer fluids, containing nanometer-sized particles because of their significant increase in thermal conductivity. Hence, they are used in several applications, such as cooling, microelectronics, transportation, fabrication of computer processors, and military gadgets. These fluids were first studied by Choi and Eastman [1].

Furthermore, high thermally characterized nanofluids such as hybrid nanofluids have been developed, which have stronger thermal conductivity than nanofluids. Li et al. [2] illustrated the homogeneous model for nanofluid behavior with appropriate thermal conditions with nanoparticle shape effect. Yang et al. [3] elaborated the hybrid nanoparticles hydrodynamics. More specifically, Fuzhang et al. [4] presented a numerical report that elucidates the heat transport properties of liquid Aniline-based fluid. The failure and success of gold nanoparticles incorporation inside Ferro/ferricyanide thermogalvanic cells was analyzed by Alzahrani et al. [5]. Madhukesh et al. [6] elaborated on the hybrid nanoliquid flow past a coiled sheet comprising AA7075 and AA7072 nanomaterial alloys. The liquid flow comprising AA7075 and AA7072 nanomaterial alloy was explicated by Khan et al. [7]. Tlili et al. [8] elaborated the nanofluid flow by suspending aluminum alloys in methanol as the carrier liquid.

Ferrofluids are fluids that are suspended with micro-sized particles such as cobalt, magnetite, or iron. Ferro liquids have superparamagnetic characteristics. Moreover, ferrofluids are pertinent in improving the rate of heat transfer and play a substantial role in the electromechanical and chemical fields. Andersson and Valnes [9] scrutinized the ferrofluid flow driven by a sheet that is in contact with a magnetic dipole. Tahir et al. [10] elaborated on the heat transfer in ferromagnetic nanoliquid flow. Nadeem et al. [11] elaborated on the consequence of the magnetic dipole with a radiative flow of ferroliquid. Kumar et al. [12,13] debriefed the ferromagnetic nanoliquid flow with several influencing factors.

A chemical reaction occurs between the working fluid and a foreign mass, which moves due to the stretching of a surface in several chemical engineering processes. The order of a chemical reaction is determined by various parameters, the most basic of which is the first-order reaction, where the reaction rate is proportional to the species concentration. The heat transfer study in nanofluids with chemical reactions has vast practical implications in engineering and scientific fields. The chemical reaction influencing the flow of different liquid models was expounded by Nadeem et al. [14,15]. The chemically reactive flow of nanofluid encountered by a permeable disk was exemplified by Hayat et al. [16]. The chemically reactive stream of nanofluid was elaborated by Gowda et al. [17]. The aspects of fluid flow through stretching cylinders placed in the permeable medium were systematically inspected by many engineers and scientists during the last decades. A permeable stretching cylinder that generates the viscous fluid flow was swotted by Khan et al. [18]. The Dusty fluid stream on a cylinder with nanomaterial suspension was pondered by Kumar et al. [19]. A detailed examination of the thermal behavior of dusty hybrid nanoliquid was done by Gowda et al. [20]. Kumar et al. [21] delineated the ferromagnetic hybrid nanoliquid flow past a cylinder. Muhammad [22] explained the non-Newtonian fluid simulations by open foam by considering flow around a stretchy cylinder. The analysis of heat origination/sink on the liquid flow established by a cylinder was swotted by Rashid et al. [23]. Gowda et al. [24] quizzed the features of heat generation for the fluid flow produced by the plate. The research exposed that the elevation of the Hartmann number enhances the temperature profile. Ramesh et al. [25] conferred the heat generation phenomenon on hybrid nanoliquid flow by an extended cylinder. Khan et al. [26] swotted the heat generation in the micropolar fluid flow through a surface.

To the best of the authors' knowledge, the ferromagnetic hybrid nanoliquid flow through an extending cylinder with heat source/sink, porous medium, and suspended alloy nanoparticles has not yet been published. As is well acknowledged, many approaches are available to provide a few appropriate solutions to this kind of issue. There has never been

a numerical solution for the specified flow. This research gap prompted researchers to employ a numerical technique (RKF-45) and a shooting strategy to study the upshot of effective parameters on the flow characteristics of ferromagnetic hybrid nanofluid. The most important goal of this research is to look at the previously described flow numerically. Finally, the persistence of this work was to address the below-mentioned research questions:

- What influence do different dimensionless parameters have on hybrid nanofluid flow, heat, and mass transport behaviour?
- What impact does an upsurge in different non-dimensional parameters have on the skin friction and Nusselt number?

## 2. Mathematical formulation

The steady-state, incompressible hybrid nanofluid flow over a stretching cylinder with chemical reaction and heat source/sink in the occurrence of a magnetic dipole is considered. Here, AA7072 and AA7075 alloys are chosen as nanoparticles suspended in 50% ethylene glycol. Let  $R$  be the radius of the cylinder with the stretching velocity  $U_w$  be directly related to  $x$ .  $T_w$  is the surface temperature, and the  $T_c$  represents the Curie temperature. We often assume that the Curie temperature is greater than the liquid temperature and that the magnetic field applied is nonuniform. The modeling equations that describe the system are given below (refs. Alshomrani and Ramzan [27], Manjunatha et al. [28])

$$\frac{\partial(ru)}{\partial x} + \frac{\partial(rv)}{\partial r} = 0, \quad (1)$$

$$u \frac{\partial u}{\partial x} + v \frac{\partial u}{\partial r} = \nu_{hnf} \left[ \frac{\partial^2 u}{\partial r^2} + \frac{1}{r} \frac{\partial u}{\partial r} \right] - \frac{\nu_{hnf}}{K^*} u + \frac{\mu_0}{\rho_{hnf}} M \frac{\partial H}{\partial x}, \quad (2)$$

$$u \frac{\partial T}{\partial x} + v \frac{\partial T}{\partial r} + \frac{\mu_0 T}{(\rho C_p)_{hnf}} \frac{\partial M}{\partial T} \left( u \frac{\partial H}{\partial x} + \frac{v}{r} \frac{\partial H}{\partial r} \right) = \alpha_{hnf} \left[ \frac{\partial^2 T}{\partial r^2} + \frac{1}{r} \frac{\partial T}{\partial r} \right] + \frac{Q_0}{(\rho C_p)_{hnf}} (T - T_c), \quad (3)$$

$$u \frac{\partial C}{\partial x} + v \frac{\partial C}{\partial r} = D_f \left[ \frac{\partial^2 C}{\partial r^2} + \frac{1}{r} \frac{\partial C}{\partial r} \right] - k_r (C - C_c), \quad (4)$$

The boundary constraints used in the modeling are

$$\left. \begin{aligned} r = R : v = 0, u = U_w = \frac{U_0 x}{l}, T = T_w, C = C_w \\ r \rightarrow \infty : u = 0, T = T_c, C = C_c \end{aligned} \right\} \quad (5)$$

Now, consider a cylinder with length  $l$ , radius  $R$ , and magnetic field strength intensity  $H$  and is consistently magnetized along its axis with  $M = M_0 i_x$  (ref. Ferdows et al. [29]).

The magnetic field intensity in terms of the scalar magnetic potential  $\varphi_M$  is introduced by

$$H = -\nabla \varphi_M, \quad (6)$$

where

$$\nabla^2 \varphi_M = -\rho_M = -\nabla \cdot M. \quad (7)$$

Here  $\rho_M$  is the magnetic charge density.

The divergence is zero inside the cylinder because of the constant magnetization there. Demonstrating a surrounded area around the surface charge density and shrinking it down leads to  $(M_2 - M_1) \cdot n = -\sigma_M$ . There is no magnetization in the exterior of the cylinder, i.e.  $M_2 = 0$  and inside we know  $M_1 = M_0 \bar{x}$  so that we have:

$$\sigma_M = \pm M_0 \bar{x} \cdot n. \quad (8)$$

In the above equation, the values of  $\sigma_M = +M_0$  on the top of the cylinder,  $\sigma_M = -M_0$  on the bottom of the cylinder,  $\sigma_M = 0$  on the sides of the cylinder.

$$\sigma_M = 0 \quad (9)$$

The general solution for magnetic scalar potential representing the Poisson equation is given by

$$\varphi_M = -\frac{1}{4\pi} \int_V \frac{(r') \rho_M}{r' - r} dv. \quad (10)$$

Along the axis of the cylinder, these integrals become (ref. Ferdows et al. [29])

$$\varphi_M = \frac{M_0}{2} \left[ \left| \frac{2x+l}{2} \right| - \left| \frac{2x-l}{2} \right| - \sqrt{R^2 + \left( \left( \frac{2x+l}{2} \right)^2 \right)} + \sqrt{R^2 + \left( \left( \frac{2x-l}{2} \right)^2 \right)} \right], \quad (11)$$

$$-\nabla \varphi_M = H = -\frac{M_0}{2} \left[ -\frac{\frac{2x+l}{2}}{\left| \frac{2x+l}{2} \right| \sqrt{R^2 + \left( \frac{2x+l}{2} \right)^2}} - \frac{\frac{2x-l}{2}}{\left| \frac{2x-l}{2} \right| \sqrt{R^2 + \left( \frac{2x-l}{2} \right)^2}} \right]. \quad (12)$$

For,  $-l/2 < x < l/2$  the magnetic field strength intensity is

$$H_x = -\frac{M_0}{2} \left[ 2 - \frac{\frac{2x+l}{2}}{\sqrt{\left( \frac{2x+l}{2} \right)^2 + R^2}} + \frac{\frac{2x-l}{2}}{\sqrt{R^2 + \left( \frac{2x-l}{2} \right)^2}} \right], \quad (13)$$

and the gradient of  $H$  is given by

$$\frac{\partial H}{\partial x} = -\frac{3lx}{R^3} \frac{M_0}{2}. \quad (14)$$



Similarity variables are as follows

$$\left. \begin{aligned} \xi &= \sqrt{\left(\frac{U_0}{\nu_f l}\right)} x, \eta = \left(\frac{r^2 - R^2}{2R}\right) \sqrt{\left(\frac{U_0}{\nu_f l}\right)}, M = K(T_c - T) \\ \theta(\xi, \eta) &= \theta_1(\eta) + \xi^2 \theta_2(\eta) = \frac{T_c - T}{T_c - T_w}, \\ \chi(\xi, \eta) &= \chi_1(\eta) + \xi^2 \chi_2(\eta) = \frac{C_c - C}{C_c - C_w}. \end{aligned} \right\} \quad (15)$$

The physical flow function is associated with the velocity components  $u$  and  $v$ .  $\psi = R\sqrt{(U_w \nu_f x)} f(\eta)$  and takes the following form

$$\begin{aligned} u &= \frac{1}{r} \frac{\partial \psi}{\partial r} = \frac{U_0 x}{l} f'(\eta) = U_w f'(\eta), \\ v &= -\frac{1}{r} \frac{\partial \psi}{\partial x} = -\frac{R}{l} \sqrt{\left(\frac{\nu_f U_0}{l}\right)} f(\eta). \end{aligned}$$

Employing these similarity transformations, Equation (1) is automatically satisfied. The remaining equations takes the following form

$$\varepsilon_1 [2\gamma \eta f'''' + f'''' + 2\gamma f''] - [f'^2 - ff''] - \varepsilon_2 \beta \theta_1 - \varepsilon_1 K^{**} f' = 0, \quad (16)$$

$$\varepsilon_3 \frac{k_{hnf}}{k_f} \frac{1}{Pr} [(2\eta\gamma + 1)\theta_1'' + 2\gamma\theta_1'] + f\theta_1' + \varepsilon_3 Q_0 \theta_1 = 0, \quad (17)$$

$$\varepsilon_3 \frac{k_{hnf}}{k_f} \frac{1}{Pr} [(2\eta\gamma + 1)\theta_2'' + 2\gamma\theta_2'] + [f\theta_2' - 2f'\theta_2] + \varepsilon_3 \frac{1}{Pr} \beta \lambda (\varepsilon - \theta_1) f' + \varepsilon_3 Q \theta_2 = 0, \quad (18)$$

$$\frac{1}{Sc} [(2\eta\gamma + 1)\chi_1'' + 2\gamma\chi_1'] + f\chi_1' - \sigma \chi_1 = 0, \quad (19)$$

$$\frac{1}{Sc} [(2\eta\gamma + 1)\chi_2'' + 2\gamma\chi_2'] + [f\chi_2' - 2f'\chi_2] - \sigma \chi_2 = 0, \quad (20)$$

$$\varepsilon_1 = \frac{1}{\left[ (1 - \phi_2) \left[ (1 - \phi_1) + \phi_1 \frac{\rho_{s1}}{\rho_f} \right] + \phi_2 \frac{\rho_{s2}}{\rho_f} \right] (1 - \phi_1)^{2.5} (1 - \phi_2)^{2.5}},$$

$$\varepsilon_2 = \frac{1}{(1 - \phi_2) \left[ (1 - \phi_1) + \phi_1 \frac{\rho_{s1}}{\rho_f} \right] + \phi_2 \frac{\rho_{s2}}{\rho_f}},$$

$$\varepsilon_3 = \frac{1}{(1 - \phi_2) \left[ (1 - \phi_1) + \phi_1 \left( \frac{(\rho C_p)_{s1}}{(\rho C_p)_f} \right) \right] + \phi_2 \frac{(\rho C_p)_{s2}}{(\rho C_p)_f}},$$

where we have equated coefficients of equal powers of  $\xi$  up to  $\xi^2$ .

With corresponding associated boundary constraints

$$\left. \begin{aligned} f(0) &= 0, f'(0) = 1, \theta_1 = 1, \theta_2 = 0, \chi_1 = 1, \chi_2 = 0, \\ f'(\infty) &\rightarrow 0, \theta_1(\infty) \rightarrow 0, \theta_2(\infty) \rightarrow 0, \chi_1(\infty) \rightarrow 0, \chi_2(\infty) \rightarrow 0. \end{aligned} \right\} \quad (21)$$

The non-dimensional parameters in the flow model are as follows

$$\gamma = \sqrt{\frac{l\nu_f}{U_0 R^2}}, K^{**} = \frac{\nu_f l}{K^* U_0}, Pr = \frac{\mu_f C_p}{k_f}, \beta = \frac{3 M_0 \mu_0 K (T_c - T_w) l^3}{2 \rho_f R^3 U_0^2},$$

$$\varepsilon = \frac{T_c}{(T_c - T_w)}, \lambda = \frac{U_0 \mu_f^2}{l k_f \rho_f (T_c - T_w)}, Sc = \frac{\nu_f}{D_f}, Q = \frac{Q_0 l}{\rho C_p U_0}, \sigma = \frac{k_f l}{U_0} \text{ and } Re = \frac{U_0 x^2}{\nu l}.$$

Engineering significant quantities, such as, rate of mass transfers, rate of heat transfer, and skin friction in their non-dimensional form are as follows

$$Re^{-1/2} Sh = -(\chi'_1 + \xi^2 \chi'_2), \quad (22)$$

$$Re^{-1/2} Nu = -\frac{k_{hnt}}{k_f} (\theta'_1 + \xi^2 \theta'_2), \quad (23)$$

$$Re^{1/2} C_f = -\frac{f''(0)}{(1 - \phi_1)^{2.5} (1 - \phi_2)^{2.5}}. \quad (24)$$

### 3. Numerical method

Although not all boundary value issues can be addressed analytically, a well-defined initial value problem (IVP) is very simple to solve. The shooting technique and the Runge-Kutta scheme are used to get numerical solutions. By selecting appropriate similarity variables, the modeling equations are simplified to a collection of nonlinear ODEs. The reduced Equations (16)–(20) are first reduced into IVP using the following substitutions  $f = y_1, f' = y_2, f'' = y_3, \theta_1 = y_4, \theta'_1 = y_5, \theta_2 = y_6, \theta'_2 = y_7, \chi_1 = y_8, \chi'_1 = y_9, \chi_2 = y_{10}, \chi'_2 = y_{11}$ .

$$y'_1 = y_2,$$

$$y'_2 = y_3,$$

$$y'_3 = \frac{-\varepsilon_1 2\gamma y_3 + [y_2^2 - y_1 y_3] + \varepsilon_2 \beta y_4 + \varepsilon_1 K^{**} y_2}{\varepsilon_1 (2\gamma\eta + 1)},$$

$$y'_4 = y_5,$$

$$y'_5 = \frac{-\varepsilon_3 \frac{k_{hnt}}{k_f} 2\gamma y_5 + Pr[-y_1 y_5 - \varepsilon_3 Q_0 y_4]}{\varepsilon_3 \frac{k_{hnt}}{k_f} (2\eta\gamma + 1)},$$

$$y'_6 = y_7,$$

$$y'_7 = \frac{-\varepsilon_3 \frac{k_{hnt}}{k_f} 2\gamma y_7 - Pr[y_1 y_7 - 2y_2 y_6] - \varepsilon_3 \beta \lambda (\varepsilon - y_4) y_2 - Pr \varepsilon_3 Q_0 y_6}{\varepsilon_3 \frac{k_{hnt}}{k_f} (2\eta\gamma + 1)},$$

$$y'_8 = y_9,$$

$$y'_9 = \frac{-\varepsilon_4 2\gamma y_9 - Sc y_1 y_9 + Sc \sigma y_8}{\varepsilon_4 (2\eta\gamma + 1)},$$

$$y'_{10} = y_{11},$$

**Table 1.** Comparison of  $-f''(0)$  for some reduced cases.

		$-f''(0)$
Previously published results	Zeeshan and Majeed [30]	0.6058427
	Olanrewaju [31]	0.605848
	Pal and Mondal [32]	0.615066
Present results		0.606938

**Table 2.** Thermophysical properties of hybrid nanofluid (ref. Tilili et al. [8]).

$\frac{\rho_{hnf}}{\rho_f} = (1 - \phi_2) \left[ (1 - \phi_1) + \phi_1 \frac{\rho_{s1}}{\rho_f} \right] + \phi_2 \frac{\rho_{s2}}{\rho_f}$
$\mu_{hnf} = \frac{\mu_f}{(1 - \phi_1)^{2.5} (1 - \phi_2)^{2.5}}$
$\frac{(\rho C_p)_{hnf}}{(C_p \rho)_f} = (1 - \phi_2) \left[ (1 - \phi_1) + \phi_1 \left( \frac{(\rho C_p)_{s1}}{(\rho C_p)_f} \right) \right] + \phi_2 \frac{(\rho C_p)_{s2}}{(\rho C_p)_f}$
$\frac{k_{bf}}{k_f} = \frac{k_{s1} + 2k_f - 2\phi_1(k_f - k_{s1})}{k_{s1} + 2k_f + \phi_1(k_f - k_{s1})}$
$\frac{k_{hnf}}{k_{bf}} = \frac{k_{s2} + 2k_{bf} - 2\phi_2(k_{bf} - k_{s2})}{k_{s2} + 2k_{bf} + \phi_2(k_{bf} - k_{s2})}$

$y'_{11} = \frac{-\epsilon_4 2\gamma y_{11} - 5c[y_1 y_{11} - 2y_2 y_{10}] + 5c_0 y_{10}}{(2\eta\gamma + 1)\epsilon_4}$ , along with corresponding boundary constraints  
Equation (21) as

$$\left[ \begin{aligned} y_1(0) = 0, y_2(0) = 1, y_4 = 1, y_6 = 0, y_8 = 1, y_{10} = 0, \\ y_2(\infty) \rightarrow 0, y_4(\infty) \rightarrow 0, y_6(\infty) \rightarrow 0, y_8(\infty) \rightarrow 0, y_{10}(\infty) \rightarrow 0. \end{aligned} \right]$$

Here, to satisfy the far-field boundary constraints asymptotically, we pick an optimum finite  $\eta_\infty$  value. In the current investigation, the appropriate definite value of  $\eta_\infty$  is contemplated to be  $\eta_\infty < 8$  so that numerical solutions not only changed but also the defined conditions are equally satisfying. During the computation, the convergence criterion is  $10^{-6}$  with the step size  $\Delta\eta = 0.001$ , and the CPU time to calculate the values of profiles in the modeled problem is up to 2.05 s. We have related the obtained numerical results to published work (see Table 1).

#### 4. Discussion

This section explains how to represent important pertinent parameters on involved gradients graphically. Here, a mix of Aluminum and Zinc in the proportions 98 and 1 with added metals Silicon, ferrous, and Copper yields AA7072 alloy. Correspondingly, in the proportion

**Table 3.** Thermophysical properties of base liquid and alloys (refs. Tilili et al. [8] and Gholinia et al. [33]).

Physical properties	50% C <sub>2</sub> H <sub>6</sub> O <sub>2</sub>	AA7072	AA7075
P	1063.8	2720	2810
k	0.387	222	173
C <sub>p</sub>	3630	893	960
Pr	20.1	—	—

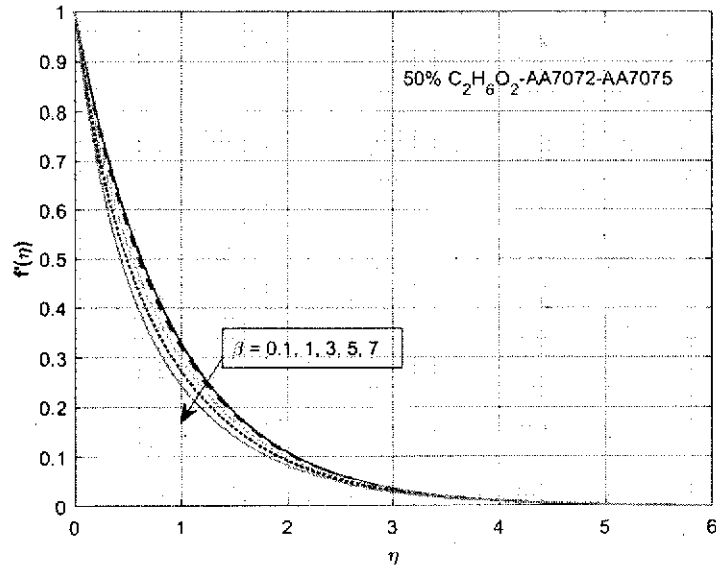


Figure 1. Leverage of  $\beta$  on  $f'(\eta)$ .

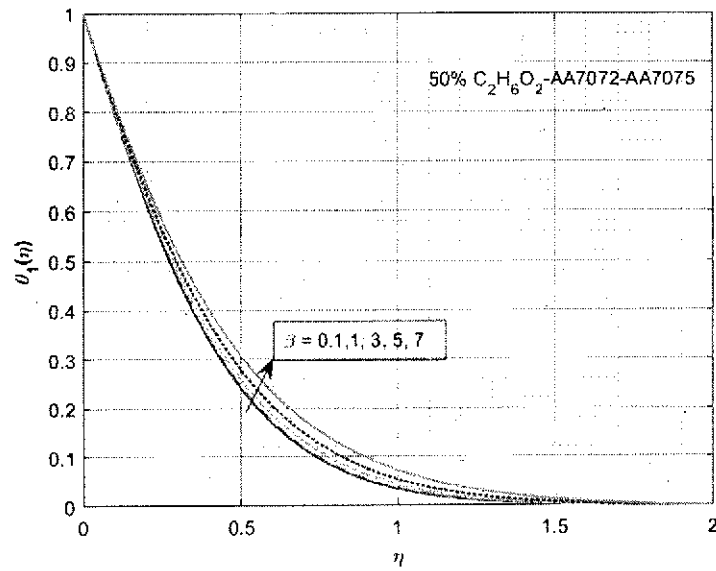
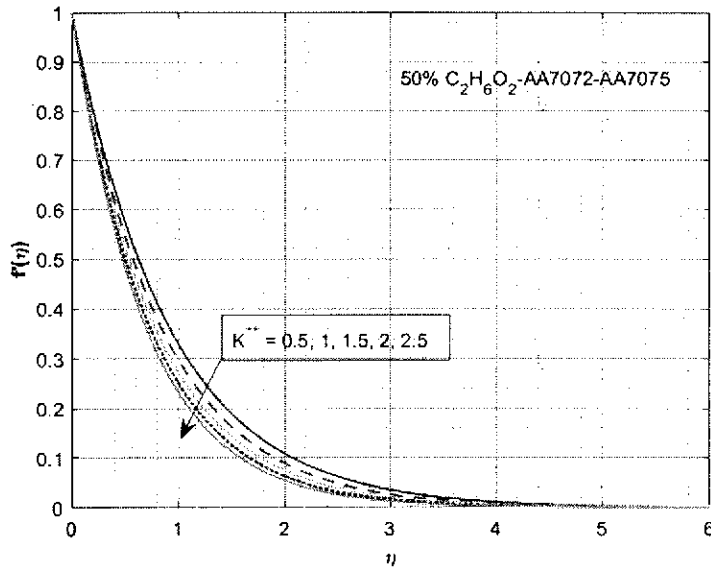
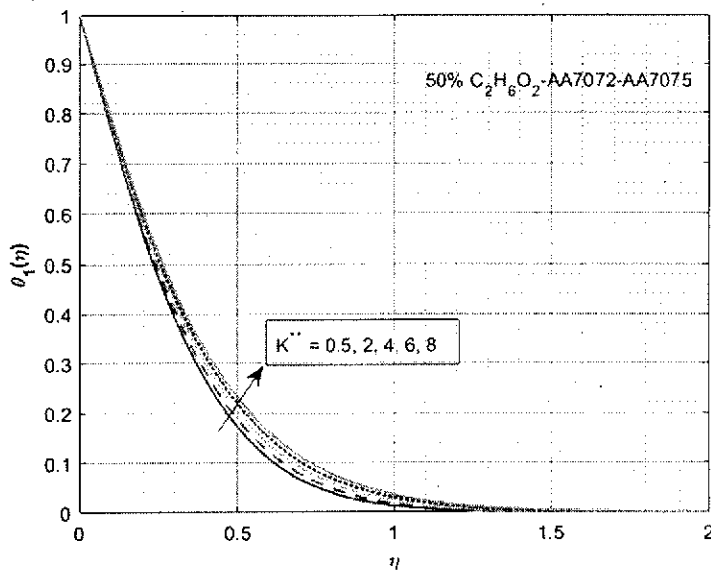


Figure 2. Leverage of  $\beta$  on  $\theta_1(\eta)$ .

of  $\sim 90$ ,  $\sim 1$ ,  $\sim 6$ , and  $\sim 3$ , of Aluminum, Copper, Zinc, and Magnesium with additional metals, Silicon ferrous and Magnesium yields AA7075 alloy. Tables 2 and 3 show the physical characteristics of these alloys and base liquids. In this study, the value of  $Pr = 20.1$  (at room temperature),  $K^{**} = 0.5$ ,  $\gamma = 1$ ,  $Sc = 0.9$ ,  $Q = 0.02$ ,  $\sigma = 0.15$ , and  $\beta = 0.5$  remains constant unless otherwise mentioned in the graph.

Figure 3. Leverage of  $K^{**}$  on  $f'(\eta)$ .Figure 4. Leverage of  $K^{**}$  on  $\theta_1(\eta)$ .

The impact of  $\beta$  on velocity field is revealed in Figure 1. The rise in  $\beta$  drops the velocity. Physically, while the magnetic effect is zero, the liquid velocity is increased. The liquid velocity lessens as the magnetic dipole upshot rises. The magnetic field presence acts as a delaying force on velocity, and this force grows as  $\beta$  increases. Following that, the velocity diminutions. Figure 2 shows the behavioral pattern of heat transfer for booming  $\beta$  values. Here, escalation in  $\beta$  improves the heat transfer. For the increased  $\beta$ , the nanofluid

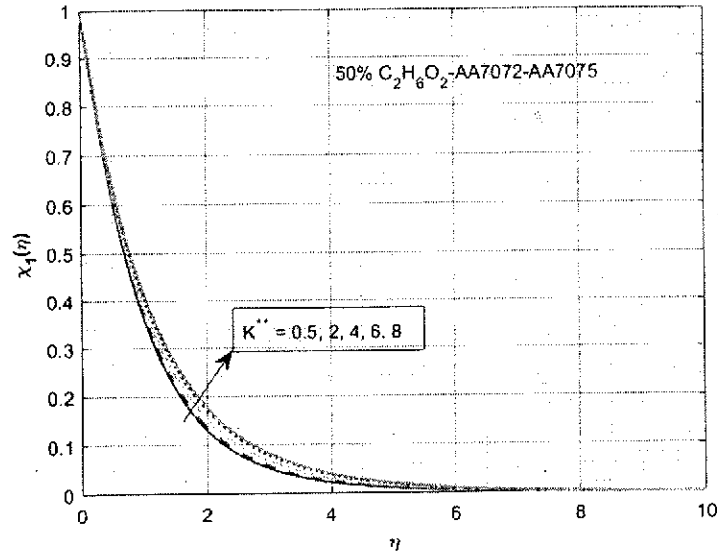


Figure 5. Leverage of  $K^{**}$  on  $\chi_1(\eta)$ .

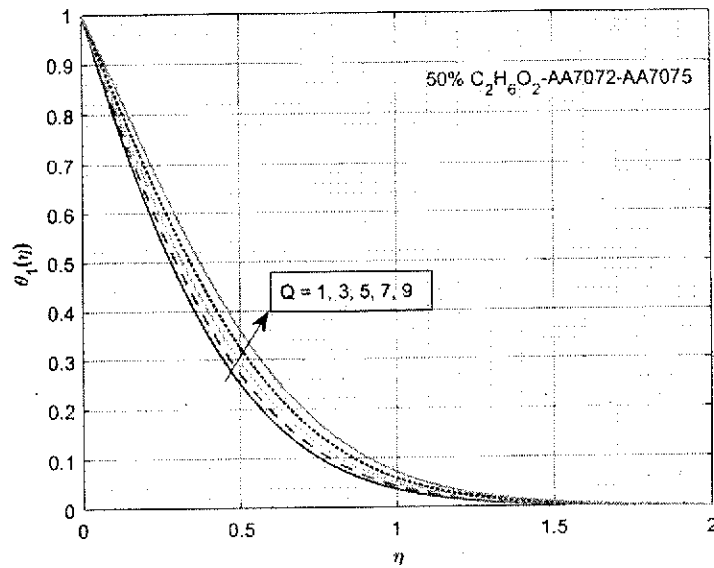
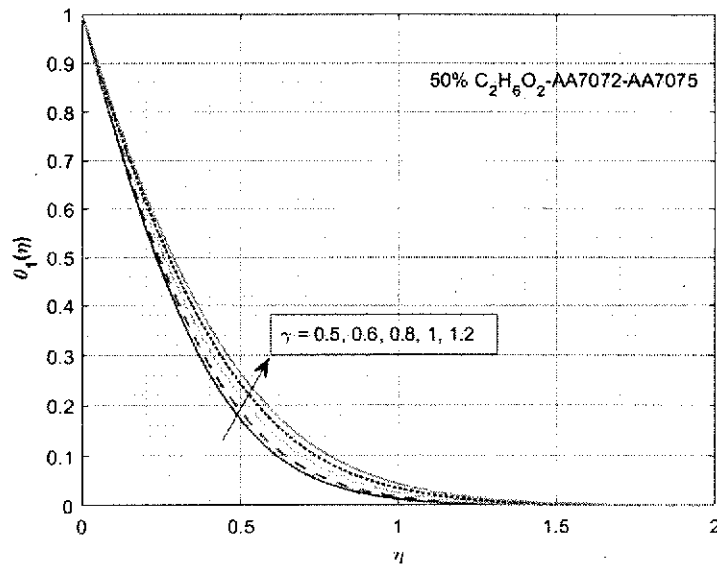
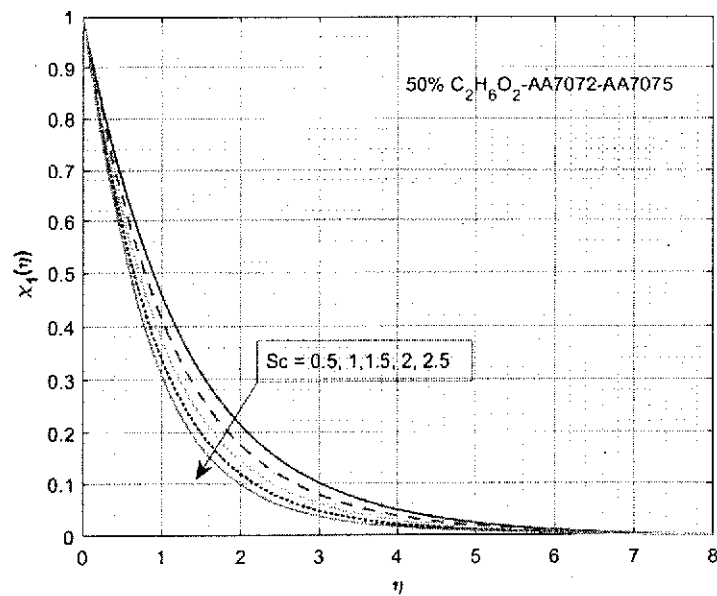


Figure 6. Leverage of  $Q$  on  $\theta_1(\eta)$ .

temperature rises in the existence of the magnetic dipole. Also, the interaction between nanoparticles and magnetic field action thins the axial velocity, increasing frictional heating among fluid layers, and ensuing in a rise in the thermal profile.

Porosity is defined as the relation between the filled and empty space of a permeable medium. Figure 3 portrays the stimulation of  $K^{**}$  on typical profile of velocity. The gain in  $K^{**}$  weakens the velocity. The porosity component's increasing values enhance the system's resistance. This enhanced resistance lowers the velocity. The stimulation of  $K^{**}$  on

Figure 7. Leverage of  $\gamma$  on  $\theta_1(\eta)$ .Figure 8. Leverage of  $Sc$  on  $\chi_1(\eta)$ .

heat passage is presented in Figure 4. The growth in  $K^{**}$  values intensifies the heat transfer. It is apparent that the occurrence of pervious medium reasons for the advanced restraint to the liquid stream results in the decay of fluid velocity, and because of this, there is an upsurge in the heat transfer. The stimulation of  $K^{**}$  on mass transference is observed in Figure 5. The increase in value of  $K^{**}$  increases the mass transference. Here, the rise in



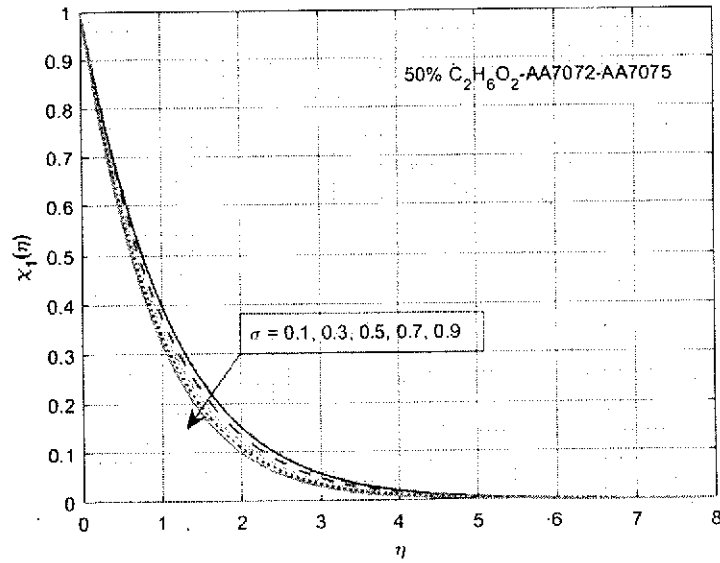


Figure 9. Leverage of  $\sigma$  on  $\chi_1(\eta)$ .

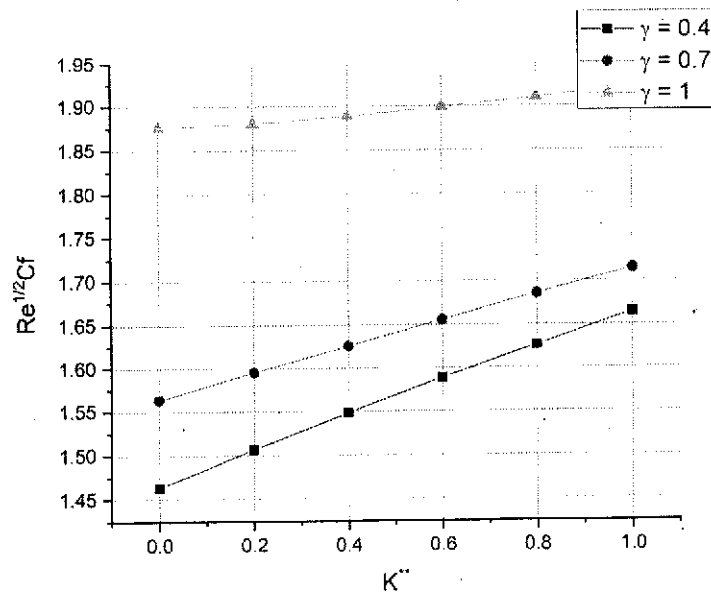


Figure 10. Leverage of  $\gamma$  on  $Re^{1/2}C_f$  versus  $K^{**}$ .

$K^{**}$  increases the concentration gradient near the surface resulting in an away movement of nanoparticles.

The variation in thermal profile for varied  $Q$  values is offered in Figure 6. The growth in  $Q$  rises the transport of heat. In this case, a rise in  $Q$  creates more heat, which increases the flow's heat passage assets, leading to an increase in heat transfer. The heat source strength

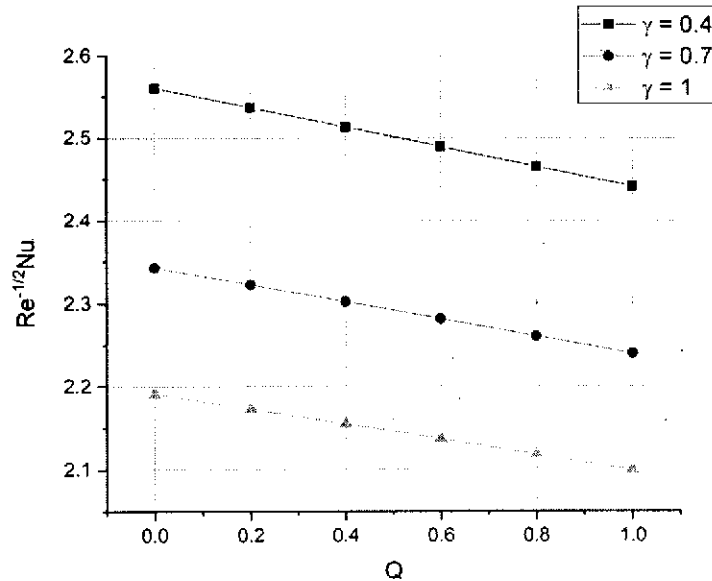


Figure 11. Leverage of  $\gamma$  on  $Re^{-1/2}Nu$  versus  $Q$ .

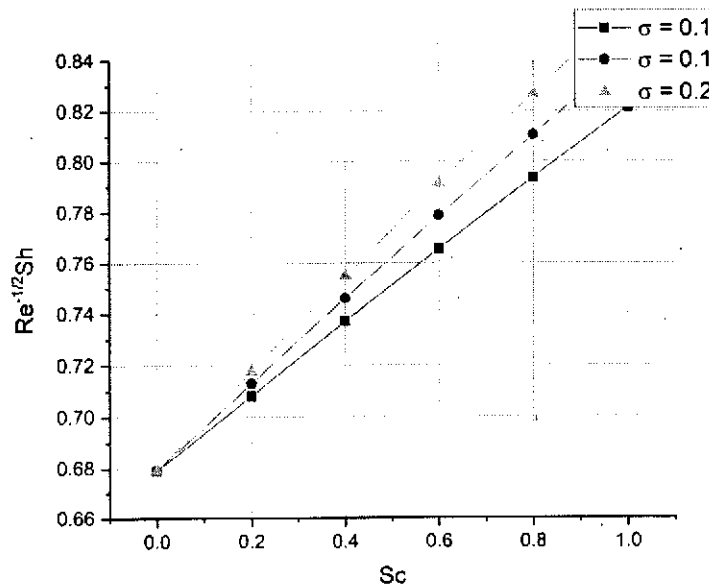


Figure 12. Leverage of  $\sigma$  on  $Re^{-1/2}Nu$  versus  $Sc$ .

increases, resulting in a greater thermal diffusion layer and perhaps a higher heat transport. The upshot of  $\gamma$  on heat transfer is portrayed in Figure 7. The boom in  $\gamma$  enhances the heat passage. Larger  $\gamma$  increase the thickness of the thermal barrier layer, decreasing heat transmission and increasing heat transfer from a physical standpoint. Here, raising the curvature parameter increases the heat transfer rate, resulting in a lower temperature profile at the surface but an increase in temperature profile away from the surface. The leverage

of  $Sc$  on mass transport is exposed in Figure 8. The advance in  $Sc$  values decays the mass transference. The upward value of  $Sc$  upsurges momentum diffusivity and reasons for the mass transport decline. The stimulation of  $\sigma$  on mass distribution is exemplified in Figure 9. It should go without saying that as the  $\sigma$  grows, the concentration profile diminishes. The mass transfer grows feeblers in a chemical reaction. As  $\sigma$  grows, the concentration boundary layer becomes thinner. As can be seen from the graph, increasing values of  $\sigma$  produce a decrease in the concentration of chemical species in the interface layer.

The deviation in  $C_f Re^{1/2}$  versus  $K^{**}$  and  $\gamma$  is shown in Figure 10. Here it is founded that  $C_f Re^{1/2}$  enhances rising values of  $\gamma$  versus  $K^{**}$ . Here, the friction factor acts as an escalating function of  $K^{**}$  and  $\gamma$ . Also, a sudden increase in skin friction is observed for  $\gamma = 1$ . Figure 11 displays the impact of  $\gamma$  against  $Q$  for heat transfer rate/Nusselt number. Here, the rise in  $\gamma$  declines the Nusselt number. Also, as  $\gamma$  grows, the thermal boundary layer thickness near the surface decreases, increasing away from the surface. The change in  $Sh Re^{-1/2}$  versus  $\sigma$  and  $Sc$  is revealed in Figure 12. Here,  $Sh Re^{-1/2}$  improves budding values of  $\sigma$ . Here,  $Sh Re^{-1/2}$  increases in  $Sc$  and  $\sigma$  values.

## 5. Conclusions

Here, we investigated the impact of heat sink/source on chemically reacting ferromagnetic hybrid nanofluid flow past a stretching cylinder with a magnetic dipole in a porous medium. AA7072 and AA7075 aluminum alloys submerged in 50% ethylene glycol are considered in the modeling. The behavior of involved profiles is scrutinized graphically. The key findings of the present study are as follows:

- A rise in  $K^{**}$  declines the liquid velocity and improves the heat and mass transport.
- The increase in  $\beta$  drops the fluid velocity but augments the temperature profile.
- Increase in values of  $Q$  improves the thermal field.
- The rise in  $\gamma$  and  $Q$  drops the heat transfer rate.
- The growth in values of  $Sc$  and  $\sigma$  drops the mass transfer.
- The upsurge in  $Sc$  and  $\sigma$  progresses the rate of mass transfer.

## Acknowledgements

The authors gratefully acknowledge technical and financial support from the Ministry of Education and King Abdulaziz University, Jeddah, Saudi Arabia, for funding this work through the research group programme under grant number IFPRC-149-135-2020.


## Disclosure statement

No potential conflict of interest was reported by the author(s).

## Funding

This research work was funded by the Institutional Fund Projects King Abdulaziz University, Jeddah, Saudi Arabia Under Grant Number IFPRC-149-135-2020.

## ORCID

Hassan A. H. Alzahrani  <http://orcid.org/0000-0002-0999-8351>

## References

- [1] Choi SUS, Eastman JA. Enhancing thermal conductivity of fluids with nanoparticles. Argonne (IL): Argonne National Lab; 1995.
- [2] Li F, Muhammad N, Abohamzeh E, et al. Finned unit solidification with use of nanoparticles improved PCM. *J Mol Liq.* 2020;314:113659. DOI:10.1016/j.molliq.2020.113659
- [3] Yang J, Abdelmalek Z, Muhammad N, et al. Hydrodynamics and ferrite nanoparticles in hybrid nanofluid. *Int Commun Heat Mass Transf.* 2020;118:104883. DOI:10.1016/j.icheatmasstransfer.2020.104883
- [4] Fuzhang W, Ali S, Nadeem S, et al. Numerical analysis for the effects of heat transfer in modified square duct with heated obstacle inside it. *Int Commun Heat Mass Transf.* 2021;129:105666. DOI:10.1016/j.icheatmasstransfer.2021.105666
- [5] Alzahrani HAH, Buckingham MA, Marken F, et al. Success and failure in the incorporation of gold nanoparticles inside ferri/ferrocyanide thermogalvanic cells. *Electrochem Commun.* 2019;102:41–45. DOI:10.1016/j.elecom.2019.03.007
- [6] Madhukesh JK, Naveen Kumar R, Punith Gowda RJ, et al. Numerical simulation of AA7072-AA7075/water-based hybrid nanofluid flow over a curved stretching sheet with Newtonian heating: a non-Fourier heat flux model approach. *J Mol Liq.* 2021;335:116103. DOI:10.1016/j.molliq.2021.116103
- [7] Khan U, Zaib A, Khan I, et al. Comparative investigation on MHD nonlinear radiative flow through a moving thin needle comprising two hybridized AA7075 and AA7072 alloys nanomaterials through binary chemical reaction with activation energy. *J Mater Res Technol.* 2020;9(3):3817–3828. DOI:10.1016/j.jmrt.2020.02.008
- [8] Tilili I, Nabwey HA, Ashwinkumar GP, et al. 3-D magnetohydrodynamic AA7072-AA7075/methanol hybrid nanofluid flow above an uneven thickness surface with slip effect. *Sci Rep.* 2020;10(1):1–13. DOI:10.1038/s41598-020-61215-8
- [9] Andersson HI, Valnes OA. Flow of a heated ferrofluid over a stretching sheet in the presence of a magnetic dipole. *Acta Mech.* 1998;128:39–47. DOI:10.1007/BF01463158.
- [10] Tahir H, Khan U, Din A, et al. Hybridized two phase ferromagnetic nanofluid with  $\text{NiZnFe}_2\text{O}_4$  and  $\text{MnZnFe}_2\text{O}_4$ . *Ain Shams Eng J.* 2021;12(3):3063–3070. DOI:10.1016/j.asej.2020.10.026
- [11] Nadeem S, Ahmad S, Muhammad N. Analysis of ferrite nanoparticles in liquid. *Pramana.* 2020;94(1):54. DOI:10.1007/s12043-019-1913-1
- [12] Naveen Kumar R, Jyothi AM, Alhumade H, et al. Impact of magnetic dipole on thermophoretic particle deposition in the flow of Maxwell fluid over a stretching sheet. *J Mol Liq.* 2021;334:116494. DOI:10.1016/j.molliq.2021.116494
- [13] Naveen Kumar R, Punith Gowda RJ, Prasanna GD, et al. Comprehensive study of thermophoretic diffusion deposition velocity effect on heat and mass transfer of ferromagnetic fluid flow along a stretching cylinder. *Proc Inst Mech Eng Part E J Process Mech Eng.* 2021. DOI:10.1177/09544089211005291
- [14] Nadeem S, Ahmad S, Muhammad N, et al. Chemically reactive species in the flow of a Maxwell fluid. *Results Phys.* 2017;7:2607–2613. DOI:10.1016/j.rinp.2017.06.017
- [15] Muhammad N, Nadeem S, Mustafa MT. Hybrid isothermal model for the ferrohydrodynamic chemically reactive species. *Commun Theor Phys.* 2019;71(4):384. DOI:10.1088/0253-6102/71/4/384
- [16] Hayat T, Haider F, Alsaedi A, et al. Unsteady flow of nanofluid through porous medium with variable characteristics. *Int Commun Heat Mass Transf.* 2020;119:104904. DOI:10.1016/j.icheatmasstransfer.2020.104904
- [17] Punith Gowda RJ, Naveen Kumar R, Jyothi AM, et al. KKL correlation for simulation of nanofluid flow over a stretching sheet considering magnetic dipole and chemical reaction. *ZAMM - J Appl Math Mech Z Für Angew Math Mech.* 2021;101(11):e202000372. DOI:10.1002/zamm.20200372
- [18] Khan MI, Tamoor M, Hayat T, et al. MHD boundary layer thermal slip flow by nonlinearly stretching cylinder with suction/blowing and radiation. *Results Phys.* 2017;7(March):1207–1211. DOI:10.1016/j.rinp.2017.03.009

- [19] Varun Kumar RS, Punith Gowda RJ, Naveen Kumar R, et al. Two-phase flow of dusty fluid with suspended hybrid nanoparticles over a stretching cylinder with modified Fourier heat flux. *SN Appl Sci.* 2021;3(3):384. DOI:10.1007/s42452-021-04364-3
- [20] Punith Gowda RJ, Naveen Kumar R, Prasannakumara BC. Two-phase Darcy-Forchheimer flow of Dusty hybrid nanofluid with viscous dissipation over a cylinder. *Int J Appl Comput Math.* 2021;7(3):95. DOI:10.1007/s40819-021-01033-2
- [21] Kumar RN, Punith Gowda RJ, Abusorrah AM, et al. Impact of magnetic dipole on ferromagnetic hybrid nanofluid flow over a stretching cylinder. *Phys Scr.* 2021;96(4):045215. DOI:10.1088/1402-4896/abe324
- [22] Muhammad N. Finite volume method for simulation of flowing fluid via OpenFOAM. *Eur Phys J Plus.* 2021;136(10):1010. DOI:10.1140/epjp/s13360-021-01983-y
- [23] Rashid M, Hayat T, Alsaedi A. Entropy generation in Darcy-Forchheimer flow of nanofluid with five nanoparticles due to stretching cylinder. *Appl Nanosci.* 2019;9(8):1649–1659. DOI:10.1007/s13204-019-00961-2
- [24] Punith Gowda RJ, Naveen Kumar R, Jyothi AM, et al. Impact of binary chemical reaction and activation energy on heat and mass transfer of marangoni driven boundary layer flow of a Non-Newtonian nanofluid. *Processes.* 2021;9(4):4. DOI:10.3390/pr9040702
- [25] Ramesh GK, Shehzad SA, Rauf A, et al. Heat transport analysis of aluminum alloy and magnetite graphene oxide through permeable cylinder with heat source/sink. *Phys Scr.* 2020;95(9):095203. DOI:10.1088/1402-4896/aba5af
- [26] Khan MN, Nadeem S, Muhammad N. Micropolar fluid flow with temperature-dependent transport properties. *Heat Transf.* 2020;49(4):2375–2389. DOI:10.1002/htj.21726
- [27] Alshomrani AS, Ramzan M. Upshot of magnetic dipole on the flow of nanofluid along a stretched cylinder with gyrotactic microorganism in a stratified medium. *Phys Scr.* 2019. DOI:10.1088/1402-4896/ab4067
- [28] Manjunatha PT, Gireesha BJ, Prasannakumara BC. Effect of radiation on flow and heat transfer of MHD Dusty fluid over a stretching cylinder embedded in a porous medium in presence of heat source. *Int J Appl Comput Math.* 2017;3(1):293–310. DOI:10.1007/s40819-015-0107-x
- [29] Ferdows M, Murtaza MG, Tzirtzilakis EE, et al. Numerical study of blood flow and heat transfer through stretching cylinder in the presence of a magnetic dipole. *ZAMM-J Appl Math Mech Für Angew Math Mech.* 2020: e201900278. DOI:10.1002/zamm.201900278
- [30] Zeeshan A, Majeed A. Effect of magnetic dipole on radiative non-Darcian mixed convective flow over a stretching sheet in porous medium. *J Nanofluids.* 2016;5(4):617–626.
- [31] Olanrewaju PO. Effects of internal heat generation on hydromagnetic non-Darcy flow and heat transfer over a stretching sheet in the presence of thermal radiation and ohmic dissipation. *World Appl Sci J.* 2012;16:37–45.
- [32] Pal D, Mondal H. Hydromagnetic non-Darcy flow and heat transfer over a stretching sheet in the presence of thermal radiation and Ohmic dissipation. *Commun Nonlinear Sci Numer Simul.* May;15(5):1197–1209. DOI:10.1016/j.cnsns.2009.05.051
- [33] Gholinia M, Armin M, Ranjbar AA, et al. Numerical thermal study on CNTs/C<sub>2</sub>H<sub>6</sub>O<sub>2</sub>-H<sub>2</sub>O hybrid base nanofluid upon a porous stretching cylinder under impact of magnetic source. *Case Stud Therm Eng.* 2019;14:100490.

# **Title: Use of essential oils as bio active substances for antimicrobial finishing of fabrics.**

## **Authors:**

**K B Ravindra, Ph.D, Associate Professor**, Department of Textile Technology, Bapuji Institute of Engineering and Technology, Davangere

**Y N Dinesh, Ph.D, Asst. Professor**, Department of Textile Technology, Bapuji Institute of Engineering and Technology, Davangere

**S M Chandrasekhara, Ph. D, Asst. Professor**, Department of Textile Technology, Bapuji Institute of Engineering and Technology, Davangere

**Address:** Department of Textile Technology, Bapuji Institute of Engineering and Technology, Davangere, KARNATAKA

**Correspondence to:** K B Ravindra ([ravi328@rediffmail.com](mailto:ravi328@rediffmail.com))

## **Abstract**

The natural extracts of Oregano leaves and Cinnamon bark were found to be highly effective as antimicrobial agents and successfully inhibit the bacterial growth. In the present study, antimicrobial compounds (essential oils) were extracted from spices such as Oregano and Cinnamon by using organic solvent (Ethylene) using the soxhlet apparatus. The above bioactive agents (5% & 10 % owf) were applied on plain cotton and polyester/cotton woven fabrics by the pad-dry-cure process. For fixation of the finishing agents, Glutaraldehyde (8% owf) was used as a cross-linking agent along with Sodium hypophosphite (2% owf) as the catalyst. Evaluation of the antimicrobial activity of untreated and treated fabrics was performed quantitatively by percentage reduction test (AATCC-147-1998) against test organisms gram-positive bacteria staphylococcus aureus (ATCC 6538) and gram-negative bacteria Escherichia coli (ATCC 11230). The results indicate that treated fabrics register above 90% antimicrobial activity against S. aureus and E. coli bacterial strains. After 10 washes the efficacy of antimicrobial activity was reduced by 10-20%. A small decrease in flexibility, breaking strength and elongation properties is observed for treated fabrics. However, treated fabrics show enhanced crease recovery.

**Key words:** antimicrobial activity, bioactive substance, biodegradable, essential oils, hygienic

## Introduction

Cross infection by pathogens leads to the development of odour when the fabric is worn next to the skin. As consumers are increasingly aware of a hygienic lifestyle and there is a necessity for the development of a wide range of textile products finished with antimicrobial properties. Apart from this microbial attack can cause discolouration and loss of functional properties of fabrics and hence prevention of microbial attack on textiles has become a matter of significant importance. In view of this, to prevent the development of objectionable odour, dermal infection and other related diseases and to prevent product deterioration antimicrobial finish is applied to textile materials<sup>1</sup>.

A variety of antimicrobial textile materials are reported. Chemical-based antimicrobial agents are synthetic non-biodegradable chemical compounds, which cause environmental and health concerns. The finishing ingredients used in antimicrobial finishing need to be effective, have selective activity towards harmful microbes, be bioactive, non-toxic, biodegradable and be permanent<sup>2</sup>. Natural extracts from various parts of some of the medicinal plants and herbs exhibit antimicrobial properties. These antimicrobial compounds, which are mostly extracted from plants such as aloe vera, tea-tree, eucalyptus, neem, tulsi leaf etc<sup>3</sup>. The textile products treated with these natural plant extracts are required to be reusable and durable antimicrobial textiles which are effective against harmful pathogens. Such products will be beneficial for both medical industry workers and the general public as well. Spices and herbal plant extracts can exhibit antimicrobial activity. The main components present in these natural antimicrobial agents such as basil, thyme, and oregano essential oils are linalool, thymol, and carvacrol, respectively exhibit antimicrobial activity against various microorganisms.

This study investigated the antimicrobial functionality of cotton and polyester/cotton fabrics finished with extracts of spices such as Oregano and Cinnamon. According to Conner *et al.*, the antimicrobial action of essential oils may be due to the impairment of a variety of enzyme systems including those involved in energy production and structural component synthesis of harmful microorganisms<sup>4</sup>. The Oregano leaves or Bay leaf (used in cooking) contain about 1.3% essential oils. Major compounds in cinnamon stick present were volatile oil component (*E*)-



cinnamaldehyde and several polyphenols mainly proanthocyanidins and catechins<sup>5,6</sup>. These components significantly contributed to the antibacterial properties. Lopez, *et al*, and Rodr'iguez-Lafuente, *et al* reported the antimicrobial activity of cinnamon, oregano, and thyme EOs against various Gram-negative Gram-positive bacteria, yeasts and molds<sup>6,7</sup>.

## Materials and methods

### Fabric

For the purpose of application of antimicrobial compounds plain-woven cotton and polyester/cotton fabrics were used. The construction particulars of the fabrics are shown in Table 1.

**Table. 1 Construction particulars of test fabrics**

Sl. No.	Fabrics	Particulars		
		Ends/cm x Picks/cm	Yarn count (Tex)	Fabric Weight (GSM)
1	Cotton Fabric	40X36	12X13	113
2	Polyester/ cotton blended fabric (67/33)	40X33	14X12	115

### Extraction of active compound

Antimicrobial compounds used for this study were extracted from Oregano leaves and Cinnamon bark pieces which are two important spices frequently used in food preparation. The respective plant parts were collected, cleaned and were dried at 40°C in a drier. These dried plant materials were powdered into fine particles with the help of a domestic grinder. The active compound (antimicrobial agent) was extracted using organic solvent (Ethylene) using the soxhlet apparatus. The extract was filtered using Whatman filter paper IV. The solvent was then distilled under reduced pressure in a rotary evaporator until it becomes completely dry.

### Application

Natural extracts at 10% (owf) concentration were applied on pre-washed cotton and polyester/cotton fabric samples using the conventional pad-dry-cure process. Glutaraldehyde as cross-linking agent (8% owf) and Sodium hypophosphite (2% owf) as a catalyst was used. Fabric samples were padded through a laboratory padding mangle with two dips and two nips to give a wet pick up of  $85 \pm 5\%$  (owf). Later the samples were dried at 85°C for 5 min and then cured for

2 min at 120°C. **Fig. 1** shows the photographs of untreated and treated cotton and polyester/cotton fabrics.

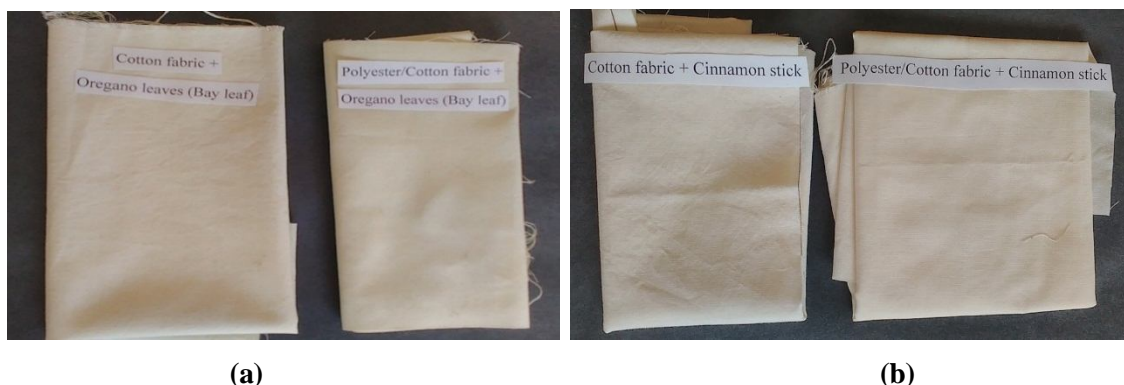


**Fig. 1** Cotton and polyester/cotton fabrics treated with extracts of (a) Oregano (b) Cinnamon

### Evaluation of Antimicrobial activity

Modified colony counting method (AATCC test method 147-1998) was used to determine the antibacterial activity of the untreated and the treated fabric samples against *Staphylococcus aureus* and *Escherichia coli* and test results were expressed in terms of % reduction of bacterial growth.

### Wash durability test

The finished fabric samples were subjected to multiple washes using a lander-o-meter as per ISO 6330-1984E. Then antimicrobial activity for washed fabric samples was determined and activity retention % was calculated.

### Fabric properties

**Bending length:** Bending length of fabric samples was measured by the cantilever principle, as per test method BS 3356.

**Crease recovery:** Shirley crease recovery tester was used to measure crease recovery angle of treated and control fabrics as per test method BS EN 22 313.

**Strength and Elongation:** Tensile strength was evaluated by using Hounsfield Universal Tester, UK (CRE) as per test method BS 2576.

## Results and Discussion

### Evaluation antimicrobial activity by suspension test (Quantitative) -AATCC test method 147-1998

Fig. 3 shows the antimicrobial plates laden with *E. coli* for untreated cotton fabric (a) and oregano (b) and cinnamon (c) treated fabrics. Substantial reduction of the number of bacterial colonies for treated fabrics can be seen in Figure 3.

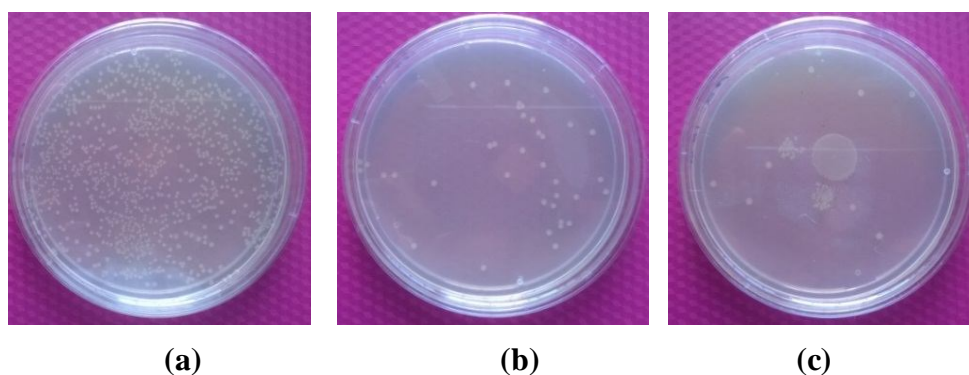


**Fig. 3** Reduction in bacterial colonies of *E. coli* (a) Untreated cotton (b) Cotton treated with oregano (c) Cotton treated with Cinnamon

**Table 2** Antimicrobial properties of cotton fabric sample against *S. aureus* and *E. coli*

Antimicrobial agent		S aureus		E coli	
		Number of colonies at $10^{-6}$ dilution	% inhibition	Number of colonies at $10^{-6}$ dilution	% inhibition
Untreated		200	--	165	--
Oregano	Before wash	7	97	18	89
	After wash	55	73	35	85
Cinnamon	Before wash	12	94	20	88
	After wash	60	70	44	73

From the above **Table 2** and **Fig. 4**, it is observed that the antimicrobial efficiency of cotton fabrics treated with oregano and cinnamon extract is ranging from 94% - 97% against test

bacteria. In general, the activity against Gram-positive bacteria is higher than gram-negative bacteria. Gupta D *et al*<sup>8</sup> have also reported that the Gram-positive bacteria are more sensitive to the bactericidal effect of antibacterial agents than Gram-negative bacteria. It is noted that the washed oregano treated cotton fabric retained its antimicrobial properties up to a maximum of 95% against *E. coli*, whereas, cinnamon treated fabric, retained 73% of its activity. The reason may be attributed to ineffective mordanting. Even though a cross-linking agent could be able to fix the antimicrobial compound with the fibre there is a small reduction of antibacterial activity which may be due to the removal of some unfixed active compounds during washing. However, all the treated fabrics retain a considerable amount of antibacterial activity even after repeated washes.

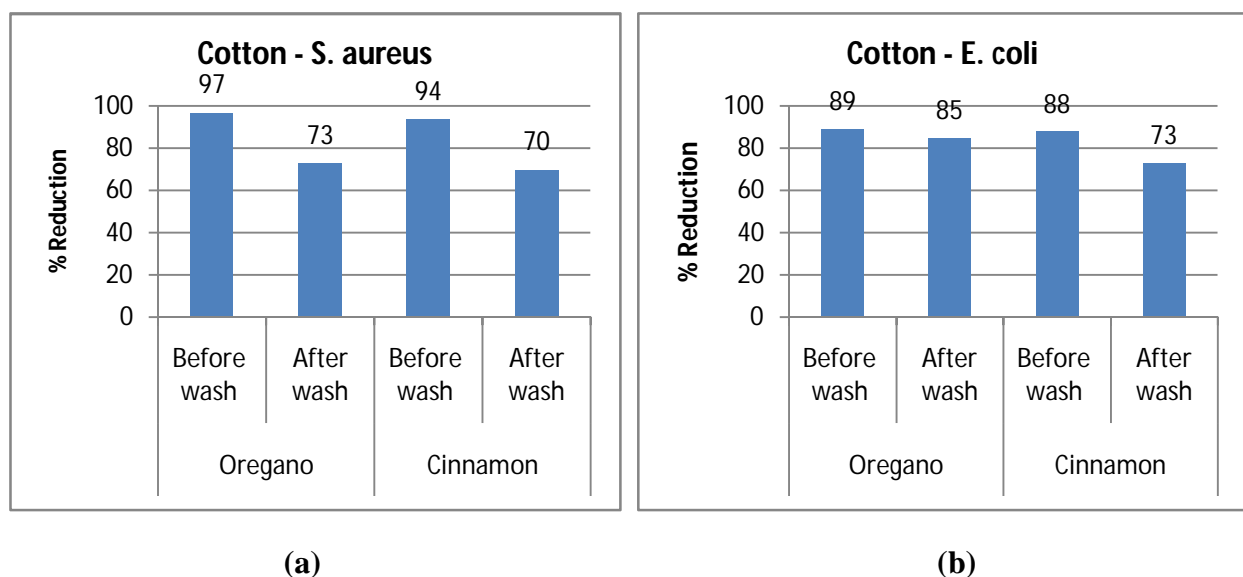


**Fig 4** Antibacterial properties of Oregano & Cinnamon extract on cotton (a) against *S. aureus* (b) against *E. coli*

From **Table 3** it is observed that the antimicrobial efficiency of the treated cotton fabric against *S. aureus* and *E. coli* is high compared to polyester/cotton blended fabrics. This indicates that the uptake % of the antimicrobial compound of cotton fabric for a given concentration of 10% is found to be higher than polyester/cotton fabric. It is observed that the loss of antimicrobial efficiency due to washing for treated cotton fabric is less than polyester/cotton blended fabric (**Fig. 5**). This is in line with observations of Joshi M *et al.*<sup>9</sup>, the active ingredients may be attached to cellulose by physical bonding and the cross-linking agent may act as a

bridging material for chemical bond formation. The cellulose part in the blend fabrics is actively involved in bond formation with the active ingredients of the natural extract.

**Table 3** Antimicrobial activity of polyester/cotton fabric against *S. aureus* & *E. coli*

Antimicrobial agent		<i>S. aureus</i>		<i>E. coli</i>	
		Number of colonies at $10^{-6}$ dilution	% inhibition	Number of colonies at $10^{-6}$ dilution	% inhibition
Untreated		118	--	135	--
Oregano	Before wash	15	87	24	82
	After wash	60	49	85	37
Cinnamon	Before wash	8	93	16	88
	After wash	46	61	56	59

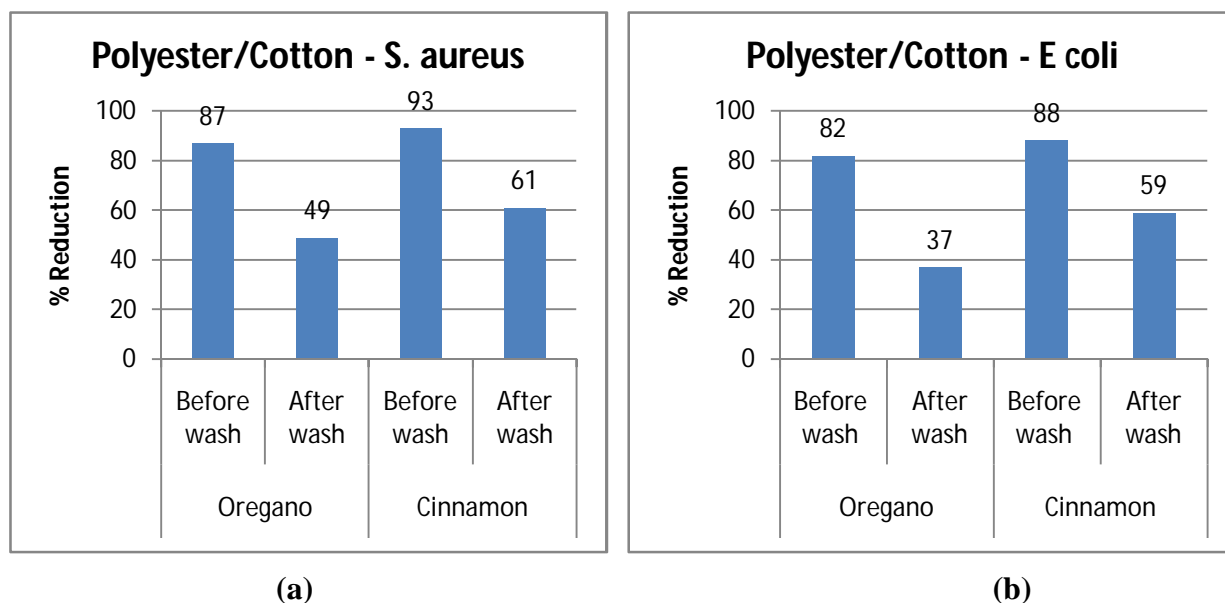


**Fig 5** Antibacterial activity of Oregano & Cinnamon extract on Polyester/cotton (a) against *S. aureus* (b) against *E. coli*

### Fabric Properties

Bending length test results shown in **Tables 4 and 5** indicate that the cotton and polyester/cotton fabrics become slightly stiffer after finishing with the extracts. It is noted that fabrics treated with antimicrobial agents along with cross-linking agents offered an improved crease recovery angle as compared to the corresponding untreated fabrics. However, the increase in the crease recovery angle of treated polyester/cotton blended fabric ranging from 182 to 186 is

found to be high as compared to 100% cotton fabric sample having crease recovery angle ranging from 140 to 151. This is due to the excellent crease recovery properties of the polyester component present in the blended fabrics.

**Table 4** Effect of finish on properties of cotton fabric treated with oregano, cinnamon

Particulars		Cotton untreated	Cotton treated	
			oregano	cinnamon
Bending length in cm	warp	1.96	1.93	1.88
	weft	1.56	1.78	1.84
	<b>Avg.</b>	<b>1.75</b>	<b>1.85</b>	<b>1.86</b>
Crease Recovery angle	warp	69	72	75
	weft	71	73	<b>76</b>
	<b>Total</b>	<b>140</b>	<b>145</b>	<b>151</b>
Breaking Strength (Kg)	warp	44.2	35.3	40
	weft	32.2	28	30
	<b>Avg.</b>	<b>38.2</b>	<b>32</b>	<b>35</b>
Elongation (%)	Warp	14.5	<b>10</b>	<b>12</b>
	Weft	26	<b>25</b>	<b>23</b>
	<b>Avg.</b>	<b>20.3</b>	<b>17.5</b>	<b>17.5</b>

**Table 5** Effect of finish on properties of Polyester/cotton fabric treated with oregano, cinnamon

Particulars		Polyester/cotton untreated	Polyester/cotton treated	
			oregano	cinnamon
Bending length in cm	Warp	2.08	2.1	2.2
	Weft	1.72	1.8	1.9
	<b>Avg.</b>	<b>1.89</b>	<b>1.94</b>	<b>2.04</b>
Crease Recovery Angle	Warp	90	93	91
	Weft	85	93	91
	<b>Total</b>	<b>175</b>	<b>186</b>	<b>182</b>
Breaking Strength (Kg)	Warp	70.3	70	68
	Weft	51.5	49	50
	<b>Avg.</b>	<b>60.9</b>	<b>59.5</b>	<b>59</b>
Elongation (%)	Warp	16.3	<b>11</b>	<b>12</b>
	Weft	24.4	<b>23</b>	<b>22</b>
	<b>Avg.</b>	<b>20.4</b>	<b>17</b>	<b>17</b>

From the results in **Tables 4 and 5**, it is observed that the breaking strength retention percentage of cotton fabric after treatment is 84 – 92 % whereas blended fabric retained breaking

strength up to 98%. It means blended fabric sample offers slightly more breaking strength retention (6.5%) as compared to cotton fabric. The loss of strength could be attributed to molecular degradation of the cotton fabrics together with rigidity conferred on the latter by factors associated with cross-linking<sup>10</sup>. This suggests that the tensile strength of polyester/cotton fabric is not seriously affected by the treatment. The retention of elongation of fabrics is 14 % which is more or less the same for both cotton and polyester/cotton fabrics before and after treatment.

## Conclusion

In the present study, antimicrobial agents extracted from spices such as oregano and cinnamon (essential oils) were utilized for the finishing of fabrics to impart antimicrobial properties. The study shows that treated fabrics register above 90% antimicrobial activity against *S. aureus* and *E. coli* bacterial strains. Hence antimicrobial agents derived from oregano and cinnamon have the potential to be used in the antimicrobial finishing of textiles. The agents impart excellent antimicrobial properties to both cotton and polyester/cotton blended fabrics. After 10 washes the efficacy of antimicrobial activity was reduced by 10-20%. The eco friendly and nontoxic properties of these herbal extracts are promising candidates for medical and health care textile applications. The treated fabrics exhibit increased crease recovery properties but their flexibility, tensile strength and elongation properties are slightly affected.

## References

1. Ramachandran, T., Rajendrakumar, K. and Rajendran, R., 2004. Antimicrobial Textiles an Overview, *IE (I) Journal* – TX, 84;42-47.  
<https://www.researchgate.net/publication/279556239>
2. Gao, Y. and Cranston, R., 2008. Recent Advances in Antimicrobial Treatments of Textiles. *Textile Research Journal*. 87; 60-72. DOI:[10.1177/0040517507082332](https://doi.org/10.1177/0040517507082332)
3. Son, Y A., Kim, B S., Ravikumar, K. and Kim, T K., 2007. Berberine finishing for developing antimicrobial nylon 6,6 fibres: Exhaustion, colourimetric analysis, antimicrobial study, and empirical modelling. *Journal of Applied Polymer Science*, 103; 1175–1182. <https://doi.org/10.1002/app.25364>



4. Conner, D. E., Beuchat, L. R., Effects of essential oils from plants on growth of food spoilage yeasts. *J Food Science*, 49(2): 1984; 429–34.
5. Gandhiraja, N., Sriram, S., Meena, V., Kavitha Srilakshmi, J., Sasikumar, C., and Rajeswari, R., Phytochemical Screening and Antimicrobial Activity of the Plant Extracts of *Mimosa pudica* L. against Selected Microbes. *Ethnobotanical Leaflets*, 13: 2009; 618–24.
6. L'opez-Malo, A., Barreto-Valdivieso, J., Palou, E., Mart'ın, F. S., *Aspergillus flavus* growth response to cinnamon extract and sodium benzoate mixtures. *Food Control*, 18(11): 2007; 1358–62.
7. Rodr'iguez-Lafuente, A., Ner'm, C., Batlle, R., Active paraffin-based paper packaging for extending the shelf life of cherry tomatoes. *J Agric Food Chem*, 58(11): 2010; 6780–6786.
8. Gupta D., and Laha A., Antimicrobial activity of cotton fabric treated with *Quercus Infectoria* extract. *Indian journal of fibre and textile research* Vol. 32, March 2007, 88-92
9. Joshi, M., Wazed Ali, S., and Rajendran, S. Antibacterial finishing of polyester/cotton blend fabrics using neem (*Azadirachta indica*): A natural bioactive agent. *Journal of Applied Polymer Science*, 106, 2007; 793–800. VVC 2007 Wiley Periodicals.
10. Aly A.S., Abdel-Mohsen A.M. and Hebeish A., Innovative multi finishing using chitosan-*O*-PEG graft copolymer/citric acid aqueous system for preparation of medical textiles, *The Journal of The Textile Institute*, Vol. 101, No. 1, January 2010, 76–90

## International Journals:

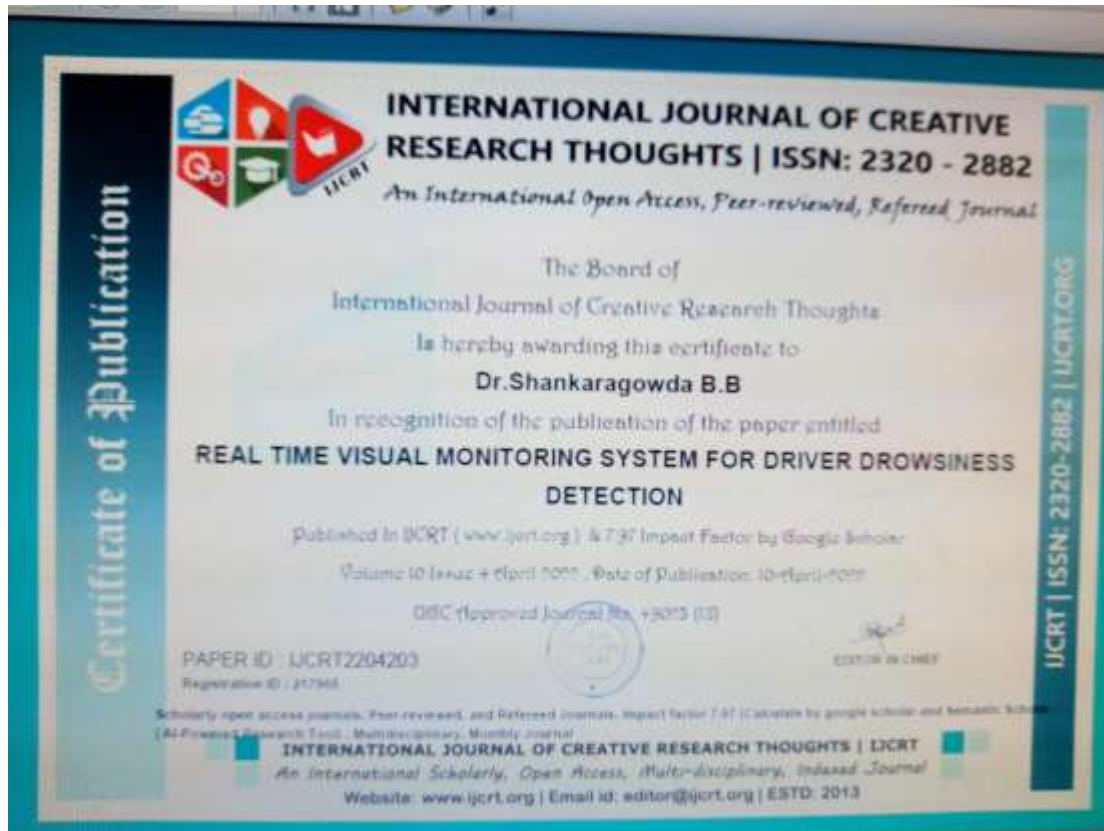
**Dr. Prasad M.** has published the paper titled “Jaffe Human Face Expressions” in <sup>the</sup> International Journal of Creative Research Thoughts(IJCRT), Vol. 10, Issue 4, DOI:10.55041/IJCRT2204605, 28<sup>th</sup> April 2022.



**Dr.Shankaragowda B.B.** and Mr. Karibasavaraja J.,“ Location Based Crop Recommendation System using Machine Learning Model ,” International Journal of Scientific Research Engineering and Management(IJSREM), Vol. 6, Issue 4,pp.1-5, DOI:10.55041/IJSREM12299, April 2022.



**Dr.Shankaragowda B.B. and Mr.Karibasavaraja J., “Real Time Visual Monitoring System for Driver Drowsiness Detection”, International Journal of Creative Research Thoughts”, Vol. 10, Issue 4,pp.b659-b666 April 2022. UGC Approved Journal No. : 49023(18).**











**CONTENTS**

MATHEMATICAL STUDY ON THERMAL POLLUTION WITH REFERENCE TO DIFFUSIONAL TRANSFER OF DISPERSANTS <b>M. L. Mallikarjuna, V.K Katiyar, K.S. Basavarajappa, Krishna Kumar T.K</b>	1-6	A NOVEL FUZZY APPROACH FOR ENHANCEMENT OF UNEVEN ILLUMINATED IMAGES <b>Rajesh Kumar Saini, Preeti Mittal, Neeraj Kumar Jain</b>	71-78
STOCHASTIC MODELING ON INTELLIGENT QUOTIENT : SURVIVAL DATA ANALYSIS A REVIEW <b>N.John Britto, V.Rajagopalan, C.Silambarasan, M.Aniji, Manimannan</b>	7-12	STOCHASTIC EPIDEMIC MODEL SEVERE ACUTE RESPIRATORY SYNDROME CORONAVIRUS 2 (SARS-COV-19) <b>N. John Britto, Dr.V. Rajagopalan, Dr. M. Selvam, E. Rathika , Dr.C. Silambarasan, S. Madasamy</b>	79-90
ONEUCLIDEAN NORMS AND FACTORIZATION IN TERNARY SEMI-DOMAINS <b>Madhu Dadhwal, Pankaj, R.P. Sharma</b>	13-26	ON THE DIOPHANTINE EQUATION $n(x-y)=xy$ , $n=pq$ , $p$ AND $q$ ARE CONSECUTIVE PRIMES <b>Surya Prakash Gautam, Hari Kishan, Megha Rani</b>	91-94
PROBABILITY MODELS IN IMAGE PROCESSING; BAYESIAN INFERENCES <b>N.John Britto, V.Rajagopalan, M.Aniji, Abi, and Manimannan G</b>	27-32	A NOTE ON STATISTICAL POPULATION GENETICS WITH WRIGHT FISHER MODEL <b>V.Rajagopalan, N.John Britto, S.Sasikala, M.Aniji and Manimannan G.</b>	95-110
ANALYSIS OF A QUEUEING PROCESS WITH BALKING, RENEGING AND PRE-EMPTIVE PRIORITY <b>Dr Meenu Gupta , Dr Man Singh, Dr Manju Tonk</b>	33-40	LATTICES IN CRYPTOLOGY <b>Auparajita Krishnaa</b>	111-124
ANALYTICAL STUDY OF A COMPLEX FEED BACK SEMI BI-TANDEM QUEUE SYSTEM DIFFER IN TRANSITION PROBABILITIES <b>Vandana Saini, Dr. Deepak Gupta, Dr.A.K.Tripathi</b>	41-54	ON THE DIOPHANTINE EQUATION $\prod_{i=1}^3 x_i - n^3$ $m \prod_{i=1}^3 (x_i - n)$ ; $m$ AND $n$ ARE POSITIVE INTEGERS <b>Surya Prakash Gautam, Hari Kishan, Megha Rani</b>	125-134
COEFFICIENT ESTIMATION OF CERTAIN SUBCLASS OF BI-UNIVALENT FUNCTIONS DEFINED BY CATAS OPERATOR <b>G. M. Birajdar, N. D. Sangle</b>	55-60		
ANALYSIS OF A STOCHASTIC MODEL OF A STANDBY SYSTEM WITH SUBSTANDARD UNIT AND CORRELATED LIFE TIME <b>Sarita, Sanjeev Kumar, Pooja Bhatia</b>	61-70		



Dr. T.P. Singh

Chief Editor & Professor in Maths & O.R.

# FOREWORD

It gives me an immense pleasure in writing this foreword for '**Aryabhatta Journal of Mathematics & Informatics**' (AJMI) Vol.14 issue 1 Jan.-June. 2022 published by Aryans Research & Educational Trust. The first issue of the journal was published in year 2009. Since then & till today the journal publication is regular & well in time. It gives us a great pleasure to put forward before the scholars and researchers that journal from its start is making an effort to produce good quality articles. The credit goes to its reviewer team which review sincerely and furnish valuable suggestions to improve the quality of papers. The Journal covers areas of mathematical and statistical sciences, Operational Research, data based managerial &, economical issues and information sciences.

**AJMI VOL.14 issue 1** is before you. I am pleased to note that research scholars, professors, executives from different parts of country have sent their papers for this issue. The papers are relevant and focus on the futuristic trends and innovations in the related areas. We have received around 34 papers for this issue from which on reviewer's report only 14 have been selected for publication. DOI no. by cross Ref. have been mentioned on each article.

1. Prof. Mallkarjuna, Krishna Kumar et.al. Proposed mathematical study to analyze the thermal pollution using continuity equation. The model results showed graphically the variation of concentration of dispersants with displacement at different time of intervals.
2. Prof. Manimannan G, John Britto et.al. presented an overview of Stochastic model and statistical testing in survival data analysis in reference to biosciences and genetic resemblance.
3. Prof. MadhuDadhwal, Pankaj et.al. studied ternary algebraic structures and introduced the notion of left Euclidean norm on a ternary semiring.
4. John Britto & Prof. Rajagopalan et.al. in their paper explored pattern recognition and image processing through Bayesian classifier approach.
5. In paper no.5, Dr. Meenu et.al. constructed a queue model with balking and reneging behavior of impatient customers and preemptive priority service.
6. Vandana et.al. discussed a complex semibi-tandem queue model in stochastic environment where transition probabilities of customers moving from one state to other are different.
7. Prof. Birajdar & Sangle introduced new subclass of the function class and established Taylor-Maclaurin coefficients using Catas operator.
8. Sarita et.al. dealt stochastic reliability model of two dissimilar units with the assumption that failure and repair times are correlated.
9. Prof. Rajesh and Preeti Proposed a novel approach using the RGB Luminance Channel for the conversion of a color image into one channel image.
10. In paper 13 A. Krishnaa presented Lattices from Discrete Mathematics in order to achieve a highly safe data transfer between two parties.
11. In paper 14 Surya P. Gautam et.al. discussed cubic non-linear Diophantine equation and obtained positive integral solution for different value of  $m$  and  $n$  in two different ways.

I would like to thank and felicitate the contributors in this issue and at the same time invite quality papers from academic and research community for Vol. 14 issue 2 to be published in Nov. 2022.

Comments, suggestions and feedback from discerning readers, scholars and academicians are always welcome.

DR. T.P. SINGH



## MATHEMATICAL STUDY ON THERMAL POLLUTION WITH REFERENCE TO DIFFUSIONAL TRANSFER OF DISPERSANTS

**M. L. Mallikarjuna\*, V.K Katiyar\*\*, K.S. Basavarajappa\*\*\*, Krishna Kumar T.K\*\*\*\***

\*Department of Physics, Adichunchanagiri Institute of Technology, Chickmagalore, Karnataka

\*\*Department of Mathematics, Indian Institute of Technology, Roorkee, Uttarakhand

\*\*\*Department of Mathematics, Bapuji Institute of Engineering and Technology, Davangere, Karnataka

\*\*\*\*Department of Physics, Bapuji Institute of Engineering and Technology, Davangere, Karnataka

E-mail : ksbraju@hotmail.com, sairamputtaparth@gmail.com

### ABSTRACT

*Mathematical study has been developed to analyze the thermal pollution using continuity equation. The diffusion equation is a partial differential equation consists of thermal dispersants such as tracer concentration  $C(x, t)$  and longitudinal mixing coefficient with respect to  $x, y$  and  $z$  directions at time  $t$ . The diffusion equation represents the dispersants has been solved analytically and the range of dispersion is considered for the range of 10ft to 1000ft. Fully mixed contour defined by equation gives the dispersants surroundings, the area as computed for solving partial differential equation (diffusion equation)*

**Key words:** Dispersants, Pollution, Thermal

### INTRODUCTION

Pollution occurs in the nature in various forms such as: industrial pollution, air pollution, water pollution, Toxic pollution, soil pollution, noise pollution and Thermal pollution. Direct effect of pollution on the surrounding vegetarian and life can always be determined by estimating the extent of pollution in a given industrial domain or land area. Therefore the pollution may be in terms of chemical or biological gases, fumes, particulate matter, polluted land and water resources. To explore the potential threat of thermal pollution which exists in the surrounding environment is studied using mathematical model. Pollution, is an undesirable change in the physical, chemical or biological characteristics of our air, land and water that may or will harmful and affect the living conditions. The thermal pollution problem consists of the larger use of electric energy, growth and construction of new electricity generating stations, and fossil fuels to nuclear reactors. There is also heat addition takes place due to industrial waste heat to waterways which increases in the heat load of the waters moderately. Also municipal discharge and irrigation return waters also causes thermal pollution. Return flows from irrigation fields are also a thermal pollutant. As in any environmental situation the actual rise is a function of initial water temperature, volume of abstraction, velocity of flow, length of time in field, and climatic conditions.



The largest single source of manmade heat (thermal) addition to our rivers and waterways is from electric generating plants. Analysis shows that steam electric cooling discharges indicates an average increase of 15<sup>0</sup>F in water temperature after passing through condensers.

Literature provides that, the temperature rise of water from initial point to discharge point of the sewage treatment plant is slightly dispersed. The dispersion and diffusion of the substances for the same density of the receiving water; but it is little known concerning with density differences exist.

J. M. Capuzzo [1], studied the relative importance physiological features like thermal, mechanical, and biocidal stress due to toxic effect of power plant operation on marine zooplankton. Victor S Kennedy [3], explains about the effect of thermal pollution due to industrial activity on vegetation from stream banks, and of disposal of heated effluents from them. M. Abbaspouret. al [4], studied the impacts of thermal pollution, i.e., disorders in reproduction, nourishment and other biological habits and was modeled using MIKE21 software to avoid a decrease on the power plant efficiency. Adrijana Radošević et.al [6], analyze the thermal pollution due to thermal power plants of the Plomin bay induced by the used cooling water released from Plomin 1 and Plomin 2 and flow simulations and temperature field analysis were made and the measurements of the bay surface temperature field were carried out using 3Dwater flow simulations. Christopher A. Ollson et.al [10], asses the results of a comprehensive human health risk assessment for energy-from-waste thermal treatment facility based on extensive sampling of baseline environmental conditions as well as 87 identified contaminants of potential concern.

From the literature it is concluded that thermal pollution has not been a pervasivethreat in the past but could become prominent unless provision is made for its control.

## FORMULATION

For thermal pollution on the reference for the heated waters, the continuity equation for the transport of a conservative tracer is given by the partial differential equation. The tracer concentration is modeled

$$\text{as,} \quad \frac{\partial c}{\partial t} = \frac{\partial}{\partial x} \left( D \frac{\partial c}{\partial x} \right) + \frac{\partial}{\partial y} \left( D \frac{\partial c}{\partial y} \right) + \frac{\partial}{\partial z} \left( D \frac{\partial c}{\partial z} \right) - \frac{\partial}{\partial x} (v_x c) - \frac{\partial}{\partial y} (v_y c) - \frac{\partial}{\partial z} (v_z c) \quad (1)$$

Where 'c' equals the tracer concentration: x, y, and z are the coordinate directions with corresponding velocities  $v_x$ ,  $v_y$  and  $v_z$ ; and D includes the effects of both molecular and turbulent diffusivity. The first

term explains the unsteady part of the conservation equation, the next three terms explain the diffusional transfer of matter, and the last three terms explain mass transfer by convective motion of the fluid.

We consider the cross-sectional average concentration, the empirical expression for velocity and the Reynolds analogy to define the variation of velocity ( $v_x$ ) and  $D$  with cross section. The transport mechanism described by equation (1) which could be represented by the following one dimensional dispersed flow model:

$$\frac{\partial c}{\partial t} = D \frac{\partial^2 c}{\partial x^2} - v_x \frac{\partial c}{\partial x}, \text{ concentration at time 't' and displacement 'x' across the cross section}$$

$$\frac{\partial c}{\partial t} = D \frac{\partial^2 c}{\partial y^2} - v_y \frac{\partial c}{\partial y}, \text{ concentration at time 't' and displacement 'y' across the cross section}$$

$$\frac{\partial c}{\partial t} = D \frac{\partial^2 c}{\partial z^2} - v_z \frac{\partial c}{\partial z}, \text{ concentration at time 't' and displacement 'z' across the cross section}$$

Defining  $D_L$  as the longitudinal mixing coefficient and  $\bar{u}$  as the average velocity,

Then we have,

$$\frac{\partial c}{\partial t} = D_L \frac{\partial^2 c}{\partial x^2} - \bar{u} \frac{\partial c}{\partial x} \quad (2)$$

Where 'c' is the function of time, displacement in x, y and z directions, it can be related to linear form,  $c(x,y,z,t)$ . In the present study, the profiles of tracer concentration has been analyzed with average values of longitudinal mixing coefficient of diffusion, ' $D_L$ ' with average velocity ' $\bar{u}$ '.

## ANALYSIS

Solving analytically for  $D_L$  using empirical data, then, for tracer concentration  $c(x,t)$  in series form with average values of  $D_L$  and  $\bar{u}$  as,

$$c(x,t) = \left[ C_1 e^{\left( \frac{\bar{u}}{D_L} + \sqrt{\left( \frac{\bar{u}}{D_L} \right)^2 + \frac{4 \times K}{D_L}} \right) x} + C_2 e^{\left( \frac{\bar{u}}{D_L} - \sqrt{\left( \frac{\bar{u}}{D_L} \right)^2 + \frac{4 \times K}{D_L}} \right) x} \right] \times C_3 e^{Kt} \quad (3)$$

$$c(x,t) = \left[ C_4 e^{\left( \sqrt{\left( \frac{\bar{u}}{D_L} \right)^2 + \frac{4 \times K}{D_L}} \right) x + Kt} + C_5 e^{-\left( \sqrt{\left( \frac{\bar{u}}{D_L} \right)^2 + \frac{4 \times K}{D_L}} \right) x + Kt} \right] \times e^{\alpha x + Kt}$$

$$c(x, t) = \left[ 1 + \alpha x + \frac{(\alpha x)^2}{2!} + \frac{(\alpha x)^3}{3!} + \dots \right] \times \left[ 1 + 2kt + \frac{4(kt)^2}{2!} + \frac{8(kt)^3}{3!} + \dots \right] \times \left\{ \left( C_4 \left[ 1 + \left( \frac{\sqrt{\alpha^2 + 4\beta}}{2} \right) x + \frac{\left[ \left( \frac{\sqrt{\alpha^2 + 4\beta}}{2} \right) x \right]^2}{2!} + \frac{\left[ \left( \frac{\sqrt{\alpha^2 + 4\beta}}{2} \right) x \right]^3}{3!} + \dots \right] \times \left[ 1 + 2kt + \frac{4(kt)^2}{2!} + \frac{8(kt)^3}{3!} + \dots \right] + \left( C_5 \left[ 1 - \left( \frac{\sqrt{\alpha^2 + 4\beta}}{2} \right) x + \frac{\left[ \left( \frac{\sqrt{\alpha^2 + 4\beta}}{2} \right) x \right]^2}{2!} - \frac{\left[ \left( \frac{\sqrt{\alpha^2 + 4\beta}}{2} \right) x \right]^3}{3!} + \dots \right] \times \left[ 1 + 2kt + \frac{4(kt)^2}{2!} + \frac{8(kt)^3}{3!} + \dots \right] \right\} \quad (4)$$

Where  $C_1 C_3 = C_4$  and  $C_2 C_3 = C_5$ , constants have been obtained using the conditions  $c(1,0)$  and  $c(1,1)$ .

For the two-dimensional case, the longitudinal velocity is computed and the surface area (A) enclosing at any specific temperature rise to be as, For the three-dimensional case

$$A = (0.496) \left( \frac{2Q_p \sqrt{Wd}}{\pi z (D_y D_z)^{\frac{1}{4}}} \right) \left( \frac{Q_p}{Q_r} \right)^{\frac{1}{2}} \left[ \frac{S_c}{S_p} \right]^{\frac{3}{2}} \quad (5)$$

For values of  $\frac{S_c}{S_p} < 0.60$ . The cross section area of the isothermal contour  $A_c$  is,

$$\frac{A_c}{A_r} = \left[ \frac{Q_p}{Q_r} + \left( \frac{\pi \sqrt{D_y D_z} L}{Q_r} \right) \right] \left[ \ln \left( \frac{S_p}{S_c} \right) \right] \left( \frac{1}{1 + \frac{\pi \sqrt{D_y D_z} L}{Q_r}} \right) \quad (6)$$

Where  $A_r$  is the cross-sectional area of the river and  $L$  is the distance from the discharge point to the cross sectional area of the interest.

The distance to the completely mixed contour is obtained as

$$L_m = \frac{Q_r}{\pi \sqrt{D_y D_z}} \left( 1 - \frac{Q_p}{Q_r} \right) \quad (7)$$

## RESULTS AND DISCUSSION

The theoretical study has been presented in the form of mathematical model. It is found that the dispersants spread over the range 100ft to 1000ft decreases as displacement increases at time 't'. The contour consists of dispersants with fully mixed pollutants which can be taken at a constant factor of pollutants in the environment. Model results are compared with [4] and [7]. Fig.(1),(2),(3) and (4) shows that the variation of concentration of dispersants with displacement at time  $t = 2\text{min.}$ ,  $t = 4\text{min.}$ ,  $t = 6\text{min.}$  and  $t = 8\text{min.}$

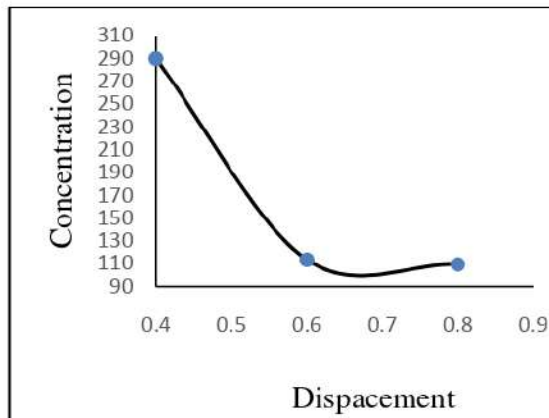


Fig.1: Variation of Concentration vs Displacement at time  $t = 2\text{min}$

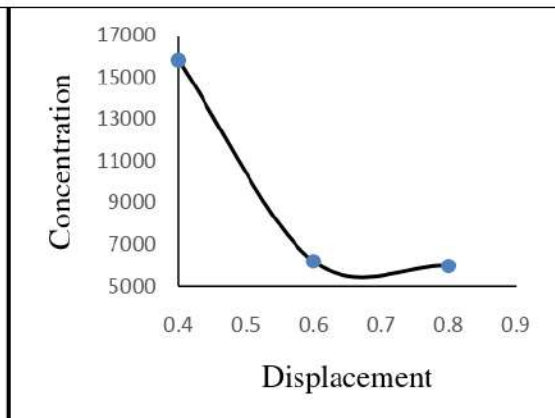


Fig.2: Variation of Concentration vs Displacement at time  $t = 4\text{min}$

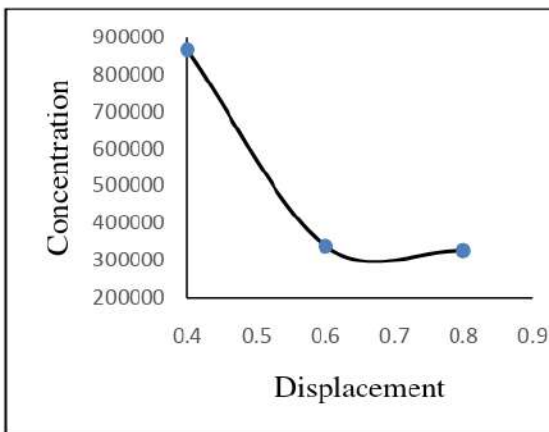


Fig.3: Variation of Concentration vs Displacement at time  $t = 6\text{min}$

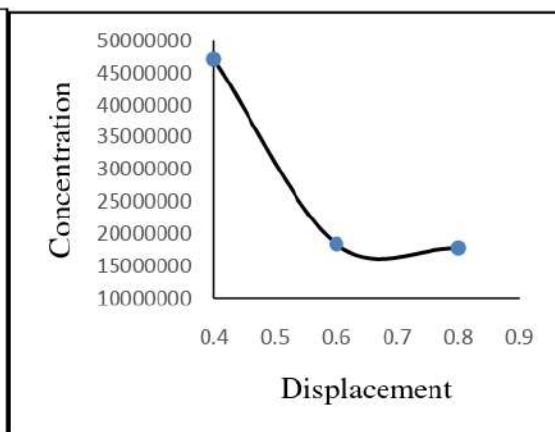


Fig.4: Variation of Concentration vs Displacement at time  $t = 8\text{min}$

## REFERENCES

1. J. M. Capuzzo, *Impact of Power-Plant Discharges on Marine Zooplankton: A Review of Thermal, Mechanical And Biocidal Effects*, *HelgoDerMeeresuntersuchungen*, vol. 33, 1980, pp 422-433.
2. I. I. Dolgikh, A. I. Pokhodun, and Yu. A. Chistyakov, *Conception Of Metrological Assurance For Monitoring Environmental Thermal Pollution*, *Measurement Techniques*, Vol. 40, 1997, pp 29-31.
3. Victor S. Kennedy, *Thermal Pollution*, *Reference Module in Earth Systems and Environmental Sciences*, *Encyclopedia of Energy*, 2004, pp 79-89.
4. M. Abbaspour, A. H. Javid, P. Moghimi K. Kayhan, *Modeling of thermal pollution in coastal area and its economical and environmental assessment*, *Int. J. Environ. Sci. Tech.* Vol. 2, 2005, pp 13-26.



5. Grant Ferguson, Allan D. Woodbury, *Observed thermal pollution and post-development simulations of low-temperature geothermal systems in Winnipeg, Canada*, *Hydrogeology Journal*, Vol. 14, 2006, pp 1206–1215.
6. Adrijana Radošević, Luka Sopta, Alfredo Višković, *Numeric modeling of thermal pollution in Plomin bay area*, *Ann Univ Ferrara*, Vol.54, 2008, pp .287–295.
7. E. N. Yadrenkina, *Ichthyofauna of the Upper Tom' Affected by Thermal Pollution (West Siberia)*, *Contemporary Problems of Ecology*, Vol. 3, 2010, pp. 541–546.
8. Daniel A. Vallero, *Thermal Pollution, Waste, A Handbook for Management*, 2011, pp 425–443.
9. Xiaofeng Zhao, Hui Jiang, Huina Wang, Juanjuan Zhao, Quanyi Qiu, Nigel Tapper, Lizhong Hua, *Remotely sensed thermal pollution and its relationship with energy consumption and industry in a rapidly urbanizing Chinese city*, *Energy Policy*, Vol. 57, 2013, pp 398–406.
10. Christopher A. Ollson, Loren D. Knopper, Melissa L. Whitfield Aslund, Ruwan Jayasinghe, *Site specific risk assessment of an energy-from-waste thermal treatment facility in Durham Region, Ontario, Canada. Part A: Human health risk assessment*, *Science of the Total Environment*, 2014, pp 345–356.
11. Catherine E. Raptis, Justin M. Boucher, Stephan Pfister, *Assessing the environmental impacts of freshwater thermal pollution from global power generation in LCA*, *Science of The Total Environment*, Vol. 580, 2017, pp 1014–1026.
12. Shikun Zhang, Zhongwei Huang Haizhu, Wang Hongyuan, Zhang Chengcheng, Zhang Chao Xiong, *Thermal characteristics analysis with local thermal non-equilibrium model during liquid nitrogen jet fracturing for HDR reservoirs*, *Applied Thermal Engineering*, Volume 143, October 2018, Pages 482–492
13. T. Lyubimova, A. Lepikhin, Ya. Parshakova, Yu. Lyakhin, A. Tiunov, *The modeling of the formation of technogenic thermal pollution zones in large reservoirs*, *International Journal of Heat and Mass Transfer*, Volume 126, Part A, November 2018, Pages 342–352.
14. Jie Lin, Xinqing Zou, Faming Huang, *Quantitative analysis of the factors influencing the dispersion of thermal pollution caused by coastal power plants*, *Water Research*, Volume 188, 1 January 2021, 116558.
15. *Thermal pollution level reduction by sweeping jet-based enhanced heat dissipation: A numerical study with calibrated Generalized k- $\omega$  (GEKO) model*, *Applied Thermal Engineering*, Volume 204, 5 March 2022, 117990.

PAPER

# Influence of divalent metal ion ( $\text{Zn}^{2+}$ ) on magnetic properties, curie temperature and DC electrical properties in $\text{Ce}^{3+}$ substituted Ni-Zn ferrites

To cite this article: Santhosh Kumar M V *et al* 2022 *Phys. Scr.* **97** 015807

View the [article online](#) for updates and enhancements.

## You may also like

- [A Comparative Study of Energy Consumption Pattern and Environmental Impact in Residential Sector of Indian Cities](#)  
G. Jangali Satish and N. Nagesha
- [One-pot green synthesis of ZnO–CuO nanocomposite and their enhanced photocatalytic and antibacterial activity](#)  
C R Rajith Kumar, Virupaxappa S Betageri, G Nagaraju et al.
- [Regulation of the adsorption and chromatographic properties of polymeric adsorbents by varying their porous structure](#)  
Lyubov D Belyakova



## PAPER

# Influence of divalent metal ion ( $\text{Zn}^{2+}$ ) on magnetic properties, curie temperature and DC electrical properties in $\text{Ce}^{3+}$ substituted Ni-Zn ferrites

RECEIVED  
29 September 2021REVISED  
24 December 2021ACCEPTED FOR PUBLICATION  
31 December 2021PUBLISHED  
11 January 2022Santhosh Kumar M V<sup>1</sup> , A Alhadhrami<sup>2</sup>, Shankarmurthy G J<sup>3</sup>, M G Thriveni<sup>4</sup> and B M Prasanna<sup>4</sup> <sup>1</sup> Department of Physics, Jain Institute of Technology, Davanagere- 577003, (Affiliated to V.T.U., Belagavi - 590018) Karnataka, India<sup>2</sup> Department of Chemistry, College of Science, Taif University, PO Box 11099, Taif 21944, Saudi Arabia<sup>3</sup> University B.D.T. College of Engineering, Davanagere- 577002, Karnataka, India<sup>4</sup> Department of Chemistry, Bapuji Institute of Engineering and Technology, Davanagere-577004, Karnataka, IndiaE-mail: [santhukphysics@gmail.com](mailto:santhukphysics@gmail.com)**Keywords:** Ni–Ce–Zn nano ferrites, activation energy, curie temperature, magnetization

## Abstract

Nanoparticles of  $\text{Ni}_{1-x}\text{Zn}_x\text{Ce}_{0.1}\text{Fe}_{1.9}\text{O}_4$  ferrite substituted with  $\text{Zn}^{2+}$  ion concentrations (0.0, 0.2, 0.4, 0.6, 0.8 & 1.0) have been synthesised via aqueous citrate precursor auto combustion method. The obtained Powder x-ray diffraction data suggests a good crystalline phase; the crystallite size exists in the range of 14 ~ 38 nm. The lattice constant of samples increases with  $\text{Zn}^{2+}$  concentration. It validates Vegard's law and the decreasing trends in porosity of the samples were identified. The inhomogeneity in the grains was confirmed from FE-SEM. The EDS spectrogram attributes the good stoichiometry in the product. The Thermogravimetric analysis reveals that the crystallization occurred within the temperature 800 °C. The high-temperature DC conductivity of the samples shows that NTC behaviour. The Curie temperature and activation energy are estimated and the activation energy of carriers are found to be more at the paramagnetic region. The magnetic saturation ( $M_s^*$ ) has maximum for  $\text{Zn}^{2+} = 0.2$  (57.7 emu g<sup>-1</sup>) and coercive field ( $H_c$ ) related with a radius of occupancy of  $\text{Zn}^{2+}$  ion validates the relation  $H_c \propto \frac{1}{r}$  and also, the value of the remanence ratio suggests that isotropic magnetization took place in the heterogeneous material.

## 1. Introduction

The Ni-Zn ferrites are iron oxides and are typically high resistive compounds whose resistivity is  $10^6 - 10^8 \Omega\text{-cm}$  [1, 2]. The resistivity of the ferrites depends on composition, processing temperature and the way of cation distribution. The high resistivity is one of the key factors for considering the material for microwave devices [3, 4]. The resistivity of the materials influences the eddy current loss; in the ferromagnetic materials, it is inversely proportional to the resistivity. In the ferrite, the shallow eddy current loss is due to its high resistivity. As a result, ferrites are widely employed in high-frequency power systems, high-density magnetic recording heads, transformer components, EMI-shielding, microwave devices, inductors, high-quality filters, radio frequency circuits, rod antennas, including high-speed digital tape read-write heads [5]. It also has applications in Medical diagnostics, site-specific drug delivery, magnetic refrigeration and ferrofluids. Gas sensing is the new domain where nano ferrites are being used [6–8]. On the other hand, if the dimensions of the magnetic particle are reduced below its critical diameter, the domain formation is no more extended vigorously favoured and the particles exist as a single domain [9]. Thereby, electrically low power loss [7, 10–12] and more importantly, particles exhibit unique magnetic properties due to a more surface-to-volume ratio of ferrite nanoparticles. In the rare earth element substituted ferrites, a part of rare-earth ions were arranged at the proximity of the grain-boundary region. Later, magnetic spin canting surface magnetocrystalline anisotropy, single-domain behaviour, and superparamagnetism (SP) are identified. Many researchers have synthesized and examined various nano ferrites. The results reveal that 'saturation magnetization' ( $M_s^*$ ) improves with the concentration of  $\text{Ni}^{2+}$  ion and also the Curie temperature and magnetization are reduced by dislocations in ferrites [13].

The property of spinel phases is more correlated with the cation distribution between tetrahedral and octahedral sites [14]. And also, the interaction between metal and oxygen ions (M–O). The M–O interaction is decided by the oxygen parameter; various nano ferrites have been reported in the previous work, i.e.  $\text{MgFe}_2\text{O}_4$ ,  $\text{NiFe}_2\text{O}_4$ ,  $\text{ZnFe}_2\text{O}_4$ ,  $\text{MnFe}_2\text{O}_4$  [15–18]. More recently, semiconducting behaviours have been identified in the case of Calcium substituted Zinc cobalt ferrites  $\text{Zn}_{0.5-x}\text{Ca}_{0.1}\text{Co}_{0.4+x}\text{Fe}_2\text{O}_4$  [19]. The  $\text{Re}^{m+}$  ( $\text{Ce}^{3+}$ ,  $\text{Gd}^{3+}$ ,  $\text{La}^{3+}$ , and  $\text{Cd}^{3+}$ ) substitution in the ferrites shows the interesting behaviour which is reported in the literature [20, 21].

This research aimed to examine the effects of  $\text{Zn}^{2+}$  ion inclusions on the structural, DC electrical and magnetic properties of Ni-Ce-Zn ferrite. We have effectively synthesized the spinel-type nanoparticles of  $\text{Ni}_{1-x}\text{Zn}_x\text{Ce}_{0.1}\text{Fe}_{1.9}\text{O}_4$  ( $x = 0.0$  to  $1.0$ ) by sol-gel auto combustion followed by heat treatment. Further, we characterized their structure, surface morphology, Thermogravimetric analysis, DC electrical conductivity and magnetic properties using Powder-XRD, FE-SEM, EDS, TGA, Two probes and VSM. This paper presented a detailed investigation of structural and electrical and magnetic properties.

## 2. Experimental procedure

### 2.1. Synthesis

Sol-gel auto combustion was used to synthesize the composition of  $\text{Ni}_{1-x}\text{Zn}_x\text{Ce}_{0.1}\text{Fe}_{1.9}\text{O}_4$  with 'x' varying from 0.0 to 1.0. The analytical grades of the chemicals was used to prepare the solutions by dissolving nitrate salts with a stoichiometric quantity in de-ionized water. The aqueous solutions of Nickel nitrate ( $\text{Ni}(\text{NO}_3)_2 \cdot 6\text{H}_2\text{O}$ ), Zinc nitrate ( $\text{Zn}(\text{NO}_3)_2 \cdot 6\text{H}_2\text{O}$ ), Ferric nitrate ( $\text{Fe}(\text{NO}_3)_3 \cdot 9\text{H}_2\text{O}$ ) and Cerium nitrate ( $\text{Ce}(\text{NO}_3)_3 \cdot 6\text{H}_2\text{O}$ ) were mixed with constant stirring. The molar ratio of  $\text{Fe}^{3+}$  to  $\text{Me}^{2+}$  ( $\text{Zn}^{2+}$  &  $\text{Ni}^{2+}$ ) ions were adjusted by the addition of citric acid solution (i.e. Nitrates/citric = 1/1.5) with constant stirring for 1 h. Further, adjusted the precursor pH ( $\approx 7$ ) by adding aqueous ammonia at a constant temperature ( $100^\circ\text{C}$ ), after 6 h gel was formed and it turned to fluffy flakes by self-ignition. The powders were calcinated at  $600^\circ\text{C}$  for 5 h. Further, disc-shaped pellets were prepared and sintered at  $600^\circ\text{C}$  for 4 h in a muffle furnace [22].

### 2.2. Analysis

The structural characterization of all the samples was carried out by using Bruker D-8 Discover Powder x-ray diffractometer at room temperature ( $\text{Cu K}\alpha$  radiation ( $\lambda$ ) =  $1.5406 \text{ \AA}$ ) by continuous scan from  $10^\circ$  to  $80^\circ$  Bragg's angle. The sample's surface morphology and EDS analysis was carried out by using the Carl Zeiss FE-SEM instrument. The thermal stability of the unsintered powder sample were obtained by thermal analysis (TGA Q500 instrument). It measures the weight loss of the compound with a resolution of  $0.1 \mu\text{g}$  from ambient temperature to  $800^\circ\text{C}$  at the standard air medium with a heating rate of  $10 \text{ K min}^{-1}$ . The significant change in the weight loss of the substance was estimated with a precision of  $\pm 0.01\%$  from the first derivatives of weight loss. The DC electrical conductivity of all the samples was measured with two probes and Keithley 2600 source meters from 300K to 650K. The magnetic characterization (M v/s H) of all powder samples was carried out at Room Temperature in the field strength 0 to 15 kOe using the Lakeshore VSM 7410 instrument.

## 3. Results and discussion

### 3.1. Structural analysis

Figure 1 shows the diffractograms of all the samples and good crystallinity is observed. The diffractograms are then matched with the JCPDS card number 00-08-0234 and labeled all the prominent peaks. The secondary phase ( $\alpha\text{-Fe}_2\text{O}_3$ ) has appeared around ' $2\theta$ ' =  $33^\circ$  for  $x \geq 0.2$ , as confirmed by comparing the pattern with standard data (ICDD card no. 33-0664) [23]. The secondary phase formed due to the difference in crystallization energy and grain boundary phase from the cerium ions [24, 25]. In general, the radius of the  $\text{Zn}^{2+}$  ion is greater than  $\text{Ni}^{2+}$  and preferentially occupies the A-site leads to pushing the trivalent metal ion to B-site can increase the chance of the grain boundary phase. This is significant at the concentrations 0.4, 0.6 it is more when at  $x = 0.8$ , 1.00 it does not form the grain boundary phase [26].

The structure of ferrites is considered as an intertwining network of positively-charged metal ions ( $\text{Fe}^{3+}$ ,  $\text{Me}^{2+}$ ) and negatively charged divalent oxygen ions ( $\text{O}^{2-}$ ) [27]. It exists in an fcc structure with space group  $\text{Fd}_{3m}$   $\text{O}_h^7$  [27]. The structural parameters are obtained and presented in figures 2(a) and (b) and also enumerated in table 1; the Lattice constant of the sample is almost linearly dependent on  $\text{Zn}^{2+}$  ion, this effect is mainly due to the occupation of  $\text{Zn}^{2+}$  ( $0.69 \text{ \AA}$ ) into the tetrahedral site lead to enlarge the A-site [28, 29]. The ionic radius of the substituted elements directly changes the lattice parameter; this observation is also reflected in the  $\text{Ce}^{3+}$  ion substituted samples [30]. However, in some  $\text{Zn}^{2+}$  substituted spinel Mn-ferrites shows the reduction in the lattice constant [31]. The Crystallite size and lattice strain have been determined using the Debye-Scherrer relation [32] and tabulated in table 1. The average crystallite size is in the range (14–37.5 nm). The crystallite size

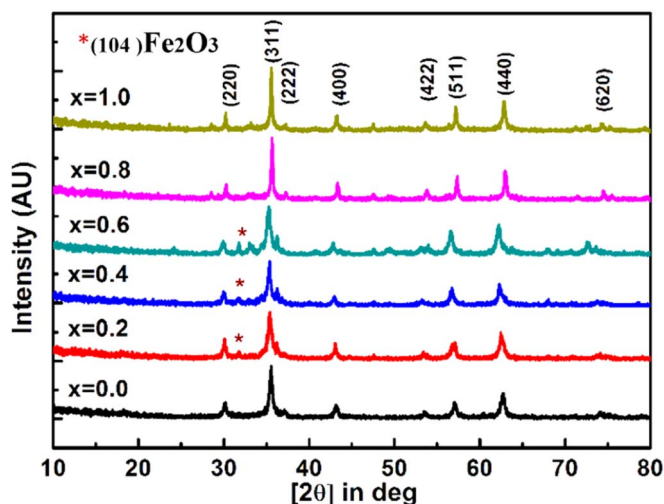


Figure 1. PXRD micrographs of  $\text{Ni}_x \text{Zn}_{1-x} \text{Ce}_{0.1} \text{Fe}_{1.9} \text{O}_4$ .

of samples is initially found to be increases up to for  $x = 0.2$  increased for  $x = 0.4$  it drops to low and for higher  $\text{Zn}^{2+}$  ion concentrations again crystallite size increases. The crystallite has a smaller dimension in comparison with the sample without  $\text{Ce}^{3+}$  ion. However, the variation of crystallite size seems to be contradictory to the material without  $\text{Ce}^{3+}$  ions [33]; similar results have been reported. The experimental density of all the samples was estimated by measuring the weight and volume of the sintered pellets in the air medium with highly sensitive instruments. The experimental density of the sample was calculated from the relation (1). The x-ray density of the material is determined by the relation (2). Similarly, the porosity of samples have estimated by using the relation (3) [32, 34]

$$d_{\text{exp}} = \frac{\text{Weight of the pellet}}{\text{volume of the pellet}} \quad \text{g/cm}^3 \quad (1)$$

$$\left[ d_{\text{xrd}} = \frac{8 \times \text{Mol.Wt.}}{N_A \times 10^3 \times a^3} \right] \quad \text{g/cm}^3 \quad (2)$$

Where; ' $N_A$ ' is the Avogadro's number.

$$\left[ P = 1 - \frac{d_{\text{exp}}}{d_x} * 100 \right] \quad (3)$$

The value of ' $d_{\text{xrd}}$ ' increases with  $\text{Zn}^{2+}$  concentration due to the heavier ion. The decrease in the porosity of the samples with a concentration of  $\text{Zn}^{2+}$  ions has been noticed. Which is the collective effect by the  $\text{Zn}^{2+}$  and  $\text{Ce}^{3+}$  ions during the formation of grains and some  $\text{Ce}^{3+}$  ions prefers the octahedral site as well some of them are present at the vicinity of grain boundary lead to a increase in the chance of closeness with nearby grains can lower the porosity and increases the probability of lattice stain [35].

### 3.2. FE-SEM- morphology and EDS of samples

The FE-SEM microstructure of all the samples of  $\text{Ni}_x \text{Zn}_{1-x} \text{Ce}_{0.1} \text{Fe}_{1.9} \text{O}_4$  prepared via citrate gel auto combustion as shown in figures 3(a)–(f), the FE-SEM micrographs demonstrate the porous morphology and inhomogeneous grain distribution due to the evolution of gas. The connectivity between the grains is more in the  $\text{Zn}^{2+}$  ions substituted samples. The distribution of grains is examined through Image-J software, the grains size has been measured and the histogram of grain distribution is displayed in the inset of figures 3(a)–(f). All the samples are found to exist in the nano regime. The quantification of chemical elements in the prepared sample is conformed by EDS measurement; all the elements are found to be in a right stoichiometric proportion the EDS spectra of  $\text{Ni}_{0.8} \text{Zn}_{0.2} \text{Ce}_{0.1} \text{Fe}_{1.9} \text{O}_4$  as shown in figure 3(g).

### 3.3. Thermogravimetric analysis (TG-DTA)

Thermal analysis is a simple and accurate method of studying the thermal behaviour of a substance. It is possible to get the temperature at which crystallization, phase change and decomposition take place in the material and also account for the kinematics of chemical reactions that can take place within the substance. These factors are essential to finding the required sintering temperature for the samples. The plots of weight loss % (TGA) and Differential weight loss (DTA) with temperature give the amount of temperature required for sintering.

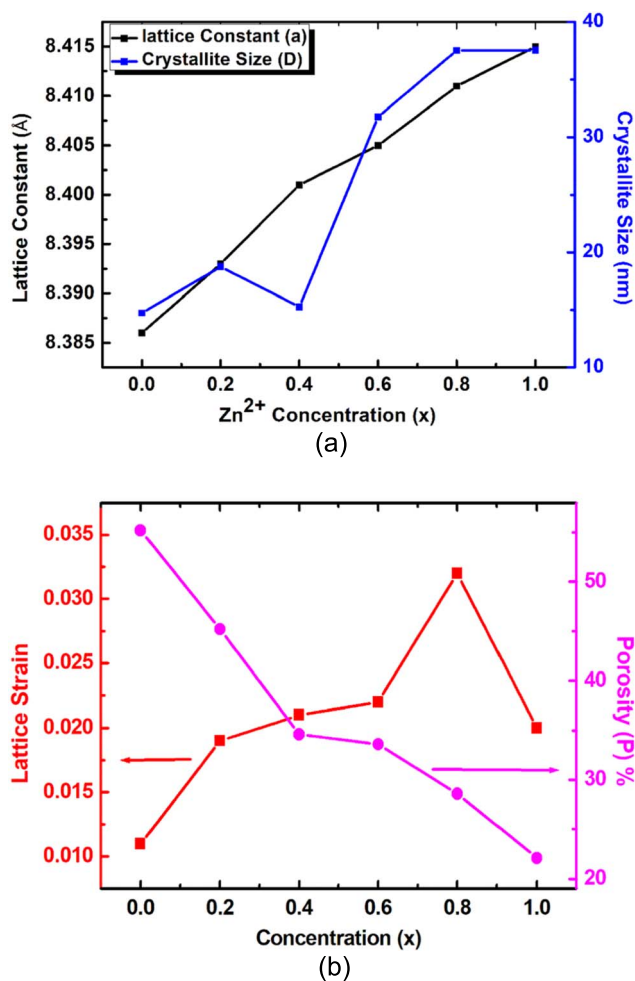


**Figure 2.** (a) lattice constant and crystallite size of  $\text{Ni}_{1-x}\text{Zn}_x\text{Ce}_{0.1}\text{Fe}_{1.9}\text{O}_4$  ( $0 \leq x \leq 1$ ). (b) Lattice strain and porosity of  $\text{Ni}_{1-x}\text{Zn}_x\text{Ce}_{0.1}\text{Fe}_{1.9}\text{O}_4$  ( $0 \leq x \leq 1$ ).

**Table 1.** Molecular weight (mol. Wt.), lattice constant (a), crystallite size (d), lattice strain ( $\epsilon$ ), bulk density ( $d_{\text{exp}}$ ), x-ray density ( $d_x$ ) & porosity (p) of  $\text{Ni}_{1-x}\text{Zn}_x\text{Ce}_{0.1}\text{Fe}_{1.9}\text{O}_4$  ferrite.

Concentration (x)	Mol. Wt. (g/mol.)	a (Å)	D (nm)	$\epsilon$	$d_{\text{exp}}$ (g/cm <sup>3</sup> )	$d_x$ (g/cm <sup>3</sup> )	P (%)
0.0	242.80	8.386	14.74	0.011	3.993	5.468	55.2
0.2	244.15	8.393	18.75	0.019	3.939	5.485	45.2
0.4	245.48	8.401	15.27	0.021	3.783	5.499	34.6
0.6	246.82	8.405	31.76	0.022	3.767	5.521	33.6
0.8	248.16	8.411	37.53	0.032	3.834	5.539	28.6
1.0	249.49	8.415	37.54	0.020	3.778	5.561	22.1

Figure 4(a); shows the weight loss % (TGA) and Differential weight loss (DTA) of the sample  $\text{NiFe}_2\text{O}_4$ . The TGA curve confirms that no significant order of weight loss takes place. However, of the three endothermic peaks in the Derivative of Thermogravimetric Analysis, the inflection points lie at 45.7 °C, 324.1 °C & 458.9 °C, respectively. The first derivative of the weight loss curve signifies three steps of apparent change in weight loss in the sample. In the first step, 0.1% of weight loss was due to the evaporation of absorbed water molecules from the sample. The second step of weight loss of 1.83% is due to the evolution of gas from remaining nitrates and organic substance from the sample [36] and in the third step sample loses 4.05%. It is due to the crystallization of  $\text{NiFe}_2\text{O}_4$  in the spinel phase.

Figure 4(b); shows the weight loss % (TGA) and Differential weight loss (DTA) of the sample  $\text{ZnFe}_2\text{O}_4$ ; the TGA curve confirms that continuous weight loss by results the three inflection points at 44.15 °C, 318.87 °C & 699.5 °C from the differential weight loss curve signifies that there are three steps of weight loss takes place in the sample, in the first step 0.48% of weight loss due to the evaporation of absorbed water molecules from the sample. In The second step, 4.32% and 12.9% in the third step of weight loss signifies the crystalline phase



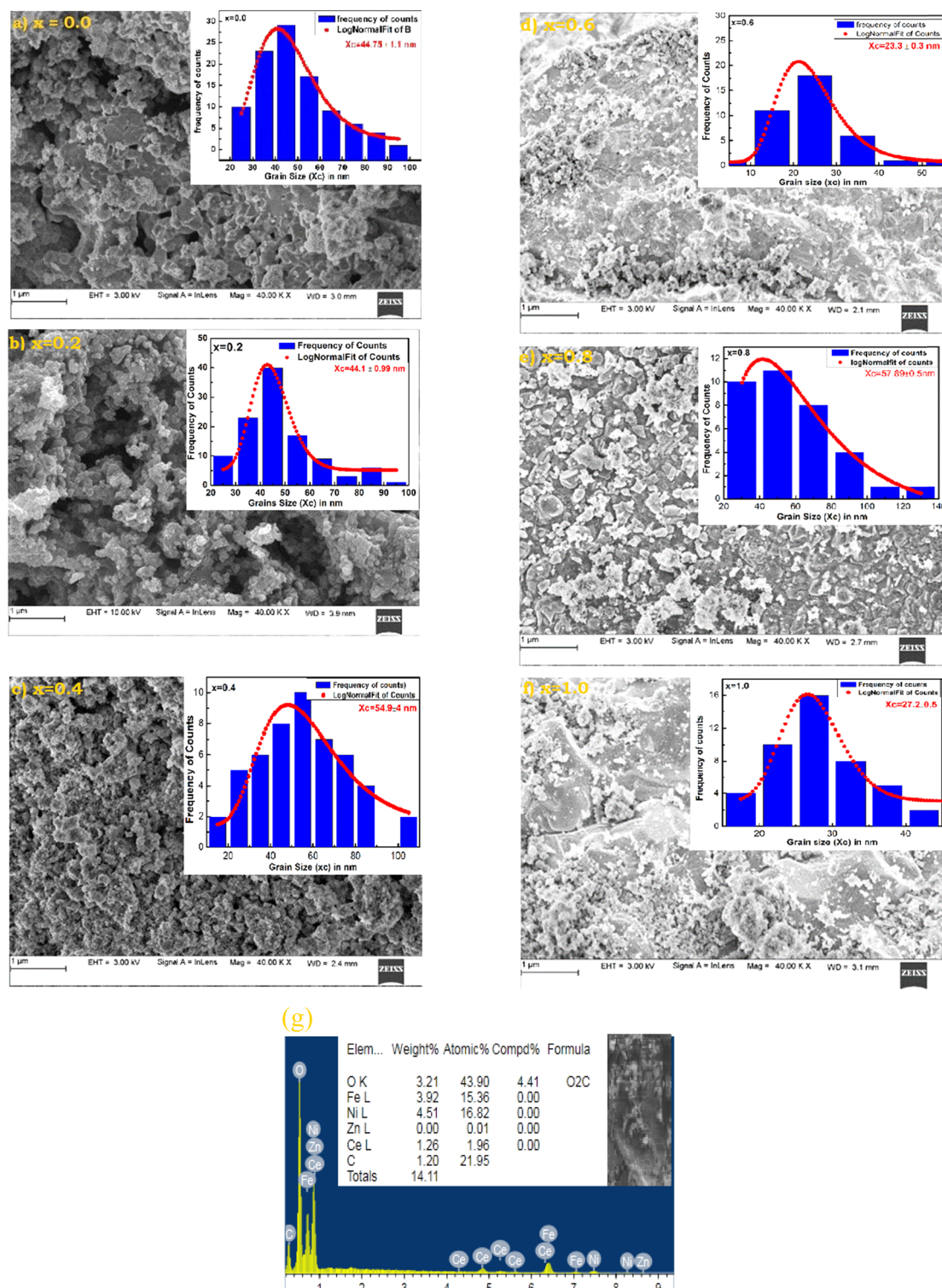
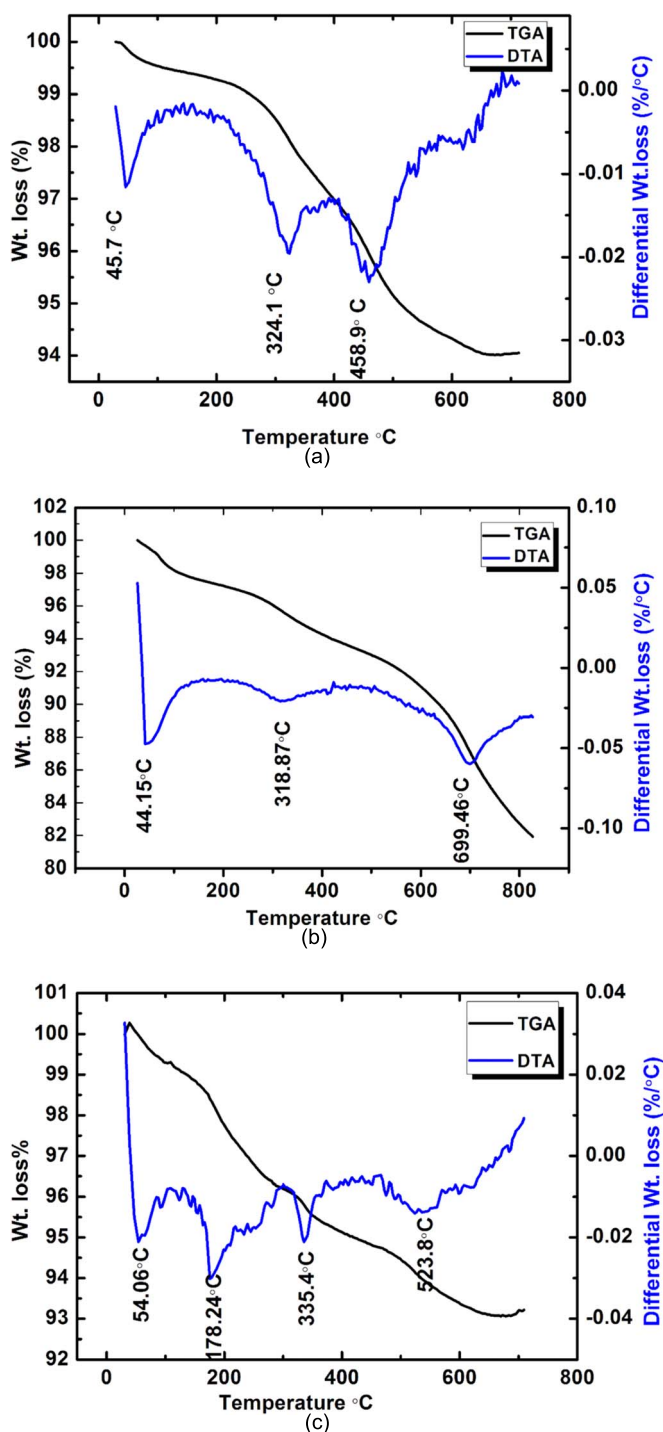


Figure 3. (a)–(f) The FE-SEM microstructure of  $\text{Ni}_{0.8}\text{Zn}_{1-x}\text{Ce}_{0.1}\text{Fe}_{1.9}\text{O}_4$ . (g) EDS. Spectra of  $\text{Ni}_{0.8}\text{Zn}_{0.2}\text{Ce}_{0.1}\text{Fe}_{1.9}\text{O}_4$ .

formation in the sample [37] and changes in the crystallographic arrangement of  $\text{ZnFe}_2\text{O}_4$  by the evaporation of zinc. Therefore, no decomposition or melting of material takes place in the measured range.

Figure 4(c); shows the weight loss % (TGA) and Differential weight loss (DTA) of the sample  $\text{Ni}_{0.8}\text{Zn}_{0.2}\text{Ce}_{0.1}\text{Fe}_{1.9}\text{O}_4$  in the plot four endothermic peaks at  $54^\circ\text{C}$ ,  $178.24^\circ\text{C}$ ,  $335.4^\circ\text{C}$  &  $523.8^\circ\text{C}$  from the differential weight loss curve signifies that there are four steps of weight loss takes place in the sample, in the first step, 0.03% of weight loss due to the evaporation of absorbed water molecules from the sample. The second step sample loses 1.66% of its weight due to the evolution of  $\text{CO}_2$  from the samples. The third step, 4.2%, is due to the crystallization of  $\text{Ni}_{0.8}\text{Zn}_{0.2}\text{Ce}_{0.1}\text{Fe}_{1.9}\text{O}_4$  and the fourth step, 5.86%, is due to the alteration in the phase by the loss of excess oxygen from the sample in the spinel phase, in all the samples, no decomposition or melting of





**Figure 4.** (a) TGA and DTA curves of the  $\text{NiFe}_2\text{O}_4$ . (b) TGA and DTA curves of the  $\text{ZnFe}_2\text{O}_4$ . (c) TGA and DTA curves of the  $\text{Ni}_{0.8}\text{Zn}_{0.2}\text{Ce}_{0.1}\text{Fe}_{1.9}\text{O}_4$ .

material takes place the measured range. Comparatively, the Cerium substituted samples are crystallized below the crystallization temperature of unsubstituted samples. The comparative thermogravimetric analysis infers the improved thermal stability of the rare earth element Ni-Zn ferrites by substituting  $\text{Zn}^{2+}$  ions [38].

### 3.4. DC Electrical conductivity

Figure 5: Shows the  $\log \sigma_{dc}$  with the  $1000/T$  plot for samples  $\text{Ni}_{(1-x)}\text{Zn}_x\text{Ce}_{0.1}\text{Fe}_{1.9}\text{O}_4$  ( $0 \leq x \leq 1$ ); the temperature dependence of  $\sigma_{dc}$  of all samples increases continuously with the increasing temperature, revealing that all samples exhibit the semiconducting property by following the Arrhenius relation (4) [39]. At a particular temperature slight change in the resistivity lead to form two distinct regions in the plot. The temperature at which alters the resistivity of the samples is known as Curie temperature (Loria method) [28].

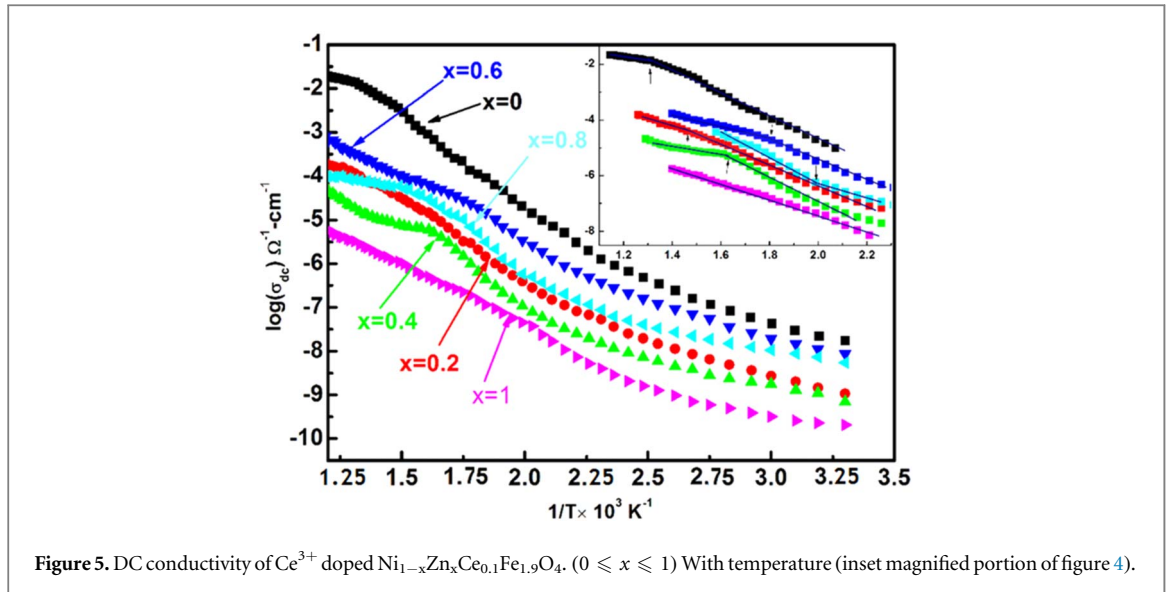


Figure 5. DC conductivity of  $\text{Ce}^{3+}$  doped  $\text{Ni}_{1-x}\text{Zn}_x\text{Ce}_{0.1}\text{Fe}_{1.9}\text{O}_4$  ( $0 \leq x \leq 1$ ) With temperature (inset magnified portion of figure 4).

$$\sigma_{dc} = \sigma_0 \exp\left(\frac{-\Delta E}{kT}\right) \Omega^{-1}\text{cm}^{-1} \quad (4)$$

Where;  $\sigma_0$  = Temperature independent constant in  $\Omega^{-1}\text{cm}^{-1}$ ,  $K$  = Boltzmann constant in  $\text{eV}/K$ ,  $\Delta E$  = activation energy in  $\text{eV}$  and  $T$  = absolute temperature in  $K$ ,

At high-temperature, phonon induced correlated electron transfer mechanism takes place. The material initially exists in the ferrimagnetic phase as a result of increment in the temperature it changes to the paramagnetic phase, it is mainly due to change in the crystal symmetry from monoclinic (below  $T_c$ ) to cubic (above  $T_c$ ) [40]. The nature of conductivity variation can be explained by the Verwey mechanism between the two adjacent tetrahedral and octahedral sites [41, 42]. This is chiefly due to the exchange mechanism of electrons between  $\text{Ni}^{2+} + \text{Fe}^{3+} \rightleftharpoons \text{Ni}^{3+} + \text{Fe}^{2+}$  ions. Similarly, the type of dopant used, microstructure and porosity of samples also impact the conductivity of the samples [43]. When compared to previously reported values, the sample's DC conductivity is reduced. The consequent impact is due to the magnetic coupling interaction of hopping elections at localized bands, tending to enlarge the energy bands in nanoparticles [44].

#### 3.4.1. Influence of $\text{Zn}^{2+}$ ion on conductivity

Figure 5; confirms the distinct value of conductivity for all the concentrations. The compositional variation of DC conductivity shows that the conductivity of the samples increases with increases in  $\text{Zn}^{2+}$  concentration [28]. This is the attribute of proportionate expansion of cell volume by the substitution of  $\text{Zn}^{2+}$  ion. Thus, the ionic radius of  $\text{Zn}^{2+}$  ( $0.67 \text{ \AA}$ ) is quite larger than the  $\text{Ni}^{2+}$  ion, which will usually prefer the tetrahedral site [42], then increase the chance of migration of  $\text{Fe}^{3+}$  ions from A-site to B-site. In the meanwhile, some ferrous ions are produced and they act as a kinetic barrier for the hopping of ions leads to an increase in the value of conductivity of material [45, 46].

The literature survey reveals that Ni–Zn–Ce ferrites are exhibiting n-type semiconducting properties. It is due to the intense hopping of  $\text{Fe}^{2+}$  and  $\text{Fe}^{3+}$  [47]. The DC conductivity increases with the increase in  $\text{Zn}^{2+}$  ion concentration. because  $\text{Zn}^{2+}$  has more conductivity value than  $\text{Ni}^{2+}$ . The conduction of materials is based on activation energy ( $\Delta E$ ), which are  $0.635 \text{ eV}$  and  $0.416 \text{ eV}$  for  $\text{NiFe}_2\text{O}_4$  and  $\text{ZnFe}_2\text{O}_4$ , respectively. The activation energy of  $\text{NiFe}_2\text{O}_4$  is higher than that of  $\text{ZnFe}_2\text{O}_4$ . Thus, more energy is required for electron exchange between  $\text{Fe}^{2+}$  and  $\text{Fe}^{3+}$  ions for the  $\text{NiFe}_2\text{O}_4$ . It is consistent with the fact that increased activation energy corresponds to decreased electrical conductivity [30].

The rise in conductivity may also, due to the manifestation of occupancy of the tetrahedral site by the  $\text{Fe}^{2+}$  and  $\text{Zn}^{2+}$  ions as well as the octahedral site by the  $\text{Ni}^{2+}$  and  $\text{Ce}^{3+}$  ions. Whereas  $\text{Fe}^{3+}$  ions partially exist in the A-site and B-site [45]. The rare-earth ion has fluctuating valence state, whenever the electrons are released during the hopping mechanism, it enhances their mobility and eventually leads to increase conduction [39].

## 4. Curie temperature ( $T_c$ ) and activation energy ( $\Delta E$ )

Figure 6: shows the variation of activation energy with  $\text{Zn}^{2+}$  ion concentrations. The reduction of magnetic ions at the A-site affects the activation energy of the material. The activation energy and Curie temperature are reduced with  $\text{Zn}^{2+}$  ions concentrations. The temperatures are pretty close to the Curie temperature ( $T_c$ ) the

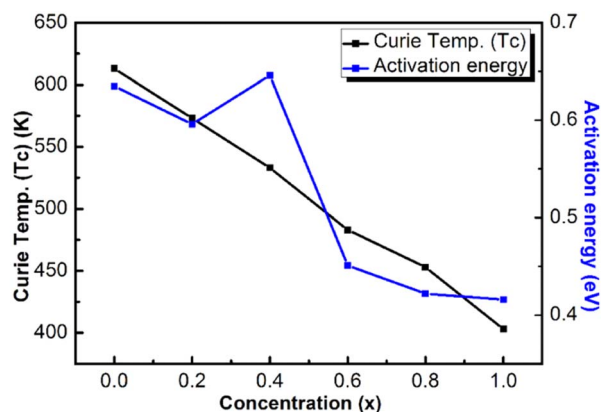


**Figure 6.** Curie temperature ( $T_c$ ) and activation energy ( $\Delta E$ ) with concentration ( $x$ ) for  $\text{Ni}_{1-x}\text{Zn}_x\text{Ce}_{0.1}\text{Fe}_{1.9}\text{O}_4$ .

**Table 2.** Values of paramagnetic and Ferrimagnetic activation energy ( $E_p$  &  $E_F$ ) & Curie temperature of  $\text{Ni}_{1-x}\text{Zn}_x\text{Ce}_{0.1}\text{Fe}_{1.9}\text{O}_4$  ferrites by DC Conductivity.

Concentration ( $x$ )	Activation energies (eV)			Curie Temperature(K) ( $T_c$ )
	$E_p$	$E_F$	$\Delta E$	
0	0.862	0.227	0.635	613
0.2	0.750	0.154	0.596	573
0.4	0.781	0.135	0.646	533
0.6	0.720	0.269	0.451	483
0.8	0.607	0.185	0.422	453
1	0.584	0.168	0.416	403

$\text{Fe}^{2+}(\text{A}) \rightleftharpoons \text{O}^{2-} \rightleftharpoons \text{Fe}^{3+}(\text{B})$  interaction decreases. Similar results are reported in K. Vijaya Kumar *et al* investigation [48], we can confirm that the Curie temperature only depends on the composition and is independent of geometry or porosity. Table 2 is the list of values of activation energy of the sample in the paramagnetic and the ferrimagnetic region they are estimated using the relation (5).

$$E_a = 2.303 \times k_B \times 10^3 \times \text{Slope}(eV) \quad (5)$$

Where;  $k_B$  is the Boltzmann constant ( $8.603 \times 10^{-5} \text{ eV K}^{-1}$ ).

And because of the ordered magnetic dipoles, the activation energy in the paramagnetic region is more than that of the ferrimagnetic region.

It indicates that when  $\text{Zn}^{2+}$  increases, activation energy decreases in the paramagnetic zone due to a decrease in the barrier height [49, 50]. The activation energy in the case of rare earth element substituted samples are more at smaller concentrations. Thus, some of the B-site is occupied by  $\text{Ce}^{3+}$  ions, which strongly block the conduction mechanism between ferrous and ferric ions. Therefore, electrons require more energy to establish conduction in the samples, for higher concentration reverses due to the partial substitution of rare-earth ions to the octahedral site and filling the voids lead to increasing the activation energy.

#### 4.1. Magnetic characterization

Figure 7: Shows the magnetization of the sample at room temperature. In the magnetic hysteresis plots, the magnetization of samples measured up to the magnetic field strength 15kOe, obtained values are given in table 3. The magnetization increases with an increase in the order of flux, and then saturation is attained within the range of selection. The respective  $\text{Zn}^{2+}$  concentration influences the saturation of magnetization of all samples. As  $\text{Zn}^{2+}$  concentration increased the saturation magnetization immediately takes the raise ( $x = 0.2$ ,  $M_s^* = 57.70 \text{ emu g}^{-1}$ ) and for higher concentrations of  $\text{Zn}^{2+}$  ions (0.4, 0.6, 0.8, and 1.00) it gradually decrease [51]. The saturation magnetization follows a similar trend, but it is slightly higher than  $\text{Gd}^{3+}$  substituted ferrites [26]; the reason is that the effective magnetic moment of  $\text{Ce}^{3+}$  is  $1.732 \mu_B$ . It is lower than  $\text{Gd}^{3+}$  is  $7.9 \mu_B$ , it prefers the B-site of spinel ferrite. In the isotropic magnetic materials, net magnetic moment obeys the relation, i.e.,  $\mu = \mu_A - \mu_B$ .  $M_s^*$  is high in the case of  $\text{Ce}^{3+}$  substituted ferrites compared to the  $\text{Gd}^{3+}$  ferrites [52].

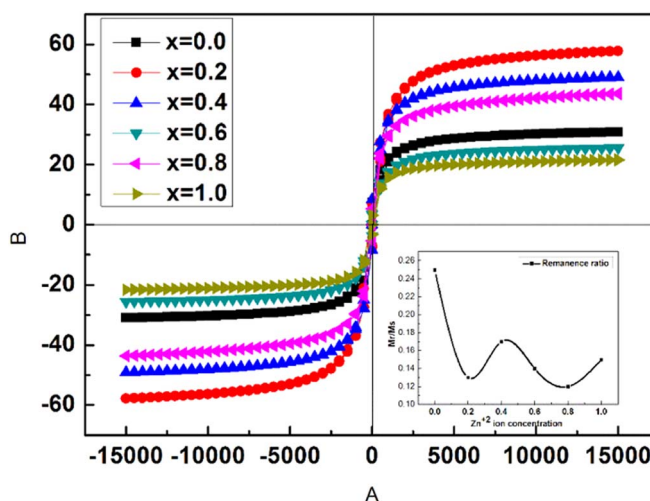


Figure 7. Magnetic hysteresis of  $\text{Ni}_{(1-x)}\text{Zn}_x\text{Ce}_{0.1}\text{Fe}_{1.9}\text{O}_4$  at room temperature. (Inset, remanence ratio v/s  $\text{Zn}^{2+}$  ions concentration).

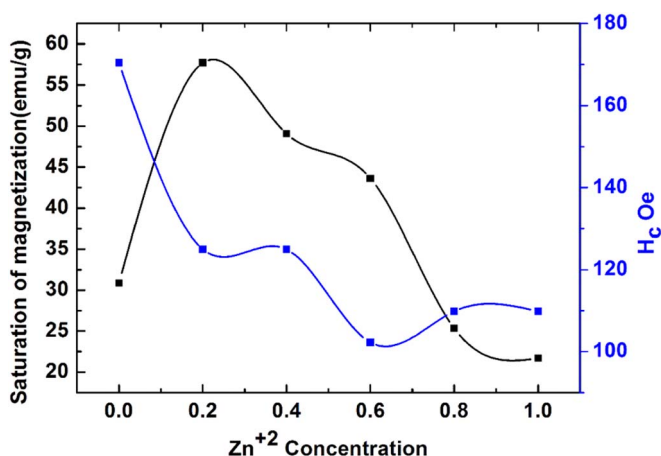


Figure 8. Variation of saturation remanence ratio, magnetization ( $M_s^*$ ) and coercive field ( $H_c$ ) with  $\text{Zn}^{2+}$  concentration.

Table 3. Saturation Magnetization ( $M_s^*$ ), Coercive Field ( $H_c$ ), Experimental value of magnetic moment ( $\eta_{\text{exp}}$ ), Retentivity ( $M_r$ ), Remanence ratio ( $S = M_r/M_s$ ).

'x'	$M_s^* (\text{emu/g})$	$H_c (\text{Oe})$	$\eta_{\text{exp}} (\text{emu})$	$M_r (\text{emu/g})$	$S (M_r/M_s)$
0.0	30.88	170.41	1.35689	7.83	0.25
0.2	57.70	124.98	2.54927	7.57	0.13
0.4	49.07	124.97	2.17971	9.24	0.17
0.6	43.63	102.25	1.94857	5.73	0.14
0.8	25.36	109.81	1.13872	3.71	0.12
1.0	21.67	109.82	0.97821	3.43	0.15

The variation of saturation remanence ratio, magnetization ( $M_s^*$ ) and coercive field ( $H_c$ ) with  $\text{Zn}^{2+}$  concentration are shown in figures 7 (inset) and 8. The remanence ratio progressively decreases with  $\text{Zn}^{2+}$  ion concentration; this indicates the isotropic nature of magnetic material and more easily finds the nearest magnetization direction after the removal of a magnetic field. The area under the hysteresis loop signifies the hysteresis loss. Therefore, the loop area is small in the case of  $\text{Ce}^{3+}$  substituted ferrite; hence, the hysteresis loss is low as in the case of  $\text{Ce}^{3+}$  substituted ferrite implied by the low magnetocrystalline anisotropy of the material. The coercive field also decreases with an increase in the concentration of  $\text{Zn}^{2+}$  ions conditions grain size, which follows the relation  $H_c \propto \frac{1}{r}$ . The radius of the  $\text{Zn}^{2+}$  ions in the cell reduces the ' $H_c$ ' [53, 54]. The marginal enhancement of magnetic parameters is due to the magnetic ordering in surface spin [55].

## 5. Conclusion

$\text{Ni}_{(1-x)}\text{Zn}_x\text{Ce}_{0.1}\text{Fe}_{1.9}\text{O}_4$  Nanoparticles are successfully synthesized for various concentrations of  $\text{Zn}^{2+}$  ion ( $0 \leq x \leq 1$ ) via aqueous citrate precursor auto combustion method with a ratio of  $\text{Fe}^{3+}$  &  $\text{Zn}^{2+}$  or  $\text{Ni}^{2+}$  to 2:1 and Nitrates/citric acid ratio of 1/1.5. The powder x-ray diffraction studies inform the crystallization in the Spinel phase and the formation of the grain-boundary phase. The crystallite size increases with  $\text{Zn}^{2+}$  concentration 14 ~ 38 nm. The compressive force will dominate the lattice strain by the grain boundary phase. The basis vector increases with  $\text{Zn}^{2+}$  validates Vegard's law. The voids are reduced due to the occupation of  $\text{Zn}^{2+}$  (0.69 Å) ion into the A-site. FE-SEM studies reveal inhomogeneity in the formation of grains. The TGA analysis identifies the multiple endothermic peaks; however, no major decomposition takes place within 800 °C. The DC conductivity measured at various temperatures up to 800 K, the variation of conductivity linear in the range of temperature and phase change from ferrimagnetic to paramagnetic is noticed, the activation energy and Curie temperature in the paramagnetic and ferrimagnetic range obtained by Arrhenius plots (Loria method). The activation energy is more at the paramagnetic region, which is reduced with  $\text{Zn}^{2+}$  concentration. The saturation magnetization at room temperature is maximum for  $\text{Zn}^{2+} = 0.2$  (57.7 emu g<sup>-1</sup>) and  $H_c'$  related by  $H_c \propto \frac{1}{r}$ . The radius of the  $\text{Zn}^{2+}$  low hysteresis loss is identified, the magnetic parameters and DC electrical factors are improved in  $\text{Ce}^{3+}$ -Ni-Zn-ferrites.

## Acknowledgments

The authors would like to thank the Ministry of education in Saudi Arabia and Taif University Researchers Supporting Project Number (TURSP-2020/47), Taif University, Saudi Arabia. Santhosh Kumar M V Acknowledge to Jain Institute of Technology. Davangere.

## Data availability statement

All data that support the findings of this study are included within the article (and any supplementary files).

## ORCID iDs

Santhosh Kumar M V  <https://orcid.org/0000-0002-3756-0517>

B M Prasanna  <https://orcid.org/0000-0002-8972-5360>

## References

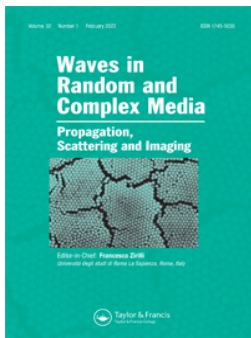
- [1] Verma A and Dube D C 2005 Processing of nickel-zinc ferrites via the citrate precursor route for high-frequency applications *J. Am. Ceram. Soc.* **88** 519–23
- [2] Zheng L J Z, Zhang H and Yang Q 2014 Enhanced high-frequency properties of nzn ferrite ceramic with co2Z-hexaferrite addition *J. Am. Ceram. Soc.* **97** 2016–9
- [3] Gul I H and Maqsood A 2008 Structural, magnetic and electrical properties of cobalt ferrites prepared by the sol-gel route *J. Alloys Compd.* **465** 227–31
- [4] Venkataraju C, Sathishkumar G and Sivakumar K 2010 Effect of nickel on the electrical properties of nanostructured MnZn ferrite *J. Alloys Compd.* **498** 203–6
- [5] Anwar H and Maqsood A 2010 Temperature-dependent structural and electrical analysis of Mn-Zn nano ferrites *J. Pak Mater Soc.* **4** 81–94
- [6] Mukherjee K and Majumder S B 2010 Reducing gas sensing behavior of nano-crystalline magnesium-zinc ferrite powders *Talanta* **51** 1826–32
- [7] Praveena K, Sadhana K, Bharadwaj S and Murthy S R 2009 Development of nanocrystalline Mn-Zn ferrites for high-frequency transformer applications *J. Magn. Magn. Mater.* **321** 2433–7
- [8] Choudhary B L, Kumar U, Kumar S, Chander S, Kumar S, Dalela S, Dolia S N and Alvi P A 2020 Irreversible magnetic behavior with temperature variation of  $\text{Ni}_{0.5}\text{Co}_{0.5}\text{Fe}_2\text{O}_4$  nanoparticles *J. Magn. Magn. Mater.* **507** 166861
- [9] Vaidyanathan G and Sendhilnathan S 2008 Characterization of  $\text{Co}_{1-x}\text{Zn}_x\text{Fe}_2\text{O}_4$  nanoparticles synthesized by co-precipitation method *Phys. B Condens. Matter.* **403** 2157–67
- [10] Hu P, Yang H, Pan D, Wang H, Tian J, Zhang S, Wang X and Volinsky A A 2010 Heat treatment effects on microstructure and magnetic properties of Mn-Zn ferrite powders *J. Magn. Magn. Mater.* **322** 173–7
- [11] Costa A C F M, Silva V J, Xin C C, Vieira D A, Cornejo D R and Kiminami R H G A 2010 Effect of urea and glycine fuels on the combustion reaction synthesis of Mn-Zn ferrites: evaluation of morphology and magnetic properties *J. Alloys Compd.* **495** 503–5
- [12] Hessien M M, Rashad M M, El-Barawy K and Ibrahim I A 2008 Influence of manganese substitution and annealing temperature on the formation, microstructure and magnetic properties of Mn-Zn ferrites *J. Magn. Magn. Mater.* **320** 1615–21
- [13] Mohd Hashima R K K et al 2013 Preparation and characterization chemistry of nano-crystalline Ni-Cu-Zn ferrite *J. Alloys Compd.* **549** 349–57



- [14] Murthy S R, Kumar S A, Ramesh T, Rao G N, Suneetha T, Shinde R S and Rajendar V 2018 Microwave-Hydrothermal synthesis of  $\gamma$ -Fe<sub>2</sub>O<sub>3</sub> nanoparticles : sintering temperature effect on structural, magnetic and dielectric properties *J. Supercond. Nov. Magn.* **31** 1899–908
- [15] Penchal Reddy M, Shakoor R A, Mohamed A M A, Gupta M and Huang Q 2016 Effect of sintering temperature on the structural and magnetic properties of MgFe<sub>2</sub>O<sub>4</sub> ceramics prepared by spark plasma sintering *Ceram. Int.* **42** 4221–7
- [16] Barati M R, Seyyed Ebrahimi S A and Badii A 2008 The role of surfactant in synthesis of magnetic nanocrystalline powder of NiFe<sub>2</sub>O<sub>4</sub> by sol-gel auto-combustion method *J. Non. Cryst. Solids.* **354** 5184–5
- [17] Zaki H M 2009 The influence of Zn ions substitution on the transport properties of Mg-ferrite *Phys. B Condens. Matter.* **404** 3356–62
- [18] Ramesh S, Dhanalakshmi B, Chandra Sekhar B, Subba Rao P S V and Rao B P 2016 Effect of Mn/Co substitutions on the resistivity and dielectric properties of nickel–zinc ferrites *Ceram. Int.* **42** 9591–8
- [19] Lal G, Punia K, Bhoi H, Dolia S N, Choudhary B L, Alvi P A, Dalela S, Barbar S K and Kumar S 2021 Exploring the structural, elastic, optical, dielectric and magnetic characteristics of Ca<sup>2+</sup> incorporated superparamagnetic Zn<sub>0.5</sub>–xCa<sub>0.1</sub>Co<sub>0.4</sub> + xFe<sub>2</sub>O<sub>4</sub> (x = 0.0, 0.05 & 0.1) nanoferrites *J. Alloys Compd.* **886** 161190
- [20] Rai B K, Mishra S R, Nguyen V V and Liu J P 2012 Author's personal copy Synthesis and characterization of high coercivity rare-earth ion doped Sr 0.9RE0.1Fe<sub>10</sub>Al<sub>2</sub>O<sub>19</sub> (RE: Y, La, Ce, Pr, Nd, Sm, and Gd) *J. Alloys Compd.* **550** 198–203
- [21] Gadkari A B, Shinde T J and Vasambekar P N 2010 Magnetic properties of rare earth ion (Sm<sup>3+</sup>) added nanocrystalline Mg–Cd ferrites, prepared by oxalate co-precipitation method *J. Magn. Magn. Mater.* **322** 3823–7
- [22] Pervaiz E and Gul I H 2013 Influence of Rare Earth (Gd<sup>3+</sup>) on Structural, gigahertz dielectric and magnetic studies of cobalt ferrite *J. Phys. Conf. Ser.* **439** 1–15
- [23] Lassoued A, Dkhil B, Gadri A and Ammar S 2017 Control of the shape and size of iron oxide ( $\alpha$ -Fe<sub>2</sub>O<sub>3</sub>) nanoparticles synthesized through the chemical precipitation method *Results Phys.* **7** 3007–15
- [24] Kadyrzhanov K K, Egizbek K, Kozlovskiy A L and Zdorovets M V 2019 Synthesis and properties of Ferrite-based nanoparticles *Nanomaterials.* **9** 1–16
- [25] Praveena K, Chen H-W, Liu H-L, Sadhana K and Murthy S R 2016 Enhanced magnetic domain relaxation frequency and low power losses in Zn<sup>2+</sup> substituted manganese ferrites potential for high-frequency applications *J. Magn. Magn. Mater.* **420** 129–42
- [26] Santhosh Kumar M V, Shankarmurthy G J, Melagiriappa E, Rao A and Nagaraja K K 2020 Cation distribution and magnetic properties of Gd<sup>3+</sup>-substituted Ni–Zn Nano-ferrites *J. Supercond. Nov. Magn.* **33** 2821–7
- [27] Goldman A 2006 *Modern Ferrite Technology* 2nd (Pittsburgh, PA, U.S.A.: Springer)
- [28] Rama Krishna K, Vijaya Kumar K and Ravinder D 2012 Structural and electrical conductivity studies in nickel–zinc ferrite *Adv. Mater. Phys. Chem.* **2** 185–91
- [29] Ishaque M, Khan M A, Ali I, Athair M, Khan H M, Asif Iqbal M, Islam M U and Warsi M F 2016 Synthesis of nickel–zinc-yttrium ferrites: structural elucidation and dielectric behavior evaluation *Mater. Sci. Semicond. Process.* **41** 508–12
- [30] Lazarević Z Ž, Jovalekić Č, Milutinović A, Sekulić D, Ivanovski V N, Rečnik A, Cekić B and Romčević N Ž 2013 Nanodimensional spinel NiFe<sub>2</sub>O<sub>4</sub> and ZnFe<sub>2</sub>O<sub>4</sub> ferrites prepared by soft mechanochemical synthesis *J. Appl. Phys.* **113** 187221
- [31] Veena Gopalan E, Al-Omari I A, Malini K A, Joy P A, Sakthi Kumar D, Yoshida Y and Anantharaman M R 2009 Impact of zinc substitution on the structural and magnetic properties of chemically derived nanosized manganese zinc mixed ferrites *J. Magn. Magn. Mater.* **321** 1092–9
- [32] Singh N, Agarwal A and Sanghi S 2011 Dielectric relaxation, conductivity behavior and magnetic properties of Mg substituted Zn–Li ferrites *Curr. Appl. Phys.* **11** 783–9
- [33] Kumar M V S, Shankarmurthy G J, Melagiriappa E, Nagaraja K K, Jayanna H S and Telenkov M P 2018 Structural and complex impedance properties of Zn<sub>2+</sub> substituted nickel ferrite prepared via low-temperature citrate gel auto-combustion method *J. Mater. Sci., Mater. Electron.* **29** 12795–803
- [34] Ridha S M A 2015 X-ray studies and electrical properties of the zinc-substituted copper nanoferrite synthesized by sol-gel method *Int. J. Compos. Mater.* **5** 195–201
- [35] Lakshmi C S, Sridhar C S L N, Govindraj G, Bangararaju S and Potukuchi D M 2016 Experimental characterization of nanocrystalline niobium-doped nickel–zinc ferrites: occurrence of superparamagnetism *J. Mater. Sci.* **51** 8382–99
- [36] Sileo E E, Rotelo R and Jacobo S E 2002 Nickel zinc ferrites prepared by the citrate precursor method *Phys. B Condens. Matter.* **320** 257–60
- [37] Rahimi M, Kameli P, Ranjbar M, Hajihashemi H and Salamati H 2013 The effect of zinc doping on the structural and magnetic properties of Ni<sub>1-x</sub>Zn<sub>x</sub>Fe<sub>2</sub>O<sub>4</sub> *J. Mater. Sci.* **48** 2969–76
- [38] Sanida A, Stavropoulos S G, Spiliotis T and Psarras G C 2019 Investigating the effect of zn ferrite nanoparticles on the thermomechanical, dielectric and magnetic properties of polymer nanocomposites *Materials* **12** 3015 (1–12)
- [39] Ali M A, Uddin M M, Khan M N I, Chowdhury F-U-Z and Haque S M 2016 *Structural, Morphological And Electrical Properties Of Sn-Substituted Ni-Zn Ferrites Synthesized By Double Sintering Technique* **424** 148–54
- [40] Srivastava C M 1983 Transport property *Bull. Mater. Sci.* **5** 247–56
- [41] Verwey E J, Haayman P W and Romeijn F C 1947 Physical properties and cation arrangement of oxides with spinel structures: II. Electronic conductivity *J. Chem. Phys.* **15** 181–7
- [42] Hashim M et al 2013 Synthesis and characterizations of Ni<sup>2+</sup> substituted cobalt ferrite nanoparticles *Mater. Chem. Phys.* **139** 364–74
- [43] Irvine J T S, Huanosta A, Valenzuela R and West A R 1990 Electrical properties of polycrystalline nickel zinc ferrites *J. Am. Ceram. Soc.* **73** 729–32
- [44] Santhosh Kumar M V, Shankarmurthy G J, Melagiriappa E, Nagaraja K K, Jayanna H S and Telenkov M P 2019 Induced effects of Zn<sub>2+</sub> on the transport and complex impedance properties of Gadolinium substituted nickel-zinc nano ferrites *J. Magn. Magn. Mater.* **478** 12–9
- [45] Ajmal M and Maqsood A 2007 Influence of zinc substitution on structural and electrical properties of Ni<sub>1-x</sub>Zn<sub>x</sub>Fe<sub>2</sub>O<sub>4</sub> ferrites *Mater. Sci. Eng. B Solid-State Mater. Adv. Technol.* **139** 164–70
- [46] Ghazanfar U, Siddiqi S A and Abbas G 2005 Study of room temperature dc resistivity in comparison with activation energy and drift mobility of NiZn ferrites *Mater. Sci. Eng. B Solid-State Mater. Adv. Technol.* **118** 132–4
- [47] Dias A and Moreira R L 1999 Chemical, mechanical and dielectric properties after sintering of hydrothermal nickel–zinc ferrites *Mater. Lett.* **39** 69–76
- [48] Vijaya Kumar K and Ravinder D 2002 Electrical conductivity of Ni–Zn–Gd ferrites *Mater. Lett.* **52** 166–8
- [49] Asif Iqbal M, Misbah-Ul-Islam, Ali I, Mustafa G and Ali I 2013 Study of electrical transport properties of Eu<sup>3+</sup> substituted MnZn-ferrites synthesized by co-precipitation technique *Ceram. Int.* **39** 1539–45

- [50] Aliuzzaman M, Manjurul Haque M, Jannatul Ferdous M, Manjura Hoque S and Abdul Hakim M 2014 Effect of sintering time on the structural, magnetic and electrical transport properties of  $\text{Mg}_{0.35}\text{Cu}_{0.20}\text{Zn}_{0.45}\text{Fe}_{1.94}\text{O}_4$  ferrites *World J. Condens. Matter Phys.* **4** 13–23
- [51] Harzali H, Saida F, Marzouki A, Megriche A, Baillon F, Espitalier F and Mgaidi A 2016 Journal of magnetism and magnetic materials structural and magnetic properties of nano-sized NiCuZn ferrites synthesized by co-precipitation method with ultrasound irradiation *J. Magn. Magn. Mater.* **419** 50–6
- [52] Abdellatif M H, El-Komy G M and Azab A A 2017 Magnetic characterization of rare earth doped spinel ferrite *J. Magn. Magn. Mater.* **442** 445–52
- [53] Sadiq I, Khan I, Aen F, Islam M and Rana M 2012 Influence of rare earth  $\text{Ce}^{3+}$  on structural, electrical and magnetic properties of  $\text{Sr}^{2+}$  based W-type hexagonal ferrites *Phys. B Phys. Condens. Matter.* **407** 1256–61
- [54] Sridhar C S L N, Lakshmi C S, Govindraj G, Bangararaju S, Satyanarayana L and Potukuchi D M 2016 Structural, morphological, magnetic and dielectric characterization of nano-phased antimony doped manganese zinc ferrites *J. Phys. Chem. Solids* **92** 70–84
- [55] Naik P P, Tangsali R B, Meena S S, Bhatt P, Sonaye B and Sugur S 2014 Gamma radiation roused lattice contraction effects investigated by Mössbauer spectroscopy in nanoparticle Mn-Zn ferrite *Radiat. Phys. Chem.* **102** 147–52





## Effect of thermal radiation on heat transfer in plane wall jet flow of Casson nanofluid with suction subject to a slip boundary condition

Hassan A. H. Alzahrani, Abdulmohsen Alsaieri, J. K. Madhukesh, R. Naveen Kumar & B. M. Prasanna

To cite this article: Hassan A. H. Alzahrani, Abdulmohsen Alsaieri, J. K. Madhukesh, R. Naveen Kumar & B. M. Prasanna (2022): Effect of thermal radiation on heat transfer in plane wall jet flow of Casson nanofluid with suction subject to a slip boundary condition, Waves in Random and Complex Media, DOI: [10.1080/17455030.2022.2030502](https://doi.org/10.1080/17455030.2022.2030502)

To link to this article: <https://doi.org/10.1080/17455030.2022.2030502>



Published online: 08 Feb 2022.



Submit your article to this journal [↗](#)



View related articles [↗](#)



View Crossmark data [↗](#)



# Effect of thermal radiation on heat transfer in plane wall jet flow of Casson nanofluid with suction subject to a slip boundary condition

Hassan A. H. Alzahrani <sup>a</sup>, Abdulmohsen Alsaiani <sup>b,c</sup>, J. K. Madhukesh <sup>d</sup>,  
R. Naveen Kumar <sup>d</sup> and B. M. Prasanna <sup>e</sup>

<sup>a</sup>Department of Chemistry, College of Science and Arts at Khulis, University of Jeddah, Jeddah, Saudi Arabia;

<sup>b</sup>Centre of Excellence in Desalination Technology, King Abdulaziz University, Jeddah, Saudi Arabia;

<sup>c</sup>Mechanical Engineering Dept., King Abdulaziz University, Jeddah, Saudi Arabia; <sup>d</sup>Department of Studies and Research in Mathematics, Davangere University, Karnataka, India; <sup>e</sup>Department of Chemistry, Bapuji Institute of Engineering and Technology, Davanagere, India

## ABSTRACT

A Glauert type laminar wall jet issuing into a stationary liquid medium lying above a wall has technical uses in wall cooling and flow control. It plays a vital role in industrial applications like cooling/heating by impingement of jet, turbine blades, film cooling, mass and heat transfer phenomena. In this regard, a steady incompressible two-dimensional laminar Glauert kind wall jet is scrutinized in this study by considering nanoparticles suspension in the base liquid sodium alginate (*NaAlg*) with suction and wall slip boundary conditions. Further, a comparative study is done by considering aluminum alloy (AA7075) and single-walled carbon nanotube (*SWCNT*) as nanoparticles. The reduced ordinary differential equations (ODEs) are numerically solved by applying Runge–Kutta–Fehlberg fourth fifth-order (RKF-45) technique along with the shooting method. Results reveal that *NaAlg*–*SWCNT* Casson nanofluid shows enhanced heat transfer than *NaAlg*–AA7075 Casson nanofluid for increased values of radiation parameter. The rising values of the Casson parameter deteriorate the heat transfer rate of both nanofluids but an inverse trend is seen for improved values of radiation parameter.

## ARTICLE HISTORY

Received 24 August 2021

Accepted 12 January 2022

## KEYWORDS

Wall jet flow; Casson nanofluid; thermal radiation; suction; slip condition

## Nomenclature

$I(x)$	Variable slip factor
$T_w$	Temperature of the plate ( $K$ )
$C_w$	Concentration at the plate
$\beta$	Casson fluid parameter
$Nu$	Nusselt number
$Sh$	Sherwood number
$\rho C_p$	Heat capacitance
$U_r$	Reference velocity ( $ms^{-1}$ )

**CONTACT** B. M. Prasanna drbmprasanna@gmail.com

$Sc$	Schmidt number
$L$	Slip parameter
$\rho$	Density ( $kgm^{-3}$ )
$\mu$	Dynamic viscosity ( $kgm^{-1}s^{-1}$ )
$\phi$	Solid volume fraction
$q_r$	Radiative heat flux
$f_\infty$	Far-field velocity
$k$	Thermal conductivity ( $Wm^{-1}K^{-1}$ )
$\chi(\eta)$	Concentration profile
$u, v$	Axial velocity ( $ms^{-1}$ )
$k^*$	Mean absorption coefficient
$C_\infty$	Far filed Concentration
$x, y$	Cartesian coordinates ( $m$ )
$Rd$	Radiation parameter
$Pr$	Prandtl number
$D_f$	Diffusion coefficient ( $m^2s^{-1}$ )
$\sigma^*$	Stephan–Boltzmann constant
$g'(\eta)$	Velocity profile
$C_p$	Specific heat capacity ( $Jkg^{-1}K^{-1}$ )
$C_f$	Skin friction coefficient
$T_\infty$	Far filed temperature ( $K$ )
$S$	Wall suction parameter
$U, V$	Dimensionless variables
$\eta$	Similarity variable
$\theta(\eta)$	Thermal profile
$Re$	Local Reynolds number

## Subscripts

$nf$	nanofluid
$CNT$	Carbon nanotube
$s$	Solid particle
$f$	Fluid

## 1. Introduction

Researchers have been focusing more on improving heat transfer efficiency in recent years as a result of serious energy and environmental issues. In the literature, numerical solutions to equations reduced from governing equations have received a lot of attention. Knowing that numerical solutions are typically the more favored and convenient option in the engineering field since they take less time to compute and are more accurate. Here, we have numerically analyzed the wall jet flow of nanofluid. The boundary layer approximations are a popular method for simplifying laminar wall jet issues. Many researchers were attracted to laminar jets because of their several potential and practical applications, such as sluice gate flows, cooling jets over turbomachinery components, and freezing systems for laptop central processing units. The associated similarity/non-similarity solutions were discovered to be sufficient for predicting their behavior. Glauert [1] initially discussed the

issue of a stationary impermeable wall jet in 1956. In this study, he discovered that, the second similarity restriction concerning a quantity, namely the external momentum flux which can be scarcely construed as a physical perception. Recently, several researchers discussed both numerical and analytical solutions for wall jet problems Jafarimoghaddam [2–4] conferred the heat and mass transport characteristics of wall jet flows of different nanoliquids with several influencing factors. Aly and Pop [5] elaborated on the wall jet issue for hybrid nanofluid flows. Alhadhrami et al. [6] numerically quizzed the particle deposition influence on Glauert wall jet slipstream of nanoliquid

The transport characteristics of nanoliquids are influenced by the thermophysical of the nanoparticles and base fluid. The accumulation of nanoparticles to the carrier fluid increases the effective thermal conductivity of the nanofluid, thereby improving heat transport performance. Here, we considered the suspension of different nanoparticles such as aluminum alloy (AA7075) and single-walled carbon nanotubes (SWCNTs) in Sodium Alginate (NaAlg) as base fluid. The nanoparticle AA7075 is a mixture of Zinc, Magnesium, Copper, and Aluminum, in the proportion of,  $\sim 6 \sim 3$ ,  $\sim 1$ , and  $\sim 90$  respectively with added metals Silicon ferrous and Magnesium. In the present study, we used SWCNT as a nanoparticle. A CNT with a single layer of graphene is called an SWCNT. SWNTs exhibit specific electronic properties and can be either semiconducting or metallic depending on their geometry. Furthermore, the base liquid Sodium alginate (SA) is a safe, very viscous and water-soluble natural Casson liquid isolated from brown algae. Because of these qualities, SA is extensively employed in a wide range of industries, including food processing, medicines, cosmetics and textiles. Edward C. Stanford, a British chemist, was the first to develop sodium alginate in 1881. SA flow has since been the subject of several publications. Hatami and Ganji [7] conferred the flow analysis for SA-TiO<sub>2</sub> nanoliquid among dual coaxial cylinders. Sheikholeslami et al. [8] quizzed the nanoliquid spraying on a spinning disk. Hatami [9] explored the migration of nanoparticles around the intense cylinder. Tang et al. [10] swotted the convective heat transport in a nanoliquid-filled cavity with dual sinusoidal wavy walls. Hatami et al. [11–13] mathematically examined the heat transfer behavior of different nanoliquids past different surfaces. Prasannakumara [14,15] numerically examined the heat and mass transfer behavior of different nanoliquids past a stretching sheet. Several researchers have recently quizzed the heat and mass transport behavior of various nanoliquids passing through a varied surface [16–25].

Due to their outstanding properties in the field of industrial and technical sciences, the researcher has fully-fledged interests in non-Newtonian liquids. The basic equations of Navier-Stokes are unable to characterize the properties of the stream field of non-Newtonian liquids at this time because of the difficulty in the mathematical formulation of the flow issue. The Jeffrey, Burger, Eyring-Powell, Carreau, Oldroyd-A, Oldroyd-B, Maxwell, and Casson models are examples of non-Newtonian fluid models [26–30]. The Casson model is the utmost important model for blood characteristics and suspensions in our everyday life among these models. Motivated by these features, many researchers scrutinized the stream of Casson fluid with nanoparticles suspension. Recently, Alotaibi et al. [31] quizzed the MHD stream of Casson nanoliquid on a stretching surface. Jamshed et al. [32] exemplified the Casson nanofluid stream on a surface. Kumar et al. [33] analyzed the performance of a magnetic field on a chemically reacting Casson nanoliquid stream on a coiled stretchable sheet. The Casson nanoliquid flow across a stretchable surface was developed by Hussain et al. [34]. Kumar et al. [35] quizzed Casson liquid flow using dual nanoparticles suspended on a disk.

Researchers have discussed the thermal radiation effect on fluid streams due to its applications in engineering areas such as space vehicles, aircraft, satellites, various propulsion devices for missiles, nuclear power plants, turbid water bodies, photochemical reactors, and gas turbines. Recently, Hamid et al. [36] conferred the Cross-nanoliquid stream towards a radially shrinking disk with radiation. Reddy et al. [37] typified the radiative flow of a nanoliquid on a sheet with a melting effect. Akbar et al. [38] quizzed the radiation effect on the peristaltic flow of nanoliquid. Li et al. [39] quizzed the radiative Falkner–Skan stream of Maxwell nanoliquid past a poignant/static wedge. Yusuf et al. [40] elaborated the impact of bioconvection on the radiative flow of Williamson nanoliquid. Many researchers have been interested in studying suction and slip effects on various liquid streams in recent years. Suction and slip conditions are significant in a variety of technological and engineering applications. In the non-Newtonian liquid's flow, the slip effect can't be unheeded. The boundary slip is used in the prosthetic heart valve polishing, the polymers melting and the creation of interior cavities. Recently, Khan et al. [41] conferred the radiative stream with suction and slip effects. The radiative heat transference in Bodewadt slipstream on a disk due to suction was studied by Mustafa et al. [42]. Yashkun et al. [43] quizzed the slip flow of nanoliquid on a sheet with a suction effect. Zhao [44] elaborated the slip effect on the magnetized flow of a hybrid nanoliquid past a stretching surface. Yusuf et al. [45] educed the slip flow of micropolar liquid on an inclined surface.

Inspired by the all above insights, we developed a model for the wall jet flow of nanofluid. From the literature part of the view, the problem is not yet studied by considering suction, slip effects along with Casson fluid model. To fill this research gap, the existing study employs the RKF-45 approach with the shooting strategy to investigate the significant factors impact on the concentration, thermal, and flow fields of Casson nanoliquid inside the boundary. Furthermore, we have done a comparative study on *NaA Ig – SWCNT* and *NaA Ig – AA7075* nanoliquids. Although there are several publications on the thermal examination of different nanoparticles in the literature. Though, the wall jet flow of *NaA Ig – SWCNT* and *NaA Ig – AA7075* nanoliquids in the existence of these phenomenon's are not offered in the dynamic literature. This study is the first to investigate the thermal properties of such a liquid model. Also, a good discussion is made with the help of graphs.

## 2. Mathematical description of the problem

Consider a laminar jet flow of Cassin nanoliquid introduced through a slit into a stagnant medium distributed across a plate. *AA7075* and *SWCNT* are considered as nanoparticles suspended in the base liquid *NaA Ig*. Further, the Glauert kind wall jet is scrutinized in this study by employing suction and slip boundary conditions. From Navier's slip law (see [46]), no-slip along the  $x$ -axis should be replaced by (see [47])  $u = l(x)u_y$  due to wall roughness. Let, the variable slip factor is denoted by  $l(x)$ , by scaling analysis  $l(x)$  value depends on the spatial coordinate  $x$ . Furthermore, a variable suction at the wall in the  $y$ -direction is assumed to control the jet-induced stream in the form  $v = -V_w(x)$ ,  $V_w(x) > 0$  (see Figure 1).

Based on the above stated assumptions the fluid flow governing equations are as follows (see Alhadhrami et al. [6], Jafarimoghaddam [3,4] and Turkyilmazoglu [46]):

$$\frac{\partial u}{\partial x} + \frac{\partial v}{\partial y} = 0, \quad (1)$$

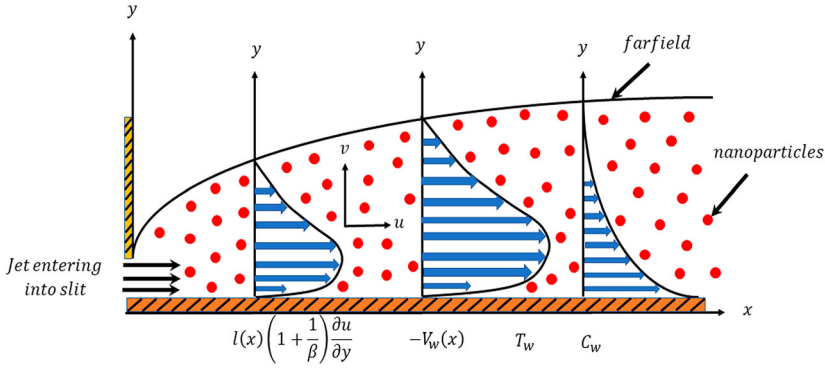


**Figure 1.** Flow geometry.

$$v \frac{\partial u}{\partial y} + u \frac{\partial u}{\partial x} = \left(1 + \frac{1}{\beta}\right) \frac{\mu_{nf}}{\rho_{nf}} \frac{\partial^2 u}{\partial y^2}, \quad (2)$$

$$u \frac{\partial T}{\partial x} + v \frac{\partial T}{\partial y} = \frac{k_{nf}}{(\rho C_p)_{nf}} \frac{\partial^2 T}{\partial y^2} - \frac{1}{(\rho C_p)_{nf}} \frac{\partial q_r}{\partial y}, \quad (3)$$

$$u \frac{\partial C}{\partial x} + v \frac{\partial C}{\partial y} = D_f \frac{\partial^2 C}{\partial y^2}. \quad (4)$$

Appropriate boundary conditions are as follows (see Turkiilmazoglu [46]):

$$\left. \begin{aligned} u &= l(x) \left(1 + \frac{1}{\beta}\right) \frac{\partial u}{\partial y}, \quad v = -V_w(x), \quad T = T_w, \quad C = C_w \quad \text{at } y = 0 \\ u &\rightarrow 0, \quad T \rightarrow T_\infty, \quad C \rightarrow C_\infty \quad \text{as } y \rightarrow \infty \end{aligned} \right\} \quad (5)$$

Where, accurate expressions for thermophysical properties of nanofluid are given by (see [49], [50] and [51]):

$$\begin{aligned} \rho_{nf} &= \rho_f \left(1 - \phi + \phi \frac{\rho_s}{\rho_f}\right), \quad (\rho C_p)_{nf} (\rho C_p)_f^{-1} = \left(1 - \phi + \phi \frac{(\rho C_p)_s}{(\rho C_p)_f}\right), \\ \mu_{nf} &= \mu_f (1 - \phi)^{-2.5}, \\ k_{nf} k_f^{-1} &= \frac{k_s + 2k_f - 2\phi(k_f - k_s)}{k_s + 2k_f + 2\phi(k_f - k_s)} \quad (\text{For nanoparticles}), \\ k_{nf} k_f^{-1} &= \frac{(1 - \phi) + 2\phi \left(\frac{k_{CNT}}{k_{CNT} - k_f}\right) \ln \left(\frac{k_{CNT} + k_f}{2k_f}\right)}{(1 - \phi) + 2\phi \left(\frac{k_f}{k_{CNT} - k_f}\right) \ln \left(\frac{k_{CNT} + k_f}{2k_f}\right)} \quad (\text{For Carbon nanotubes}). \end{aligned}$$

We can make equations (1-4) and (5) dimensionless by introducing reference velocity  $U_r$  (entrance velocity of the jet) and the following dimensionless variables are considered (see Turkiilmazoglu [46]).

$$u = U_r U, \quad v = U_r V, \quad x = \frac{v_f}{U_r} X, \quad y = \frac{v_f}{U_r} Y \quad (6)$$

With the help of Rosseland approximation for radiation, the term radiative heat flux  $q_r$  is stated as follows:

$$q_r = -\frac{16T_\infty^3 \sigma^*}{3k^*} \frac{\partial T}{\partial y}. \quad (7)$$

With the help of (6) and (7) in the equations (1-5), we obtain dimensionless system as follows:

$$\frac{\partial U}{\partial X} + \frac{\partial V}{\partial Y} = 0, \quad (8)$$

$$U \frac{\partial U}{\partial X} + V \frac{\partial U}{\partial Y} = \left(1 + \frac{1}{\beta}\right) \frac{1}{A_1 A_2} \frac{\partial^2 U}{\partial Y^2}, \quad (9)$$

$$U \frac{\partial \theta}{\partial X} + V \frac{\partial \theta}{\partial Y} = \left[\frac{k_{nf}}{k_f} + \frac{4}{3} Rd\right] \frac{1}{Pr A_3} \frac{\partial^2 \theta}{\partial Y^2}, \quad (10)$$

$$U \frac{\partial \chi}{\partial X} + V \frac{\partial \chi}{\partial Y} = \frac{1}{Sc} \frac{\partial^2 \chi}{\partial Y^2}, \quad (11)$$

and

$$\left. \begin{aligned} U &= \frac{l(x)}{v_f} U_r \left(1 + \frac{1}{\beta}\right) \frac{\partial U}{\partial Y}, V = -V_w(x) U_r^{-1}, T = T_w, C = C_w \text{ at } Y = 0, \\ U &\rightarrow 0, T \rightarrow T_\infty, C \rightarrow C_\infty \text{ as } Y \rightarrow \infty. \end{aligned} \right\} \quad (12)$$

Along with  $f(\eta) = g'(\eta)f_\infty$ , where,  $f_\infty = f(\infty)$  is to be found out, considering the below Glauert transformations.

$$V = -\frac{f_\infty}{4} X^{-\frac{3}{4}} (g(\eta) - 3\eta g'(\eta)), \quad U = \frac{f_\infty^2}{\sqrt{X}} g'(\eta), \quad \eta = \frac{f_\infty}{X^{\frac{3}{4}}} Y, \quad (13)$$

$$T = T_\infty + (T_w - T_\infty)\theta(\eta), \quad C = C_\infty + (C_w - C_\infty)\chi(\eta).$$

The reduced equations are as follows:

$$\left(1 + \frac{1}{\beta}\right) \frac{g'''}{A_1 A_2} + 2(g')^2 + gg'' = 0, \quad (14)$$

$$\left[\frac{k_{nf}}{k_f} + \frac{4}{3} Rd\right] 4\theta'' + Pr A_3 \theta' g = 0, \quad (15)$$

$$4\chi'' + Sc \chi' g = 0. \quad (16)$$

Reduced Boundary conditions are as follows:

$$\left. \begin{aligned} g'(0) &= L \left(1 + \frac{1}{\beta}\right) g''(0), g(0) = S, \theta(0) = 1, \chi(0) = 1, \\ g'(\infty) &\rightarrow 0, \theta(\infty) \rightarrow 0, \chi(\infty) \rightarrow 0. \end{aligned} \right\} \quad (17)$$

Where,

$$Rd = \frac{4T_\infty^3 \sigma^*}{k^* k_f}, \quad Sc = \frac{v_f}{D_f}, \quad Pr = \frac{\mu_f C p_f}{k_f}, \quad L = \frac{l_0 f_\infty U_r}{v_f}, \quad l(X) = \frac{l_0}{X^{\frac{3}{4}}}, \quad S = \frac{4v_w}{U_r f_\infty},$$

$$V_w = \frac{v_w}{X^{\frac{3}{4}}}, \quad A_1 = (1 - \phi)^{2.5}, \quad A_2 = \left(1 - \phi + \phi \frac{\rho_s}{\rho_f}\right), \quad A_3 = \left(1 - \phi + \phi \frac{(\rho C p)_s}{(\rho C p)_f}\right).$$



### 3. Physical quantities of engineering interests

The resistance to flow, rate of heat, and mass transfer are calculated using important engineering interests like local skin friction, Nusselt, and Sherwood numbers relations. They are stated as follows (see [48]):

$$C_f \propto \frac{\left(1 + \frac{1}{\beta}\right) g''(0)}{(1 - \phi)^{2.5}}, \quad Nu \propto - \left[ \frac{k_{nf}}{k_f} + \frac{4}{3} Rd \right] \theta'(0), \quad Sh \propto -\chi'(0). \quad (18)$$

### 4. Numerical procedure

The RKF-45 method and shooting approach are used to numerically solve the reduced equations (14-16) and the boundary constraints given in equation (17). Because the derived equations are higher-order and have two points. To solve this, we must first convert arrange these simplified equations and boundary conditions into first order.

Let us take,  $g = p_1, g' = p_2, g'' = p_3, g''' = p_3^1$

$$p_3^1 = - \frac{A_1 A_2}{\left(1 + \frac{1}{\beta}\right)} (2(p_2)^2 + p_1 p_3) \quad (19)$$

$$\theta = p_4, \theta' = p_5, \theta'' = p_5^1$$

$$p_5^1 = - \frac{\text{Pr} A_3 p_5 p_1}{\left[ \frac{k_{nf}}{k_f} + \frac{4}{3} Rd \right] 4}, \quad (20)$$

$$\chi = p_6, \chi' = p_7, \chi'' = p_7^1$$

$$\chi'' = \frac{-Sc p_7 p_1}{4} \quad (21)$$

And,

$$p_1(0) = S, \quad p_2(0) = L \left(1 + \frac{1}{\beta}\right) p_3(0), \quad p_4(0) = 1, \quad (22)$$

$$p_5(0) = \varepsilon_1, \quad p_6(0) = 1, \quad p_7(0) = \varepsilon_7.$$

The converted initial value problem stated in equations (19-21) and (22) are solved numerically with the help of the RKF-45 process and the unknown values in equation (22) are determined with the assistance of the shooting process by choosing the step size  $10^{-6}$  and 0.01 as step size. The numerical values are gathered with the aid of the bvp4c MATLAB inbuilt function. The algorithm and flow chart (Figure 2) for the RKF-45 order and the numerical scheme are shown below.

Runge-Kutta technique 4th order

$$y_{i+1} = y_i + \frac{25}{216} a_1 - \frac{1}{5} a_5 + \frac{2197}{4104} a_4 + \frac{1408}{2565} a_3, \quad (23)$$

Runge-Kutta technique 5th order

$$z_{i+1} = y_i + \frac{16}{135} a_1 + \frac{2}{55} a_6 - \frac{9}{50} a_5 + \frac{28561}{56430} a_4 + \frac{6656}{12825} a_3, \quad (24)$$

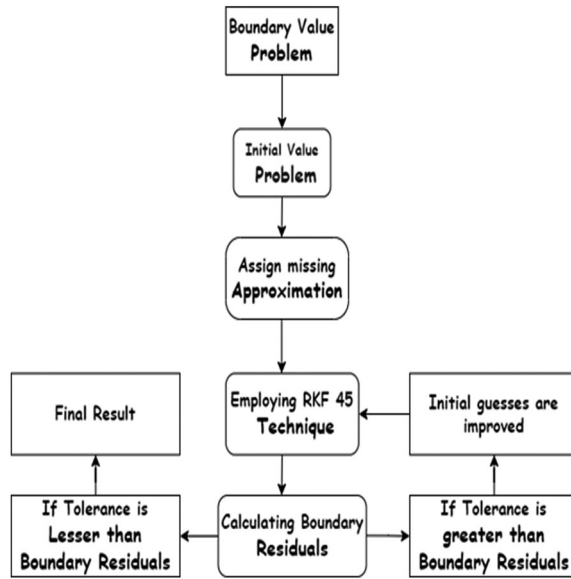


**Figure 2.** Flow chart for the numerical procedure.

and 6 steps sizes as follows

$$a_1 = f(x_i, y_i)h, \quad (25)$$

$$a_2 = f\left(x_i + \frac{1}{4}h, y_i + \frac{1}{4}a_1\right)h, \quad (26)$$

$$a_3 = f\left(x_i + \frac{3}{8}h, y_i + \frac{3}{32}a_1 + \frac{9}{32}a_2\right)h, \quad (27)$$

$$a_4 = f\left(x_i + \frac{12}{13}h, y_i + \frac{1932}{2147}a_1 - \frac{7200}{2147}a_2 + \frac{7296}{2147}a_3\right)h, \quad (28)$$

$$a_5 = hf\left(x_i + h, y_i + \frac{439}{216}a_1 - \frac{845}{4104}a_2 - 8a_3 + \frac{3680}{513}a_4\right), \quad (29)$$

$$a_6 = hf\left(x_i + \frac{1}{2}h, y_i - \frac{8}{27}a_1 + 2a_2 - \frac{11}{40}a_3 - \frac{3544}{2565}a_4 - \frac{1859}{4104}a_5\right). \quad (30)$$

## 5. Results and discussion

The study relied on the similarity solution of the Glauert kind, which is further developed here by including nanoliquid, wall slip and suction boundary constraints. The impact of numerous non-dimensional characteristics on fluid flow profiles is examined in depth using appropriate graphs, as well as the skin friction coefficient, mass, and heat transfer rate. Table 1 displays the thermophysical properties of nanoparticles and the base liquid. In Table 2, we've also compared our findings to previous research.

Figures 3 and 4 exhibit the variation of Casson parameter ( $\beta$ ) on both  $g'(\eta)$  and  $\theta(\eta)$  respectively. Increase in values of  $\beta$  declines the  $g'(\eta)$  but inclines  $\theta(\eta)$ . Here, for larger values of  $\beta$  the liquid behaves as a Newtonian fluid. Moreover, the cumulative values of the  $\beta$

**Table 1.** Material properties of carrier liquid and nanoparticles (see [49], [50] and [51]).

Particle and Base fluid	$\rho$ [ $kgm^{-3}$ ]	$C_p$ [ $Jkg^{-1}K^{-1}$ ]	$k$ [ $Wm^{-1}K^{-1}$ ]
Sodium Alginate (SA)	989	4175	0.6376
SWCNT	2600	425	6600
AA7075	2810	960	173

**Table 2.** Comparison for velocity profile for some reduced cases.

$\eta$	Shahmohamadi and Rashidi [52]		Present study
	VIM-Pade	Exact results	RKF-45
0.5	0.0277	0.0277	0.027702
1	0.1091	0.1091	0.109103
1.5	0.2865	0.2865	0.286501
2	0.3149	0.3149	0.314902
2.5	0.2949	0.2949	0.294903
3	0.2428	0.2428	0.242801
3.5	0.1810	0.1810	0.181002
4	0.1256	0.1256	0.125604
4.5	0.0829	0.0830	0.083002
5	0.0530	0.0531	0.053101
5.5	0.0329	0.0333	0.033303
6	0.0198	0.0206	0.020605
6.5	0.0111	0.0126	0.012602
7	0.0049	0.0077	0.007701

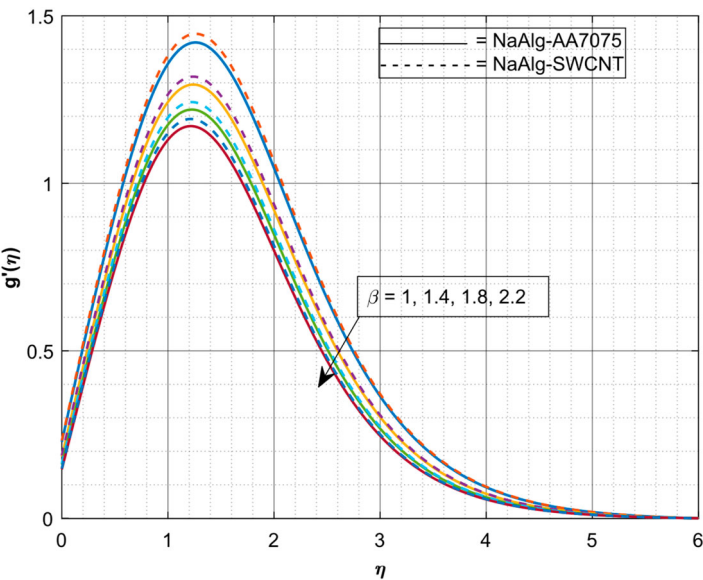


**Figure 3.** Significance of  $\beta$  on  $g'(\eta)$ .

decline the yield stress and suppress the velocity field. Here, the velocity of NaA lg –AA7075 decreases faster when compared to NaA lg –SWCNT. Further, it is noticed from the figures that, heat transfer in NaA lg –SWCNT is faster than NaA lg –AA7075 nanoliquid. Figure 5 is

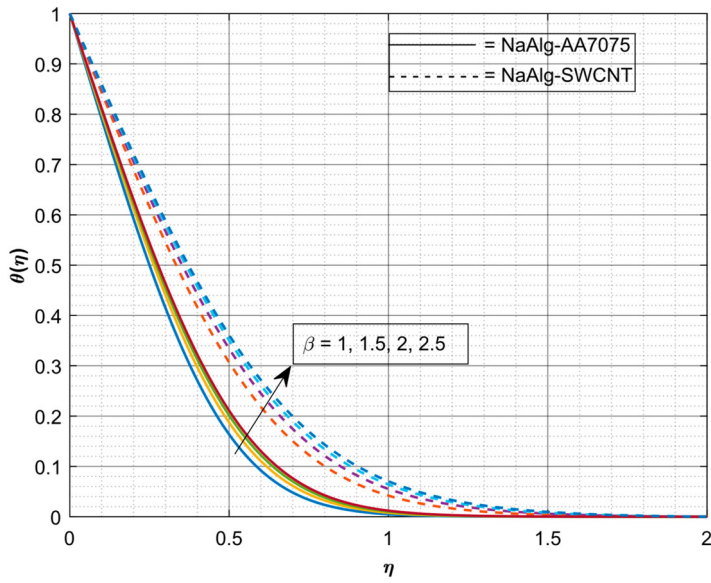


**Figure 4.** Significance of  $\beta$  on  $\theta(\eta)$ .

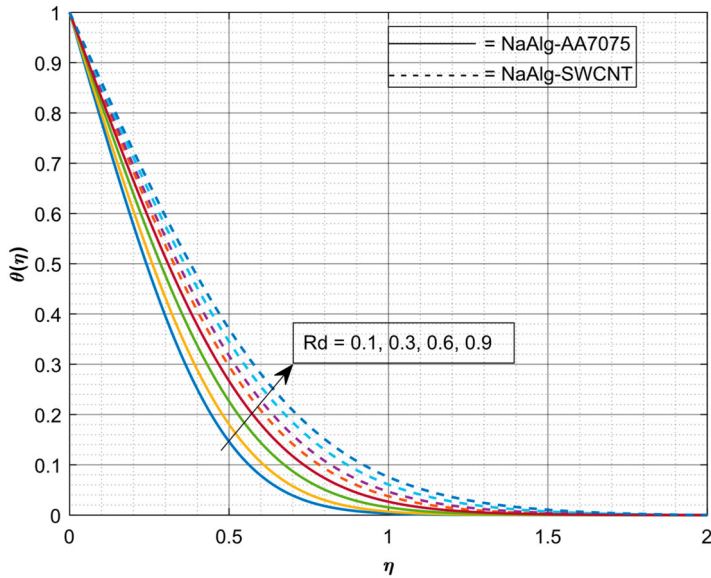


**Figure 5.** Significance of  $Rd$  on  $\theta(\eta)$ .

drawn to distinguish the behavior of both  $NaAlg-AA7075$  and  $NaAlg-SWCNT$  nanofluids on  $\theta(\eta)$  for increase in values of  $Rd$ . Increasing values of  $Rd$  inclines the  $\theta(\eta)$ . Radiation is a thermal transferring phenomenon in which heat is transferred via fluid molecules. As a result, with large  $Rd$  values, the liquid is heated more and more which results in augmentation of  $\theta(\eta)$ . Further, heat transfer in  $NaAlg-SWCNT$  is faster than  $NaAlg-AA7075$  for increase in values of  $Rd$ . Figure 6 enlightens the impact of  $L$  on  $g'(\eta)$ . Upsurge in

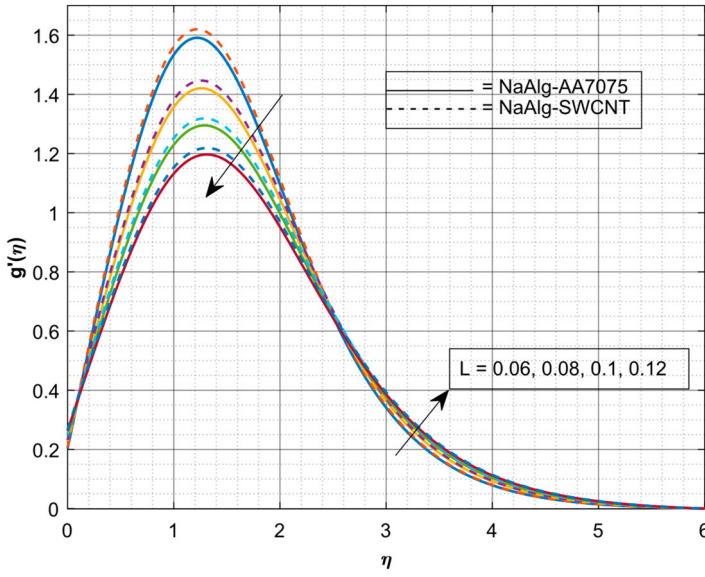


**Figure 6.** Significance of  $L$  on  $g'(\eta)$ .

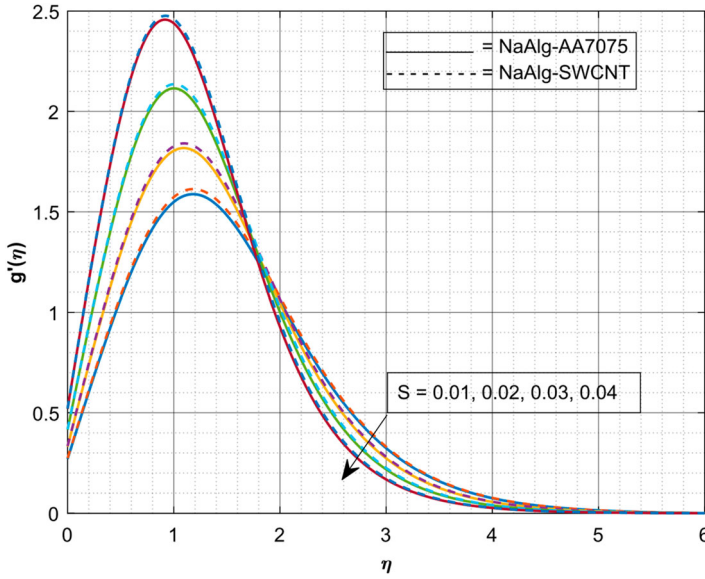


**Figure 7.** Significance of  $S$  on  $g'(\eta)$ .

$L$  decays the  $g'(\eta)$  near the surface and augments away from the wall. Because of the stretched surface that may convey the liquid, as the  $L$  grows, the fluid velocity drops. Because the stretched surface can only partly communicate to the fluid with the slip constraint, as the  $L$  rises, the slip velocity increases, and then  $g'(\eta)$  decreases. Further, velocity declines slower in NaAlg-SWCNT than NaAlg-AA7075 nanofluid for an increase in values of  $L$ . Figure 7 exposes the encouragement of  $S$  on  $g'(\eta)$ . Booming  $S$  values

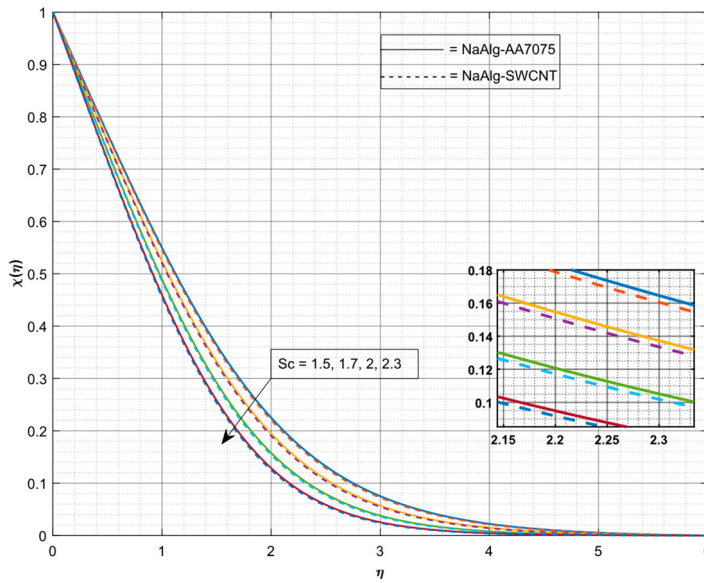


**Figure 8.** Significance of  $Sc$  on  $\chi(\eta)$ .

drops down the  $g'(\eta)$ . The suction causes the fluid velocity in the boundary layer region to drop, meaning that suction causes the  $g'(\eta)$  in the boundary layer area to decrease. This motion reduces the shear stress on the wall. The boundary layer thins as the suction level rises. Further, velocity declines faster in  $NaAlg-SWCNT$  than  $NaAlg-AA7075$  nanofluid for growth in values of  $S$ . Figure 8 discloses the impact of  $Sc$  on  $\chi(\eta)$ . The rise in values of  $Sc$  decays the  $\chi(\eta)$ . In a liquid flow, the  $Sc$  is a non-dimensional number that characterizes the linking between mass and momentum diffusivities. The growing  $Sc$  value causes  $\chi(\eta)$  to reduce due to increased momentum diffusivity. Further, mass transfer declines faster in  $NaAlg-SWCNT$  than  $NaAlg-AA7075$  nanofluid for an increase in values of  $Sc$ .

Figure 9 describes the impact of  $\phi$  on  $Re^{1/2}C_f$  versus  $\beta$  of both  $NaAlg-SWCNT$  and  $NaAlg-AA7075$  nanoliquids. The improved  $\phi$  improve the  $Re^{1/2}C_f$  of both nanoliquids. But the inverse trend is seen in  $Re^{1/2}C_f$  for growing  $\beta$  values. This is due to improvement in the  $\phi$  will improves the boundary layer thickness which decreases the flow of the liquid as a consequence surface drag force will decrease. Hence, a rise in the value of the  $\beta$  and  $\phi$  will reduce the  $Re^{1/2}C_f$ . Further, skin friction coefficient inclines faster in  $NaAlg-AA7075$  than  $NaAlg-SWCNT$  nanofluid for an increase in values of both  $\phi$  and  $\beta$ . The encouragement of  $\beta$  on  $Re^{-1/2}Nu_f$  versus  $Rd$  for both nanoliquids is shown in Figure 10. The improvement in  $\beta$  deteriorates the  $Re^{-1/2}Nu_f$  of both liquids but the conflicting movement is seen for improved  $Rd$  values. Improvement in the  $\beta$  will decline the rate of thermal distribution. As the values of  $Rd$  increase along with the  $\beta$  which removes the additional heat from the system as the result  $Re^{-1/2}Nu_f$  declines. Moreover, the rate of heat transfer declines faster in  $NaAlg-AA7075$  nanoliquid. The change in  $ShRe^{-1/2}$  versus  $\beta$  and  $Sc$  is revealed in Figure 11. Here,  $Re^{-1/2}Sh$  improves for booming  $Sc$  values. But declines for rising  $\beta$  values. Physically  $Sc$  is the ratio between kinematic viscosity to the diffusion coefficient. As the values of  $Sc$  enhances the rate of mass transfer declines.

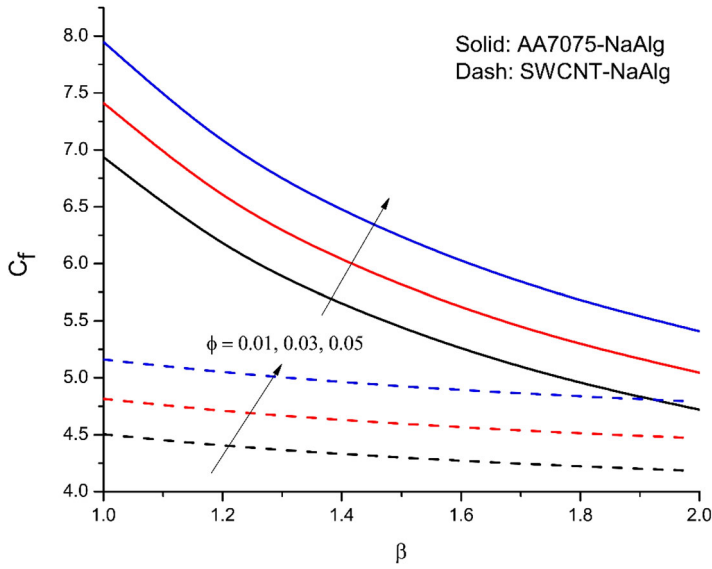


**Figure 9.** Significance of  $\phi$  on skin friction along with varied  $\beta$ .

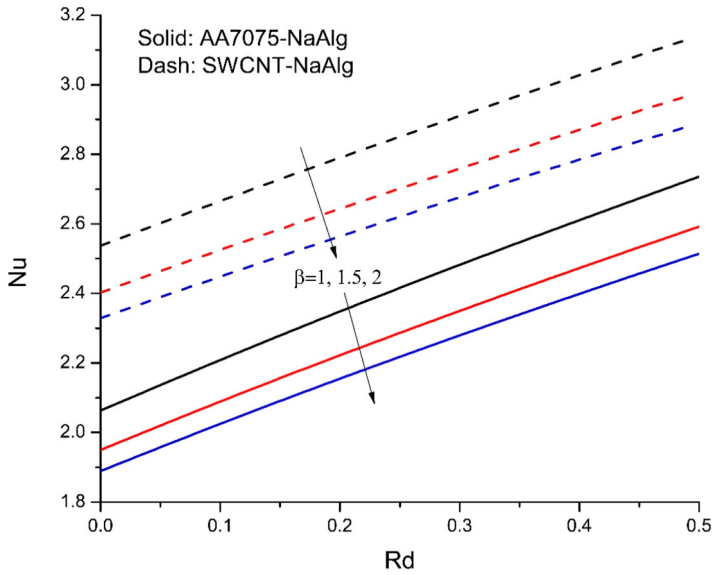


**Figure 10.** Significance of  $Rd$  on Nusselt number along with varied  $\beta$ .

Further, both nanoliquid shows approximately the same mass transfer rate for rising values of  $\beta$ .

## 6. Conclusions

The key intention of this article is to discuss the steady incompressible laminar wall jet flow of Glauert kind with suspended nanoparticles AA7075 and SWCNT in the base fluid



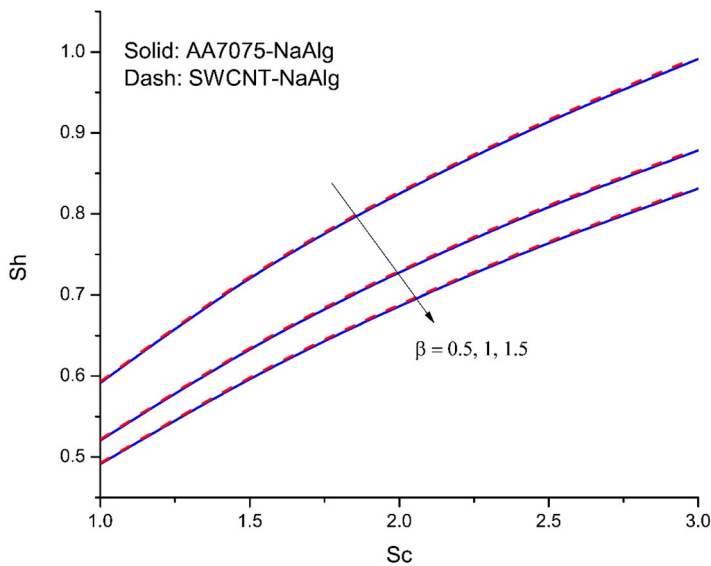


**Figure 11.** Significance of  $Sc$  on Sherwood number along with varied  $\beta$ .

*NaAlg* with wall slip and suction boundary constraints. Also, the non-Newtonian Casson fluid model is considered. Further, a comparative study is done by considering AA7075 and SWCNT nanoparticles. The numerical solutions are obtained by applying the RKF-45 technique with a shooting scheme. The considerable outcomes of this study are given below:

- Increase in values of  $\beta$  declines the  $g'(\eta)$  but inclines  $\theta(\eta)$ .
- *NaAlg* –SWCNT Casson nanofluid shows enhanced heat transfer than *NaAlg* –AA7075 Casson nanofluid for increased values of radiation parameter which transfer more heat via fluid molecules.
- Upsurge in  $L$  drops down the  $g'(\eta)$  near the surface and augments away from the wall.
- The fluid velocity declines faster in *NaAlg* –SWCNT than *NaAlg* –AA7075 nanofluid for an increase in values of  $S$ .
- *NaAlg* –SWCNT based Casson nanofluid show improved rate of heat transfer than *NaAlg* –AA7075 based Casson nanofluid for increased values of radiation parameter.
- The mass transfer rate improves for improved  $Sc$  values. But declines for rising values of  $\beta$ .
- *NaAlg* –SWCNT based Casson nanofluid show improved mass transfer rate than *NaAlg* –AA7075 based Casson nanofluid for increased values of  $Sc$ .

Future studies might focus on a number of various Newtonian and non-Newtonian fluid models with various nanoparticle suspensions, varied slip conditions and convective boundary conditions, non-uniform/uniform heat sink/source, and Stefan blowing. To create appropriate mathematical models and simulate a range of thermal boundary limitations under various situations, as well as to create a mathematical model for various nanofluid flows.

## Acknowledgements

The authors would like to thank the Ministry of education in Saudi Arabia and Jeddah University for their support.

## Disclosure statement

No potential conflict of interest was reported by the author(s).

## Funding

This work was supported by Jeddah University.

## ORCID

Hassan A. H. Alzahrani  <http://orcid.org/0000-0002-0999-8351>

J. K. Madhukesh  <http://orcid.org/0000-0003-1676-7700>

R. Naveen Kumar  <http://orcid.org/0000-0002-0056-1452>

B. M. Prasanna  <http://orcid.org/0000-0002-8972-5360>

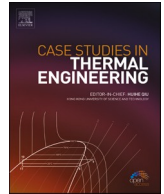
## References

- [1] Glauert MB. The wall jet. *J Fluid Mech.* Dec. 1956;1(6):625–643. doi:10.1017/S002211205600041X
- [2] Jafarimoghaddam A. Wall jet flows of Glauert type: heat transfer characteristics and the thermal instabilities in analytic closed forms. *Eur J Mech - BFluids.* Sep. 2018;71:77–91. doi:10.1016/j.euromechflu.2018.04.002
- [3] Jafarimoghaddam A. Two-phase modeling of magnetic nanofluids jets over a stretching/shrinking wall. *Therm Sci Eng Prog.* Dec. 2018;8:375–384. doi:10.1016/j.tsep.2018.09.008
- [4] Jafarimoghaddam A. Closed form analytic solutions to heat and mass transfer characteristics of wall jet flow of nanofluids. *Therm Sci Eng Prog.* Dec. 2017;4:175–184. doi:10.1016/j.tsep.2017.09.006
- [5] Aly EH, Pop I. Merkin and needham wall jet problem for hybrid nanofluids with thermal energy. *Eur J Mech - BFluids.* Sep. 2020;83:195–204. doi:10.1016/j.euromechflu.2020.05.004
- [6] Alhadhrami A, Alzahrani HAH, Naveen Kumar R, et al. Impact of thermophoretic particle deposition on Glauert wall jet slip flow of nanofluid,” case stud. *Therm Eng.* Dec. 2021;28:101404. doi:10.1016/j.csite.2021.101404
- [7] Hatami M, Ganji DD. Heat transfer and flow analysis for SA-TiO<sub>2</sub> non-Newtonian nanofluid passing through the porous media between two coaxial cylinders. *J Mol Liq.* Dec. 2013;188:155–161. doi:10.1016/j.molliq.2013.10.009
- [8] Sheikholeslami M, Hatami M, Ganji DD. Numerical investigation of nanofluid spraying on an inclined rotating disk for cooling process. *J Mol Liq.* Nov. 2015;211:577–583. doi:10.1016/j.molliq.2015.07.006
- [9] Hatami M. Nanoparticles migration around the heated cylinder during the RSM optimization of a wavy-wall enclosure. *Adv Powder Technol.* Mar. 2017;28(3):890–899. doi:10.1016/j.appt.2016.12.015
- [10] Tang W, Hatami M, Zhou J, et al. Natural convection heat transfer in a nanofluid-filled cavity with double sinusoidal wavy walls of various phase deviations. *Int J Heat Mass Transf.* Dec. 2017;115:430–440. doi:10.1016/j.ijheatmasstransfer.2017.07.057
- [11] Hatami M, Sheikholeslami M, Domairry G. High accuracy analysis for motion of a spherical particle in plane couette fluid flow by multi-step differential transformation method. *Powder Technol.* Jul. 2014;260:59–67. doi:10.1016/j.powtec.2014.02.057
- [12] Hatami M, Song D, Jing D. Optimization of a circular-wavy cavity filled by nanofluid under the natural convection heat transfer condition. *Int J Heat Mass Transf.* Jul. 2016;98:758–767. doi:10.1016/j.ijheatmasstransfer.2016.03.063

- [13] Hatami M, Zhou J, Geng J, et al. Optimization of a lid-driven T-shaped porous cavity to improve the nanofluids mixed convection heat transfer. *J Mol Liq.* **Apr. 2017**;231:620–631. doi:10.1016/j.molliq.2017.02.048
- [14] Prasannakumara BC. Numerical simulation of heat transport in Maxwell nanofluid flow over a stretching sheet considering magnetic dipole effect. *Partial Differ Equ Appl Math.* **Dec. 2021**;4:100064. doi:10.1016/j.padiff.2021.100064
- [15] Prasannakumara BC. Assessment of the local thermal non-equilibrium condition for nanofluid flow through porous media: a comparative analysis. *Indian J Phys.* **Nov. 2021**. doi:10.1007/s12648-021-02216-9
- [16] Hatami M, Ganji DD. Motion of a spherical particle in a fluid forced vortex by DQM and DTM. *Particuology.* **Oct. 2014**;16:206–212. doi:10.1016/j.partic.2014.01.001
- [17] Pourmehran O, Rahimi-Gorji M, Hatami M, et al. Numerical optimization of microchannel heat sink (MCHS) performance cooled by KKL based nanofluids in saturated porous medium. *J Taiwan Inst Chem Eng.* **Oct. 2015**;55:49–68. doi:10.1016/j.jtice.2015.04.016
- [18] Hatami M, Jing D. Optimization of wavy direct absorber solar collector (WDASC) using Al<sub>2</sub>O<sub>3</sub>-water nanofluid and RSM analysis. *Appl Therm Eng.* **Jul. 2017**;121:1040–1050. doi:10.1016/j.applthermaleng.2017.04.137
- [19] Jamshed W, Nisar KS, Ibrahim RW, et al. Thermal expansion optimization in solar aircraft using tangent hyperbolic hybrid nanofluid: a solar thermal application. *J Mater Res Technol.* **Sep. 2021**;14:985–1006. doi:10.1016/j.jmrt.2021.06.031
- [20] Sajid T, et al. Study on heat transfer aspects of solar aircraft wings for the case of reiner-philippoff hybrid nanofluid past a parabolic trough: keller box method. *Phys Scr.* **Jun. 2021**;96(9):095220. doi:10.1088/1402-4896/ac0a2a
- [21] Nouar A, Dib A, Kezzar M, et al. Numerical treatment of squeezing unsteady nanofluid flow using optimized stochastic algorithm. *Z Für Naturforschung A.* **Oct. 2021**;76(10):933–946. doi:10.1515/zna-2021-0163
- [22] Boumaiza N, Kezzar M, Eid MR, et al. On numerical and analytical solutions for mixed convection falkner-Skan flow of nanofluids with variable thermal conductivity. *Waves Random Complex Media.* **Nov. 2021**;31(6):1550–1569. doi:10.1080/17455030.2019.1686550
- [23] Al-Hossainy AF, Eid MR. Combined theoretical and experimental DFT-TDDFT and thermal characteristics of 3-D flow in rotating tube of [PEG + H<sub>2</sub>O/SiO<sub>2</sub>-Fe<sub>3</sub>O<sub>4</sub>]C hybrid nanofluid to enhancing oil extraction. *Waves Random Complex Media.* **Jul. 2021**. doi:10.1080/17455030.2021.1948631
- [24] Eid MR, Al-Hossainy AF. Combined experimental thin film, DFT-TDDFT computational study, flow and heat transfer in [PG-MoS<sub>2</sub>/ZrO<sub>2</sub>]C hybrid nanofluid. *Waves Random Complex Media.* **Jan. 2021**. doi:10.1080/17455030.2021.1873455
- [25] Raja MAZ, Shoaib M, Tabassum R, et al. Intelligent computing for the dynamics of entropy optimized nanofluidic system under impacts of MHD along thick surface. *Int J Mod Phys B.* **Oct. 2021**;35(26):2150269. doi:10.1142/S0217979221502696
- [26] Jamshed W, Shahzad F, Safdar R, et al. Implementing renewable solar energy in presence of Maxwell nanofluid in parabolic trough solar collector: a computational study. *Waves Random Complex Media.* **Nov. 2021**. doi:10.1080/17455030.2021.1989518
- [27] Waqas H, Hussain M, Alqarni MS, et al. Numerical simulation for magnetic dipole in bioconvection flow of Jeffrey nanofluid with swimming motile microorganisms. *Waves Random Complex Media.* **Jul. 2021**. doi:10.1080/17455030.2021.1948634
- [28] Shoaib M, Kausar M, Ijaz Khan M, et al. Muhammad Asif Zahoor Raja, "Intelligent back-propagated neural networks application on darcy-Forchheimer ferrofluid slip flow system,". *Int Commun Heat Mass Transf.* **Dec. 2021**;129:105730. doi:10.1016/j.icheatmasstransfer.2021.105730
- [29] Shoaib M, Zubair G, Nisar KS. Muhammad Asif Zahoor Raja, Muhammad Ijaz khan, R. J. Punith Gowda, B.C. prasannakumara, "ohmic heating effects and entropy generation for nanofluidic system of Ree-Eyring fluid: Intelligent computing paradigm,". *Int Commun Heat Mass Transf.* **Dec. 2021**;129:105683. doi:10.1016/j.icheatmasstransfer.2021.105683

- [30] Madhukesh J, Alhadhrami A, Naveen Kumar R, et al. Physical insights into the heat and mass transfer in Casson hybrid nanofluid flow induced by a Riga plate with thermophoretic particle deposition. *Proc Inst Mech Eng Part E J Process Mech Eng*. Aug. 2021. doi:10.1177/09544089211039305
- [31] Alotaibi H, Althubiti S, Eid MR, et al. Numerical treatment of mhd flow of casson nanofluid via convectively heated non-linear extending surface with viscous dissipation and suction/injection effects. *Comput Mater Contin*. 2020;66(1):229–245.
- [32] Jamshed W, Uma Devi S S, Safdar R, et al. Comprehensive analysis on copper-iron (II, III)/oxide-engine oil Casson nanofluid flowing and thermal features in parabolic trough solar collector. *J Taibah Univ Sci*. Jan. 2021;15(1):619–636. doi:10.1080/16583655.2021.1996114
- [33] Kumar RSV, Dhananjaya PG, Kumar RN, et al. Modeling and theoretical investigation on Casson nanofluid flow over a curved stretching surface with the influence of magnetic field and chemical reaction. *Int J Comput Methods Eng Sci Mech*. Mar. 2021;23(1):12–19. doi:10.1080/15502287.2021.1900451
- [34] Hussain SM, et al. Computational analysis of thermal energy distribution of electromagnetic Casson nanofluid across stretched sheet: shape factor effectiveness of solid-particles. *Energy Rep*. Nov. 2021;7:7460–7477. doi:10.1016/j.egy.2021.10.083
- [35] Naveen Kumar R, Gowda RJP, Gireesha BJ, et al. Non-Newtonian hybrid nanofluid flow over vertically upward/downward moving rotating disk in a darcy–Forchheimer porous medium. *Eur Phys J Spec Top*. Apr. 2021;230:1227–1237. doi:10.1140/epjs/s11734-021-00054-8
- [36] Hamid A, Chu Y-M, Khan MI, et al. Critical values in axisymmetric flow of magneto-cross nanomaterial towards a radially shrinking disk. *Int J Mod Phys B*. Mar. 2021;35(07):2150105. doi:10.1142/S0217979221501058
- [37] Gnaneswara Reddy M, Punith Gowda R, Naveen Kumar R, et al. Analysis of modified Fourier law and melting heat transfer in a flow involving carbon nanotubes. *Proc Inst Mech Eng Part E J Process Mech Eng*. Oct. 2021;235(5):1259–1268. doi:10.1177/09544089211001353
- [38] Akbar Y, Abbasi FM, Shehzad SA. Thermal radiation and Hall effects in mixed convective peristaltic transport of nanofluid with entropy generation. *Appl Nanosci*. Dec. 2020;10(12):5421–5433. doi:10.1007/s13204-020-01446-3
- [39] Li Y-X, Hamid A, Ijaz Khan M, et al. Dual branch solutions (multi-solutions) for nonlinear radiative falkner–Skan flow of Maxwell nanomaterials with heat and mass transfer over a static/moving wedge. *Int J Mod Phys C*. Apr. 2021;32(10):2150130. doi:10.1142/S0129183121501308
- [40] Yusuf TA, Mabood F, Prasannakumara BC, et al. Magneto-Bioconvection flow of Williamson nanofluid over an inclined plate with gyrotactic microorganisms and entropy generation. *Fluids*. Mar. 2021;6(3):109. doi:10.3390/fluids6030109
- [41] Khan MI, Tamoor M, Hayat T, et al. MHD boundary layer thermal slip flow by nonlinearly stretching cylinder with suction/blowing and radiation. *Results Phys*. Jan. 2017;7:1207–1211. doi:10.1016/j.rinp.2017.03.009
- [42] Mustafa M, Pop I, Naganthran K, et al. Entropy generation analysis for radiative heat transfer to bödewadt slip flow subject to strong wall suction. *Eur J Mech - BFluids*. Nov. 2018;72:179–188. doi:10.1016/j.euromechflu.2018.05.010
- [43] Yashkun U, Zaimi K, Bakar NAA, et al. Nanofluid stagnation-point flow using tiwari and Das model over a stretching/shrinking sheet with suction and slip effects. *J Adv Res Fluid Mech Therm Sci*. 2020;70(1):62–76.
- [44] Zhao T-H, Khan MI, Qayyum S, et al. Comparative study of ferromagnetic hybrid (manganese zinc ferrite, nickle zinc ferrite) nanofluids with velocity slip and convective conditions. *Phys Scr*. Apr. 2021;96(7):075203. doi:10.1088/1402-4896/abf26b
- [45] Yusuf TA, Naveen Kumar R, Prasannakumara BC, et al. Irreversibility analysis in micropolar fluid film along an incline porous substrate with slip effects. *Int Commun Heat Mass Transf*. Jul. 2021;126:105357. doi:10.1016/j.icheatmasstransfer.2021.105357
- [46] Navier CLMH. Memoire sur les du mouvement des. *Mem Acad Sci Inst France*. 1823;1(6):414–416.
- [47] Turkyilmazoglu M. Laminar slip wall jet of Glauert type and heat transfer. *Int J Heat Mass Transfer*. May 2019;134:1153–1158. doi:10.1016/j.ijheatmasstransfer.2019.02.051

- [48] Jafarimoghaddam A, Shafizadeh F. Numerical modeling and spatial stability analysis of the wall jet flow of nanofluids with thermophoresis and Brownian effects. *Propul Power Res.* [Sep. 2019;8\(3\):210–220](#). doi:[10.1016/j.jppr.2019.06.002](#)
- [49] Madhukesh JK, Naveen Kumar R, Punith Gowda RJ, et al. Sami ullah Khan and Yu-ming Chu “numerical simulation of AA7072-AA7075/water-based hybrid nanofluid flow over a curved stretching sheet with Newtonian heating: A non-Fourier heat flux model approach,”. *J Mol Liq.* [Aug. 2021;335:116103](#). doi:[10.1016/j.molliq.2021.116103](#)
- [50] Kumar V, Madhukesh JK, Jyothi AM, et al. Analysis of single and multi-wall carbon nanotubes (SWCNT/MWCNT) in the flow of Maxwell nanofluid with the impact of magnetic dipole. *Comput Theor Chem.* [Jun. 2021;1200:113223](#). doi:[10.1016/j.comptc.2021.113223](#)
- [51] Khan A, Khan D, Khan I, et al. MHD flow of Sodium alginate-based Casson type nanofluid passing through A porous medium With Newtonian heating. *Sci Rep.* [Dec. 2018;8\(1\):8645](#). doi:[10.1038/s41598-018-26994-1](#)
- [52] Shahmohamadi H, Rashidi MM. A novel solution for the glauert-Jet problem by variational iteration method-padé approximant. *Math Probl Eng.* [Apr. 2010;2010:e501476](#). doi:[10.1155/2010/501476](#)



# Heat transfer augmentation in a solar air heater with conical roughness elements on the absorber

Abdulmohsen O. Alsaiani<sup>a,b</sup>, Hassan A.H. Alzahrani<sup>c</sup>, Madhukeshwara N<sup>d,\*</sup>,  
B.M. Prasanna<sup>e</sup>

<sup>a</sup> Mechanical Engineering Department, College of Engineering, King Abdulaziz University, 80200, Jeddah, 21589, Saudi Arabia

<sup>b</sup> Center of Excellence in Desalination Technology, King Abdulaziz University, P.O. Box 80200, Jeddah, 21589, Saudi Arabia

<sup>c</sup> Department of Chemistry, College of Science and Arts at Khulis, University of Jeddah, P. O. Box 355, Jeddah, Saudi Arabia

<sup>d</sup> Department of Mechanical Engineering, Jain Institute of Technology, Davanagere, 577003, Karnataka, India

<sup>e</sup> Department of Chemistry, Bapuji Institute of Engineering and Technology, Davanagere, 577 004, India

## ARTICLE INFO

### Keywords:

Efficiency index

SAH

Cone-shaped rib roughness

## ABSTRACT

Adding flow-disturbing components to the absorber plate's effective heat transfer zone is the most efficient Thermo-hydraulic performance enhancement approach for a solar air heater (SAH). Researchers are attempting to decide the best geometrical parameters for a SAH when the turbulent flow has fully established with fabricated roughness protrusions on the absorber surface plate in a cone-shaped contour. The Thermo-hydraulic performance of the proposed SAH design is taken into account throughout the optimization process. Air flow rate and geometrical variables such as the Reynolds number ( $Re = 3000$  to  $8000$ ), relative rib pitch ( $p/e = 10$  to  $20$ ), and relative rib gap ( $w/e = 4$  to  $8$ ) are varied in a series of experiments to assess the SAH's performance. Flow angle of attack ( $\alpha = 90^\circ$ ), relative roughness height ( $e/D_h = 0.08$ ), and rectangular flow passage aspect ratio ( $W/H = 5$ ) are maintained constant in all the trials for inline and staggered configurations. Series of tests are carried out to establish statistical correlations between the average Nusselt number and the average friction factor. Thermo-hydraulic performance is affected by the Reynolds number ( $Re$ ) as well as relative roughness gaps ( $w/e$ ) and relative roughness pitch ( $p/e$ ) of the conical protrusions. There was a 64.5% increase in Nusselt number and a 153.3% increase in friction factor at  $Re = 8000$ ,  $p/e = 10$  and  $w/e = 4$ . Cone-shaped roughness, as suggested, has a Thermo-hydraulic efficiency index of 0.8233, which occurs at  $p/e = 20$  and  $w/e = 8$  at  $Re = 3000$ .

## Nomenclature

$A_c$	Absorber plate area ( $m^2$ )
$a_o$	Orifice area ( $m^2$ )
$a_1$	Pipe cross sectional area ( $m^2$ )
$C_p$	Air specific heat ( $J/kgK$ )
$C_d$	Coefficient of discharge of orifice
$D_h$	Ducts hydraulic diameter ( $m$ )

\* Corresponding author.

E-mail addresses: [madhukeshwara.n@jitd.in](mailto:madhukeshwara.n@jitd.in), [madhukeshwara.n@gmail.com](mailto:madhukeshwara.n@gmail.com) (M. N).

$e$	Roughness element height (m)
$e/D_h$	Relative roughness height
$f$	Friction factor
$f_{av}$	Average friction factor
$f_r$	Friction factor of roughened air duct
$f_s$	Friction factor of smooth air duct
$g$	Acceleration due to gravity ( $m/s^2$ )
$H$	Height of the air duct (m)
$h$	Convective heat transfer coefficient ( $W/m^2K$ )
$h_m$	Manometer reading (m)
$k$	Air thermal conductivity ( $W/mK$ )
$L$	Test length (m)
$m$	Mass flow rate of the air (kg/s)
$Nu_{av}$	Average Nusselt number
$Nu_s$	Nusselt number of all smooth sided duct
$Pr$	Prandtl number
$p$	Rib pitch (m)
$p/e$	Relative roughness pitch
$q$	Heat transfer rate to air (W)
$R_{av}$	Average radial distance of the duct (m)
$Re$	Reynolds number
$t_f$	Average air temperature ( $^{\circ}C$ )
$t_i$	Average inlet air temperature ( $^{\circ}C$ )
$t_o$	Average outlet air temperature ( $^{\circ}C$ )
$t_p$	Average absorber surface temperature ( $^{\circ}C$ )
$V$	Average air velocity inside the duct (m/s)
$W$	Width of the air duct (m)
$W/H$	Aspect ratio of the duct
$w$	Gap between roughness elements (m)
$w/e$	Relative roughness gap
$\Delta p$	Pressure drop across the test length ( $N/m^2$ )
<b>Greek symbols</b>	
$\alpha$	Angle of attack of flow ( $^{\circ}$ )
$\rho$	Air density ( $kg/m^3$ )
$\rho_w$	Water density ( $kg/m^3$ )
$\mu$	Viscosity of air ( $Ns/m^2$ )

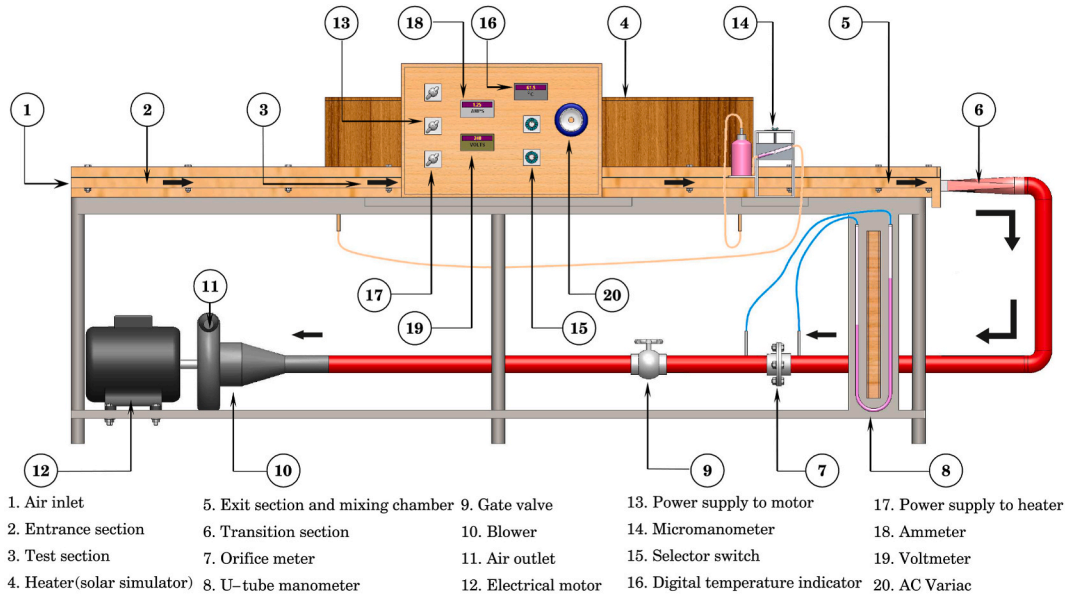
## 1. Introduction

Humans are extracting radiant light, solar energy and heat energy from the sun through a variety of ever-evolving means since the dawn of civilization [1]. Insolation is perhaps the most extensively used source of energy and has the prominent potential of all non-conventional and renewable sources of energy [2]. Prior to 1970, a few countries invested heavily in research activities to better harvest solar energy, but much of this research was mainly theoretical and intellectual. Following the noticeable increase in oil cost in the 1970's, several countries started to invest heavily in solar energy research and development.

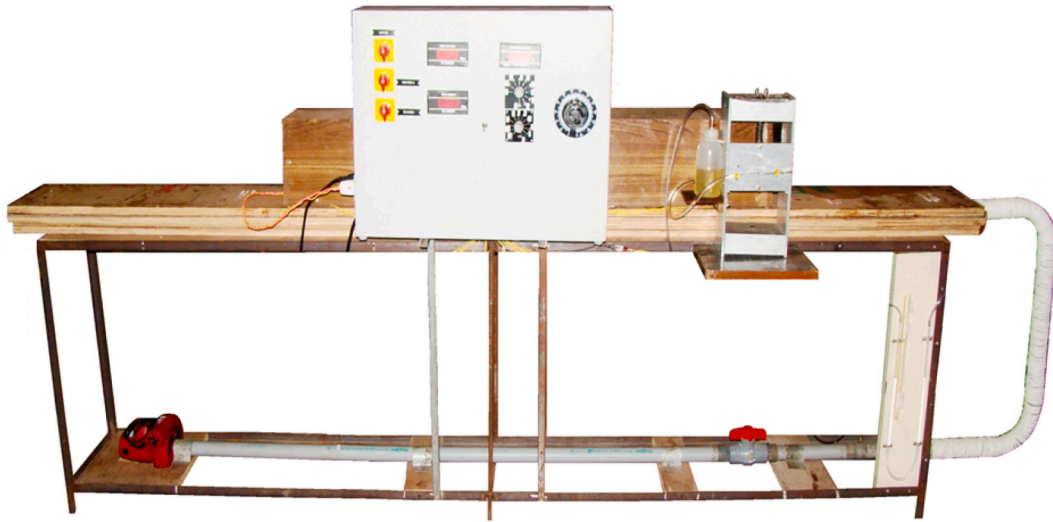
SAHs consist of a black absorber surface that absorbs sun radiation and delivers it to the air through conduction heat transfer. Agricultural crop drying applications include [3–6], wood seasoning applications include [7], and space or process heating applications include [8,9]. It is also used as a energy source in a wide range of engineering industries, such as SAHs, to generate heat ranging from 30 °C to 70 °C temperatures [10,11]. Due to low heat transfer coefficient between the circulating air and the absorber surface, SAHs function poorly. This makes the surface temperature of the absorber plate to raise, resulting in substantial heat losses to the surrounding environment [12].

To promote heat flow from a surface, incorporating artificial protrusions on the absorber surface is a common way. Several researchers suggest SAHs as a way to collect more solar energy. The porous bed air heater [13], honeycomb overlapped glass plate air heater [14], pebble bed air heater [15], matrix solar air heater [16], and jet plate air heater [17] are the ones to look out for. These designs, on the other hand, obviously promote heat transmission while also increasing flow resistance. They don't completely remove the power losses that come with pumping. Many researchers also attempted to create a SAH (artificially roughened absorber) that may improve heat transfer while reducing pumping losses. These investigations demonstrated that fabricating artificial protrusions to the absorber surface to improve thermal performance is an uncomplicated and worthwhile way [18,19]. The purpose of this research is to develop a novel method for improving heat transmission in artificially roughened absorber SAHs. The present study investigates how





(a)



(b)

Fig. 1. (a) Schematic view of experimental setup (b) Photograph of the experimental setup.

incorporating artificial protrusions to the absorber plate in the shape of a cone might improve SAH performance. Heat flow and fluid flow friction tendencies in the SAH duct are influenced by percent  $Re$ ,  $w/e$ ,  $p/e$ , and the placement of roughness components. Even a little improvement in SAH performance decreases the price of pumping electricity as well as the potent area needed to acquire thermal energy from a given source. To analyse the efficiency of a SAH, a thermo-hydraulic performance, specifically the efficiency index ( $\eta$ ), is used [20,21]. Many factors are included in the trials to assess the efficiency of such systems.

The experimental test rig is built, and tests are performed on it, taking into account a number of parameters that impact system efficiency. Experimental discoveries by some of the pioneers in the field are contrasted to theoretical findings. To create turbulence in the air flow near the wall, artificial cone-shaped roughness contours are brazed on the absorber plate surface near the laminar sublayer. Some study materials are available to help you pick from a range of roughness components to reduce friction and increase heat transfer. The next section goes over some research that has been published.

Momin et al. [22] accomplished studies to assess the influence of rib geometric parameters on the heat flow and fluid flow capacities of SAH rectangular ducts fitted with absorber surface having V-shaped ribs at the bottom of plate. To increase heat

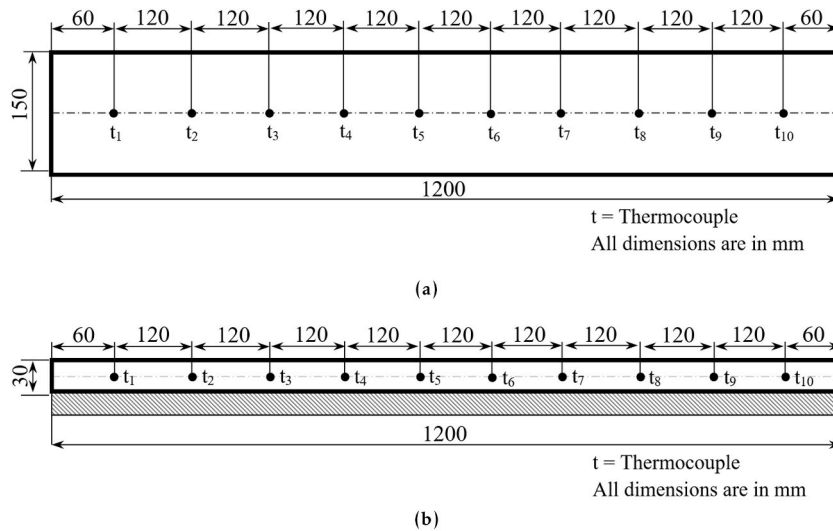


Fig. 2. Thermocouples position in the air duct (a) Top view (b) Profile view.

transmission rate, Prasad and Mullick [23] employed transverse rib protrusions underneath the absorber surface to increase the abrasion resistance. The authors of Gupta et al. [24] then provide a complete study of the inclined rib to determine the impact of flow attack angle, relative roughness height, and Reynolds number on heat transfer and pressure drop inside a rectangular air passage. Kumar et al. [25] experimented the impact of roughened dimple SAH on the three corners of smooth curves in an experimental and theoretical study. Roughness geometrical characteristics have a significant impact on heat exchange between the absorber plate and flowing air, according to further study. The small space between the ribs that are continuously inclined [26], V ribs [27–29], arc shaped ribs [30], multiple V-ribs [31], multiple arc ribs [32], or cubical roughness elements [33] significantly enhances heat transfer. The interval between the consecutive ribs enables the generated secondary flow and vortex to mix with the main flow. To increase thermo-hydraulic performance, a few studies recommended adding the distinct zigzag ribs after the gap. When compared to identical configurations without staggered ribs, the thermo-hydraulic performance of intermittent V rib [34,35], inclined discrete rib [36], intermittent arc rib [37], discrete multi V-rib [38], and transverse discrete rib [39] with staggered ribs was reported to be 24%, 9.51%, 14.6%, 12%, and 10–15% higher. Because of the prominent intermingling of two vortices (flowing on both sides of the staggered rib roughness) with the mainstream flow, the results of all of these investigations [34–39] determined that staggered ribs positioned downstream of the broken rib pattern improve the Thermo-hydraulic performance of SAH. Some of the researchers have also used aluminium fin turbulators [40], perforated vortex generators [41], helical coiled inserts [42], winglet vortex generators [43], V-down shaped perforated baffles [44], Anchor shaped inserts [45], inclined ribs in circular tube [46], and inclined turbulators [47] on absorber plate and studied their influence on the Thermo-hydraulic performance of the SAH. For several SAH performance-enhancing approaches, the optimal Nusselt number and friction factor augmentation, along with their optimum roughness parameters, are examined.

SAH thermal hydraulic efficiency is likely to be improved by using staggered and low-friction arc-shaped ribs downstream of broken ribs, as shown by research into the use of staggered ribs in other techniques of enhancing SAH thermal hydraulic efficiency. All roughness factors mentioned in this research are optimized to increase heat transfer and flow characteristics. The pressure loss and Nusselt number are quantified using empirical correlations for the optimized geometries. Consequently, an extensive experimental study is carried out to assess the influence of cone shaped protrusions on thermo-hydraulic performance.

## 2. Experimental program and procedure

Fig. 1a and Fig. 1b depicts the layout of the experimental setup and photograph respectively. Among the most important components of the arrangement is the duct, which is composed of 25 mm thick timber boards. The duct is having 2.6 m length, 0.15 m width, and 0.03 m height, with an aspect ratio of 5/1. It is made up of an 800 mm long smooth entry part, a 1200 mm long roughened test segment, and a 600 mm long exit section. There's a mixing chamber consisting of baffles at the last part of the exit portion for homogeneous mixing of hot air. Except for the absorber plate side, the duct is insulated on the other three sides to guarantee that all heat flux is delivered to the duct and to reduce heat loss. A rectangular to circular transition piece connects the duct's end to a circular pipe. In the air flow channel, there is also a flow metre and an air blower. Because thermally completely established flow will be produced in such a little length, i.e. two to three times the hydraulic diameter, a roughened duct is designed with a short entrance length to accommodate this. As per ASHRAE standard 93–77 [48], the least possible entrance and exit portion lengths are 338 mm and 170 mm, respectively, for the turbulent flow regime.

As an absorber plate, with 1200 mm × 150 mm dimension is manufactured using a 16 SWG, 1.626 mm thick aluminium sheet having roughness in the shaped of a cone on the absorber bottom surface. Conical protrusions are brazed underneath the absorber

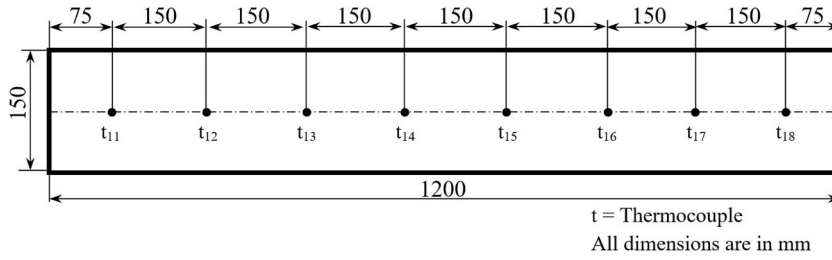


Fig. 3. Thermocouples position on the absorber plate (top view of test length).

**Table 1**  
Uncertainties in the calculated parameters.

Sl. No.	Parameters	Uncertainty (%)
1.	Reynolds number (Re)	1.66 – 2.28
2.	Heat transfer coefficient ( $h$ )	3.43 – 4.58
3.	Nusselt number ( $Nu$ )	3.51 – 4.73
4.	Stanton number ( $St$ )	4.31 – 4.89
5.	Friction factor ( $f$ )	2.83 – 3.95

plate, which comes in direct contact with the duct's air flow. A solar simulator is used with electric bulbs as a heater to produce a consistent heat flux to the absorber plate of up to  $1500 \text{ W/m}^2$ . An AC dimmerstat is used to monitor the heater electricity power supply.

### 2.1. Instrumentation

An orifice metre is a device with a coefficient of discharge of 0.62 is utilized to find the air mass flow rate flowing through the duct. At the test section, a minimum pressure drop of 0.00436 mm can also be recorded by a inclined single column micro-manometer. Fig. 2a and b and Fig. 3 demonstrate how K-type Chromel-Aluminum thermocouples are used to detect absorber plate and flowing air temperatures at different places. These thermocouples are calibrated against standard mercury thermometer of  $0.1^\circ\text{C}$  least count. These thermocouples can be used for the temperature range of  $-180$  to  $+1300^\circ\text{C}$ . Calibrated voltmeter and ammeter readings are also used to measure the amount of power provided to the heater. A blower which is driven by a single phase, 230 V, 600 W and 16,000 rpm, AC motor with a capacity of  $3.3 \text{ m}^3/\text{min}$  sucks air through the rectangular duct. The air flow rate via the duct is controlled by the control valve. The air flow rate in the rectangular duct is measured with a pitot tube-calibrated orifice metre. With water as the manometric fluid, a U-tube manometer detects the pressure decrease across the orifice metre.

### 2.2. Experimental program and procedure

To begin with, SAH duct is built and a roughened absorber plate with cone-shaped roughness is fitted. The heater provides the energy for heating until a quasi-steady condition is established. The blower is then turned on, confirming that there is no leakage in the flow channels, and the ducts flow rate is regulated via control valves. All readings are collected after the system has reached a quasi-steady state, as defined by the ASHRAE standard. To cover the complete range of Reynolds numbers from 3000 to 8000, it was chosen to perform testing for eleven different air mass flow rates. Pressure drop between the orifice meter and the test length, power supply to the heater, air temperature at intake and exit, the air temperatures and absorber plate temperatures are monitored throughout the experiment.

### 2.3. Uncertainty analysis

When doing experimental measurements, the approach given by Kline and McClintock [49] is used to quantify the uncertainty in the results. It is used to estimate the level of uncertainty in experimental findings based on the data collected. If  $T$  is the considered property that is dependent on other variables, the expression may be phrased as follows:

$$T = k x_1^a x_2^b x_3^c x_4^d \dots x_n^m \quad (1)$$

The fundamental outcome of the uncertainty  $\delta T$  in  $T$  is:

$$\delta T = \sqrt{\left(\frac{\partial T}{\partial x_1} \delta x_1\right)^2 + \left(\frac{\partial T}{\partial x_2} \delta x_2\right)^2 + \dots + \left(\frac{\partial T}{\partial x_n} \delta x_n\right)^2} \quad (2)$$

As indicated in Table 1, there are uncertainties in the values of the major parameters.

### 2.4. Roughness geometries and their ranges

Artificial roughness element generation is a time-consuming procedure that may not be financially feasible for large-scale

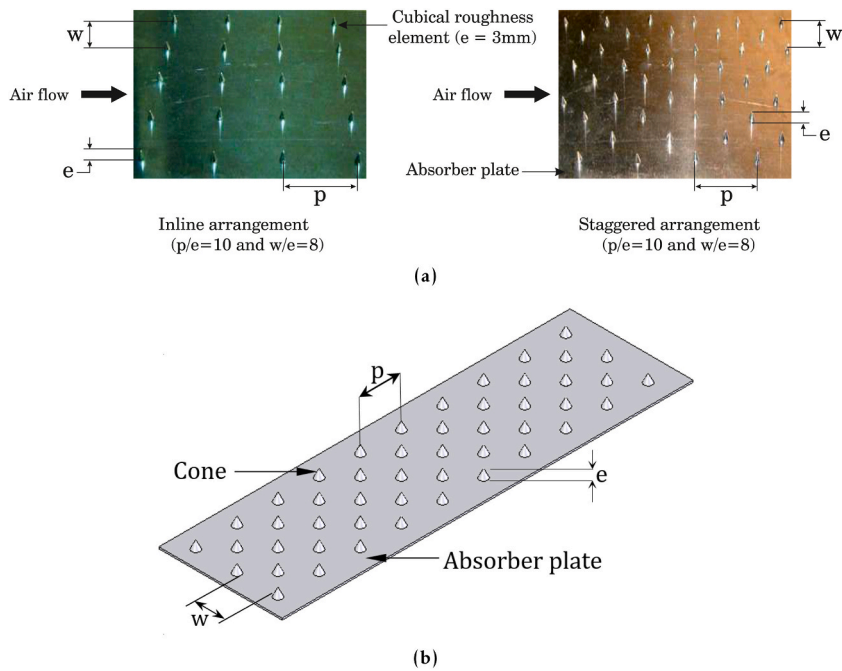


Fig. 4. (a) Pictorial (b) Schematic view of cone shaped roughness on the absorber surface.

Table 2

Specifications and range of cone shaped roughness parameters and flow parameter.

Plate No.	$w/e$	$p/e$	Arrangement	$\alpha$	$e/D_h$	$W/H$	$Re$
1	4	10	Inline	$90^\circ$ (Fixed parameter)	0.06 (Fixed parameter)	5 (Fixed parameter)	3000 to 8000 (For each plate)
2	6						
3	8						
4	4	15					
5	6						
6	8						
7	4	20					
8	6						
9	8						
10	4	10	Staggered				
11	6						
12	8						
13	4	15					
14	6						
15	8						
16	4	20					
17	6						
18	8						

manufacture of SAHs for a variety of applications. The roughness of a cone form, as seen in Fig. 4a and b, is employed in this work to increase heat transmission while reducing frictional cost.

The details of three dimensional roughness elements geometrical parameters and flow parameter of the investigation are as follows.

- Reynolds number ( $Re$ ):  $3000 \leq Re \leq 8000$ .
- Relative roughness pitch ( $p/e$ ):  $10 \leq p/e \leq 15$ .
- Relative roughness gap ( $w/e$ ):  $4 \leq w/e \leq 8$ .

The plates are examined on a total of eighteen. Each set consists of 11 trials with varying flow rates that span the Reynolds number range of 3000–8000 for each of the 11 runs. Flow parameters and three-dimensional roughness elements are included in Table 2 together with their specifications and ranges.

## 2.5. Data reduction

For a calculated heat flux input and air flow rate, the quasi-steady state temperatures values of the absorber and air temperatures in

the duct are determined at different places across the duct. These data are utilized to compute the rate at which heat is transferred to the moving air through the duct. The Nusselt number and friction factor are also computed in order to determine the influence of roughness configuration and operational conditions on heat flow and friction characteristics.

It is necessary to utilize the following formulae in order to determine air flow rate  $m$ , air velocity  $V$ , heat furnished to the air  $q$ , and convective heat transfer coefficient  $h$ .

$$m = \rho C_d a_o \sqrt{\frac{2gH}{1 - \left(\frac{a_o}{a_1}\right)^2}} \quad (3)$$

Using a pitot tube with a coefficient of discharge  $C_d$  of 0.62, the orifice plate is calibrated. Where,  $H = h_m(\rho_w/\rho)$  and  $h_m$  is manometer reading. The air velocity inside the duct is computed as follows.

$$V = \frac{m}{\rho WB} \quad (4)$$

The following equation is used to calculate the effective heat addition to the flowing air [50],

$$q = m \times C_p \times (t_o - t_i) \quad (5)$$

The heat transfer coefficient of air in the test length is calculated as [51,52],

$$h = \frac{q}{[A_c \times (t_p - t_f)]} \quad (6)$$

The average Nusselt number is derived using the heat transfer coefficient ( $h$ ) and is defined in the relationship as [53],

$$Nu_{av} = \frac{(h \times D_h)}{k} \quad (7)$$

The friction factor ( $f_r$ ) is calculated over the whole length of the test section ( $L$ ) as [53],

$$f_r = \frac{D_h \times \Delta p}{(2 \times L \times V^2 \times \rho)} \quad (8)$$

The friction factor for an air duct (smooth inside surfaces) is determined using the most popular Blasius equation [54] as follows.

$$f_s = \frac{0.079}{Re^{0.25}} \quad (9)$$

The average friction factor is computed using equation suggested by Refs. [20,55] and as per equation (1) topside rough wall and other three sides smooth walls.

$$f_{av} = \frac{\left[\left(\frac{W}{B}\right) + 2\right] f_s + \left[\left(\frac{W}{B}\right)\right] f_r}{2\left[\left(\frac{W}{B}\right) + 1\right]} \quad (10)$$

Stanton number for duct (all inside surfaces are smooth) is computed using correlation [56],

$$St_s = \frac{0.023}{Re^{0.2} Pr^{0.6}} \quad (11)$$

Average Stanton number is computed using average Nusselt number as shown below.

$$St_{av} = \frac{Nu_{av}}{Re Pr} \quad (12)$$

Efficiency index is calculated using formula as per investigations carried out by Refs. [20,21].

$$\eta = \frac{\left(\frac{St_{av}}{St_s}\right)}{\left(\frac{f_{av}}{f_s}\right)} \quad (13)$$

### 3. Validity test

In this study an approach is used determine the Nusselt number and the friction factor for a smooth inside surface duct and compare them to the values derived from correlations of the Nusselt number and the friction factor with the modified Dittus-Boelter equation for Nusselt number and friction factor with the modified Blasius equation.

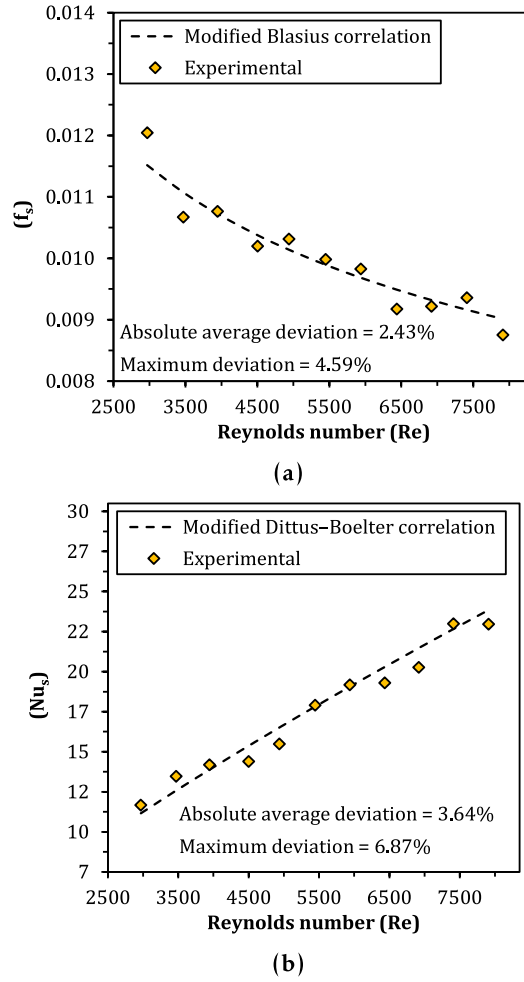


Fig. 5. Comparison of predicted and experimental (a)  $f_s$  values (b)  $Nu_s$  values.

$$Nu_s = 0.023 Re^{0.8} Pr^{0.4} \left( \frac{2R_{av}}{D_h} \right)^{-0.2} \quad \text{Where,} \quad \left( \frac{2R_{av}}{D_h} \right) = \left( \frac{1.156 + \frac{H}{W} - 1}{\frac{H}{W}} \right) \quad (14)$$

Using velocity of air 'V', the Reynolds number is computed as below,

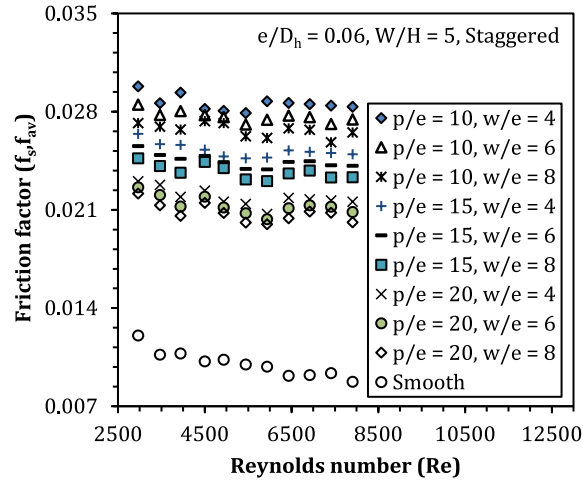
$$Re = \frac{\rho V D_h}{\mu} \quad \text{Where,} \quad V = \frac{m}{\rho W H} \quad (15)$$

Using below shown modified Blasius equation, friction factor for a smooth duct is calculated.

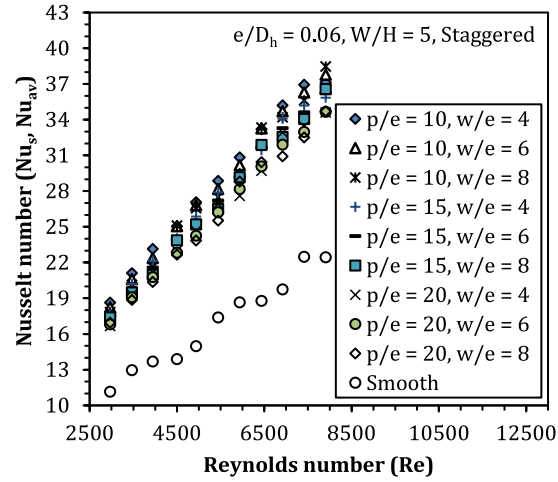
$$f_s = 0.085 Re^{-0.25} \quad (16)$$

Tests for validity are carried out on a traditional smooth absorber plate under identical overall duct geometry and flow conditions, with the results being compared to the heat transfer and friction factor values obtained from the equations applicable for smooth ducts in the literature as a basis for comparison.

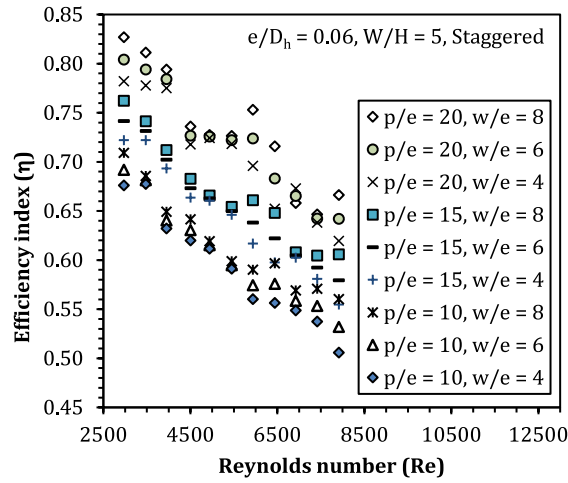
It is discovered that the friction factor and Nusselt number are much greater when these trial findings are compared to the numbers estimated using modified Blasius correlation and modified Dittus-Boelter correlation, respectively. Visual comparisons of the two techniques may be seen in Fig. 5a and Fig. 5b, respectively. Compared to the numbers predicted using modified Blasius equation, the absolute average percentage divergence of the current experimental friction factor data is  $\pm 2.43\%$ , and the highest absolute percentage divergence is  $\pm 4.59\%$ , according to the data, with the highest absolute percentage divergence being  $\pm 4.59\%$ . On the same lines, the absolute average percentage divergence of the current experimental Nusselt number data is  $\pm 3.64\%$ , and the highest divergence is  $\pm 6.87\%$ , compared to the values predicted using a modified Dittus-Boelter correlation. The minimum divergence is  $\pm 3.64\%$ , and the maximum divergence is  $\pm 6.87\%$ . Because of the high degree of agreement between experimented and predicted



(a)



(b)



(c)

Fig. 6. Effect of Re on (a)  $f_s$  &  $f_{av}$  (b)  $Nu_s$  &  $Nu_{av}$  (c)  $\eta$  for various values of  $p/e$  &  $w/e$ .



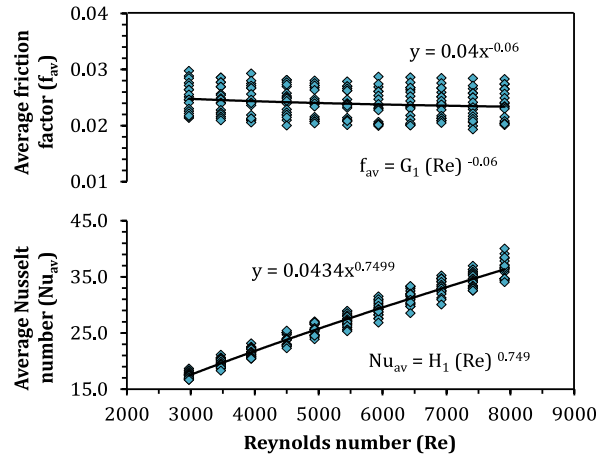


Fig. 7.  $f_{av}$  and  $Nu_{av}$  versus  $Re$  for all data points of the plates with cone roughness.

values, it is possible to rely on the experimental data collected for investigatory purposes to be reliable in the vast majority of situations.

#### 4. Results and discussions

Fig. 6a and Fig. 6b depict the influence of  $Re$  on  $f_s$  &  $f_{av}$  and  $Nu_s$  &  $Nu_{av}$  for different values of  $p/e$  &  $w/e$  for a staggered arrangement of conical roughness elements on the absorber plate, respectively. Results show that when the Reynolds number rises, a minor drop in friction factor is found, which is associated with a significant increase in Nusselt. Higher values of Reynolds number, i.e.  $Re = 7909$ , result in the greatest increase in friction factor and Nusselt number for absorber plates with a variety of relative roughness pitch values. At lower Reynolds numbers, i.e., at  $Re = 3000$ , the least amount of enhancement happens in a same manner.

Fig. 6a and b show the influence of relative roughness pitch ( $p/e$ ) on friction factor and Nusselt number, respectively, for a staggered arrangement of conical roughness elements on an absorber plate with a range of relative roughness gap ( $w/e$ ). The relative roughness pitch increases with the amount of roughened duct that has conical roughness components on the absorber surface, and this results in large reductions in friction factor and a modest drop in Nusselt number. In order to get the lowest enhancement of friction factor of about 91.3% and the lowest enhancement of Nusselt number of approximately 59.4%, the greatest value of relative roughness pitch (i.e. at  $p/e = 20$ ) must be reached.

Fig. 6a and b also depict the influence of the relative roughness gap ( $w/e$ ) on the friction factor and Nusselt number, respectively, for a staggered arrangement of conical roughness elements on the absorber plate for a variety of Reynolds number values. In roughened ducts, an increase in the value of relative roughness gap results in significant reductions in the friction factor throughout a wide range of different flow Reynolds numbers. However, a rise in the values of the relative roughness gap does not result in significant changes in the values of the Nusselt number. For all values of the Reynolds number, the highest value of the relative roughness gap (i.e.,  $w/e = 8$ ) provides the lowest friction factor possible. Because of the fact that this plate has the highest relative roughness pitch and gap values, it exhibits the highest enhancement of Nusselt number (59.4%) for a relatively smaller enhancement of friction factor (91.3%) at Reynolds number 3000. The reason behind this is because, this plate has the highest relative roughness pitch and gap values.

On the absorber plate, Fig. 6c illustrates the influence of  $Re$  on  $\eta$  for different values of  $p/e$  and  $w/e$  for a staggered arrangement of conical roughness elements with respect to the absorber plate's surface roughness. The efficiency index drops as Reynolds number rises for all numbers of relative roughness pitch (i.e.,  $p/e = 10, 15$  and  $20$ ) regardless of the relative roughness pitch value. This is owing to the fact that, as the Reynolds number grows from 3000 to 7909, the ratio of enhancement of friction factor ( $f_{av}/f_s$ ) predominates over the ratio of enhancement of Nusselt number ( $Nu_{av}/Nu_s$ ) as the Reynolds number increases. To improve the performance of an air heater duct, the Reynolds number should be increased since it generates turbulence, which increases friction. As predicted, roughened SAHs with a lower Reynolds number have better Thermo-hydraulic performance than their smooth counterparts.

Refer to Fig. 6c to see how the relative roughness pitch affects the efficiency index for an inline arrangement of conical roughness elements on an absorber plate with a variety of relative roughness gap values when the roughness elements are conical in shape. When the relative roughness pitch rises, the efficiency index enhances for all relative roughness gap values (i.e.,  $w/e = 4, 6$ , and  $8$ ), which is a notable trend. The reason for this is that as relative roughness pitch increases, the ratio of Nusselt number enhancement to friction factor enhancement ( $Nu_{av}/Nu_s$ ) predominates over the ratio of Nusselt number enhancement to friction factor enhancement ( $f_{av}/f_s$ ) as the ratio of relative roughness pitch increases. Higher values of relative roughness pitch result in improved Thermo-hydraulic performance due to the lowest enhancement of friction factor for the relative maximum increase in Nusselt number, which is achieved by using higher values of relative roughness pitch.

Fig. 6c also illustrates the impact of the relative roughness gap on the efficiency index for a staggered configuration of conical roughness protrusions on the absorber plate at different Reynolds numbers using a staggered arrangement of conical roughness elements. It is notable that the efficiency index grows as the relative roughness gap increases for all Reynolds numbers, and this is true for

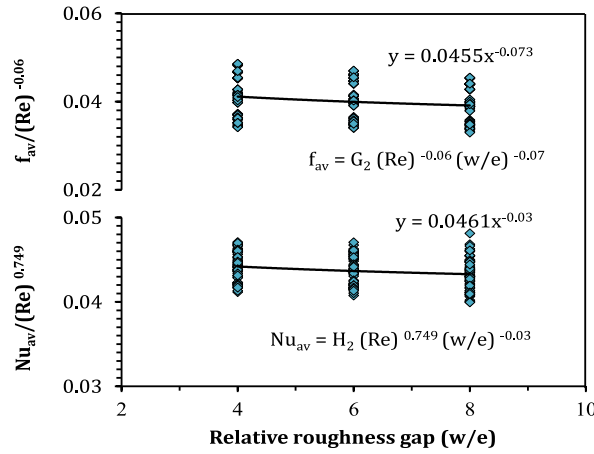


Fig. 8. Plot of  $f_{av}/(Re)^{-0.06}$  and  $Nu_{av}/(Re)^{0.749}$  versus  $(w/e)$ .

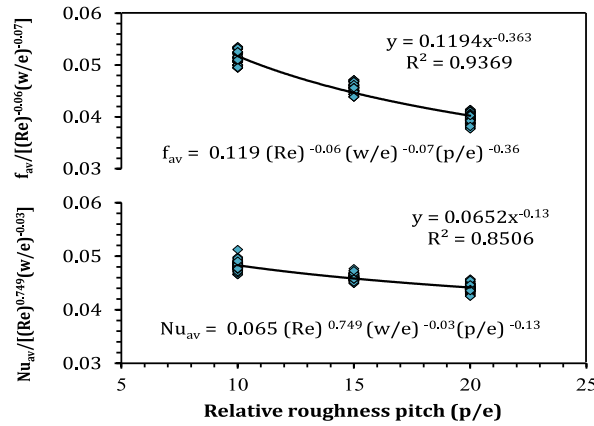


Fig. 9. Plot of  $f_{av}/[(Re)^{-0.06}(w/e)^{-0.07}]$  and  $Nu_{av}/[(Re)^{0.749}(w/e)^{-0.03}]$  versus  $(p/e)$ .

all Reynolds numbers. As a result of the fact that a rise in relative roughness gap values results in a considerable reduction in friction in the duct by providing less turbulence, without causing a major change in Nusselt number, this is the case. To get greater Thermo-hydraulic performance, it is preferable to have a larger value of relative roughness gap (e.g.,  $w/e = 8$ ).

#### 4.1. Correlations for friction factor and Nusselt number

Statistical correlations for average Nusselt number ( $Nu_{av}$ ) and average friction factor ( $f_{av}$ ) are developed by analysing experimental data gathered on a range of three-dimensional roughness geometries employed in the current inquiry. In order to create these correlations, Saini and Saini reference [57] a process provided by Saini and Saini citesaini2008development as follows: Reynolds number ( $Re$ ), relative roughness pitch ( $p/e$ ), and relative roughness gap ( $w/e$ ) are all multiplied by a constant. It is common practise to utilize the correlations that have been created to anticipate the performance of an artificially roughened duct that has three-dimensional roughness geometries on the absorber surface. The following is an example of how such connections are stated.

$$f_{av} = f[Re, p/e, w/e] \quad (17)$$

$$Nu_{av} = f[Re, p/e, w/e] \quad (18)$$

The experimental data for plates with cone-shaped roughness are utilized in conjunction with regression analysis to derive an equation for the average friction factor ( $f_{av}$ ) and the average Nusselt number ( $Nu_{av}$ ). The average friction factor ( $f_{av}$ ) and average Nusselt number ( $Nu_{av}$ ) are shown as a function of the Reynolds number ( $Re$ ) in Fig. 7.

A regression analysis performed to fit a straight line across the data points yielded the power law correlations shown in the accompanying table.

$$f_{av} = G_1(Re)^{-0.06} \quad (19)$$

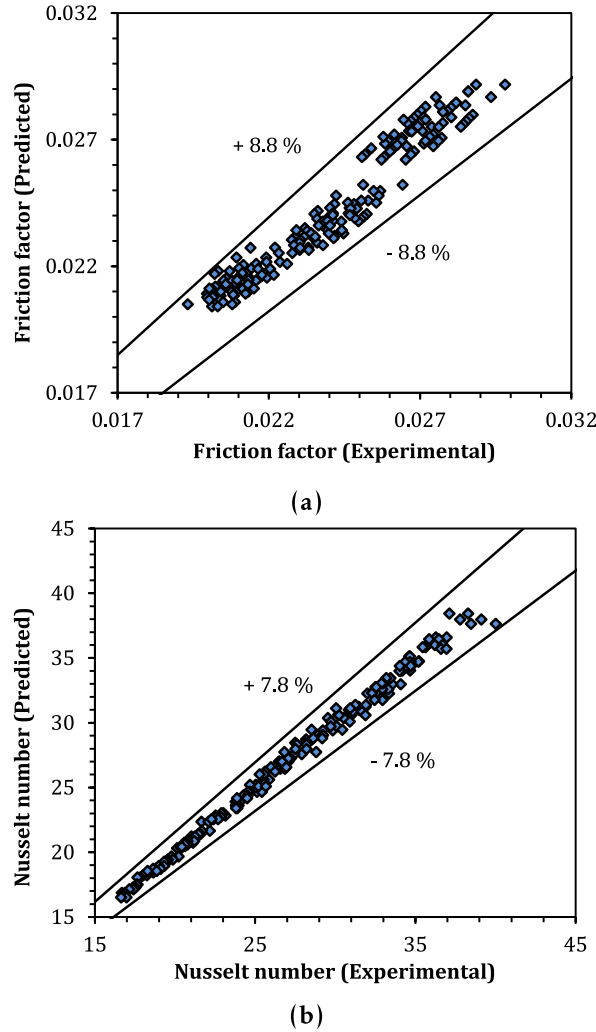


Fig. 10. Comparison of predicted and experimental values of (a)  $f_{av}$  (b)  $Nu_{av}$ .

$$Nu_{av} = H_1(Re)^{0.749} \quad (20)$$

Each of these coefficients  $G_1$  and  $H_1$  are functions of the other factors that go into determining the value. Now, considering the relative roughness gap parameter ( $w/e$ ), the value of  $G_1$  and  $H_1$  are plotted against ( $w/e$ ) as shown in Fig. 8. Using regression analysis to fit a straight line between two points, the following expressions are generated.

$$f_{av}/(Re)^{-0.06} = G_2(w/e)^{-0.07} \quad (21)$$

$$Nu_{av}/(Re)^{0.749} = H_2(w/e)^{-0.03} \quad (22)$$

Further, the coefficients  $G_2$  and  $H_2$  are the functions of other parameter i.e. relative roughness pitch ( $p/e$ ). Now values of  $G_2$  and  $H_2$  are plotted against ( $p/e$ ), as shown in Fig. 9. The regression analysis to best fit curves through these data points yields the following expressions of average friction factor ( $f_{av}$ ) and average Nusselt number ( $Nu_{av}$ ).

$$f_{av} = 0.119(Re)^{-0.06}(w/e)^{-0.07}(p/e)^{-0.36} \quad (23)$$

$$Nu_{av} = 0.065(Re)^{0.749}(w/e)^{-0.03}(p/e)^{-0.13} \quad (24)$$

These are the final correlations for average friction factor ( $f_{av}$ ) and average Nusselt number ( $Nu_{av}$ ) for roughened ducts having cone shape roughness on the absorber.

The difference of the anticipated and experimental values of the average friction factor and the average Nusselt number is represented in Fig. 10a and Fig. 10b, respectively. Predictions of average friction factor ( $f_{av}$ ) and average Nusselt number values ( $Nu_{av}$ ) for

cone shaped protrusions made using statistical correlations generated using the technique of regression analysis are within the error limitations of  $\pm 7.8\%$  to  $\pm 8.8\%$ , respectively. As a result, it may be said that the correlations for the prediction of average friction factor ( $f_{av}$ ) and average Nusselt number ( $Nu_{av}$ ) for a roughened duct with cone shaped protrusions on the absorber plate surface are relatively adequate in terms of accuracy.

## 5. Conclusions

The findings of this investigation will be used to build an acceptable approach for choosing the most optimal designs of artificial cone shaped protrusions on the absorber surface, as well as to enhance the characteristics of heat flow by reducing the amount of pumping energy required.

1. Increases in the Reynolds number are accompanied by decreases in the friction factor as well as Nusselt number. In comparison to the results recorded for smooth absorber plates, friction factor and Nusselt number values are much greater for rough absorber plates. As a result of roughness, the different properties of airflow are triggered, resulting in air flow deviations, re-attachments, and the formation of derived secondary flow.
2. For cone shaped roughness corresponding to ( $p/e$ ) value of 10 and ( $w/e$ ) value of 4 at Reynolds number (Re) value of 8000, the maximum enhancement in Nusselt number is determined to be 64.5%.
3. According to the results, the maximum enhancement in friction factor is determined to be 153.3% for cone shaped roughness with  $p/e = 10$  and  $w/e = 4$  at  $Re = 8000$ .
4. Cone-shaped roughness has a maximum efficiency index of 0.8233 at  $Re = 3000$  and  $p/e = 20$  and  $w/e = 8$ .
5. The results of the experimental work that was carried out indicate a high degree of consistency between theoretical and experimental results.
6. A similar result is that the average friction factor ( $f_{av}$ ) and average Nusselt number ( $Nu_{av}$ ) values predicted for cone shaped roughness elements are within the error bounds of  $\pm 8.8\%$  compared to the actual values. Accordingly, it can be decided that the correlations are reasonably agreeable for the prediction of average friction factor ( $f_{av}$ ) and average Nusselt number ( $Nu_{av}$ ) for the roughened duct with conical roughness protrusions on the absorber surface.

## Author statement

Abdulmohsen O. Alsaiari: Conceptualization and Methodology, Writing - Original Draft. Hassan A. H. Alzahrani: Software and Validation. Madhukeshwara. N.; Formal analysis. Prasanna B.M: Writing - Review & Editing; Supervision.

## Declaration of competing interest

The authors declare that they have no known competing financial interests or personal relationships that could have appeared to influence the work reported in this paper.

## Acknowledgments

This research work was funded by institutional fund projects under grant number IFPRC-149-135-2020. Therefore authors gratefully acknowledge technical and financial support from the Ministry of Education and King Abdul Aziz University, Jeddah, Saudi Arabia.


## References

- [1] M.K. Alawiye, O.R. Ewulo, Awareness and use of solar energy as alternative power source for ict facilities in nigerian university libraries and information centres, *Libr. Philos. Pract.* (2019) 1–18.
- [2] A. Kumar, R. Saini, J. Saini, A review of thermohydraulic performance of artificially roughened solar air heaters, *Renew. Sustain. Energy Rev.* 37 (2014) 100–122.
- [3] H.K. Ghritlahre, R.K. Prasad, Prediction of exergetic efficiency of arc shaped wire roughened solar air heater using ANN model, *Int. J. Heat Technol.* 36 (3) (2018) 1107–1115.
- [4] G. Roa, I. Macedo, Grain drying in stationary bins with solar heated air, *Sol. Energy* 18 (5) (1976) 445–449.
- [5] T. Koyuncu, Performance of various design of solar air heaters for crop drying applications, *Renew. Energy* 31 (7) (2006) 1073–1088.
- [6] A.R. Womac, F.D. Tompkins, K.E. DeBusk, Evaluation of solar air heaters for crop drying, *Energy Agric.* 4 (1985) 147–157.
- [7] K. Ong, Crop and timber drying in Malaysia proposed plans for studies, in: *Solar Energy International Progress*, Elsevier, 1980, pp. 1654–1665.
- [8] A.S. Yadav, J. Bhagoria, A cfd based thermo-hydraulic performance analysis of an artificially roughened solar air heater having equilateral triangular sectioned rib roughness on the absorber plate, *Int. J. Heat Mass Tran.* 70 (2014) 1016–1039.
- [9] E. Bilgen, B. Bakeka, Solar collector systems to provide hot air in rural applications, *Renew. Energy* 33 (7) (2008) 1461–1468.
- [10] A. Boulemtafes-Boukadoum, A. Benzaoui, CFD based analysis of heat transfer enhancement in solar air heater provided with transverse rectangular ribs, *Energy Proc.* 50 (2014) 761–772.
- [11] N. Madhukeshwara, E. Prakash, An investigation on the performance characteristics of solar flat plate collector with different selective surface coatings, *Int. J. Energy Environ.* 3 (1) (2012).
- [12] J.A. Duffie, W.A. Beckman, *Solar Engineering of Thermal Processes*, John Wiley & Sons, 2013.
- [13] M. Selvaraj, P. Sadagopan, M. Vairavel, Review on latent heat solar air collectors, *Int. J. Adv. Res. Eng. Technol.* 10 (6) (2019) 112–121.
- [14] K. Visagavel, *Performance Analysis of Overlapped Solar Air Heater Using CFD*, 2018.
- [15] M. Nazari, D.J. Vahid, R.K. Saray, Y. Mahmoudi, Experimental investigation of heat transfer and second law analysis in a pebble bed channel with internal heat generation, *Int. J. Heat Mass Tran.* 114 (2017) 688–702.
- [16] A. Thakre, A. Singh, A. Verma, *Experimental Analysis of Comparative Performance of Conventional and Matrix Aluminium Mesh Wire Absorber Solar Air Heater*, 2017.

- [17] A. Kumar, R. Kumar, A.K. Behura, Investigation for jet plate solar air heater with longitudinal fins, *Int. Res. Adv. Eng. Sci.* 2 (3) (2017) 112–119.
- [18] H.K. Ghritlahre, R.K. Prasad, Exergetic performance prediction of a roughened solar air heater using artificial neural network, *Strojinski Vestnik/J. Mech. Eng.* 64 (3) (2018).
- [19] C. Prakash, R. Saini, Use of artificial roughness for performance enhancement of solar air heaters—a review, *Int. J. Green Energy* 16 (7) (2019) 551–572.
- [20] M. Nanjundappa, Optimum thermo-hydraulic performance of solar air heater provided with cubical roughness on the absorber surface, *Exp. Heat Tran.* (2019) 1–14.
- [21] R. Webb, E. Eckert, R. Goldstein, Heat transfer and friction in tubes with repeated-rib roughness, *Int. J. Heat Mass Tran.* 14 (4) (1971) 601–617.
- [22] A.M.E. Momin, J. Saini, S. Solanki, Heat transfer and friction in solar air heater duct with v-shaped rib roughness on absorber plate, *Int. J. Heat Mass Tran.* 45 (16) (2002) 3383–3396.
- [23] K. Prasad, S. Mullick, Heat transfer characteristics of a solar air heater used for drying purposes, *Appl. Energy* 13 (2) (1983) 83–93.
- [24] D. Gupta, S. Solanki, J. Saini, Thermohydraulic performance of solar air heaters with roughened absorber plates, *Sol. Energy* 61 (1) (1997) 33–42.
- [25] R. Kumar, A. Kumar, V. Goel, Effect of rounded corners on heat transfer and fluid flow through triangular duct, *J. Heat Tran.* 140 (12) (2018).
- [26] K. Aharwal, B.K. Gandhi, J. Saini, Heat transfer and friction characteristics of solar air heater ducts having integral inclined discrete ribs on absorber plate, *Int. J. Heat Mass Tran.* 52 (25–26) (2009) 5970–5977.
- [27] S. Singh, S. Chander, J. Saini, Heat transfer and friction factor correlations of solar air heater ducts artificially roughened with discrete v-down ribs, *Energy* 36 (8) (2011) 5053–5064.
- [28] N. Madhukeshwara, E. Prakash, An investigation of heat transfer augmentation and friction characteristics in solar air heater duct with v-shaped wire as artificial roughness on absorber plate, *Int. J. Energy Environ.* 4 (2013).
- [29] N. Madhukeshwara, A. Alhadhrami, H.A. Alzahrani, B. Prasanna, Thermal–hydraulic analysis of a solar air heater fitted with a wire-roughened absorber plate, in: *Proceedings of the Institution of Mechanical Engineers, Part E: Journal of Process Mechanical Engineering*, 2021, 09544089211059044.
- [30] R.S. Gill, V.S. Hans, R.P. Singh, Optimization of artificial roughness parameters in a solar air heater duct roughened with hybrid ribs, *Appl. Therm. Eng.* 191 (2021), 116871.
- [31] A. Jaurker, J. Saini, B. Gandhi, Heat transfer and friction characteristics of rectangular solar air heater duct using rib-grooved artificial roughness, *Sol. Energy* 80 (8) (2006) 895–907.
- [32] N. Pandey, V. Bajpai, et al., Experimental investigation of heat transfer augmentation using multiple arcs with gap on absorber plate of solar air heater, *Sol. Energy* 134 (2016) 314–326.
- [33] M. Nanjundappa, Nusselt number and friction factor correlations for the solar air heater duct furnished with artificial cube shaped roughness elements on the absorber plate, *Heat Mass Tran.* 57 (12) (2021) 1997–2013.
- [34] K. Muluwork, Investigations on Fluid Flow and Heat Transfer in Roughened Absorber Solar Heaters, IIT, India, 2000. *Roorkee-247667*.
- [35] A.K. Patil, J. Saini, K. Kumar, Nusselt number and friction factor correlations for solar air heater duct with broken v-down ribs combined with staggered rib roughness, *J. Renew. Sustain. Energy* 4 (3) (2012), 033122.
- [36] Y. Rathor, K. Aharwal, Heat transfer enhancement due to a staggered element using liquid crystal thermography in an inclined discrete rib roughened solar air heater, *Int. Commun. Heat Mass Tran.* 118 (2020), 104839.
- [37] R. Gill, V. Hans, J. Saini, S. Singh, Investigation on performance enhancement due to staggered piece in a broken arc rib roughened solar air heater duct, *Renew. Energy* 104 (2017) 148–162.
- [38] A. Kumar, M.-H. Kim, Effect of roughness width ratios in discrete multi v-rib with staggered rib roughness on overall thermal performance of solar air channel, *Sol. Energy* 119 (2015) 399–414.
- [39] S. Lau, R. McMillin, J. Han, Turbulent Heat Transfer and Friction in a Square Channel with Discrete Rib Turbulators, 1991.
- [40] A. Abdullah, M. Amro, M. Younes, Z. Omara, A. Kabeel, F. Essa, Experimental investigation of single pass solar air heater with reflectors and turbulators, *Alex. Eng. J.* 59 (2) (2020) 579–587.
- [41] S. Chamoli, R. Lu, P. Yu, Thermal characteristic of a turbulent flow through a circular tube fitted with perforated vortex generator inserts, *Appl. Therm. Eng.* 121 (2017) 1117–1134.
- [42] I. Singh, S. Vardhan, Experimental investigation of an evacuated tube collector solar air heater with helical inserts, *Renew. Energy* 163 (2021) 1963–1972.
- [43] S. Chamoli, R. Lu, D. Xu, P. Yu, Thermal performance improvement of a solar air heater fitted with winglet vortex generators, *Sol. Energy* 159 (2018) 966–983.
- [44] S. Chamoli, N. Thakur, Heat transfer enhancement in solar air heater with v-shaped perforated baffles, *J. Renew. Sustain. Energy* 5 (2) (2013), 023122.
- [45] S. Chamoli, R. Lu, J. Xie, P. Yu, Numerical study on flow structure and heat transfer in a circular tube integrated with novel anchor shaped inserts, *Appl. Therm. Eng.* 135 (2018) 304–324.
- [46] S. Bhattacharyya, H. Chattopadhyay, A.C. Benim, Computational investigation of heat transfer enhancement by alternating inclined ribs in tubular heat exchanger, *Prog. Comput. Fluid Dynamic. Int. J.* 17 (6) (2017) 390–396.
- [47] S. Bhattacharyya, H. Chattopadhyay, A. Guin, A.C. Benim, Investigation of inclined turbulators for heat transfer enhancement in a solar air heater, *Heat Tran.* Eng. (2018).
- [48] A. Standard, “93-77, Methods of Testing to Determine the Thermal Performance of Solar Collectors, american society of heating,” *Refrigeration and Air Conditioning Engineers, Inc.*, New York, NY, 1977.
- [49] S. Kline, F. McClintock, Describing uncertainties in single-sample experiments, *asme mech. Eng. Times* 75 (1952) 3–8.
- [50] R. Saini, J. Saini, Heat transfer and friction factor correlations for artificially roughened ducts with expanded metal mesh as roughness element, *Int. J. Heat Mass Tran.* 40 (4) (1997) 973–986.
- [51] H.K. Ghritlahre, R.K. Prasad, Prediction of heat transfer of two different types of roughened solar air heater using artificial neural network technique, *Therm. Sci. Eng. Prog.* 8 (2018) 145–153.
- [52] S. Pawar, D. Hindolia, J. Bhagoria, Experimental study of nusselt number and friction factor in solar air heater duct with diamond shaped rib roughness on absorber plate, *Am. J. Eng. Res.* 2 (6) (2013) 60–68.
- [53] K. Aharwal, B. Gandhi, J. Saini, Experimental investigation on heat-transfer enhancement due to a gap in an inclined continuous rib arrangement in a rectangular duct of solar air heater, *Renew. Energy* 33 (4) (2008) 585–596.
- [54] A. Kumar, A. Gholap, R. Gangarde, S.M. Shinde, M.P. Vyavahare, V.B. Mete, S.A. Borude, Performance of solar air heaters with corrugated absorber plate—a cfd approach, *Int. J. Innovat. Res. Adv. Stud.* 4 (11) (2017) 76–86.
- [55] B. Prasad, J. Saini, Effect of artificial roughness on heat transfer and friction factor in a solar air heater, *Sol. Energy* 41 (6) (1988) 555–560.
- [56] B. Prasad, J. Saini, Optimal thermohydraulic performance of artificially roughened solar air heaters, *Sol. Energy* 47 (2) (1991) 91–96.
- [57] S. Saini, R. Saini, Development of correlations for nusselt number and friction factor for solar air heater with roughened duct having arc-shaped wire as artificial roughness, *Sol. Energy* 82 (12) (2008) 1118–1130.

## RESEARCH ARTICLE

# Comparative study of chitosan derivatives through CoM-polynomial

M. C. Shanmukha<sup>1</sup>  | A. Usha<sup>2</sup>

<sup>1</sup>Department of Mathematics, Bapuji Institute of Engineering and Technology, Davanagere, India

<sup>2</sup>Department of Mathematics, Alliance School of Applied Mathematics, Alliance University, Bangalore, India

**Correspondence**

M. C. Shanmukha, Department of Mathematics, Bapuji Institute of Engineering and Technology, Davanagere 577004, Karnataka, India.

Email: [mcshanmukha@gmail.com](mailto:mcshanmukha@gmail.com)

**Abstract**

Most abundant polysaccharides having numerous applications in biopolymers, bioscience and other fields are chitin and chitosan. Hydrogels are their derivatives, widely used in biomedical applications. Other applications include adsorbent of metals and dyes from industrial wastes. Hydrogels based chitosan is used in drugs and proteins in pharmaceutical fields. This work mainly focuses on the polysaccharides such as, chitosan and its derivatives, whose chemical structure is modeled as a chemical graph and the data regarding edge and vertex partitioning are studied. In this work, using non-adjacent pairing of vertices approach, their polynomials are determined for various topological coindices for the polysaccharides chitosan and their chemical derivatives. These polynomials are termed CoM-polynomials, extension of M-polynomials for non-adjacent vertices. Topological coindices are the real numbers, representing the molecular structure of the chemical compound whose physicochemical characteristics can be studied that relates Quantitative Structure Property Relationship/Quantitative Structure Activity Relationship (QSPR/QSAR) investigations. CoM-polynomials are computed for the derivatives of chitosan such as alpha, beta and gamma chitin. CoM-polynomials of 11 degree-based topological coindices are determined and are compared for the derivatives of chitosan.

**KEYWORDS**

chitosan derivatives, CoM-polynomial, topological coindex

## 1 | INTRODUCTION

The natural biopolymers that are found in the exoskeletons of insects, shell of crustaceans are very popularly known as chitin and chitosan. They are artificial polymers which are non-toxic, biocompatible and biodegradable in nature. Annually, lakhs of tons of synthetic polymers are produced globally. These polymers are stable and biodegradable necessitates compatibility with the ecosystem. Out of these polymers, chitin and chitosan have attracted many scientists because of their wide applications in drug delivery, wound healing, gene therapy and tissue engineering as they can be easily processed into various forms such as gels, scaffolds, membranes, nanofibers, and nanoparticles [1, 2]. Archivaly, chitin an abundant mucopolysaccharide available in nature was earlier named fungine by Braconnot in 1811 as it was first isolated from the cell walls of mushrooms. In 1823, Odier renamed it as chitin. After three decades of renaming fungine as chitin, it was isolated from cellulose by Knorr in 1984. Rouget in 1859 first discovered chitosan as it was extensively studied because of its significant chemical, physical and biological properties and ample applications. Studies revealed that chitosan is mostly obtained from chitin deacetylation. The diverse applications include polymers belonging to polyesters that are obtained from bacteria, polymers from animals, proteins and polypeptides are a class of polysaccharides of which chitosan is one of them. It is used in waste treatment, biomaterials as gels, cosmetics, food, textile, agriculture, and pharmaceutical industries [3]. Additionally, chitosan finds its applications as it has healing, antifungal and antimicrobial properties. This has gained a lot of attention in the development of hydrogels. Hydrogels have the capacity to absorb water or biological fluids as they are formed by hydrophilic polymers. Because of the absorption

capacity, it is used extensively in the fields of pharmacy, biomedicine and environmental chemistry. The applications of chitin and chitosan are several, be it in tissue engineering, drug and growth delivery, wound healing and many more. Chitin originated from the shrimps, cray fish, crabs, lobsters and other insects as well as from squids which occur in the granular sheets or powder forms. Chitin originated from porifera or sponge like structure are found their applications in biomedical and bio engineering science. Chitin also occurs in marine invertebrates except marine sponges. Tissue engineering includes clinical treatment of organ replacement in which recuperates the damaged body tissues and organs. It also fosters surgical reconstruction through cells thereby gaining successful survival rates over autografts. Combination of diverse polymers like chitin and chitosan have remarkable applications in the biomedical field where it is applied in the surgical treatment of ligament, cartilage, tendon, neural, bone and skin regeneration.

In chemical graph theory a topological descriptor is a real number that is obtained from the molecular structure of a chemical compound [4–11]. It illustrates molecular features of the chemical compound and helps in the development of new drugs as they are data rich, and faster to calculate to predict the properties of the compound through the molecular graph [12–15].

The chemical compounds are modeled as molecular graphs where the atoms are considered the vertices while their bonds as edges.  $G = (V, E)$  represents a molecular graph where  $V(G)$  and  $E(G)$  are the vertex and edge set respectively. The usual notations such as  $a \in V(G)$  is a vertex and  $d(a)$  represents the degree of the vertex  $a$  which denotes the number of edges incident to the vertex  $a$ . Let  $\bar{G}$  be the complement of the graph  $G$  such that  $ab \in \bar{G}$  if  $ab \notin G$  [16].

Lot of research has taken place in degree based topological indices which consider adjacent vertex pairs. Overtime, studies have begun based on non-adjacent pair of vertices resulting in degree based topological indices termed as coindices.

Berhe et al. [17] focused on the study related to  $C_4C_8(S)$  nanotubes, nanotorus and graphene sheets for which various coindices were computed. Many researchers have worked on coindices, for more literature, readers might refer to [18–20].

Recently, Syed Ajaj et al. [21], studied the topological coindices through CoM polynomial which contributes to the non-adjacent pair of vertices. The following are the First Zagreb  $\overline{M}_1(G)$ , Second Zagreb  $\overline{M}_2(G)$ , Second modified Zagreb  $\overline{m}M_2(G)$ , Redefined third Zagreb  $\overline{ReZG}_3(G)$ , Forgotten  $\overline{F}(G)$ , Randic  $\overline{R}_k(G)$ , Inverse Randic  $\overline{RR}_k(G)$ , Symmetric division  $\overline{SDD}(G)$ , Harmonic  $\overline{H}(G)$ , Inverse sum indeg  $\overline{I}(G)$ , and Augmented Zagreb  $\overline{A}(G)$  coindices.

## 2 | CoM-POLYNOMIAL

In this study, using non-adjacent pairing of vertices, its polynomials are determined for various topological coindices for the polysaccharide's chitosan and their chemical derivatives. These polynomials are termed CoM-polynomials which are an extension of M-polynomials for non-adjacent vertices. Degree-based topological indices contribute to the adjacency of vertex pairs. Studies have also extended for non-adjacency vertices whose topological indices are referred to as coindices. As the non-adjacent vertices consume a lot of time for calculations, a new concept of coindices is introduced. M-polynomials are associated with degree-based indices [22–31] whereas CoM-polynomials with that of non-adjacency vertices [32].

**Definition 2.1.** For a simple connected graph  $G$ , the CoM-polynomial is defined as,

$$\text{CoM}(G; x, y) = \overline{M}(G; x, y) = \sum_{i \leq j} \overline{m}_{ij}(G) x^i y^j$$

where  $\overline{m}_{ij}$ ,  $i, j \geq 1$  represents the number of edges  $ab \notin E(G)$  such that  $\{d(a), d(b)\} = \{i, j\}$ . Here  $d(a)$ ,  $d(b)$  represent the degrees of the vertices  $a$  and  $b$  in the graph  $G$ .

List of CoM-polynomials through which various topological coindices are derived tabulated in Table 1.

Applying the following notations in the paper,

$$\begin{aligned} n_i &= |V_i| \text{ for } V_i = \{a \in V(G) | d(a) = i\} \\ m_{ij} &= |E_{ij}| \text{ for } E_{ij} = \{ab \in E(G) | d(a) = i \text{ and } d(b) = j\} \\ \overline{m}_{ij} &= |\overline{E}_{ij}| \text{ for } \overline{E}_{ij} = \{ab \in \overline{E}(G) | d(a) = i \text{ and } d(b) = j\} \end{aligned}$$

**Lemma 2.2.** For a connected graph  $G$  of order  $n$ , we have

$$\overline{m}_{ij} = |\overline{E}_{ij}| = \begin{cases} \frac{n_i(n_i - 1)}{2} - m_{ii} & \text{for } i = j \\ n_i n_j - m_{ij} & \text{for } i < j \end{cases}$$

where  $n_i$ ,  $m_{ij}$  and  $\overline{m}_{ij}$  are defined above.



**TABLE 1** The relation between various topological coindices with CoM-polynomial

Topological coindex	Formula $\phi(d(a), d(b))$	Derivation from $f(x, y) = \text{CoM}(G; x, y)$
$\overline{M}_1(G)$	$\sum_{ab \notin E(G)} d(a) + d(b)$	$(D_x + D_y)(f(x, y))_{x=1=y}$
$\overline{M}_2(G)$	$\sum_{ab \notin E(G)} d(a)d(b)$	$(D_x D_y)(f(x, y))_{x=1=y}$
${}^m\overline{M}_2(G)$	$\sum_{ab \notin E(G)} \frac{1}{d(a)d(b)}$	$(S_x S_y)(f(x, y))_{x=1=y}$
$\overline{ReZG}_3(G)$	$\sum_{ab \notin E(G)} d(a)d(b)(d(a) + d(b))$	$D_x D_y (D_x + D_y)(f(x, y))_{x=1=y}$
$\overline{F}(G)$	$\sum_{ab \notin E(G)} d^2(a) + d^2(b)$	$(D_x^2 + D_y^2)(f(x, y))_{x=1=y}$
$\overline{R}_k(G)$	$\sum_{ab \notin E(G)} \{d(a)d(b)\}^k$	$(D_x^k D_y^k)(f(x, y))_{x=1=y}$
$\overline{RR}_k(G)$	$\sum_{ab \notin E(G)} \frac{1}{\{d(a)d(b)\}^k}$	$(S_x^k S_y^k)(f(x, y))_{x=1=y}$
$\overline{SDD}(G)$	$\sum_{ab \notin E(G)} \frac{d^2(a) + d^2(b)}{d(a)d(b)}$	$(D_x S_y + S_x D_y)(f(x, y))_{x=1=y}$
$\overline{H}(G)$	$\sum_{ab \notin E(G)} \frac{2}{d(a) + d(b)}$	$2S_x J(f(x, y))_{x=1}$
$\overline{I}(G)$	$\sum_{ab \notin E(G)} \frac{d(a)d(b)}{d(a) + d(b)}$	$S_x J D_y (f(x, y))_{x=1}$
$\overline{A}(G)$	$\sum_{ab \notin E(G)} \left\{ \frac{d(a)d(b)}{d(a) + d(b) - 2} \right\}^3$	$S_x^3 Q_{-2} J D_x^3 D_y^3 (f(x, y))_{x=1}$
where		
$D_x = x \frac{\partial(f(x, y))}{\partial x},$	$D_y = y \frac{\partial(f(x, y))}{\partial y},$	$S_x = \int_0^x \frac{f(t, y)}{t} dt,$
$S_y = \int_0^y \frac{f(x, t)}{t} dt,$	$J(f(x, y)) = f(x, x),$	$Q_k(f(x, y)) = x^k f(x, y).$

### 3 | DISCUSSION AND MAIN RESULTS

In this work, the topological coindices are computed through the CoM-polynomial approach for chitosan derivatives (Figure 1). The molecular structure of the said compounds is modeled as simple graphs and the techniques used for computing the results include combinatorial methods, vertex partition and edge partition.

### 4 | MOTIVATION

After cellulose, the amplest polysaccharide is chitosan. Chitosan has varied applications because of its interesting properties, in the fields of waste treatment, food, textile, biodegradable, and pharmaceutical industries such as gels, films, polymer membranes and nanofibers. In addition to its amazing properties, it can be included with properties like healing, antimicrobial, and antifungal. Hydrogels formed from chitosan are the biopolymers that have attracted a lot of attention in the field of pharmacy as lysozyme and fabrication of dressings. It is used in the wound secretions as it can absorb and manage the hydration of the affected region. Hydrogels are used extensively in medical purposes, proving chitosan derivatives to be the safe choice for the applications of biomaterials [33]. This is obvious as there is a large volume of studies and research being carried out on the considered polysaccharide (CS). Hydrogels that are synthesized from chitosan and its derivatives are used in drugs, gene factors, protein delivery, dressing devices, and for tissue culture. Chitosan and its derivatives exhibit mucoadhesive, able to transiently open epithelial tight joints and biodegradable properties that have made their applications very significant in the pharma and biomedical fields. To increase the mechanical properties of hydrogel, chitosan is associated with other synthetic polymers to increase liquid uptake capacity. Topological coindices is a real number that represents the molecular structure of the chemical compound whose physicochemical characteristics can be studied that relates QSPR/QSAR investigations. Recent studies on coindices have shown that there is a notable relationship with the physicochemical properties and anti-viral drugs. It is evident that for upcoming research in drugs and QSPR analysis, topological coindices will be a powerful tool. In this study we define the CoM-polynomial of chitosan and its derivatives.

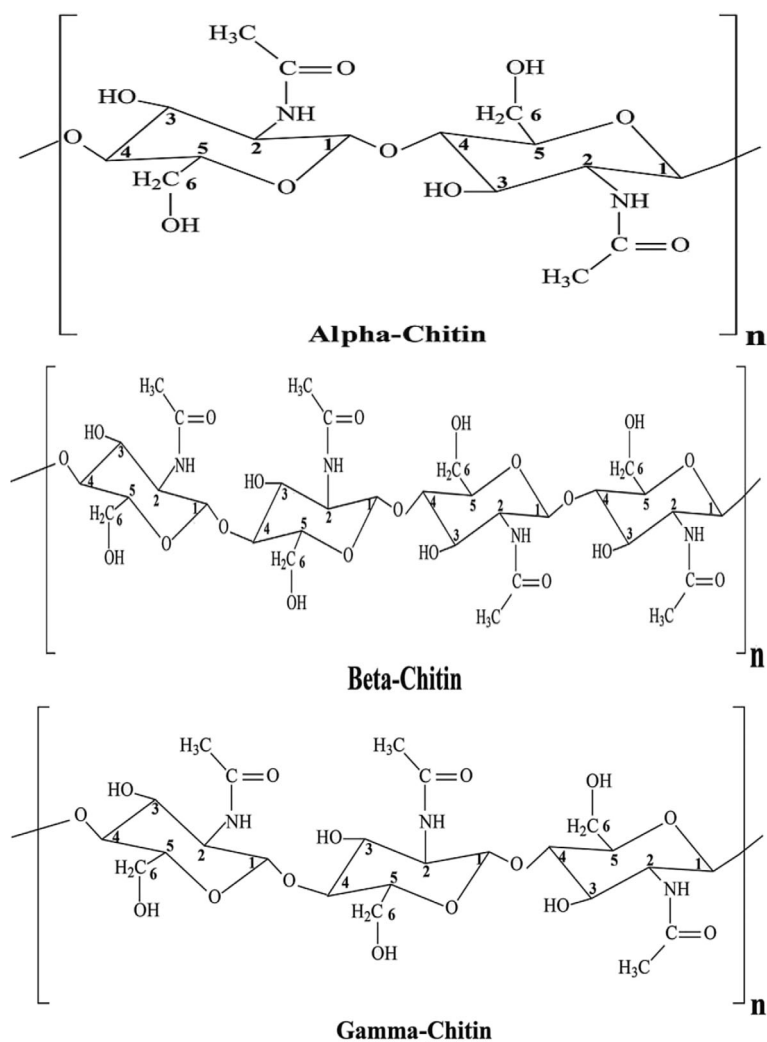


**FIGURE 1** Molecular structure of  $\alpha$ -chitin,  $\beta$ -chitin, and  $\gamma$ -chitin

#### 4.1 | CoM-polynomial of $\alpha$ -chitin( $\alpha C$ )

**Theorem 4.1.** The CoM-polynomial for  $\alpha$ -chitin is given by (Figures 2 and 3)

$$\text{CoM}(\alpha C; x, y) = (64n^2 + 6n - 2)xy^2 + (96n^2 + 18n - 2)xy^3 + (96n^2 - 26n + 2)x^2y^3 + (72n^2 - 14n)x^3y^3$$

*Proof.* From the Figure 2, it is easy to see that  $|V(\alpha C)| = 28n + 1$  and  $|E(\alpha C)| = 30n$ . Also, the edge set of  $\alpha C$  may be categorized into four partitions based on the degree of vertices are as follows

$$E_{12} = \{ab \in E(\alpha C) | d(a) = 1, d(b) = 2\},$$

$$E_{13} = \{ab \in E(\alpha C) | d(a) = 1, d(b) = 3\},$$

$$E_{23} = \{ab \in E(\alpha C) | d(a) = 2, d(b) = 3\},$$

$$E_{33} = \{ab \in E(\alpha C) | d(a) = 3, d(b) = 3\},$$

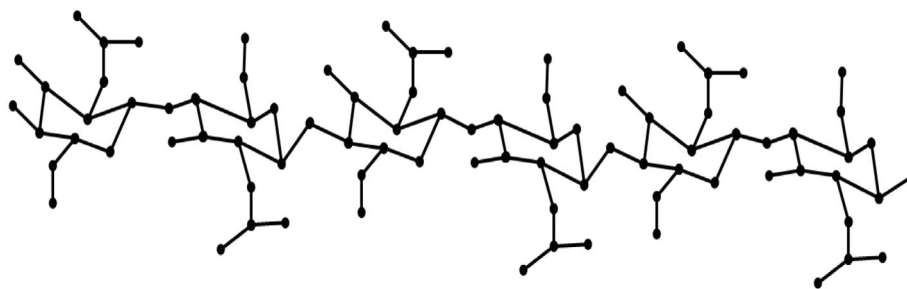


**FIGURE 2** Molecular graph of  $\alpha$ -chitin for  $n = 3$

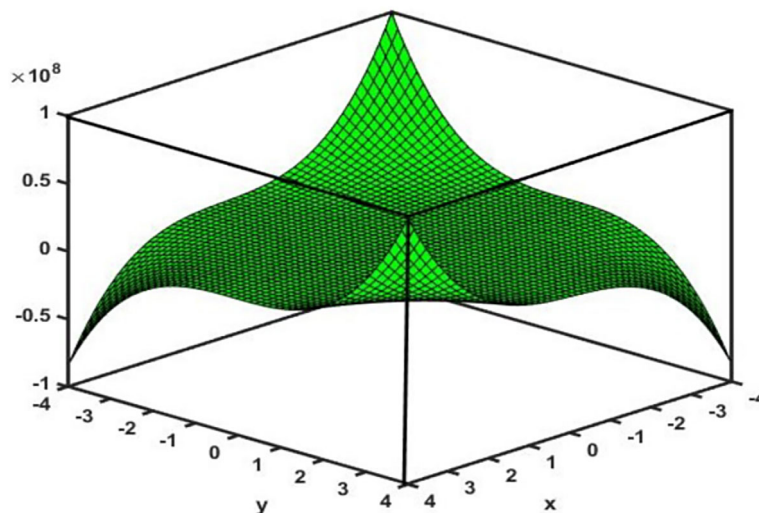


**FIGURE 3** 3D plot of CoM-polynomial of  $\alpha$ -chitin

such that

$$m_{12} = 2n, \quad m_{13} = 6n + 2, \quad m_{23} = 14n - 2, \quad \text{and} \quad m_{33} = 8n.$$

Similarly,  $V(\alpha C)$  can be divided into three classes depending on the degree of vertex are given by

$$n_1 = |V_1| = 8n + 2, \quad n_2 = |V_2| = 8n - 1, \quad \text{and} \quad n_3 = |V_3| = 12n.$$

Using Lemma 1, we have

$$\begin{aligned} \bar{m}_{12} &= n_1 n_2 - m_{12} = (8n + 2)(8n - 1) - 2n = 64n^2 + 6n - 2. \\ \bar{m}_{13} &= n_1 n_3 - m_{13} = (8n + 2)(12n) - (6n + 2) = 96n^2 + 18n - 2. \\ \bar{m}_{23} &= n_2 n_3 - m_{23} = (8n - 1)(12n) - (14n - 2) = 96n^2 - 26n + 2. \\ \bar{m}_{33} &= \frac{n_3(n_3 - 1)}{2} - m_{33} = \frac{(12n)(12n - 1)}{2} - 8n = 72n^2 - 14n. \end{aligned}$$

Using the definition of CoM-polynomial

$$\begin{aligned} \text{CoM}(G; x, y) &= \bar{M}(G; x, y) = \sum_{i \leq j} \bar{m}_{ij}(G) x^i y^j \\ \text{CoM}(\alpha C; x, y) &= \sum_{1 \leq 2} \bar{m}_{12} x y^2 + \sum_{1 \leq 3} \bar{m}_{13} x y^3 + \sum_{2 \leq 3} \bar{m}_{23} x^2 y^3 + \sum_{3 \leq 3} \bar{m}_{33} x^3 y^3 \\ &= (64n^2 + 6n - 2) x y^2 + (96n^2 + 18n - 2) x y^3 + (96n^2 - 26n + 2) x^2 y^3 + (72n^2 - 14n) x^3 y^3. \end{aligned}$$

Adopting Theorem 1 and Table 1, some degree based topological coindices of the  $\alpha$ -chitin are derived in the following proposition

**Proposition 4.2.**

$$\begin{aligned}\overline{M}_1(\alpha C) &= 1488n^2 - 124n - 4. \\ \overline{M}_2(\alpha C) &= 1640n^2 - 216n + 2. \\ {}^m\overline{M}_2(\alpha C) &= 88n^2 + 3.1111n - 1.3333. \\ \overline{ReZG}_3(\alpha C) &= 8304n^2 - 128n + 24. \\ \overline{F}(\alpha C) &= 3824n^2 - 380n - 4. \\ \overline{R}_k(\alpha C) &= 2^k(64n^2 + 6n - 2) + 3^k(96n^2 + 18n - 2) + 6^k(96n^2 - 26n + 2) + 3^{2k}(72n^2 - 14n). \\ \overline{RR}_k(\alpha C) &= \frac{(64n^2 + 6n - 2)}{2^k} + \frac{(96n^2 + 18n - 2)}{3^k} + \frac{(96n^2 - 26n + 2)}{6^k} + \frac{(72n^2 - 14n)}{3^{2k}}. \\ \overline{SDD}(\alpha C) &= 831.990n^2 - 9.332n - 7.3334. \\ \overline{H}(\alpha C) &= 153.06n^2 - 2.0666n - 1.5332. \\ \overline{I}(\alpha C) &= 337.8624n^2 - 34.7004n - 0.4332. \\ \overline{A}(\alpha C) &= 2424.1232n^2 - 258.7184n - 6.75.\end{aligned}$$

*Proof.* Let

$$\begin{aligned}f(x, y) &= CoM(\alpha C; x, y) = (64n^2 + 6n - 2)xy^2 + (96n^2 + 18n - 2)xy^3 + (96n^2 - 26n + 2)x^2y^3 + (72n^2 - 14n)x^3y^3 \\ \text{then,} \\ D_x f(x, y) &= (64n^2 + 6n - 2)x^1y^2 + 2(96n^2 + 18n - 2)x^1y^3 + 2(96n^2 - 26n + 2)x^2y^3 + 3(72n^2 - 14n)x^3y^3, \\ D_y f(x, y) &= 2(64n^2 + 6n - 2)x^1y^2 + 3(96n^2 + 18n - 2)x^1y^3 + 3(96n^2 - 26n + 2)x^2y^3 + 3(72n^2 - 14n)x^3y^3, \\ (D_x + D_y)f(x, y) &= 3(64n^2 + 6n - 2)x^1y^2 + 4(96n^2 + 18n - 2)x^1y^3 + 5(96n^2 - 26n + 2)x^2y^3 + 6(72n^2 - 14n)x^3y^3, \\ D_y D_x f(x, y) &= 2(64n^2 + 6n - 2)x^1y^2 + 3(96n^2 + 18n - 2)x^1y^3 + 6(96n^2 - 26n + 2)x^2y^3 + 9(72n^2 - 14n)x^3y^3, \\ (D_x^2 + D_y^2)f(x, y) &= 5(64n^2 + 6n - 2)x^1y^2 + 10(96n^2 + 18n - 2)x^1y^3 + 13(96n^2 - 26n + 2)x^2y^3 + 18(72n^2 - 14n)x^3y^3, \\ D_x^k D_y^k f(x, y) &= 2^k(64n^2 + 6n - 2)x^1y^2 + 3^k(96n^2 + 18n - 2)x^1y^3 + 6^k(96n^2 - 26n + 2)x^2y^3 + 3^{2k}(72n^2 - 14n)x^3y^3, \\ D_x D_y (D_x + D_y)f(x, y) &= 6(64n^2 + 6n - 2)x^1y^2 + 12(96n^2 + 18n - 2)x^1y^3 + 30(96n^2 - 26n + 2)x^2y^3 + 54(72n^2 - 14n)x^3y^3, \\ S_x S_y f(x, y) &= \frac{(64n^2 + 6n - 2)}{2}xy^2 + \frac{(96n^2 + 18n - 2)}{3}xy^3 + \frac{(96n^2 - 26n + 2)}{6}x^2y^3 + \frac{(72n^2 - 14n)}{9}x^3y^3, \\ S_x^k S_y^k f(x, y) &= \frac{(64n^2 + 6n - 2)}{2^k}xy^2 + \frac{(96n^2 + 18n - 2)}{3^k}xy^3 + \frac{(96n^2 - 26n + 2)}{6^k}x^2y^3 + \frac{(72n^2 - 14n)}{3^{2k}}x^3y^3, \\ (S_y D_x + S_x D_y)f(x, y) &= \frac{5(64n^2 + 6n - 2)}{2}xy^2 + \frac{10(96n^2 + 18n - 2)}{3}xy^3 + \frac{13(96n^2 - 26n + 2)}{6}x^2y^3 + \frac{18(72n^2 - 14n)}{9}x^3y^3, \\ S_x J f(x, y) &= \frac{(64n^2 + 6n - 2)}{3}x^3 + \frac{(96n^2 + 18n - 2)}{4}x^4 + \frac{(96n^2 - 26n + 2)}{5}x^5 + \frac{(72n^2 - 14n)}{6}x^6, \\ S_x J D_x D_y f(x, y) &= \frac{2(64n^2 + 6n - 2)}{3}x^3 + \frac{3(96n^2 + 18n - 2)}{4}x^4 + \frac{6(96n^2 - 26n + 2)}{5}x^5 + \frac{9(72n^2 - 14n)}{6}x^6, \\ S_x^3 Q_{-2} J D_x^3 D_y^3 f(x, y) &= \frac{(2)^3(64n^2 + 6n - 2)}{(1)^3}x^1 + \frac{(3)^3(96n^2 + 18n - 2)}{(2)^3}x^2 + \frac{(6)^3(96n^2 - 26n + 2)}{(3)^3}x^3 + \frac{(9)^3(72n^2 - 14n)}{(4)^3}x^4.\end{aligned}$$

Using the above results in Table 1, we obtain

$$\overline{M}_1(\alpha C) = (D_x + D_y)f(x, y)|_{x=1=y} = 1488n^2 - 124n - 4.$$

$$\overline{M}_2(\alpha C) = (D_x D_y)f(x, y)|_{x=1=y} = 1640n^2 - 216n + 2.$$

$${}^m\overline{M}_2(\alpha C) = (S_x S_y)f(x, y)|_{x=1=y} = 88n^2 + 3.1111n - 1.3333.$$

$$\overline{ReZG}_3(\alpha C) = D_x D_y (D_x + D_y)f(x, y)|_{x=1=y} = 8304n^2 - 128n + 24.$$

$$\overline{F}(\alpha C) = (D_x^2 + D_y^2)f(x, y)|_{x=1=y} = 3824n^2 - 380n - 4.$$

$$\begin{aligned}\overline{R_k}(\alpha C) &= \left(D_x^k D_y^\beta\right) f(x, y) \Big|_{x=1=y} = 2^k (64n^2 + 6n - 2) + 3^k (96n^2 + 18n - 2) + 6^k (96n^2 - 26n + 2) + 3^{2k} (72n^2 - 14n). \\ \overline{RR_k}(\alpha C) &= \left(S_x^k S_y^k\right) f(x, y) \Big|_{x=1=y} = \frac{(64n^2 + 6n - 2)}{2^k} + \frac{(96n^2 + 18n - 2)}{3^k} + \frac{(96n^2 - 26n + 2)}{6^k} + \frac{(72n^2 - 14n)}{3^{2k}}. \\ \overline{SDD}(\alpha C) &= (D_x S_y + S_x D_y) f(x, y) \Big|_{x=1=y} = 831.990n^2 - 9.332n - 7.3334. \\ \overline{H}(\alpha C) &= 2S_x J f(x, y) \Big|_{x=y=1} = 153.06n^2 - 2.0666n - 1.5332. \\ \overline{I}(\alpha C) &= S_x J D_x D_y f(x, y) \Big|_{x=y=1} = 337.8624n^2 - 34.7004n - 0.4332. \\ \overline{A}(\alpha C) &= S_x^3 Q_{-2} J D_x^3 D_y^3 f(x, y) \Big|_{x=y=1} = 2424.1232n^2 - 258.7184n - 6.75.\end{aligned}$$

## 4.2 | CoM-polynomial of $\beta$ -chitin( $\beta C$ )

**Theorem 4.3.** The CoM-polynomial for  $\beta$ -chitin is given by (Figures 4 and 5)

$$CoM(\beta C; x, y) = (240n^2 + 26n)xy^2 + (384n^2 + 36n - 2)xy^3 + (360n^2 - 28n + 2)x^2y^3 + (288n^2 - 38n)x^3y^3$$

*Proof.* From the Figure 4, it is easy to see that  $|V(\beta C)| = 55n + 2$  and  $|E(\beta C)| = 60n$ . Also, the edge set of  $\beta C$  may be categorized into four partitions based on the degree of vertices are as follows

$$E_{12} = \{ab \in E(\beta C) | d(a) = 1, d(b) = 2\},$$

$$E_{13} = \{ab \in E(\beta C) | d(a) = 1, d(b) = 3\},$$

$$E_{23} = \{ab \in E(\beta C) | d(a) = 2, d(b) = 3\},$$

$$E_{33} = \{ab \in E(\beta C) | d(a) = 3, d(b) = 3\},$$

such that

$$m_{12} = 4n, m_{13} = 12n + 2, m_{23} = 28n - 2, \text{ and } m_{33} = 16n.$$

Similarly,  $V(\beta C)$  can be divided into three classes depending on the degree of vertex are given by

$$n_1 = |V_1| = 16n + 2, n_2 = |V_2| = 15n, \text{ and } n_3 = |V_3| = 24n.$$

Using Lemma 1, we have

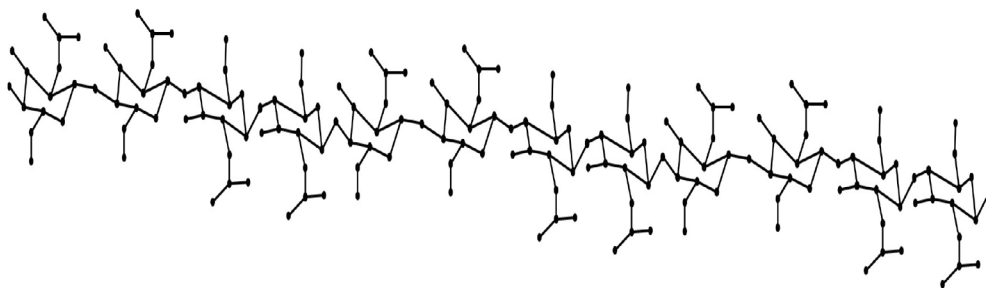


**FIGURE 4** Molecular graph of  $\beta$ -chitin for  $n = 3$

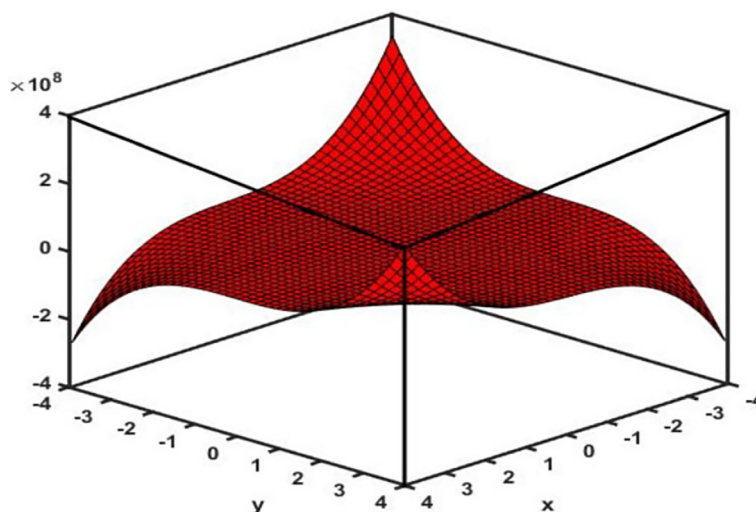


FIGURE 5 3D plot of CoM-polynomial of  $\beta$ -chitin

$$\begin{aligned}\bar{m}_{12} &= n_1 n_2 - m_{12} = (16n + 2)(15n) - 4n = 240n^2 + 26n. \\ \bar{m}_{13} &= n_1 n_3 - m_{13} = (16n + 2)(24n) - (12n + 2) = 384n^2 + 36n - 2. \\ \bar{m}_{23} &= n_2 n_3 - m_{23} = (15n)(24n) - (28n - 2) = 360n^2 - 28n + 2. \\ \bar{m}_{33} &= \frac{n_3(n_3 - 1)}{2} - m_{33} = \frac{(24n)(24n - 1)}{2} - 16n = 288n^2 - 38n.\end{aligned}$$

By definition of CoM-polynomial

$$\begin{aligned}\text{CoM}(G; x, y) &= \bar{M}(G; x, y) = \sum_{i \leq j} \bar{m}_{ij}(G) x^i y^j \\ \text{CoM}(\beta C; x, y) &= \sum_{1 \leq 2} \bar{m}_{12} x y^2 + \sum_{1 \leq 3} \bar{m}_{13} x y^3 + \sum_{2 \leq 3} \bar{m}_{23} x^2 y^3 + \sum_{3 \leq 3} \bar{m}_{33} x^3 y^3 \\ &= (240n^2 + 26n) x y^2 + (384n^2 + 36n - 2) x y^3 + (360n^2 - 28n + 2) x^2 y^3 + (288n^2 - 38n) x^3 y^3.\end{aligned}$$

Adopting Theorem 2 and Table 1, some degree based topological coindices are derived for the  $\beta$ -chitin in the following proposition

**Proposition 4.4.**

$$\begin{aligned}\bar{M}_1(\beta C) &= 5784n^2 - 146n + 2. \\ \bar{M}_2(\beta C) &= 6384n^2 - 350n + 6. \\ {}^m\bar{M}_2(\beta C) &= 340n^2 + 16.1111n - 4.5555. \\ \text{ReZG}_3(\beta C) &= 32400n^2 - 2304n + 36. \\ \bar{F}(\beta C) &= 14904n^2 - 558n + 6. \\ \bar{R}_k(\beta C) &= 2^k(240n^2 + 26n) + 3^k(384n^2 + 36n - 2) + 6^k(360n^2 - 28n + 2) + 3^{2k}(288n^2 - 38n). \\ \overline{RR}_k(\beta C) &= \frac{(240n^2 + 26n)}{2^k} + \frac{(384n^2 + 36n - 2)}{3^k} + \frac{(360n^2 - 28n + 2)}{6^k} + \frac{(288n^2 - 38n)}{3^{2k}}. \\ \overline{SDD}(\beta C) &= 3235.9632n^2 + 48.344n - 2.3334. \\ \bar{H}(\beta C) &= 591.9744n^2 + 11.4662n - 0.2. \\ \bar{I}(\beta C) &= 1311.984n^2 - 46.2684n + 0.9. \\ \bar{A}(\beta C) &= 9376.4928n^2 - 327.3428n + 9.25.\end{aligned}$$

Proof. Let

$$\begin{aligned}
 f(x, y) &= \text{CoM}(\beta C; x, y) = (240n^2 + 26n)xy^2 + (384n^2 + 36n - 2)xy^3 + (360n^2 - 28n + 2)x^2y^3 + (288n^2 - 38n)x^3y^3 \\
 \text{then,} \\
 D_x f(x, y) &= (240n^2 + 26n)x^1y^2 + 2(384n^2 + 36n - 2)x^1y^3 + 2(360n^2 - 28n + 2)x^2y^3 + 3(288n^2 - 38n)x^3y^3, \\
 D_y f(x, y) &= 2(240n^2 + 26n)x^1y^2 + 3(384n^2 + 36n - 2)x^1y^3 + 3(360n^2 - 28n + 2)x^2y^3 + 3(288n^2 - 38n)x^3y^3, \\
 (D_x + D_y)f(x, y) &= 3(240n^2 + 26n)x^1y^2 + 4(384n^2 + 36n - 2)x^1y^3 + 5(360n^2 - 28n + 2)x^2y^3 + 6(288n^2 - 38n)x^3y^3, \\
 D_y D_x f(x, y) &= 2(240n^2 + 26n)x^1y^2 + 3(384n^2 + 36n - 2)x^1y^3 + 6(360n^2 - 28n + 2)x^2y^3 + 9(288n^2 - 38n)x^3y^3, \\
 (D_x^2 + D_y^2)f(x, y) &= 5(240n^2 + 26n)x^1y^2 + 10(384n^2 + 36n - 2)x^1y^3 + 13(360n^2 - 28n + 2)x^2y^3 + 18(288n^2 - 38n)x^3y^3, \\
 D_x^k D_y^k f(x, y) &= 2^k(240n^2 + 26n)x^1y^2 + 3^k(384n^2 + 36n - 2)x^1y^3 + 6^k(360n^2 - 28n + 2)x^2y^3 + 3^{2k}(288n^2 - 38n)x^3y^3, \\
 D_x D_y (D_x + D_y)f(x, y) &= 6(240n^2 + 26n)x^1y^2 + 12(384n^2 + 36n - 2)x^1y^3 + 30(360n^2 - 28n + 2)x^2y^3 + 54(288n^2 - 38n)x^3y^3, \\
 S_x S_y f(x, y) &= \frac{(240n^2 + 26n)}{2}xy^2 + \frac{(384n^2 + 36n - 2)}{3}xy^3 + \frac{(360n^2 - 28n + 2)}{6}x^2y^3 + \frac{(288n^2 - 38n)}{9}x^3y^3, \\
 S_x^k S_y^k f(x, y) &= \frac{(240n^2 + 26n)}{2^k}xy^2 + \frac{(384n^2 + 36n - 2)}{3^k}xy^3 + \frac{(360n^2 - 28n + 2)}{6^k}x^2y^3 + \frac{(288n^2 - 38n)}{3^{2k}}x^3y^3, \\
 (S_y D_x + S_x D_y)f(x, y) &= \frac{5(240n^2 + 26n)}{2}xy^2 + \frac{10(384n^2 + 36n - 2)}{3}xy^3 + \frac{13(360n^2 - 28n + 2)}{6}x^2y^3 + \frac{18(288n^2 - 38n)}{9}x^3y^3, \\
 S_x J f(x, y) &= \frac{(240n^2 + 26n)}{3}x^3 + \frac{(384n^2 + 36n - 2)}{4}x^4 + \frac{(360n^2 - 28n + 2)}{5}x^5 + \frac{(288n^2 - 38n)}{6}x^6, \\
 S_x J D_x D_y f(x, y) &= \frac{2(240n^2 + 26n)}{3}x^3 + \frac{3(384n^2 + 36n - 2)}{4}x^4 + \frac{6(360n^2 - 28n + 2)}{5}x^5 + \frac{9(288n^2 - 38n)}{6}x^6, \\
 S_x^3 Q_{-2} D_x^3 D_y^3 f(x, y) &= \frac{(2)^3(240n^2 + 26n)}{(1)^3}x^1 + \frac{(3)^3(384n^2 + 36n - 2)}{(2)^3}x^2 + \frac{(6)^3(360n^2 - 28n + 2)}{(3)^3}x^3 + \frac{(9)^3(288n^2 - 38n)}{(4)^3}x^4,
 \end{aligned}$$

Using the above results in Table 1, we obtain

$$\begin{aligned}
 \overline{M_1}(\beta C) &= (D_x + D_y)f(x, y)|_{x=1=y} = 5784n^2 - 146n + 2. \\
 \overline{M_2}(\beta C) &= (D_x D_y)f(x, y)|_{x=1=y} = 6384n^2 - 350n + 6. \\
 {}^m\overline{M_2}(\beta C) &= (S_x S_y)f(x, y)|_{x=1=y} = 340n^2 + 16.1111n - 4.5555. \\
 \overline{\text{ReZG}_3}(\beta C) &= D_x D_y (D_x + D_y)f(x, y)|_{x=1=y} = 32400n^2 - 2304n + 36. \\
 \overline{F}(\beta C) &= (D_x^2 + D_y^2)f(x, y)|_{x=1=y} = 14904n^2 - 558n + 6. \\
 \overline{R_k}(\beta C) &= (D_x^k D_y^k)f(x, y)|_{x=1=y} = 2^k(240n^2 + 26n) + 3^k(384n^2 + 36n - 2) + 6^k(360n^2 - 28n + 2) + 3^{2k}(288n^2 - 38n). \\
 \overline{RR_k}(\beta C) &= (S_x^k S_y^k)f(x, y)|_{x=1=y} = \frac{(240n^2 + 26n)}{2^k} + \frac{(384n^2 + 36n - 2)}{3^k} + \frac{(360n^2 - 28n + 2)}{6^k} + \frac{(288n^2 - 38n)}{3^{2k}}. \\
 \overline{SDD}(\beta C) &= (D_x S_y + S_x D_y)f(x, y)|_{x=1=y} = 3235.9632n^2 + 48.344n - 2.3334. \\
 \overline{H}(\beta C) &= 2S_x J f(x, y)|_{x=y=1} = 591.9744n^2 + 11.4662n - 0.2. \\
 \overline{I}(\beta C) &= S_x J D_x D_y f(x, y)|_{x=y=1} = 1311.984n^2 - 46.2684n + 0.9. \\
 \overline{A}(\beta C) &= S_x^3 Q_{-2} J D_x^3 D_y^3 f(x, y)|_{x=y=1} = 9376.4928n^2 - 327.3428n + 9.25.
 \end{aligned}$$

### 4.3 | CoM-polynomial of $\gamma$ -chitin( $\beta C$ )

**Theorem 4.5.** The CoM-polynomial for  $\gamma$ -chitin is given by (Figures 6 and 7)

$$\text{CoM}(\gamma C; x, y) = (144n^2 + 9n - 2)xy^2 + (216n^2 + 27n - 2)xy^3 + (216n^2 - 39n + 2)x^2y^3 + (162n^2 - 21n)x^3y^3$$



*Proof.* From the Figure 6, it is easy to see that  $|V(\gamma C)| = 28n + 1$  and  $|E(\gamma C)| = 30n$ . Also, the edge set of  $\gamma C$  may be categorized into four partitions based on the degree of vertices are as follows

$$E_{12} = \{ab \in E(\gamma C), d(a) = 1 | d(b) = 2\},$$

$$E_{13} = \{ab \in E(\gamma C), d(a) = 1 | d(b) = 3\},$$

$$E_{23} = \{ab \in E(\gamma C), d(a) = 2 | d(b) = 3\},$$

$$E_{33} = \{ab \in E(\gamma C), d(a) = 3 | d(b) = 3\},$$

such that

$$m_{12} = 3n, m_{13} = 9n + 2, m_{23} = 21n - 2, \text{ and } m_{33} = 12n.$$

Similarly,  $V(\gamma C)$  can be divided into three classes depending on the degree of vertex are given by

$$n_1 = |V_1| = 12n + 2, n_2 = |V_2| = 12n - 1, \text{ and } n_3 = |V_3| = 18n.$$

Using Lemma 1, we have

$$\bar{m}_{12} = n_1 n_2 - m_{12} = (12n + 2)(12n - 1) - 3n = 144n^2 + 9n - 2.$$

$$\bar{m}_{13} = n_1 n_3 - m_{13} = (12n + 2)(18n) - (9n + 2) = 216n^2 + 27n - 2.$$

$$\bar{m}_{23} = n_2 n_3 - m_{23} = (12n - 1)(18n) - (21n - 2) = 216n^2 - 39n + 2.$$

$$\bar{m}_{33} = \frac{n_3(n_3 - 1)}{2} - m_{33} = \frac{(18n)(18n - 1)}{2} - 12n = 162n^2 - 21n.$$

By definition of CoM-polynomial

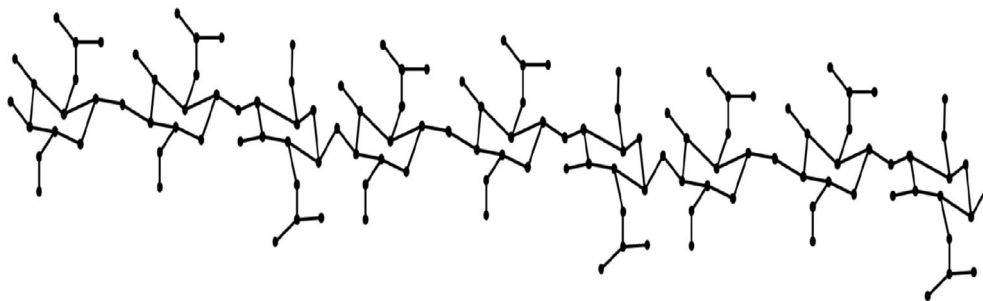


**FIGURE 6** Molecular graph of  $\gamma$ -chitin for  $n = 3$

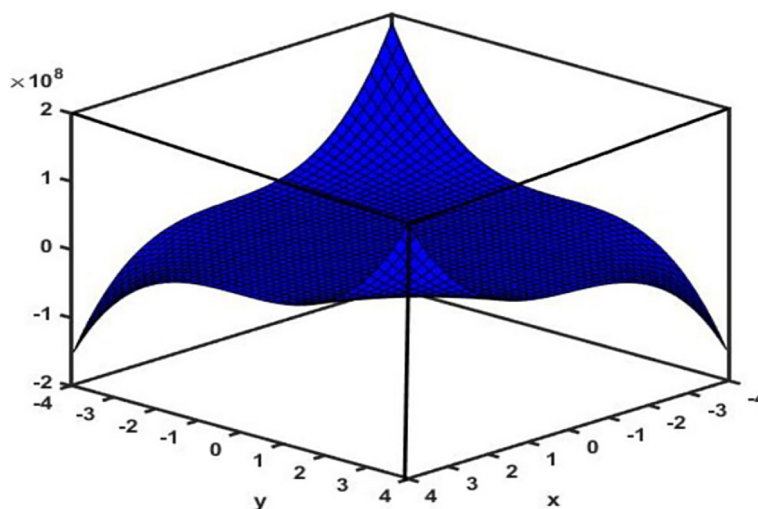


**FIGURE 7** 3D plot of CoM-polynomial of  $\gamma$ -chitin

$$\begin{aligned}\text{CoM}(G; x, y) &= \overline{M}(G; x, y) = \sum_{i \leq j} \overline{m}_{ij}(G) x^i y^j \\ \text{CoM}(\gamma C; x, y) &= \sum_{1 \leq 2} \overline{m}_{12} x y^2 + \sum_{1 \leq 3} \overline{m}_{13} x y^3 + \sum_{2 \leq 3} \overline{m}_{23} x^2 y^3 + \sum_{3 \leq 3} \overline{m}_{33} x^3 y^3 \\ &= (144n^2 + 9n - 2)xy^2 + (216n^2 + 27n - 2)xy^3 + (216n^2 - 39n + 2)x^2y^3 + (162n^2 - 21n)x^3y^3.\end{aligned}$$

Adopting Theorem 3 and Table 1, some degree based topological coindices of the  $\gamma$ -chitin are derived in the following proposition.

**Proposition 4.6.**

$$\begin{aligned}\overline{M}_1(\gamma C) &= 3348n^2 - 186n - 4. \\ \overline{M}_2(\gamma C) &= 3690n^2 - 324n + 2. \\ {}^m\overline{M}_2(\gamma C) &= 198n^2 + 4.6666n - 1.3333. \\ \text{ReZG}_3(\gamma C) &= 18684n^2 - 1926n + 24. \\ \overline{F}(\gamma C) &= 8604n^2 - 570n - 4. \\ \overline{R}_k(\gamma C) &= 2^k(144n^2 + 9n - 2) + 3^k(216n^2 + 27n - 2) + 6^k(216n^2 - 39n + 2) + 3^{2k}(162n^2 - 21n). \\ \overline{RR}_k(\gamma C) &= \frac{(144n^2 + 9n - 2)}{2^k} + \frac{(216n^2 + 27n - 2)}{3^k} + \frac{(216n^2 - 39n + 2)}{6^k} + \frac{(162n^2 - 21n)}{3^{2k}}. \\ \overline{SDD}(\gamma C) &= 1871.9784n^2 - 13.9983n - 7.3334. \\ \overline{H}(\gamma C) &= 344.385n^2 - 3.0999n - 1.5332. \\ \overline{I}(\gamma C) &= 760.7904n^2 - 52.0506n - 0.4332. \\ \overline{A}(\gamma C) &= 5454.2772n^2 - 388.0776n - 6.75.\end{aligned}$$

*Proof.* Let

$$\begin{aligned}f(x, y) &= \text{CoM}(\gamma C; x, y) = (64n^2 + 6n - 2)xy^2 + (96n^2 + 18n - 2)xy^3 + (96n^2 - 26n + 2)x^2y^3 + (72n^2 - 14n)x^3y^3 \\ \text{then,} \\ D_x f(x, y) &= (144n^2 + 9n - 2)x^1y^2 + 2(216n^2 + 27n - 2)x^1y^3 + 2(216n^2 - 39n + 2)x^2y^3 + 3(162n^2 - 21n)x^3y^3, \\ D_y f(x, y) &= 2(144n^2 + 9n - 2)x^1y^2 + 3(216n^2 + 27n - 2)x^1y^3 + 3(216n^2 - 39n + 2)x^2y^3 + 3(162n^2 - 21n)x^3y^3, \\ (D_x + D_y)f(x, y) &= 3(144n^2 + 9n - 2)x^1y^2 + 4(216n^2 + 27n - 2)x^1y^3 + 5(216n^2 - 39n + 2)x^2y^3 + 6(162n^2 - 21n)x^3y^3, \\ D_y D_x f(x, y) &= 2(144n^2 + 9n - 2)x^1y^2 + 3(216n^2 + 27n - 2)x^1y^3 + 6(216n^2 - 39n + 2)x^2y^3 + 9(162n^2 - 21n)x^3y^3, \\ (D_x^2 + D_y^2)f(x, y) &= 5(144n^2 + 9n - 2)x^1y^2 + 10(216n^2 + 27n - 2)x^1y^3 + 13(216n^2 - 39n + 2)x^2y^3 + 18(162n^2 - 21n)x^3y^3, \\ D_x^k D_y^k f(x, y) &= 2^k(144n^2 + 9n - 2)x^1y^2 + 3^k(216n^2 + 27n - 2)x^1y^3 + 6^k(216n^2 - 39n + 2)x^2y^3 + 3^{2k}(162n^2 - 21n)x^3y^3, \\ D_x D_y (D_x + D_y)f(x, y) &= 6(144n^2 + 9n - 2)x^1y^2 + 12(216n^2 + 27n - 2)x^1y^3 + 30(216n^2 - 39n + 2)x^2y^3 + 54(162n^2 - 21n)x^3y^3, \\ S_x S_y f(x, y) &= \frac{(144n^2 + 9n - 2)}{2}xy^2 + \frac{(216n^2 + 27n - 2)}{3}xy^3 + \frac{(216n^2 - 39n + 2)}{6}x^2y^3 + \frac{(162n^2 - 21n)}{9}x^3y^3, \\ S_x^k S_y^k f(x, y) &= \frac{(144n^2 + 9n - 2)}{2^k}xy^2 + \frac{(216n^2 + 27n - 2)}{3^k}xy^3 + \frac{(216n^2 - 39n + 2)}{6^k}x^2y^3 + \frac{(162n^2 - 21n)}{3^{2k}}x^3y^3, \\ (S_y D_x + S_x D_y)f(x, y) &= \frac{5(144n^2 + 9n - 2)}{2}xy^2 + \frac{10(216n^2 + 27n - 2)}{3}xy^3 + \frac{13(216n^2 - 39n + 2)}{6}x^2y^3 + \frac{18(162n^2 - 21n)}{9}x^3y^3, \\ S_x J f(x, y) &= \frac{(144n^2 + 9n - 2)}{3}x^3 + \frac{(216n^2 + 27n - 2)}{4}x^4 + \frac{(216n^2 - 39n + 2)}{5}x^5 + \frac{(162n^2 - 21n)}{6}x^6, \\ S_x J D_x D_y f(x, y) &= \frac{2(144n^2 + 9n - 2)}{3}x^3 + \frac{3(216n^2 + 27n - 2)}{4}x^4 + \frac{6(216n^2 - 39n + 2)}{5}x^5 + \frac{9(162n^2 - 21n)}{6}x^6, \\ S_x^3 Q_{-2} J D_x^3 D_y^3 f(x, y) &= \frac{(2)^3(144n^2 + 9n - 2)}{(1)^3}x^1 + \frac{(3)^3(216n^2 + 27n - 2)}{(2)^3}x^2 + \frac{(6)^3(216n^2 - 39n + 2)}{(3)^3}x^3 + \frac{(9)^3(162n^2 - 21n)}{(4)^3}x^4,\end{aligned}$$

Using the above results in Table 1, we obtain

$$\overline{M}_1(\gamma C) = (D_x + D_y)f(x, y)|_{x=1=y} = 3348n^2 - 186n - 4.$$

TABLE 2 Numerical comparison of degree based coincides of  $\alpha$ -chitin for  $n = 1-10$ 

$n$	$\overline{M}_1$	$\overline{M}_2$	$\overline{mM}_2$	$\overline{ReZG}_3$	$\overline{F}$	$\overline{R}$	$\overline{RR}$	$\overline{SDD}$	$\overline{H}$	$\overline{I}$	$\overline{A}$
1	1472	1426	89.7778	7044	3440	161.462	572.514	815.325	149.460	302.729	2158.7
2	5924	6130	356.889	30 672	14 532	652.397	2432.3	3302	606.574	1281.6	9172.3
3	13 352	14 114	800	70 908	33 272	1471.1	5579.9	7452.6	1369.8	2936.2	21 034
4	23 756	25 378	1419.1	127 752	59 660	2617.4	10 015	13 267	2439.2	5266.6	37 744
5	37 136	39 922	2214.2	201 204	93 696	4091.5	15 739	20 746	3814.6	8272.6	59 303
6	53 492	57 746	3185.3	291 264	135 380	5893.3	22 750	29 888	5496.2	11 954	85 709
7	72 824	78 850	4332.4	397 932	184 712	8022.9	31 049	40 695	7483.9	16 312	116 960
8	95 132	103 234	5655.6	521 208	241 692	10 480	40 636	53 165	9777.8	21 345	153 070
9	120 416	130 898	7154.7	661 092	306 320	13 265	51 511	67 300	12 378	27 054	194 020
10	148 676	161 842	8829.8	817 584	378 596	16 378	63 674	83 098	15 284	33 439	239 820

**TABLE 3** Numerical comparison of degree based coincides of  $\beta$ -chitin for  $n = 1-10$ 

$n$	$\overline{M}_1$	$\overline{M}_2$	$\overline{mM}_2$	$\overline{ReZG}_3$	$\overline{F}$	$\overline{R}$	$\overline{RR}$	$\overline{SDD}$	$\overline{H}$	$\overline{I}$	$\overline{A}$
1	5640	6040	351.556	30 132	14 352	649.064	2402.3	3282	603.241	1266.6	9058.4
2	22 846	24 842	1387.7	125 028	58 506	2567.1	9823.8	13 038	2390.6	5156.3	36 861
3	51 620	56 412	3103.8	284 724	132 468	5753.8	22 266	29 266	5362	11 670	83 416
4	91 962	100 750	5499.9	509 220	236 238	10 209	39 729	51 966	9517.3	20 808	148 720
5	143 872	157 856	8576	798 516	369 816	15 933	62 212	81 138	14 856	32 569	232 780
6	207 350	227 730	12 332	1 152 612	533 202	22 926	89 716	116 780	21 380	46 955	335 600
7	282 396	310 372	16 768	1 571 508	726 396	31 187	122 240	158 900	29 087	63 964	457 170
8	369 010	405 782	21 884	2 055 204	949 398	40 717	159 790	207 490	37 978	83 598	597 490
9	467 192	513 960	27 680	2 603 700	1 202 208	51 516	202 350	262 550	48 053	105 860	756 560
10	576 942	634 906	34 157	3 216 996	1 484 826	63 583	249 940	324 080	59 312	130 740	934 390

TABLE 4 Numerical comparison of degree based coincides of  $\gamma$ -chitin for  $n = 1-10$ 

$n$	$\overline{M}_1$	$\overline{M}_2$	$\overline{mM}_2$	$\overline{ReZG}_3$	$\overline{F}$	$\overline{R}$	$\overline{RR}$	$\overline{SDD}$	$\overline{H}$	$\overline{I}$	$\overline{A}$
1	3158	3368	201.333	16 782	8030	365.964	1341.4	1850.6	339.752	707.707	5059.4
2	13 016	14 114	799.9999	70 908	33 272	1471.1	5579.9	7452.6	1369.8	2936.2	21 034
3	29 570	32 240	1794.7	162 402	75 722	3313.5	12 716	16 798	3088.6	6685.1	47 918
4	52 820	57 746	3185.3	291 264	135 380	5893.3	22 750	29 888	5496.2	11 954	85 709
5	82 766	90 632	4972	457 494	212 246	9210.5	35 682	46 722	8592.6	18 744	134 410
6	119 408	130 898	7154.7	661 092	306 320	13 265	51 511	67 300	12 378	27 054	194 020
7	162 746	178 544	9733.3	902 058	417 602	18 057	70 238	91 622	16 852	36 885	264 540
8	212 780	233 570	12 708	1 180 392	546 092	23 586	91 863	119 690	22 014	48 235	345 960
9	269 510	295 976	16 079	1 496 094	691 790	29 853	116 390	151 500	27 866	61 107	438 300
10	332 936	365 762	19 845	1 849 164	854 696	36 857	143 810	187 050	34 406	75 498	541 540

$$\overline{M}_2(\gamma C) = (D_x D_y) f(x, y) \Big|_{x=1=y} = 3690n^2 - 324n + 2.$$

$$\overline{mM}_2(\gamma C) = (S_x S_y) f(x, y) \Big|_{x=1=y} = 198n^2 + 4.6666n - 1.3333.$$

$$\overline{ReZG}_3(\gamma C) = D_x D_y (D_x + D_y) f(x, y) \Big|_{x=1=y} = 18684n^2 - 1926n + 24.$$

$$\overline{F}(\gamma C) = (D_x^2 + D_y^2) f(x, y) \Big|_{x=1=y} = 8604n^2 - 570n - 4.$$

$$\overline{R}_k(\gamma C) = (D_x^k D_y^k) f(x, y) \Big|_{x=1=y} = 2^k (144n^2 + 9n - 2) + 3^k (216n^2 + 27n - 2) + 6^k (216n^2 - 39n + 2) + 3^{2k} (162n^2 - 21n).$$

$$\overline{RR}_k(\gamma C) = (S_x^k S_y^k) f(x, y) \Big|_{x=1=y} = \frac{(144n^2 + 9n - 2)}{2^k} + \frac{(216n^2 + 27n - 2)}{3^k} + \frac{(216n^2 - 39n + 2)}{6^k} + \frac{(162n^2 - 21n)}{3^{2k}}.$$

$$\overline{SDD}(\gamma C) = (D_x S_y + S_x D_y) f(x, y) \Big|_{x=1=y} = 1871.9784n^2 - 13.9983n - 7.3334.$$

$$\overline{H}(\gamma C) = 2S_x J f(x, y) \Big|_{x=y=1} = 344.385n^2 - 3.0999n - 1.5332.$$

$$\overline{I}(\gamma C) = S_x J D_x D_y f(x, y) \Big|_{x=y=1} = 760.7904n^2 - 52.0506n - 0.4332.$$

$$\overline{A}(\gamma C) = S_x^3 Q_{-2} J D_x^3 D_y^3 f(x, y) \Big|_{x=y=1} = 5454.2772n^2 - 388.0776n - 6.75. \quad \square$$

## 5 | NUMERICAL AND GRAPHICAL COMPARISON OF COINDICES

A comparison of 11 topological coindices are computed for the derivatives of chitosan tabulated in the Tables 2–4 for the values of  $n$  varying through 1–10. It is evident that all the coindices increase as  $n$  approaches greater value. The coindices for all the three derivatives of chitosan are as follows.

## 6 | CONCLUSION

The amino polysaccharides considered in this study are the chitosan and its derivatives. They are significantly used in most of the fields as they are non-toxic, biodegradable and biocompatible. This work concentrates on three chemical compounds, chitosan and its derivatives for which the non-adjacency vertex partition is noted and coindices are computed. A novel type of polynomials especially for the non-adjacency of vertices, such as CoM polynomials are established for the said three polysaccharides. A comparative study of the coindices, pertaining to degree based topological coindices are discussed. A 3D plot of CoM-polynomial of chitosan derivatives are made as shown in the Figures 3, 5, and 7. As the considered compounds have vast applications, this study would be useful for the chemists/pharmacists/researchers who would make advanced study on the same compounds. This data may be used by them for their further studies.

### AUTHOR CONTRIBUTIONS

**Shanmukha M. C.:** Conceptualization; investigation; methodology; writing – original draft; writing – review and editing. **Usha A.:** Formal analysis; investigation; visualization; writing – review and editing.

### CONFLICT OF INTEREST

There are no conflicts of interest among the authors.

### DATA AVAILABILITY STATEMENT

Data sharing is not applicable to this article as no new data were created or analyzed in this study.

### ORCID

M. C. Shanmukha  <https://orcid.org/0000-0002-9560-1209>

### REFERENCES

- [1] A. Anitha, S. Sowmya, P. S. Kumar, S. Deepthi, K. P. Chennazhi, H. Ehrlich, M. Tsurkan, R. Jayakumar, *Prog. Polym. Sci.* **2014**, 39(9), 1644.
- [2] M. M. Abo Elsoud, E. M. El Kady, *Bull. Natl. Res. Cent.* **2019**, 43(1), 1.
- [3] A. Francesko, M. D. González, G. R. Lozano, T. Tzanov, *Adv. Text. Biotechnol.* **2010**, 288.
- [4] I. Gutman, O. E. Polansky, *Mathematical Concepts in Organic Chemistry*, Springer Science & Business Media, Berlin **2012**.
- [5] N. Trinajstić, *Chemical Graph Theory*, CRC Press, Boca Raton, FL **1992**.

- [6] R. Todeschini, V. Consonni, *Handbook of Molecular Descriptors*, John Wiley & Sons, New York **2008**.
- [7] B. Furtula, A. Graovac, D. Vukićević, *J. Math. Chem.* **2010**, 48(2), 370.
- [8] B. Furtula, I. Gutman, *J. Math. Chem.* **2015**, 53(4), 1184.
- [9] C. K. Gupta, V. Lokesh, S. B. Shwetha, P. S. Ranjini, *Southeast Asian Bull. Math.* **2016**, 40(1), 280.
- [10] D. Vukićević, M. Gašperov, *Croat. Chem. Acta* **2010**, 83(3), 243.
- [11] M. Ghorbani, M. A. Hosseinzadeh, *Optoelectron. Adv. Mater. Rapid Commun.* **2010**, 4(September), 1419.
- [12] M. Randić, *New J. Chem.* **1996**, 20(10), 1001.
- [13] S. Hayat, M. Imran, J. B. Liu, *Int. J. Quantum Chem.* **2019**, 119(23), e26016.
- [14] M. C. Shanmukha, N. S. Basavarajappa, K. C. Shilpa, A. Usha, *Heliyon* **2020**, 6(6), e04235.
- [15] M. Azeem, M. Imran, M. F. Nadeem, *J. King Saud Univ. Sci.* **2022**, 34(2), 101779.
- [16] I. Gutman, B. Furtula, Z. K. Vukicevic, G. Popivoda, *MATCH Commun. Math. Comput. Chem* **2015**, 74(1), 5.
- [17] M. Berhe, C. Wang, *Appl. Math. Nonlin. Sci.* **2019**, 4(2), 455.
- [18] H. Hua, A. R. Ashrafi, L. Zhang, *Filomat* **2012**, 26(6), 1215.
- [19] B. Bommanahal, I. Gutman, C. S. Gali, *Kragujev. J. Sci.* **2015**, 37, 113.
- [20] N. De, S. Nayeem, M. Abu, A. Pal, *Springerplus* **2016**, 5(1), 1.
- [21] S. A. K. Kirmani, P. Ali, F. Azam, *Int. J. Quantum Chem.* **2021**, 121(9), e26594.
- [22] E. Deutsch, S. Klavžar, M-polynomial and degree-based topological indices. arXiv preprint arXiv:1407.1592 **2014**.
- [23] B. Basavanagoud, A. P. Barangi, A. P. Barangi, *Open J. Discret. Appl. Math.* **2019**, 2(2), 59.
- [24] S. Mondal, N. De, M. K. Siddiqui, A. Pal, *Biointerface Res. Appl. Chem.* **2021**, 11(3), 9915.
- [25] Y. C. Kwun, M. Munir, W. Nazeer, S. Rafique, S. Min Kang, *Sci. Rep.* **2017**, 7(1), 1.
- [26] A. Q. Baig, M. Imran, A. L. H., *Optoelectron. Adv. Mater. Rapid Commun.* **2015**, 9, 248.
- [27] H. Ali, M. K. Shafiq, M. R. Farahani, M. Cancan, M. S. Aldemir, *Eurasian Chem. Commun.* **2020**, 2(11), 1093.
- [28] M. F. Nadeem, M. Imran, H. M. A. Siddiqui, M. Azeem, A. Khalil, Y. Ali, *Arabian J. Chem.* **2021**, 14(6), 103157.
- [29] G. Abbas, M. Ibrahim, A. Ahmad, M. Azeem, K. Elahi, *Math. Probl. Eng.* **2021**, 2021, 2021.
- [30] G. Abbas, M. Ibrahim, A. Ahmad, M. Azeem, K. Elahi, *Polycyclic Aromat. Compd.* **2021**, 2021, 1.
- [31] M. C. Shanmukha, A. Usha, K. C. Shilpa, N. S. Basavarajappa, *Eur. Phys. J. Plus* **2021**, 136(10), 1.
- [32] S. A. K. Kirmani, P. Ali, *Arabian J. Chem.* **2022**, 15(7), 103911.
- [33] K. B. Rufato, J. P. Galdino, K. S. Ody, A. G. Pereira, E. Corradini, A. F. Martins, A. T. Paulino, A. R. Fajardo, F. A. Aouada, F. A. La Porta, A. F. Rubira, E. C. Muniz, Hydrogels based on chitosan and chitosan derivatives for biomedical applications. in *Hydrogels-Smart Materials for Biomedical Applications*, IntechOpen, London **2018**.

**How to cite this article:** M. C. Shanmukha, A. Usha, *Int. J. Quantum Chem.* **2022**, e26976. <https://doi.org/10.1002/qua.26976>